UNIVERSITÄT
DUISBURG
ESSEN

Open-Minded

26th Numerical Towing Tank Symposium

NuTTS'24

23rd – 25th October 2024

Mülheim/Ruhr, Germany

Proceedings

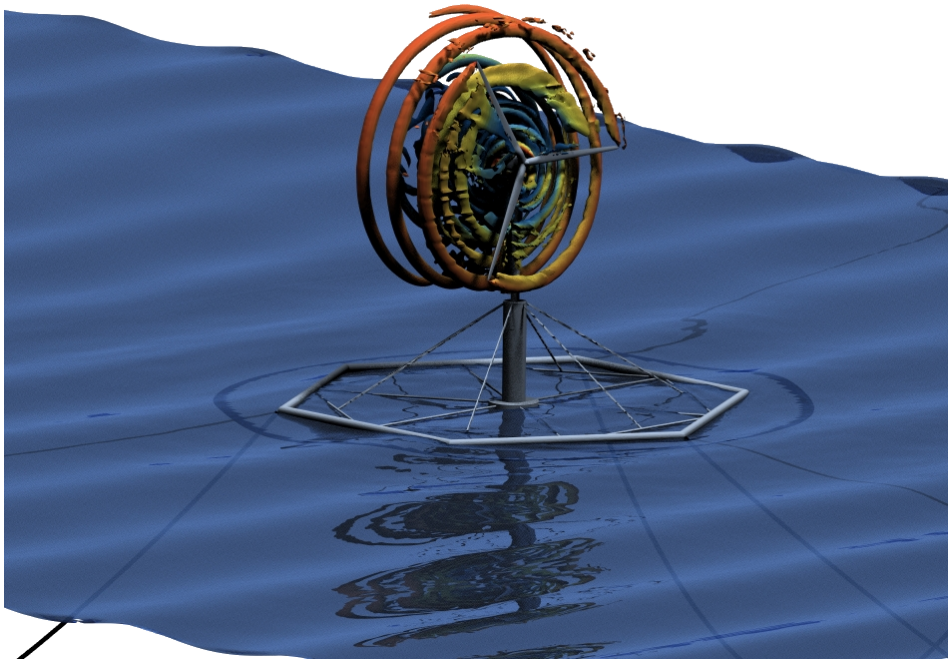

Bettar Ould el Moctar, Udo Lantermann (Eds.)

List of Extended Abstracts

P01	Philipp Mucha	Computational Fluid Dynamics Analysis of Inland Waterway Ship Maneuvering in Extremely Shallow Water
P02	Georg Göbel, Lahbib Zentari, Cristian Brutto, Jacek A. Jankowski	Full Scale Prediction of Ship Induced Waves in Restricted Waters with Numerical Tools – a Comparative Study
P03	Muhammed Talha Özdenoglu, Yao Zhang, Stephen Turnock, Tahsin Tezdogan	Development of a CFD-based Collision Avoidance Model for Maritime Autonomous Surface Ships in Restricted Waters
P04	Guillermo Chillcce, Lahbib Zentari, Bettar Ould el Moctar	Ship hydrodynamics in steady circular motion in shallow waters - Experience from the SHINING workshop
P05	Genís Masjoan Vallés, Juha Tanttari, Ville Vuorinen	Development and validation of underwater radiated noise analysis method using computational fluid dynamics simulations
P06	Arne Heuvelman, Sasha Zverkhovskyi, Scott Terry	CFD Analysis of Air Lubrication Effects on Ship Propulsive Performance
P07	Roya Shademani, Tommi Mikkola, Teemu Manderbacka, Sasan Tavakoli, Heikki Remes	CFD Modeling Approaches for Simulating Air Lubricating System in Ships: Preliminary Findings
P08	Ian Hubbard, Themistoklis Melissaris	Detecting Numerical Instabilities in Propeller Cavitation Erosion Modelling Using Unsupervised Learning
P09	Carlos Eduardo Simões de Almeida, Claudio Mueller Prado Sampaio, Mariana Lopes Pinto, Philip Pritzelwitz	Hydrodynamic performance enhancement of Newcastlemax bulk carriers via parametric modelling and Computational Fluid Dynamics (CFD)
P10	Aaron Harrison Godfrey, Miles Wheeler	Multiphase Computational Fluid Dynamics Based Optimization of Hydrofoil Envelope Performance
P11	Ines Ivković, Matija Vasilev, Milan Kalajdžić	A CFD-Based Analysis of Bow Modification Influence on Ship Resistance and Energy Efficiency
P12	Yanxin Feng, Bettar Ould el Moctar	Hull Optimizaion of a Catamaran in both Deep and Shallow Water
P13	Marco Lugaresi, Diego Villa, Stefano Gaggero	Gap effect of a Rim Driven thruster in convergent and divergent duct configuration
P14	Kenshiro Takahashi	Numerical study on tip-leakage flow for a stationary hydrofoil
P15	Daniel Akinmulewo, Simon Froitzheim	Propeller Prediction in Behind Condition using a RANS-Based Artificial Body Force Method
P16	Laurens-Jan Lagendijk, Arjan Lampe, Jaap Windt, Stefan Hickel, Tom van Terwisga	Simulation workflow for flexible marine propellers
P17	Negin Donyavizadeh, Arash Eslamdoost, Rickard Bensow	Optimization of the Open Water Performance of a Ducted Propeller
P18	Ahmet Soydan, Widar W. Wang, Hans Bihs	Ship Hydrodynamic Simulations Using an Upgraded Direct Forcing Immersed Boundary Method

P19	Noh Zainal Abidin, Frederic Grondin, Pol Muller Muller, Jean-François Sigrist	Assessment of hydrodynamic characteristics and computational resources for submarine resistance analysis: A comparative study between CFD Codes with application of the BB2 Submarine
P20	Charles Badoe, Merrick Stanley, Peter Bull, Richard Pattenden	Calibration of RANS Wall Model for Accuracy Improvement of Submarine CFD Resistance Prediction
P21	Gert J. Dekkers, Artur K. Lidtke, Thomas P. Lloyd, Fernanda L. Dos Santos, Gabriel D. Weymouth	Quantifying the effect of turbulence intensity on turbulence-interaction noise of an airfoil using scale-resolving simulations
P22	Fabian Knoblauch, Widar Weizhi Wang, Hans Bihs	A VOF-PLIC Algorithm for Modeling the Impact of Breaking Waves on Structures in the CFD Solver REEF3D::CFD
P23	Eric Heilshorn, Kevin J. Maki, Robinson Perić, Jannes Berndt, Moustafa Abdel-Maksoud	Comparison of different approaches to couple the high-order spectral (HOS) method with computational fluid dynamics solvers
P24	Claes Eskilsson	Water wave simulations using fully nonlinear potential flow: spectral/hp element models implemented in nektar++
P25	Andreas Peters, Bettar Ould el Moctar, Robert Potthoff	Effects of Density Ratio on Sloshing-Induced Impact Pressures
P26	Chaitanya Sanghavi, Isabel Michel, Fabian Castelli, Jörg Kuhnert	MESHFREE Simulations for Maritime Applications
P27	Mazyar Dawoodian, Bettar Ould el Moctar	Effects of Oxygen Molecules on nucleation and growing of nanobubbles
P28	Jeroen Wackers, Gaétan Rousseau, Ganbo Deng	Simulation practice and scale effects for sail-driven cargo ships in sideslip
P29	Ricardo Francisco Suarez Fernandez, Moustafa Abdel-Maksoud, Carlos Jahn	Evaluation of the Performance of Model-Based Identification Method of Ship Manoeuvring Parameters using Convex Programming
P30	Benjamin Kossmann, Bettar Ould el Moctar	Development of an azimuth propeller duct for shallow water applications
P31	Wout Opdam, Maarten Bijlard, Bart van Esch, Themis Melissaris	Hydrodynamic Characteristics of a Gate Rudder During Straight-sailing And Sailing With a Ship Drift Angle
P32	Qi Zhang, Bettar Ould el Moctar, Changqing Jiang	Extreme-event analysis of a floating structure with mooring dynamics in an irregular sea state
P33	João Muralha, Tiago Gomes, António Maximiano, Guilherme Vaz	Modelling turbine-turbine interactions using techniques learned from Naval Engineering
P34	Eduardo Tadashi Katsuno, Simon Tödter, Jörn Linde, Andreas Peters, Bettar Ould el Moctar	Hydroelasticity Effects During Helicopter Ditching

List of Participants

Daniel Jonas Ahl	Kongsberg Maritime Sweden AB
Daniel Akinmulewo	Schiffbau-Versuchsanstalt Potsdam
Charles Erzan Badoe	QinetiQ
Jannes Christian Berndt	Hamburg University of Technology (TUHH)
Volker Bertram	DNV
Guillermo Chillcce	University of Duisburg-Essen
Álvaro Crespillo Novoa	C-Job Naval Architects
Mazyar Dawoodian	University of Duisburg-Essen
Gerbert Johan Dekkers	MARIN
Negin Donyavizadeh	Chalmers University of Technology
Maik Dunkerbeck	Bundeswehr, WTD
Bettar Ould el Moctar	University of Duisburg-Essen
Claes Eskilsson	RISE - Research Institutes of Sweden
Yanxin Feng	University of Duisburg Essen
Georg Göbel	Bundesanstalt für Wasserbau
Arne Heuvelman	Damen Shipyards Group
Ian Hubbard	Wärtsilä Netherlands B.V.
Ines Ivković	Faculty of Mechanical Engineering University of Belgrade
Changqing Jiang	University of Duisburg-Essen
Eduardo Tadashi Katsuno	University of Duisburg-Essen
Fabian Knoblauch	Norwegian University of Science and Technology (NTNU)
Benjamin Kossmann	University of Duisburg-Essen
Niklas Kühl	Hamburg Ship Model Basin (HSVA)
Laurens-Jan Lagendijk	TU Delft
Udo Lantermann	University of Duisburg-Essen
Marco Lugaresi	Università degli Studi di Genova
Genís Masjoan Vallés	Elomatic Oy
Themistoklis Melissaris	Wärtsilä Netherlands B.V.
Philipp Mucha	Siemens Digital Industries Software
João Muralha	blueOASIS
Wout Opdam	Wärtsilä Netherlands B.V.
Geir Åge Øye	Kongsberg Maritime
Muhammed Talha Ozdenoglu	University of Southampton
Robinson Perić	Hamburg University of Technology (TUHH)
Andreas Peters	University of Duisburg-Essen
Heikki Piippo	Meyer Turku Oy
Chaitanya Yogendra Sanghavi	Fraunhofer ITWM
Roya Shademani	Aalto University
Carlos Eduardo Simões de Almeida	University of São Paulo
Ahmet Soydan	Norwegian University of Science and Technology (NTNU)
Ricardo Francisco Suarez Fernandez	Fraunhofer Center for Maritime Logistics and Services CML
Kenshiro Takahashi	University of Tasmania
Jeroen Wackers	Ecole Centrale de Nantes (CNRS)
Noh Zainal Abidin	Ecole Centrale de Nantes (CNRS)

26th Numerical Towing Tank Symposium (NuTTS)
23.10-25.10.2024
Mülheim a.d. Ruhr, Germany

Computational Fluid Dynamics Analysis of Inland Waterway Ship Maneuvering in Extremely Shallow Water

Philipp Mucha, Siemens Digital Industries Software, Waltham, MA, USA
philipp.mucha@siemens.com

Introduction

The advance of digitalization and green shipping have led to requirements to assess the impact of alternative fuels, novel engine configurations and systems for autonomous operations on maneuverability in adverse conditions like wind, waves, and shallow water. Simulation technology has also become a resource for forensic analysis of shipping accidents like the obstruction of the Suez Canal by a large container ship in 2021 or the collapse of the Francis Scott Key Bridge in Baltimore (MD, USA) in 2024 following impact from a large container ship. The present paper presents computational fluid dynamics (CFD) based maneuverability analyses of an inland waterway ship under extremely shallow water conditions. Simulations of straight-line self-propulsion and zig-zag maneuvers at water depth H to draft T ratio of 1.2 were utilized to provide a quantification of the reliability of CFD to contribute to the limited pool of benchmarking data for these conditions and ships. The critical elements of CFD are turbulence modeling to account for the altered near-wall flow in the under-keel clearance (UKC) region and motion modeling to consider dynamic trim and sinkage in presence of only a small gap between the keel and the bottom. A comprehensive review of simulation technology for hydrodynamic problems in confined waters can be found in Mucha (2017). Carrica et al. (2016) discuss the simulation of a zig-zag maneuver in extremely shallow water for the Kriso containership (KCS) based on Delayed Detached Eddy Simulation (DDES). Overshoot angles were underpredicted by 13% and 18.9% for the first and second rudder execution, respectively, stemming from a 19% underprediction of the maximum yaw rate. The period of the resulting yaw oscillation was predicted in good agreement to the experiment (<1%). The finite width of the shallow water tank was not considered in simulations, representing a source of error, while the underprediction of yaw kinematics was attributed to turbulence modeling. From the few available studies, it can be observed that comparison errors to experiments are usually 5-10% higher than for simulations in deep water conditions.

Ship test case

The model used in the study (Fig. 1, Tab.1) represents a typical inland waterway ship encountered on European waterways which can be used for bulk carriers, container, or tanker ships. A detailed description of the ship, resistance and propulsion tests under various shallow water conditions is available from Mucha et al. (2018). Free-running zig-zag maneuvers were conducted at the Maritime Research Institute Netherlands (MARIN), Mucha et al. (2019). The tank at MARIN is 220m in length, 15.8m wide and with adjustable water depth from 0-1.1 m. Experiments were run at conditions of H/T=1.2 and 3.0. Zig-zag maneuvers were performed starting to both port and starboard side with yaw checking angle of Ψ= +/- 5° and application of rudder angle δ= +/- 35°. Tests at H/T=1.2 were repeated four times to each side. Approach speed was 0.556 m/s, corresponding to depth Froude number F_{nh}=0.086, respectively, and 4.3 kts at full scale. Prior to maneuvering experiments, speed runs were conducted to determine propulsion characteristics. A right-handed Cartesian coordinate system with origin located at the center of gravity participating in the motion of the model was used. Axes x, y, z pointed forward, to port and upward, respectively. Details of the propeller geometry can be found in Mucha et al. (2018). The twin propellers followed inward over-the-top rotation seen from astern.

Figure 1. Inland waterway ship model, built at Schiffbauversuchsanstalt Potsdam (SVA), designed by DST.

Table 1. Main particulars of the inland waterway ship.

	Length between perpendiculars L_{pp} [m]	Beam B [m]	Draft T [m]	Wetted Surface Are S_W [m^2]	Longitudinal center of gravity wrt. $L_{pp}/2$ x_{CG} [m]	Block coefficient c_B [-]	Volume V [m^3]
Ship	135	11.45	3.5	2376.1	-0.1718	0.92	4992
Model	8.4375	0.7150	0.2188	9.2817	-0.01074		1.2187

Numerical Method

The CFD application Simcenter™ STAR-CCM+ (Siemens, 2024) was used in the current study. In Simcenter STAR-CCM+ numerical solution methods based on Finite Volume (FV) approximation for the Navier-Stokes equations are available. Unsteady Reynolds-averaged Navier-Stokes (URANS) equations formed the basis of the solution procedure. The transport of turbulent momentum was accounted for by introducing time-averaged and fluctuating terms of the flow variables to the equations, while approximations were made for the resulting stress tensor. The k-ω Shear Stress Transport (SST) model was utilized. In Simcenter STAR-CCM+ the constitutive order can be chosen to be linear, quadratic, or cubic. Details on the approximation schemes and VOF-HRIC based free surface modeling can be found in Mucha (2017). Rigid body motions were solved for by the Dynamic Fluid Body Interaction (DFBI) method which provides an implicit coupling scheme between the flow and rigid body equations of motion in six degree of freedom (DoF). Two kinds of mesh configurations were investigated, Fig. 2. The first one is valid for laterally unrestricted water neglecting relative motions between the ship and tank walls. In this case a single region can be used for the tank and ship. The entire region moves with the maneuvering ship while heave and pitch motions are modelled using mesh morphing. Propellers were modeled using sliding interfaces. Rudders were added by way of overset mesh technology. With the second configuration the ship is included in a separate overset region and the tank region only participates in longitudinal motions enabling relative motions between the ship and side tank walls. Mesh morphing is active inside the ship overset region for heave and pitch modeling. This configuration comes at additional computational cost due to overset hole cutting, interpolation and additional grid refinement in the tank region to cover horizontal motions of the overset ship region (factor 2.8). The computational mesh for the tank, ship, rudders and duct consisted of hexahedral CVs in unstructured arrangement. Propeller regions were meshed with polyhedral cells. Prismatic cells were used on the hull, rudder and propeller boundaries (y^+<=1). Anisotropic refinement was employed in the zone of free surface motions. Further anisotropic refinement was requested in the UKC region extending beyond the main dimensions of the ship model to account for six DoF body motions. These refinements represented 44% of the total number of cells in the domain. Here, cells had a vertical grid spacing of 2mm and horizontal grid spacing of 8mm (medium grid resolution, total number of cells: 17M). The computational domain extended 1.25L upstream of the fore perpendicular and 2.75L downstream of the aft perpendicular. The distance to the side and bottom tank wall were in accordance with the physical experiments at MARIN, i.e., the tank was 15.8m wide. Its vertical extent to the top boundary was 1L measured from the deck. The upstream and downstream boundaries were modelled as velocity inlets. In Simcenter STAR-CCM+ this constitutes a Dirichlet type

boundary condition and, consistent with the forward motion of the region, the velocity vector was [0,0,0] m/s here. The volume fraction definition was based on calm-water condition and prescribed directly in analogy to the velocity. Pressure was interpolated from adjacent cells. Wave forcing was used to mitigate reflection of numerical free surface disturbances from the upstream and downstream boundaries. The forcing zone length at the inlet was 4m and 7m at the outlet, respectively. In configuration one the side boundaries were velocity inlets with 4m wave forcing zones. The bottom relative velocity was [$-U_x$,$-U_y$,0] m/s, U_i being the instantaneous rigid body velocity of the ship model. In configuration two the sides and lower boundary of the background region were no-slip walls with relative tangential velocity of [$-U_x$,0,0] m/s. The top boundary was a pressure outlet with direct specification of atmospheric pressure, volume fraction and interpolation of velocity and turbulence values from neighboring cells. The ducted propeller was modelled using a moving reference frame (MRF). The presence of the duct partially mitigates the errors in the capturing of transient cross-flow and side forces on the blades introduced by MRF, Mucha et al. (2023). The setup and simulation of open-water propeller tests followed an equivalent study presented in Aram and Mucha (2023). Three grids were generated comprising 2.2M, 3.7M and 6.6M, respectively. Comparison errors across all grids for the practically relevant range (advance coefficient J=0.1 to 0.5) to the operational point of the maneuver (J=0.42) show a mean comparison error of 6.27% for the total thrust generated by the duct-propeller unit. The coarse grid was chosen.

Results and Discussion

Comparison error E% is defined as 100(E-S)/E, where S is the simulation result and E is the experimental result, respectively. Bare-hull towing test results were available for the slow speed range from the Development Center for Ship Technology (DST), Mucha et al. (2018) on the fixed model moving in x-direction only due to negligible effect of squat. A factor of √2 was used to perform one level of coarsening and refining for a 17M cell grid to arrive at 7.9M and 42.7M cells, respectively. Grid sensitivity was checked for the production run speed of 0.556 m/s. Additionally, based on the converged solution from employing the conventional k-ω-SST model, the cubic constitutive option was activated to allow for anisotropic production of turbulence. Enabling anisotropic production improved the results for speeds greater than 0.556 m/s. The maximum deviation was found at -8.7% for the highest considered speed and the linear constitutive option. For both higher speeds considered E% decreased by three to four percentage points. Due to the low depth Froude number, it was not as pronounced as observed by Yahfoufi and Deng (2014), who demonstrated that differences of E%>15 between isotropic and anisotropic modeling started to show for F_{rh}>0.2. For the approach speed to the maneuver of 0.556 m/s the difference to the experiment was -1.6%. Results indicate a small deviation between the coarse and medium, and the medium and fine grid, Tab. 2. A pronounced zone of recirculation was visible behind the

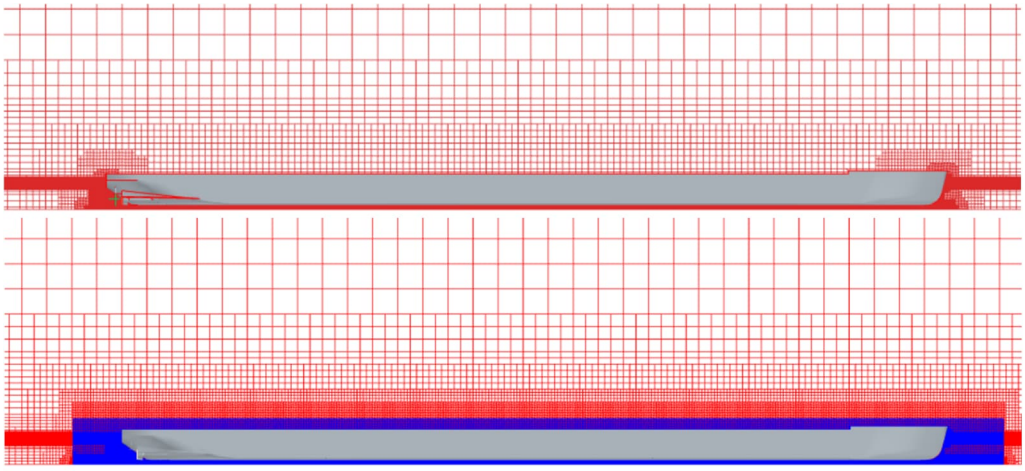

Figure 2. Detail side views of the computational mesh for configuration one (top, open water, single mesh for tank and ship) and two (relative motion to tank considered, blue overset mesh region inside tank region).

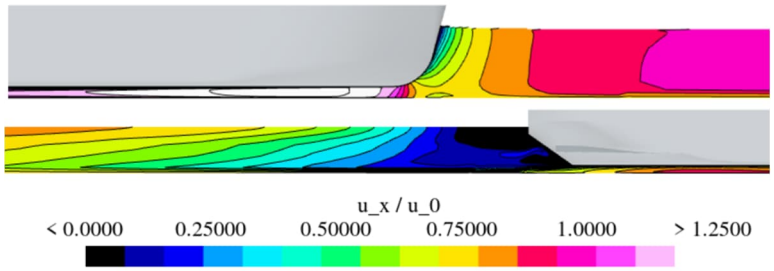

Figure 3. Detail side views on bow and stern regions of the velocity in the center plane (y=0).

Table. 2. Results of X in [N] of bare-hull towing tests, grid and turbulence modeling sensitivity studies.

U [m/s]	0.415	0.555	0.555	0.695	0.695
F_{rh} [-]	0.065	0.086	0.086	0.108	0.108
Constitutive Order	Linear	Linear	Cubic	Linear	Cubic
Coarse (7.9M)	-	8.51	-	-	-
Medium (17M)	4.45	7.89	8.11	13.05	13.7
E% Medium	**-5.56**	**-4.36**	**-1.6**	**-8.7**	**-4.19**
Fine (42.7M)	-	7.79	8.33	-	-
EFD	4.71	8.25	8.25	14.3	14.3

skeg. Fig. 3 provides expanded insight into the flow fields near the bow and stern region. Besides the large recirculation zone behind the stern, the acceleration of the flow near the fore shoulder, where the flow encounters the maximum obstruction, stands out as a prominent feature of the flow around the ship model. The pronounced flow features proximal to the fore and after shoulders are critical to the understanding of squat and the dynamic trim bias (bow-down) which is important for UKC management to prevent grounding of the rudders. Due to acceptable differences between the medium and fine grid, the medium grid was selected for further simulation work. In free-running mode the model was controlled using a proportional-derivative (PD) control law for the course angle with an additional proportional gain for offset in sway, both with set point Ψ=0° and y=0 m, see Mucha et al. (2018). The time step during the approach phase (only x-motion allowed) was 0.1s. A small number of 5 inner iterations was sufficient to achieve reasonable decline of residuals in each time step. After 100s it was decreased to 0.05s, then further decreased to 0.025s when heave and pitch motions were activated. The solution was stabilized by a temporally limited increase of the number of inner iterations to 50 and an artificial damping force and moment in heave and pitch modes of motion to absorb the numerical impact of switching from one to three DoF. Upon settling of the heave and pitch response to a steady state the remaining modes of motion and course controller were activated. Propeller rate of revolution was varied using a P-controller and the final value for the approach speed of U_0=0.556 m/s was 830 RPM compared to 780 RPM in the experiments (E%=6.4). Sinkage settled at 5.22 mm compared to 6.1 mm in the experiment (E%=16.8). Trim was negligibly small in both experiment and computation (<0.1°). Fig. 5a-b show the time histories of port (l.h.s.) and starboard (r.h.s) 35°/5° zig-zag maneuvers. Measurements from the first run using experimental fluid dynamics (EFD) are represented by black lines. Blue lines refer to CFD configuration one (open water). Configuration two (modeling relative motion to the tank) was only run for the maneuver starting to port and is represented by red lines. Overall good agreement between CFD and EFD was attained. The first overshoot angle for both CFD configurations was 3.28° which is only slightly higher than the average of 3.18° with a variance of 0.1° from experiments, resulting in a comparison error of 3.2%. The second overshoot angle was 4.6° (open water) and 4.5° (tank) in CFD compared to the average of 5.98° with 0.1° variance in EFD, resulting in a comparison error of 12.5%. Analysis of motion responses in surge and sway revealed that speed loss predictions by CFD were close to measurements,

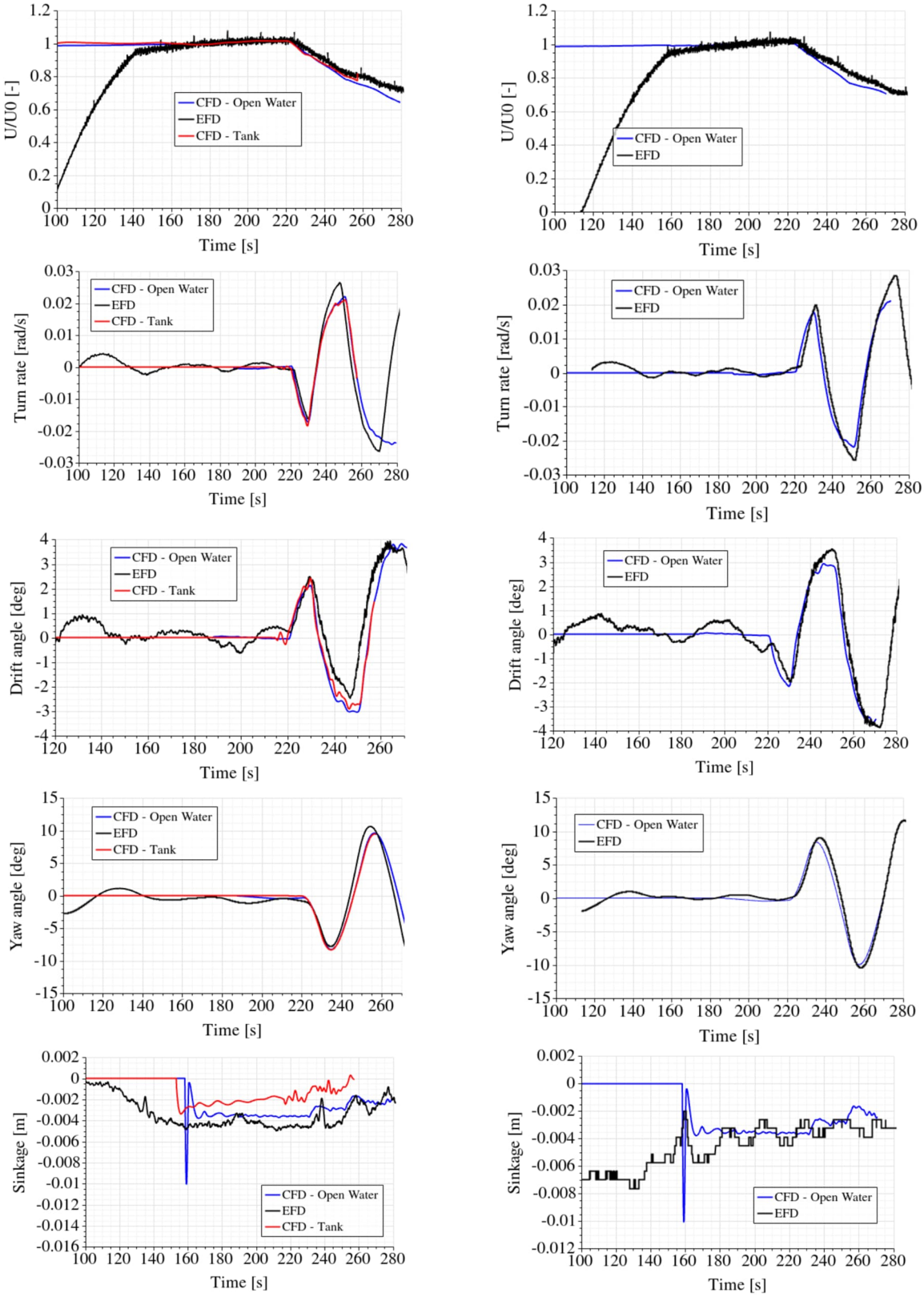

Figure 5a. Time histories of port (l.h.s.) and starboard (r.h.s) 35°/5° zig-zag maneuvers.

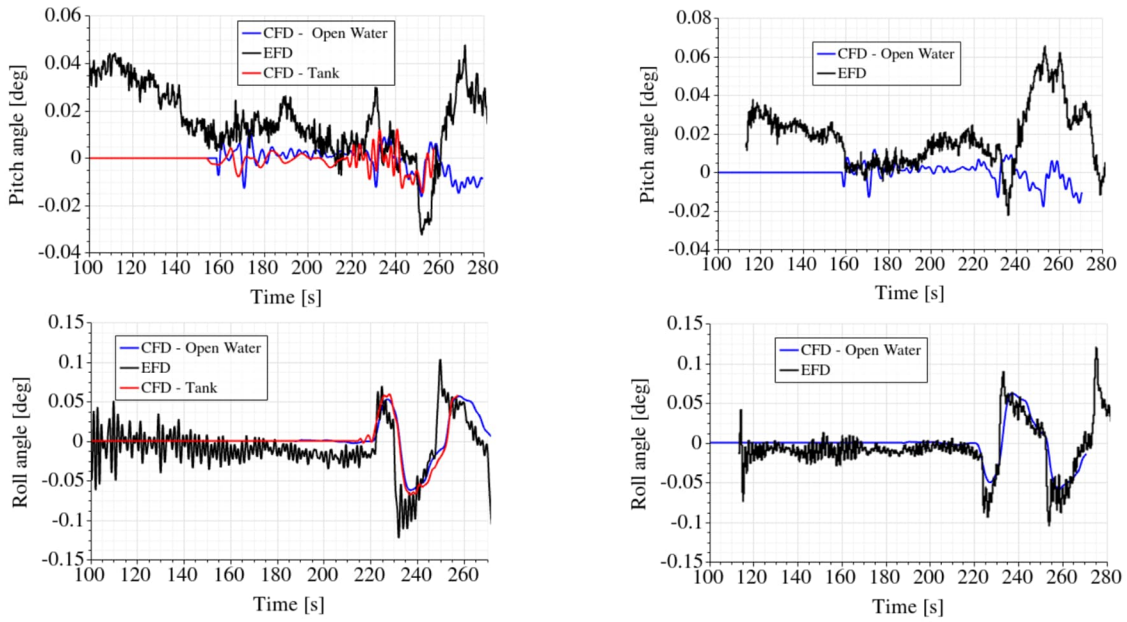

Figure 5b. Time histories of port (l.h.s.) and starboard (r.h.s) 35°/5° zig-zag maneuvers.

albeit showing a slightly faster decline of forward speed during the first two rudder executions. Drift angle agreed well up until the second overshoot angle, when CFD predicted a slightly larger drift angle. The same applies to the turn rate. The maximum amplitude was underpredicted in CFD by 15%. Dynamic sinkage and trim were very small and qualitative trends in good agreement. The same observation applies to roll motions which were negligibly small. With the exception of dynamic sinkage the differences between the two CFD configurations were marginal which is attributed to the wide tank and MARIN and negligible wall effects. The 2.8-fold increase in cell count for configuration two translated to a 85% increase in solver time. Using 20x40 cores for configuration one the total solution time was 2.97 days. For configuration two it was 5.5 days. The value of validating configuration two refers to applications where neglecting relative motions to boundaries is not admissible, e.g. maneuvering in narrow channels, entry to locks, or passing and overtaking of other ships.

References

P. Mucha. 2017. On Simulation-based Ship Maneuvering Prediction in Deep and Shallow Water. PhD-Thesis, Univ Duisburg-Essen

P. Carrica, A. Mofidi, K. Eloot, G. Delefortrie. 2016. Direct simulation and experimental study of zigzag maneuver of KCS in shallow water. Ocean Eng. 112, 117–133.

Siemens. 2024. Simcenter STAR-CCM+ User Guide 2402.

N. Yahfoufi,G. Deng, 2013. Resistance prediction of the DTC container ship model in shallow water. Ship Technology Research – Schiffstechnik 61(3)

P. Mucha, T. Dettmann, V. Ferrari, O. el Moctar. 2019. Experimental investigation of free-running ship manoeuvers under extreme shallow water conditions. Applied Ocean Engineering 63(155-162)

P. Mucha, O. el Moctar, T. Dettman, M. Tenzer. 2018. An experimental study on the effect of confined water on resistance and propulsion of an inland waterway ship. Ocean Engineering 167(11–22).

P. Mucha, S. Aram. 2023. Computational fluid dynamics analysis of different propeller models for a ship maneuvering in calm water. Ocean Engineering 276(114226)

P. Mucha, S. Aram, M. Wheeler, D. Radosavljevic, J. Singh. 2023. Propeller Modeling for Ship Maneuvering Simulations in Simcenter STAR-CCM+. Proc. 25th NuTTS, Ericeira, Portugal.

26th Numerical Towing Tank Symposium (NuTTS)
23-25 October 2023
Mühlheim an der Ruhr, Germany

Full Scale Predictions of Ship Induced Waves in Restricted Waters with Numerical Tools – a Comparative Study

Georg Göbel[*], Lahbib Zentari[*], Cristian Brutto[†] and Jacek A. Jankowski[*]
[*] Bundesanstalt für Wasserbau, Karlsruhe, Germany, [†] University of Trento, Trento, Italy
georg.goebel@baw.de

1 Introduction

Banks of inland waterways are subject to hydrodynamic loads induced by primary and secondary waves generated by passing ships. To counteract these loads, banks are typically reinforced with riprap, as well as nature-based solutions.
The design and dimensioning of bank reinforcements are based on predicting the largest wave loads caused by passing inland ships, which underscores the importance of accurate predictions of a ship's primary wave. Several factors influence the primary wave height, including the ship's shape, size, and speed. Additionally, these waves are significantly affected by the vertical and lateral confinement of the waterway. Furthermore, waves generated by inland ships approaching critical speed in confined waterways are characterized by relatively high wave steepness and complex effects, such as wave breaking and reflections.
Ship wave simulations can be performed using various approaches. High-fidelity CFD codes, which employ Reynolds-averaged Navier-Stokes equations solved with two-phase Volume of Fluid methods, are commonly used in marine applications to predict ship forces and maneuvering characteristics. In contrast, codes based on the Shallow Water Equation with a height function to describe the free surface are more commonly used for the simulating larger water bodies like river stretches and for wave propagation over extensive domains.
The present study compares the ability of four different tools to predict ship-induced waves in a confined waterway. The comparison is conducted from a practical engineering perspective, without delving into the specifics of numerical procedures, and presents preliminary results in the search for software suitable for the estimation of ship-wave loads on the banks of inland waterways. This work focuses solely on model accuracy; aspects related to numerical efficiency and computational effort are not considered in the comparison.

2 Ship Geometry and Validation Data

In 2004, BAW conducted an extensive measurement campaign at the Wesel-Datteln-Canal (WDK) with a 105 m long and 11 m wide ship passing a straight, uniform stretch at different speeds and varying distances from the bank. The canal is trapezoidal in the cross-section and the width of the gravel bottom is 33,4 m. The slope of the riprap reinforced banks is 1:2.43. With a water depth of 3.95 m, the width of the free surface is 52,6 m. The height of the ship-generated wave was measured using an ultrasonic probe located halfway up the bank (Figure 1).
Based on the grain size of the gravel bottom and dimension of the riprap stones the equivalent sand-grain roughness of the canal is estimated $k_{s,bed}$ = 0,03 and $k_{s,slope}$ = 0,3. Ship-hull roughness is estimated $k_{s,hull}$ = 0,0003.

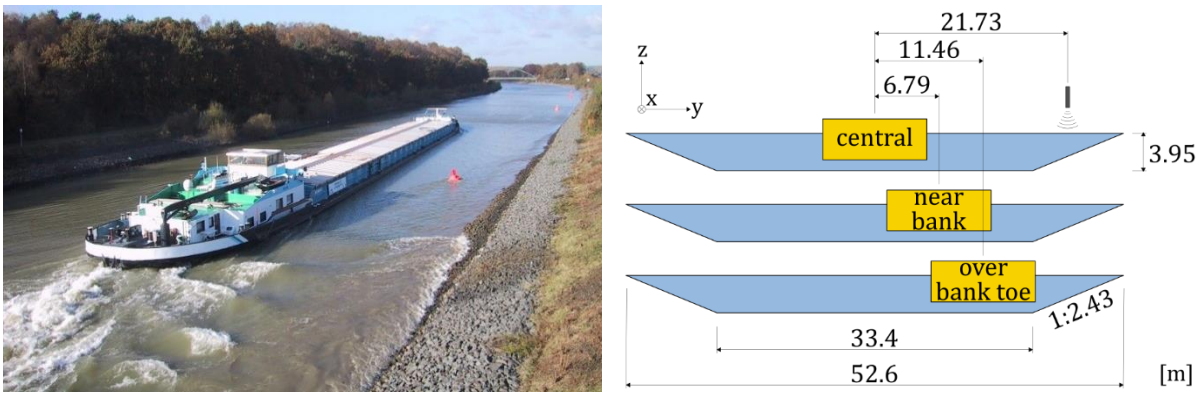

Figure 1: Ship in canal during measurement (left) and sketch of canal geometry with location of the ultrasonic probe and three different ship positions (right).

The collected data were never fully published, parts can be found in Söhngen and Doychev (2018). For the presented work, measurement data from three different lateral positions and three ship speeds v_s were used. Lateral position was as depicted in Figure 1. Ship speed was varied relative to the critical ship speed v_{crit}, which was calculated as described in GBB (Bundesanstalt für Wasserbau 2010) (Table 1).

Table 1: Ship-speed v_s and corresponding depth Froude Number Fr_h for all nine measurement runs.

	central, v_{crit} = 2,69 m/s		near bank, v_{crit} = 2,67 m/s		over bank toe, v_{crit} = 2,67 m/s	
	v_s [m/s]	Fr_h [-]	v_s [m/s]	Fr_h [-]	v_s [m/s]	Fr_h [-]
100% v_{crit}	2,66	0,42	2,66	0,42	2,65	0,42
90% v_{crit}	2,53	0,40	2,54	0,41	2,52	0,40
80% v_{crit}	2,39	0,38	2,32	0,37	2,22	0,35

The measurements are shown in Figure 2. All cases display the typical ship-induced wave pattern, with surface elevation at the bow and stern, and a drawdown along the length of the hull. When the ship speed approaches v_{crit}, the drawdown increases further, and the slope supply flow transforms to a breaking wave (Dempwolff et al. 2022a), as seen in Figure 1.
The results are averaged from four to five measurement runs which introduces some high-frequency filtering. That implies that the superimposed secondary wave may appear smaller than it is in reality.

3 Numerical Methods

Simulations were performed using four different solvers with the aim of resolving the primary wave system and, if possible, the secondary wave systems generated by a typical inland cargo ship in a canal at full scale.
Two high-fidelity CFD solvers of the URANS-type (OpenFOAM and STAR CCM+) were employed in which the ship is kept fixed while the fluid around the ship is moved. The flow around the ship is established by applying a velocity or flow-rate inlet condition and a pressure outlet. The lateral banks and the bottom of the canal were defined as a no-slip wall with a relative velocity equal to the inlet velocity. The ship's hull was treated with a no-slip surface as well.

This approach has been shown to give satisfactory results in other studies, see e.g. Bechthold and Kastens (2020). In both applications, the domain consisted of approximately 25 million cells and extended 1.5 ship lengths forward of the test ship and 3.5 ship lengths aft. Mesh refinements were applied around the ship, extending to the lateral boundaries of the canal as well as in the underkeel region. Additional refinements were defined in the free surface region in order to capture its deformation accurately.
Two solvers of the non-hydrostatic Shallow-Water-Equation (SWE) type (REEF3D SFLOW and SIFSI) were used, in which the ship moves through the canal with a constant velocity. The domain size was chosen long enough to establish a stable ship-wave system, uninfluenced by precursor soliton waves or reflections from both open boundaries. A full-scale model is employed in all four approaches.
Since not all codes are able to handle ship dynamics, the draft was fixed to T = 2.8 m (h/T = 1.41) and dynamic squat and trim are neglected for consistency and simplicity. The applied canal shape and water depth are sketched in Figure 1.
All models were calibrated by improving mesh quality, numerical parameters, and numerical schemes. The calibration was performed for the central position at 100% of v_{crit}; all other cases are based on this calibration.

OpenFOAM

OpenFOAM is an open source C++ library for solving partial differential equation systems (Weller et al. 1998). The library consists of a variety of solvers for modelling specific physical phenomena. *interFoam* is a two-phase model for the simulation of free surface flows that is based on the Volume-of-Fluid method (VoF) by Hirt and Nichols (1981). Mass and momentum equations are solved using the PIMPLE algorithm, an iterative pressure-velocity coupling method. The distribution of air and water in the domain is described by the volume fraction α. The transport equation of α is solved with the OpenFOAM specific MULES-algorithm. In this work, OpenFOAM v2212 is used. The k-ω-SST model by Menter et al. (2003) is employed for turbulence modelling. Second order schemes are applied for both temporal and spatial discretization. The time step is adjusted in relation to the CFL-number that is below 0.5 for cells with $0 < \alpha < 1$ and 0.8 for cells with $\alpha = 0$ and $\alpha = 1$.
The cell size in vicinity of the ship hull is 0.125 m. Based on the assumption that the primary wave of the ship is pressure-dominated and the influence of ship's surface roughness is negligible, a prism layer was omitted and a wall function was used.

Simcenter™ STAR-CCM+

The commercial flow solver Simcenter STAR-CCM+ has been validated for various ship flow cases in restricted waters, see Mucha (2017). The simulation is based on the numerical solution of the unsteady Reynolds-Averaged Navier-Stokes (URANS) equations. Closure of the equations is provided by the k-ω-SST turbulence model. A VoF approach is used to resolve the air-water interface. A fixed time step was chosen to maintain a Courant number CFL < 1, ensuring a sharp interface between water and air when using the HRIC scheme. The system of equations was solved in a segregated manner using the SIMPLE algorithm.
Considering the scale of the simulation, a $y^+ > 300$ was targeted at the ship and canal boundaries by the application of a prism layer. Second order schemes are applied for both temporal and spatial discretizations.

REEF3D SFLOW

REEF3D is an open-source software package containing various solvers for hydraulic engineering applications. It includes multiple solvers, such as the non-hydrostatic shallow-water-model SFLOW which is used in this investigation (Wang et al. 2020). In all four solvers high order schemes can be applied, like the 5th-order WENO for discretization in space and the 3rd-order TVD Runge-Kutta for discretization in time.
The mesh size used is 2 x 2 m, and the domain length is 1410 m. The ship is represented as a moving pressure field on the water surface. The specific pressure field is derived from the geometry of the ship as described and validated in Dempwolff et al. (2022b). The surface elevation is measured 570 m from the start of the domain.
A 3rd-order TVD Runge-Kutta is used for discretization in time and a 5th-order WENO for discretization in space. A linear non-hydrostatic approach is applied for dynamic pressure, with roughness set to k_s = 0.3 m.

SIFSI

The newly developed SIFSI model is based on a semi-implicit finite volume scheme and is designed for solving fluid-structure-interaction problems (Brutto and Dumbser 2022; Brutto 2024). It efficiently simulates multiple objects moving on the free surface of water bodies such as rivers, lakes, and harbors, while simultaneously analyzing long-distance wave propagation from these bodies. The motion of these objects is influenced by gravity, hydrostatic pressure and the shear stress in their six degrees of freedom, whose evolution is controlled by the ODE system of the linear and angular momentum equations. Forces acting on the bodies are calculated using the free surface solution derived from the partial differential equation system that governs the motion of water. This enables the study of interactions with waterways, allows ship's course tracking and aids in the design of waterways and ports infrastructure. The position and orientation of the bodies modify the nonlinear volume function applied in each computational cell. The water flow dynamics is currently based on the 3D shallow water equations, which allow solving the flow equations in mesoscale domains in a context where the horizontal dimensions are greater than the vertical dimension. The discretization follows the scheme of Casulli and Cheng (1992), where the dimension of the linear equation system to be solved is only weakly affected by vertical discretization, ensuring computational efficiency. Additionally, treating mass fluxes and the pressure gradients as implicit terms reduces the limitation on the timestep by the CFL condition. Dispersion effects are introduced through a Boussinesq-type term in the momentum equation. The calculations have been done on a 4 m x 2 m grid with 4 x 4 subgrid, a timestep of 0.5 sec and without skin-friction.

4 Results and Discussion

The ship-induced wave is evaluated as the surface elevation above the slope, as illustrated in Figure 1. Figure 2 presents the results of the measurement campaign, including a 95% confidence interval, along with the results from the four different numerical tools. The first observation is that none of the tools consistently predict the ship-generated wave with satisfying accuracy. Additionally, some tendencies can be observed as ship speed and lateral position increase.

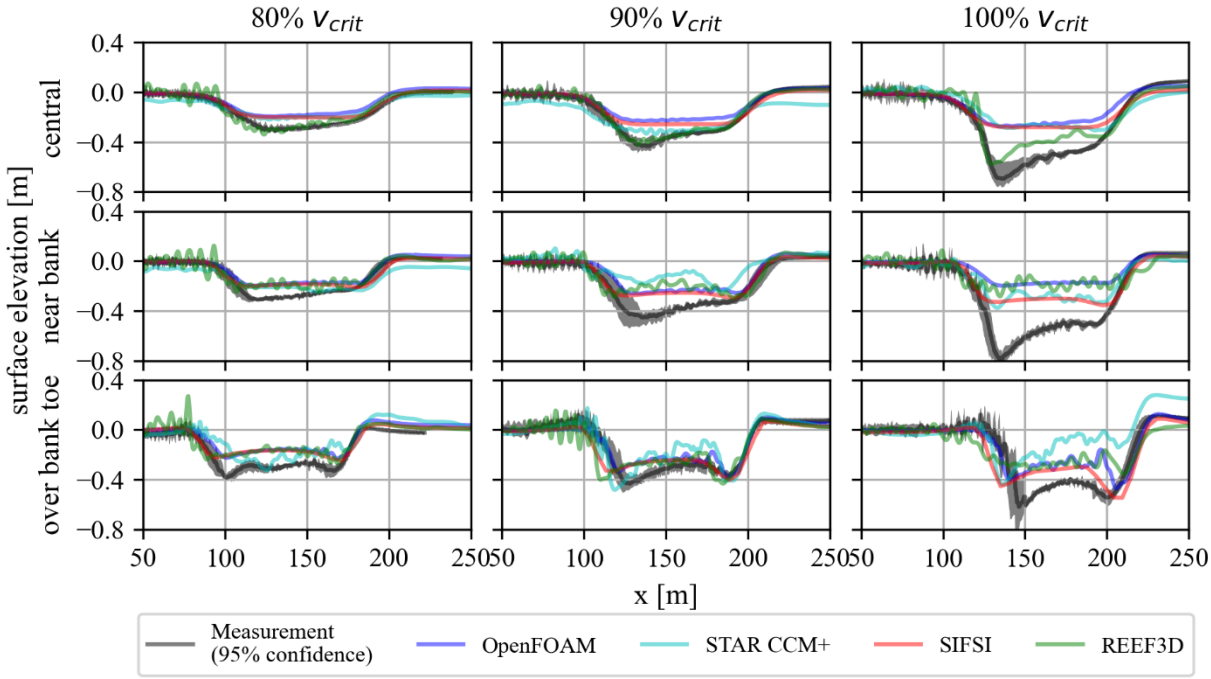

Figure 2: Surface elevation along the canal for different ship speeds vs and lateral positions. Measurement data, shown in black, represents the average of five measurement runs, with the 95% confidence interval shaded in grey.

While both URANS methods are further from the reference results than the SWE solvers, their accuracy appears to improve when the ship is closer to the shore. This indicates, that the prediction of drawdown is more reliable in near vicinity of the hull but become less accurate as the wave propagates into the far field. The prediction of the orbital motion of the wave requires high precision in the interface region, which may not have been fully achieved in this case, despite mesh refinements based on previous operational experience. A more accurate prediction is possible, as Kochanowski and Kastens (2022) showed, however further refinement of the free surface region would significantly increase computational costs. They also included ship dynamics and a propeller in their simulation which may also be a reason for the better accuracy in their work.

Comparing STAR-CCM+ and OpenFOAM, the secondary wave is slightly more pronounced in STAR-CCM+. The reason for this is unclear and may be related to differences in interface-capturing methods or the finer mesh on the hull surface in STAR-CCM+, since the mesh resolution on the water surface area is similar in both cases.

Across all solvers, REEF3D demonstrates highest accuracy, though the results still deviate from the reference data in most cases. REEF3D performs best for the central ship position but shows discrepancies in near-bank and over-bank-toe positions. A recalibration of the ship-induced moving pressure field may improve accuracy in these eccentric positions.

By the SIFSI results presented in Fig. 2 it should be stressed that no skin friction was applied. Brutto (2024) shows, that there are big differences in the size and shape of the primary wave, when skin-friction is considered or not. His work also shows good accuracy with validation data, when skin-friction is applied.

The propagation of ship waves in natural, more complex bathymetries will be a topic for future research. In particular, the propagation of ship waves in water bodies laterally connected to waterways is of interest, as wetland restoration and riverbank renaturation become increasingly important. This study

demonstrates that none of the applied tools provide perfect results. Since the SWE solvers have shown better accuracy in ship waves prediction, future research will focus on these methods. However, further work is needed in terms of calibration and development.
The comparison of URANS solvers will remain a topic of research interest as well, as they presently excel in predicting ship forces and addressing maneuvering questions over the SWE-based methods (Brutto 2024). However, they are unlikely to serve as reliable and computationally efficient tools for predicting ship waves. Moreover, for all compared methods, the validation of simulated ship wave systems is still an ongoing research. Regarding the validation dataset, new data needs to be collected, processed, and published. This dataset should include water surface levels and fluid velocities at various lateral positions, as well as information on ship dynamics and machine data such as propeller thrust.

5 References

Bechthold, J.; Kastens, M. (2020): Robustness and quality of squat predictions in extreme shallow water conditions based on RANS-calculations. In *Ocean Engineering* (197).

Brutto, C. (2024): Development of an efficient fluid-structure interaction model for floating objects. Doctoral thesis. University of Trento, Trento. Department of Civil, Environmental and Mechanical Engineering.

Brutto, C.; Dumbser, M. (2022): A semi-implicit finite volume scheme for a simplified hydrostatic model for fluid-structure interaction. In *International Journal of Numerical Methods in Fluids* 36 (1).

Bundesanstalt für Wasserbau (2010): BAWMerkblatt Grundlagen zur Bemessung von Böschungs- und Sohlensicherungen an Binnenwasserstraßen. GBB.

Casulli, V.; Cheng, R. T. (1992): Semi-implicit finite difference methods for three-dimensional shallow water flow. In *International Journal of Numerical Methods in Fluids* (15), pp. 629–648.

Dempwolff, L.-C.; Melling, G.; Windt, C.; Lojek, O.; Martin, T.; Holzwarth, I. et al. (2022a): Loads and effects of ship-generated, drawdown waves in confined waterways - A review of current knowledge and methods. 46 Pages / Journal of Coastal and Hydraulic Structures, Vol. 2 (2022). DOI: 10.48438/JCHS.2022.0013.

Dempwolff, L.-C.; Windt, C.; Melling, G.; Martin, T.; Bihs, H.; Holzwarth, I.; Goseberg, N. (2022b): The influence of the hull representation for modelling of primary ship waves with a shallow-water equation solver. In *Ocean Engineering* 266, p. 113163. DOI: 10.1016/j.oceaneng.2022.113163.

Hirt, C. W.; Nichols, B. D. (1981): Volume of fluid (VOF) method for the dynamics of free boundaries. In *Journal of Computational Physics* 39 (1), pp. 201–225. DOI: 10.1016/0021-9991(81)90145-5.

Kochanowski, C.; Kastens, M. (2022): Simulation and Validation of ship induced Waves in shallow and confined Water. In Ghent University, University of Strathclyde und Flanders Hydraulics (Ed.): 6th Mashcon - Proceedings. International Conference on Ship Manoeuvring in Shallow and Confined Water with special focus on port manoeuvres. 6th MASHCON. Glasgow, UK, 22.-26.5.2022, pp. 89–101.

Menter, F. R.; Kuntz, M.; Langtry, R. (2003): Ten Years of Industrial Experience with the SST Turbulence Model. In C. Hanjalic, Nagano Y, M. J. Tummers (Eds.): Fourth Internal Symposium, Turbulence, heat and mass transfer, vol. 4. New York, Wallingford: Begell House (Turbulence, heat and mass transfer, 4), pp. 625–632.

Mucha, P. (2017): On Simulation-based Ship Maneuvering Prediction in Deep and Shallow Water. Doctoral Thesis. Universität Duisburg-Essen, Duisburg. Fakultät für Ingenieurwissenschaften, Abteilung Maschinenbau.

Söhngen, B.; Doychev, S. (2018): Impact of ship size on induced waves and currents in confined water. In *3rd International Conference on Ship Manouvering in Shallow and Confined Water, June 03 - 05, 2013, Ghent, Belgium*, pp. 1–6.

Wang, W.; Martin, T.; Kamath, A.; Bihs, H. (2020): An improved depth-averaged nonhydrostatic shallow water model with quadratic pressure approximation. In *Numerical Methods in Fluids* 92 (8), pp. 803–824. DOI: 10.1002/fld.4807.

Weller, H. G.; Tabor, G.; Jasak, H.; Fureby, C. (1998): A tensorial approach to computational continuum mechanics using object-oriented techniques. In *Computers in Physics* 12 (6).

Development of a CFD-based Collision Avoidance Model for Maritime Autonomous Surface Ships in Restricted Waters

Muhammed Talha Ozdenoglu[1], Yao Zhang, Stephen Turnock, and Tahsin Tezdogan

Department of Civil, Maritime and Environmental Engineering, School of Engineering, University of Southampton, Boldrewood Innovation Campus, Building 176, SO16 7QF, U.K.

1. Introduction

The rise of automation in the maritime industry, driven by the need to enhance safety and efficiency, has led to the development of Maritime Autonomous Surface Ships (MASS). A critical challenge in autonomous ship design is ensuring reliable collision avoidance, particularly in confined or restricted waters such as ports, locks, or narrow channels. These environments involve complex hydrodynamic interactions influenced by factors like waves, currents, and ship proximity, requiring advanced modeling techniques to predict and mitigate risks.

The main objective of this research is to develop a computational fluid dynamics (CFD)-based collision avoidance model specifically tailored for MASS operating in restricted waters. The ultimate goal is to create a model that can accurately simulate real-world conditions, including wave forces, currents, and ship proximity, to ensure safe and efficient autonomous navigation.

To achieve this, the study integrates experimental towing tank data, full-scale CFD simulations, and advanced control strategies, such as Model Predictive Control (MPC), which will allow the ship to make real-time adjustments to its trajectory. Additionally, by comparing traditional resistance estimation methods, such as Holtrop-Mennen and Michell's Thin-Ship Theory, with CFD simulations, the research aims to provide a more reliable prediction of ship behavior under dynamic conditions. This project will result in a robust collision avoidance system for MASS, contributing valuable insights to the future development of autonomous navigation systems.

Literature review :

The development of control systems for MASS has attracted significant attention, particularly in the areas of path-following and maneuverability under adverse weather conditions. Daejeong Kim et al. (2022) explored control issues for MASS under low-speed conditions using unsteady RANS CFD simulations, highlighting the importance of robust control strategies in varying wave heights.

Tezdogan et al. (2019) further investigated the maneuverability and course-keeping performance of ships in different wave conditions, leveraging CFD techniques to predict hydrodynamic forces affecting ship stability. These studies underscore the potential of CFD simulations in simulating realistic environmental conditions for autonomous ships.

[1] Corresponding author.
E-mail address: M.T.Ozdenoglu@soton.ac.uk

Thor Fossen's (1994) work on guidance and control of ocean vehicles serves as a key reference for applying MPC in path tracking for maritime vessels. Fossen's research into adaptive control methodologies in disturbed environments is crucial for the real-time control models for MASS in restricted waters.

Predictive models, as explored by Wang et al. (2017) and Guo et al. (2020), offer insights into using wave-based disturbances for path tracking under uncertain environmental conditions. Traditional empirical methods, such as the Holtrop-Mennen method, have been valuable for estimating ship resistance in calm waters. However, their application in dynamic, wave-influenced environments is limited. Therefore, this study emphasizes CFD-based simulations, which provide more accurate predictions for ship behavior in complex sea states, particularly for MASS in restricted waters.

2. Methodology

This section presents the methodologies employed in this research, covering numerical simulations, experimental validation, and mathematical modelling.

The study focuses on a ship with a length ranging from 100 to 150 meters, representing a typical size for Maritime Autonomous Surface Ships (MASS) operating in restricted waters. The CFD simulations were conducted using STAR-CCM+ software, with the computational domain designed to capture the essential hydrodynamic interactions. The domain was sufficiently large, extending five ship lengths in all directions from the model, to minimize the effects of boundary reflections in both calm water and regular wave conditions. This low blockage ratio setup was crucial for accurate flow predictions. Figures 1 and 2 illustrate the computational domain and the overset mesh used to accommodate the ship's motions, respectively.

The meshing strategy was developed to ensure high accuracy while maintaining computational efficiency, resulting in approximately 5.6 million cells. The average non-dimensional wall distance (y+) was controlled around 50, following the recommendations of the ITTC 7.5-03-02-03 guidelines for CFD simulations of full-scale ships (ITTC, 2011). A time step of 0.001 seconds was chosen to resolve the unsteady flow characteristics, based on best practices and prior work on full-scale unsteady flow simulations (Tezdogan et al., 2016).

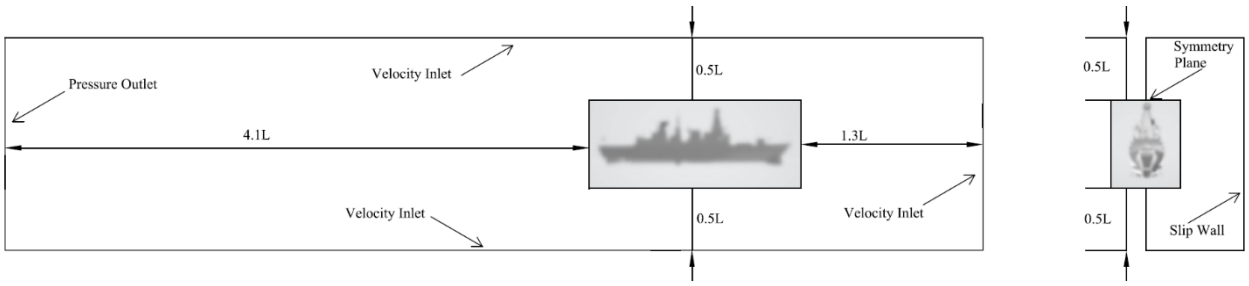

Figure 1 Dimensions and boundary conditions of the background domain of the computational domain (sample ship) (L: Ship Length)

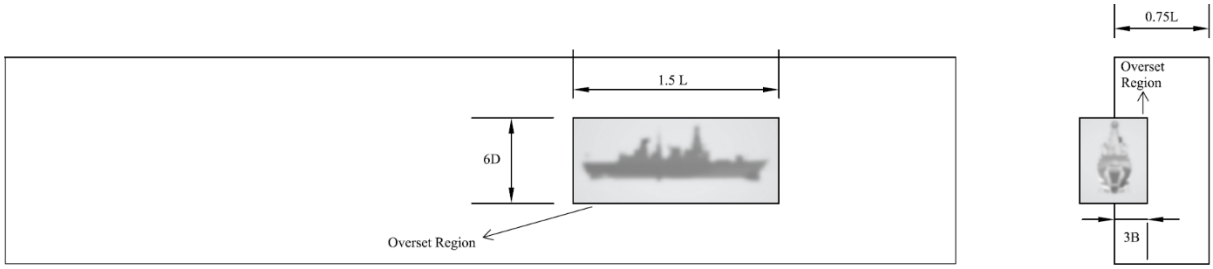

Figure 2 Dimensions of the overset domain of the computational domain (Sample Ship) (B: Beam of the Ship, D: Ship Depth)

2.1. CFD Simulation Setup

The CFD simulations were carried out using STAR-CCM+, focusing on evaluating hydrodynamic behavior in two distinct conditions: flat wave (calm water) and regular wave (for added resistance). These simulations were conducted in the Boldrewood Innovation Towing Tank at the University of Southampton, with dimensions of 138 meters in length, 6 meters in width, and 3.5 meters in depth. The towing tank environment was modeled to closely replicate experimental conditions, providing a benchmark for numerical results and validating the computational models used in this study.

2.2. Numerical Methods: Holtrop-Mennen and Thin-Ship Theory

- **Holtrop-Mennen Method:** The widely adopted empirical model developed by Holtrop (1977), which provides a statistical analysis of performance test results, was utilized in this study to estimate ship resistance in calm water. This method, based on extensive model test data, offers a general estimation of resistance components, including both frictional and residuary resistance. In this study, the method was applied to predict ship resistance over a range of speeds, from 0 to 25 knots, and for various draughts (4.8 m to 5.8 m). While the Holtrop-Mennen method is effective for initial approximations, its accuracy in dynamic environments, such as waves, is limited due to the absence of wave-induced resistance factors. The Maxsurf software was used to calculate the total resistance across a range of ship speeds, and the accuracy of this method was validated by comparison with Computational Fluid Dynamics (CFD) results and towing tank tests.
- **Thin-Ship Theory:** Michell's Thin-Ship Theory (Michell, 1898), which provides an analytical approach for calculating wave resistance, was also applied in this study. This method relies on assumptions regarding the slenderness of the ship's form and was implemented using MATLAB for the same draught and speed range as the Holtrop-Mennen method. Thin-Ship Theory is particularly useful for analyzing wave resistance at lower speeds but demonstrates limitations in more complex hydrodynamic environments due to its linear assumptions (Tsubogo, 2014). The comparison of results across different draughts (4.8 m to 5.8 m) highlighted its strengths in the lower draught ranges, where wave-making effects are minimal.

2.3. CFD Simulations

Two distinct CFD simulations were conducted as part of the hydrodynamic analysis:

2.3.1 Flat Wave (Calm Water): In calm water conditions, simulations focused on the baseline resistance, similar to towing tank experiments without external wave forces. The goal was to isolate the inherent resistance components of the ship model at various speeds, specifically at Froude numbers of 0.22 and 0.36.

2.3.2 Regular Wave (Added Resistance): Regular wave conditions were modeled to study the added resistance due to waves at varying frequencies, ranging from 0.45 to 0.75 Hz. This range, corresponding to wavelength-to-ship length ratios (λ/L) from 1.82 to 0.65, was selected to simulate typical wave conditions experienced in operational environments. These simulations are currently ongoing and will provide crucial insights into the ship's performance in dynamic sea states.

2.4. Towing Tank Tests

Two sets of towing tank experiments were performed to validate the numerical and CFD results:

2.4.1 Flat Wave (Calm Water) Experiments: Resistance tests were conducted at two Froude numbers (0.22 and 0.36) for a single draught of 5.2m. These experiments served as a benchmark for validating the CFD flat wave simulations and the empirical predictions from the Holtrop-Mennen and Thin-Ship methods.

2.4.2 Regular Wave (Added Resistance) Experiments: The added resistance in waves was measured for wave frequencies between 0.45 Hz and 0.75 Hz, matching the conditions used in the CFD simulations. This data will be crucial for validating the CFD model's performance in predicting added resistance and other hydrodynamic effects.

3. Results & Discussions

The results from the numerical methods, CFD simulations, and towing tank experiments were compared to assess their accuracy and reliability for resistance predictions. The primary findings are summarized below:

Numerical Methods Evaluation:

The numerical analysis using both the Holtrop-Mennen and Thin-Ship Theory methods provided an initial estimate of resistance under calm water conditions. As shown in Figure 3, the Holtrop-Mennen method produced reliable predictions at lower speeds, closely following the CFD results up to 15 knots. However, the Thin-Ship Theory displayed significant deviations at higher speeds, particularly beyond 20 knots, due to its linearized assumptions about wave resistance. These deviations were most pronounced for draughts above 5.2 m, where wave interactions had a more substantial impact on resistance.

CFD Simulations:

At this stage, we have completed the CFD simulations for flat wave (calm water) conditions. As illustrated in Figure 3, preliminary results suggest a close correlation with the experimental data for the 5.2 m draught case at Froude numbers of 0.22 and 0.36. However, we are still awaiting the completion of the regular wave simulations to compare the added resistance predictions with experimental data and empirical methods. These ongoing simulations will help further refine the accuracy of the hydrodynamic model, particularly in dynamic environments.

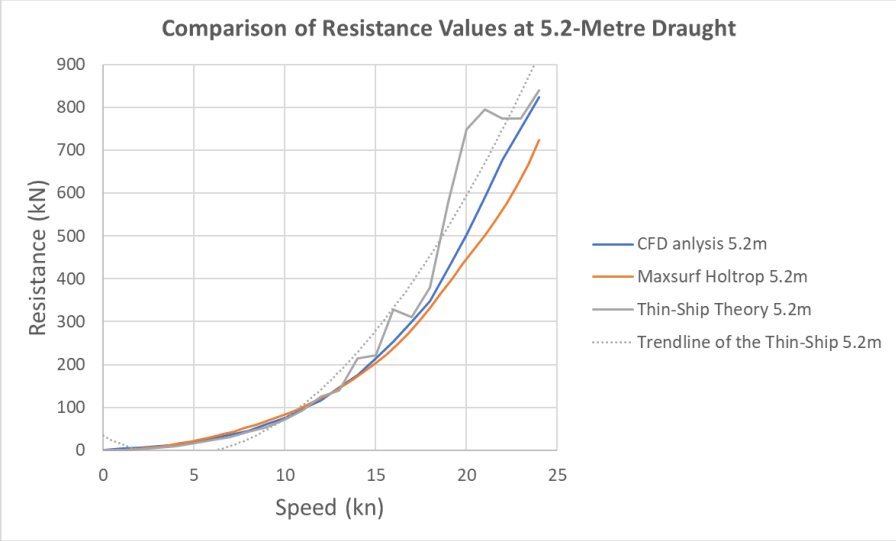

Figure 3 Resistance comparison for the 5.2m draught case across different methods.

4. Conclusions and Future Work

Conclusions:

The comparison of empirical methods and CFD simulations under calm water conditions showed that while traditional methods like Holtrop-Mennen and Thin-Ship Theory are useful for initial resistance estimates, they lack accuracy in complex hydrodynamic environments. The CFD simulations, validated by towing tank experiments, provided a more robust prediction of ship resistance and will serve as the foundation for further control model development.

Future Work:

Future research will focus on completing the CFD simulations for regular wave conditions and comparing the results with experimental data. Additionally, the Double Body Method will be explored as a potential tool to enhance the accuracy of resistance predictions, particularly in separating viscous resistance from wave-making components. This method, as discussed by Larsson and Raven (2010), will be applied to analyze the form factor more precisely, especially in cases where non-linear hydrodynamic interactions are significant. Incorporating the Double Body Method is expected to improve the overall understanding of ship resistance, particularly for bluff body forms.

The next phase of this research will focus on completing the regular wave condition CFD simulations and comparing them with experimental results. Once these comparisons are validated, the results will also be compared with empirical methods to assess the accuracy of added resistance predictions. Future work will extend this analysis to irregular wave conditions using established spectral methods, such as JONSWAP or ITTC, to simulate more realistic sea states.

Additionally, the research will incorporate **Model Predictive Control (MPC)** strategies for developing a collision avoidance system that complies with the International Regulations for Preventing Collisions at Sea (COLREGs). Drawing on the work of Fossen (2017), particularly in the field of adaptive control for marine vehicles, the control model will be designed to predict and adjust ship trajectories in real time based on wave-induced disturbances and proximity to other vessels.

4.1 Limitations

- **Thin-Ship Theory:** As a linearized theory, it fails to account for the non-linear wave interactions that become significant at higher speeds or in short wavelength conditions, resulting in underestimation of resistance.
- **Holtrop-Mennen:** This method, while effective at lower speeds, struggled with accurate resistance predictions in waves due to its empirical nature and lack of wave resistance components.
- **CFD Simulations:** Although accurate, the CFD simulations were computationally expensive, particularly in terms of meshing and convergence times. Further optimization of the meshing strategy may be necessary to reduce computational costs for future simulations.

4.2 Recommendations

- Conduct further experimental analysis, particularly in irregular waves, to enhance the robustness of the CFD model.
- Refine the meshing strategy in CFD simulations to improve computational efficiency.
- Develop and implement the MPC-based control model for autonomous collision avoidance.
- Investigate the integration of sensor data with CFD simulations for real-time collision avoidance system validation.
- Include additional ship motions such as heave, roll, and pitch in the future analysis to fully capture the ship's dynamic response.

5. Acknowledgements

The authors would like to thank the University of Southampton for supporting this research through the FEPS scholarship and Dean bursary. Results were obtained using the Iridis High-Performance-Computer of the University of Southampton.

6. References

Fossen, T.I. *Guidance and Control of Ocean Vehicles*. John Wiley & Sons, 1994.
Fossen, T.I. "Wave based adaptive control of unmanned surface vehicles subject to disturbances and model uncertainties." *Ocean Engineering*, 197, 106924, 2020.
Guo, W., Li, Y., Fossen, T.I., et al. "Wave based adaptive control of unmanned surface vehicles subject to disturbances and model uncertainties." *Ocean Engineering*, 197, 106924, 2020.
Holtrop, J. "A Statistical Analysis of Performance Test Results." *International Shipbuilding Progress*, February 1977.
ITTC. *Recommended Procedures and Guidelines: Testing and Extrapolation Methods*.
Kim, Daejeong, Soonseok Song, Byongug Jeong, Tahsin Tezdogan, and Atilla Incecik. "Unsteady RANS CFD simulations of ship manoeuvrability and course keeping control under various wave height conditions." *Ocean Engineering*, 2022.
Larsson, L., & Raven, H.C. *Ship Resistance and Flow*. The Netherlands: Society of Naval Architects and Marine Engineers, 2010.
Tezdogan, T., Demirel, Y.K., Incecik, A., and Turan, O. "Full-scale unsteady RANS CFD simulations of ship behavior and performance in head seas due to slow steaming." *Ocean Engineering*, 2019.
Tsubogo, T. "Michell's Thin Ship Theory Considering the Gradient of Ship Form in Depth Direction." *Journal of the Japan Society of Naval Architects and Ocean Engineers*, 2014.
Turnock, S. *Resistance and Propulsion*. University of Southampton.
Wang, Y., Sørensen, A.J., Cui, W., and Fossen, T.I. "Wave induced roll motion reduction of a monohull vessel using model predictive control." *Ocean Engineering*, 136, 79-87, 2017.

26th Numerical Towing Tank Symposium (NuTTS)
23-25 October 2024
Mülheim a.d. Ruhr, Germany

Ship hydrodynamics in steady circular motion in shallow waters – Experience from the SHINING workshop

Guillermo Chillcce*, Lahbib Zentari†, Bettar Ould el Moctar*
†Bundesanstalt für Wasserbau (BAW), Karlsruhe/Germany
*University of Duisburg-Essen, Duisburg/Germany,
guillermo.chillcce@uni-due.de

1 Introduction

Water levels on major European rivers are expected to remain low for prolonged periods, as observed in the summers of 2018 and 2022. These conditions negatively affect inland navigation by increasing the risk of grounding and reducing the manoeuvrability of inland vessels. In this context, navigability analyses play a key role in supporting the development of safety-oriented navigation policies.

Currently, most navigability analyses are based on mathematical manoeuvring models. These models use hydrodynamic coefficients derived from captive tests in experimental facilities or from simulations of captive manoeuvring tests using RANS-based solvers. Consequently, the accuracy of navigability analyses is highly dependent on the physical fidelity of the underlying mathematical manoeuvring model. This is particularly true when considering manoeuvring in shallow or confined waters.

RANS-based solvers have proven effective in calculating hydrodynamic forces and moments on a ship's hull in deep water, challenges arise when considering ship hydrodynamics in extremely shallow water. In order to evaluate the reliability and accuracy of RANS-based methods for the calculation of hydrodynamic forces in shallow and extremely shallow inland waterways, the SHINING research group was established, consisting of five European institutions: the German Federal Waterways Engineering and Research Institute (BAW), the Development Centre for Ship Technology and Transport Systems (DST), Flanders Hydraulics (FH), the Maritime Research Institute Netherlands (MARIN) and the University of Duisburg-Essen (UDE). The common goal is to deepen the understanding of shallow water hydrodynamics by applying computational methods to benchmark the hydrodynamic forces acting on a typical inland waterway vessel manoeuvring in shallow water. This paper presents two representative computational methods from the SHINING 2023 workshop and investigates the hydrodynamics of an inland waterway vessel during a steady circular motion in shallow water.

2 Test case

We conducted the study using a typical inland waterway vessel that travels on the river Rhine. The hull geometry was made publicly available by BAW in Mucha et al. (2017). The vessel is characterized by a high block coefficient of 0.92 and sharp edges at the stern. The vessel is equipped with two ducted propellers and twin fish-tail rudders behind each propeller. Table 1 lists the main particulars of the ship. In this study, only the bare hull was considered in order to reduce the complexity of the hydrodynamic problem.

Table 1: Main particulars of the test inland waterway cargo vessel

Main particulars	symbol	full-scale	units
Length between perpendiculars	L_{pp}	135.0	m
Breadth	B	14.45	m
Draft	T	3.5	m
Block coefficient	C_b	0.92	-
Mass	M	4984.6	t

3 Computational procedure

We compared two computational approaches, both implemented in the commercial flow solver STAR-CCM+, aimed at resolving the quasi-steady captive circular motion of the inland test ship, albeit using different methods. The first method aims to physically resolve the circular motion of a floating ship, as is typically conducted in model scale tests. In this approach, the problem is solved in an inertial frame, in which the numerical domain rotates with a prescribed rotation rate r, see Figure 1 left sketch. The ship, located at the centre of the numerical domain, is free to heave and pitch using the overset grid technique. Additionally, the VoF method is used to account for air and water phases, with interface sharpness enhanced using the HRIC scheme. Closure to the system equations is provided by the k-omega-SST model by Menter et al. (1994) with curvature correction. The governing equations are solved in a segregated manner using the SIMPLE algorithm with 10 outer iterations. The time step is chosen to keep the Courant number on the free surface below 0.5.

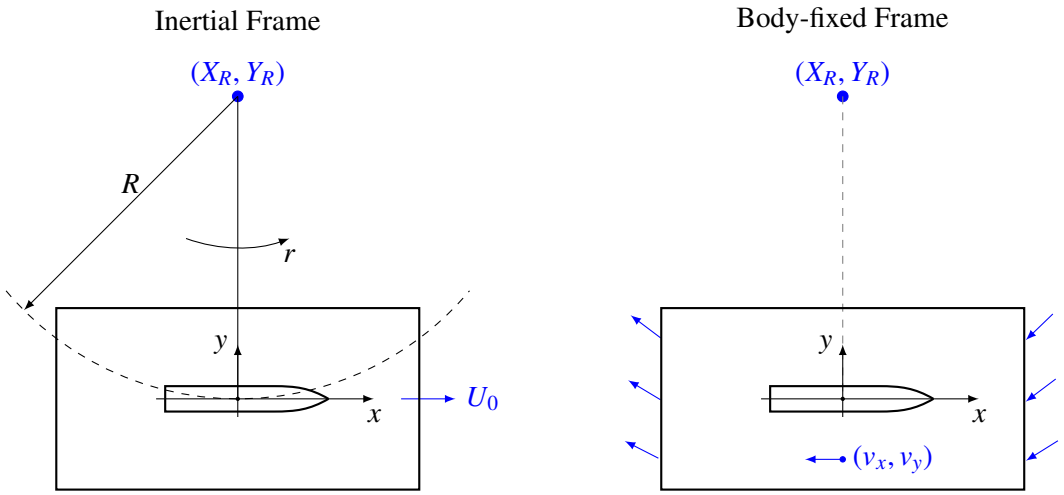

Fig. 1: The steady circular motion can be calculated in an inertial frame (left) or in a body-fixed frame (right). In the inertial frame, the numerical domain rotates at a constant rotation rate around the centre of rotation. In the body-fixed frame the numerical domain does not move but rather the water flows around the ship.

The second method solves the problem in a body-fixed frame, see Fig. 1 right sketch. Since ship manoeuvring in shallow water occurs at low speeds, a simplification has been made to consider only the water phase with a steady-state method (double-body), where the RANS equations are solved in a segregated manner. Closure is provided by the Reynolds Stress Model (Lardeau and Manceau (2014)), which gives better results for bluff bodies in restricted waters. Circular motion is induced by adding source terms to the momentum conservation equation to account for centrifugal and Coriolis forces.

In this method, the velocity vectors within the domain vary based on the ship's distance from the centre of rotation, located outside the vessel. The computational domain has a length of $4.2L_{pp}$ and a width of $2.8L_{pp}$. All boundaries are assigned inlet conditions, while the bottom surface has a relative velocity equal to that of the velocity vectors. Both the ship and the bottom are treated with a no-slip wall condition. Hydrodynamic forces are calculated by integrating pressure and shear stresses over the ship's surface. A novel approach to account for sinkage was also implemented. This method consists of solving the vertical equilibrium forces iteratively until convergence. The non-dimensional rotation rate, r', Radius of rotation R, length between perpendiculars L_{Lpp} and ship speed U_0 are related by the following formulas:

$$r = \frac{r' U_0}{L_{pp}}, \quad r' = \frac{L_{pp}}{R}, \quad R = \frac{U_0}{r} \tag{1}$$

Both methods resolve the same physics and produce similar results, though with significant differences in computational efficiency.

4 Results and Discussion

In this section, we present the forces obtained by the presented methods, additionally we added the results from the SHINING 2023 workshop, with the author's permission. Figure 2 plots the hydrodynamic forces and moments acting on the hull during a steady circular motion for three water depth-draft ratios: $h/T = 3.0, 1.5, 1.2$. The calculations were performed by varying the nondimensional turning rate r'. For a ship in steady circular motion, the yaw moment is the most important quantity. The magnitude of the yaw moment is well captured by the different methods and a small scatter of the values is observed for most of the methods. For the sway force, slightly different slopes are observed for the different methods, but the magnitude of this component is relatively small. The surge force shows the larger scatter. Although the different calculations show similar trends, the offset between the lines can be up to 20%. This may indicate a higher sensitivity to the numerical setup, in particular to the turbulence model. In fact, the surge force is equally dependent on accurate predictions of pressure and shear, while the sway force and yaw moment are pressure-driven.

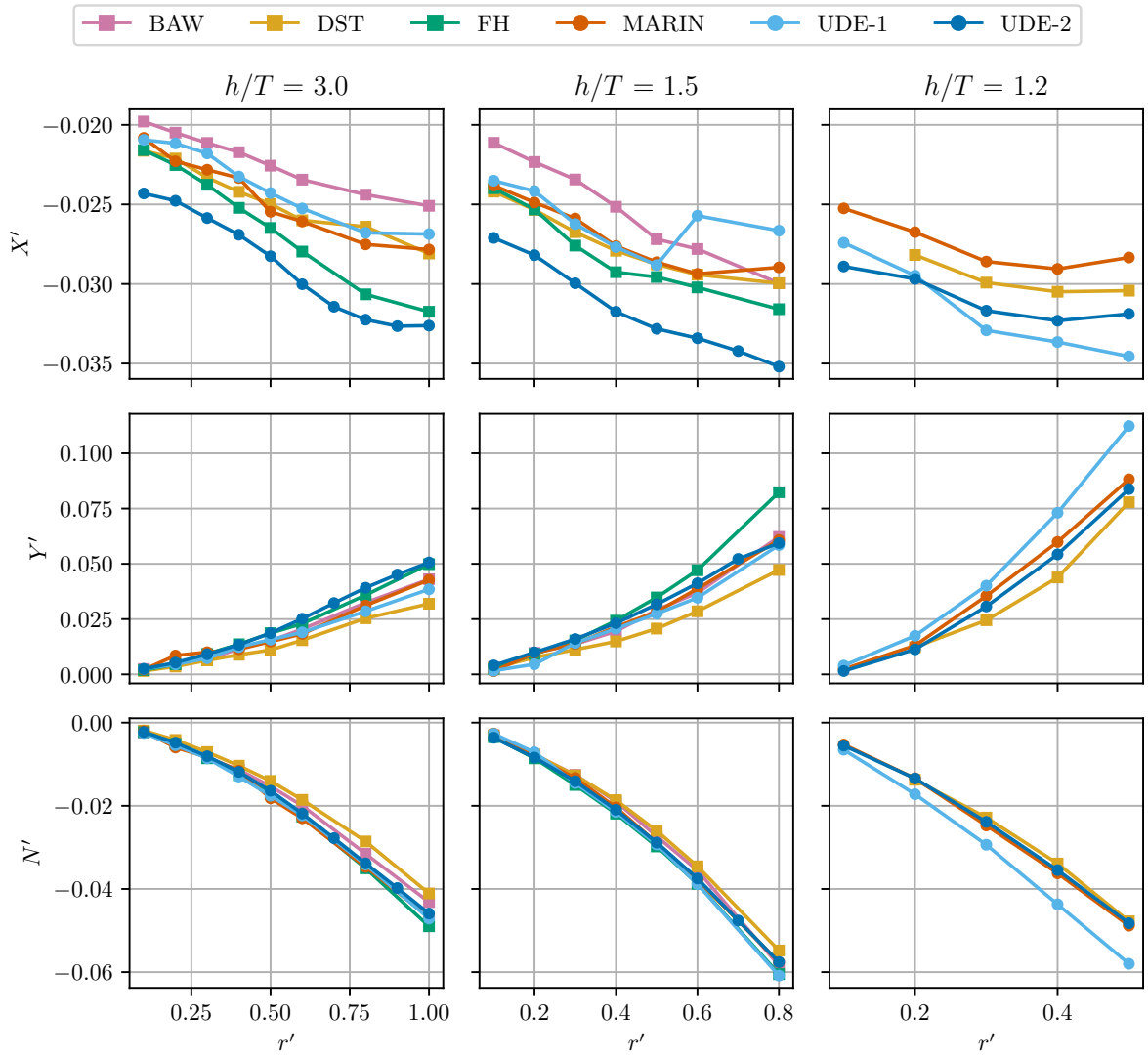

Fig. 2: Comparison of hydrodynamic surge force, sway force, yaw moment and sinkage of the reference inland waterway vessel during circular motion for $h/T = 3.0$ (left), for $h/T = 1.5$ (centre), and for $h/T = 1.2$ (right). Each line correspond to a unique method present at the SHINING 2023 workshop (Results used with the permission of the institutions).

Figure 3 provides a statistical overview of the numerical results presented in Fig. 2. Average values for forces and moments were calculated from all simulations and are represented by a red line, with the red shaded area indicating the standard deviation between the numerical submissions. In addition, the plots include two averages related to two turbulence models. The green line represents the average of the methods using SST k-ω (four methods), while the blue line represents the average of the methods using Reynolds stress models (two methods). The results show that the different turbulence models give comparable results for the sway force and the yaw moment. However, the surge force is influenced by the turbulence model, confirming thus the hypothesis stated above. The SST k-ω model gives relatively lower surge forces than the RSM model, especially for the deeper conditions.

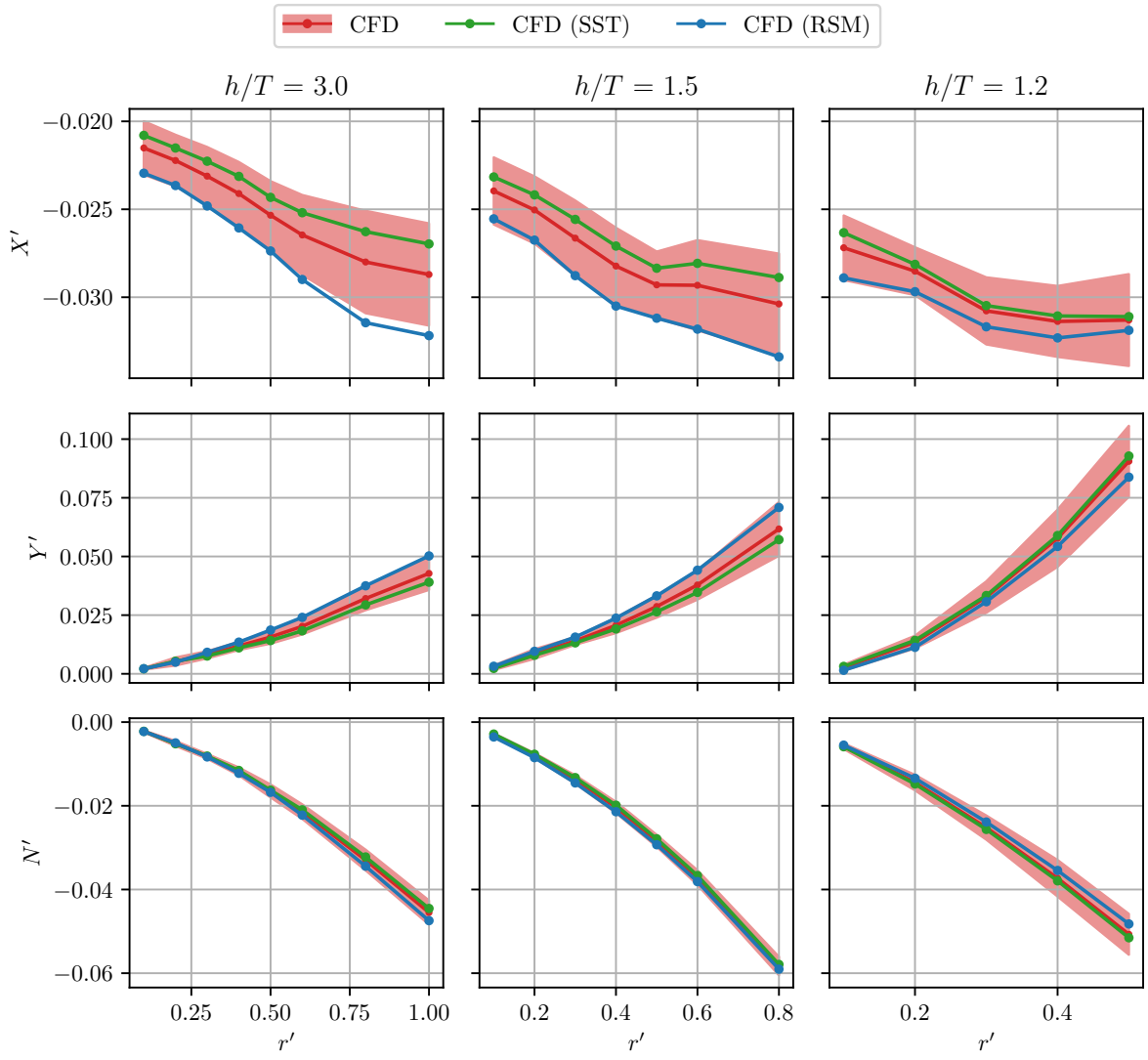

Fig. 3: RANS-based mean hydrodynamic forces, moments and sinking calculated from all submissions (red lines) with their respective standard deviations (reddish area). In addition, the submissions were divided into two turbulence modelling schemes, $k\omega$-SST (green lines) and RSM (blue lines). In the left column for $h/T = 3.0$, in the middle column for $h/T = 1.5$ and in the right column for $h/T = 1.2$.

As an example of the complexity of the flow, Figure 4 shows the vorticity in transverse planes along the ship's longitudinal direction. As seen, a vortex is formed at the starboard bow of the ship and travels downstream through the starboard side of the ship, passes under the bottom of the hull and continues to travel through the port side at the stern of the ship. To see how the turbulence modelling affects the vorticity around the hull, Figure 5 shows the vorticity at plane $x = -0.45Lpp$ computed with two

turbulence models: k-ω SST and RSM. The high level of vorticity under the hull correlates well between both modelling methods. However, the intensity of the RSM turbulent model predicts higher vorticity under the hull.

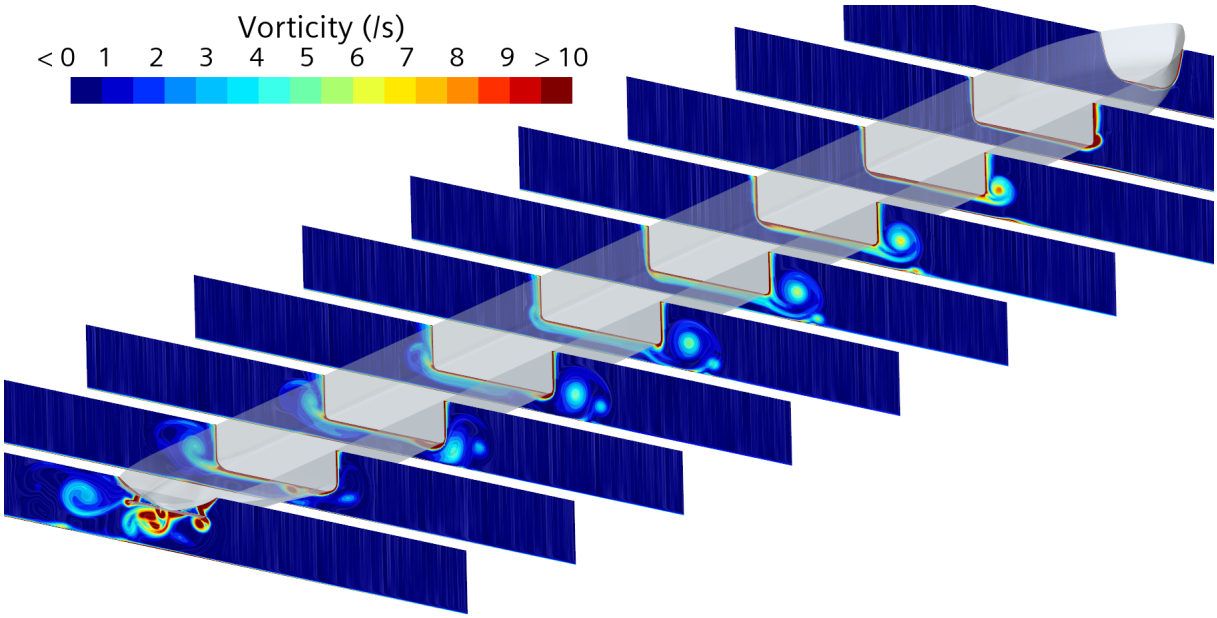

Fig. 4: Vorticity around the hull during circular steady motion at h/T=1.5 and $r' = 0.5$ using UDE-2 method. We can see how a vortex is formed at the starboard bow and travelling downstream along the starboard side

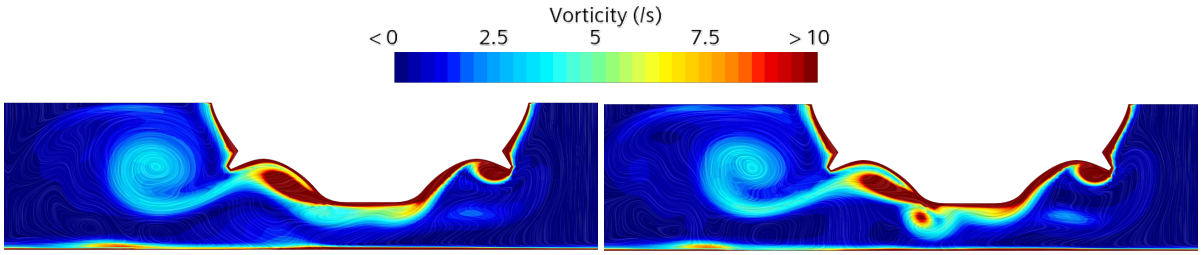

(a) k-ω SST (b) RSM

Fig. 5: Vorticity at plane $x = -0.45Lpp$ for the case $U_0 = 0.556\,\mathrm{m/s}$, $r' = 0.5$, $h/T = 1.5$.

Acknowledgements

The results presented in this paper originated from the SHINING research group members. We thank DST, FH, and MARIN for kindly allowing us to use their results.

References

Mucha, Philipp; El Moctar, Ould; Dettmann, Thorsten; Tenzer, Matthias. (2017). Inland waterway ship test case for resistance and propulsion prediction in shallow water. *Ship Technology Research* **64**, 106-113. DOI: 10.1080/09377255.2017.1349723.

Menter, Florian R.(1994). Two-equation eddy-viscosity turbulence models for engineering applications. *AIAA Journal* **32**, DOI: 10.2514/3.12149.

Lardeau, S; Manceau, Remi. (2014). Computations of complex flow configurations using a modified elliptic-blending Reynolds-Stress model. *10th International ERCOFTAC Symposium on Engineering Turbulence Modelling and Measurements*. Marbella, Spain. hal-01051799.

Development and validation of underwater radiated noise analysis method using computational fluid dynamics simulations

Genís Masjoan Vallés [1,2], Juha Tanttari [1], Ville Vuorinen[2]
[1]Elomatic Oy, Finland, [2]Aalto University, Finland
genis.masjoanvalles@elomatic.com

1 Introduction

Several studies have shown that Underwater Radiated Noise (URN) produced by marine traffic have a relevant negative impact for marine wildlife, especially mammals [1]. Although IMO guidelines aimed to monitor and reduce noise emission are currently non-mandatory a rising interest to address this issue has appeared. Consequently, stakeholders in marine industry are seeking to promote strategies and innovative solutions to decrease underwater noise emission. To develop such solutions, it is crucial to have the possibility to efficiently and accurately predict the production and radiation of underwater noise. URN can originate from various sources related to the vessel operation but the most relevant sources to the acoustic signature are often the propeller wake and cavitation [2].

In this work, a CFD method for predicting noise production and radiation coming from cavitating flow has been carried out. The method aims to be suitable for its use in industrial design, what imposes that it must be efficient in terms of computational demand. The method has been validated and the results analyzed in two cases posing different flow patterns. The first case consists in a NACA0009 Hydrofoil with a chord of 0.15m and a wingspan of 0.025m. The second case consists in a five bladed model scale propeller of 0.22m in diameter, commonly known as Princess Royal propeller. Both cases were analyzed under cavitation conditions. The method uses the Ffowcs Williams-Hawkings (FW-H) acoustic analogy for the prediction of sound production and radiation. The models were selected with the aim of finding a compromise solution between accuracy and computational demand. The effects of using impermeable or permeable noise emitting surfaces has been investigated, revealing a higher precision of the permeable surfaces in predicting high-frequency noise. The effect of the shape of the permeable surface has also been detected to have significant impact, especially for the pseudo-loading sources at high frequencies. The models used have been proven to be accurate enough to give a good indication of noise produced by cavitating flow.

This work was carried out in the context of Genís Masjoan's Master thesis for Aalto University, with funding from Elomatic Oy.

2 Methodology

The flow consists in two incompressible and isothermal fluids having water as the primary phase and vapor as the secondary phase, appearing as a result of cavitation. The software used for fluid modelling is StarCCM+. The Navier-Stokes equations are solved using the Segregated flow solver with the pressure-velocity coupling handled by the SIMPLE algorithm.

The multiphase flow is modelled by the Eulerian Volume of Fluid method (VOF) [3]. The phase change is accounted by the mass-transfer model Schnerr-Sauer which is based in a simplified version of the Rayleigh-Plesset equation to obtain the cavitation bubble growth velocity. The need for accurate turbulence modelling to capture complex cavitation patterns requires the use of the hybrid RANS-LES model Detached Eddy Simulation (DES) [4], providing good accuracy while maintaining the computational cost within an acceptable range. The volume fraction transport convection term is discretized using the High-Resolution Interface Capturing scheme (HRIC) allowing to capture the sharp interface. The convective term for the rest of the transported variables is discretized using Hybrid-BCD scheme which is based in the central differencing scheme and the second-order upwind scheme, what provides good accuracy and stability respectively. The temporal discretization is done with a second-order implicit scheme.

The prediction of noise production and radiation is achieved by the Ffowcs Williams-Hawkings acoustic analogy [5]. This analogy extends Lighthill's acoustic analogy [6] and Curle expansion [7] to not only include the noise produced by turbulence and static solid boundaries, but also include the effects of surfaces in motion. Through this analogy the acoustic pressure, p', felt at

arbitrary receivers in the far-field is calculated based in the noise sources obtained from the flow solution in the near-field. The acoustic pressure at the receiver is expressed as,

$$p'(x,t) = p'_T(x,t) + p'_L(x,t) + p'_Q(x,t)\,. \tag{1}$$

Showing it can be decomposed according to the noise source type. The noise produced by the surfaces consists in the thickness pressure, p'_T,and the loading pressure, p'_L, which are produced by the monopoles and the dipoles respectively. The noise produced by the movement of the fluid in the region surrounding the solid body is the quadrupole pressure, p'_Q, generated by turbulence. The acoustic pressures are calculated in the receivers by integrating the noise sources over the surface, S, or volume, V, where they are being produced,

$$p'_T(x,t) = \frac{1}{4\pi}\left(\left(\frac{\partial}{\partial t}\right)\int_S \left[\frac{Q}{r(1-M_r)}\right]_{ret} dS\right), \tag{2}$$

$$p'_L(x,t) = \frac{1}{4\pi}\left(\left(-\frac{\partial}{\partial x_i}\right)\int_S \left[\frac{L_i}{r(1-M_r)}\right]_{ret} dS\right), \tag{3}$$

$$p'_Q(x,t) = \frac{1}{4\pi}\left(\left(\frac{\partial^2}{\partial x_i \partial x_j}\right)\int_V \left[\frac{T_{ij}}{r(1-M_r)}\right]_{ret} dV\right), \tag{4}$$

where r is the position of the receiver, M_r is the Mach number, and the subindex *ret* indicates the retarded time to account for the time needed for the sound wave to travel from the production location to the receiver. The source terms creating the acoustic waves consist in the monopole strength, Q, for Equation 2. It represents the volumetric changes of the flow due to the presence of the body surface. In Equation 3 the Loading term, L_i, accounts for the net force after the momentum fluctuation introduced by a solid object immersed in the fluid. For Equation 4 the Lighthill Stress Tensor, T_{ij}, accounts for the internal stress in the fluid due to non-uniform distribution of vorticity. These sources are obtained after a flow solution is reached at each time step.

Another approach, developed by Di Francescantiono [8], is by considering that the noise is being produced in permeable surfaces encasing the near-field region where the relevant flow events producing noise are taking place. This approach saves computational time and memory as Equation 4 is disregarded, avoiding the volume integral. The pseudo-thickness and pseudo-loading terms resulting from Equations 2 and 3 include monopoles, dipoles, and quadrupoles. This approach is unable to identify the precise location where the sources are being produced. The FW-H equations are solved using the Farrasat 1A formulation [9]. Post-processing is needed to present the Sound Pressure Level (SPL) in decibels (dB). To do so, the acoustic pressure signal is translated to the frequency domain through FFT and a power level is applied with a reference pressure of 1 μPa in case the transmitting fluid is water.

The first test case consists in a NACA0009 Hydrofoil with a chord of 0.15 m, a wingspan of 0.025 m, and an angle of attack of 9º. The reference data for this case is taken from the paper by Lidtke et al. [10]. The inlet velocity is set to 6.97 m/s, the gauge pressure to 29 kPa, and the water saturation pressure is 2970 Pa to have a cavitation number of 0.53 and a Reynolds number of 1045500. The mesh for this case consists in a 1.9 million hexahedral cell mesh with a prism layer designed to achieve a y+ ≤ 1.

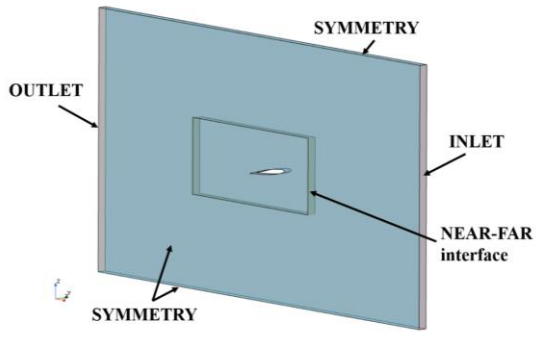

Figure 1. NACA0009 Hydrofoil domain boundaries. Note the near and far field interface delimiting the noise region.

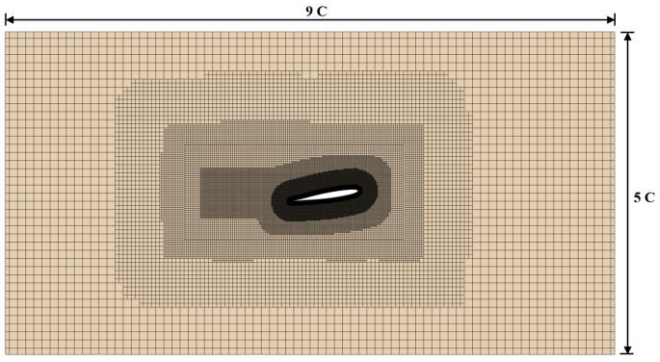

Figure 2. NACA0009 Hydrofoil mesh.

The second test case consists in the five bladed model scale Princess Royal (PR) propeller with a diameter of 0.22 m and a constant rotation rate of 35 rps. The results are validated against the experimental data contained in the paper by Tani et al. [11]. The inlet velocity is set to 3.08 m/s and the gauge pressure is found to be 35 kPa. The water saturation pressure is 3171 Pa to have a cavitation number of 1.311 and a Reynolds number of 2187337. The mesh for the propeller case consists in a 41.8 million polyhedral cell mesh in a cylindrical domain with a prism layer aimed to achieve a $y+ \leq 1$. To obtain the necessary refinement to capture the blade tip cavitation extending downstream a vorticity based Adaptive Mesh Refinement (AMR) is used.

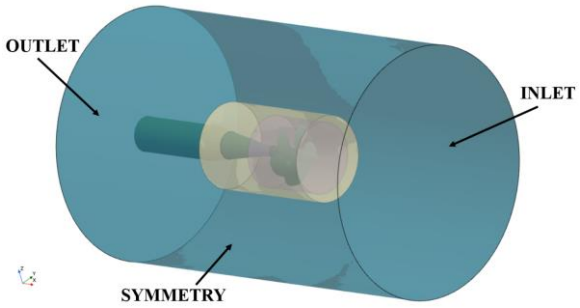

Figure 3. PR domain boundaries. The yellow region corresponds to the noise region and the purple region corresponds to the rotating region.

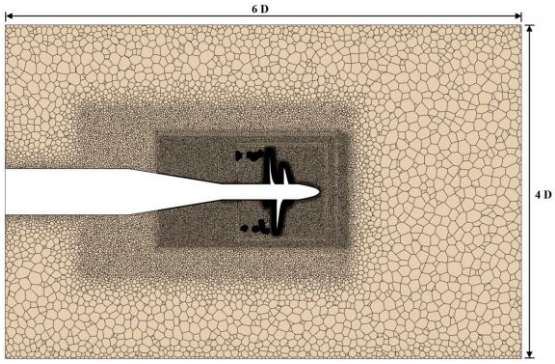

Figure 4. PR case mesh. Note the fine refinement produced by the AMR in the wake of the propeller.

3 Results and discussion

The evolution of the lift coefficient and the total volume of steam in the domain are compared against the reference data [10], being the mean in the reference 0.8761, and 0.8865 in the simulation. The oscillation of the lift coefficient shows a similar trend both in amplitude and periodicity (Figure 5). In the same way, the total steam volume shows a good agreement in simulation and the reference data (Figure 6). These both figures suggest that the cavitation shedding process is being correctly simulated, implying that the main flow event influencing the noise production is accurate.

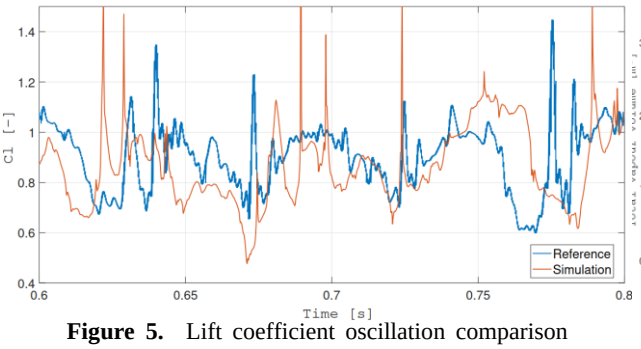

Figure 5. Lift coefficient oscillation comparison showing similar oscillation in period and amplitude.

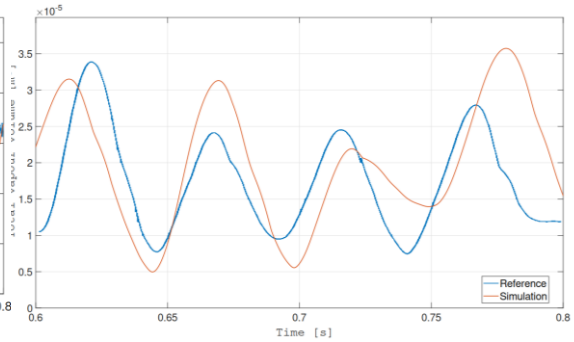

Figure 6. Comparison between the total volume oscillation showing satisfactory agreement.

When observing the Hydrofoil noise mitigation with the distance (Figure 7) from the foil, the intensity of the SPL in all the receivers show good agreement with a variation of less than 5 dB with the reference data. Notable disagreement is observed in the high-frequency range where the trough of the signal appears with a deviation of around 300 Hz.

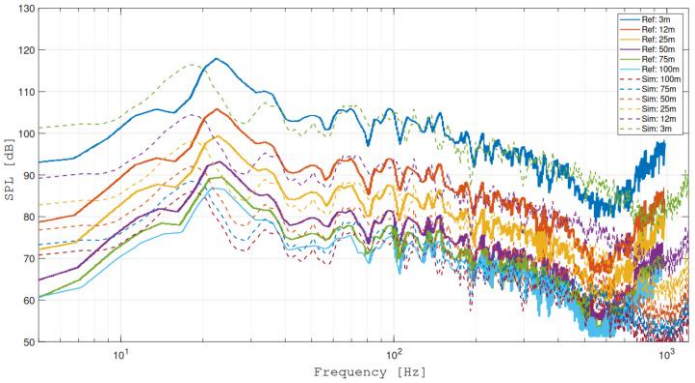

Figure 7. Comparison of the SPL measured at different distances from the source. Dashed line is the data form the simulations and solid lines is the data extracted from the reference. Accurate noise dissipation results are obtained having similar SPL decay with the increase of frequency.

The effects of using the impermeable and permeable approach have also been observed. The noise was recorded using both methods resulting in the SPL comparison observed in Figure 8. It is seen that the impermeable approach is more accurate for capturing the low frequency noise. As can be understood from the paper by Lighthill [12], the small-scale turbulence is usually responsible of high frequency noise while the large-scale turbulence is responsible for the production of low frequency noise. This implies that the low frequency sources located on the surface of the foil are better predicted when the emitting surface is the real physical boundary itself. However, in the high-frequency range the permeable approach shows better agreement as it can predict the SPL trough at 900 Hz. This can be explained since permeable approach ignores less noise sources located in the vorticity field as not only quadrupoles are detected but also other types of sources. Although the permeable approach is computationally faster and gives better results, specially in the high frequency range, it fails to show the location of the noise sources. This poses a problem when the user is interested in identifying where the noise is being produced.

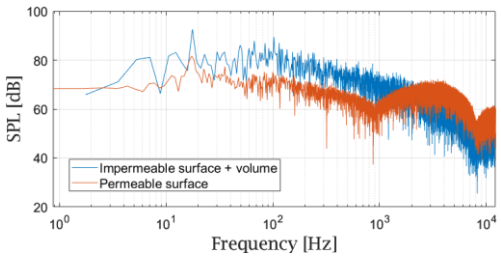

Figure 8. Comparison between the total SPL obtained through permeable and impermeable approach at the receiver located at 25 meters from above the foil.

It has been detected that the shape of the permeable surface can impact the results, two permeable surfaces have been tested, consisting in the ones seen in Figure 9. The simple permeable surface is box-like shaped while the adapted permeable surface has a rounded front to adapt to the acoustic wave formed in the front of the foil. Recording the noise at a receiver located 50 m behind the trailing edge of the foil using both surfaces result in the SPL shown in Figure 10. It is observed that in the lower to mid frequency range the SPL show relatively good agreement with both surfaces. However, notable differences are observed above 1100 Hz, especially for the pseudo-loading terms. These differences may be because the adapted surface is more capable of capturing the pressure disturbances in a more efficient and realistic way. In the case of the simple surface, the fact that it has right angles may induce some error or unrealistic sound detection. In this work, the permeable surface has not been fully optimized, but it has been proved that the design of this surface influences the results.

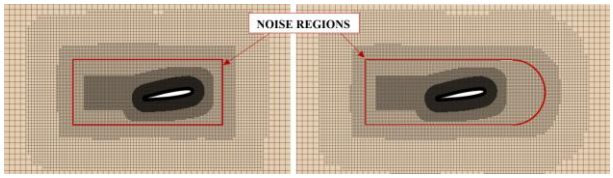

Figure 9. Permeable surfaces used, marked in red. In the left the simple geometry and in the right the adapted surface.

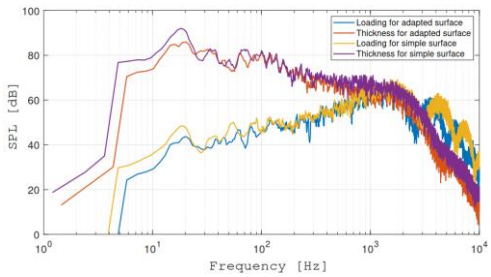

Figure 10. Comparison of the pseudo-loading and pseudo-thickness noise sources obtained from the simple and adapted permeable surfaces.

Cavitation is linked to the noise through the vorticity appearing because of the presence of vapor structures. The lift coefficient is severely affected by the shedding process, as is confirmed by the coincident oscillations of the lift coefficient (Figure 5) and the cavitation vapor volume (Figure 6). Looking at the frequency spectrum of the lift coefficient (Figure 11) it is observable how the peak frequency, which is probably close to the resonance frequency, is located at 18 Hz. Equally, for the SPL results, as in Figures 7, 8, and 10, the peak frequency is located also at 18 Hz. Therefore, it can be confirmed that noise and cavitation are coupled and that the noise is directly related to the dynamics generated by the shedding process.

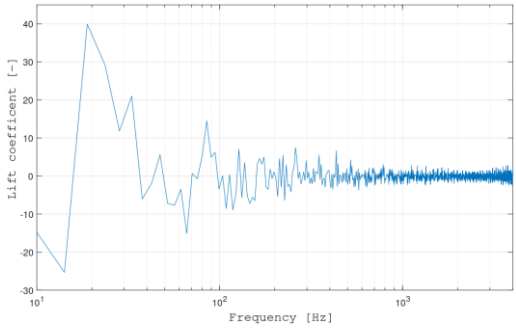

Figure 11. Lift coefficient signal in the frequency domain. Note that the peak frequency is located at 18 Hz, the same frequency as the peak noise frequency.

Another relevant effect that cavitation has in noise production are the shock waves produced by cavitation bubble implosions. In this works the use of incompressible assumption implies that the sound produced by these shock waves is not detected as the bubble implosions cannot be modelled.

The second test case has been used to test the applicability of the method to propellers and assess its accuracy against the experimental data in Tani et al. [11]. In first place, the cavitating flow solution accuracy is assessed. Obtaining the blade tip vortices was necessary to capture the vortex cavitation in the wake as this type of cavitation was expected to have relevant impact to noise. The thrust coefficient (Kt) obtained from the simulations shows an error of around 10%, being the mean Kt 0.269 in the simulations and 0.242 in the experiments. This error is considered acceptable for this work. The cavitation pattern observed in the simulations before the activation of FW-H is observed in Figure 12.

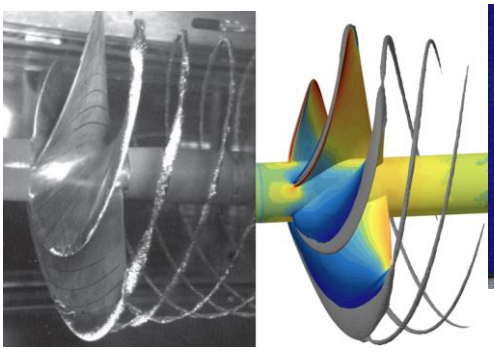

Figure 12. Comparison of cavitation appearance between cavitation tunnel experiments from [11] and from simulation with the pressure contour.

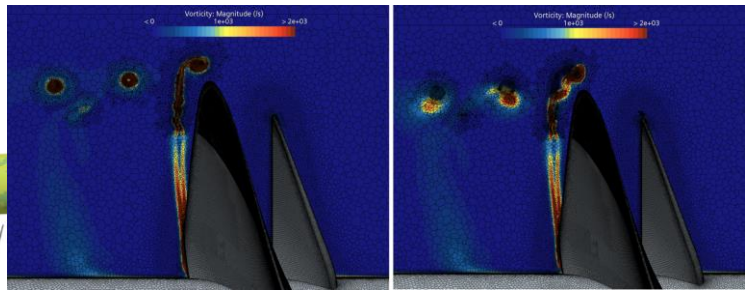

Figure 13. Misalignment of the mesh caused after the deactivation of vorticity guided AMR (right). Vorticity field is shown in the background.

In StarCCM+ AMR model is incompatible with the FW-H model, meaning that AMR must be deactivated during noise recording time steps. This caused the misalignment between the refinement and the flow solution (Figure 13), what causes the non-physical destruction of cavitation.

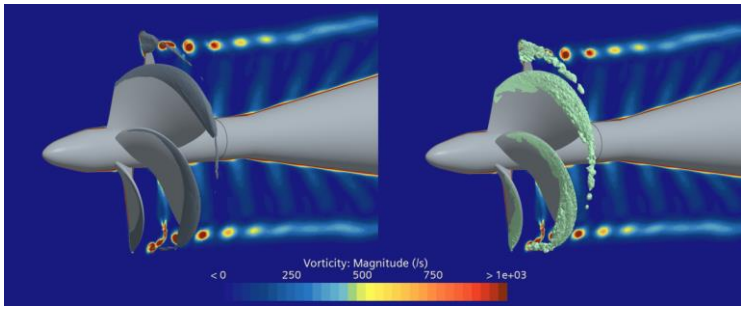

Figure 14. Cavitation (left) and main Quadrupole noise sources (right) location. The isovalue for cavitation is 0.1 and 1000 $kg/m4 \cdot s2$ for the quadrupole noise sources. The vorticity field is represented in the background. The location of cavitation and main quadruple sources coincide representing the direct relation between cavitation and noise.

This reduction in the extension of cavitation has a negative impact on sound prediction accuracy as observed in Figure 14, where it is seen how the location of cavitation coincides with the location where the main quadrupole sources are found. It can be assumed that cavitation extending downstream would also impact the high frequency noise produced by quadrupole sources.

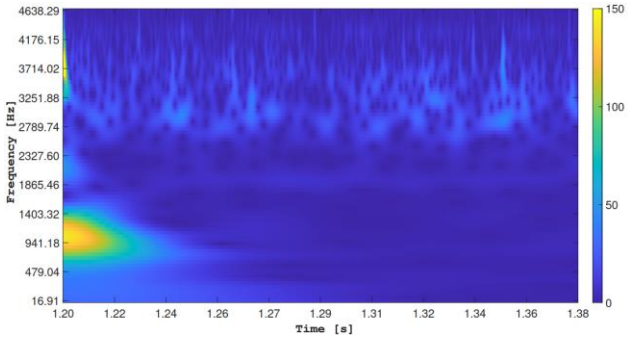

Figure 15. Wavelet analysis of the PR acoustic pressure. The colorbar at the left indicates the acoustic pressure in Pascals.

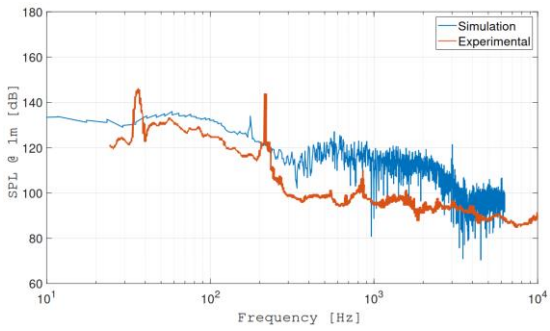

Figure 16. Comparison between simulation and experimental noise from [11] showing acceptable agreement with experimental data.

Several noise features can be linked to the flow solution when performing a Wavelet analysis to the acoustic pressure signal (Figure 15). It is noticeable the high acoustic pressure bursts in the initial time of the recording. Those are produced by the destruction of the vortex cavitation in the wake. This observation reinforces the previous comments related to the reduction of noise accuracy by the loss of tip vortex cavitation. Darker spots can be distinguished, specially at frequencies higher than 1865 Hz. These are likely produced by transient acoustic phenomena related to blade passages interacting with each other. Also, the 11th harmonic of the blade passing frequency is identifiable as a light blue line at 1925 Hz.

As have been proven, the inability of the model to maintain vortex cavitation during time implies that some unrealistic and undesired noise appear in the solution when cavitation collapses. However, the results still give a good approximation of the noise being produced. Although the results comparison with experimental data show discrepancies (Figure 16), the results are close in low-frequency range showing only a deviation between 5 and 10 dB. In higher frequencies the deviation of the results is more relevant. A deviation of approximately 20 dB is found beyond 300 Hz frequency.

4 Conclusions

The proposed method, which relies on DES for turbulence, Schnerr-Sauer for cavitation, and FW-H for noise prediction, has demonstrated its capability to provide a good indication of the SPL generated by cavitating flow. However, some discrepancies were observed, primarily due to the incompressible flow assumption and the inability to accurately capture vortex cavitation. The comparison between impermeable and permeable surface approaches revealed that the permeable approach is more accurate for detecting high-frequency noise. Additionally, the shape of the permeable surface was found to impact noise prediction, particularly for pseudo-loading noise sources at higher frequencies.

References

[1] C. Peng, X. Zhao, and G. Liu. “Noise in the sea and its impacts on marine organisms”. In: International Journal of Environmental Research and Public Health 12 (Sept. 2015), pp. 12304–12323.
[2] A. MacGillivray, L. Ainsworth, J. Zhao, H. Frouin-Mouy, J. Dolman, and M. Bahtiarian. ECHO Vessel Noise Correlations Study. Vancouver Fraser Port Authority, 2020.
[3] C. W. Hirt and B. D. Nichols. “Volume of fluid (VOF) method for the dynamics of free boundaries”. In: J. Comput. Phys 39 (1981), pp. 201-225.
[4] M.L. Shur, P.R. Spalart, M.K. Strelets, and A.K. Travin. “A hybrid RANS-LES approach with delayed-DES and wall-modelled LES capabilities”. In: International Journal of Heat and Fluid Flow 6 (2008), pp. 1638–1649.
[5] J.E. Ffowcs Williams and D.L. Hawkings. “Sound Generation by Turbulence and Surfaces in Arbitrary Motion”. In: Philosophical Transactions of the Royal Society of London. Series A, Mathematical and Physical Sciences 264 (1969), pp. 321–342.
[6] M.J. Lighthill. On sound generated aerodynamically I. General theory. The Royal Society, 1951.
[7] N. Curle. “The influence of solid boundaries upon aerodynamic sound”. In: Proceedings of the Royal Society of London. Series A. Mathematical and Physical Sciences 231 (1187 Sept. 1955), pp. 505–514.
[8] P. DiFrancescantonio. “A new boundary integral formulation for the prediction of sound radiation”. In: Journal of Sound and Vibration 202 (1997), pp. 491–509.
[9] F. Farassat. Derivation of Formulations 1 and 1A of Farassat. NASA Center for AeroSpace Information, 2007.
[10] A.K. Lidtke, S.R. Turnock, and V.F. Humphrey. “Characterisation of sheet cavity noise of a hydrofoil using the Ffowcs Williams-Hawkings acoustic analogy”. In: Computer Fluids (2016).
[11] G. Tani, B. Aktas, M. Viviani, and M. Atlar. “Two medium size cavitation tunnel hydro-acoustic benchmark experiment comparisons as part of a round robin test campaign”. In: Ocean Engineering 138 (2017), pp. 179–207.
[12] M.J. Lighthill. On sound generated aerodynamically II. Turbulence as a source of sound. The Royal Society, 1953.

CFD Analysis of Air Lubrication Effects on Ship Propulsive Performance

Arne Heuvelman, Sasha (Oleksandr) Zverkhovskyi, and Scott Terry
Damen Shipyards, the Netherlands
arne.heuvelman@damen.com

1 Introduction

Air lubrication is a promising and effective method for reducing the frictional resistance of ships. The Damen Air Cavity System (DACS) is an air lubrication system that creates stable air cavities on the bottom of a ship, thereby reducing the wetted area of the hull. In literature, it has been observed that air lubrication can also change the propulsive efficiency of a ship. Air cavities can decrease the wake fraction, (Gorbachev & Amromin, 2012). Furthermore, propeller efficiency might change due to a shift in the propeller's operating point. In the present study, the change is propulsive efficiency for ships with DACS is assessed using CFD.

2 Damen Air Cavity System (DACS)

The Damen Air Cavity System (DACS) is an air lubrication system developed by Damen Shipyards Group. Instead of injecting air bubbles underneath the ship, the system creates stable air cavities on the flat bottom of a ship. The air cavities separate the ship hull from water and by that effectively reduce the wetted area of a ship. This causes a reduction in frictional resistance. The air cavities can be created by injecting air behind a cavitator, an obstruction in the transverse direction, which separates the mean flow from the wall. The air cavities require side fences (skegs) to remain stable. (Damen Shipyards Group, 2023)

3 Method

An effective approach to assess changes in propulsive efficiency for ships with air cavities is through CFD. However, CFD modeling of air cavities is challenging and computationally expensive, primarily due to the difficulties in turbulence modeling of multiphase flow and the air-water interface in the closure region of an air cavity (Rotte et al., 2019, 2023). A simpler method at lower computational cost models air cavities as surfaces with a slip boundary condition (Zverkhovskyi, 2023). Zverkhovskyi (2023) used this method to model an inland ship with air cavities. Furthermore, Zverkhovskyi et al. (2015) showed good comparison of this method with computational results. However, this method requires a priori knowledge of the cavity shape, as air flow is not resolved. The air cavity shape can be approximated from experimental data, (Zverkhovskyi, 2014). The cavities are modeled as flat surfaces due to the large length-to-thickness ratio, with the cavitators and side fences omitted for simplicity. Added resistance of these appendages can be estimated and included separately. Literature suggests that air inflow into the propeller due to air lubrication is minimal (Mäkiharju et al., 2012), a finding supported by self-propulsion model tests at Damen. This indicates that air lubrication's impact on thrust deduction and the propeller wake field can be modeled accurately without resolving air flow.

The resistance, thrust, and nominal wake fields of two ships with different hull shapes and propulsion configurations—a cruise ship and a general cargo ship—were computed using CFD. The computations were performed for both ships, with and without air cavities. Cadence Fine Marine software was used, and vessel trim and sinkage were solved to allow dynamic equilibrium. Only half of the hull was modeled due to symmetry. Turbulence was modeled using the k-ω SST model, with wall functions resolving the boundary layer as the ships were modeled at full-scale. The computational mesh, created with Hexpress, consisted of 12.5 and 16 million cells for the cruise ship, and 9 and 14.7 million cells for the cargo ship, respectively without and with air cavities. The increased cell count for air cavities is due to higher refinement needed for surfaces between cavities. Though no boundary layer exists on the air cavities themselves due to the slip boundary condition, a new boundary layer forms on surfaces between and behind the cavities, requiring sufficient cells in the longitudinal direction. Figure 1 shows the surface mesh on the bottom of the cruise ship with air cavities.
An actuator disk model is used to model the thrust deduction effect. An axial body-force distribution is applied on the actuator disk. The force distribution is axisymmetric and varies in radial direction based

on the Goldstein optimum circulation distribution, without any loading at the propeller root and tip. Integration of the body forces over the actuator disk volume recovers the prescribed thrust. Tangential velocities induced by the propeller are not modelled.

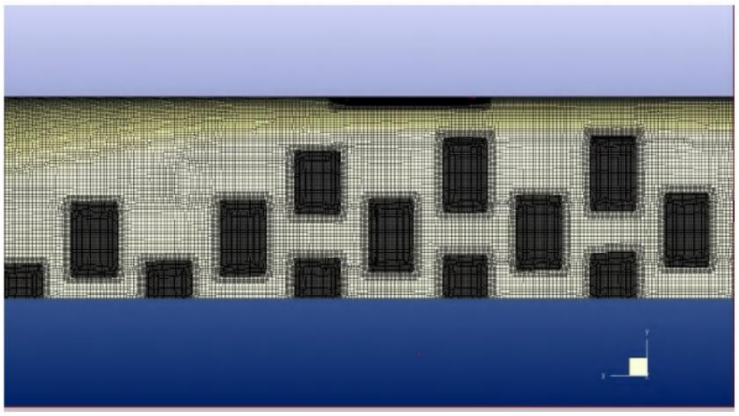

Figure 1: Surface mesh on the bottom of the cruise ship (half ship) with air cavities.

3 Cruise ship

The first case study is performed on a cruise ship. This ship has a relatively slender hull shape and a small flat bottom area. The ship is a twin-screw vessel with podded propulsion. The main particulars of this ship are presented in table1.

Table 1: Main particulars of the cruise ship.

Length waterline [m]	160.7
Beam [m]	21.4
Draught	5.15
Displacement [ton]	11845
Block coefficient [-]	0.65

Model tests of the cruise ship were performed at the Maritime Research Institute Netherlands (MARIN). The model test investigation aimed to optimize and determine the gain in propulsive power of the Damen Air Cavity System (DACS). Resistance and propulsion tests were performed. Also, some runs were made with an underwater camera being present , to investigate the development of the air cavities under the ship hull. The underwater camera's allowed to approximate the cavity length for the present analysis. Figure 2 shows the layout of the air cavities on the bottom of the ship.

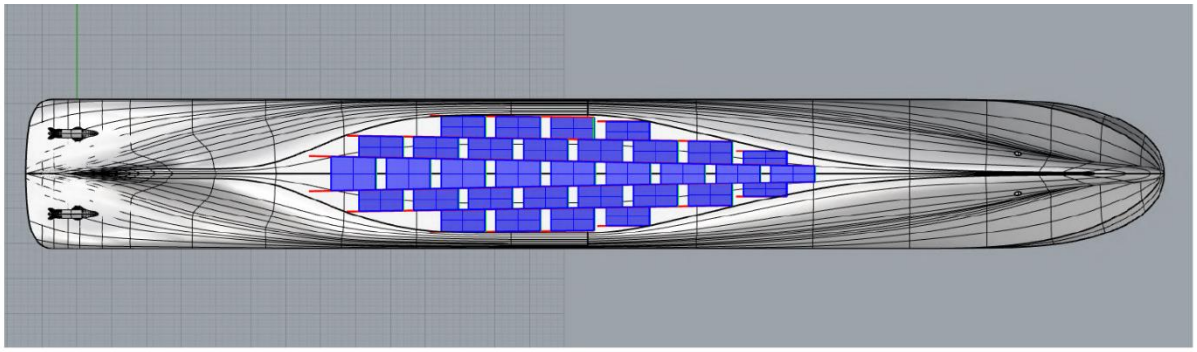

Figure 2: Cruise ship: schematic layout of the air cavity system on the bottom. (Blue: air cavities, Red: skegs, Green: cavitators)

3.1 CFD results

Table 2 compares the resistance components calculated via CFD for the ship without air cavities (reference) and with air cavities (air on) at various speeds. No correction is applied for DACS appendages resistance. The table indicates that the reduction in frictional resistance remains nearly constant across speeds. The relative reduction in friction drag is less than the 16.8% reduction in

wetted area, as noted by Zverkhovskyi (2023). This is due to the formation of a new boundary layer behind each cavity, increasing local skin friction. Additionally, the table shows negligible changes in pressure resistance, except for a 3% reduction at 9 knots, which is not understood.
Table 3 compares the resistance reduction from CFD with that measured in model tests (extrapolated results). In this case, the CFD resistance with air cavities is corrected for DACS appendage resistance, which was measured at 2% of total resistance during model tests. The table shows a small difference between CFD and model test results, suggesting that resistance reduction from air cavities can be predicted relatively accurately with the applied modeling method when the air-covered area is known.

Table 2: Cruise ship: CFD resistance components comparison between the reference case and air on

	Total resistance [kN]			Pressure resistance [kN]			Viscous resistance [kN]		
v_s [kn]	Ref	Air on	Diff. [%]	Ref	Air on	Diff. [%]	Ref	Air on	Diff. [%]
9	96.1	86.4	-10.2	21.5	20.8	-3.2	74.7	65.6	-12.2
11	143.5	130.0	-9.4	34.4	34.2	-0.7	109.0	95.8	-12.1
14	232.0	210.5	-9.3	59.4	59.0	-0.6	172.6	151.5	-12.3
17	356.9	325.5	-8.8	106.8	106.2	-0.6	250.1	219.4	-12.3
19	479.8	440.9	-8.1	170.3	169.3	-0.6	309.5	271.5	-12.3

Table 3: Cruise ship: comparison of change in resistance due to DACS between extrapolated model test results and CFD.

	Total (corrected resistance reduction [%]	
v_s [kn]	Model tests	CFD
11	-9.5	-7.2
14	-7.7	-7.3
17	-8.6	-7.0

A comparison between the nominal wake field in the reference case and with air on is presented in figure 3. The nominal wake fraction and the thrust deduction factor for both cases are also given in table 4. From these results it can be concluded that the nominal wake field is almost not affected by air cavities for this ship. This is because the ship's propellers are located mostly out of the ship's boundary layer. A change in the boundary layer due to the air cavities will therefore not cause a big change in the wake field. Also the change in the thrust deduction effect is negligible. This is also observed in literature for Russian barges with a large internal air cavity, (Gorabchev & Amromin, 2012). The same observations for change in thrust deduction and wake field were made during the model tests.

Table 4: Cruise ship comparison of CFD results of the thrust deduction and wake factor between the reference case and air on.

	(1-t) [-]			(1-w_n) [-]		
v_s [kn]	Ref	Air on	Diff. [%]	Ref	Air on	Diff. [%]
9	0.914	0.915	0.1	0.914	0.916	0.2
11	0.911	0.912	0.2	0.914	0.916	0.2
14	0.905	0.907	0.2	0.916	0.918	0.2
17	0.899	0.900	0.1	0.915	0.917	0.2
19	0.895	0.896	0.1	0.917	0.919	0.2

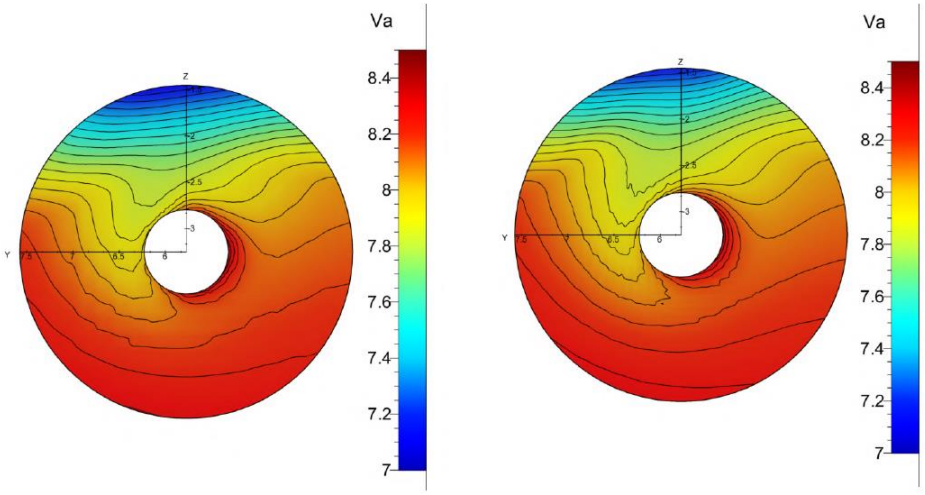

(a) Reference *(b) Air on*

Figure 3: Cruise ship: comparison of the nominal wake field at 17 knots.

4 Cargo ship

A second case study was performed on a cargo ship. This ship has a relatively full hull form and sails at a lower speed than the cruise ship. The main particulars of this ship are presented in table 5. In contrast to the cruise ship, the cargo ship is a single-screw vessel.

Table 5: Main particulars of the cargo ship

Length waterline [m]	114.1
Beam [m]	16.5
Draught aft [m]	5.0
Draught fore [m]	4.65
Displacement [ton]	7668
Block coefficient [-]	0.82

Figure 4 shows the layout of the air cavities on the bottom of the ship. In this case the cavity length is approximated based on the experimental observations of Zverkhovskyi (2014). He observed that the length-to thickness ratio of an air cavity is rather constant. Therefore, the cavity length can be predicted based on the height of the side fences.

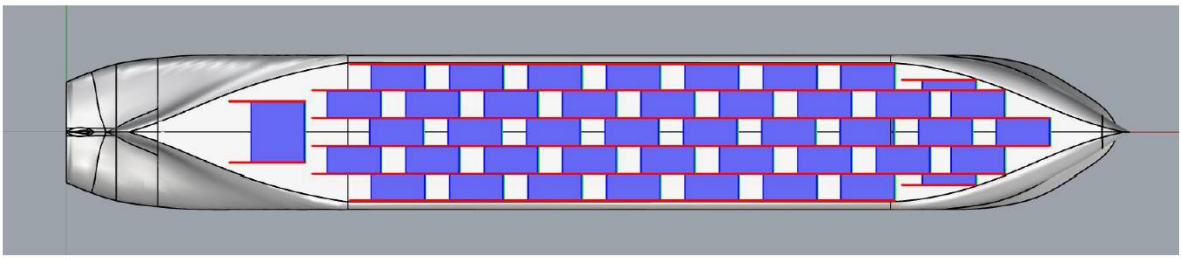

Figure 4: Cargo ship: schematic layout of the air cavity system on the bottom. (Blue: air cavities, Red: skegs, Green: cavitators)

4.1 CFD results

Table 6 shows a comparison between CFD resistance components (not corrected for DACS appendage resistance) between the ship without (reference) and with air cavities (air on). Also for this ship a rather constant frictional resistance reduction is observed. Again the relative frictional drag reduction is lower than the relative wetted area reduction. Surprisingly, also a reduction in pressure resistance is observed.

This ships experiences flow separation at the gondola. The boundary layer development on the bottom of the ship is affected and reduced by the air cavities. In general a thinner boundary layer is less prone to flow separation. Therefore the air cavities could cause a reduction in flow separation on the gondola. This statement is supported by the fact that the relative pressure resistance reduction decreases with increasing speed. Generally the viscous pressure resistance (due to flow separation) is most dominant at lower speed. During model tests on a ship with a large internal air cavity also a reduction in flow separation on the stern was observed, **(**Sverchkov & Borusevich, 2019). Further research into possible reduction of flow separation by air cavities is recommended, especially using more sophisticated turbulence models.

Table. 6 Cargo ship: CFD resistance components comparison between the reference case and air on

	Total resistance [kN]			Pressure resistance [kN]			Viscous resistance [kN]		
v_s [kn]	Ref	Air on	Diff. [%]	Ref	Air on	Diff. [%]	Ref	Air on	Diff. [%]
9.07	79.4	63.2	-20.4	28.6	23.5	-17.8	50.9	39.8	-21.8
10.67	112.1	93.0	-17.1	42.9	38.8	-9.4	69.3	54.2	-21.8
11.95	152.1	129.8	-14.7	66.6	62.9	-5.4	85.5	66.8	-21.8
12.41	181.3	156.0	-14.0	91.9	84.2	-8.4	89.4	71.8	-19.8
12.97	228.5	201.5	-11.8	128.5	123.5	-3.9	100.0	78.0	-21.9

Table 7 shows a comparison between the nominal wake fraction and the thrust deduction fraction of the ship with and without air cavities. Again the change of the thrust deduction effect is negligible. However the change in the nominal wake field is significant. A comparison is also made in figure 5. The nominal wake field is significantly reduced by air cavities. This can be explained in the following way. The boundary layer in the aft region is much thinner due to the air cavities. Due to the air cavities it could not grow as much as it would have done without the air cavities. As a result, the average axial velocity in the wake field is higher. The structure of the nominal wake field itself is not really affected. The higher axial velocity in the nominal wake field will cause a reduction of the hull efficiency. However, the resistance reduction is significantly larger than the reduction of the hull efficiency. Therefore, the air cavity still causes a reduction in propulsion power.

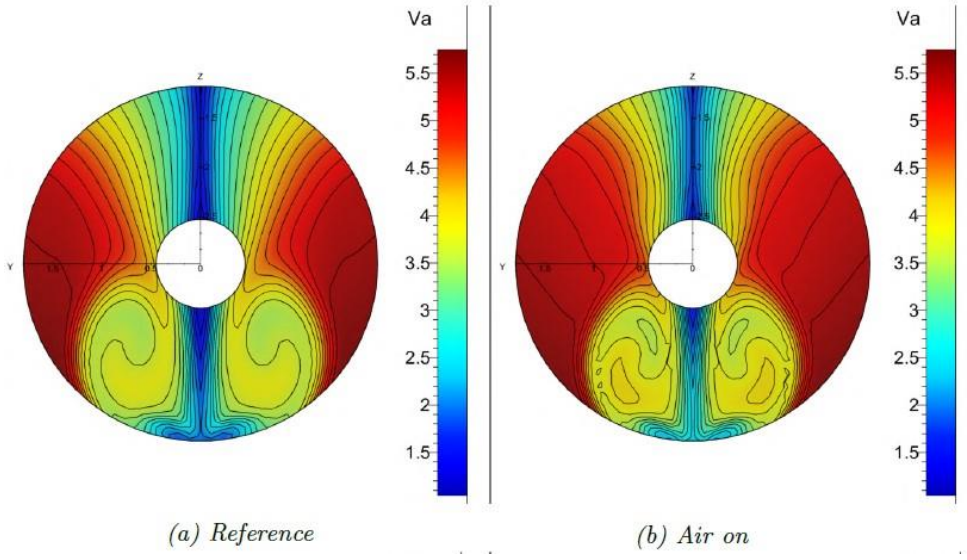

Figure 5: Cargo ship: comparison of the nominal wake field at 12.97 knots

Table 7: Cargo ship comparison of CFD results of the thrust deduction and wake factor between the reference case and air on.

	(1-t) [-]			(1-w_n) [-]		
v_s [kn]	Ref	Air on	Diff. [%]	Ref	Air on	Diff. [%]
9.07	0.810	0.806	-0.5	0.610	0.660	8.1
10.67	0.809	0.804	-0.6	0.614	0.662	7.9
11.95	0.809	0.805	-0.6	0.617	0.664	7.6
12.41	0.812	0.806	-0.7	0.614	0.661	7.7
12.97	0.815	0.813	-0.2	0.607	0.656	8.0

5 Conclusion

Two ships with air cavity drag reduction were modeled using CFD. For the cruise ship, good comparison for the resistance reduction caused by the air lubrication was found between CFD and model test results. This means that modeling the air cavities as surfaces with a slip boundary condition is relatively accurate, provided that the air covered area is known. For both ships it was observed that the change of the thrust deduction effect due to air cavities is negligible. The nominal wake field however can be reduced due to the change in boundary layer development caused by the air cavities. The change of the nominal wake field depends on the propeller(s) location(s) and the influence of the bottom boundary layer on the propeller wake field. However, the reduction of the wake field and hence, the hull efficiency is secondary to the resistance reduction so still power savings can be made.

For further research is recommended to repeat this study with a more sophisticated propeller model, e.g. a fully discretized propeller with a sliding mesh. This allows to study the effect of air cavities on the effective wake field rather than the nominal wake field. Furthermore, the possible reduction of pressure resistance and flow separation due to air cavities should be studied in more detail. A next step after this research could be propeller optimization of ships with air cavities.

References

Damen Shipyards Group. (2023). Damen Air Cavity System (DACS). https://www.damen.com/equipment/green-solutions/damen-air-cavity-system

Gorabchev, Y. & Amromin, E. (2012). Ship drag reduction by hull ventilation from laval to near future: Challenges and successes. In ATMA (Ed.), *Proceedings of the conference of association technique maritime et aeronautique*, https://www.atma.asso.fr/dyn/memoires/memoire_20.pdf

Mäkiharju, S. A., Perlin, M., & Ceccio, S. L. (2012). On the energy economics of air lubrication drag reduction. *International Journal of Naval Architecture and Ocean Engineering*, 4 (4), 412–422. https://doi.org/10.2478/IJNAOE-2013-0107

Rotte, G., Kerkvliet, M., & van Terwisga, T. (2019). Exploring the limits of RANS-VoF modelling for air cavity flows. *International Shipbuilding Progress*, 66 (4), 273–293. https://doi.org/10.3233/ISP-190270

Rotte, G., Kerkvliet, M., & van Terwisga, T. (2023). The resolved and unresolved issues and phenomena in numerical modelling of air cavity closure using a scale-resolving method. *Proceedings of the NuTTS 2023*. https://blueoasis.pt/wp-content/uploads/2023/10/Nutts2023_proceedings_v4.pdf

Sverchkov, A., & Borusevich, V. (2019). Artificial cavity as a tool for reducing ship resistance [in Russian]. *Transactions from the Krylov State Research Centre*, 1 (387), 20–31. https://doi.org/10.24937/2542-2324-2019-1-387-20-31

Zverkhovskyi, O. (2014). *Ship drag reduction by air cavities* [Doctoral dissertation, Delft University of Technology]. https://doi.org/10.4233/uuid:a5754f75-55c1-4407-bebb-41458e6c9a11

Zverkhovskyi, O., Kerkvliet, M., Lampe, A., Vaz, G., & van Terwisga, T. (2015). Numerical study on air cavity flows. *Proceedings of NuTTS 2015*. https://www.researchgate.net/publication/281834294_Numerical_Study_on_Air_Cavity_Flows

Zverkhovskyi, O. (2023). CFD Study on a Flow Around a Vessel With Air Cavities on the Bottom. *Proceedings of NuTTS 2023*. https://blueoasis.pt/wpcontent/uploads/2023/10/Nutts2023_proceedings_v4.pdf

CFD Modeling of Air Lubrication Systems in Ships

Roya Shademani[1], Tommi Mikkola[1], Teemu Manderbacka[1],

Sasan Tavakoli[2], Heikki Remes[1]

[1]Department of Mechanical engineering, Aalto University,[2] University of Melbourne, Australia

Roya.shademani@aalto.fi

1 Introduction

Maritime transportation dominates global trade, with oceangoing ships, including container vessels, bulk carriers, and tankers, handling most of the freight. However, these large, human-made vessels require substantial energy, primarily generated by diesel engines. This reliance on diesel engines has contributed significantly to CO2 emissions, prompting the International Maritime Organization (IMO) to mandate emission reductions across the shipping industry. To address this, two primary approaches are being explored: the adoption of alternative fuels, such as ammonia, and hydrodynamic retrofitting of ships. The latter includes innovations like Air Lubrication Systems (ALS) and wind-assisted propulsion technologies.

Hydrodynamic retrofitting solutions have garnered significant interest, driving companies and industries to develop new methods for implementing these technologies on ships. However, engineering the setup for each vessel must be tailored in advance, as each ship exhibits unique hydrodynamic behavior. Therefore, before installing retrofitting technologies, a thorough understanding of the related fluid dynamics is essential. This requires a hydrodynamic study of ships equipped with such systems, which can be performed either via numerical modeling of the air-water (+bubble) flow around the vessel or via physical experiments, such as towing tank tests. Unfortunately, our understanding of the flow dynamics around ships with air-lubrication systems—one of the most promising retrofitting solutions—remains limited, as research in this area has only gained momentum in recent years.

To better understand the problem and move towards numerical modeling, it is essential to first review the foundational literature, beginning with early studies from the 1970s. However, the Air Lubrication System was proposed a century ago, in 1907 Frederick W. Lanchester [1] explored how aerodynamics and fluid mechanics could be applied to watercraft to minimize resistance, laying the groundwork for later research on air lubrication systems. Most of these studies introduced the concept of drag reduction on wet surfaces through bubble generation. Initial experiments were conducted in tunnels or tanks, where symmetric submerged bodies, such as submarines, were tested to observe frictional drag reduction. This early research sparked more practical studies, where scholars tested ships equipped with air-bubble generators on their hulls in towing tank experiments. While experimental research in this field has provided valuable insights, it is limited in scope, and conducting new experiments for each design can be prohibitively expensive. This is why numerical simulations done using Computational Fluid Dynamics (CFD), have become favored for conceptualizing, and engineering such systems in the early stages. Although CFD modeling of fluid flow around ships without air lubrication has been extensively studied over the past decades, research on ships equipped with air lubrication systems (ALS) remains limited. Replicating this problem

in a CFD environment is particularly challenging due to the complexity of the system and the various methods needed to solve it. Furthermore, few studies have transparently reported CFD simulations of ALS-equipped ships.

To address this gap, this article presents a CFD-based study on ships equipped with ALS, offering new findings that can assist other researchers in modeling this problem. The remainder of this paper is structured as follows: Section 2 introduces the ship model and provides a general overview of the numerical schemes used to solve the problem. Section 3 presents the results and compares CFD predictions against towing tank data. Section 4 presents concluding remarks.

2 Methodology

2.1. Ship Model

In the present study, a three-dimensional ship model equipped with an air injection chamber at its bottom is considered, as shown in Fig. 1(a). Experimental results for the same case were reported in [2]. The fluid flow around the ship is simulated in a virtual towing tank via computational fluid dynamics. To do so, a computational domain with prescribed boundary conditions (BCs) shown in Fig. 1(b) is generated. A symmetry BC is prescribed for the upper surface, which cancels out effects of the free surface and wave making resistance. This helps us to single out the effects of air injection on the frictional drag. Inlet and outlet BCs are respectively set for front and back surfaces. These two surfaces are set to be L and $2L$ far from the ship to avoid the influence of these boundaries on the results, where L represents the length of the ship model.

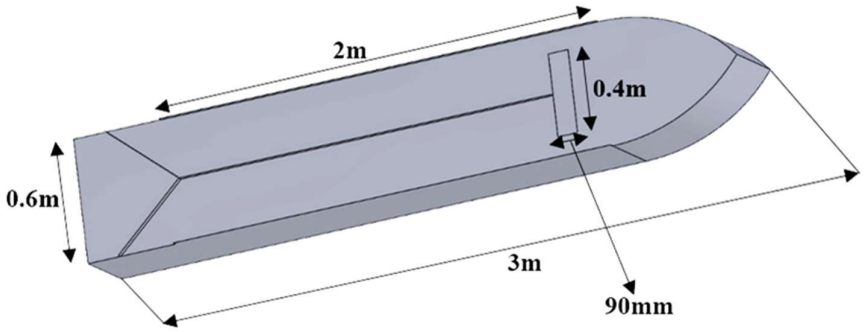

(a)

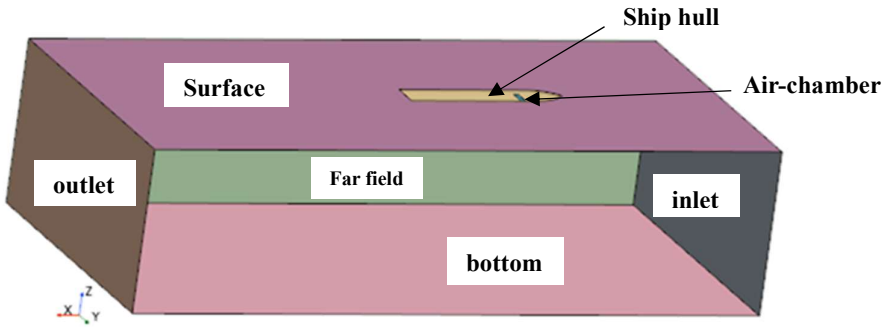

(b)

Fig.1 (a) Geometry of ship model, (b) Numerical computational domain.

2.2 Numerical scheme

The fluid is assumed to be viscous and incompressible. We formulate the fluid motion equation using a Eulerian approach. In addition, we expect the fluid flow to be turbulent due to the relatively large Reynolds number and the expected fluid regime around the ship. In addition, we use a two-phase (air and water) fluid flow approach to model the problem. Hence, the flow field around the ship should satisfy the continuity and RANS (Reynolds-Averaged Navier Stokes Equation) equations as follows.

$$\nabla . \boldsymbol{V} = 0 \tag{1}$$

$$\frac{\partial(\rho_{eff}\boldsymbol{V})}{\partial t} + \nabla \cdot \left(\rho_{eff}\boldsymbol{V}\boldsymbol{V}\right) = -\nabla p + [\mu_{eff}(\nabla \boldsymbol{V} + (\nabla \cdot \boldsymbol{V})] + \rho_{eff}\boldsymbol{g} \tag{2}$$

Here, $\boldsymbol{V}$ is the averaged speed, and p is the averaged pressure, and $\boldsymbol{g}$ is the gravity acceleration. ρ_{eff} and μ_{eff} are the effective density and dynamic viscosity, respectively (as in each cell a mixture of air and water would exist). The air-water mixture flow is solved using a volume fraction method that introduces an extra conservative equation to the system of equations, which is not presented in this paper for the sake of brevity. A realizable k-epsilon two-layer turbulence model is used as a turbulence closure.

The fluid flow around the ship is simulated using the commercial package of Star-CCM+ (Version 2402).

3 Results and Discussion

In this paper, we present three different sets of results. First, we illustrate the pattern of air distribution on the bottom of the ship hull to demonstrate how a realistic pattern can be achieved in CFD simulations. Next, we present the drag reduction observed during numerical simulations and compare the results against experimental data to validate the model. Finally, we show how the addition of appendages to the hull affects the CFD results.

3.1 Air Distribution Pattern

The distribution pattern of air emerging on the bottom of a ship following injection is a critical indicator that provides valuable physical insights into the problem, helping us understand how air injection contributes to drag reduction. Hence, air distribution on the bottom of the ship needs to be predicted accurately. The pattern of air distribution on the bottom of the ship is expected to form a continuous air layer, which can effectively reduce the drag. One question regarding the modeling of fluid flow around a ship under the effects of air lubrication is whether gravity needs to be considered to achieve a realistic pattern of air distribution on the bottom of the ship. So, we modeled the problem using two different settings: in one, gravity was turned off, and in the other, gravity was turned on. Fig. 2 shows the results. As seen, an incorrect and unrealistic air distribution pattern is obtained when gravity is turned off, while a realistic distribution is achieved after activating the gravity model.

The results also closely match those from the numerical simulations in [2]. This phenomenon occurs because, in the absence of gravity, there is nothing to drive the air towards the hull surface, so the air bubbles tend to collect near the air chamber, but the only exception is the low pressure area aft of the inclined arranged strips close to the stern of the model, and eventually the air injected disperses throughout the fluid domain rather than forming an air carpet. However, under the influence of gravity, the air bubbles generated beneath the ship are more likely to rise towards the bottom of the hull, partially drying the ship's hull. The strips close to the stern of the model are higher than the thickness of the air layer and block the transport of air towards the transom.

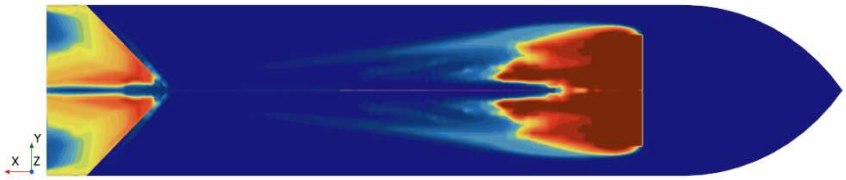

(a) No gravity model

(b) With gravity model

(c) Validation case [2]

Fig.2 Air distribution at the air flow rate of 8 m^3/h and ship speed of 0.542 m/s.

3.2 The calculated drag reduction

The effect of the air lubrication system on drag reduction is investigated at various air flow rates (ranging from 0 m^3/h to 10 m^3/h). The drag reduction is quantified as follows:

$$\Delta R = \frac{\Delta R_f}{R_0} \times 100\% \tag{3}$$

Here ΔR_f is the relative friction drag reduction in comparison to the case with no air-injection. R_0 is the total drag of the ship model without air injection.

The numerical and experimental results of the drag reduction rate at Froude number of 0.16 are compared in Fig. 3. Here, the drag reduction is plotted versus air flow rate for a complete ship model equipped with all strips configured identically to the experimental control case. As seen, the frictional drag would reduce up to 15% at very high injection rates, though it converges as the injection rate becomes relatively high. The results indicate that having a very large injection rate would just waste the energy and does not lead to further drag reduction.

We now turn our attention to the accuracy of the numerical model in calculating drag reduction. The numerical results seem to follow the experimental data, though they may slightly overpredict drag reduction at low injection rates. This can be explained by the nature of the numerical model. While the two-phase flow approach helps model the problem at these low rates, it does not fully capture the real physics. In the simulations, bubbles are not generated, and a homogenous mixture of air and water exits the chamber, whereas in real physical tests, bubbles do form. Consequently, the two-phase flow modeling results in a thicker air layer under the ship's hull, leading to a larger drag reduction than observed in the tank tests.

At higher injection rates, the numerical model does not appear to overpredict the results, which is a very promising observation. In these cases, the two-phase model yields a more realistic air injection. During physical tests, higher air injection rates resemble the air layer more than bubble formation. Therefore, the numerical model produces a similar air layer thickness and drag reduction to what is observed in real experiments.

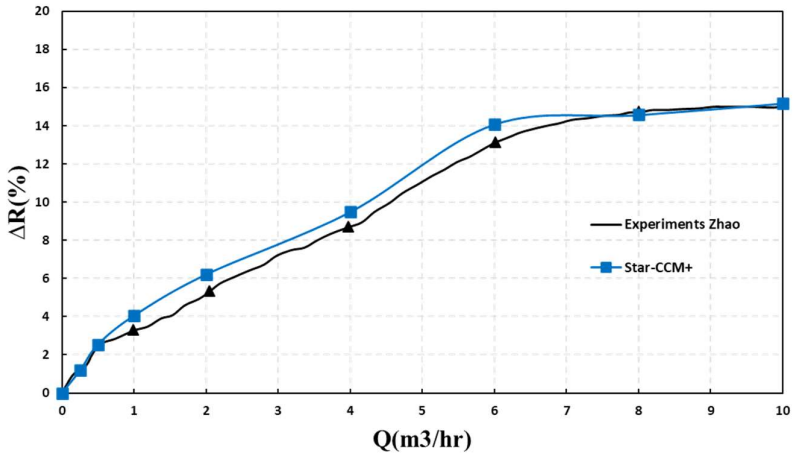

Fig.3 The comparison of drag reduction rates at different air flow rates.

3.3 Strips effect

We now present some results that provide physical insights into the setup used to increase the effects of air lubrication. When air is injected, our goal is to prevent its leakage from the sides and trap the air beneath the ship. From an engineering perspective, this is achieved by adding strips to the hull to control airflow and stop it from escaping. In the experimental tests conducted in [2], two side strips, one middle strip, and two inclined strips were installed on the ship model. We have run simulations both for a bare ship with no strips and for a ship equipped with these strips.

When these strips were added to the numerical model in the CFD tank, the drag reduction was found to be more significant. The installation of inclined strips, by facilitating the escape of air along the sides of the ship's hull, helps to make the friction drag more dominant and mitigate the effect of air on the pressure drag at the stern.

Figure 4 shows examples of the time history of shear drag developed on the hull surface of the ship under air injection, both for the bare hull and the hull equipped with strips. The results correspond to the Froude Number of 0.10 and the air flow rate of 10 m^3/h. As seen, the case with the ship equipped with strips exhibits lower shear drag.

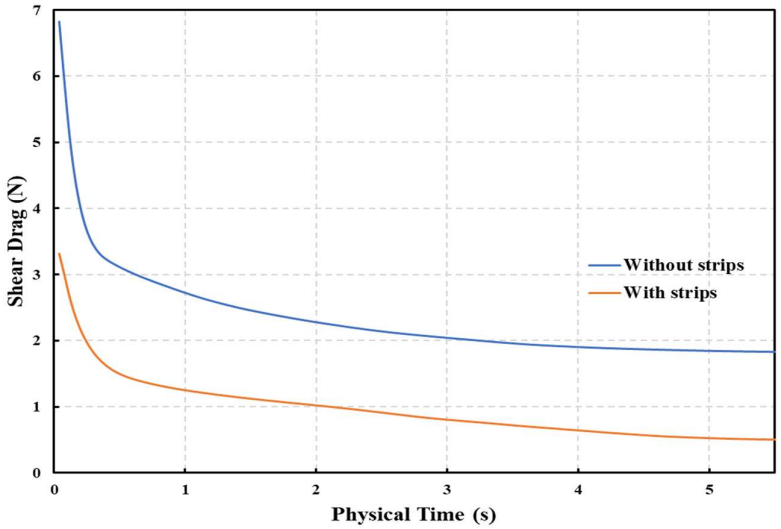

Fig.4 Impact of strip installation on shear drag at a flow rate of Q = 10 m³/h

4 Concluding remarks

This study presents a detailed CFD analysis of air layer drag reduction based on early CFD simulations of drag reduction for a flat-bottomed ship hull equipped with an air-lubrication system, conducted using Star-CCM. The fluid flow is modeled using a volume fraction method. The results indicated that the CFD model can predict the drag reduction up to 15% at the highest considered airflow, which is like what was measured at experimental tank tests. The simulation results closely aligned with experimental data, yet the model was seen to slightly over-predict drag at low injection rates.

Additionally, it was shown that activating gravity in CFD modeling of the problem allows for prediction of a more realistic pattern of air distribution on the bottom of a ship equipped with an air lubrication system. Additionally, it was demonstrated that when the problem is solved using the CFD model, strips need to be added to the ship hull to effectively address the influences of friction drag on the numerical results.

Future work will focus on using the Eulerian Multiphase (EMP) model for simulating the problem, providing a significant opportunity to compare the capabilities of EMP with those of the Volume of Fluid (VOF) method. This will also involve a numerical evaluation of the wave effects on the performance of air lubrication systems (ALS).

Acknowledgements

The authors acknowledge research funding received from the Horizons Europe project" RETROFIT solutions to achieve 55% GHG reduction by 2030 (RETROFIT55) – Project No.: 101096068". The views set out in this paper are those of the authors and do not necessarily reflect the views of their sponsors.

References

[1] F. W. Lanchester, Aerodynamics, Constituting the First Volume of a Complete Work on Aerial Flight. London: A. Constable & Co., Ltd., 1907.
[2] Xiaojie Zhao, Zhi Zong, Experimental and numerical studies on the air-injection drag reduction of the ship model.

26th Numerical Towing Tank Symposium (NuTTS)
23-25 October 2024 - Mülheim an der Ruhr, Germany

Detecting Numerical Instabilities in Propeller Cavitation Erosion Modelling Using Unsupervised Learning

Ian Hubbard*, **Themistoklis Melissaris***
*Propulsion Technology R&D, Wärtsilä Netherlands B.V.
ian.hubbard@wartsila.com

1 Introduction

Predicting cavitation erosion and propeller noise requires accurate prediction of the vapor volume and its dynamics around the propeller blades. Ship scale validation of cavitation dynamics and its nuisance is therefore very important; however, few validation cases can be found in the literature. Melissaris et. al. (2022, 2023) have compared the erosion risk on the propeller blades of several full-scale propellers and thruster units, using a novel erosion model developed by Schenke et al. (2019) to validate the predicted cavitation impact loads, and compare them with the actual erosion on the real surface. In Melissaris and Hubbard (2024), a first attempt at identifying the limit above which cavitation starts to become erosive has been carried out on various full-scale test cases, where numerical instabilities that could result in abnormally higher energy radiation may potentially depicting a distorted erosion energy assessment.

Lower mesh quality, high cell curvature, as well as the incompressibility of the liquid phase, may lead to extreme pressure changes. Despite cell quality filtering efforts, these corrupted cell pressures remain in the final solution and pollute the results. Manual filtering of such cells becomes case-by-case dependent and too involved for the analysis at hand, hence an unsupervised machine learning approach from the field of anomaly detection; Isolation Forests (IF), was implemented allowing for an automated detection scheme of such corrupted cells with success in de-noising the results.

The drawback of using IF is that there is a possibility of mis-identifying high intensity, highly localized impact loads as anomalies which instead should not be discarded. In attempt to circumvent this issue, another unsupervised method is tested and compared against the isolation forests on available test cases and the suitability of their usage is then further outlined. A relationship-based approach is attempted in the form of an autoencoder (AE) neural network architecture (Hawkins, 2002), proven successful in Gupta et al. (2024), albeit for a different application. The aim of the approach, at a high level, is to utilize the networks feature extraction ability on the dataset and respective energy distribution in a more robust and generalized way. The intention is to then be able to better and more reliably isolate true anomalies (corrupted cells), without also mis-identifying true high intensity collapse events.

2 Case overview

Erosion risk assessment has been performed in four different propeller designs and eight different operating conditions in total. All four propeller designs have exhibited erosion on the pressure side of the blades. One of the designs operates partly at an operating condition with large amount of suction side cavitation (C8). However, there are no signs of erosion on the suction side on this blade. Therefore, that design should show the lowest risk for erosion. The other seven operating conditions should demonstrate a higher erosion risk on the blade surface. An overview of the designs and the operating conditions are given in Table 1. It should be noted that all the thruster cases concern open water simulations without the presence of the hull geometry, and it has been assumed that the housing of the thruster unit is mainly responsible for the velocity variation on the propeller plane. On the other hand, test cases C5 and C6 were simulated behind the actual vessel geometry, and the ship wakefield was therefore considered.

To determine the erosion risk, the radiated surface energy e_s is derived from the CFD solution using cavitating flow conditions where, the energy content radiated by the collapsing cavities within a prescribed volume around the blade is collected over a revolution and projected to the blade surface through a volume-to-surface methodology, further outlined in Schenke et al. (2019). The radiated surface energy distribution on any given blade has been non-dimensionalized in order to make a fair comparison of

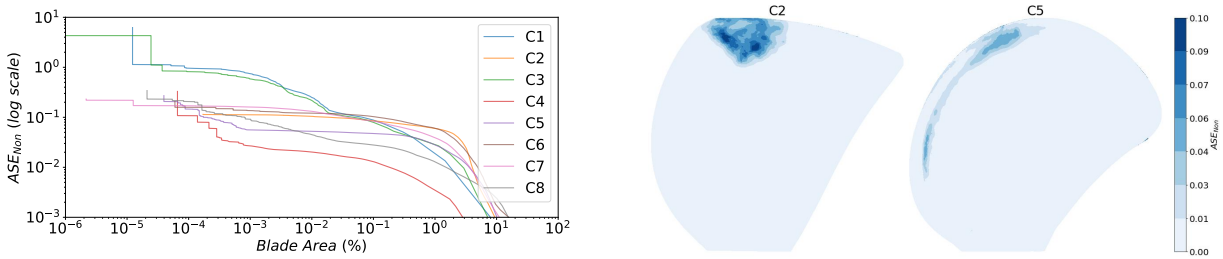

Fig. 1: Example ASE_{Non} distributions over the percentage impacted surface area and over the blades.

energy levels between an individual blade design and another, detailed in Melissaris & Hubbard (2024) and the non-dimensional surface energy is given as follows,

$$ASE_{Non} = \frac{e_s}{\rho A_f n^2 D^3}$$

Where A_f the surface cell face area, n is the propeller rotational velocity, D the propeller diameter and e_s is the radiated surface energy, further detailed in Schenke et al. (2019). An example of the distribution of ASE_{Non} over a blade design is shown in Fig.1. Here designs C2 and C5 are shown and the areas of the blade in which are exposed to higher intensity surface accumulated energies can be identified. Furthermore, the risk energy levels as raw data distributed over a percentage of the blade area are also shown.

Table 1: An overview of the propeller designs and the different operating conditions.

	Type	Dprop [m]	RPM	Ship Speed [kn]	Erosion
C1	Thruster	3.0	217.7	0	Yes (PS)
C2	Thruster	3.0	217.7	0	Yes (PS)
C3	Thruster	3.0	217.7	7	Yes (PS)
C4	Thruster	3.0	217.7	0	Yes (PS)
C5	Open	5.6	134	13.5	Yes (PS)
C6	Open	5.6	134	13.5	Yes (PS)
C7	Thruster	2.6	256	0	Yes (PS)
C8	Thruster	2.6	256	10	No

When attempting to judge this risk energy against a threshold energy level, the raw data may have skewed results due to potential numerical instabilities in the solution. Lower mesh quality, high cell curvature, as well as the incompressibility of the liquid phase, may lead to extreme pressure changes. Despite cell quality filtering efforts, these corrupted cell pressures remain in the final solution and pollute the results as shown in Fig.1 for lower percentages of the blade area. Manual filtering of such cells becomes case-by-case dependent and too involved for the analysis at hand, with the data sets containing ≈150k-350k data points in each analysis. Hence, an unsupervised machine learning approach from the field of anomaly detection has been implemented allowing for an automated detection scheme of such corrupted cells.

3 Unsupervised Learning & Methodology

In contrast to supervised learning, which is typically used in regression type tasks containing target prediction data which has been labelled, in unsupervised learning, a model is instead trained using unlabelled data in order to exploit underlying patterns and extract features within the context or distribution of the data itself. This is particularly useful for anomaly detection. A machine learning type model can be fed a dataset not containing any labels (i.e. whether a data point should be an outlier or not) and then be subsequently used to identify which data points seem to be anomalous within that dataset. Various algorithms can handle this separation between data points that fit the data's distribution and those that do

not. In this paper, two approaches are investigated, a decision-tree based approach via Isolation forests (Lui et al. 2008) and a relationship-based approach using autoencoder neural networks (Hawkins, 2002).

Isolation forests (IF) process the training data and detect anomalous points within such data using a decision-tree approach further outlined in Lui et al. (2008). An important parameter of the algorithm is the contamination threshold T, which is used to adjust the percentage of data points expected to be anomalies in the dataset. This can be a sensitive parameter and taking too high a value can lead to the IF over-marking anomalies, while a small threshold can lead to missing outliers. In Melissaris & Hubbard (2024) an IF was used with a contamination threshold $T = 0.005$ which was found to be conservative enough to mark the outlier numerical instabilities in the solution, but not perfectly as in some cases, outliers were marked in the region of expected high intensity impact loads. The results of Melissaris & Hubbard (2024) using an IF will be the base line comparison here.

To compare against the IF, a relationship-based approach using an autoencoder (AE) will be used. As described in Burkov (2019), autoencoders utilise a feed-forward neural network architecture

$$f_l(X) = \sigma_l(\mathbf{W}_l \cdot f_{l-1}(X) + \mathbf{b}_l)$$

where σ_l is the activation function, $\mathbf{W}_l$ the weight matrix and $\mathbf{b}_l$ the bias of the l^{th} layer in the model. This network is trained to reconstruct its input, with a training set consisting of (X, X). The hidden layers of the network are connected in an hour-glass fashion, exploiting dimensional reduction. This structure contains two sections, the encoder and the decoder. In the encoder, the input vector X is compressed in each i^{th} layer to a reduced dimensionality towards the centre layer, known as the embedding layer. The decoder stage then aims to decompress the information from the embedding layer back to the input vector dimensionality, attempting to reconstruct the entire input vector. The reconstruction will have a form of compression loss and will not be perfect. This reconstruction error can be determined by the Mean Squared Error between input vector X and its reconstruction $\hat{X} = f(X)$ given as;

$$\epsilon = \frac{1}{n}\sum_{i=1}^{n} \left\| X_i - \hat{X}_i \right\|^2$$

where n is the sample size and X_i and $\hat{X}_i$ represent the input and reconstruction vectors respectively. In this study, the autoencoder architecture considered here consists of 5 layers, 2 in the encoder, 1 embedding layer and 2 in the decoder. The encoder layers are L_2 regularized. The well known Adam stochastic optimizer is used in the weight optimization together with ReLU activation functions within the layers. A scheduled variable learning rate is used during training, starting from 5e-5 to as low as 1e-7 and the loss function is also taken as MSE.

In order to determine the outliers from the reconstruction error, a statistical filtering approach is applied on the resulting ϵ reconstruction error distribution. This can be done using a percentile or a confidence interval (CI) method. When using a confidence interval, a normal distribution is fit to the resulting reconstruction errors and using the determined confidence interval as a threshold, error values falling outside of the interval threshold can be identified as anomalous. To avoid making assumptions about the normality of the error distributions, a percentile method has been implemented in this study. This approach does not require the data to follow a normal distribution and is more interpretable than using a confidence interval. Taking lead from Gupta et al. (2024), errors beyond a 99^{th} percentile threshold have been considered. The errors falling outside this threshold are then marked as outliers and then removed from the ASE_{Non} data in order to re-evaluate the energy distribution.

4 Results & Discussion

In the initial application of a 99^{th} percentile starting point on the reconstruction error, ϵ appears to be an excessive threshold for identifying true outliers, as a significant amount of data is marked as anomalous. To sufficiently identify the outliers, the threshold needs to be adjusted to a lower percentage of errors such as a 99.9% threshold for instance. This however, may be too low or high, under- and over-detecting the anomalies in different cases and also introducing the need for the tuning of the AE embedding layer compression and hyper-parameters in addition for each case being investigated. On a case-by-case basis,

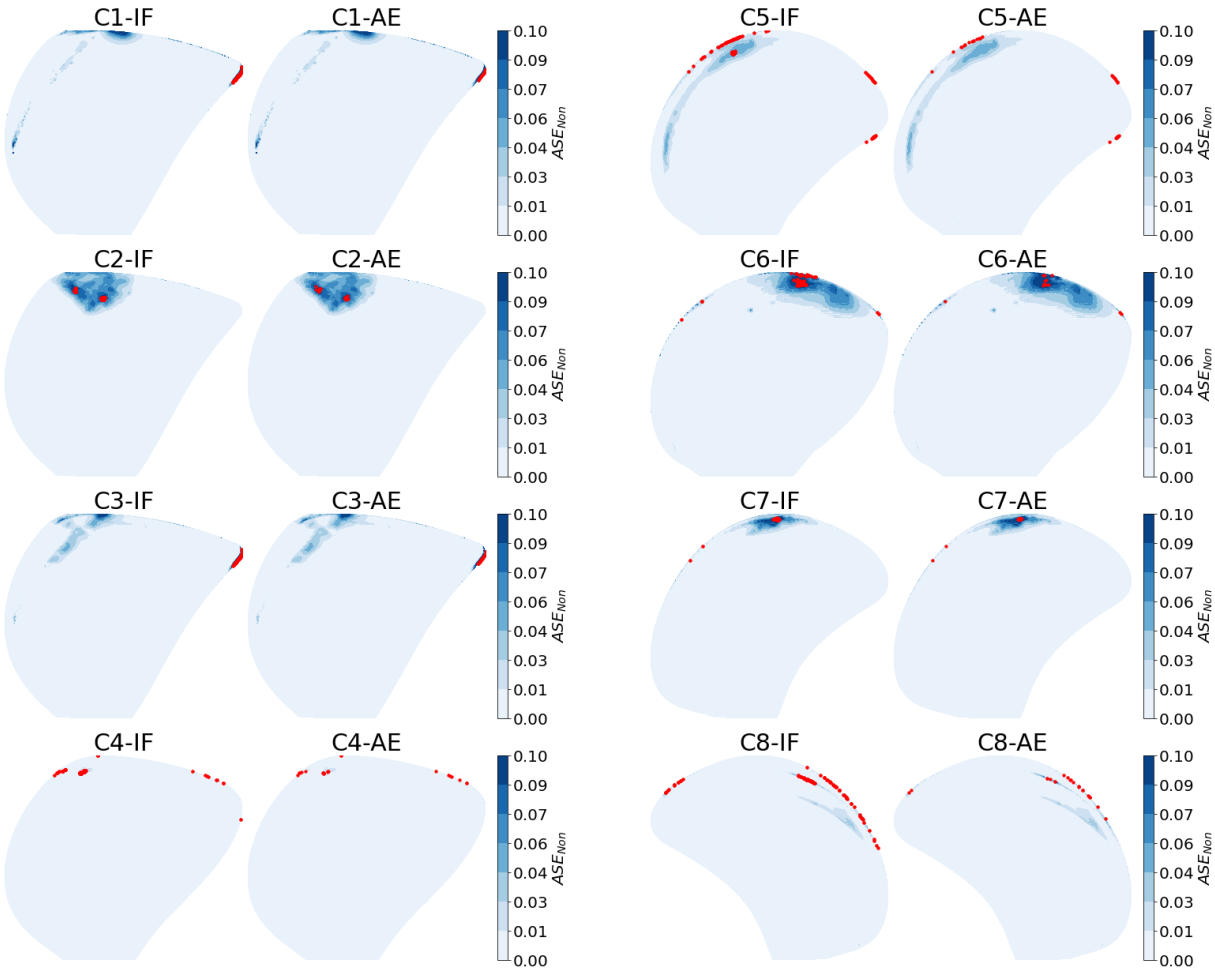

(a) Detected outliers in same design for conditions C1-C4

(b) Detected outliers for the other designs C5-C8

Fig. 2: Comparison of outliers detected in the ASE_{Non} data by both IF and AE methods, marked in red

the amount of adjustment to the AE architecture and to the threshold required is non-trivial, as it requires manual trial-and-error intervention using the visual inspection of the error distribution as a guide.

The aim of this detection methodology is to have a more generalized approach, which can be applied to any resulting blade design and operating condition to remove any numerical errors present in the final solution. If there is a need for visual inspection of the resulting ϵ distribution, followed by a threshold adjustment on a case-by-case basis, then this algorithm and approach would not be fit for our purpose. To avoid this and generalize the AE methodology, a two-stage filtering has been attempted. Here, the first stage gathers the reconstruction errors from the 99^{th} percentile threshold, then a new 99^{th} percentile threshold is applied from the already isolated reconstruction errors. This new threshold is re-applied to the ASE_{Non} data to detect the outliers.

The comparison of the detected anomalies in the data for both the IF and the AE using the two-stage filter are shown in Fig.2 (a,b). The AE has a lower marking rate of false positives, especially when it comes to the marking of points in the regions of high energy intensity. Based on the current IF contamination threshold, a larger quantity of points are obtained from the high-intensity regions, resulting in them being falsely marked as anomalies. This current state affects the gauging of the ASE_{Non} erosion risk threshold, as the over-marking by the IF reduces the energy content on the lower % blade area notably for most designs, shown in the side-by-side comparisons of both methods in Fig.3.

While the amount of anomalies detected in the regions of high impact have been reduced (cases C2, C6, C7, C8) or even not considered any more such as in case C5 (see Fig.2(b)), there still remains to be some points in these regions. It may be observed that for particular designs & conditions such as

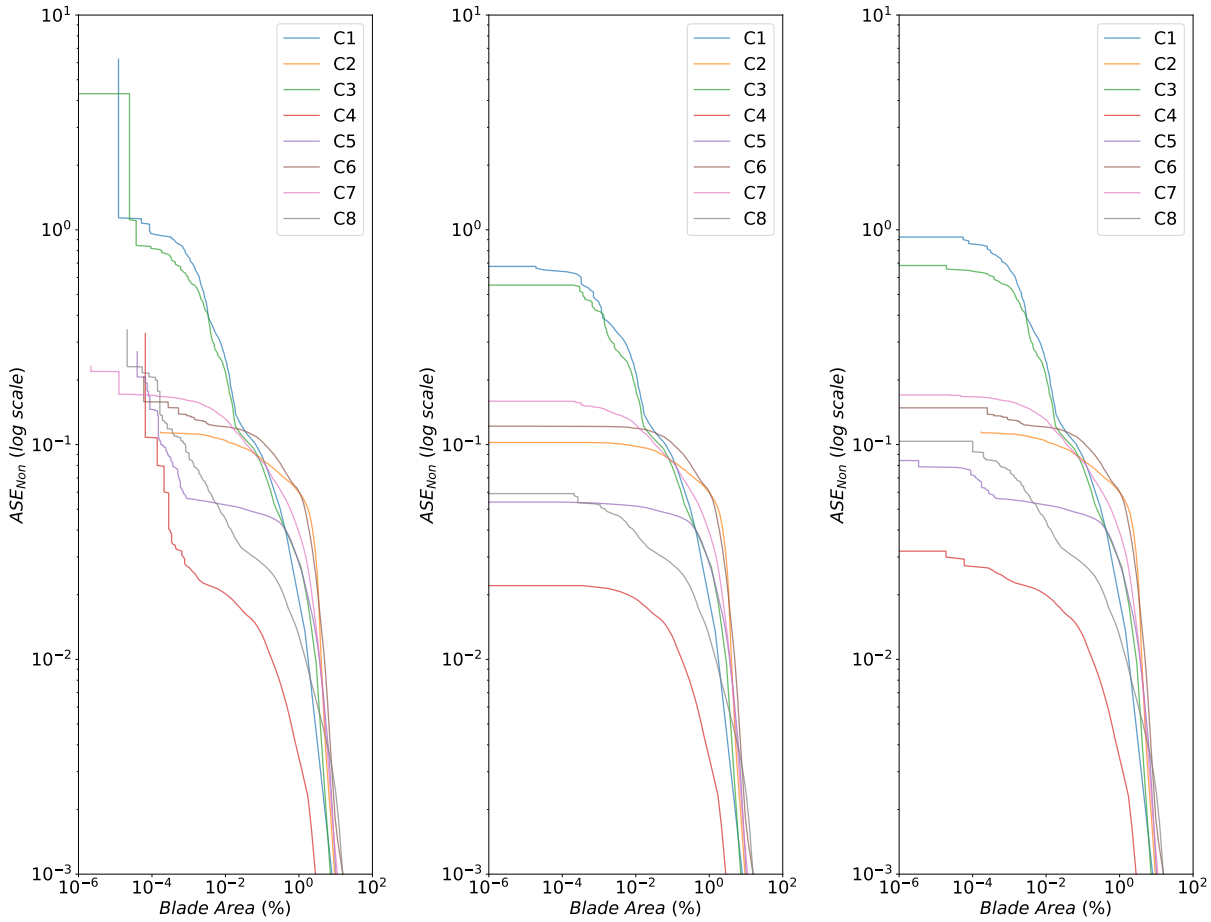

(a) Raw Data (b) Isolation Forest (IF) (c) Autoencoder (AE)

Fig. 3: Surface energy over the percentage of the impacted surface area comparing the raw data to the data after outlier detection has been applied for both IF and AE approaches.

in C2, the highest errors are found in the high-intensity region for both the IF and AE. When further inspecting the distribution of ϵ from the AE, shown in Fig.4(a), the resulting error distribution appears to be smoother and more closely clustered than in C8 as a comparison example in Fig.4(c). This could be for various reasons, such as that there are potentially no highly corrupted cells, containing numerical instabilities for this particular case, implying that the highest intensity events are being marked as outliers since they are the hardest to reconstruct accurately by the AE. Alternatively, these energies could be actual outliers that have been introduced from a corrupt cell within the volume and cavitation volume, subsequently projected to surface during the volume-to-surface projection step of the erosion energy methodology. Further work will be done to identify whether this is the case or not and whether anomalies should be identified per time step within the volume, rather than at the end during the final energy projection to the blade surface.

5 Conclusion

In this study, two unsupervised algorithms have been applied on accumulated surface energy data, acquired from cavitating RANS-based calculations for various blade designs and operating conditions. These algorithms have been successfully applied in order to automatically identify numerical instabilities from the results, which are evidently polluting the final erosion assessments. In general, both the AE and IF perform similarly on the task, however the AE provides additional information, interpretability and flexibility in comparison to the IF, due to the two-stage statistical filtering approach utilized here. When using the AE, the regions of interest (i.e. the impact areas) can be automatically identified and

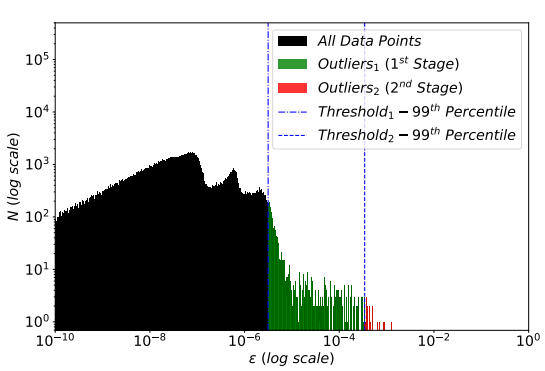

(a) C2 distribution of ϵ & percentile thresholds

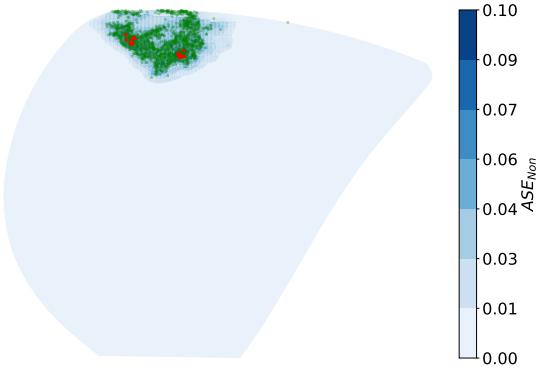

(b) C2 marked ϵ: Stage-1 in green, Stage-2 in red

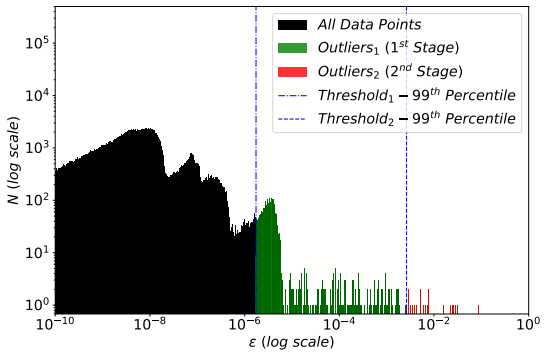

(c) C8 distribution of ϵ & percentile thresholds.

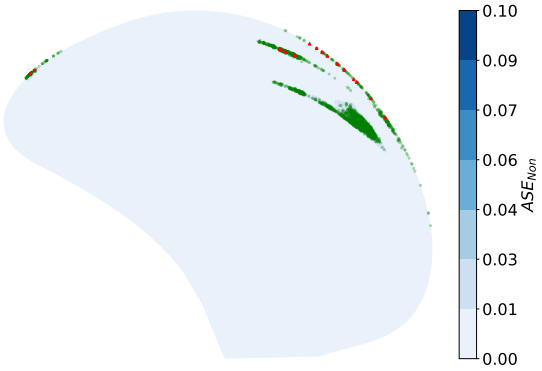

(d) C8 marked ϵ: Stage-1 in green, Stage-2 in red

Fig. 4: Comparison of distribution of reconstruction errors for blades C2 and C8 and the corresponding outliers marked on the blades by the two-stages of the 99th percentile thresholds.

isolated if needed within the first stage, and furthermore the percentile method, more specifically in the second filtering stage, offers more flexibility and accuracy in identifying the outliers. The two-stage filtering approach effectively generalizes the AE methodology, removing the need for individual fine-tuning or modifications. This results in a more robust detection of outliers compared to the IF method, which may require case-by-case tuning of the contamination parameter. Consequently, the AE method significantly reduces the chances of misidentifying regions of interest as outliers. Using both methods have shown however that there still are some common issues when anomalies are found in the high-intensity regions, prompting the requirement for further study into the current energy accumulation methodology.

References

T. Melissaris, S. Schenke, N. Bulten, and T.J.C. van Terwisga, (2022). Cavitation erosion risk assessment on a full-scale steerable thruster, *Ocean Engineering*, **251**

T. Melissaris, S. Schenke, and T.J.C. van Terwisga, (2023). Cavitation erosion risk assessment for a marine propeller behind a RoRo container vessel, *Phys. Fluids*, **35**, 013342

S. Schenke, T. Melissaris, and T.J.C. van Terwisga, (2019). On the relevance of kinematics for cavitation implosion loads, *Phys. Fluids*, **31**, 052102

T. Melissaris and I. Hubbard (2024). An Overview of Cavitation Erosion Risk Assessment on Propeller Blades in Full Scale. in *Proceedings of the 12th International Symposium of Cavitation*, Chania, Greece.

F. Liu, T. Ting, K. Ming and Z. Zhou. (2008) Isolation forest. *Data Mining, Eighth IEEE International, ICDM08*

S. Hawkins, H. He, G. Williams and R. Baxter, (2002). Outlier detection using replicator neural networks, in *International Conference on Data Warehousing and Knowledge Discovery*, p.170-80.

P. Gupta, A. Rasheed and S. Steen, (2024). Correlation–based outlier detection for ships' in–service datasets, *Journal of Big Data*, **11**(85)

A. Burkov (2019). The hundred-page machine learning book. *Quebec City, Canada: True Positive Inc*, 17 pp. ISBN: 978-1-9995795-0-0.

26th Numerical Towing Tank Symposium (NuTTS)
23-25 October 2024 - Duisburg, Germany

Hydrodynamic performance enhancement of Newcastlemax bulk carriers via parametric modelling and Computational Fluid Dynamics (CFD)

Carlos E. S. de Almeida*, Claudio Mueller Prado Sampaio*, Mariana Lopes Pinto†, and Philip Pritzelwitz†
*TPN - USP, Sao Paulo/Brazil, †ITV Vale, Ouro Preto/Brazil
carlossimoes@usp.br

1 Introduction

Optimizing the hull forms of Very Large Bulk Carriers (VLBCs) is crucial for enhancing efficiency and reducing fuel consumption in the maritime industry. In today‘s competitive shipping environment, even minor improvements in vessel performance can lead to significant cost savings and reduced environmental impact, making the pursuit of optimized hull designs increasingly important. This need is further amplified by the International Maritime Organization‘s (IMO) new regulations on greenhouse gases (GHGs) emissions (IMO, 2023), which mandate stricter limits on the carbon footprint of ships. These regulations propel the necessity for innovative solutions in ship design projects in order to meet environmental standards while still ensuring that the ships remain economically viable.

Traditional ship design approaches often lack the precision and flexibility needed to address the complexities of modern ship geometries and operational conditions, so this paper presents a method for assessment of novel bow forms of Newcastlemax bulk carriers by integrating parametric modeling with Computational Fluid Dynamics (CFD). This is a Simulation-Based Design (SBD), an invaluable design approach to Naval Architecture. The parametric modeling is conducted using CAESES (CAE System Empowering Simulation), a powerful tool that enables a comprehensive exploration of the design space. Through CAESES, hull parameters can be systematically varied to identify the most effective configurations, leading to smooth surfaces based on F-Splines. CFD is then employed to accurately predict hydrodynamic performance, guiding the iterative refinement of hull form designs.

2 Methodology

The generation of the parametric model in CAESES involves five stages: defining the parameters and design variables; creating the basic longitudinal curves, as well as the auxiliary ones; creating the sections; generating the surfaces; and constructing the solid model. This approach has been done and described by Harries (1998; 2011), Sanches (2016) and others. A traditional Newcastlemax hull form was used as the basis for the parametric modeling.

In the first stage, the design variables and parameters are defined. The design variables are usually the main dimensions of the hull and the parameters are derived from the design variables. For example, the length of the parallel middle body (L_P) is a function of the length between perpendiculars (L_{PP}), a design variable.

The main design variables that control the parametric hull globally - meaning that they are not associated with only one longitudinal curve - are the main dimensions, the lengths of the entrance and run bodies and the position of the stern: length overall (LOA); length between perpendiculars (LPP); beam; draft; height; length of the run body (lAftBody); length of the entrance body (lFwdBody); and position of the transom stern (xTransom). Overall, 50 parameters control the hull shape, including global parameters - meaning that they are not associated with only one longitudinal curve - and the local ones, used to control the shape of the hull in specific areas. Being the majority of the longitudinal curves F-Splines, the local parameters are their start and end positions, as well as the angles of such curves at those positions.

The longitudinal and auxiliary curves used in the present work are F-Splines and NURBS. The second stage is the generation of such curves, as shown in Fig. 1: (1) Midframe; (2) Stem; (3) Flat of Bottom (FOB), the curve on the z = 0 plane; (4) Deck Line; (5) Flat of Side (FOS); (6) Transom Stern; (7) Center Plane Curve (CPC), the curve defining the aft body, especially the bulb; (8)-(10) Diagonals: Auxiliary curves for the aft body; and (11)-(13) Isos: Auxiliary curves for the forward body. The red

curves represent the sections, generated only in the aft body due to its inherent complexity. These curves are created using the vertical angle distribution - referred to as splay in the present work - along the longitudinal curves. The splay angles at the third section are shown in Fig. 2.

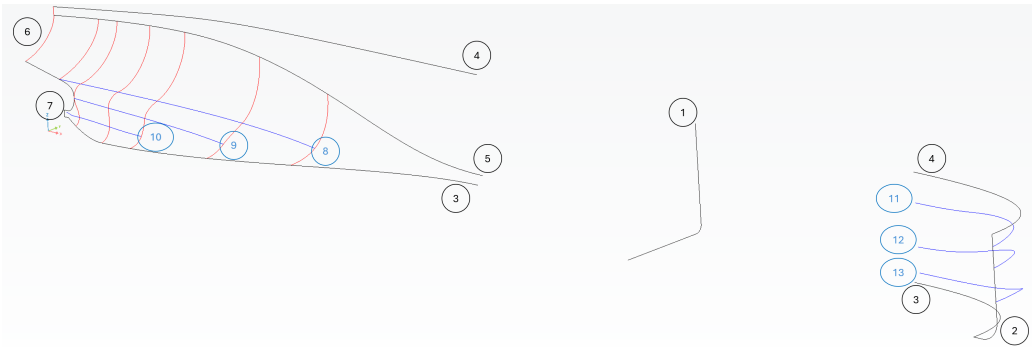

Fig. 1: Parametric longitudinal curves.

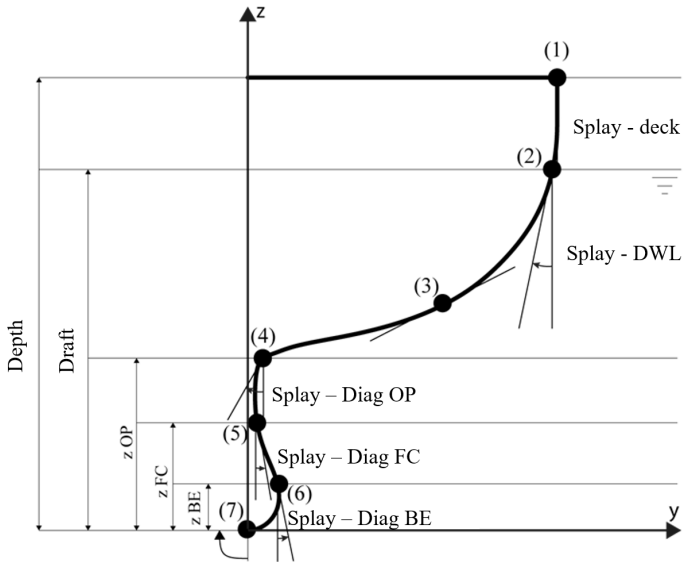

Fig. 2: Definition of the splay angle.

The surfaces that form the parametric hull model are generated during the fourth stage. These surfaces are either constructed using the ruled method or Meta Surfaces. The first is used in the construction of simple surfaces (parallel middle body, FOS, FOB, and stern bulb), while the second is used for the forward body (2 meta-surfaces) and aft body (8 meta-surfaces). The ruled method simply involves generating a linear surface between two arbitrary curves, while the Meta Surface is inherently complex and requires three steps:

- Curve Definition: first, the curve (section) is defined through a feature. A feature is a code, written in the specific language of the software, that takes input data (parameters) and uses them to construct the desired curve. For example, when defining a cross-section represented by an F-Spline, four basic inputs are required: the start point, the end point, and the slope of the curve (splay) at both points.
- Definition of Parametric Distribution Curves: The parameters used as input data in item 1 vary along the longitudinal direction of the hull. The parametric distribution curves define how this variation occurs. The so-called curve engine links the base curve (section) to the parametric distribution curves (longitudinal variation of the points and angles of the section).

- Generation of the Meta-Surface: The meta-surface uses the data from the curve engine for its generation. After that, the meta-surface is represented as a NURBS surface, a standardized type of surface that can be used by other CAE software.

The parametric hull surfaces are shown in Fig.3. The colors of such surfaces are selected in a way that it expresses their complexity: the light gray ones are ruled surfaces, namely the FOB, the parallel middle body; the FOS; and the stern bulb; the gray ones are the two meta surfaces in the entrance body, which don't need predefined sections to be created; and the dark gray ones are the nine meta surfaces that compose the run body and present higher complexity. The solid parametric hull is generated by simply mirroring these surfaces and closing the rear end and the deck with flat surfaces.

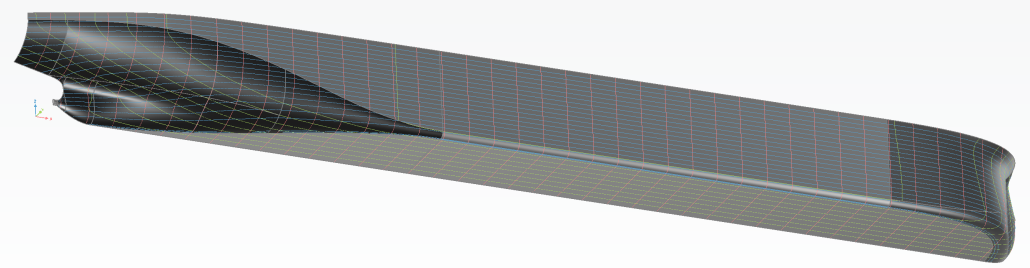

Fig. 3: Hull parametric surfaces.

A significant portion of the parametric models generated throughout this work exhibit variations in their Sectional Area Curve (SAC). The SAC is of utmost importance to the naval architect as it represents the distribution of the ship's displaced volume along the longitudinal axis. In other words, each point on the curve corresponds to the cross-sectional area at that specific position. Thus, the area under the SAC equals the ship's displaced volume, and the x-coordinate of the centroid of this area corresponds to the LCB (Longitudinal Center of Buoyancy).

The lengths of the entrance and run bodies roughly correspond to the positions of the shoulders at the forward and aft sections of the ship, respectively. Fig. 4 shows the SAC of the Newcastlemax in project, where the red points delineate the lengths of the parallel body (L_P), entrance body (L_E), and run body (L_R), as stated in Eq. (1). The area of the midship section is denoted as A_M.

$$LPP = L_R + L_P + L_E. \tag{1}$$

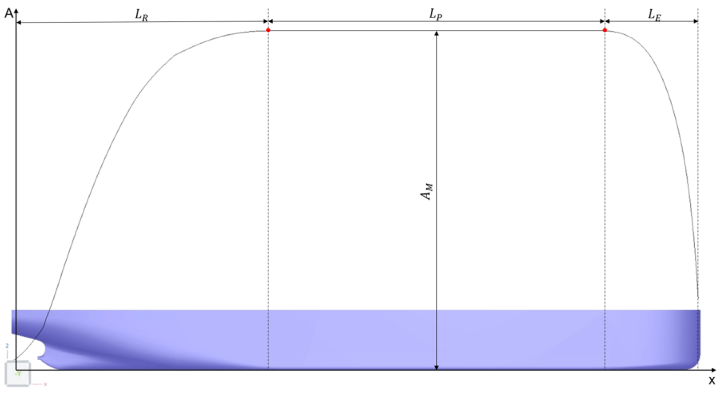

Fig. 4: Sectional Area Curve.

The Generalized Lackenby Method was employed to shift the LCB forward or aft while preserving the hull's overall shape and displacement. This technique allows for targeted variations to assess hydrodynamic performance without significantly altering the vessel's form, as it only changes the centroid of the SAC.

All CFD simulations in the present work were performed under calm water conditions and with a stationary hull. Each simulation used 128 cores and Star-CCM was used. The software has only a frictional (R_F) and a total pressure resistance (R_P) as the output, so in order to obtain the viscous pressure resistance (R_{VP}), a two-step approach was adopted.

The first step involved a symmetry simulation, where the flow was steady, and there was no free surface. This setup allowed the calculation of the frictional and viscous pressure resistance, focusing mainly on the hull interactions with the fluid around it. In the next step, an unsteady simulation with a free surface and using the Volume of Fluid (VOF) method was done. This part was crucial for determination of the wave-making resistance, as it accurately represents the interaction between the hull and the water surface, including the creation of waves. In this study, the SST $k-\omega$ turbulence model was employed to simulate the flow dynamics around the hull. To discretize the terms of the governing equations, the Upwind method was used. For the pressure-velocity coupling, the SIMPLE algorithm (Semi-Implicit Method for Pressure-Linked Equations) is employed.

In all simulations the same meshing methods were used: Surface Remesher for the surface mesh, Trimmed for the volumetric mesh and the Prism Layer mesher for capturing the phenomena on the boundary layer. The mesh was refined near the hull and in the free surface, in order to capture the complex flow in such regions. The total cell count stayed between 7 to 8 million to balance precision with computational efficiency, one of the main trade-offs of CFD (Larson; Stern; Bertram, 2016). Fig.5 shows the domains and 3D mesh views of both simulations.

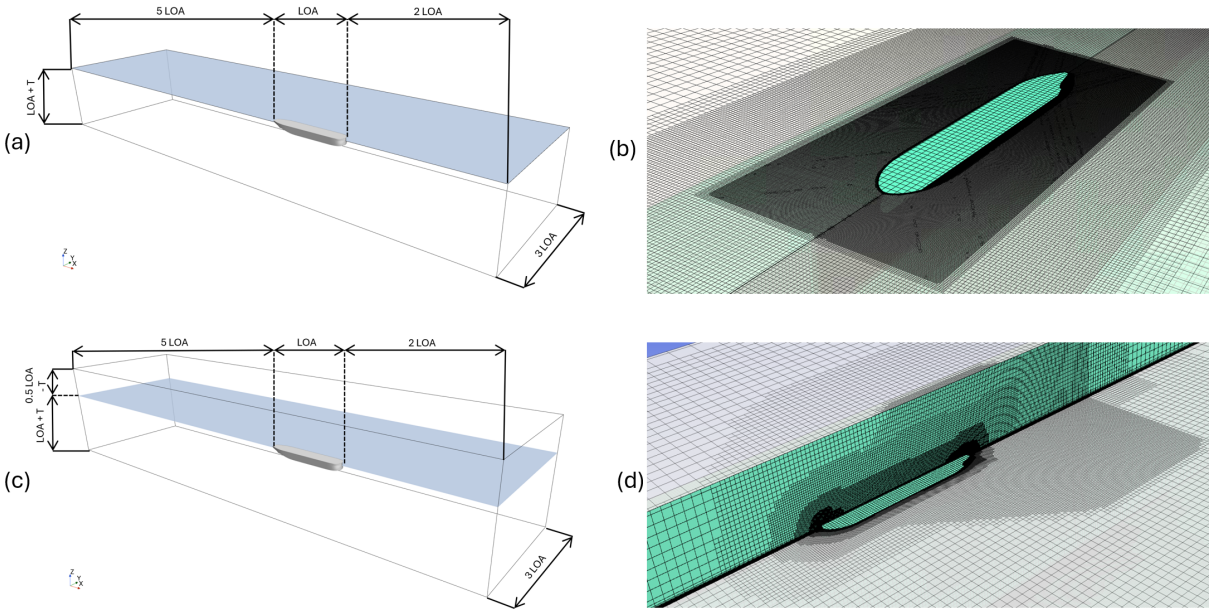

Fig. 5: (a) Domain - Symmetry - S, (b) Mesh - Symmetry, (c) Domain - Free Surface and (d) Mesh - Free Surface.

3 Results

This study involved three key steps: first, the validation of a parametric model by comparing it to the original Newcastlemax hull (called 350); second, the analysis of how the LCB influences resistance, guiding the development of new bow forms; and third, the evaluation of two novel bow designs against the original one, with a focus on identifying the most efficient configuration in terms of the effective power. All simulations were conducted at a ship velocity of 14 knots.

The parametric model was validated by comparing its performance with that of the original hull. The two hulls are not identical, as the original hull provided only the main parameters and the positions of key points in the lines. Any parametric model will inherently differ from the original hull design; otherwise, it would represent a traditional approach rather than a parametric one. Even with such differences, the

variation in the displacement was only $-0.4\%\Delta_{350}$, which is reflected in the small differences between their Normalized Effective Power ($NEP = EffectivePower/\Delta$), as shown in Fig.7.

The parametric model generated has an LCB of 3.45%F. By changing and analyzing the LCB positioning within the parametric model, it was verified that a shift towards the bow (400PM, LCB = 4.0%F, Fig.6(b)) resulted in a larger wave-making resistance and a diminished viscous pressure resistance, with the opposite being true for a shift towards amidships (200PM, LCB = 2.0%F, Fig.6(a)). This finding was crucial in guiding the design and evaluation of novel bow forms.

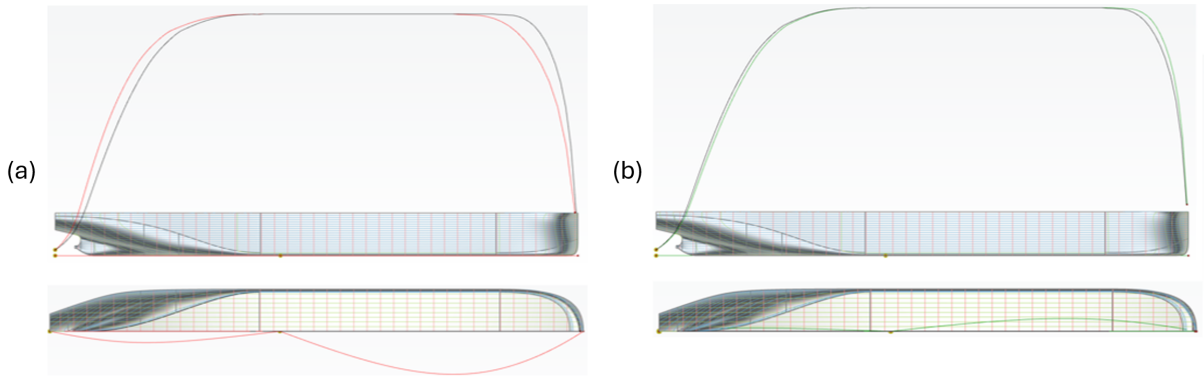

Fig. 6: Generalized Lackenby: (a) 200PM and (b) 400PM.

Analyzing the results in Fig. 7, it is clear that at 14 knots, the wave-making resistance of the Newcastlemax constitutes a significant portion of the total resistance. Therefore, two novel bow forms for a VLBC were analyzed: a spoon bow, a subtype of the cylindrical bow named for its spoon-like shape; and a bow called SEA-Dao, which has an entrance angle of 0° at the Design Water Line (DWL).

The spoon bow was considered for its potential to generate a smoother flow around the hull, while the SEA-Dao was selected for its shape, which is designed to allow the entrance body to cut through the water more effectively. The spoon bow hull has an LCB = 3.67%F, which means that it should have a larger wave-making resistance. However, the results (Fig.7) and the analysis of the flow around the hull show the contrary: due to the smoother flow over the entrance body, the wave-making resistance decreases. The viscous pressure resistance decreases with the larger LCB, as expected. The analyses of the free surface around the original and spoon hulls are shown in Fig.8 as the height of the generated wave divided by the draft (h/T). The SEA-Dao bow hull has a larger wave-making resistance and is discarded.

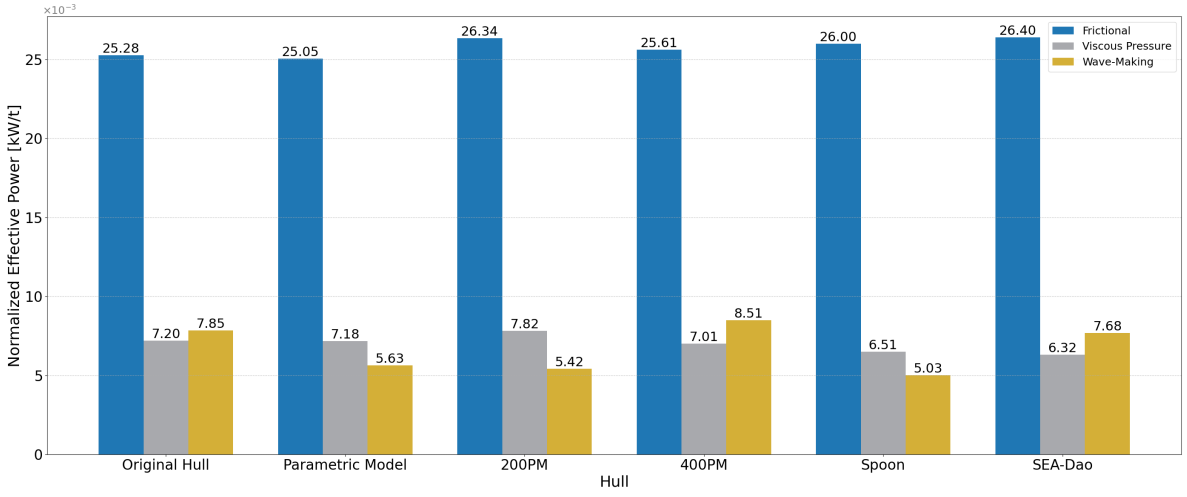

Fig. 7: Normalized Effective Power of the hulls.

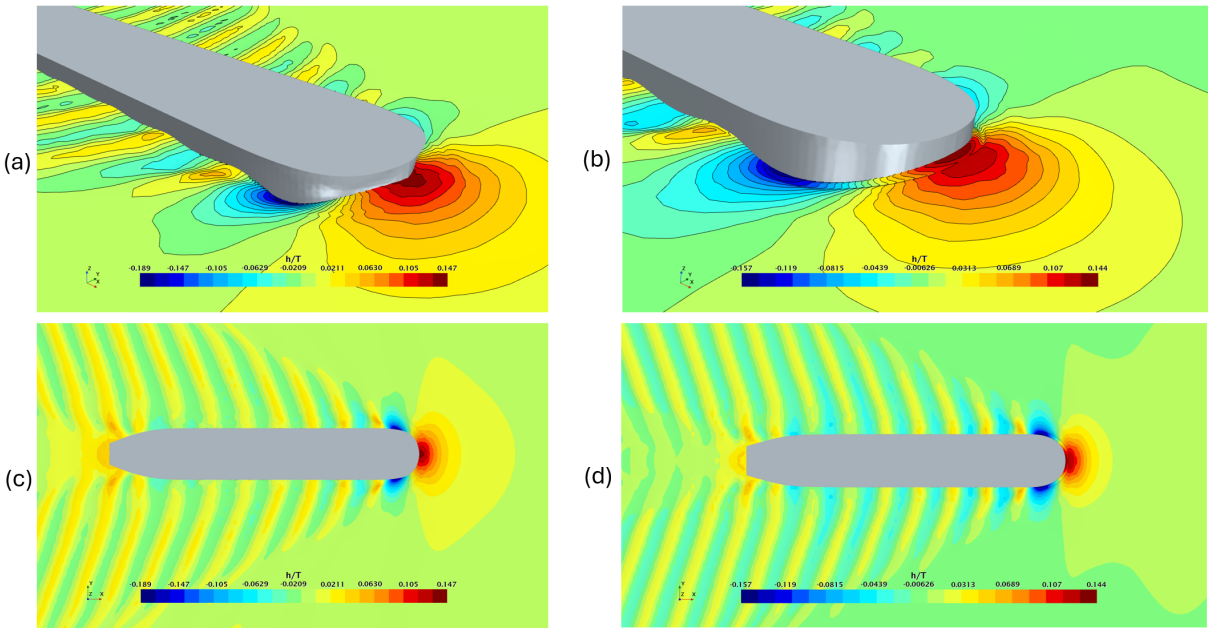

Fig. 8: Free surface analysis: (a) Original - bow view, (b) Spoon - bow view, (c) Original - top view and (d) Spoon - top view.

For the Newcastlemax operating at 14 knots, wave-making resistance plays a significant role in the overall ship resistance. Due to their size and large block coefficients, this component of resistance is usually considered negligible in VLBCs. However, this paper demonstrates that it is not negligible, and therefore, an optimized bow form can be of utmost importance - particularly in today's context, where any reduction in effective power is highly valued.

4 Conclusion

The Newcastlemax hull with the new bow form showed more than a 10% reduction in wave resistance, making it an extremely desirable option in bulk carrier ship design. The next steps towards a full optimization of the hull would be an analysis of the run body forms, focusing on the viscous pressure resistance reduction; alongside a hull-propeller integration procedure. Additionally, exploring the interaction between hull form and varying operational conditions, such as different speeds and sea states, will be crucial.

Finally, integrating this optimization with considerations of structural integrity and cargo capacity will guarantee that the Newcastlemax design remains not only efficient but also practical and feasible for bulk carrier operations. This holistic approach to optimization could lead to a new standard in VLBC design, balancing hydrodynamic performance and operational efficiency.

Acknowledgements

Financial support for this study was provided by Vale Institute of Technology (ITV) and Vale. The authors wish to thank all the professors and colleagues who, directly or indirectly, contributed intellectually to this study.

References

International Maritime Organization (2023). *2023 IMO strategy on reduction of GHG emissions from ships.*

S. Harries (1998). *Parametric design and hydrodynamic optimization of ship hull forms.*

S. Harries et al. (2011). An Integrated Approach for Simulation in the Early Ship Design of a Tanker. *10th International Conference on Computer and IT Applications (COMPIT).*

F. Sanches (2016). *Parametric Modelling of Hull Form for Ship Optimization.*

L. Larsson; F. Stern; V. Bertram (2016). Benchmarking of Computational Fluid Dynamics in Ship Hydrodynamics: The Gothenburg 2010 Workshop. *Ocean Engineering*, **124**, 50–60.

26th Numerical Towing Tank Symposium (NuTTS)
23-25 October 2024 - Mülheim, Germany

Multiphase Computational Fluid Dynamics Based Optimization of Hydrofoil Envelope Performance

Aaron Godfrey*, **Miles Wheeler***
*Siemens Industry Software, Bellevue, WA, USA
aaron.godfrey@siemens.com

1 Introduction

Hydrofoils are streamlined bodies that operate below or in the vicinity of a free surface and are intended to generate large lift forces while keeping drag forces low in comparison. As such, their lift-to-drag ratios can be considerably larger than those of typical high-speed craft (McLeavy (1976)). Traditionally, the limited operating regime of hydrofoils has prevented their widespread use within industry. But, high-fidelity tools, such as computational fluid dynamics (CFD), have made it possible to simulate the important physical effects of hydrofoils (Matveev et al. (2019),Wheeler and Matveev (2023)). As such, it seems as if hydrofoil operating regimes have become more understood and their overall use is growing (Hydrofoil Boats (2024)), and the need for finding optimal hydrofoils is increasing. Traditional hydrofoil optimization has been problematic for two reasons: first, the parametric space is typically defined within a systematic series (e.g. NACA) and the optimal shape is therefore constrained within the bounds of the foil series; secondly, optimizations have historically focused on a single operating condition (Malathi et al. (2016)). Garg et al. (2015) performed a multi point optimization of a tapered NACA foil but used an adjoint technique to overcome the restriction of systematic series parameterization. However, adjoint methods are not typically well suited for multi-phase applications, so the use of these methods are difficult to apply for surface piercing foils where ventilation and cavitation may need to be explicitly modelled. This study focuses on creating the framework for optimizing a surface-piercing hydrofoil across multiple angles of attack while utilizing a parameterization technique that does not confine the foil to a systematic series. The framework is employed on a practical example by utilizing a commercial CFD tool on a previously well studied hydrofoil that is subject to ventilation phenomena.

2 Geometry and Numerical Model

The hydrofoil investigated in this research is a high lift hydrofoil and has a section profile originally studied by Wadlin et al. (1955) . Wheeler and Matveev (2023) performed several investigations on this foil in surface piercing conditions. The foil section is shown in Figure 3. In this study, the foil is placed in a completely vertical orientation and the chord of the foil is fixed to 0.5 m. The length of the foil is 3 m, with 2 m placed below the nominal free surface. The speed of the incoming flow was set to 10 m/s, the lift force is defined as the force perpendicular to the incoming flow, and the drag force is defined as the force acting parallel to the flow.

Wheeler and Matveev (2023) performed extensive validation studies with this foil, and numerically modelled hysteresis and ventilation effects of surface piercing foils were analyzed in great detail in their other study (Matveev et al. (2019)). The numerical modelling techniques used in these studies are largely the same as performed in those investigations. Simcenter STAR-CCM+ 2310 was used to create the CFD models. A single region model was created that employed a first order, implicit time discretization scheme with a time step of 0.001s. 2nd order upwind convection schemes were applied to the remaining equations. The realizable 2 layer all Y+ K-ε RANS-based turbulence model was used. The free surface was modelled using the single-step VOF technique with the HRIC scheme. Parametric-based volume refinements were placed in the domain to ensure adequate mesh resolution for all foils examined in this study, using a base mesh size of chord / 100 as the smallest meshing parameter. The prism layer mesh used 6 layers with a stretch factor of 1.5 to capture the boundary layer and employed wall functions with a target Y+ of 50. Typical meshes used in the study can be seen in Figures 1 and 2.

Simulation operations available within Simcenter STAR-CCM+ were used to remesh and run the model between 0° and 25° angle of attack for all geometries studied. The angle of attacks were varied

systematically and would promote a more wetted foil if hysteresis effects were of concern (i.e. a single operating point being able to operate in a ventilated or wetted state). CAD geometry was created in Siemens NX and transferred into Simcenter STAR-CCM+ using the NX CAD client.

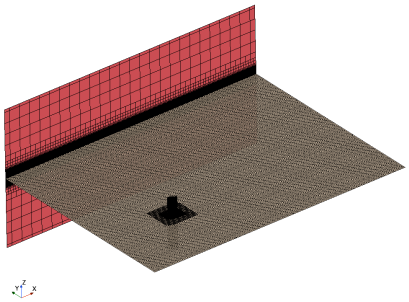

Fig. 1: Mesh of domain and volumetric refinements

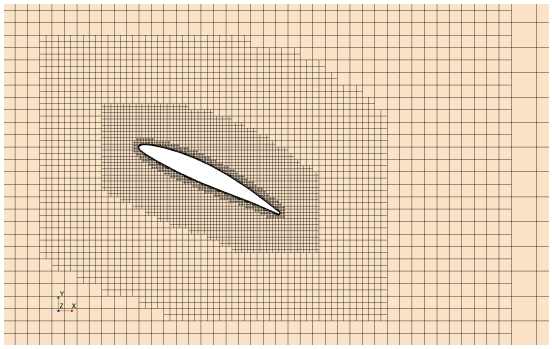

Fig. 2: Section of mesh near foil

3 Parameterization

A suitable parametric model was created using the popular class function shape function transformation (CST) technique described in Kulfan and Bussoletti (2006). The parametric curve is defined as the product of a class function which is taken as a constant and a shape function which is taken as the weighted sum of the Bernstein polynomials of a specified order. The individual polynomial weights are the parameters used to modify the geometry. The baseline design is created by extracting the coordinates of the Wadlin geometry and performing a least squares fit of the individual Bernstein polynomial weights to these coordinates. A single parametric CST is used for the suction side and a separate one is used for the pressure side. With 7^{th} order Bernstein polynomials used for both CSTs a final parameterization with 17 degrees of freedom is the result (16 shape function weights and the trailing edge thickness). Figure 3 shows the construction of the parametric Wadlin model. The upper left chart shows the unweighted Bernstein polynomials while the upper center and upper right charts show the weighted basis functions for the suction and pressure shape functions respectively. The resultant shape functions and the final parametric Wadlin geometry are shown in the bottom left chart. The local error between the parametric hydrofoil and the original Wadlin coordinates are shown in the bottom right chart. The error is everywhere less than $15/10{,}000^{ths}$ with the majority of the surface having an error less than $5/10{,}000^{ths}$. The CST parametric profile was then drawn in the commercial CAD package NX to create the final geometry to be used for the CFD calculations. The upper and lower bounds of the 17-dimensional parameter space were taken to be ±50% of the baseline values determined by the least-squares fit.

4 Optimization

Simcenter STAR-CCM+ includes access to automated design exploration techniques such as optimization. The hybrid-adaptive global search algorithm SHERPA was selected for the current work. SHERPA is a proprietary algorithm intended to search large and complex design spaces without the need for model simplification or design space reduction as these can significantly limit potential design improvements. The search processes is characterized by the simultaneous deployment of multiple search techniques from among those included in the SHERPA algorithm. This selection includes various global and local search techniques. Each technique is dynamically tuned to the specific optimization problem at runtime by the algorithm itself. A well-posed problem statement in the form of design parameters P_i and bounds for each parameter, objectives, constraints, and a total number of design evaluations allowed for the optimization is required. The current work investigates the hydrofoil performance at angles of attack from 0° to 25° in 5° increments which results in 6 distinct operating conditions with 6 associated Lift (L) and Drag (D) values. The optimization problem statement is given in Eq. (1). A weighted sum is applied so that design performance is reduced to a single function of all objectives and constraints which is to be maximized by SHERPA. All operating conditions and Lift and Drag values were considered equally

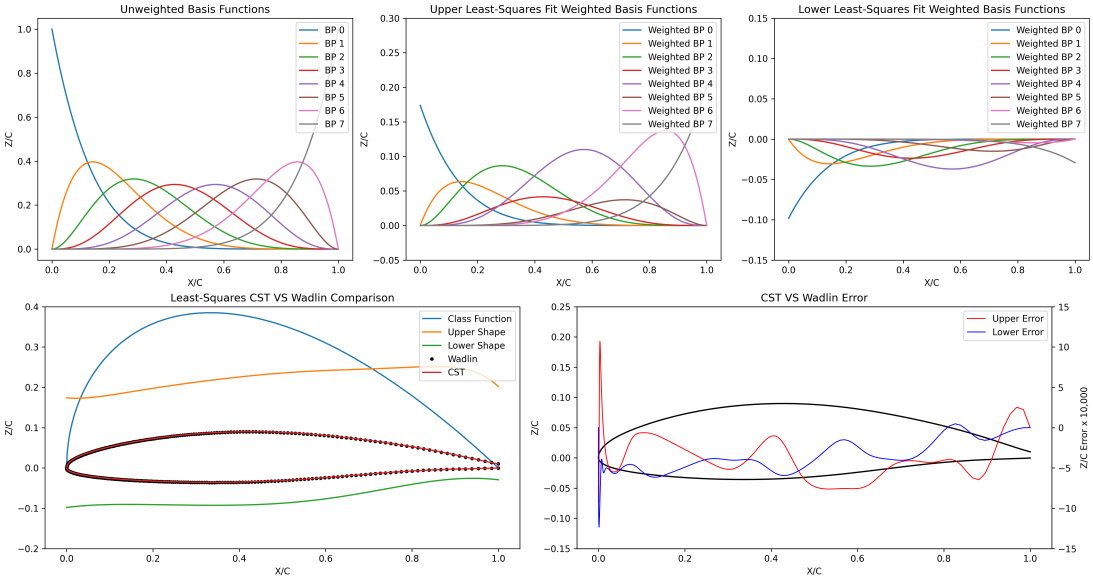

Fig. 3: Wadlin hydrofoil geometry with least squares fit CST parameterization and resultant error

important. SHERPA was allowed 135 designs for the optimization.

$$\min_{P_i} \begin{Bmatrix} D_{00} \\ D_{05} \\ D_{10} \\ D_{15} \\ D_{20} \\ D_{25} \end{Bmatrix} \quad \max_{P_i} \begin{Bmatrix} L_{05} \\ L_{10} \\ L_{15} \\ L_{20} \\ L_{25} \end{Bmatrix} \quad \text{s.t.} \begin{Bmatrix} L_{15} \\ L_{20} \geq 40,000 \text{ N} \\ L_{25} \end{Bmatrix} \tag{1}$$

5 Results

The baseline geometry was shown to be infeasible due to violations of the lift constraints at 20° and 25° angle of attack. A first feasible design (satisfying all constraints) was identified within the initial generation of designs explored. In total 76 feasible designs were identified during the study and the best design found was design 121. Figures 4 and 5 show the history of Drag and Lift values for the optimization study. The geometry of the best design as compared to the Wadlin geometry is shown in Fig. 6. The Wadlin is in red and the best design is in blue. The center chart compares the shape functions for the upper and lower surfaces between the two designs and the right chart compares the thickness and camber distributions. It is noted that the best design has the effect of shifting both the thickness and camber distributions towards the leading edge; the maximum thickness and camber are also slightly increased.

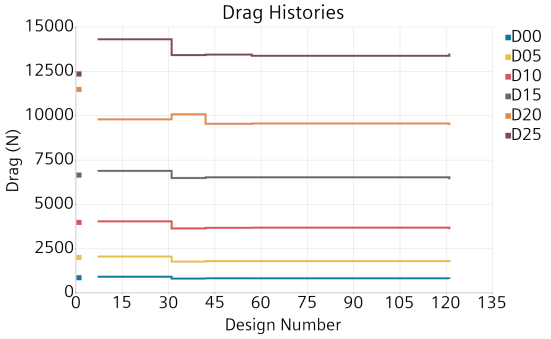

Fig. 4: Optimization drag history

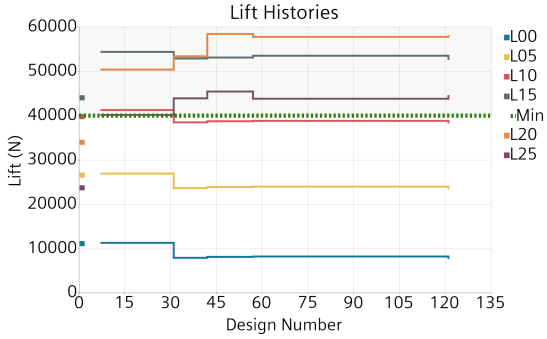

Fig. 5: Optimization lift history

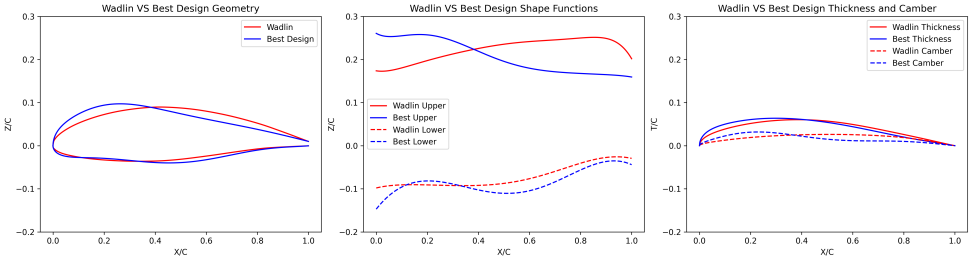

Fig. 6: Comparison of baseline hydrofoil geometry with best design found by SHERPA optimization

Figure 7 is a parallel coordinate plot of the parameter space explored by the optimization. Each vertical axis represents one of the 17 parameters and the lines that traverse the axes' are individual designs. L0 - L7 are the basis function weights for the pressure side CST while U0 - U7 are those of the suction side. The axes bounds represent the full parameter space available to SHERPA for the optimization. The black line down the center shows the parameter values of the Wadlin geometry and the gold line shows the value of all the parameters for the best design. It is seen that for many of the parameters the best design is at or near either the min or max value of the parameter space. This could indicate that additional performance gains may be available by expanding the bounds of the parameter space, especially for those that have settled at the max or min.

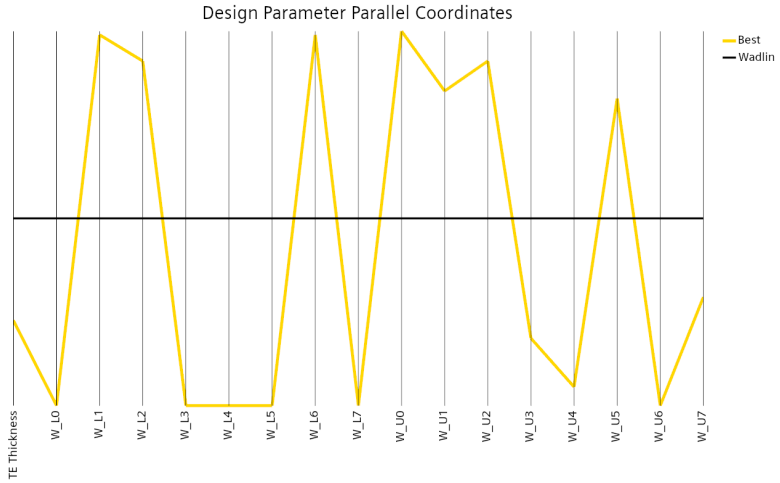

Fig. 7: Parallel coordinate plot of the optimization parameter space.

The best design satisfies all constraints and achieved an improvement in 8 of the 11 objectives, with the remaining 3 seeing some degradation. A detailed comparison of the forces at all angles of attack is given in Table 1. Any decreased performance in an objective, or values that violate constraints, are in red while objectives that show improved performance are in green.

The performance improvement of the best design was due to the flow speeding up around the leading edge which allowed it to remain intact across the initial section on the suction side of the foil, even at larger angles of attack, as seen in Figures 8 and 9. In fact, the best design is completely wetted across all angles of attack studied, whereas the original foil exhibits large ventilation effects and a hollow cavity as seen in Figures 10 and 11. The original design starts to see large ventilation effects at an angle of attack of 20°, as can be seen in the drag spike in Figure 12. This ventilation effect causes the suction side to be close to atmospheric pressure, whereas when wetted, the pressure can be significantly lower than that of atmospheric pressure, dramatically improving the lifting characteristics of the foil. The best design reduces the void from separation; consequently stall is significantly delayed, and lift is improved across larger angles of attack as shown in Figure 13. These improvements lead to an overall more efficient foil with improved or comparable lift to drag characteristics across angle of attacks between 5° and 25°.

Table 1: Lift and Drag comparison for baseline and best design (satisfied constraints or improved objectives , violated constraints or worsened objectives).

Angle of Attack	Baseline (N)	Best (N)	Difference (N)	% Difference
0° Drag	859	792	−67	−7.8
5° Drag	1,997	1,729	−268	−13.4
10° Drag	3,976	3,588	−388	−9.8
15° Drag	6,647	6,409	−238	−3.6
20° Drag	11,475	9,472	−2,003	−17.5
25° Drag	12,349	13,511	1,162	9.4
0° Lift	11,115	7,629	−3,486	−31.4
5° Lift	26,587	23,371	−3,215	−12.1
10° Lift	39,779	38,206	−1,573	−4.0
15° Lift	44,024	52,590	8,566	19.5
20° Lift	33,978	58,148	24,170	71.1
25° Lift	23,719	44,637	20,918	88.2

As noted in the optimization section, each operating condition and objective were considered to be of equal weight. This decision may not be appropriate to every hydrofoil design and will require careful upfront consideration by an engineer with a clear understanding of the principal vessel service requirements. The modification of these weights as well as the selection of appropriate constraints determine what, if any, trade-offs between individual objectives result in increased performance.

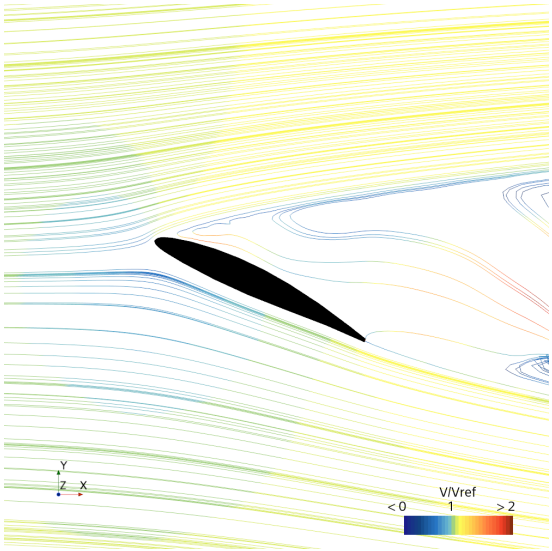

Fig. 8: Baseline Foil Streamlines at 25°

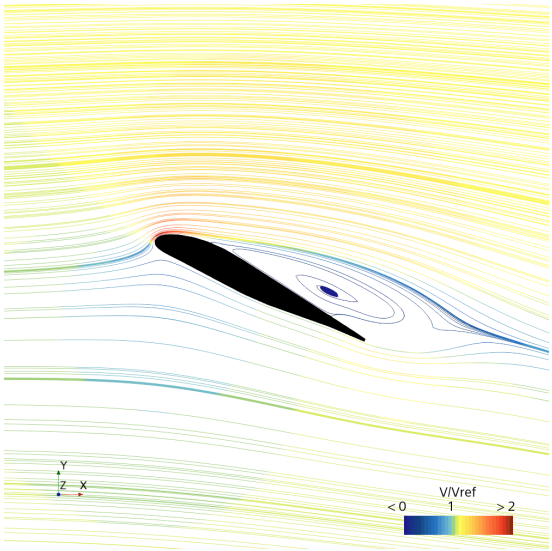

Fig. 9: Optimized Foil Streamlines at 25°

6 Conclusion

This research focused on creating a workflow that can be used to engineer hydrofoil shapes when the foil is subjected to severe multi-phase interaction. The use of CST parameterization avoids the issues of classical parameter based optimization being performed within a predefined series shape while allowing for investigation of multi-phase phenomena. A demonstration of a surface piercing foil was performed, and the final best design was shown to operate in a fully wetted regime while gaining lift and improving efficiency across larger attack angles than the baseline geometry.

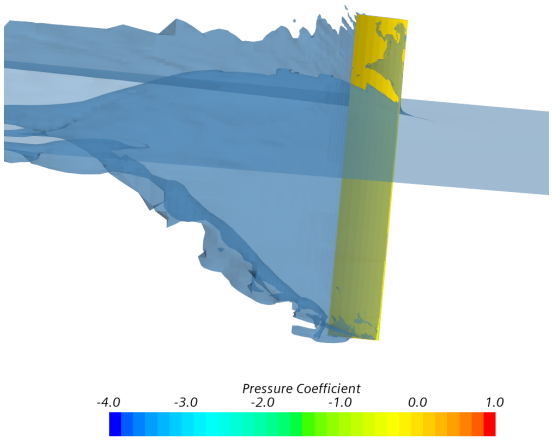

Fig. 10: Baseline Foil CP and Free Surface at 25°

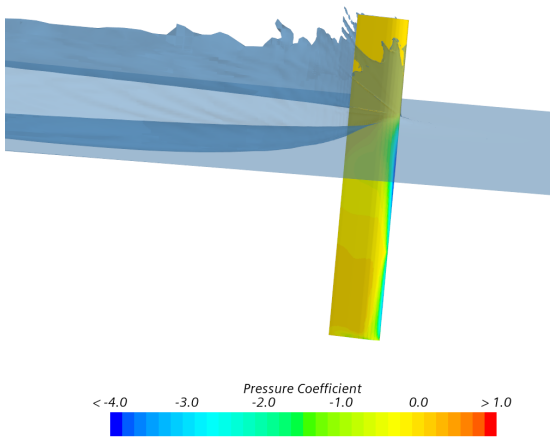

Fig. 11: Optimized Foil CP and Free Surface at 25°

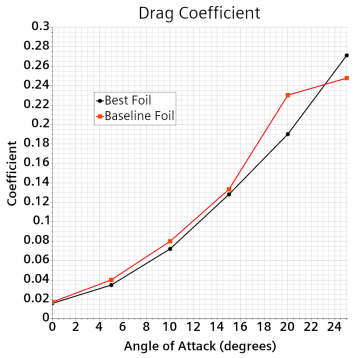

Fig. 12: Drag Coefficient

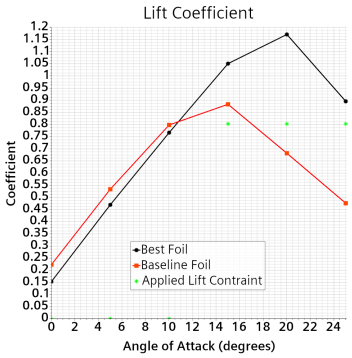

Fig. 13: Lift Coefficient

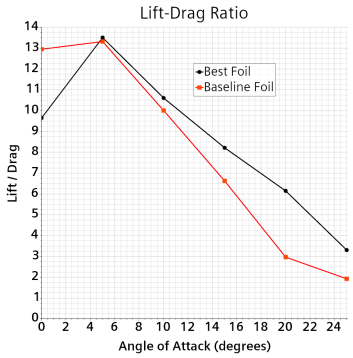

Fig. 14: Lift-Drag Ratio

References

Garg, N., Kenway, G. K., Lyu, Z., Martins, J. R., & Young, Y. L. (2015). High-fidelity hydrodynamic shape optimization of a 3-D hydrofoil. *Journal of Ship Research*, *59*(04), 209-226.

Hydrofoil Boats Market - Forecast (2024 - 2030). IndustryARC. (n.d.). https://www.industryarc.com/Research/hydrofoil-boats-market-research-800224.

Kulfan, B., & Bussoletti, J. (2006, September). "Fundamental" Parameteric Geometry Representations for Aircraft Component Shapes. In *11th AIAA/ISSMO Multidisciplinary Analysis and Optimization Conference* (p. 6948).

MALATHI, Y. L., & SEKHAR, B. G. C. (2016). Design and Optimization of Hydrofoil using CFD and Structural Analysis. *International Journal of Scientific Engineering and Technology Research*, *5*(44), 9107-9116.

Matveev, K. I., Wheeler, M. P., & Xing, T. (2019). Numerical simulation of air ventilation and its suppression on inclined surface-piercing hydrofoils. *Ocean Engineering*, *175*, 251-261.

McLeavy, R. *Hovercraft and Hydrofoils*. Poole, UK: Blanford Press, 1976.

Wadlin, K.L., Shuform, C.L., and McGehee, J.R. "A Theoretical and Experimental Investigation of the Lift and Drag Characteristics of Hydrofoils at Subcritical and Supercritical Speeds." *NACA Technical Report* No. 1232, 1955.

Wheeler, M. P., & Matveev, K. I. (2023). Numerical Modeling of Surface-Piercing Flexible Hydrofoils in Waves. *Journal of Ship Research*, *67*(02), 140-149.

A CFD-Based Analysis of Bow Modification Influence on Ship Resistance and Energy Efficiency

Ines Ivković[†], Matija Vasilev[*†], Milan Kalajdžić[*†]
[*]Ocean Pro Marine Engineers LTD & [†]Faculty of Mechanical Engineering University of Belgrade, Serbia
iivkovic@mas.bg.ac.rs, matija@oceanpro.eu, mdkalajdzic@mas.bg.ac.rs

1 Introduction

With the upgrowth of merchant ships over the centuries, engineers and shipbuilders intended on expanding the existing boundaries when it comes to dimensions, speed, cargo space and overall performance of ships. Since 2013, when the International Maritime Organization (IMO) introduced the Energy Efficiency Design Index (EEDI) for new ships and in 2023 the Energy Efficiency for Existing Ships Index (EEXI), an ongoing challenge arose on how to reduce the total resistance of ships, optimize operational aspects, implement more renewable energy sources and/or use new fuel types, etc. A ship's total resistance is mainly composed of wave resistance and frictional resistance, whose ratio varies depending on ship type and speed. Reduction of wave resistance can be accomplished by improving the ships hydrodynamic characteristics. For example, a precise and well-designed bulbous bow would generate a wave with the opposite phase to the one generated solely by the non-bulbous bow at a specific draft and speed. Therefore, a possibility of reducing the wave resistance occurs by implementing a bulbous bow that would attenuate the generated wave system. The impact of modifications made to the bow was analyzed on an existing general cargo ship, locally reshaping its existing bow. In this study, several configurations were subjected to numerical simulations, of which three are the standard bulb nabla-type (∇), delta-type (Δ) and O-type (Kracht 1978), and three are variations of vertical stem. Computational Fluid Dynamics (CFD) simulations have become a standard tool for enhancing the design process of ships, thanks to the development of computers and software. In comparison to traditional model tests conducted in specialized basins, CFD tools provide a more cost efficient and accessible solution with rising accuracy. Peri et al (2001) and Vakilabadi et al (2017) with towing tank test results at disposal, conducted CFD simulations respectively for a tanker and navy surface combatant and confirmed the accuracy of obtained results. Based on a number of CFD results of modified ship hulls, Peri et al (2001) built two models with optimized forebody geometry and verified the gained values for the two cases through experiments. The wave amplitude was reduced by 18% (Steepest Descent schemes) and 21% (Sequential Quadratic Programming). Regarding various wave resistance reducing techniques, Chen et al (2024) did research on the impact of hydrofoil appendages on resistance for the same ship as in Vakilabadi et al (2017). While Vakilabadi et al (2017) attained resistance reduction through bow and aft modification, Chen et al (2024) demonstrated through CFD simulations and verifying experiments a maximum total resistance reduction ratio of 14.6%, under the influence of simultaneously installed hydrofoil appendages at bow and stern. Yu et al (2017) obtained a reduction of 13.2% in wave-making resistance and a 13.8% reduction in added resistance at $\lambda/L=0.5$ after modifying a 66,000 DWT Supramax bulbous bow to a LEADGE bow shape. Total resistance was expected to be reduced by around 5% in that case. The beneficial impact of a vertical stem on ship resistance, and therefore energy efficiency, was presented in Vasilev et al (2023), with potential CO_2 emission reduction of 9%. The aim of this study was to examine the impact of bulb and bow shape on the results of CFD self-propulsion simulations, and compare the calculated Energy Efficiency of Existing Ship Index (EEXI) of every modified version to the EEXI of the original ship.

2 Methodology

For the analysis of bulb modification, a box-shaped general cargo ship built in 2010, which is still in operation today, was used. The ship has a DWT of 50,640 tons, a length overall of 189.9 meters, and a beam of 30.49 meters. It was designed to sail at a speed of 14.5 knots on a draft of 11 meters, while the scantling draft is 12.8 meters. By analyzing the ship's operational history over the past period, it was concluded that the ship often sails at a draft greater than that originally intended by the design, i.e., the ship more frequently operates at drafts closer to the scantling draft than at the design draft, for which the bulb was originally optimized. Therefore, research into optimizing the bow for the scantling draft at a speed of 14 knots was conducted. Additionally, a feasibility study was requested, which includes a generic study evaluating different types of bulbs based on Kracht, 1978. These types include nabla-type (∇, current design bow), delta-type (Δ), and O-type. Regarding the dimensional parameters of these bulbs, no precise formulas for determining the ideal bulb dimension parameters can be found. Model tests have been the safest solution for estimating which bulb type and bulb dimensions have the best impact on the total resistance of a specific ship. Papanikolaou A. in his book "Ship Design" mentions that the ratio of the bulb's section area at forward perpendicular and the midship section area varies between 5% and 15%. The ratio, as well as the bulb's length, depends on the design speed and bulb type. For the purposes of this study, the section area ratio is about 10% for all three bulb types and the original bulb's length was increased by 70%, which represents the bulb length for the first set of calculations. A number of models with less increasement of bulb length will in the future be tested with CFD simulations and the results will be compared with the ones achieved in this first iteration. In addition to the three main bulb shapes, the option of a vertical stem was also considered, as it has been found in Vasilev et al (2023) that a vertical stem can reduce delivered power. Vertical stems are especially beneficial for ships whose draft and trim varies during their exploitation since the fore part of the actual waterline does not vary significantly compared to the fore part of the design waterline. Other advantages of vertical stems are increased volume and cargo space at the fore peak, simpler manufacturing, and better stability in rough seas.

Based on the available construction drawings, a digital twin of the original version of the ship was created (see Fig. 1), which was later modified in the area in front of the forward watertight bulkhead and beneath the upper deck, which also serves as the watertight deck. For the three versions of the vertical stem, the original model's fore part was modified, in relation to three different reference boundaries. Version one was modified forward from the front end of the ship's parallel midbody. For the second version, the area forwards from the bulkhead that separates cargo holds number one and number two was modified, and the third version was modified in relation to the forward watertight bulkhead. The form of the vertical stem was adopted from a digital twin from another cargo vessel which has similar dimensions and displacement, but reached greater speed than the cargo ship which is the subject of interest of this study.

Fig. 1: Reference hull model – view from stern (left), view from stem (right)

All 3D models were implemented into CFD simulations to assess resistance in calm water, as well as a self-propulsion test using an actuator disk. The methodology used for mesh generation, as well as the entire setup of these types of simulations, is detailed in Vasilev et al (2024). To verify the reliability of the CFD simulations, an initial CFD analysis of resistance in calm water and a self-

propulsion test of the ship with the original bulb was conducted at both design and scantling drafts, for speeds of 12, 14, and 16 knots. The results were then compared with the available results from extrapolated model tests. According to IMO (2022), results obtained from CFD analysis should not deviate more than 5% from reference values recorded during model tests (extrapolated to full scale).

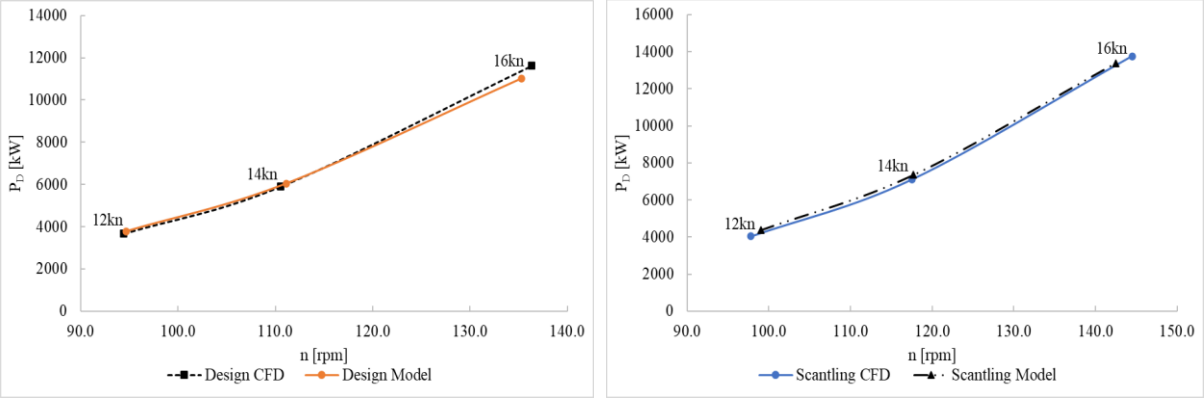

Fig. 2: CFD vs model test at design draft (left) and at scantling draft (right)

To observe the effect of bulb modification on energy efficiency, the attained EEXI was also calculated according to IMO (2021). Based on the available data provided in the shop test of the installed engine, the specific fuel oil consumption (SFOC) and daily fuel oil consumption (FOC) were determined. Using the average fuel price, which can be easily found, the economic savings in fuel for one year were calculated.

The six generated models are displayed in Figure 3. A red line can be identified at the front part of each model. The red line represents the borderline between the original model and the modified area at the front part.

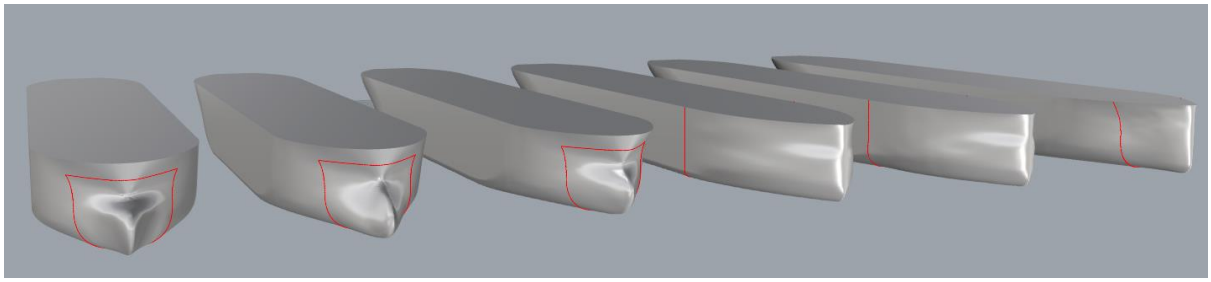

Fig. 3: Model with ∇-type bulb is first on the left, following to the right are models with Δ-type bulb, O-type bulb and versions of vertical stem number one, two and three

3 Results

The results for design draft conditions are shown in the form of 3D surface plots in Figures 4 and 5, while the results obtained for scantling draft are displayed in Figures 6 and 7. Values of brake power for every considered case and their comparative analysis are presented in Figures 4 and 6. Since the underwater volume of every redesigned model differs to a certain extent from the underwater volume of the original ship, a dimensionless ratio R_T/D was introduced for a more accurate comparison of the influence of bow modification on the ship's resistance. Figures 5 and 7 give a clearer insight into the effectiveness of the redesigns. On the x-axis are the cases 1 to 7 arranged (1 – nabla-type bulb; 2 – delta-type bulb; 3 – O-type bulb; 4 – original model; 5 – first version of vertical stem; 6 – second version of vertical stem; 7 – third version of vertical stem), on the y-axis are the ship speeds presented, while on the z-axis are values for brake power (Figures 4 and 6) or R_T/D ratio sorted (Figures 5 and 7).

Every calculated point is labeled with the percentage of increasement or reduction of brake power or R_T/D ratio in relation to the values for the original ship.

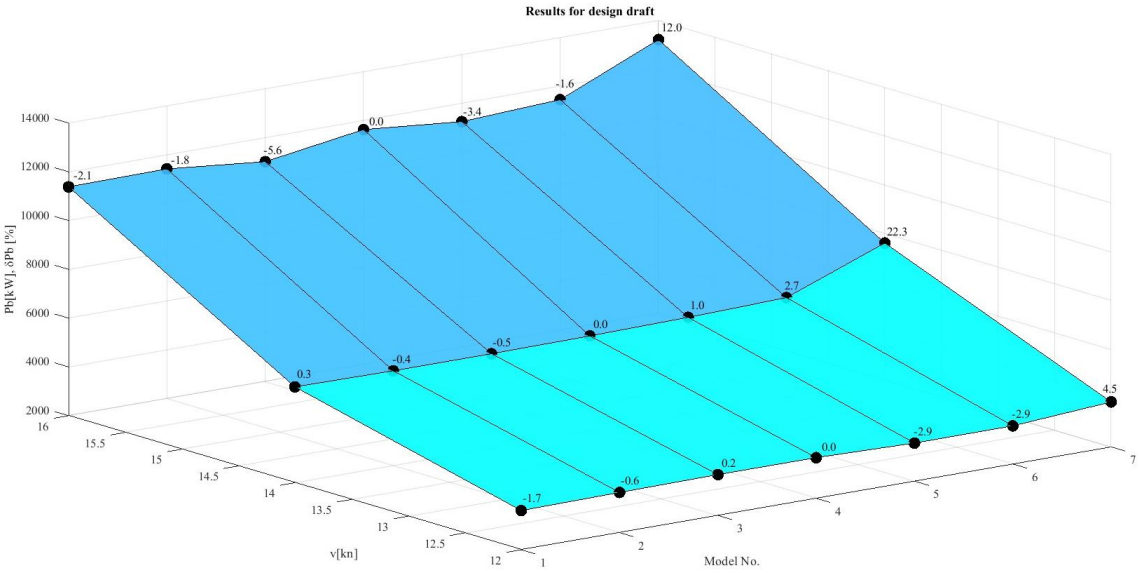

Fig. 4: Comparative analysis of brake power for considered ship bow configurations and speeds at design draft

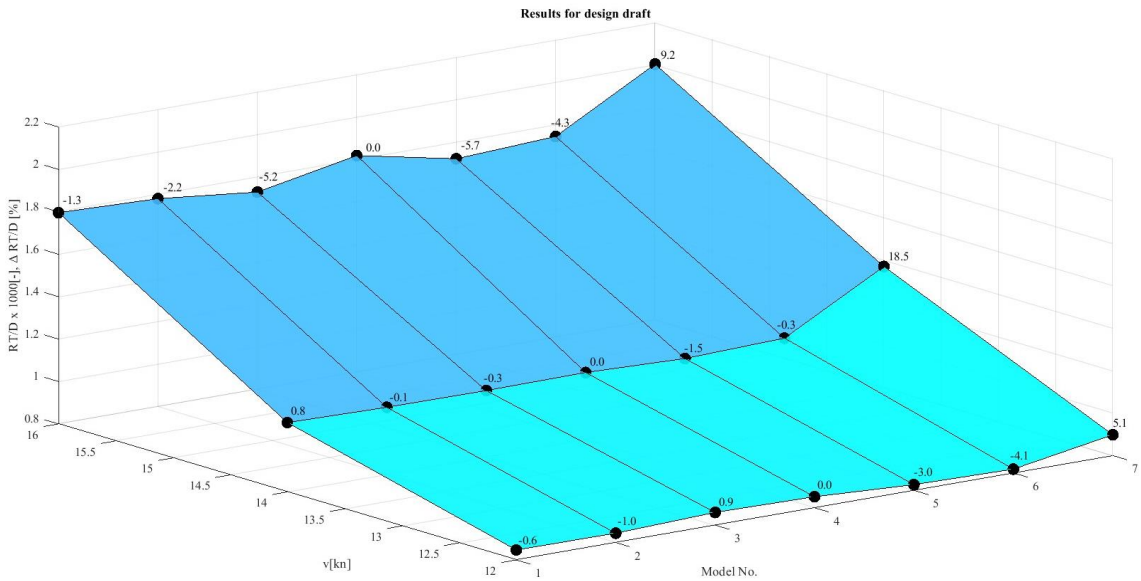

Fig. 5: Comparative analysis of *R_T/D* ratios for considered ship bow configurations and speeds at design draft

The maximum average reduction in brake power at design draft of 1.9% was obtained for the O-type bulb and 6.7% at scantling draft with the first version of vertical stem. When comparing the R_T/D ratio, the first version of vertical stem emerged as the optimal solution with an average reduction of 3.4% at design draft and 8.5% at scantling draft, followed by the second version of vertical stem with a 2.9% average reduction of R_T/D ratio at design draft and 7.4% average reduction at scantling draft. The third most beneficial version, and with the least need for modification and retrofit, is the modified O-type bulb, which reduced the R_T/D ratio by an average of 1.5% at design draft and an average of 1.1% at scantling draft. According to the CFD results, the third version of vertical stem is the worst case that was considered, with an average increase of 10.9% and 7.6% at scantling draft. It can be

noted that the original bulb was well-designed for the design draft and design speed since the relative reductions of R_T/D ratio for the three modified bulb versions are below 1%.

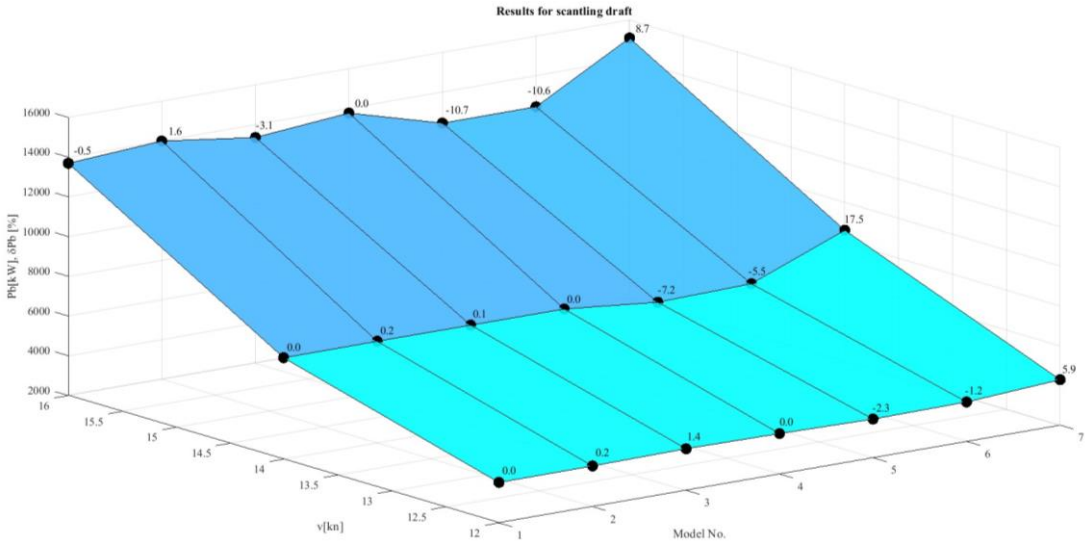

Fig. 6: Comparative analysis of brake power for considered ship bow configurations and speeds at scantling draft

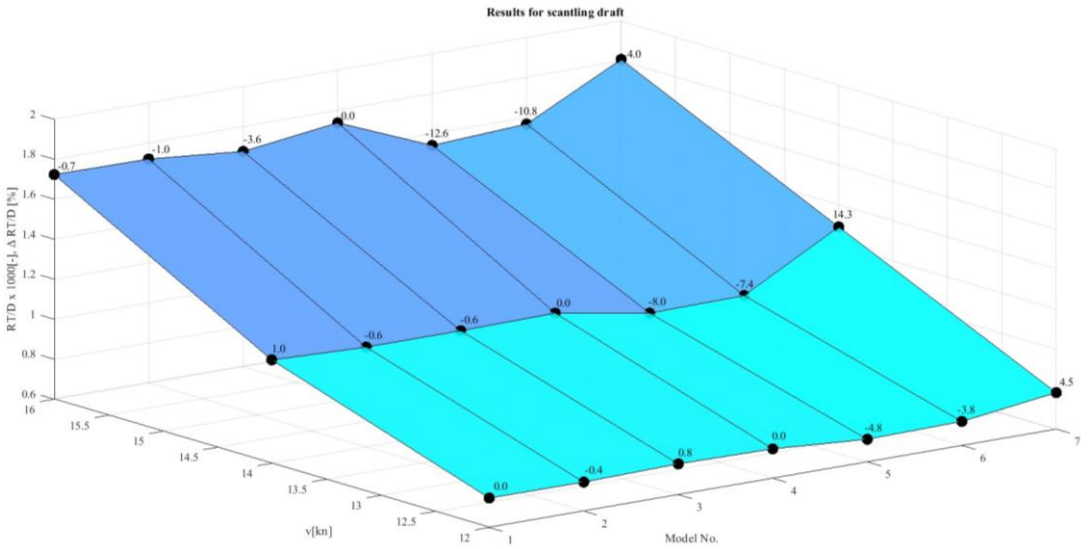

Fig. 7: Comparative analysis of R_T/D ratios for considered ship bow configurations and speeds at scantling draft

For a better insight into how redesigning the bow impacts the energy efficiency of the cargo ship, calculations of EEXI and daily fuel consumption were conducted for every case. The attained EEXI for all cases was lower than the required value, and therefore the required EEXI condition is satisfied. As expected, the model with the first version of vertical stem attained the lowest EEXI, and therefore the greatest average fuel savings of 3.2%, with a referent speed increasement of 0.3kn. Considering the fact that the ship operates more often on a draft closer to the scantling draft than the design draft, about 300 thousand to 350 thousand dollars per year could be saved in the most favorable condition

(with an average fuel price of 598 dollars per ton). Although the attained EEXI of the third version of vertical stem satisfied the condition regarding the required EEXI, an increasement of 20.6% in average fuel consumption excludes this case from further consideration. The results for EEXI and fuel saving are shown in Table 1.

Table 1: EEXI and fuel consumption calculations for 7 analyzed cases

				11m		12.8m		11m	12.8m	
	Vref [kn]	att. EEXI	req. EEXI	SFOC [g/kWh]	FOC [t/day]	SFOC [g/kWh]	FOC [t/day]	δFOC [%]	δFOC [%]	Average Fuel Savings
Original	14.00	5.723	7.249	170.89	24.24	170.88	29.13	[-]	[-]	[-]
Nabla	14.00	5.724	7.249	170.87	24.32	170.89	29.13	0.3%	0.0%	0.2%
Delta	14.00	5.727	7.249	170.91	24.15	170.90	29.19	-0.4%	0.2%	-0.1%
O-type	14.00	5.725	7.249	170.91	24.13	170.89	29.16	-0.4%	0.1%	-0.2%
V1	**14.29**	**5.609**	**7.249**	**170.84**	**24.47**	**170.65**	**27.12**	**1.0%**	**-7.4%**	**-3.2%**
V2	14.22	5.636	7.249	170.77	24.90	170.68	27.58	2.6%	-5.6%	-1.5%
V3	13.37	5.996	7.249	171.42	31.31	173.18	35.77	22.6%	18.6%	20.6%

4 Conclusion

Through comprehensive CFD simulations, the impact of bow modifications on the hydrodynamic performance of a ship was successfully demonstrated in this study, illustrated with the example of an existing cargo ship. The findings reveal a certain potential for reducing fuel consumption with modifications featuring vertical stems. The validity of this idea is justified by the CFD results which show a possibility of reducing the daily fuel consumption of the ship by 7.4% when the ship sails at scantling draft.

These results highlight the effectiveness of bow modifications in enhancing fuel efficiency and compliance with regulations such as the Energy Efficiency Existing Ship Index (EEXI). The implications for the maritime industry are profound, optimizing hull forms contributes to reduced operational costs and it also aligns with the global need for more sustainable shipping practices. The findings not only affirm the importance of innovative hull designs but also present a pathway for shipowners to achieve significant operational efficiencies.

By integrating advanced computational methods and experimental validation, we can further refine our understanding of hydrodynamics in ship design. As the maritime industry increasingly prioritizes sustainability and efficiency, the insights gained from these simulations will inform future design strategies, promoting advancements that align with both economic and environmental goals.

Acknowledgements

Authors would like to thank Ocean Pro Marine Engineers LTD who provided necessary support in CFD simulations and guidelines and Argo Navis Ltd. who provided technical software support. This work was supported by the Ministry of Education, Science and Technological Development of Serbia (Project no. 451–03−65/2024−03/200105 from 5 February 2024).

References

Chen, Q.; Liu, Z.; Liu, W.; Zhao, G. (2024). Design and PrinciplesAnalysis of Hydrofoil Appendages for Reducing Resistance of High-SpeedShips. J. Mar. Sci. Eng., 12, 1394.

IMO. (2021). Resolution MEPC. 328(76). Amendments to the Annex of Protocol of 1997 to amend the International Convention for the Prevention of Pollution from Ships, 1973, as Modified by the Protocol of 1978 Relating Thereto (2021 Revised MARPOL Annex VI). IMO, London, England. Available online. https://docs.imo.org/. (Accessed 9 July 2024).

IMO. (2022). Development of Draft 2022 IACS Guidelines for the Use of Computational Fluid Dynamics (CFD) for the Purposes of Deriving the in the Framework of the EEXI Regulation, Resolution MEPC.78/INF.16; IMO, London, England. Available online. https://docs.imo.org/. (Accessed 9 July 2024).

Kracht, A. M. (1978). Design of Bulbous Bows, SNAME Transactions, Vol. 86, pp. 197-217, 1978.

Papanikolaou A. (2014). Ship Design-Methodologies of Preliminary Design (1st ed.). Springer.

Peri, D.; Rossetti, M.; Campana, E. F. (2001). Design optimization of ship hulls via CFD techniques. Journal of Ship Research, 45, 140–149.

Schneekluth, H.; Bertram, V. (1988). Ship Design for Efficiency and Economy, Butterworth-Heinemann, Second edition.

Vakilabadi K. A., Motahari H. (2017). Analysis of Bow and Aft Modification Effect on DTMB 5115 Ship Resistance. American Journal of Mechanical Engineering, vol. 5, no. 1: 14-17.

Vasilev, M.; Kalajdžić; M., Suvačarov, A. (2023). A Practical Approach to Bulbous Bow Retrofit Analysis for Enhanced Energy Efficiency, 25th Numerical Towing Tank Symposium (NuTTS 2023), 15-17 October 2023 – Ericeira, Portugal.

Vasilev, M.; Kalajdžić, M.; Ivković, I. (2024). CFD-Powered Ship Trim Optimization: Integrating ANN for User-Friendly Software Tool Development. J. Mar. Sci. Eng, 12, 1265. https://doi.org/10.3390/jmse12081265

Yu, J.W.; Lee, C.M.; Lee, I.; Choi, J.E. (2017). Bow hull-form optimization in waves of a 66,000 DWT bulk carrier. Int. J. Naval Arch. OceanEng., 9, 499–508.

26th Numerical Towing Tank Symposium (NuTTS)
23-25 October 2024 - Mülheim a. d. Ruhr, Germany

Hull Optimization of a Catamaran in both Deep and Shallow Water

Yanxin Feng* **and Ould el Moctar**
Institute for Sustainable and Autonomous Maritime Systems
University of Duisburg-Essen, Duisburg/Germany
*yanxin.feng@uni-due.de

1 Introduction

Catamarans are increasingly popular in maritime applications due to their superior stability, reduced wave-making resistance, and larger deck area compared to monohulls. However, optimizing catamaran hull designs for efficiency in various operating conditions, particularly in deep and shallow water, remains challenging. Water depth significantly affects hydrodynamic resistance, influencing fuel consumption, operational costs, and overall performance. This dual-environment challenge motivates the optimization of catamaran hulls to minimize resistance across a range of speeds and water depths.

The main approach we used in this study was the boundary element method (BEM). The BEM has evolved significantly since its inception, finding widespread application across various fields due to its efficiency in solving boundary value problems. In fluid dynamics, BEM is applied to potential flow and Stokes flow problems, providing accurate solutions with reduced computational cost compared to volumetric methods. BEM is widely used to predict wave resistance and analyze flow fields around ship hulls. Hino (1997) provided a comprehensive review of BEM applications in calculating wave resistance. BEM has been employed in the hydrodynamic optimization of ship hulls to minimize resistance and improve performance. Campana et al. (2006) discussed optimization techniques using BEM for hull form design. Söding et al. (2014) developed a three-dimensional Rankine panel method based on BEM accounts for the interaction of the linear periodic wave-induced flow with the nonlinear steady flow caused by the ship's forward speed in calm water, taking into account nonlinear free surface conditions and dynamic squat. Later, Riesner and el Moctar (2018) applied this method to predict wave-added resistance and ship motions in small amplitude waves. As research continues, BEM is poised to play an even more significant role in the design, analysis, and optimization of marine structures and systems.

In this study, a multi-objective optimization (MOO) algorithm, known as Surrogate-based Global Optimization (SBGO), is employed. This algorithm is designed to efficiently handle complex optimization problems by using surrogate models to approximate objective functions, enabling faster convergence and more effective exploration of the design space. Numerous researchers have contributed to the sustainable development of the SBGO algorithm. Jin (2011) provided a concise overview of recent advances in surrogate-assisted applications, highlighting remaining challenges for future research. Additionally, Dong et al. (2018) presented a multi-surrogate-based differential evolution method with multi-start exploration for computationally expensive optimization tasks. Ye (2019) outlined fundamental issues in SBGO from a practitioner's perspective, covering concepts, methods, techniques, and engineering applications.

Shallow water introduces additional hydrodynamic complexities, such as increased wave resistance due to restricted water depth, leading to different performance behaviors compared to deep-water conditions. The scarcity of research addressing this dual-environment optimization highlights the need for more comprehensive approaches that can enhance catamaran performance across diverse operating conditions. This study addresses this gap by investigating the optimization of catamaran hull geometry and inter-hull spacing to minimize total resistance at different speeds in deep and shallow waters. A parametric hull model is developed to facilitate systematic adjustments to hull geometry and spacing during the optimization process. The SBGO algorithm is utilized to identify the optimal design configurations, while a potential flow solver based on the Rankine source panel method (GL Rankine code) provides

accurate fluid dynamics simulations around the catamaran hulls. This combined approach significantly reduces total resistance, achieving improvements of up to 10% at higher speeds.

2 Optimization process description

Figure 1 illustrates the flowchart of the entire hydrodynamic optimization procedure utilized in this study. The ideal geometry file of the original hull is provided in IGES format. Utilizing this file, we can extract the coordinate values of points and compare the surfaces between the original and parametric catamaran hulls. By employing the fully parametric modeling capabilities of CAESES, a parametric hull is generated for the catamaran. Selected design variables define the hull shape. Computations of the flow around the hulls are performed using a validated nonlinear potential flow boundary element method. By applying an effective optimization algorithm, SBGO, we obtain the optimized ship hull for the catamaran.

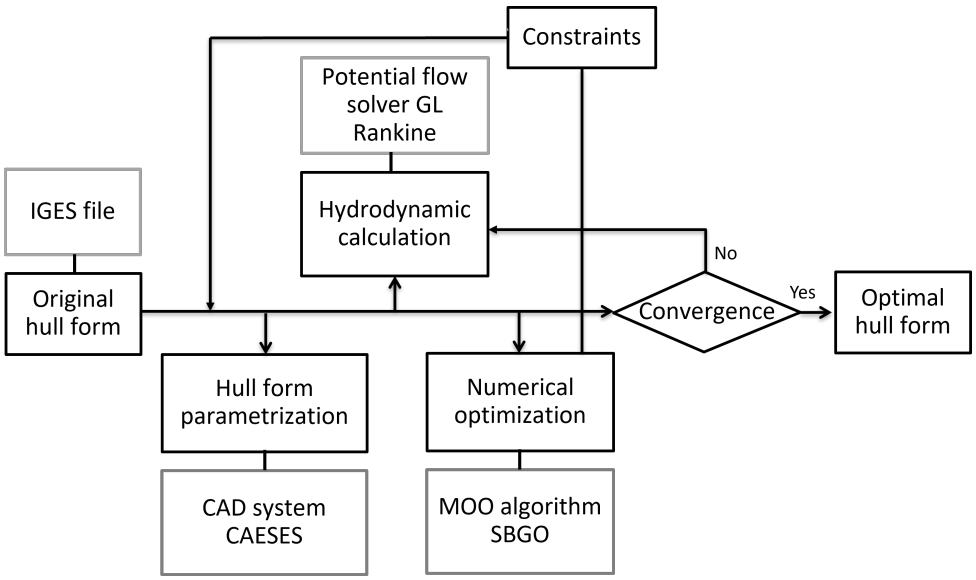

Fig. 1: The flowchart of the hydrodynamic optimization process

3 Results and discussion

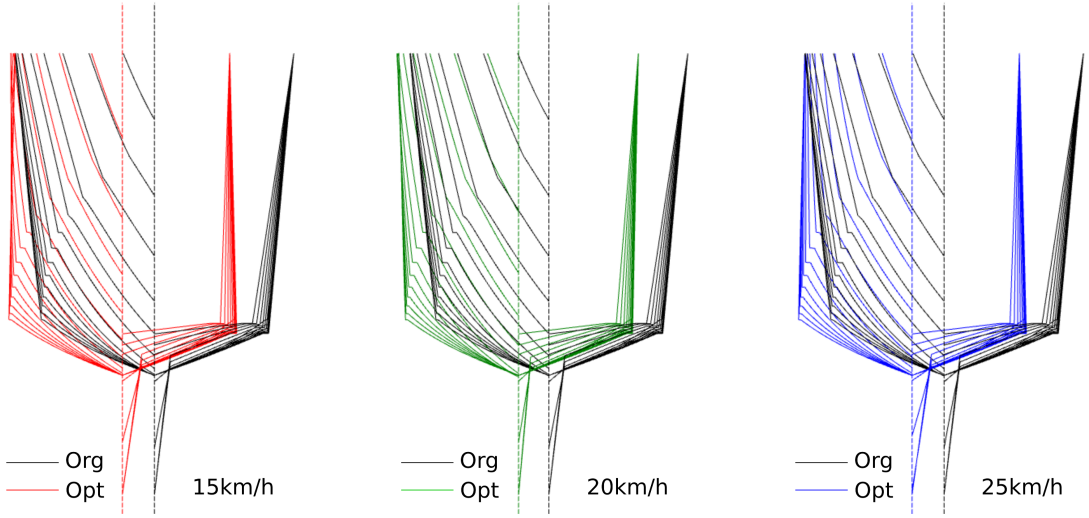

Fig. 2: Comparative body plans of the parametric hull (black) and the optimized hull (colored) for the catamaran at speeds 15 km/h (red), 20 km/h (green), and 25 km/h (blue)

Figure 2 compared the body plans for one body of the catamaran at the cross-section of the parametric hull and optimized hull at different speeds. In this figure, the black line is for the parametric hull, the red line for the optimized hull at a speed of 15 km/h, the green line for the optimized hull at 20 km/h, and the blue line for the optimized hull at 25 km/h. From the comparison results, it is evident that a longer distance between two hulls helps reduce the resistance of the catamaran. In other words, the wider the catamaran is, the more minor resistance it will encounter. Besides, the optimized hulls at different speeds all have a slimmer single hull. The influence of the width of the single hull is opposite to the beam of the catamaran. The slimmer the single hull is, the less resistance the catamaran will experience.

Figure 3 shows the wave pattern comparison between parametric hulls and optimized hulls at speed of 15 km/h, 20 km/h, and 25 km/h in a water depth of 2.5m. The color gradient from blue to red indicates the range of wave elevation, with lower values depicted in blue and higher values in red. After optimization, there is a noticeable reduction in the range of wave elevation at speeds of 20 km/h and 25 km/h. For a water depth of 4 m, a similar reduction in wave elevation on the optimized hull can be observed. Due to text length limits, this figure will not be included in the report.

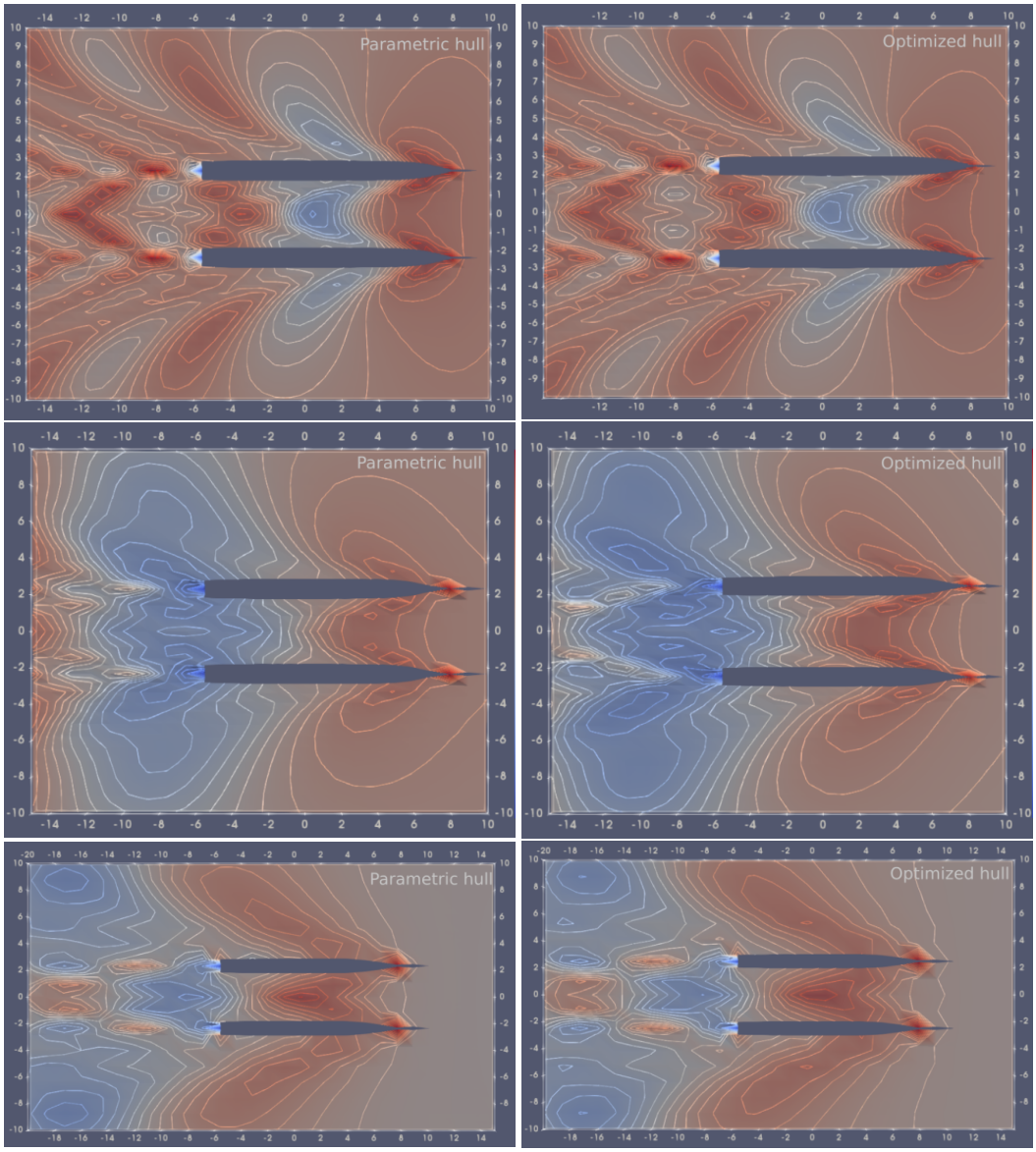

Fig. 3: The wave pattern comparison between parametric hull (left) and optimized hull (right) at speed 15 km/h (top), 20 km/h (middle), and 25 km/h (bottom) in water depth 2.5m

After optimization, the catamaran hull featured a slimmer hull, a sharper and straighter skeg-stern, and a fuller bow. Despite the influence of parameters on a single hull, the distance between the two hulls significantly affects the resistance of the catamaran. The greater the distance between the hulls, the more the resistance of the optimized hull decreases. From the comparison results between the parametric hull and the optimized hull under different conditions, it was found that the difference in resistance reduction of the optimized catamaran in different water depths is not remarkable. However, the reduction in total resistance is more significant at high speeds, with the reduction percentage value reaching more than 10%.

References

Campana, D., P., B., T., F., S., and R., W. (2006). Automatic hull generation and optimization with a cfd parametric design tool. *SNAME Transactions*, 114:203–232.

Dong, H., Li, C., Song, B., and Wang, P. (2018). Multi-surrogate-based differential evolution with multi-start exploration (mdeme) for computationally expensive optimization. *Advances in Engineering Software*, 123:62–76.

Hino, T. (1997). A review of computational techniques for predicting ship resistance and flow field. *Journal of Marine Science and Technology*, 2, Issue 4:163–170.

Jin, Y. (2011). Surrogate-assisted evolutionary computation: Recent advances and future challenges. *Swarm and Evolutionary Computation*, 1(2):61–70.

Riesner, M. and el Moctar, O. (2018). A time domain boundary element method for wave added resistance of ships taking into account viscous effects. *Ocean Engineering*, 162:290–303.

Söding, H., Shigunov, V., Schellin, T. E., and Moctar, O. e. (2014). A rankine panel method for added resistance of ships in waves. *Journal of Offshore Mechanics and Arctic Engineering*, 136(3):031601.

Ye, P. (2019). A review on surrogate-based global optimization methods for computationally expensive functions. *Software Engineering*, 7(4):68.

26th Numerical Towing Tank Symposium (NuTTS)
23-25 October 2024 - Mülheim an der Ruhr, Germany

Gap Effect of a Rim Driven Thruster in Convergent and Divergent Duct Configuration

Marco Lugaresi, Diego Villa and Stefano Gaggero
University of Genoa, Genoa, Italy

1 Introduction

In the last years, due to the increase in maritime trade, the size of the ships and consequentially the power required has increased, highlighting the scalability problems of traditional shaft lines. In fact, as their size increases, the global ship efficiency, understood not directly as hydrodynamic efficiency but as system efficiency including loss of space on board, non-linear increase in weight and all the effects that contribute to reducing the performance of the ship in carrying out its mission, is reduced and greater design and construction difficulties and costs arise (Su et al. (2020)). In this context and thanks to important technological developments in the field of materials, electric propulsion and 3D printing, the rim driven thruster (RDT) gains more and more research interest for the use in naval propulsion. Initially proposed by Kort (1940), the RDT is a type of integrated engine propeller, also known as a shaftless propeller, in which the driving torque of the blades is given by a structural circular ring (rim) connected to the tip of the blades, in opposition to traditional propellers which are driven through the shaft (Grümmer (2016)). The configuration of the RDT fits very well with an electric motor. The stator can be contained inside the duct while the permanent magnet rotor can be included inside the rim. The main advantages of the RTD can be summarized in: it does not require watertight hull passages for rotating elements, being completely immersed in water it does not require dedicated cooling systems, it has a compact design which reduces overall dimensions and weight on board, it has no mechanical performance losses due to power transmission in the shaft line, the environmental impact due to radiated noise is significantly reduced both due to the use of the electric motor and to the absence of tip vortex thanks to the presence of the rim (Gaggero (2020)). Structurally, the RDT resembles a ducted propeller, however, unlike the latter, the RDT does not have tip clearance since the blades are structurally connected to the rim. Instead a gap clearance exists between the rim and the duct. This difference generates significant variations in the flow field and in the fluid phenomena involved, causing remarkable differences in the open water performance and in the flow characteristics. In recent years, several studies have been conducted on RDTs and significant progress has been made especially in improving electromagnetic performance, decreasing weight and bearings. Several works have also focused on the hydrodynamic efficiency which is influenced by several factors including the blade structure, the shape and size of the shroud and the gap characteristics (Yan et al. (2017)). The first studies on RDT were conducted using potential methods and in particular lifting line based panel codes (Pashias and Turnock. (2003)). Another approach proposed by Kinnas et al. (2009) used potential methods combining the lifting surface with a boundary element method. In particular, a mixture of lifting surface and RANS equations is used to calculate the effective wake at each iteration which is then used as input for the BEM method allowing the performance to be calculated. More recent studies have shown that, although the computational efficiency of potential methods makes them attractive for geometry selection and design, they are not suitable for correctly predicting the performance of an RDT. Song et al. (2015) conducted a comparative analysis between RDTs with and without axis concluding that the absence of the axis improves efficiency by up to 2%. The presence of the hub in fact causes an axial acceleration of the fluid which reduces the angle of attack radially along the blade and also induces greater vorticity which causes a greater loss of energy. Cao et al. (2012) investigated through RANS simulations the radial and the along-chord distribution in different RDT configurations, identifying the presence of combined root vortices and the formation of tip vortexes at a certain distance from the propeller disk. Dubas et al. (2015) conducted an analysis comparing stationary and unsteady simulations for the prediction of rotor-stator interaction and testing different turbulence models, concluding that the k-ω SST model is the most suitable for RDT simulations at low advance coefficients. Lea et al. (2003) through experiments on commercial RDTs have highlighted that, compared

to ducted propellers, RDT have a higher tip load and less cavitation, effects which can be attributed to the presence of the rim. Liu et al. (2022) conducted simulations on RDTs with different shroud geometries presenting the results in terms of efficiency and flow field to better understand the effects of duct on propeller performance.
In general, the experimental works of Hughes et al. (2000) and Abu Sharkh et al. (2001) highlighted that the hydrodynamic efficiency of RDTs is lower with respect of ducted propellers, in fact the efficiency of RDTs is generally lower than 0.5 (Liu and Vanierschot (2021), Jiang et al. (2022), Liu et al. (2023)). This result, however, is partly attributable to the fact that the geometries typically used for RDTs are not designed ad hoc but derive from well known ducted propellers shapes. In fact, as highlighted by Peng et al. (2023) little RDT geometry data is available that can be freely used for academic research and, for this reason, as also highlighted in Liu and Vanierschot (2021) combinations of Ka4-70 propellers and MARIN 19A or MARIN 37 duct are often used. Moreover, most studies on the efficiency of RDTs have focused on the performance of the duct and propeller but the influence of the gap also plays an important role. In fact, the analysis conducted in Liu and Vanierschot (2021) highlight that the gap has a negative influence on RDT performance, leading this type of thruster to be less efficient when compared to ducted propellers. Cao et al. (2014) analyzed the effect of the radial and axial dimensions of the gap with and without a propeller, the results show that widening the gap increases the torque needed to move the propeller. The same result is confirmed by the study by Lin et al. (2023) which achieves this result increasing the front and rear side angle of the rim in order to reduce its width. Furthermore, they propose an empirical formula to estimate the torque increase which however has very limited application since the effect not only depends on the characteristics of the gap but also on the pressure field and therefore on the shape of the duct and of the propeller. Is also important to note that the literature currently available is related to accelerating (or converging) duct geometries which have the purpose of increasing the thrust of the RDT by accelerating the flow. However, in applications where the focus is on the cavitation reduction, the duct can be of a divergent type with the aim of increasing the pressure upstream of the rotor.
In this study, the effect of the gap on a convergent and a divergent duct RDT is analyzed. The geometries of propellers and ducts came from the work of Gaggero (2020) which implements a RDT design based on RANS simulations and optimization via genetic algorithm. On these geometries, the fluid dynamic fields were analyzed both with and without the gap geometrically resolved. Morover a parametric study on the gap shape is conducted applying some changes in shape and in the operating conditions. Section 2 presents the geometries used, the governing equations, the modeling hypotheses, the mesh, the boundary conditions and the numerical method used in the study. In section 3 the results obtained are presented and discussed. Finally, in section 4 we draw conclusions and indicate some recommendations for future work.

2 Numerical simulation methodology

2.1 Geometries description

The RDT geometries used in this article are obtained from the works of Gaggero (2020), Gaggero (2020b) and Gaggero et al. (2013). The geometry of rim driven configuration with decelerating duct (DRD), shown in figure 1a, is made up of the six blades propeller (z6-4097) obtained in Gaggero (2020) associated with the divergent nozzle of the ducted propeller reference presented in Gaggero et al. (2013). This geometry was designed to avoid the inception of cavitation as much as possible and, in fact, the purpose of the divergent duct is to increase the pressure upstream of the propeller. The propeller obtained is, thanks to the optimization process, designed specifically to work in the flow conditions of the associated duct at the selected design condition.
The geometry of the rim driven configuration with accelerating duct (CRD), shown in figure 1b, is taken from Gaggero (2020b) and is made up of a convergent duct (19A) designed to axially accelerate the flow, contributing to the thrust especially in bollard pull conditions, combined with a 5-blades propeller, specifically designed to work in the flow conditions generated by the duct.

Both RDT geometries are obtained on the basis of RANS simulations performed on a geometry

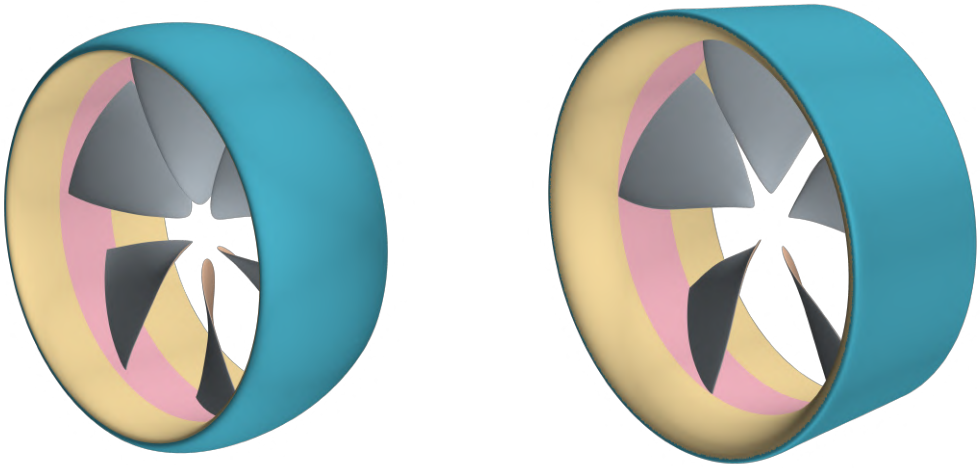

(a) (b)

Fig. 1: DRD (a) and CRD (b) geometries without geometrically resolved gap.

which, as visible in figure 1, does not explicitly contain the geometry of the gap. The rim is in fact modeled as a portion of the internal duct surface that extends axially from just before the propeller to shortly after. This choice, which has the aim of limiting computational costs can be accepted in a relative comparison based, quite demanding, design process but become a limit in correctly determining the absolute performance of the RDT considered. In fact, as highlighted by various works including for example Liu and Vanierschot (2021), the effect of the gap is not negligible and can lead to a loss of efficiency up to 2%. To investigate this aspect on above introduced optimized RDT, the geometries shown in figures 2 were produced.

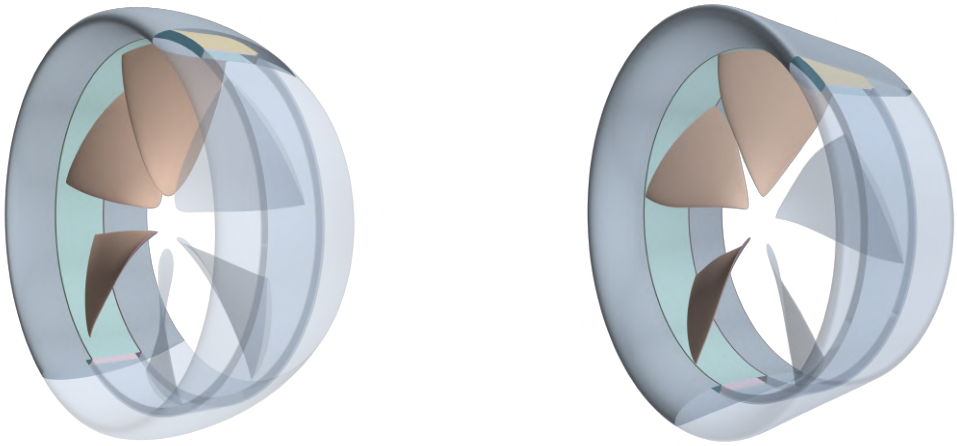

(a) (b)

Fig. 2: DRD (a) and CRD (b) geometries with geometrically resolved gap.

In these geometries the gap is built using the same parametric philosophy illustrated in figure 3 where the gap geometry is obtained using the parameters listed in table 1.

Table 1: Example of gap geometry parameters

ID	w [mm]	d [mm]	t [mm]	α_1 [°]	α_2 [°]
15/-45	40	5	1	15	-45

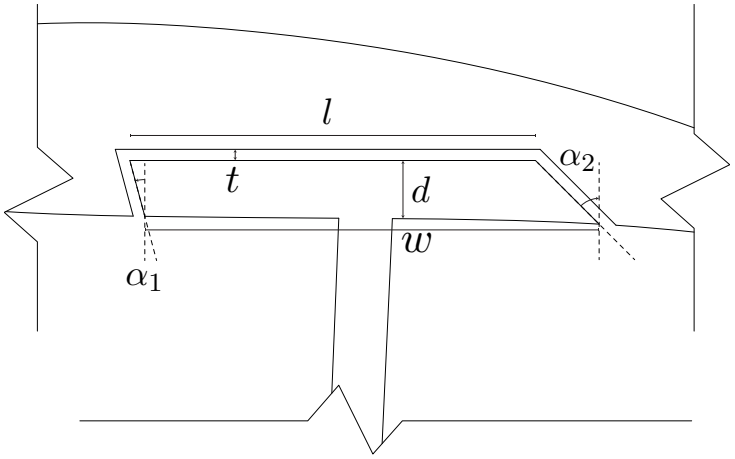

Fig. 3: Gap geometrical description.

Keeping constant w and d, the geometric characteristics of the gap were then varied parametrically in terms of:

1. gap thickness (t) with the values: [0.1, 0.3, 0.5, 0.8, 1.0, 1.2, 1.5] mm
2. front angle of the gap (α_1) with the values from -60° to 60°, step 15°
3. rear angle of the gap (α_2) with the values from -60° to 60°, step 15°

to better understand which characteristics, in addition to the width of the gap already highlighted by various works, had an impact on the performance of the RDT and how the gap affects the efficiency in both DRD and CRD configurations of thruster and considering the geometry of duct and propeller.

2.2 Simulations set-up

Most calculations were carried out using RANS for a single-phase fluid and incompressible flow. Star-CCM+ (Siemens (2021)) was used as solver on an unstructured mesh made of polyhedra using the Finite Volume method and second order discretization schemes for all the physical quantities. By using a Moving Reference Frame and by exploiting the periodicity of the problem, only one blade passage is considered in the stationary analyses while local mesh refinements account for the propeller and the duct wake. The computational domain, shown in figure 4 has a cross area at the propeller plane one hundred times higher than the area of the propeller disk (D_{domain}/D_{prop} = 10), the inlet is placed four propeller diameters in front of the propeller, the outlet six propeller diameters aft, and uniform inflow is assumed as the initial condition.

The k-ω SST turbulence model is used to compute the turbulent viscosity in a simulation where the turbulence intensity is set equal to 1% and the turbulent to molecular viscosity ratio is equal to 10.
To validate the assumptions made using stationary analyzes and exploiting the symmetry of the problem, unsteady simulation of the gap resolved reference RDTs were carried out. In these, the basic assumptions of the modeling and the mesh parameters are the same as in the stationary analysis with the following differences:

- the calculation domain is a full cylinder with diameter 10 D_{prop}, containing all the propeller blades so the number of cells is about $Z \cdot n_{steady}$ where Z is the number of blades and n_{steady} is the number of cells in steady state simulations,
- the geometries of the rim and propeller blades are inserted in a small cylindrical domain actually rotating thanks to the movement of the mesh,
- the second order time-marching scheme use a time step set to have a rotation of 1° per time-step, the stopping criteria are set to simulate at least 5 complete revolutions of the propeller and with a convergence of 1% in the average thrust of the last revolution compared to the previous one.

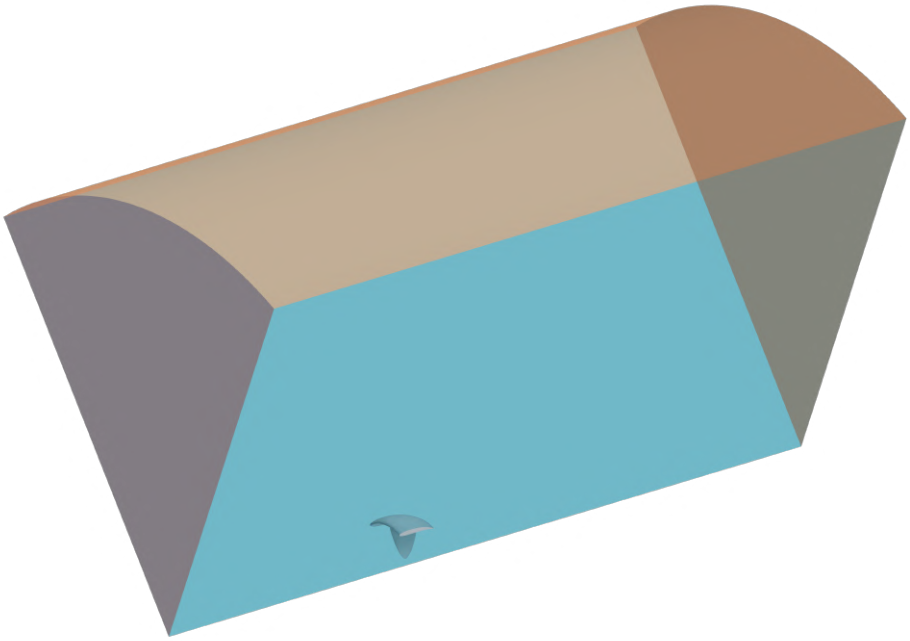

Fig. 4: Computational domain of steady simulations.

2.3 Mesh analysis

The thruster performances are typically expressed by thrust and torque coefficients and the open water efficiency η_0. In RDT we define those coefficients including not only the propeller forces and torque but also the rim ones generated by rim and duct. In particular we define:

$$K_t = \frac{T_{propeller} + T_{duct} + T_{rim}}{\rho n^2 D^4} \tag{1}$$

$$K_q = \frac{Q_{propeller} + Q_{rim}}{\rho n^2 D^5} \tag{2}$$

$$\eta_0 = \frac{J}{2\pi}\frac{K_t}{K_q} \tag{3}$$

where $J = V_a/nD$ is the commonly defined advance coefficient.
The mesh used for geometrically non-resolved gap RANS simulations is made following the guidelines consolidated in Gaggero and Villa (2018), obtaining an average of 1.3 million cells. Of course, keeping the same mesh parameters but including the gap geometry, the number of cells in the gap resolved simulation increases. In order to determine the number of cells needed to capture the relevant gap fluid dynamic effect, starting using the same mesh parameters of the non-resolved gap, a convergence analysis by changing only the number of added cells in the gap was conducted. The gap geometry used for this analysis is the reference one obtained with the parameters in Tab. 2.

Table 2: Initial gap geometry parameters

ID	w [mm]	d [mm]	t [mm]	α_1 [°]	α_2 [°]
0/0	40	5	1	0	0

Note that, to quickly refer to the different parametric configurations of the gap geometry, the nomenclature: (α_1/α_2) is used. In these cases, where not otherwise specified, it means that all other geometric characteristics are kept equal to the reference values reported in table 2.

Table 3 shows, in terms of KT, the results of this analysis, conducted using the procedure proposed in Eça and Hoekstra (2014), which indicate the need of adding about 300 000 cells to achieve an uncertainty and an error respectively less than 2% and 1%.

Table 3: Mesh convergence analysis in DRD gap-resolved simulations, K_t values normalized with respect to modeled-gap performances for confidentiality reasons

cells	$K_t/K_{t_{ref}}$	uncertainty [%]	extrapolated error [%]
1 371 102	0.9715	2.0	0.68
1 565 886	**0.9703**	**1.9**	**0.55**
3 243 345	0.9669	1.3	0.22
10 542 940	0.9665	0.6	0.17

This increment of about 15% in the cells number with respect to the non-resolved gap mesh, produces a calculation grid with approximately 1.6 million cells. A typical example of such mesh is shown in figure 5.

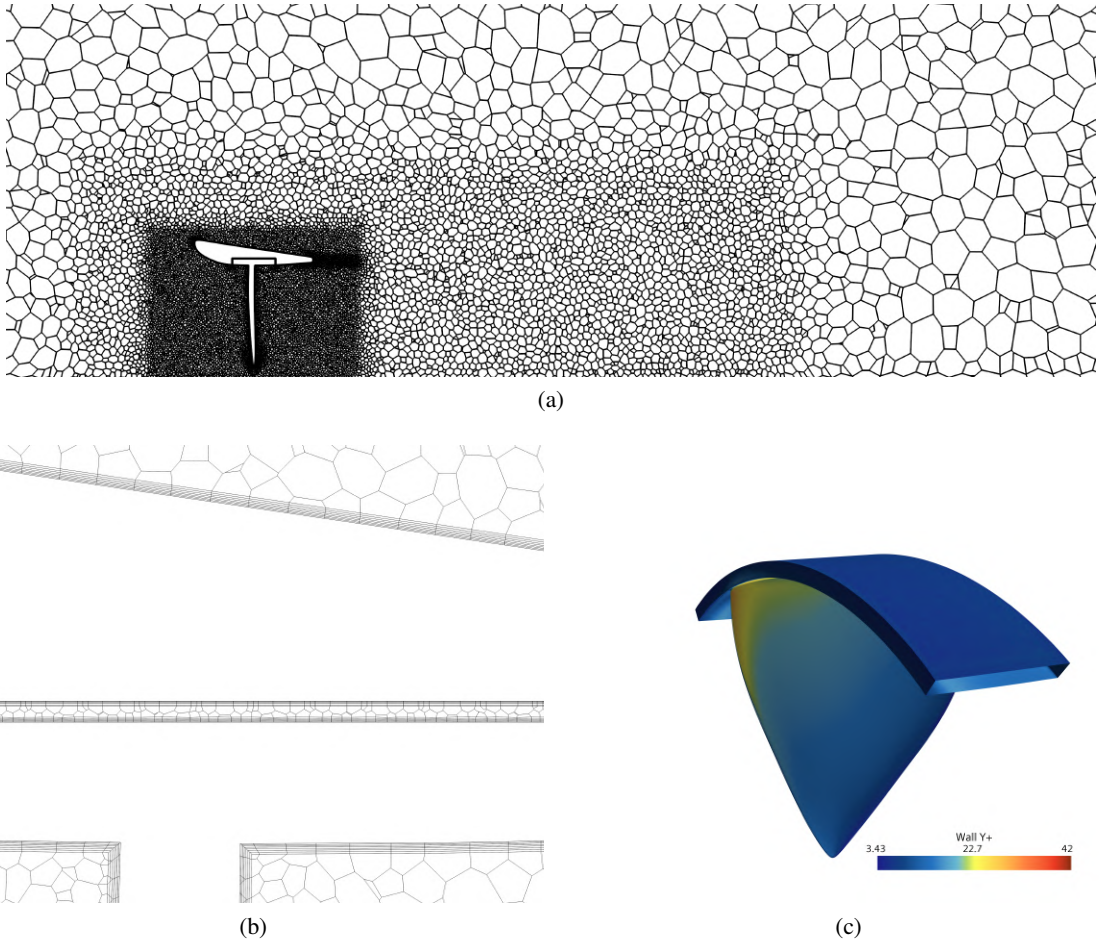

(a)

(b)

(c)

Fig. 5: Typical mesh of gap-resolved, steady simulations (a) with gap mesh detail (b) and $y+$ values in gap and blade (c).

Furthermore, an analysis was conducted on the mesh of the boundary layer inside the gap. In fact, while for the external flow the parameters already validated by Gaggero and Villa (2018) were used, for the flow inside the gap, due to the different geometric and characteristic velocity scales, it was necessary to investigate the size of the cells necessary to correctly capture the effects in the boundary layer. The first guess of thickness was obtained using the relations for turbulent boundary layer (Schlichting (1979))

where was used the Reynolds number defined as:

$$Re = \frac{t\, nD/2}{\nu} \tag{4}$$

Using the simulations results, the first guess thickness was corrected to obtain a gap $y+$ distribution in line with the values already used in similar works (Zhai et al. (2022)). In particular, the $y+$ distribution shown in figure 5c was obtained, where $y+_{max \simeq 17}$.

3 Results and discussion

The first analysis conducted concerns the comparison between the performances of the RDT in both CRD and DRD configurations, obtained using a mesh with and without a geometrically resolved gap. These simulations were carried out on the reference geometry of the gap whose characteristics are shown in table 2, i.e. rim thickness $d = 5\,mm$, gap thickness $t = 1\,mm$, rim width $w = 40\,mm$, and front and rear angles equal to $\alpha_1 = \alpha_2 = 0°$. Furthermore, on these geometries, to verify that the modeling hypotheses provided acceptable results, unsteady analysis without exploiting the periodicity of the problem were also conducted. The results of this analysis are presented in 4 in terms of K_t, K_q and η_0. Note that for confidentiality reasons the values relating to the DRD have been normalized with respect to modeled-gap performances.

Table 4: Results in standard (0/0) configurations, DRD values normalized with respect to modeled-gap performances for confidentiality reasons.

Case	J	K_t	K_q	η_0
CRD w/o gap	0.7	0.4296	0.0854	0.5603
CRD with gap	0.7	0.4221	0.0881	0.5340
CRD Unsteady with gap	0.7	0.4217	0.0887	0.5296
Case	J/J_{ref}	$K_t/K_{t_{ref}}$	$K_q/K_{q_{ref}}$	η_0
DRD w/o gap	1	1	1	0.5850
DRD with gap	1	0.9703	0.9911	0.5730
DRD Unsteady with gap	1	0.9619	0.9852	0.5716

First of all we noted that the error on performance between gap resolved steady state simulation using periodic BC and MRF and the unsteady ones, extracted as the mean of the last propeller revolution, is less than 1% so it's confirmed that the assumptions adopted in simplified model are accurate enough to correctly solve the physics of the problem. Moreover, from the results obtained we note that the efficiency loss due to the gap is much higher in the CRD case compared to the DRD. This aspect can be explained by physically analyzing the gap effect. Mainly, the loss of efficiency due to the gap is due to two distinct phenomena. The first is the increase in torque compared to the case without gap due to the fact that an extra face is added in contact with the water and therefore a bigger wet surface causing friction is considered. This component is present in both RDT configurations substantially in the same way. Note that this effect is not exactly the same in the two configurations due to the fact that it is slightly influenced by the pressure field. In fact, depending on the pressure difference downstream and upstream of the gap, an axial flow opposite to the direction of the inflow develops within the gap. This axial flow, as highlighted by various works on the Taylor-Couette flow (Hwang (2004)), influences and, in particular, reduces the torque necessary to rotate the rim. Moreover, the effect of the increase in torque due to friction is not directly observable from the K_q values. These, in fact, also contain the contribution of the propeller blades and, consequently, are influenced by the modification of the driving torque on the blade due to the modification of the pressure field induced by the propeller and the duct. In fact, while in the CRD case we notice an increase in torque in the case of a resolved gap compared to the modeled-gap case, in the DRD we notice the opposite. It is important to note that this effect on the pressure field due to the gap is in the cases analyzed more relevant than the friction contribution due to the increase in the wetted surface and is strongly dependent not only on the geometry of the gap, but also, on the pressure

field developed by the propeller and duct. The gap, in fact, puts the pressure and the suction sides of the blade in "communication", near the tip of the blade which, in the RD configuration is a loaded area. It is therefore clear that the higher the pressure difference across the blades, the greater the effect of the gap will be in "restoring" it. Considering the pressure fields of the two configurations shown, in terms of $C_{PN} = \frac{2P}{\rho n^2 D^2}$, in figure 6 we note that in the case of CRD the pressure difference is much higher than in the DRD case. In fact, despite pressure, as expected, is overall higher in divergent configuration, we note that across propeller blade there is a C_{PN} jump of about 1.42 in the convergent case while in the divergent this value is about 0.95.

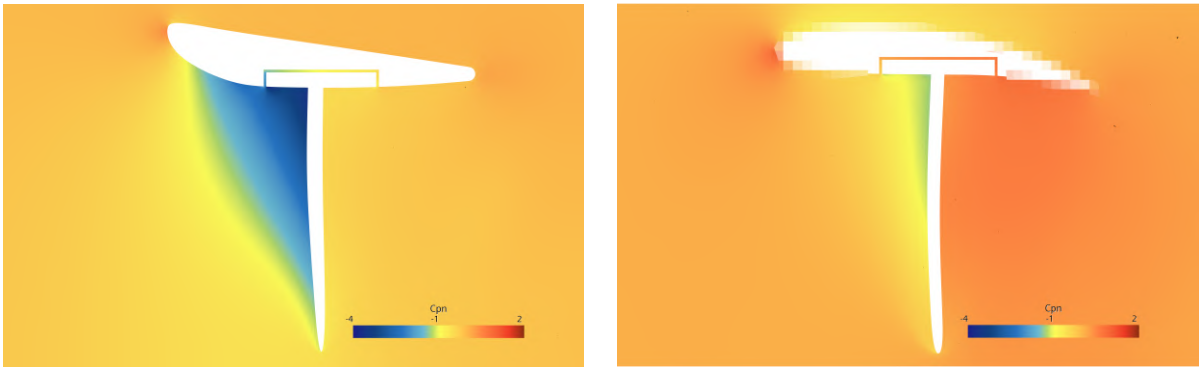

(a) (b)

Fig. 6: Pressure coefficient (C_{PN}) field in CRD (a) and DRD (b) configurations. DRD duct geometry hidden for confidentiality reasons

This pressure jump causes an axial velocity component to develop inside the gap which adds to the rotational one caused by the friction with the rim. A typical gap flow is shown in figure 7b. Due to the fact that the pressure is higer in the pressure side with respect to the suction side of the propeller blade, the axial component has a direction opposite to the main flow. For this reason, considering the inflow as x-direction, in the gap the x-component of the velocity is negative. In the analyzed cases this velocity has the profile shown in figure 7a. We note that given the greater driven pressure gradient in the CRD case, the maximum axial speed reached is about -1.5 m/s and the flow rate approximately 0.7 kg/s while in the DRD case the maximum speed is approximately -1.2 m/s and the flow rate near 0.42 kg/s

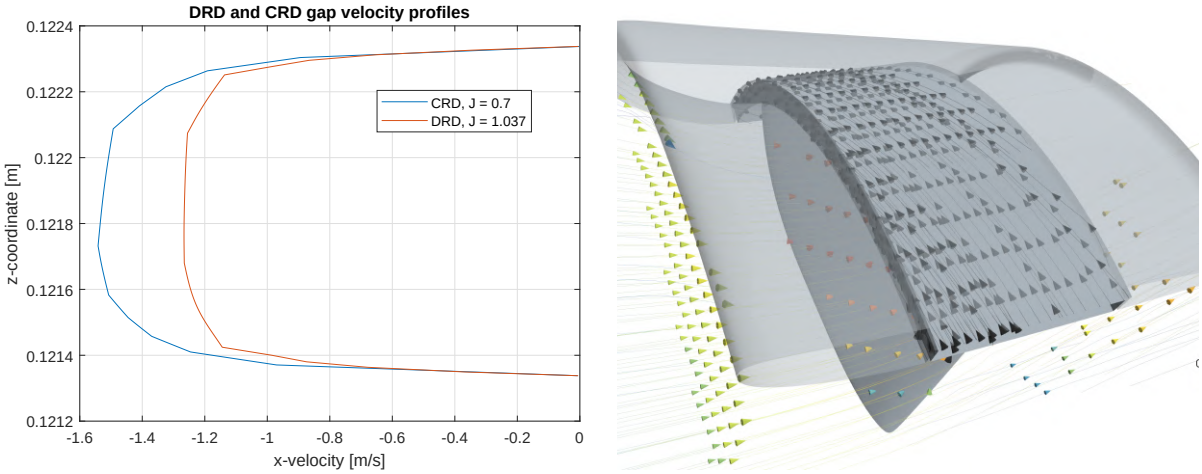

(a) (b)

Fig. 7: Gap x-velocity profile in CRD and DRD thruster (a) and typical gap flow (b).

Despite that, the contribution given by the interaction between the pressure field and flow in the gap

is not immediately and generically understandable. In fact, with what has been stated above, one could expect that the effect of the gap due to the pressure delta between the face side and the suction side is to reduce the thrust compared to the case without the gap and that consequently the greater the pressure difference, the greater the loss of thrust due in the presence of the gap. In reality the numbers obtained deny this interpretation. In fact, although there is a decrease in both the DRD and CRD configurations of the thrust due to the presence of the gap, the entity of this reduction is equal to approximately 1.5% in the CRD case (greater ΔC_{PN}) while it is approximately 2.5% in the DRD case (smaller ΔC_{PN}). On the other hand, the increase in parasitic torque due to the gap is approximately 3% in the CRD case, while in the DRD case it is almost -1%. This means that the effect of the gap in the DRD configuration is to reduce the driving torque of the propeller compared to the case without the gap resolved. In other words, the variation in the pressure field induced by the gap unload the propeller blade near the tip causing both a reduction in thrust and in torque. In any case, the effect of the gap also in the DRD case leads to a decrease in efficiency since the loss of thrust is greater than the reduction in torque. It appears clear from these considerations that the effect of the gap on the propeller performance is not trivial and strongly depends on the pressure field generated by both the blade and duct.

After having analyzed the impact of the gap on the flow and performance of the RDTs, parametric analyzes were carried out on the geometric characteristics of the gap itself to better understand how, individually, these were linked to the loss of efficiency of the thruster. Two families of analyzes were conducted: the first to understand the effect of the gap thickness and the second to determine the influence of the gap shape. The first parametric analysis, in particular, has been conducted varying the gap thickness while keeping the other geometric characteristics constant and equal to the reference ones. The performance of the RDT was evaluated in both CRD and DRD configurations for gap thicknesses varying from 0.5 to 1.5 mm. The results of the analysis conducted are presented in table 5.

Table 5: Gap thickness effect on RDT performances. DRD values normalized with respect to modeled-gap performances for confidentiality reasons.

DRD thruster, J/J_{rif} = 1					CRD thruster, J = 0.7			
t [mm]	$K_t/K_{t_{ref}}$	$K_q/K_{q_{ref}}$	η_0		t [mm]	K_t	K_q	η_0
1.5	0.9511	0.9823	0.5664		1.5	0.4167	0.0878	0.5287
1.2	0.9609	0.9867	0.5697		1.2	0.4201	0.0881	0.5312
1.0	0.9703	0.9911	0.5730		1.0	0.4221	0.0881	0.5340
0.8	0.9711	0.9926	0.5723		0.8	0.4243	0.0881	0.5366
0.5	0.9805	0.9955	0.5762		0.5	0.4278	0.0885	0.5385

The results obtained indicate that the greater the thickness of the gap, the lower the efficiency of the thruster and so that is appropriate to minimize the thickness of the gap. These results foster the assumption previously mentioned, on the phisical effect of the gap and are valid in the range of thicknesses reported in table 5 but it has been verified that by further reducing the thickness of the gap a point is reached where, due to the viscous effects and the increase of viscous shear stress in gap, the torque increases significantly causing a loss of efficiency. However, this effect occurs using gap thickness values that are not technologically achievable and are therefore not of interest. In fact, although the technologically achievable gap value does not depends directly to the diameter, for standard blade, the minimum gap reference values are between 0.5% and 1% of D, which in the analyzed configurations correspond to 1.1 - 2.3 mm.

The second parametric analysis conducted concerns the shape of the gap. In particular, keeping the thickness $t = 1\,mm$ fixed and the blade-side rim width $w = 40\,mm$, the front and rear angles were varied in a range from $-60°$ and $60°$ with $15°$ step. Naturally, since the rim width w is kept constant in order to contain the blade root, varying the angles causes a variation in the width of the duct-side of the gap l. The results in terms of efficiency of the analysis for both the CRD and the DRD are shown in the figure

8.

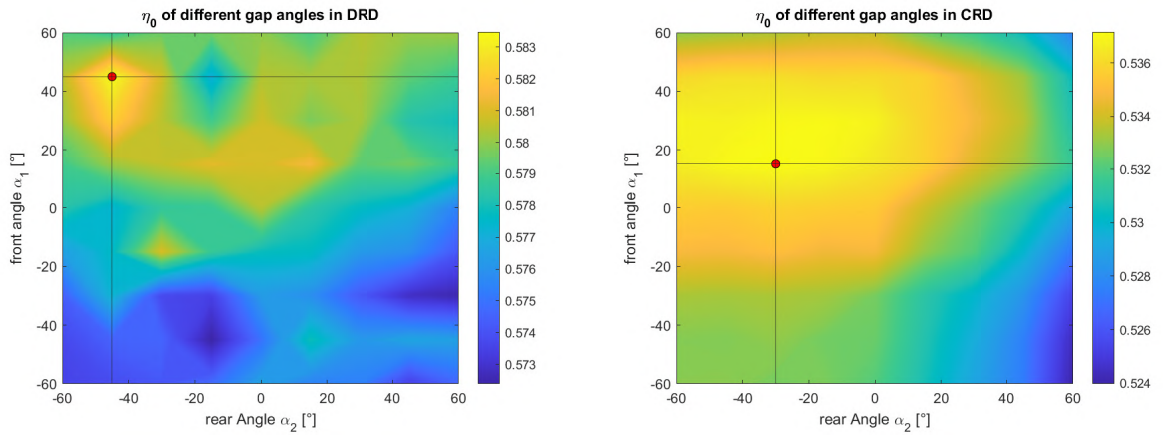

(a) optimal: $\alpha_1 = 45°, \alpha_2 = -45°$ (b) optimal: $\alpha_1 = 15°, \alpha_2 = -30°$

Fig. 8: Open water efficiency vs front (α_1) and rear (α_2) angles in DRD (a) and CRD (b) configurations.

From the analysis of CRD geometries it emerges that the optimum is obtained in the (15/-30) configuration whose pressure field, in terms of pressure coefficient C_{PN}, is shown in figure 9a.

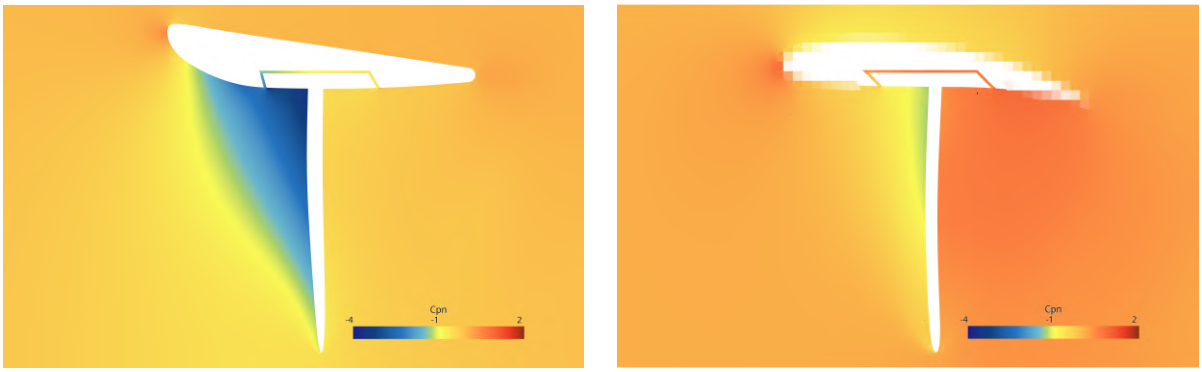

(a) optimal: $\alpha_1 = 15°, \alpha_2 = -30°$ (b) optimal: $\alpha_1 = 45°, \alpha_2 = -45°$

Fig. 9: Pressure coefficient (C_{PN}) fields in optimal CRD (a) and DRD (b) configurations. DRD duct geometry hidden for confidentiality reasons

In this case we note that the inner gap length l is not the minimum that would be obtained in the (60/-60) configuration and that therefore minimizing the wetted surface is not always the best solution. The contribution of pressure, in fact, has generally a great influence on the RDTs performances. For example in the optimal case the inner gap surface torque is greater than in the (60/-60) configuration of about 40%. However in the optimal configuration the pressure field is such that the torque required from the blade and the rim surface in contact with the blade is smaller with respect to the 60/-60 configuration. Overall the pressure effect on the blade is greater than the torque increment due the increase in wetted surface. This effect is even more evident in the optimal DRD configuration whose pressure field, in terms of pressure coefficient (C_{PN}), is shown in figure 9b where the duct geometry has been hidden for confidentiality reasons. In the DRD case, as shown in figure 8a, the efficiency is much more irregular and presents a fairly clear peak in the (-45/45) configuration. In any case the effect of the gap remains not trivial, in fact there is not a direct correlation between gap ΔC_{PN} or gap-flow speed and the loose in efficiency. This is due to the fact that there are two opposite effects: on one side the axial velocity in the gap reduce the required driving torque as documented in studies on the Taylor-Couette flow (Hwang (2004)), on the other the greater the velocity and the mass flow in the gap, the greater the induced variation in the

pressure field across the blade and so a change in blade torque and thrust. It is not therefore possible to generalize the gap effect but is necessary to consider the interaction between the gap flow and the specific duct and the propeller geometries in the working point conditions.

Figure 10 shows the results of the analysis of the gap effect as the operating point varies. In both the CRD and DRD cases we note from the open water diagrams obtained that the effect of the gap is substantially a constant offset in performance, manily due to the variation of the torque. In the DRD configuration we notice that there is a slight decrease on the gap effect at high advance coefficients ($J/J_{ref} \simeq 1.25$). However, given the small extent of this effect, it can be concluded that the gap effect does not vary substantially if the engine finds itself working in a condition different from the design one for any reason during its operational life.

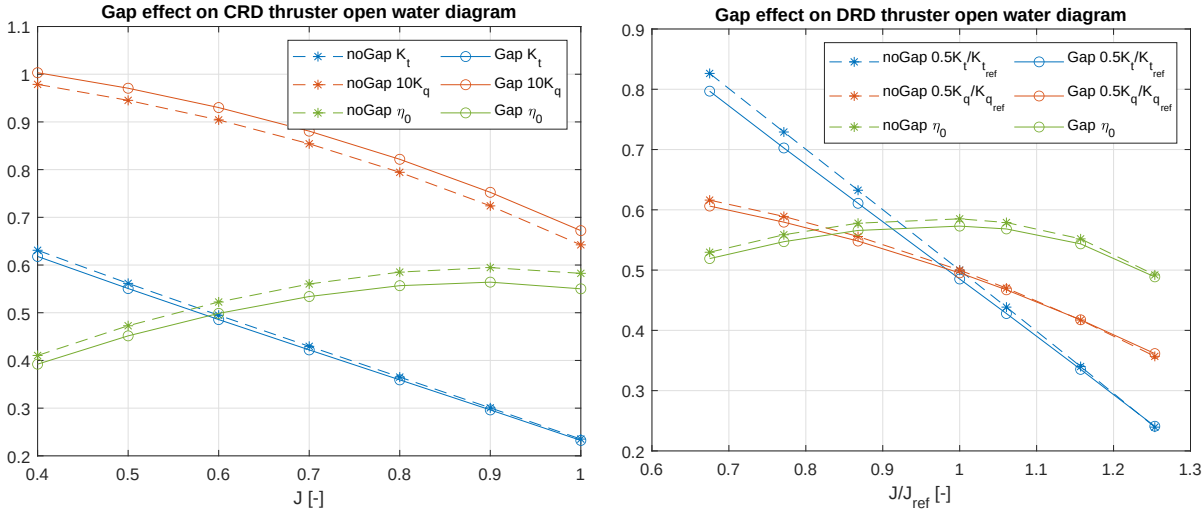

(a) (b)

Fig. 10: Gap effect on RDT open water diagram in CRD (a) and DRD (b) configurations.

4 Conclusions and future work

Several simulations have been carried out in order to better understand the effects of the gap in both convergent and divergent RDT thrusters. It was found that the effect of the gap on the propulsive efficiency is more marked in convergent configurations while it is substantially negligible in divergent ones. Moreover, by carrying out convergence analyzes on the meshes, it was noted that to correctly resolve the gap effects it is necessary to increase the size of the calculation grid by 15-20%. By exploiting the periodicity of the problem and using stationary MRF simulations it is therefore possible to perform simulations on RDTs with a gap resolved with a mesh of approximately 1.6 million cells while maintaining the thrust error within approximately 2%.

As far as the geometry of the gap is concerned, it has been noted that the thickness has a negative influence, and it is therefore advisable to limit it to the minimum possible while the angles (shape) of the gap do not have an obvious optimal configuration. Certainly, as already confirmed by the literature, reducing l reduces the added torque due to the friction of the rim in the gap. However, also considering the effect of the pressure field, it is not certain, and indeed in the cases analyzed it was not the case, that the configuration with minimum l is the one with the highest efficiency.

In conclusion, therefore, considering the relatively small increase in computational cost and the difficulties in generalizing the gap effect as it is strongly dependent on the pressure field and therefore on the duct and propeller geometries, it is believed that for future work it is preferable to investigate the RDTs by including the gap in the simulations geometry.

Acknowledgements

This work has been partially supported by Spoke 3 "Waterways" within the Italian PNRR National Centre for Sustainable Mobility (MOST) funded by the European Union - NextGenerationEU. Opinions expressed are those of the authors only and do not necessarily reflect those of the European Union or the European Commission. Neither the European Union nor the European Commission can be held responsible for them.

References

Y. Su, J. Lin, D. Zhao, C. Guo, C. Wang and H. Guo (2020). Real-time prediction of large scale ship model vertical acceleration based on recurrent neural network. *Journal of Marine Science and Engineering*, **8**(10), 777.

H. Grümmer (2016). Design and Optimization of a Hubless rim-driven Thruster for an Autonomous Surface Vehicle using RANSE Simulation. *Doctoral dissertation, MS Dissertation, Department of Dynamics of Maritime Systems, Technical University of Berlin, German*.

X. Yan, X. Liang, W. Ouyang, Z. Liu, B. Liu and J. Lan (2017). A review of progress and applications of ship shaft-less rim-driven thrusters. *Ocean Engineering*, **144**, 142?156.

C. Pashias and S. R. Turnock (2003). Hydrodynamic design of a bi-directional, rim-driven ducted thruster suitable for underwater vehicles. *Ocean Engineering*, **144**, 142?156.

S. A. Kinnas, S. H. Chang, L. He and J. T. Johannessen (2009). Performance prediction of a cavitating RIM driven tunnel thruster. *In First International Symposium on Marine Propulsors SMP*, **Vol. 9**, 435-442.

B. W. Song, Y. J. Wang and W. L. Tian (2015). Open water performance comparison between hub-type and hubless rim driven thrusters based on CFD method. *Ocean Engineering*, **103**, 55-63.

Q. M. Cao, F. W. Hong, D. H. Tang , F. L. Hu and L. Z. Lu (2012). Prediction of loading distribution and hydrodynamic measurements for propeller blades in a rim driven thruster. *Journal of Hydrodynamics*, **24**, 50-57.

A. J. Dubas, N. W. Bressloff and S. M. Sharkh (2015). Numerical modelling of rotor?stator interaction in rim driven thrusters. *Ocean engineering*, **106**, 281-288.

M. Lea, D. Thompson, B. Blarcom, J. Eaton, J. Friesch and J. Richards (2003). Scale model testing of a commercial rim-driven propulsor pod. *Journal of ship production*, **19**(02), 121-130.

B. Liu, M. Vanierschot and F. Buysschaert (2022). Effects of transition turbulence modeling on the hydrodynamic performance prediction of a rim-driven thruster under different duct designs. *Ocean Engineering*, **256**, 111-142.

A. W. Hughes, S. A. Sharkh and S. R. Turnock (2000). Design and testing of a novel electromagnetic tip-driven thruster. In ISOPE International Ocean and Polar Engineering Conference (pp. ISOPE-I). ISOPE.

S. M. Abu Sharkh, S. R. Turnock and G. Draper (2000). Performance of a tip-driven electric thruster for unmanned underwater vehicles. In ISOPE International Ocean and Polar Engineering Conference (pp. ISOPE-I). ISOPE.

B. Liu and M. Vanierschot (2021). Numerical study of the hydrodynamic characteristics comparison between a ducted propeller and a rim-driven thruster. *Applied Sciences*, **11**(11), 4919.

H. Jiang, W. Ouyang, C. Sheng, J. Lan and R. Bucknall (2022). Numerical investigation on hydrodynamic performance of a novel shaftless rim-driven counter-rotating thruster considering gap fluid. *Applied Ocean Research*, **118**, 102967.

B. Liu, M. Vanierschot and F. Buysschaert (2023). Optimization design of the duct of a rim-driven thruster using the adjoint approach. *Ocean Engineering*, **278**, 114293.

L. Peng, Y. Hua-Dong, W. Chao and W. Kaiqiang (2023). Improved efficiency with concave cavities on S3 surface of a rim-driven thruster. *Physics of Fluids*, **35**(10), 107102.

Q. Cao, X. Wei, D. Tang and F. Hong (2014). Study of gap flow effects on performance of rim driver thrusters. In Proceedings of the 13th National Conference on Hydrodynamics and the 26th National Symposium on Hydrodynamics, Tsingtao, China, 1197-1206.

J. Lin, H. D. Yao, C. Wang, Y. Su and C. Yang (2023). Hydrodynamic performance of a rim-driven thruster improved with gap geometry adjustment. *Engineering Applications of Computational Fluid Mechanics*, **17**(1), 2183902.

S. Gaggero (2023). Numerical design of a RIM-driven thruster using a RANS-based optimization approach. *Applied Ocean Research*, **94**, 101941.

S. Gaggero, M. Viviani, G. Tani, F. Conti, P. Becchi and F. Valdenazzi (2013). Comparison of different approaches for the design and analysis of ducted propellers. In proceedings of the V International Conference on Computational Methods in Marine Engineering.

S. Gaggero (2020). RIM driven propellers design using a Simulation Based Design Optimization approach. In proceedings of the 5th International Conference on Maritime Technology and Engineering - MARTECH. Lisbon.

S. Gaggero and D. Villa (2018). Cavitating propeller performance in inclined shaft conditions with openfoam: Pptc 2015 test case. *Journal of Marine Science and Application*, **17**(1), 1-20.

L. Kort (1940). Elektrisch angertriebene schiffsschraube. German Patent, 688 (1940), p. 13.

L. Eça and M. Hoekstra (2014). A procedure for the estimation of the numerical uncertainty of CFD calculations based on grid refinement studies. *Journal of Computational Physics*, **262**, 104-130.

J. Y. Hwang and K. S. Yang (2004). Numerical study of Taylor–Couette flow with an axial flow. *Computers & Fluids*, **33**, 97-118.

Siemens Digital Industries Software, (2021). Simcenter STAR-CCM+, version 2021.2.1.

S. Zhai, S. Jin, J. Chen, Z. Liu and X. Song (2022). CFD-based multi-objective optimization of the duct for a rim-driven thruster. *Ocean Engineering*, **264**, 112467.

H. Schlichting (1979). *Boundary Layer Theory.* 7th Edition, McGraw-Hill, New York.

26th Numerical Towing Tank Symposium (NuTTS)
23–25 October 2024 – Mülheim an der Ruhr, Germany

Numerical study on tip-leakage flow for a stationary hydrofoil

Kenshiro Takahashi*
*Australian Maritime College, University of Tasmania, Tasmania/Australia
kenshiro.takahashi@utas.edu.au

1 Introduction

Ducted propellers are expected to provide hydrodynamic and hydroacoustic advantages for future underwater vehicles compared to conventional open propellers. However, an additional critical issue is raised due to its mechanical structure: those propellers typically possess a tip gap, also recognised as a tip clearance, between the blades and duct surface. The tip gaps of such propellers can cause flow instability and global pressure minimum, resulting in undesirable cavitation. In this context, experimental works on tip-leakage flows (TLFs) and relevant cavitation using stationary hydrofoils have been conducted at the University of Tasmania (UTAS) variable pressure water tunnel to clarify the underlying physical phenomena. Russell et al. (2020) performed an experiment of a cavitating flow for a hydrofoil. A tip-separation vortex (TSV) formed in the clearance flow from the sharpened end of the hydrofoil. The TSV and bubbles swept across the end of the hydrofoil by the leakage flow and wound around the tip-leakage vortex (TLV). Russell et al. (2023) developed a mathematical tool to design a hydrofoil geometry with faired endwall edges to suppress flow separation in the tip gap. The cavitation associated with shedding flow on the pressure side was not observed for the evaluated incident angles. Thereafter, Russell et al. (2024) investigated the influence of boundary-layer thickness on incipient and developed cavitation in a stationary TLF using the faired hydrofoil. Takahashi (2024) performed a fundamental analysis of the tip-gap flow of a hydrofoil using Reynolds-averaged Navier-Stokes (RANS) simulations and determined the formation mechanism of the leakage vortices.

The present study was performed to test the effectiveness of computational predictions for acquiring complementary flow field information. The experiments at the UTAS revealed the deviation of the TLV cavitation trajectory with the decreased gap height. Furthermore, the acoustic cavitation event rate and sound pressure level generally increased with decreasing the tip-gap height and reached a maximum value. Thereafter, they dropped dramatically, suggesting that the boundary layer on the test section ceiling mitigated the leakage flow within the gap. Thus, this study characterises the TLF of a stationary hydrofoil for distinct tip-gap heights using computational fluid dynamics (CFD).

2 Computational setup

The test condition of the simulations was based on those in the experiment at the UTAS variable-pressure water tunnel reported in Russell et al. (2023). The tunnel test-section is 0.6 m × 0.6 m at the entrance and 2.6 m long. The hydrofoil blade, which had a chord (c) of 280 mm, was rigidly mounted to the bottom of the test section. The tip-gap height (h_g), which was the clearance between the hydrofoil blade tip and test-section ceiling, was varied from 3.36 to 67.2 mm. A gap ratio of $\tau = h_g/t = 0.1$–2.0 was obtained when non-dimensionalised by the maximum hydrofoil thickness ($t = 33.6$ mm). Experiments were performed at a hydrofoil incidence of $\alpha = 6.0$ [°]. The Reynolds number based on the blade chord (c) was $Re_c = (U_\infty \cdot c)/\nu = 3.0 \times 10^6$, where U_∞ is the mainstream velocity [m/s] and ν is kinematic viscosity [m^2/s].

Fig. 1 shows the hydrofoil mounted in the test section. The hydrofoil leading edge was located 900 mm downstream of the test-section entrance. The origin of the xyz-coordinate system located at the intersection between the test section centreline on ceiling and mid-chord of the hydrofoil, where the x-axis was positive to the downstream and the y-axis was positive upwards. The incident angle of the hydrofoil was adjusted about the y-axis. Fig. 2 shows the computational domain modelling the tunnel. The computational domain consisted of the upstream, contraction, test, and downstream sections to account for the possible boundary effects of the tunnel. The upstream section entrance was used as the inlet boundary, and uniform velocity was implemented. A zero-velocity gradient and a constant pressure

were applied to the outlet boundary. A slip condition was implemented to the upstream section, whereas a no-slip condition was implemented to the other tunnel walls and hydrofil surface. This tunnel model can simulate the boundary layer flow on the test section ceiling, as reported in Takahashi (2024).

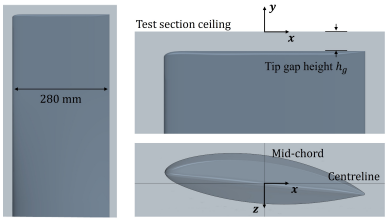

Fig. 1: Hydrofoil mounted in test section.

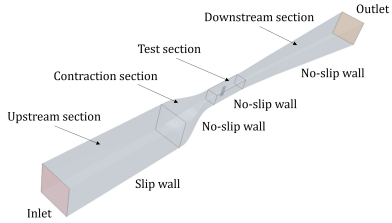

Fig. 2: Computational domain modelling UTAS tunnel.

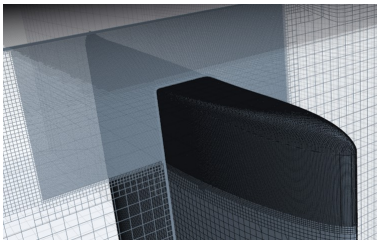

Fig. 3: Volume cells near tip-gap region.

The commercially available CFD package Simcenter STAR-CCM+ 2302, which employs a finite-volume method solver, was adopted for the RANS simulations. A second-order accuracy scheme was used for the spatial computation. The governing equations were determined using a segregated approach, and the semi-implicit method for pressure-linked equations (SIMPLE) algorithm was used to combine the pressure and velocity equations. The $k-\omega$ shear stress transport (SST) turbulence model was adopted, and steady simulations were performed to evolve the computations. The gamma transition model was adopted to predict the onset of the transition in a turbulent boundary layer by solving an additional transport equation for turbulence intermittency. The curvature correction approach was employed to incorporate the effects of rotation and curvature into the scalar eddy viscosity model.

An unstructured trimmed mesh was used to discretise the computational domain. Mesh refinement for the computational domain was performed in the contraction and test sections. Prism layer meshes were generated on the upstream-, contraction-, and test-section walls to resolve the boundary layer flow at an expansion ratio of 1.15. The nondimensional initial layer thickness of the prism layers on the test section ceiling was ensured, i.e. $y^+_{\min} = \Delta_{\min} \cdot u_\tau/\nu = 30$, where $\Delta_{\min}$ is the initial layer thickness [m] and $u_\tau (= \sqrt{\frac{1}{2}U^2_\infty C_f})$ is the frictional velocity [m/s]. Here, C_f is the Schoenherr friction coefficient ($\frac{0.242}{\sqrt{C_f}} = \log_{10}(Re_l \cdot C_f)$), where Re_l is the Reynolds number based on the test section length (l). Further mesh refinement was performed in the tip-gap region to compute the convoluted TLFs. Fig. 3 shows the mesh configuration in the tip-gap region determined based on a mesh convergence study. Prism layer meshes were generated on the hydrofoil surface to ensure $y^+_{\min} = 1.0$. Here, the Reynolds number based on the blade chord (Re_c) was used to calculate the Schoenherr friction coefficient (C_f).

3 Mesh convergence study

Mesh convergence study was conducted to verify the CFD procedure for computing the TLF by decreasing the cell size at the mesh refinement ratio $r_k = 2^{1/2}$. The cavitation inception number (σ_i) was selected for the study owing to the comparable experimental result. Here, the cavitation inception number ($\sigma_i = -C_{P\min} = (p_{\min} - p_\infty)/\frac{1}{2}\rho U^2_\infty$) is defined as presented by Ji et al. (2023), where $p_{\min}$ is the minimum pressure in the TLV [Pa], p_∞ is the ambient pressure [Pa], and ρ is the water density [kg/m^3]. The mesh size in the tip-gap region varied from approximately 0.546 to 0.273 mm. The total number of cells varied by approximately 14–112 million: 14–20 million, 34–48 million, and 84–112 million, for the rough, medium, and fine mesh, respectively. Notably, the total number of cells depended on the tested tip-gap height and was not exactly proportional to the refinement ratio because an unstructured volume mesh was employed, and the prism layer mesh property was constant through mesh refinement.

Fig. 4 shows that the computed cavitation inception numbers converged monotonically for all evaluated tip-gap heights (τ): the differences between the fine and medium meshes were smaller than those between the medium and rough meshes. Fig. 5 presented the acoustic cavitation event rate across the investigated tip-gap heights in Russell et al. (2023). Here, σ is the cavitation number defined as $\sigma =$

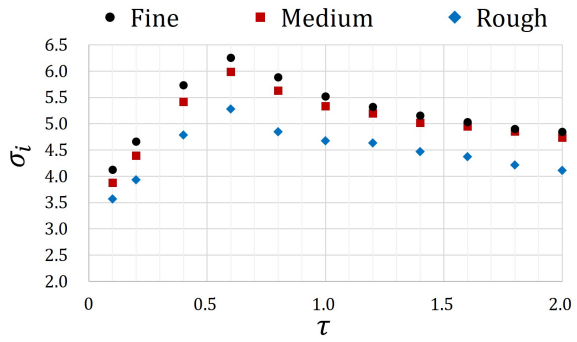

Fig. 4: Computed cavitation inception numbers (σ_i) in mesh convergence study.

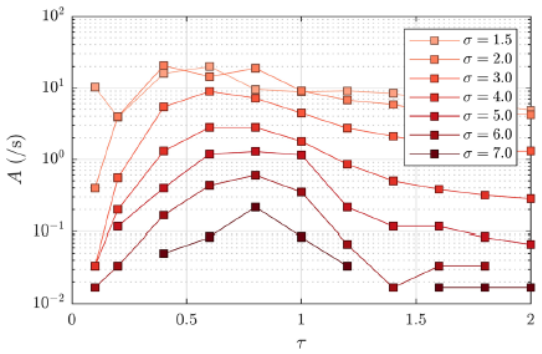

Fig. 5: Acoustic cavitation event rate across the range of τ and σ reported in Russell et al. (2023).

$(p - p_v)/\frac{1}{2}\rho U_\infty^2$, where p is the static pressure at the tunnel ceiling [Pa] and p_v is the water vapour pressure [Pa]. The cavitation event rate was used to evaluate the cavitation susceptibility because of the intermittent character and stochastic nature of cavitation inception. The computed σ_i were within the range $4.0 < \sigma < 7.0$. Furthermore, the CFD values presented the trend similar to the experimental result: σ_i increased with the decrease in the tip-gap height and reached the maximum values at $\tau \approx 0.6$. Then, σ_i decreased significantly towards the minimum tested $\tau = 0.1$. Validation studies may be required to improve computational accuracy in the future. However, the CFD model consisting of the presented mesh refinement was reasonable for computing the TLFs, and the simulation results of the fine mesh were used to analyse the flow fields.

4 Results

Fig. 6 depicts the iso-surface of the Q-criteria ($Q = \frac{1}{2}(\|\Omega\|^2 - \|S\|^2)$) at $\tau = 0.1$, 0.2, 0.4, 0.8, and 1.6, where $\|\Omega\|$ is the vorticity magnitude [s^{-1}] and $\|S\|$ is the strain rate magnitude [s^{-1}]. Fig. 7 depicts the extracted frames from the high-speed recordings of the developed cavitation. The simulations computed the deviated vortex structures for the smaller tip-gap heights: the TLV shifted away the hydrofoil with the decease in τ, and the location of the upstream end moved towards the leading edge. Although the extensions of the iso-surfaces depends on the Q value, the TLV developed further downstream for the larger gap heights, whereas it diffused for the smaller gap heights. This result and the lower cavitation inception numbers (Fig. 4) indicate that the TLV was mitigated for the lower tip-gap heights.

Fig. 8 depicts the the z-axis velocity component ($|u_z|/U_\infty$), termed 'leakage flow,' at the slices perpendicular to the x-axis for $\tau = 0.2$, 0.4, 0.8, and 1.6. The greater z-axis velocity was observed over the blade chord for $\tau = 0.2$ and 0.4, whereas the velocity acceleration was limited near the trailing edge for $\tau = 0.8$ and 1.6. Furthermore, the transverse component was dominant in the leakage flow for the lower tip-gap height when it crossed the clearance. However, the leakage flow curved from the pressure to the suction sides for the higher tip-gap height. These results support that the leakage flow became more significant with the decrease in the tip-gap height and shifted the TLVs away the hydrofoil.

Fig. 9 shows the turbulence intensity ($I = u'/U$) contours for $\tau = 0.2$, 0.4, 0.8, and 1.6, where $u'(= \sqrt{\frac{2}{3}k})$ is the root-mean-square of the turbulent velocity fluctuations [m/s] and $U(= \sqrt{u_x^2 + u_y^2 + u_z^2})$ is the mean velocity [m/s]. Here, k and $u_{x,y}$ are the turbulence kinetic energy [m^2/s^2] and x, y-axis velocity components [m/s]. The TLV was immersed in the boundary layer for $\tau = 0.2$. The mainstream flow was slightly entrained in the TLV for $\tau = 0.4$ as the TLV shifted downwards, whereas it was more interacted with the TLV and boundary layer for $\tau = 0.8$. For $\tau = 1.6$, the TLV existed below the boundary layer. The higher ambient turbulence in the boundary layer can disperse the formation of TLV for the smaller tip-gap height, thus resulting in the mitigated pressure drop near the vortex core.

Fig. 10 shows the minimum pressure coefficient ($C_{P\mathrm{min}}$) of the TLV at each plane perpendicular to the centreline (top left) and vorticity contour with the iso-surface of $Q = 1.0 \times 10^6$ [s^{-2}] coloured with the pressure coefficient ($C_P = P/\frac{1}{2}\rho U_\infty^2$) for $\tau = 0.2$, 0.4, and 0.8, where P is the pressure [Pa].

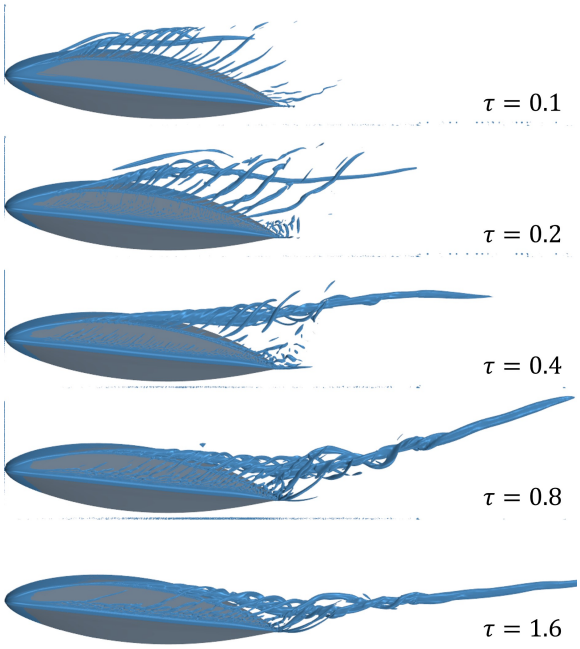

Fig. 6: Iso-surface of $Q = 1.0 \times 10^6$ [s^{-2}] to visualise vortex structures.

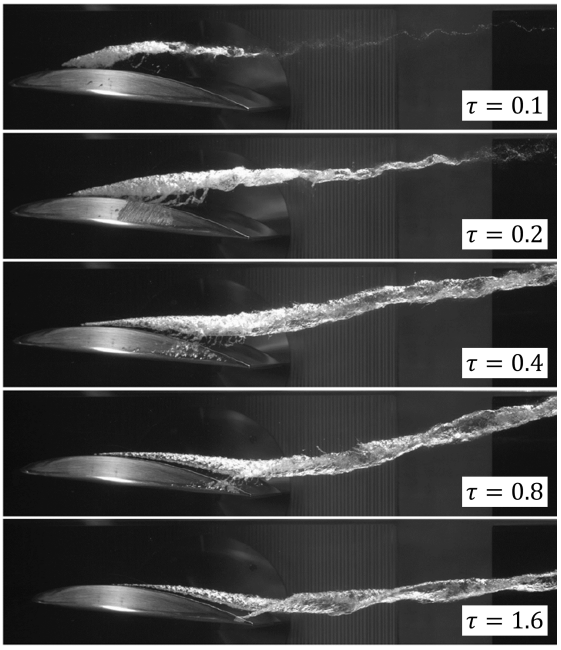

Fig. 7: Developed cavitation topology reported in Russell et al. (2023).

The pressure typically decreased from the leading edge and reached the minimum value. Thereafter, it recovered towards the downstream. The minimum pressure was presented at $x/c = -0.2$ and 0 (mid-chord) for $\tau = 0.1$ and 0.2, respectively, whereas it was observed in the downstream of the mid-chord for $\tau = 0.4$–1.6. The lower minimum pressure was observed for $\tau = 0.4$ and 0.8, indicating the higher cavitation susceptibility. The plane in which the minimum pressure was depicted was visualised by the vorticity contour. Multiple vortices (secondary vortices) with higher vorticity surrounded the TLV, and the lower pressure existed on the iso-surface in its vicinity. These results suggest that the secondary vortices intensified the TLV and caused the pressure drop near the vortex core. Fig. 11 depicts the vorticity contour with the iso-surface of $Q = 1.0 \times 10^6$ [s^{-2}] at $\tau = 0.2$ and 0.8 as viewed from the upstream. The smaller vortices winding around the TLV formed from the suction side edge for $\tau = 0.2$. Conversely, the larger vortices extended from the pressure side edge for $\tau = 0.8$, entraining the smaller vortices from the suction side edge. Thus, the secondary vortices became more significant with the increased gap height, resulting in the further pressure drop in the TLV. The proximity of the TLV to the trailing edge could induce the more significant interaction with the trailing edge vortices.

Another peak of the minimum pressure existed (i.e. $x/c = 0.8$ for $\tau = 0.8$ and $x/c = 0.9$ for $\tau = 1.6$), as shown in Fig. 10. Fig. 12 shows the iso-surface of $Q = 1.0 \times 10^6$ [s^{-2}] and vorticity (left) and pressure coefficient (right) contours at $x/c = 0.9$ plane for $\tau = 1.6$. Two vortices yielding from the trailing edge merged together, forming a strengthened vortex. A significant low pressure was presented near the vortex core at $x/c = 0.9$ with the vortex approaching to the TLV. Chesnakas (2003) remarked an incipient cavitation caused by an unsteady secondary vortical structures via the experiment using a ducted propeller. Thus, further investigation will be performed to analyse the pressure fluctuations caused by the secondary vortex for the hydrofoil blade using a detached eddy simulation.

5 Conclusion

The leakage flow became more significant with the decrease in the tip-gap height and shifted the TLV away the hydrofoil. The TLV immersed in the boundary layer for the smaller gap height, and the higher ambient turbulence could disperse the formation of TLV, resulting in the mitigated pressure drop near the vortex core. The significant secondary vortices forming from the pressure side edge intensified the TLV and caused the further pressure drop in the vortex. These results can support the TLV cavitation features

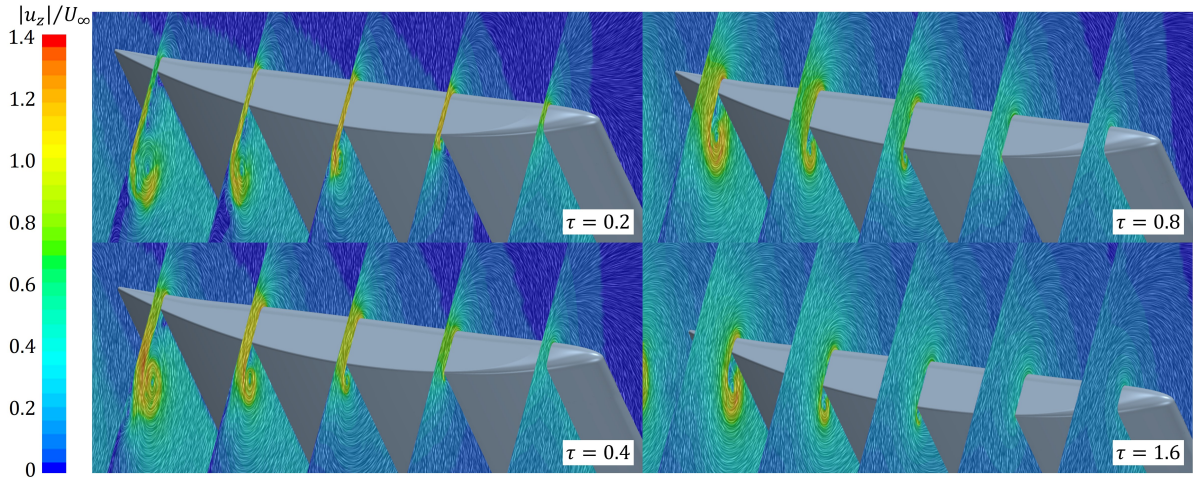

Fig. 8: z-axis velocity component contours at $\tau = 0.2$, 0.4, 0.8, and 1.6.

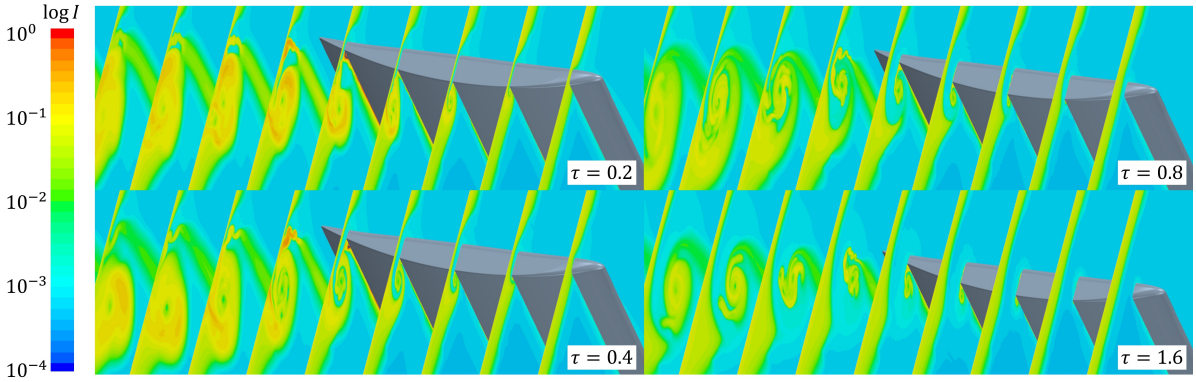

Fig. 9: Turbulence intensity contours at $\tau = 0.2$, 0.4, 0.8, and 1.6.

obtained in Russell et al. (2023). In a future study, this research will be extended to analyse the unsteady interaction between the primary TLV and secondary vortices using a detached eddy simulation.

Acknowledgements

This work is supported by the U.S. Office of Naval Research (ONR) Global through NICOP S&T grant number N62909-22-1-2058.

The author expresses gratitude to his colleagues at the Cavitation Research Laboratory and the research resources of the University of Tasmania for providing support for this study.

References

P.S. Russell, L. Barbaca, J.A. Venning, B.W. Pearce, and P.A. Brandner (2020). Nucleation Effects on Tip-gap Cavitation. Proceedings of 22nd AFMC, Brisbane, Australia.

P.S. Russell, L. Barbaca, J.A. Venning, B.W. Pearce, and P.A. Brandner (2023). Influence of nucleation on cavitation inception in tip leakage flows. *Phys Fluids*, **35**(1):013341.

P.S. Russell, K. Takahashi, L. Barbaca, J.A. Venning, B.W. Pearce, and P.A. Brandner (2024). The influence of boundary-layer thickness on incipient and developed cavitation in tip-leakage flow. Proceedings of SNH 2024, Nantes, France.

K. Takahashi (2024). Numerical study on tip-gap flow of a hydrofoil. Proceedings of OMAE 2024, Singapore.

B. Ji, X. Wang, X. Bai, H. Cheng, and X. Peng (2023). Cavitation inception noise excited by a tip leakage vortex with various gap sizes: A Eulerianâ-Lagrangian investigation. *Phys Fluids*, **35**(12):122107.

C.J. Chesnakas and S.D. Jessup (2003). Tip-vortex induced cavitation on a ducted propulsor. Proceedings of FEDSM 2003, Honolulu, Hawaii, USA.

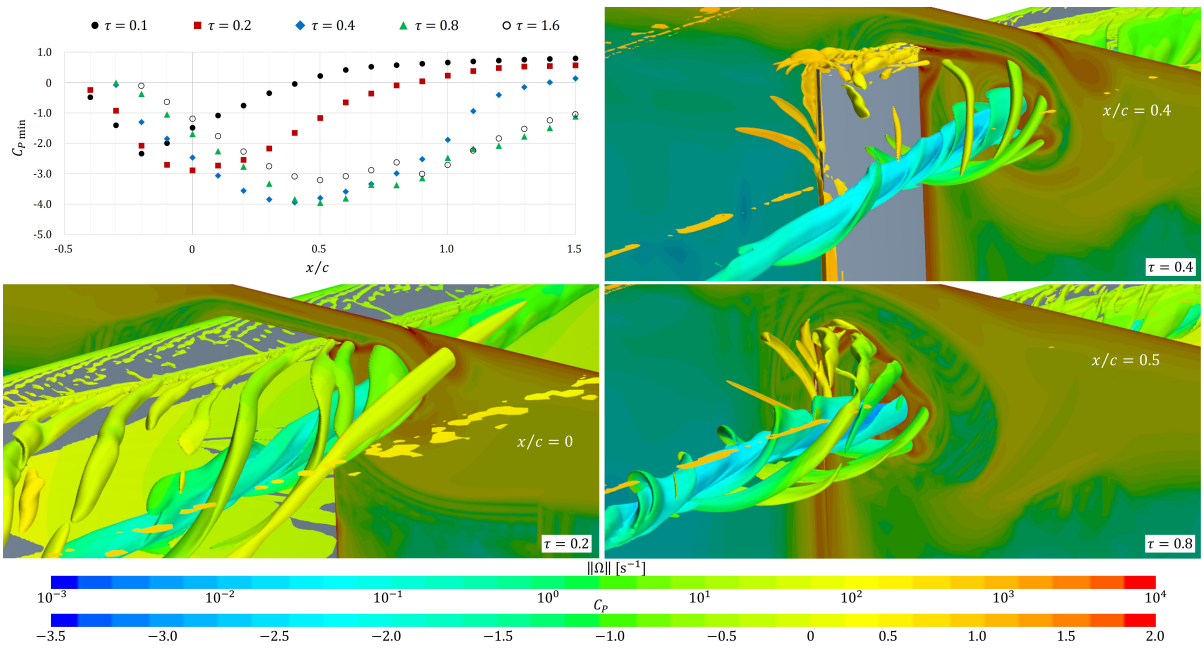

Fig. 10: Minimum pressure coefficient of TLVs at each plane perpendicular to the centreline (top left). Vorticity contour and iso-surface of $Q = 1.0 \times 10^6$ [s^{-2}] coloured with pressure coefficient for $\tau = 0.2$, 0.4, and 0.8.

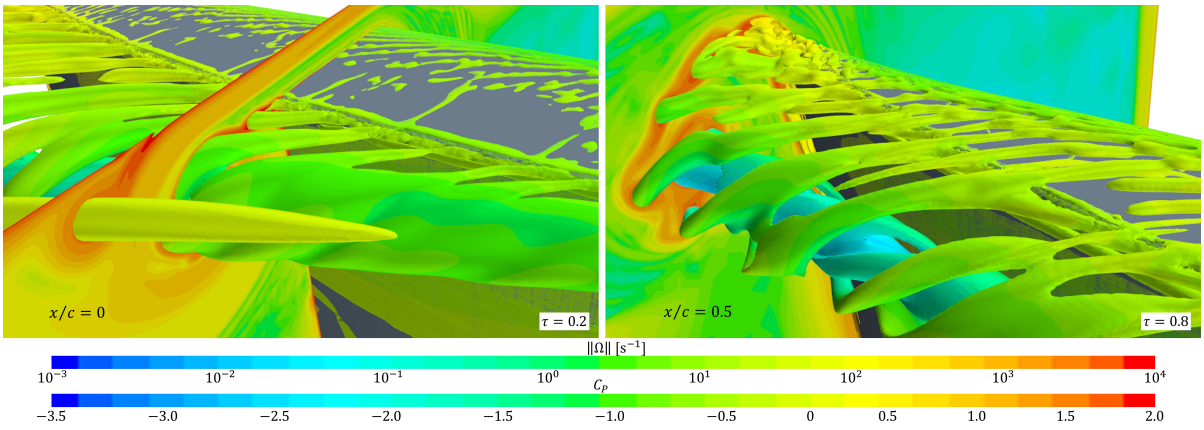

Fig. 11: Vorticity contour and iso-surface of $Q = 1.0 \times 10^6$ [s^{-2}] coloured with pressure coefficient for $\tau = 0.2$ (left) and 0.8 (right) as viewed from upstream.

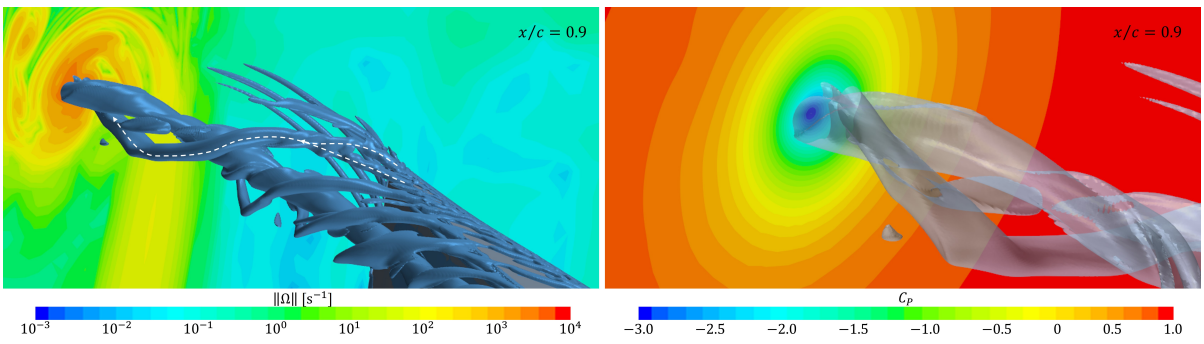

Fig. 12: Iso-surface of $Q = 1.0 \times 10^6$ [s^{-2}] and vorticity (left) and pressure coefficient (right) contours at $x/c = 0.9$ plane for $\tau = 1.6$.

Propeller Prediction in Behind Condition using a RANS-Based Artificial Body Force Method

Daniel Akinmulewo[a,1], Simon Froitzheim[a]
[a] *Schiffbau-Versuchsanstalt Potsdam GmbH*
akinmulewo.sva-potsdam.de

1.0 Introduction

RANS (Reynolds-Averaged Navier-Stokes) propeller simulation is a modern workhorse and a standard tool for practical industrial applications in predicting flows around propellers and determining the complex hull-propeller interactions. However, for unsteady propeller performance prediction in behind condition, RANSE solvers are often associated with large computational requirements and lengthy simulation times.

The previous studies conducted by Baltazar et al. [1]; Mikkelsen et al. [2]; Shin et al. [3], and others have demonstrated the feasibility of predicting propeller performance without modelling the ship hull. This approach significantly reduces computational costs due to the elimination of the need for a high number of cells required for modelling the hull, including its boundary layers.

In this study, approach to predict propeller performance without modelling the ship hull is investigated. This method involves using the wake field, calculated from a previous RANS simulation, and applying it with the use of body forces upstream of the propeller plane. The propeller performance and cavitation pattern predictions in this artificial wake field are compared to those obtained behind the ship under both steady and unsteady conditions. The effects of body force thickness and its position upstream of the propeller are examined, and the influence of mesh refinements in the wake field region on accuracy and computational cost is observed.

The paper is organized as follows: a short description of the numerical method is presented in Section 2; the test case and numerical setup are described in Section 3; the results from the numerical setup are shown in Section 4, followed by the conclusion in Section 5.

2.0 Numerical method

The numerical simulation to predict the flow around the ship hull and propeller was carried out in single phase using the open-source CFD code OpenFOAM v2212. To model the turbulence effects, the k −ω SST model with wall functions was used. For the non-uniform nominal wake field modelling needed for the predictions of propeller performance without the presence of the hull, a loss model (acting similarly to a porous baffle or to a wake-screen used in the cavitation tunnel) is applied as a body force at an upstream distance to the propeller plane. These body forces are added to the momentum equation to generate the wake field (by accelerating and decelerating the flow using the additional momentum imparted by the body forces).
According to the Rankine-Froude momentum theory and the method proposed by Baltazar et al. [1] to iteratively calibrate the body forces due to the strong interaction between the axial and the transversal flows, the velocity components are expressed as:

$$F_x^{(n)} = -0.5.\rho\left(V_s - V_{wx}^{(n)}\right)\left(V_s + V_{wx}^{(n)}\right)\frac{1}{\Delta V^{\frac{1}{3}}} \tag{1}$$

$$F_y^{(n)} = 0.5.\rho\left(V_s - V_{wx}^{(n)}\right)\left(V_{wy}^{(n)}\right)\frac{1}{\Delta V^{1/3}} \tag{2}$$

$$F_z^{(n)} = 0.5.\rho\left(V_s - V_{wx}^{(n)}\right)\left(V_{wz}^{(n)}\right)\frac{1}{\Delta V^{1/3}} \tag{3}$$

With the corrected velocities given by:

$$V_{w(x,y,z)}^{(n)} = V_{w(x,y,z)}^{(0)} - \beta\sum_{k=1}^{n-1}\left(V_{w(x,y,z)}^{(k)} - V_{w(x,y,z)}^{(0)}\right) \tag{4}$$

Where V_s is the ship speed, $V_{w(x,y,z)}^{(0)}$ is the intended wake field, ΔV is the cell volume, ρ is the fluid density and β is a relaxation factor. $V_{w(x,y,z)}^{(k)}$ represent the cell velocity in previous iteration (time step).

Based on the assumption provided by Baltazar et al. [1], the relaxation factor can be considered a forcing factor used to control the strength of the local velocities in each cell within the body force region in order to achieve the intended wake field. However, the size of the region or the thickness of the body force can also influence the strength of the body force and is such a parameter that must be adjusted to obtain the desired wake field. Therefore, the optimal combination of these two parameters needed to reproduce the desired wake on the propeller disk must be determined.

To generalize the body force implementation independent of specific parameter combinations, in Eqns. (1-3) the body forces are normalized by multiplying the r.h.s by the ratio of length of each cell to the prescribed thickness. Thus, Eqns. (1-3) becomes:

$$F_x^{(n)} = -0.5.\rho\left(V_s - V_{wx}^{(n)}\right)\left(V_s + V_{wx}^{(n)}\right)\frac{1}{W_{fb}} \quad (5)$$

$$F_y^{(n)} = 0.5.\rho\left(V_s - V_{wx}^{(n)}\right)\left(V_{wy}^{(n)}\right)\frac{1}{W_{fb}} \quad (6)$$

$$F_z^{(n)} = 0.5.\rho\left(V_s - V_{wx}^{(n)}\right)\left(V_{wz}^{(n)}\right)\frac{1}{W_{fb}} \quad (7)$$

Where the relaxation factor $\beta = 1$ or can be ignored and W_{fb} represents the prescribed thickness.

3.0 Case study and numerical setup

For this study, a single skew vessel, with a four bladed propeller was selected for full-scale analysis. The basic parameters of the vessels are provided below:

Table 1: Main ship parameters

			Single skew
Length	L_{PP}	[m]	72.000
Breadth	B_{wl}	[m]	14.400
Draught	T_d	[m]	5.550
Froude No.	*Fr*	[-]	0.2709
Propeller diameter	D_P	[m]	3.1635
Propeller rotational speed	*n*	[rpm]	160.00
Number of propeller blades	*Z*	[-]	4

3.1 Numerical setup

The numerical simulation of the viscous flow around the ship hull and propeller was conducted in three stages. In the first stage, a steady calculation of the ship hull was performed to predict the nominal wake at the propeller plane. This was followed by both steady and unsteady numerical simulations involving the propeller to predict the propeller performance in behind condition. For the steady calculations, a Multiple Reference Frame (MRF) method was used to replicate the action of the propeller, while a sliding mesh approach was employed to simulate the effect of propeller rotation in the unsteady calculations.

In the second stage, the nominal wake field was modelled using the calibrated body force approach. Numerical calculations were conducted to determine the influence of body force thickness in reproducing the desired wake on the propeller disk. Finally, propulsion simulations were carried out in both steady and unsteady states with the propeller in behind the artificially generated wake field. The effects of the body force position upstream of the propeller were also examined, along with the influence of mesh refinements in the wake field region on the accuracy of the simulations.

In this study, in addition to predicting propeller performance in behind conditions, the risk of cavitation occurrence is also determined for a specified cavitation number. This is achieved by identifying instances where the local pressure at a cell falls below the vapor pressure. The local pressure is determined by:

$$p_{local} = p_{cell} + p_{atm} + \rho_{water} \cdot g \cdot h_{sp} \quad (8)$$

$$\sigma_N = \frac{p_{local} - p_{vapor}}{0.5 \cdot \rho \cdot n^2 \cdot {D_P}^2} \quad (9)$$

Where p_{atm} is the atmospheric pressure at sea level (typically p_{atm} 101325 Pa) and h_{sp} takes into account the influence of the propeller immersion depth or reference height.

3.2 Computational domain and mesh generation

The computational domain consists of a rectangular multi-block structured grid with a hexagonal dominated mesh, generated using the OpenFOAM SnappyHexMesh utility. For simulations involving the hull and propeller, the computational domain extends $2L_{pp}$ upstream, $3L_{pp}$ downstream, and $2L_{pp}$ in both the transverse and vertical directions. A total of 7.7 million cells were used in this case, with mesh refinement around the hull and propeller regions.

For the numerical simulation to generate the artificial wake field and predict propeller performance using the calibrated body force approach (i.e., without the presence of the ship hull), a grid similar to that of the ship-propeller setup was used, except without the hull geometry. In this case, a long hub running across the length of the domain was employed. In this setup, the mesh consists of approximately around 2.9 million and 3.3 million cells respectively.

4.0 Results and Discussions

The outcome of the flow simulations is presented in this section, followed by the general prediction of propulsion performance in behind conditions.

4.1 Wake field modelling

The nominal wake field obtained from the steady-state simulation of the bare hull serves as input for the wake field modelling. Wake velocities are extracted from discrete points in the propeller plane, with an angular resolution of 0.5 degrees across 30 radial sections. A fine resolution was adopted to accurately capture the wake velocities due to the strongly non-homogeneous nature of the flow at the propeller plane.

Implementing the iterative calibrated body force approach proposed by Baltazar et al. [1], the wake field is reconstructed including both the axial and tangential velocities.

As stated in section 2.0, to determine the optimal combinations of these two parameters for reproducing the wake field, three prescribed thickness values (W_{fb} = 0.15D_p, 0.25D_p, and 0.30D_p) were selected while keeping the relaxation factor constant (β = 1). Similarly, simulation using the normalized formulation was also conducted to reproduce the desired wake field. The results of the generated artificial wake field are presented in Fig. 1, alongside the extracted wake velocities from the bare hull simulations.

	Bare hull nominal wake field	**Artificial wake field W_{fb} = 0.15D_p**	**Artificial wake field W_{fb} =0.25D_p**	**Artificial wake field W_{fb} =0.30D_p**	**Artificial wake field W_{fb} = 0.15D_p Normalized force**
	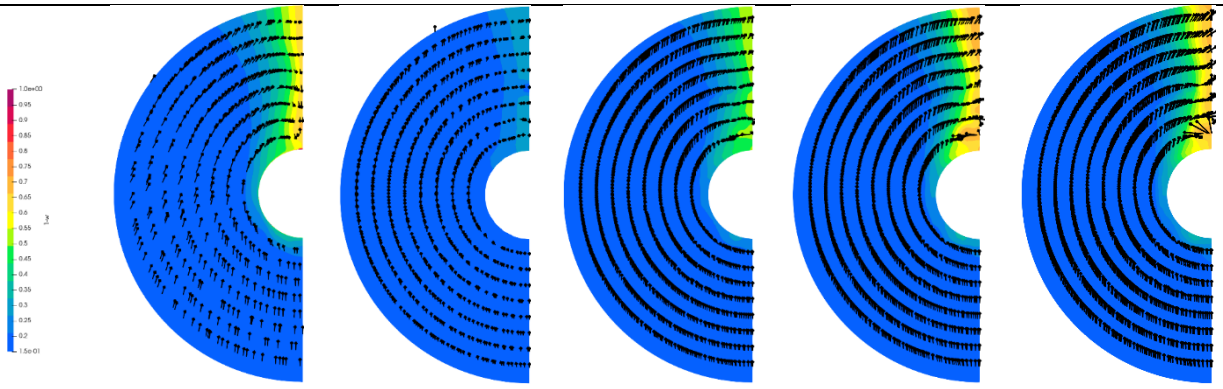				
Wake fraction	0.3099	0.1656	0.2464	0.2994	0.2930

Figure 1: Wake field

In Fig. 1, the influence of body force thickness while maintaining a constant relaxation factor are presented. As the thickness of the body force increases, the wake velocities are observed to be almost fully reconstructed. The numerical simulation indicates the body force thickness as a major parameter influencing local velocities and is thus crucial for accurately reproducing the desired wake on the propeller disk. In this case, an error of 3.51% in wake fraction was obtained with a body force thickness relative to 0.30D_p. Conversely, when the body forces were normalized according to Eqns. (5-7) and the prescribed thickness of 0.15D_p was applied, the wake velocities were again nearly fully reconstructed, yielding results similar to those previously obtained.

From the artificially modelled wake field, the wake velocities are slightly overpredicted at the 12 o'clock position, particularly in the inner radii region ($r/R \leq 0.5$). These differences can be attributed to the strong interaction

between the axial and transversal flows within the body force region. To further improve the wake field reconstruction, mesh refinement around this region could be a possible solution.

In Fig. 2, the non-dimensional wake velocities at different radii are plotted against those from the bare hull simulation, showing a good agreement in the results.

Non-dimensional wake velocities

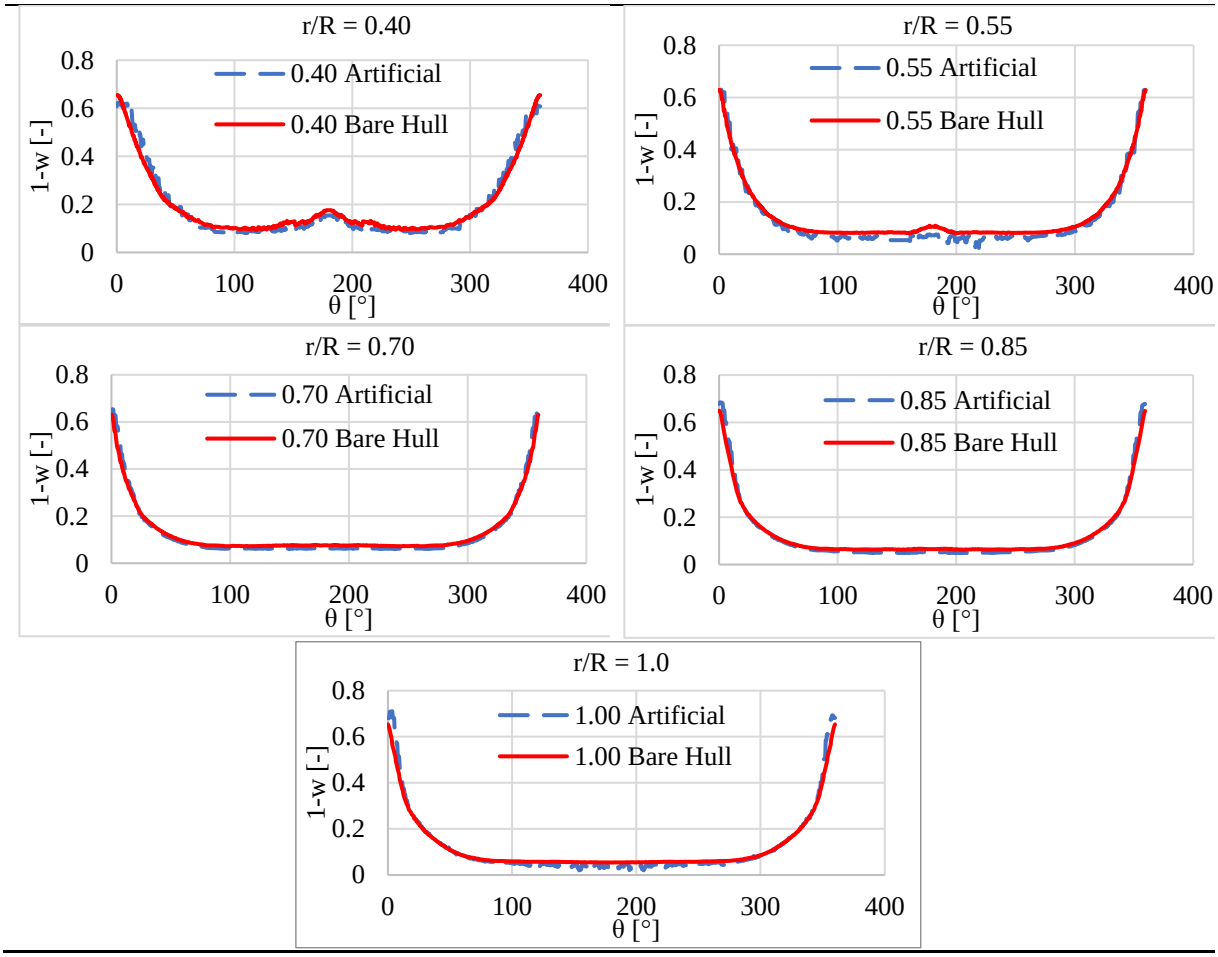

Figure 2: Non-dimensional wake fraction

4.2 Propeller in behind condition

For the prediction of propeller performance in behind conditions, both steady and unsteady simulations were conducted without considering the effect of the free surface. This applies to simulations involving both the hull and the artificially reconstructed wake field. The results from the steady state calculation are presented in table 2, including the effect of artificial wake field position upstream of the propeller and grid refinement on propeller performance.

Table 2: Propeller prediction in behind condition (steady calculation)

	Wake Position x/D_p [-]	KT [-]	error [%]	10KQ [-]	error [%]	Remarks [-]
	-	0.2205	-	0.3745	-	Propeller with Hull
Coarse Mesh	0.15	0.2209	0.19%	0.3739	-0.15%	
	0.25	0.2221	0.70%	0.3749	0.11%	
	0.35	0.2168	-1.72%	0.3691	-1.46%	
						Propeller with artificial wake field
Fine Mesh	0.15	0.2202	-0.12%	0.3730	-0.39%	
	0.25	0.2208	0.15%	0.3734	-0.30%	
	0.35	0.2164	-1.90%	0.3685	-1.63%	

Considering mesh refinements and the influence of the artificial wake field position upstream of the propeller, the results from propeller predictions in behind conditions with the artificially generated wake field show qualitatively good accuracy. The computed errors for propeller thrust and torque are less than 2% when compared to those obtained from full RANS simulations with both the hull and propeller. However, when the position of the artificial wake field is moved further upstream of the propeller, the propeller thrust and torque are slightly underpredicted.

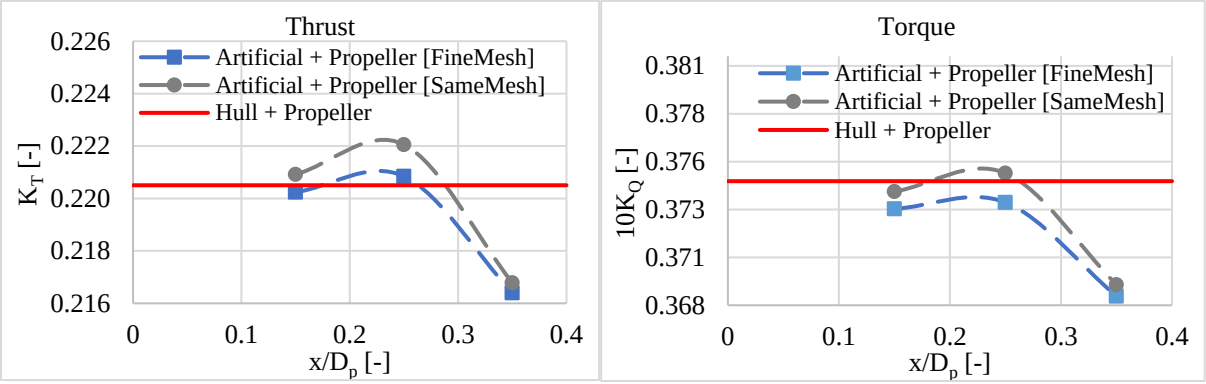

Figure 3:Steady state propeller prediction in behind condition

For the unsteady propeller simulations, the time step was adjusted to achieve an angular step of 0.5 degree in both the behind-hull and behind-artificial-wake-field conditions, with the maximum Courant number of 60. In the propeller prediction in behind-artificial-wake-field condition, the artificial wake was positioned at an upstream distance of $x/D_p = 0.15$. The predicted time-averaged results from the unsteady propeller simulations are presented in Table 2, while the unsteady thrust and torque over one propeller rotation are shown in Fig. 4.

Table 3: Propeller prediction in behind condition (unsteady calculation)

KT [-]	error [%]	10KQ [-]	error [%]	Remarks [-]
0.2207	-	0.3835	-	Propeller with Hull
0.2215	0.33%	0.3782	1.42%	Propeller with artificial wake field

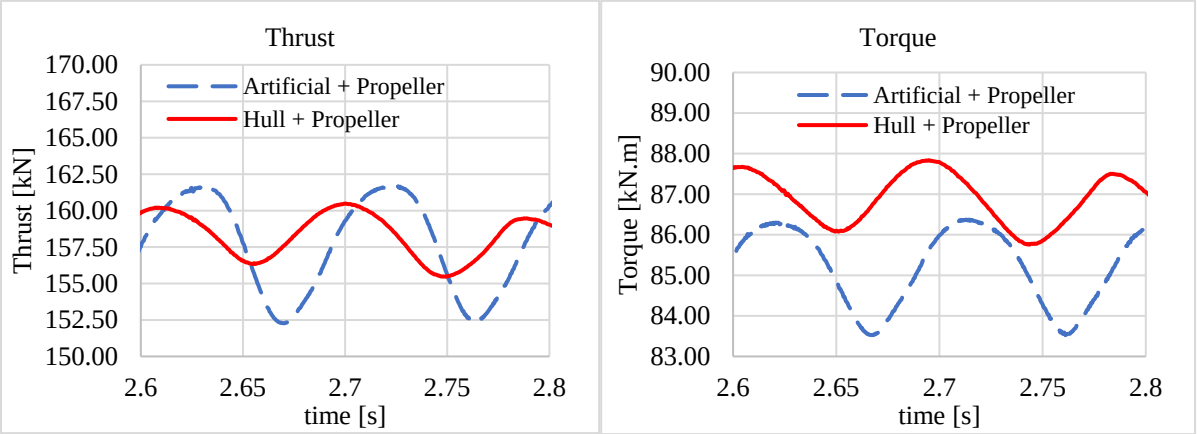

Figure 4: Unsteady thrust and Torque

From the results of the unsteady thrust and torque over one propeller rotation presented in Fig. 4, two major discrepancies were observed: underprediction of propeller torque in the behind-artificial-wake-field condition, and a phase shift. These discrepancies may be attributed to changes in the angle of attack experienced by the propeller blades, influenced by tangential velocities in the artificial wake. In principle, the tangential component of the wake field directly influences the hydrodynamic rotation speed of the propeller, resulting in a virtual shift in propeller speed due to accelerated or decelerated tangential inflow into the propeller. The combined effects of both axial and tangential velocities ultimately define the local advance ratio experienced by the propeller profile at each point in the wake field.

As mentioned earlier, the differences observed in the nominal wake field and the artificially reconstructed wake field, which is largely due to the strong interaction between the axial and tangential velocities at the 12 o'clock position, could explain these discrepancies. This strong interaction could also influence the cavitation behaviour of the propeller. One way to mitigate such effects would be to transform the tangential wake velocities into the axial ones, by maintaining a constant local advance ratio for each point in the wake field. To see the influence due to the strong interaction, the pressure distribution on the blade profile at blade positions (θ = 0° and 180°) and at radii (r/R = 0.55, 0.70 0.75) are presented in Fig. 5.

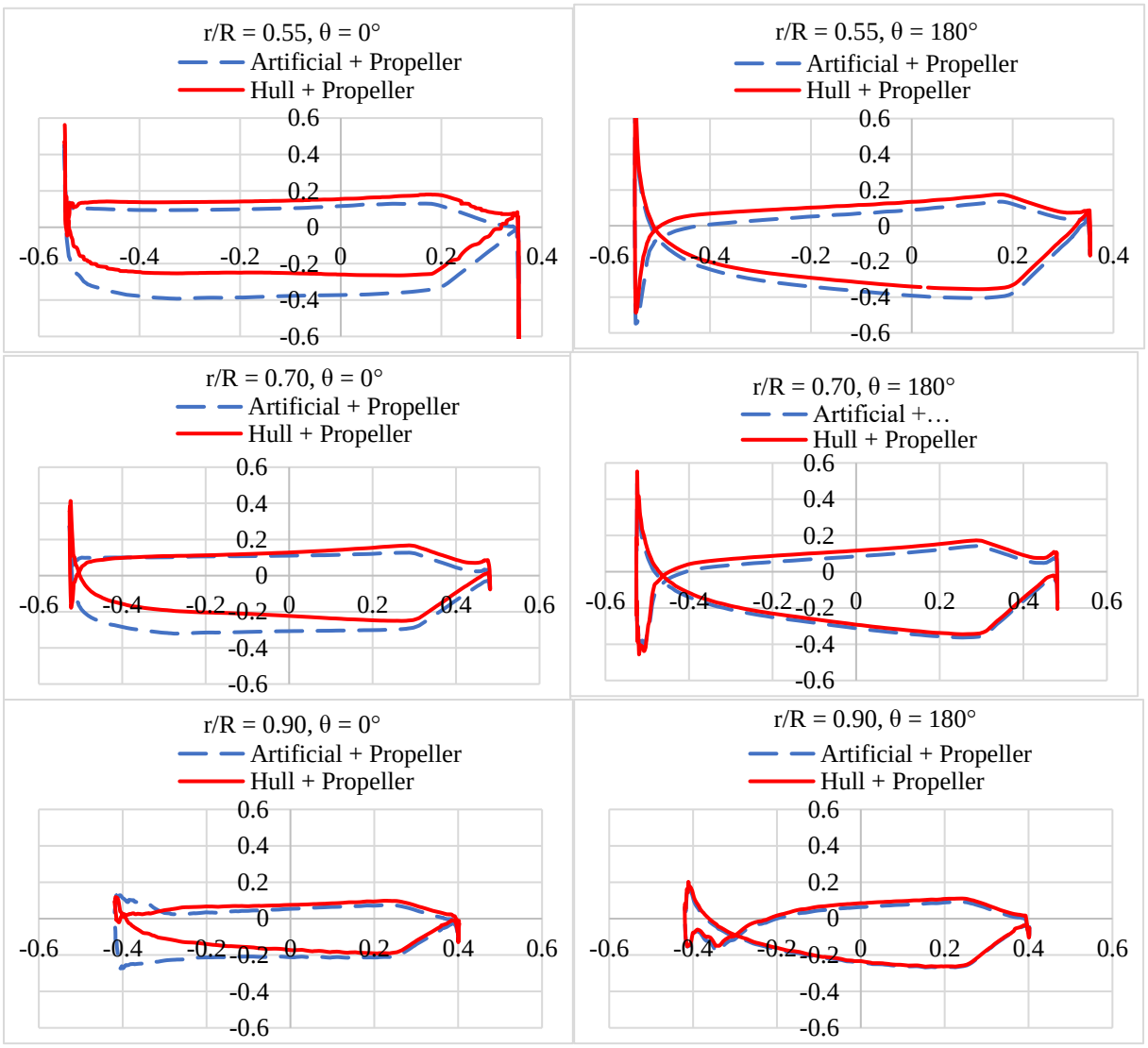

Figure 5: Pressure distributions.

4.3 Cavitation prediction

Cavitation occurs when local pressure drops below the vapor pressure of the fluid, causing a phase transition. To predict cavitation risk in this case, it is sufficient to check for pressure values below the vapor pressure in the simulation. Contour plots for visualizing potential cavitating regions and the pressure distribution are shown in Fig. 6, using a propeller immersion depth of 3.4m and ρ_{vapour} = 1.736 kPa.

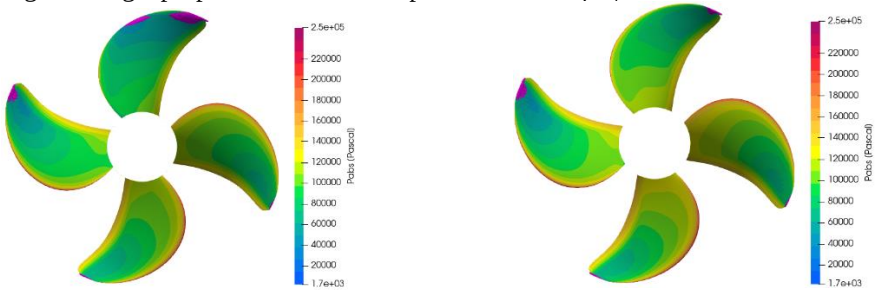

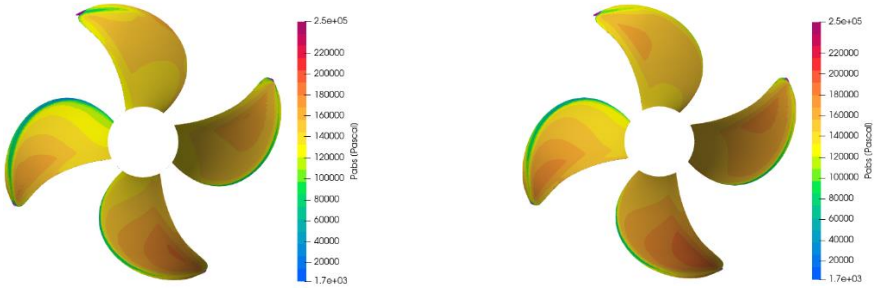

(a) Behind-artificial-wake-field condition (b) Behind ship condition

Figure 6: Pressure distribution and potential cavitating regions

Fig. 6 compares the discussed methods. The cavitation pattern observed in the behind-artificial-wake-field condition shows a much greater extent of cavitation on the suction side at the blade position ($\theta = 0°$) compared to the cavitation observed in the behind-hull condition. This could be said to be influenced by the strong interaction in the axial and tangential wake velocities as mentioned earlier.

4.4 Performance evaluation

The computational costs in real time for this case study are presented in this section. Simulations were performed on the HPC network, and for a fair comparison, the same number of CPUs (48 CPUs) were used for each simulation.

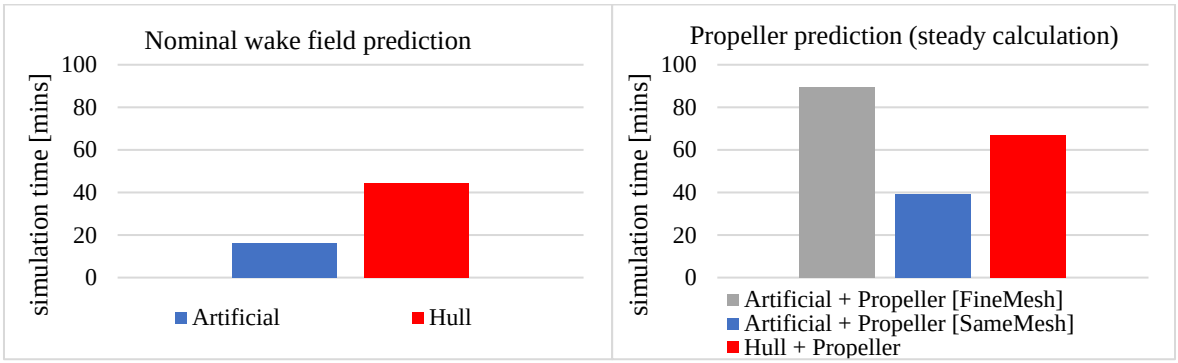

Figure 7: Performance evaluation

Simulations for predicting propeller performance in the behind-artificial-wake-field condition are 1.7 times faster than those in the behind-hull condition. However, most of the effort in the behind-artificial-wake-field condition comes from the algorithm responsible for the interpolation scheme needed to reproduce the desired wake on the propeller disk. More time could be saved in this scenario if the computational domain is reduced, as the hull is not present.

5.0 Conclusions

In this study, a thorough investigation was conducted to predict propeller performance in an artificially generated wake field using the calibrated body force approach. The strategy implemented to reproduce the desired wake field on the propeller disk, including the effects of body force thickness and its position upstream of the propeller, was examined. The computational efficiency and accuracy for predicting propeller performance and cavitation risk in the behind-artificial-wake-field condition were compared with RANS simulations in the behind-hull condition.

The numerical results demonstrated qualitatively good accuracy, with computed errors of the forces less than 2% for propeller thrust and torque in both steady and unsteady simulations. A notable advantage of the artificial wake field method is its significantly reduced computational cost compared to full RANS simulations involving the hull. Future improvements could explore transforming the tangential wake velocities into axial ones, by taking into account the propeller-induced influence on the wake field.

Reference

[1] Baltazar, J., Schuiling, B., & Rijpkema, D. (2019). Propeller Performance Prediction in an Artificially Generated Wake Field Using RANSE. In 22nd Numerical Towing Tank Symposium, Tomar, Portugal.

[2] R. Mikkelsen, P. Andersen, J.N. Sorensen (2007). Modeling of behind condition wake flow in RANS computation on a conventional and high skew propeller. 10th Numerical Towing Tank Symposium, Hamburg, Germany.

[3] K.W. Shin, P. Andersen, R. Mikkelsen (2011). Cavitation simulation on conventional and highly-skewed propellers in the behind-hull condition. Second International Symposium on Marine Propulsors, smp'11, Hamburg, Germany.

Simulation workflow for flexible marine propellers

Laurens-Jan Lagendijk[1,*], Arjan Lampe[2], Jaap Windt[2], Stefan Hickel[1], and Tom Van Terwisga[1,2]

[1]TU Delft, The Netherlands
[2]MARIN (Maritime Research Institute Netherlands), The Netherlands
[*]L.P.Lagendijk@tudelft.nl

October 2024

Abstract

This study demonstrates the use of a simulation workflow to perform FSI simulations for a flexible C4-40 propeller of various material stiffnesses and operating conditions. Grid convergence studies for both the fluid and the structure grid have been performed. The loading is found to be non-monotonic with the change in stiffness: The stiffer deformable propellers can result in increased thrust, whereas more flexible propellers result in a thrust reduction. The increased thrust is attributed to the camber deformation within the blade sections, whereas the reduction in thrust is due to a reduction of pitch, mainly near the tip region, due to the twisting of the blades.

1 Introduction

Flexible marine propellers provide additional freedom to design the desired deformation of a propeller under loading. The flexural behavior is influenced by the blade geometry, loading, and material properties. As the propeller moves through the non-uniform wake behind a ship, the blade shape is passively adjusted to the inflow conditions, this has the potential to relieve cavitation and reduce radiated noise. Understanding of the deformation behavior is required to design flexible propellers for the purpose of increased efficiency and reduced radiated noise.
A workflow has been developed for time domain simulations of a flexible propeller. Several software packages are combined in this simulation setup. The geometry is modeled, discretized, and analyzed. A modal analysis and FSI simulations of the propeller are performed. The fluid domain is discretized, and URANS simulations with a linear two-way coupling to the structural code are performed. This workflow enables the evaluation of a range of flexible propeller designs and variations in material properties.

2 Methodology

Simulations of flexible marine propellers have been performed to evaluate the deformation behavior and to test the developed workflow. These simulations are performed with the 4-bladed, 40% blade area ratio, C4-40 propeller with a pitch ratio of $P/D = 0.8$. This geometry has also been used in model tests on flexible propellers. Figure 1 shows the outline of this propeller. The C-series is a modern variable pitch propeller series of which the geometries are publicly available [5].
This study considers simulations in open water conditions for a propeller, including the hub. The propeller features a diameter of $D = 0.34[m]$ and a hub with $D_{hub}/D = 0.2389$. The propeller is operated at a constant rotational speed of 700 RPM. The axial inflow velocity is varied to attain different advance ratios. This ensures the Reynolds number over the blades remains more constant and allows for the evaluation in bollard pull condition.
The reference material is a thermoplastic polymer named POM-C. This is an isotropic material with a density of $\rho_{structure} = 1410[kg/m^3]$, a Poisson's ratio of $\nu_{structure} = 0.43$ and a Young's modulus of $E = 3[GPa]$.

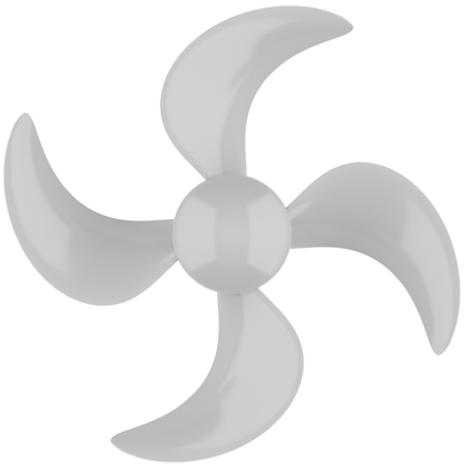

Figure 1: Outline of the C4-40 propeller

The workflow described in this paper is a method to simulate flexible propellers of various initial geometries, material properties, grid refinements, and operational conditions. The benefit of this workflow is the automation of a large part of the computational setup. This takes the total setup time for the FSI simulation from $\mathcal{O}(days)$ to $\mathcal{O}(minutes)$.

The input of the workflow consists of a geometry description of the undeformed propeller shape in the form of a .ppg (Procal Propeller Geometry) file. This propeller description uses classical design parameters: propeller diameter, hub diameter, number of blades, and radial distributions of the chord, skew, rake, pitch, thickness, camber, and section profile description at various sections. The CAD program Rhinoceros with the visual programming language Grasshopper and an in-house tool package of Marin is used to transform this geometry into a .stp file for the solid propeller geometry. Additionally, a .stl file is created to define the boundary surfaces of the computational fluid domain. An additional file is generated where the names of the boundary surfaces of the fluid domain are assigned.

The Salome-Meca [10] platform is used to generate the structural grid and perform the structural analyses. This platform incorporates multiple software modules. The Salome geometry module is used to load the .stp file and assign names to different parts of the geometry.
The Gmsh [4] meshing package within Salome is used to automatically generate the structural grid. Only one blade is discredited, this is copied to make a mesh for all the blades. The hub is assumed to be rigid, therefore it is not included in the structural analyses. These grids consist of hexahedral elements where the propeller is discretized over the face- and back surface and in the thickness direction. The refinement over the face- and back surface is referred to as surface refinement. The desired number of cells over the surface is equal and is prescribed as an input to the simulation ($N_{face,setting}$). The distribution of the surface discretization depends on the aspect ratio of the blades. This ensures the cells are approximately square. To improve the convergence behavior of the FSI simulations, the region at the blade root has additional refinement in the radial direction. The discretization in chordwise direction is increased accordingly to retain approximately rectangular cells over the surface of the blades. Because the calculated number of cells in radial and chordwise directions is unlikely to be an integer, these discretizations are rounded up to the actual radial (N_r) and chordwise (N_c) refinement. This ensures the number of cells at the surface is always at least the specified value regardless of the propeller geometry. The thickness discretization is explicitly prescribed. Quadratic elements are used to prevent shear locking as explained by Zienkiewicz [11].

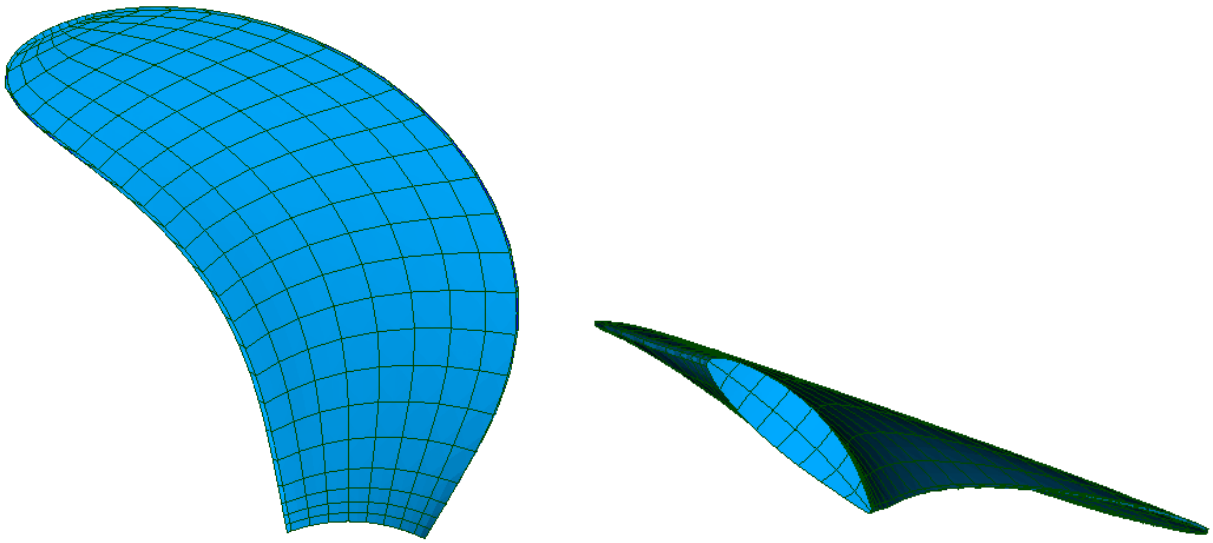

(a) Surface discretization

(b) Thickness discretization

Figure 2: Propeller discretization

A grid convergence study with structural grids ranging from 140 to 960 cells has been conducted. This convergence study uses the thrust force as the quantity of interest. The results of this structural mesh refinement study are presented in Appendix B using the method of Eça and Hoekstra [8]. This method uses the refinement of geometrically similar grids to determine the convergence behavior and the error of the selected refinement setting. This method is also used for the fluid grid refinement study and the time step refinement study. Based on this study, structural refinement settings of 91 cells over the surface and 2 cells in thickness direction have been selected. This resulting grid is presented in Figure 2.

The structure is simulated using the code_Aster [6] structural solver within Salome. The hub is assumed to be rigid, and the blade-hub connection is a fixed boundary condition. The simulation provides the mass matrix and stiffness matrix of the entire propeller, and modes of a single blade. The matrices are exported in a sparse matrix format in order not to run out of memory.
The first mode is the first bending mode, which affects the rake. The second and third modes are twisting modes. The modal frequencies provide a first insight into the sensitivities of grid refinement for surface and thickness refinement. The modal frequencies for coarse surface refinement settings tend to be too high, whereas the modal frequencies for coarse thickness refinement settings are mostly too low. The frequencies of the first modes are accurate, even for coarse meshes, but the sensitivity for cell refinement in simulated frequencies becomes larger for the higher modes. The higher modes, therefore, require finer mesh refinement. The convergence of the modal frequencies relative to the frequency with the largest refinement is presented in Figure 3 and Figure 4.

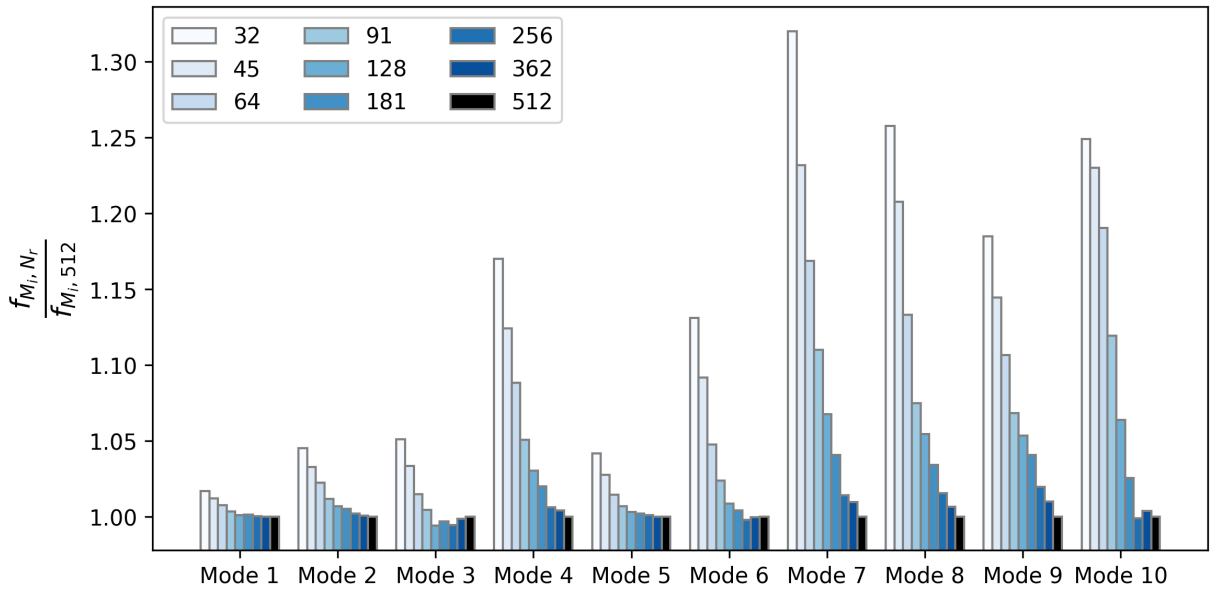

Figure 3: Modal frequency convergence for different levels of surface refinement of the structural grid, fraction relative to the finest surface refinement setting of $N_{face,setting} = 512$. All results are for $N_t = 2$.

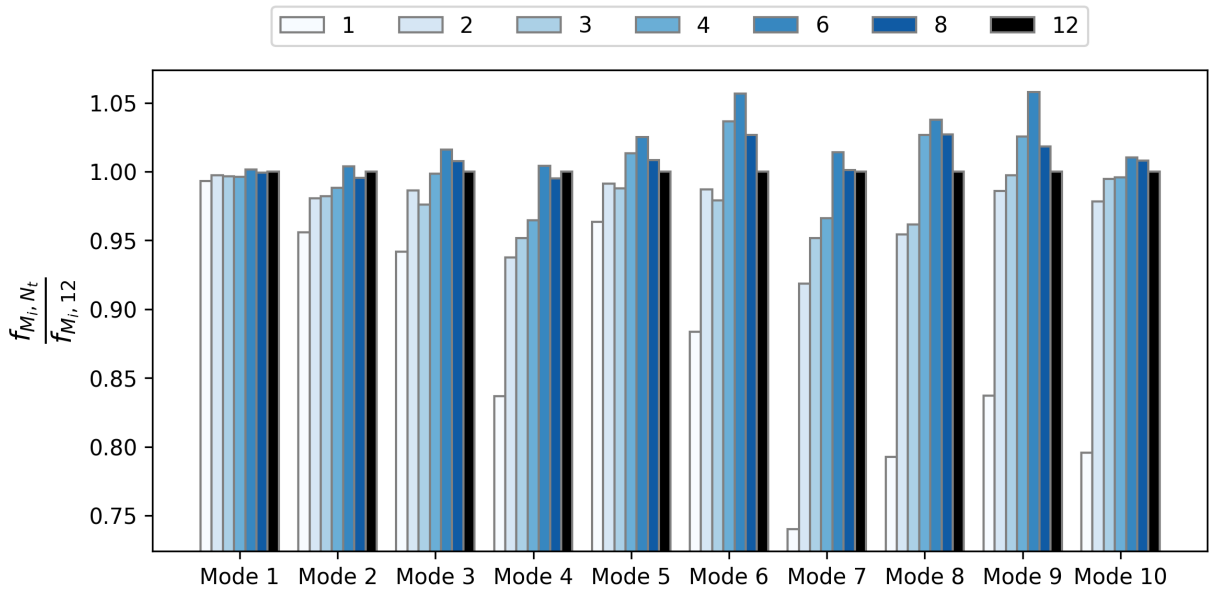

Figure 4: Modal frequency convergence for different levels of thickness refinement of the structural grid, fraction relative to the finest thickness refinement setting of $N_t = 12$. All results are for $N_{face,setting} = 64$.

The output of code_Aster is post-processed to a Hardwell-Boeing (HB) file format for the matrices and a so-called intnodes file, which contains the nodes at the interface between fluid and structure. Mapping files are also constructed for the mass and stiffness matrix. These mapping files relate the surface nodes to specific locations in the matrices.

Cadence Fidelity [2] is used to generate a cylindrical fluid grid around the propeller with a diameter and height of 10 times the propeller diameter. This is an unstructured grid that mostly consists of hexahedral elements and some tetrahedrons and pyramids at the layers between refinement levels. A grid convergence study with fluid grids ranging from 2.1 to 31 million cells has been conducted. This convergence study uses the thrust force as a measure of convergence. The wall refinement for all these grids is scaled with the length

of the cell edges, the coarsest grid has a y^+ value of 0.5. The results of this fluid mesh refinement study are presented in Appendix B. The selected grid has 5.1 million cells and a wall refinement of $y^+ = 0.5$. Slices of this grid are presented in Figure 5.

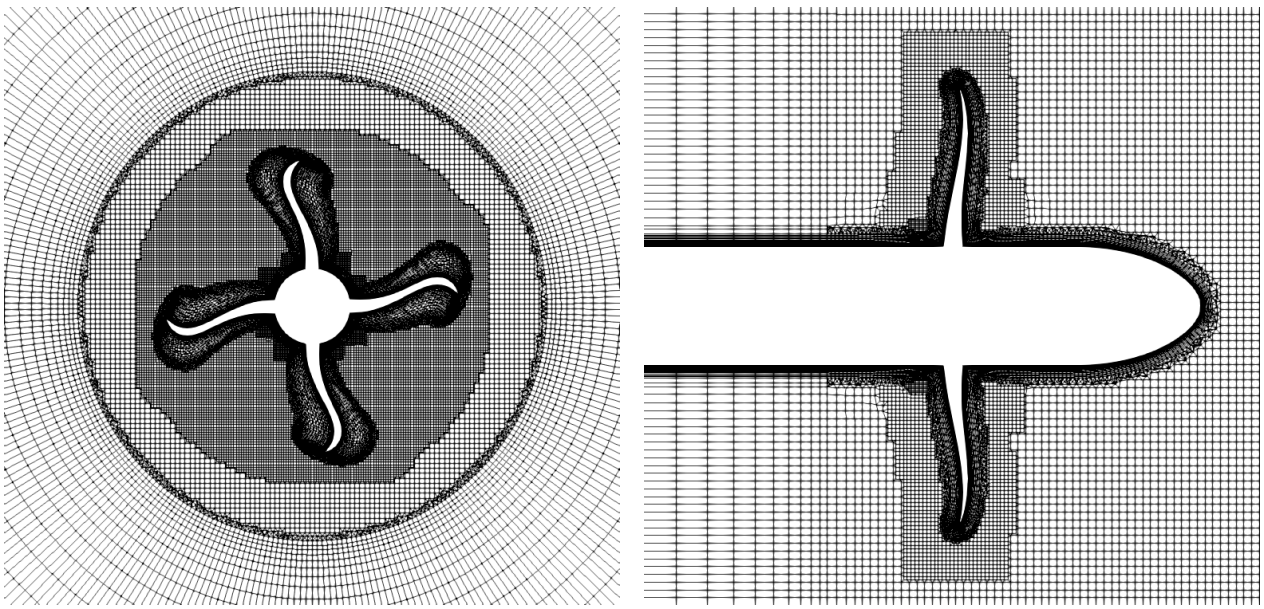

(a) Front view (b) Side view

Figure 5: Reference fluid grid

The FSI simulation is carried out with the Refresco [7] URANS flow solver. First, a rigid simulation is carried out to obtain a converged initial flowfield to start the FSI simulation.
The solver uses a grid deformation method where the loads and displacement are transferred using radial basis functions. The grid deformation is set up using compact support radial basis functions, with a support radius equal to $D/6$. This determines to what distance from the surface nodes the grid is deformed. Outside this radius, the grid remains undeformed.

For the unsteady simulations, a timestep convergence study has been conducted with timesteps ranging from 180 to 2 degrees of rotation. Based on this study, a time step of 10 degrees rotation per timestep is selected. This is sufficiently fine to only capture the first dry natural frequency. This setting is robust and converges after 15-30 rotations depending on the simulation case. The simulation always continues for 15 iterations. The simulations converge to a steady deformation, therefore the deformation of all blades is the same; this would not be the case when the propeller is operating in a non-uniform flowfield like the wake behind a ship. All the results are obtained from solutions where the residuals and forces are converged. There can be small periodic oscillations on the force signal. Therefore the method of Brouwer et al. [1] and the code of Lemaire and Klapwijk [9] is used to determine when the forces are converged.

The result of the workflow is a new geometry description of the deformed geometry in the form of a ppg file, similar to the geometry input of the workflow. This can be compared to the initial geometry to determine the deformation from the change in classical design parameters. This also enables the evaluation of the sectional deformations of the blades at different radial positions.

3 Results

The workflow is used to simulate the flexible propeller for a range of advance ratios and blade stiffness settings. The resulting thrust, torque, and blade deformation are investigated. The performance of flexible propellers is expressed in an open-water diagram, which is presented in Figure 6.
The thrust for the Young's modulus of $E = 3[GPa]$ is lower at high advance ratios and higher for $J < 0.6$,

which is around the optimum efficiency for all propellers. In this case, the efficiency curve of the flexible propellers does not exceed the efficiency curve of the rigid propeller and is equal for $J < 0.6$. The efficiency at equal thrust of the deformed propeller, therefore, exceeds the efficiency of the rigid propeller at advance ratios below $J < 0.6$, because of the change in working point J.
For the most flexible results of $E = 1[GPa]$, the thrust is reduced for all advance ratios. The efficiency for this case is also lower compared to the rigid case. Therefore, this case is less efficient for all levels of thrust.

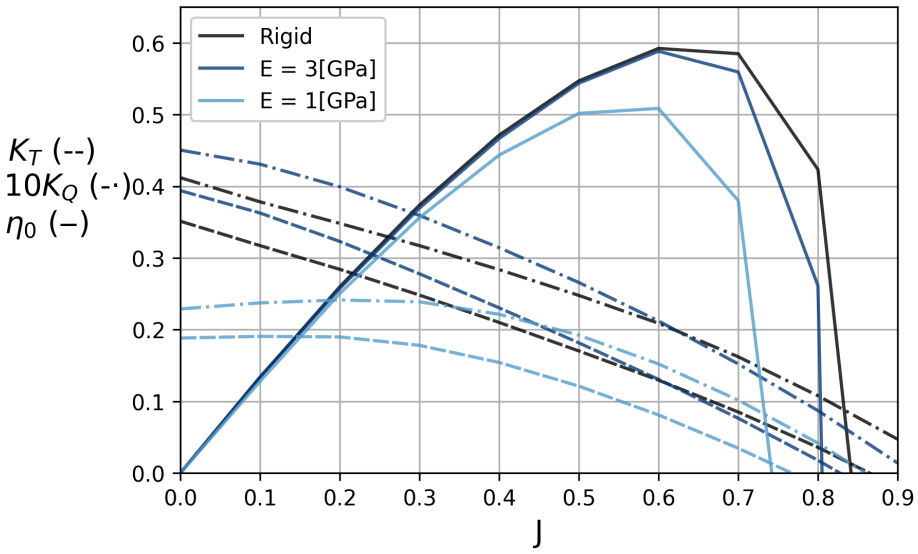

Figure 6: Open water diagram for material properties of various stiffness

The thrust force of flexible propellers depends not only on the operating condition but also on the material stiffness. This stiffness determines the deformation amplitude and type of deformation. Very flexible materials have been simulated up to $E = 1/16[GPa]$. This presents the non-monotonic behavior of the thrust with respect to the material stiffness, as shown in Figure 7.

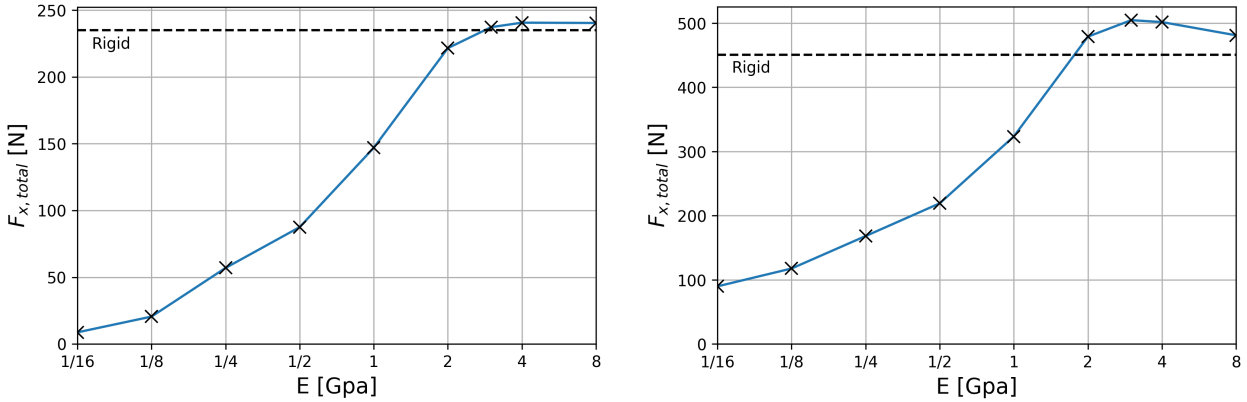

(a) $J = 0.6$ (b) $J = 0.3$

Figure 7: Thrust for various material stiffness

The most flexible cases show the thrust approaching zero but not reaching zero due to some thrust that remains from the blade root region because this is rigidly connected to the hub. From $E = 3[GPa]$ to $E = 1[GPa]$, there is a sharp drop-off in thrust. This can be explained by the reduction in pitch at the tip of the blade due to twisting. The pitch reduction at the tip results in reduced tip loading. This is visually shown in Figure 8. Figure 10 shows a graph of the reduction of pitch in the tip region.

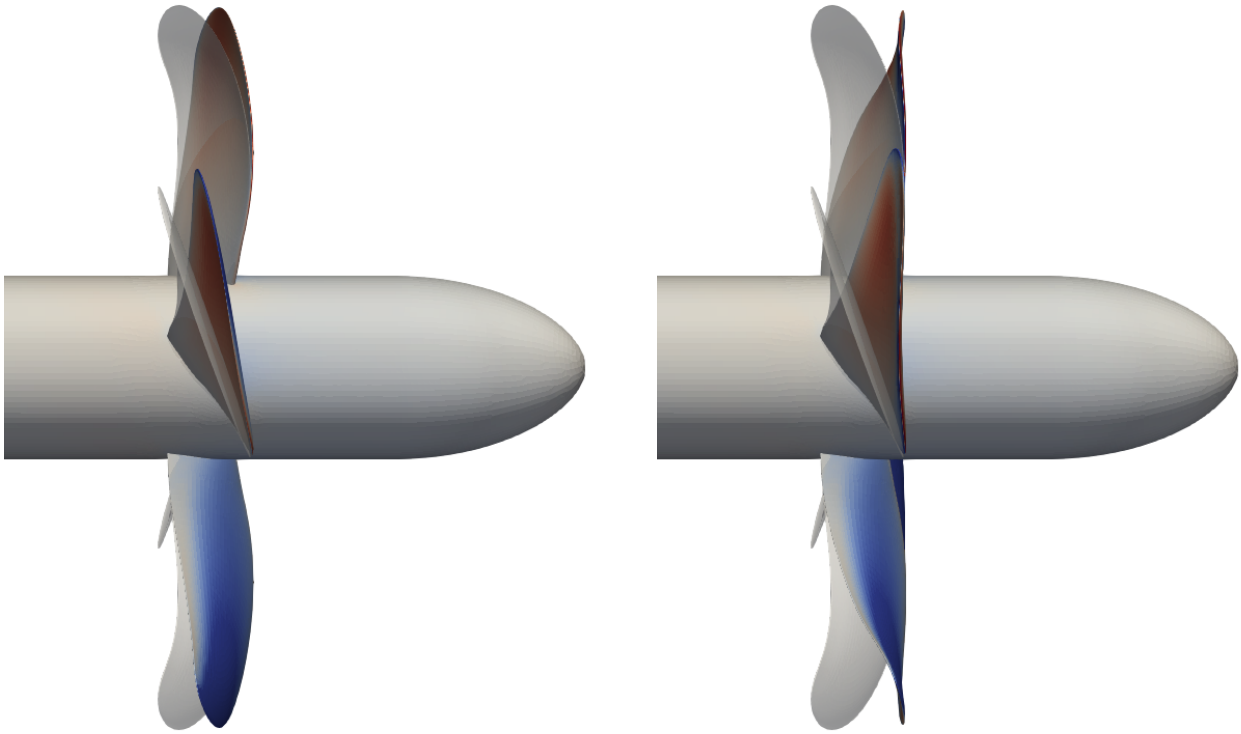

(a) $E = 3[GPa]$ (b) $E = 1[GPa]$

Figure 8: Propeller deformation, transparent rigid geometry and pressure distribution on the deformed blades, $J = 0.3$

The larger stiffness settings in Figure 7a and Figure 7b respectively indicate an increased thrust up to 2.3% for $J = 0.6$ and up to 12% for the heavier loading at $J = 0.3$. The open water diagram also indicates this effect is more pronounced for lower advance ratios. To determine the cause of this increase in thrust, we look in more detail at the deformation of the blades. Radial plots of characteristic propeller properties are made to investigate the deformation. All radial parameter changes are presented in Appendix E.
The thickness remains almost constant, and chord distribution shows only minimal deformation. This is because the plane-axial stiffness is larger than the flexural stiffness for out-of-plane deformations.
There is some increase of skew near the tip. This is a side effect of the blade twist because the twist of a skewed propeller can increase the skew.
The most trivial deformation is rake because the propeller thrust provides a bending force in the forward direction on the blades in this operating condition. This rake deformation is not presumed to cause the increased thrust. The rake deformation is largest for the case where $J = 0.3$ because this is the heaviest loadcase.

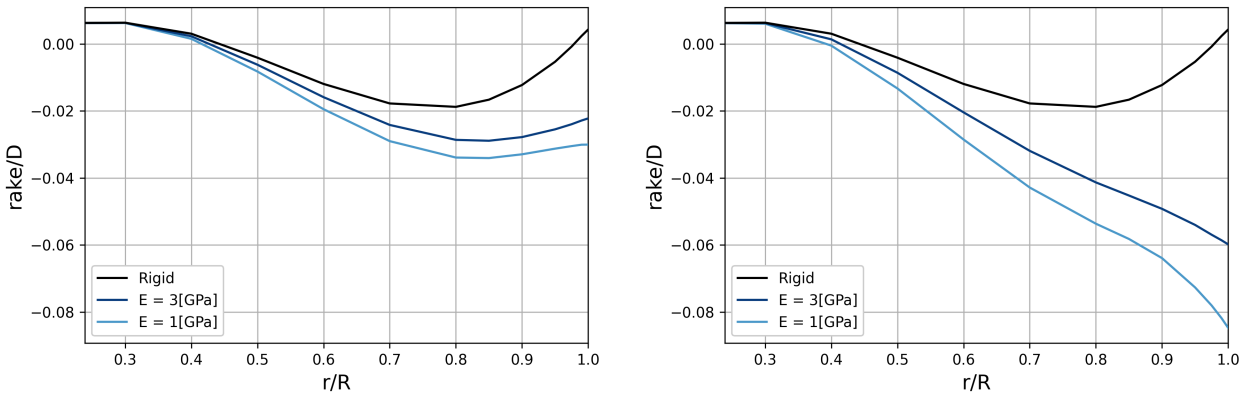

(a) $J = 0.6$ (b) $J = 0.3$

Figure 9: Propeller rake deformation

Changes in pitch and camber have a major effect on thrust, therefore the changes in these parameters are investigated. The pitch at the hub is fixed by the boundary condition at the hub. There is also no large twist near the root of the blade because the sections in this region are thicker and more resistant to twisting. The skewed blade shape enables twisting near the tip, which affects the pitch. The simulation results for both advance ratios show a reduction in pitch, mainly near the tip region. This would contribute to a reduction in thrust and is, therefore, no explanation for the increased thrust.

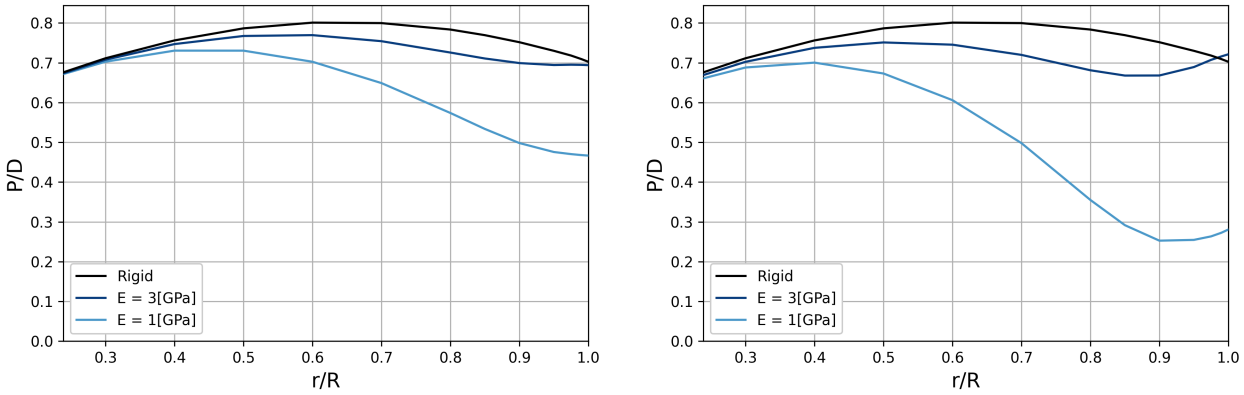

(a) $J = 0.6$ (b) $J = 0.3$

Figure 10: Propeller pitch deformation

The camber of the blades can also influence the thrust. For both conditions, we see an increase in camber over the entire radius, this increased camber is largest near the tip region. This is found in flexible propellers of all stiffness settings. Therefore, the increase in camber explains the increased thrust. This cambering effect is largest for larger stiffness in heavily loaded conditions $J < 0.6$. Here, the increased camber is sufficiently large to increase the thrust even though the pitch is reduced.
This increased cambering effect is also present in the more flexible case where $E = 1[GPa]$, but here, the reduction in pitch outweighs the increased camber, resulting in reduced thrust for the more flexible cases.
The increased camber also explains the small reduction in chord length for the case of $E = 1[GPa]$.

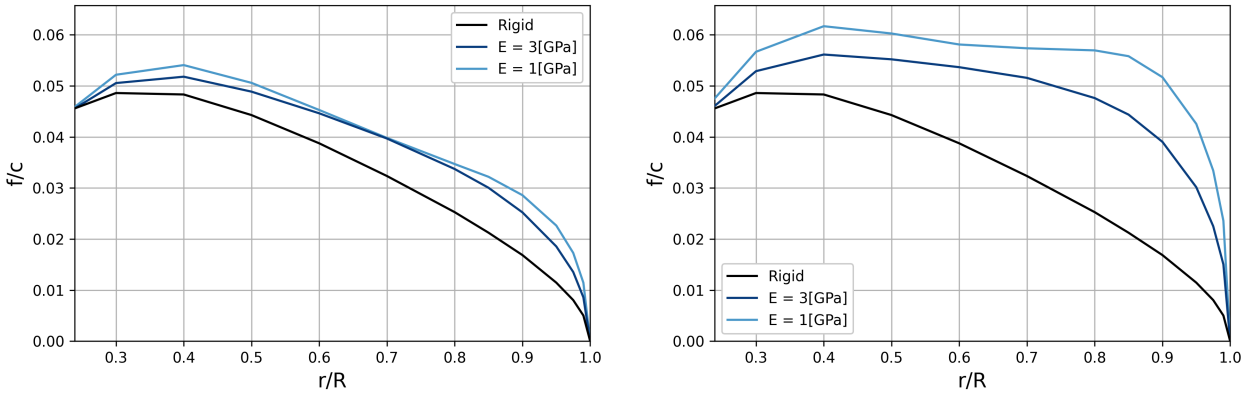

(a) $J = 0.6$ (b) $J = 0.3$

Figure 11: Propeller camber deformation

The camber (f) is expressed as the maximum amplitude of the camber line to the chord line. This is an indicative parameter, but the section profiles at $r/R = 0.7$ are plotted to visualize the change in camber. This radial location is selected to be a representative section for propeller performance, as explained by Carlton [3] based on Lerbs' equivalent profile procedure. The camber change is substantial, especially for the case of $E = 1[GPa]$ where the maximum camber location shifts towards the trailing edge. This makes the deformed section profile look similar to a morphing flap.

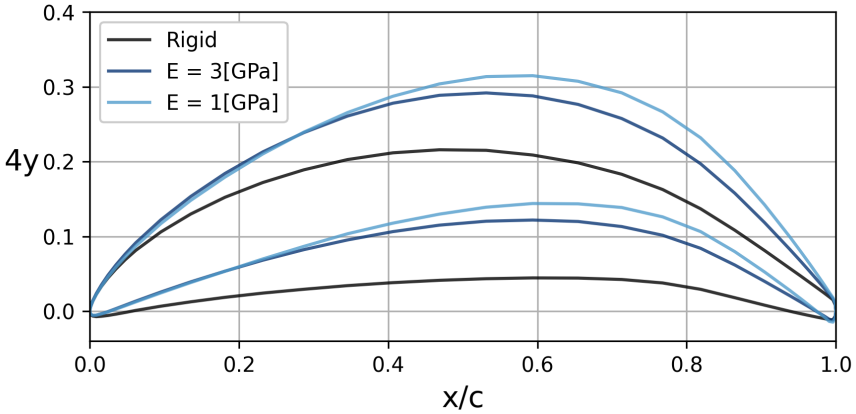

Figure 12: Propeller section profiles at $r/R = 0.7$, $J = 0.3$, thickness increased by a factor 4

4 Discussion

The developed workflow can simulate isotropic flexible propellers of stiffness as low as $E = 1/16[GPa]$. This stiffness is 48 times lower than the reference POM-C material. The selected grid and timestep settings used in this study work well for a modern propeller such as the Wageningen C4-40 but might not hold for different geometries.

The simulations in this study are performed in open water conditions. To investigate the in-behind performance a wake should be included.

Isotropic materials can be used to twist the blades. It should be noted that this is accompanied by raking deformations.

It has been found that flexible propellers can increase efficiency by shifting the working point to a higher efficiency regime. For this case, increased efficiency is only seen for low advance ratios where the propeller material is not too flexible.

The flexibility of the Wageningen C4-40 propeller has been found to reduce pitch and increase the camber.

The amplitude of these effects depends on the material stiffness and the operating conditions. The camber increase is found to be less prevalent at lighter loading conditions. In some conditions, the thrust can be increased due to increased camber provided that the pitch deformation is sufficiently small. The increase in thrust is largest for stiffer materials and lower advance ratios. The increase in camber was found to be key for improved efficiency, this should be further investigated by showing deformations at multiple radial locations and blade loading.
To show the change in performance solely due to camber deformation, the performance of the rigid and deformed geometry should be compared to the rigid geometry, where the camber distribution is adjusted to the camber of the deformed geometry and the deformed geometry with the original camber distribution. The cause of the cambering effect should be further investigated.
It is hypothesized that deformation effects on camber and pitch can be decoupled by increasing the aspect ratio of the blades whilst retaining the blade area ratio. This could increase the twist deformation and reduce the twist deformation. This can possibly also be achieved by design with anisotropic materials.
Further research will look into the sensitivities of different design parameters and how the efficiency can be improved for a range of operating conditions.

5 Conclusion

This study presents a workflow that combines multiple software packages to reduce the setup time to simulate flexible marine propellers of various material properties and operating conditions. Simulations on a flexible Wageningen C4-40 propeller design have been performed to demonstrate the workflow and indicate changes in performance and deformations of the blades.
The propeller thrust and efficiency have been found to depend on the material stiffness and operating conditions. A non-monotonic relationship has been found between thrust and material stiffness. This is attributed to two opposing effects on thrust: a reduction of pitch and an increase in camber. The material stiffness and operating condition determine if the combination of deformations results in increased or decreased thrust. Therefore, the change of camber should be considered when designing flexible marine propellers.
This study found that the propulsive efficiency could potentially be increased by using a flexible propeller where the efficiency is increased for increased propeller loading by shifting the propeller working point into the higher efficiency regime. The maximum attainable efficiency of the propeller is not increased.

References

[1] Joris Brouwer, Jan Tukker, and Martijn van Rijsbergen. Uncertainty analysis of finite length measurement signals. In *The 3rd International Conference on Advanced Model Measurement Technology for the EU Maritime Industry*, 09 2013.

[2] Cadence. Fidelity, version 2024. `http://www.cadence.com`, 2024.

[3] J.S. Carlton. Chapter 6 - propeller performance characteristics. In J.S. Carlton, editor, *Marine Propellers and Propulsion (Third Edition)*, pages 79–136. Butterworth-Heinemann, Oxford, third edition edition, 2012.

[4] Jean-Francois Remacle Christophe Geuzaine. 3d finite element mesh generator with a built-in cad engine and post-processor. Open source on gmsh.info, 2024.

[5] Marin: Jie Dang. Wageningen cd-propeller series (original), October 2024.

[6] Electricité de France. Finite element *code_aster*, analysis of structures and thermomechanics for studies and research. Open source on www.code-aster.org, 1989–2017.

[7] Marin et al. Refresco, version 2024.1. `https://www.marin.nl/en/about/facilities-and-tools/software/refresco`, 2024.

[8] L. Eça and M. Hoekstra. A procedure for the estimation of the numerical uncertainty of cfd calculations based on grid refinement studies. *Journal of Computational Physics*, 262:104–130, 2014.

[9] Sébastien Lemaire and Maarten Klapwijk. pytst, January 2021.

[10] Maximilien Siavelis. Salome-meca 2021 for windows. Open source on https://code-aster-windows.com/2022/04/22/salome-meca-2021-for-windows, 2021.

[11] O.C. Zienkiewicz, R.L. Taylor, and J.Z. Zhu. *The Finite Element Method: Its Basis and Fundamentals*. Butterworth-Heinemann, 2005.

Nomenclature

Symbol	Description	Unit
D_{hub}	Hub diameter	m
D	Propeller diameter	m
E	Young's modulus	GPa
$F_{x,total}$	Total thrust force	N
J	Advance ratio	–
M_i	Mode number with integer index	–
N_c	Blade surface refinement in chord wise direction	–
$N_{face,setting}$	Blade surface refinement setting	–
N_{face}	Blade surface refinement	–
N_r	Blade surface refinement in radial direction	–
N_t	Blade thickness refinement	–
P	Pitch	m
R	Propeller radius	m
Z	Number of blades	–
η_0	Open water efficiency	–
$\nu_{structure}$	Poisson's ratio	–
$\rho_{structure}$	Structure density	kg/m^3
ρ_{water}	Water density	kg/m^3
c	Chord length	m
f_M	Modal frequency	Hz
f	Camber	m
r	Propeller radial location	m
y^+	Dimensionless wall distance	–

Acronyms

CAD	Computer Aided Design
FSI	Fluid Structure Interaction
ppg	Procal Propeller Geometry
RPM	Rounds Per Minute
URANS	Unsteady Reynolds Averaged Navier Stokes

Appendices

A Signal convergence

This appendix shows an example of the signal convergence procedure used to determine the effective force or moment of an oscillating signal, using the procedure of Lemaire and Klapwijk [9].

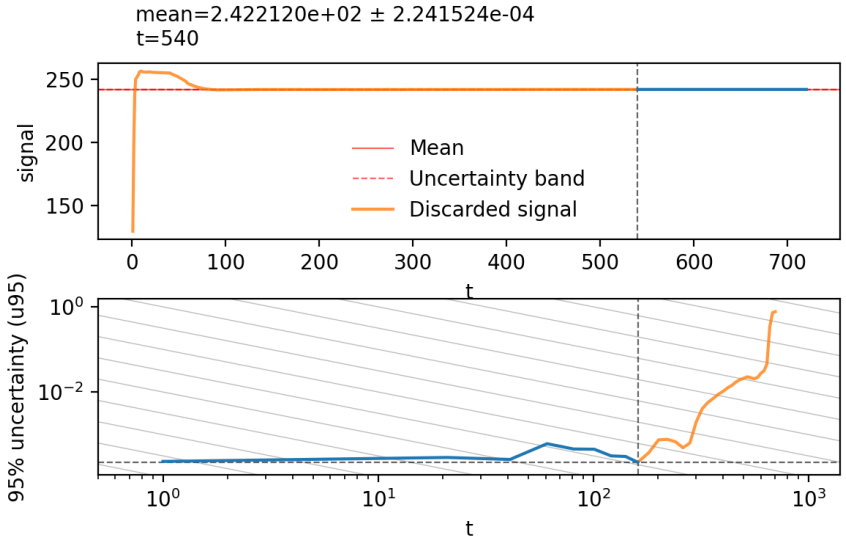

Figure 13: Thrust force convergence of a flexible simulation with $E = 3[GPa]$ and $J = 3$

B Refinement study

This appendix shows the refinement studies for different discretization settings. The method of Eça and Hoekstra [8] is used where larger relative step sizes represent coarser grids or larger time steps.

B.1 Fluid mesh refinement

This appendix shows the fluid mesh refinements from 2.2, 3.2, 5.3, 9.6, 19 to 31 million cells. The number of cells in the 3D grid is used to determine the relative step size. A grid with 5.1 million cells is selected.

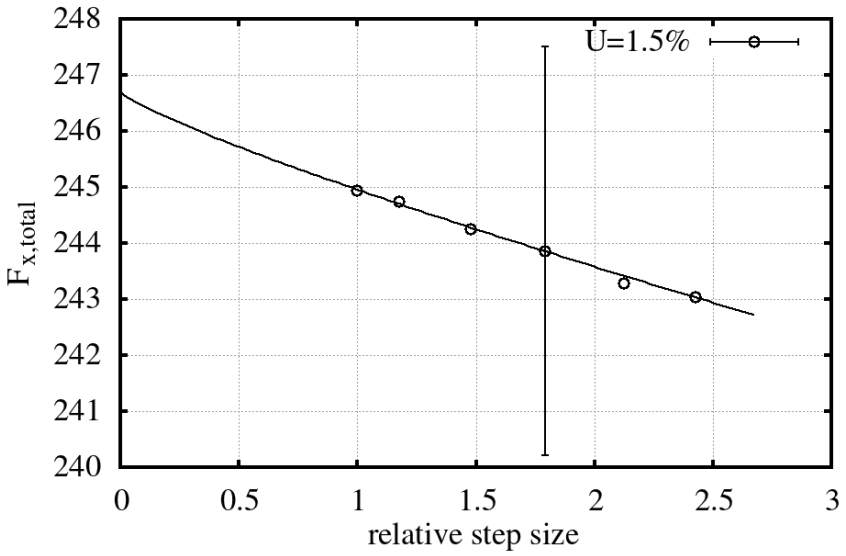

Figure 14: Fluid mesh refinement with the method of Eça and Hoekstra [8]

B.2 Structure surface mesh refinement

This appendix shows the surface mesh refinement of the structure grid. Refinement settings are increased by a factor of $sqrt(2)$. The setting number of cells in the 2D grid is used to determine the relative step size. The settings and resulting refinements are shown in Table 2. The refinement setting of $N_{face,setting} = 91$ is selected.

Table 2: Surface refinement settings

$N_{face,setting}$	N_c	N_r	N_{face}
32	5	14	70
45	5	17	85
64	6	20	120
91	8	24	192
128	9	28	252
181	10	33	330
256	12	40	480

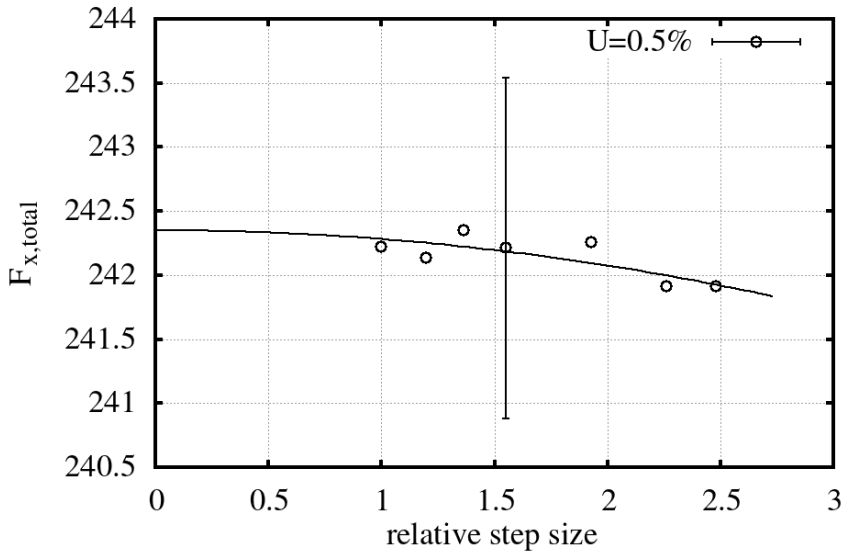

Figure 15: Structure surface mesh refinement with the method of Eça and Hoekstra [8]

B.3 Structure thickness mesh refinement

This appendix shows the thickness refinement of the structure grid. The number of cells along one direction is used to determine the relative step size. The thickness refinement is evaluated at 2, 3, 4, 5, 6 and 8 cells in thickness direction. The refinement setting of $N_t = 2$ is selected.

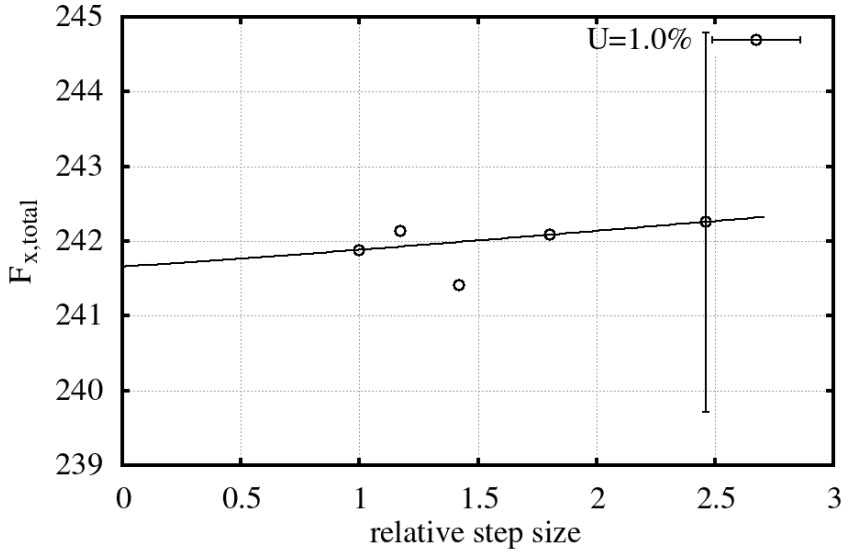

Figure 16: Structure thickness mesh refinement with the method of Eça and Hoekstra [8]

B.4 Timestep refinement

The time step size is evaluated for 180, 60, 30, 10, 5 and 2 degrees of rotation per time step. This time step in degrees is used to determine the relative step size. A time step size of 10 degrees is selected.

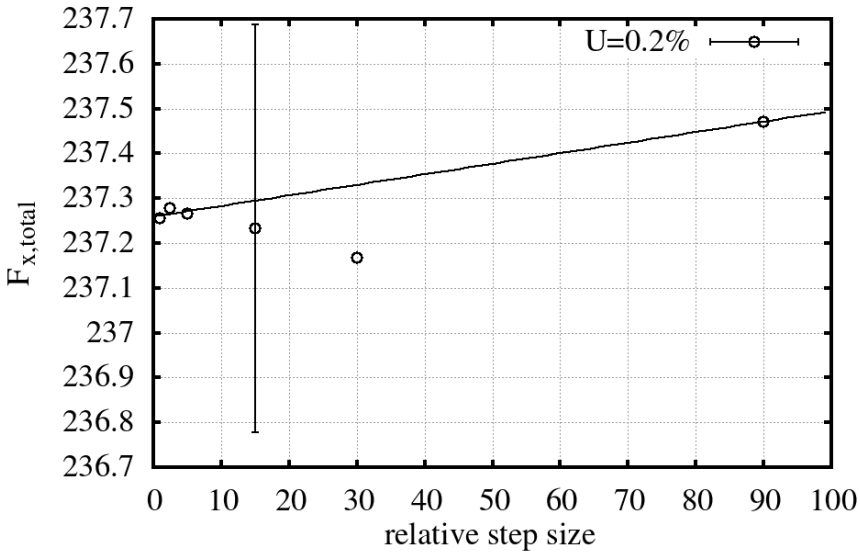

Figure 17: Timestep refinement with the method of Eça and Hoekstra [8]

C Modal frequency convergence

This appendix shows the non-normalized modal frequency convergence for the first 5 dry modal frequencies of a C4-40 propeller blade with a stiffness of $E = 3[GPa]$. As stated in Appendix B, a refinement of 91 cells at the surface and 2 cells in the thickness direction is selected.

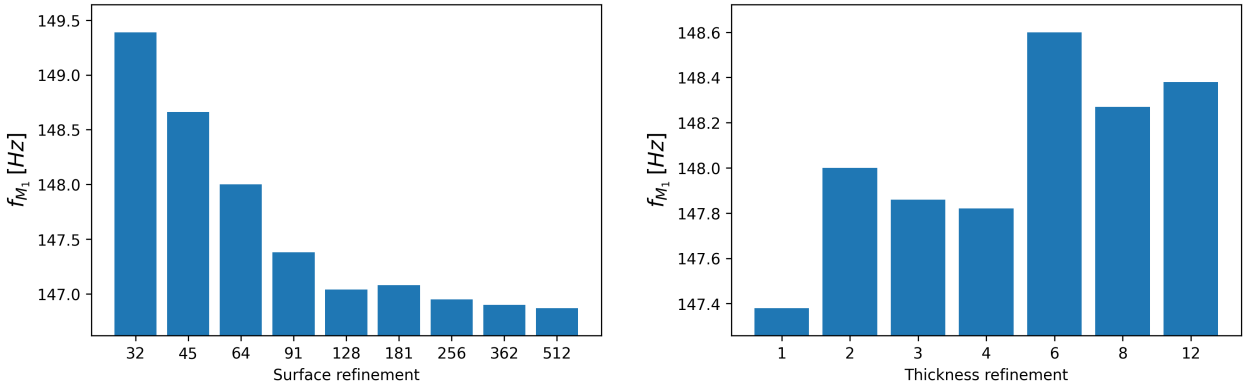

Figure 18: Mode 1 frequency convergence for different levels of structural grid refinement

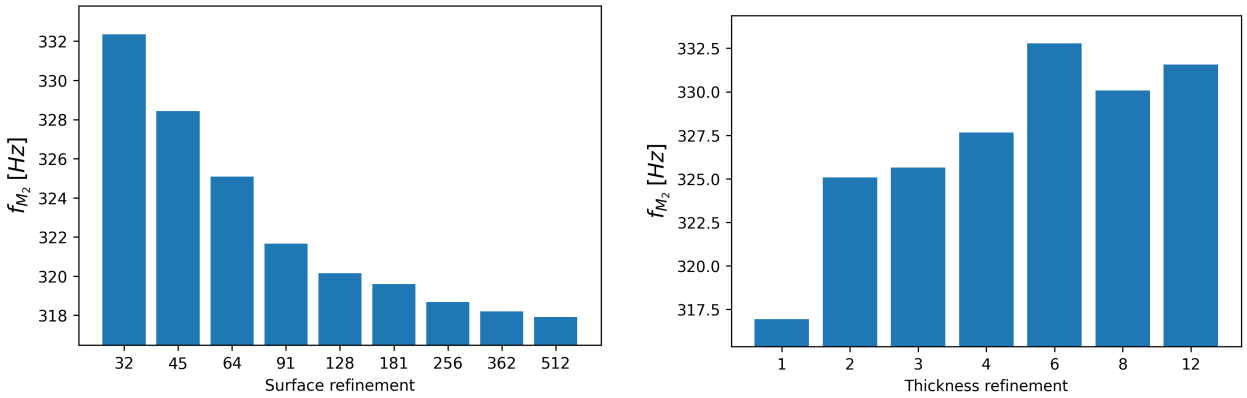

Figure 19: Mode 2 frequency convergence for different levels of structural grid refinement

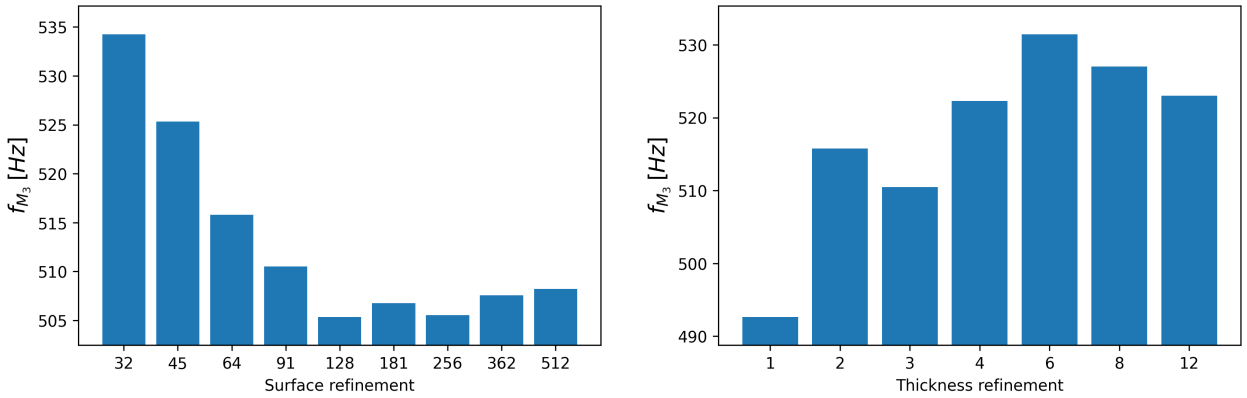

Figure 20: Mode 3 frequency convergence for different levels of structural grid refinement

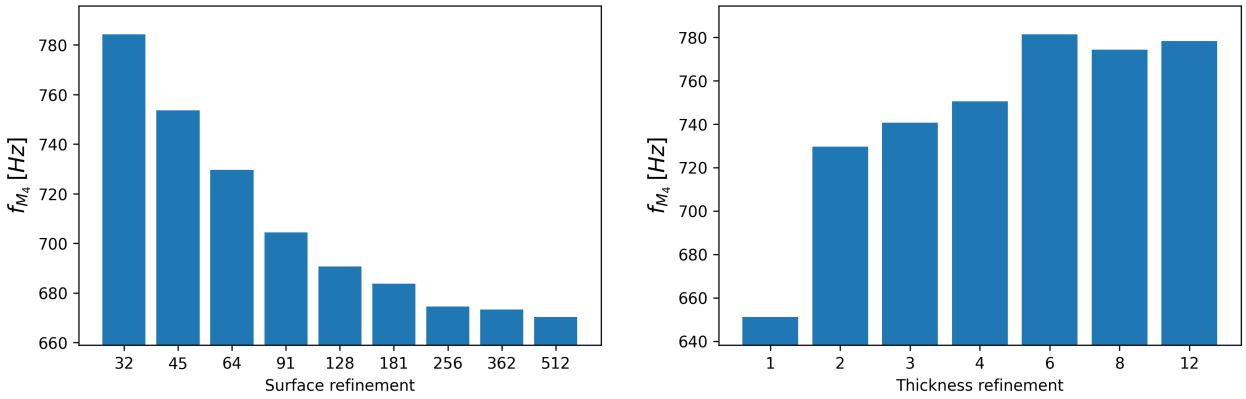

Figure 21: Mode 4 frequency convergence for different levels of structural grid refinement

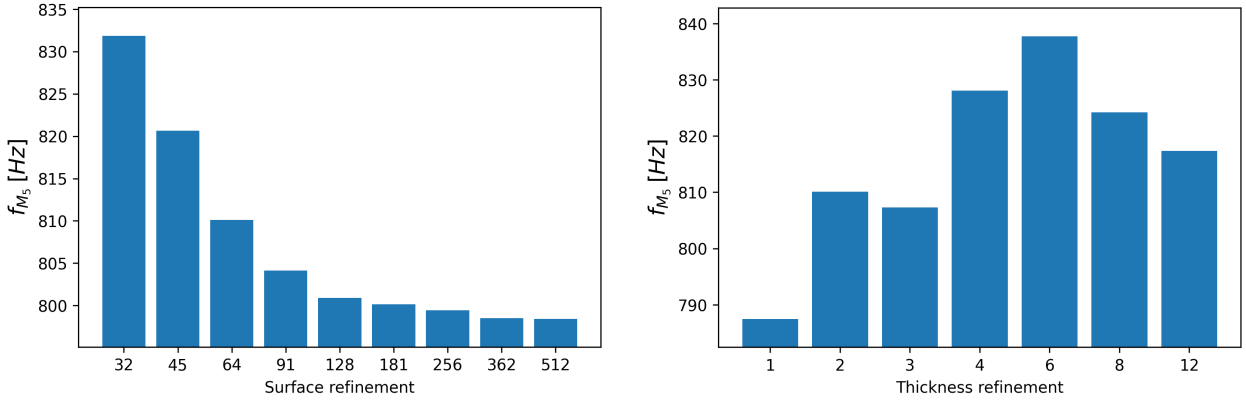

Figure 22: Mode 5 frequency convergence for different levels of structural grid refinement

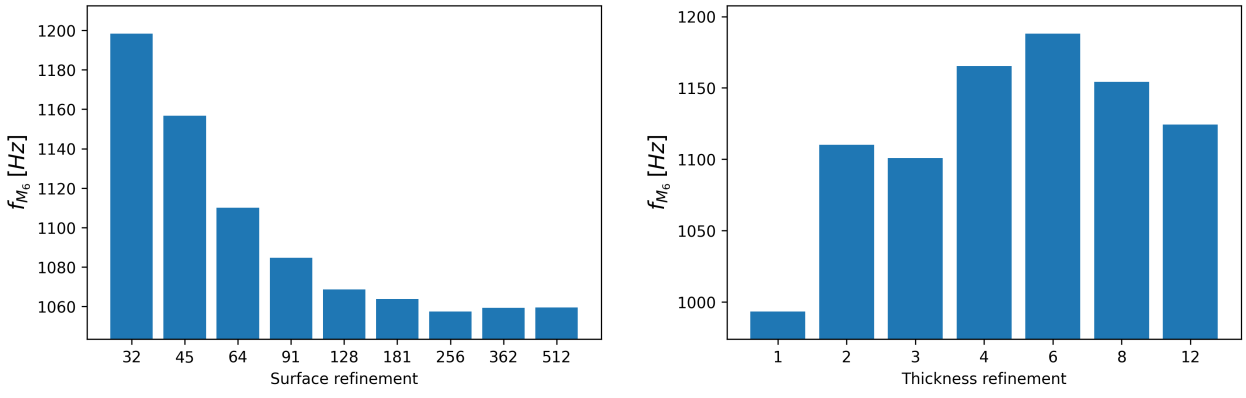

Figure 23: Mode 6 frequency convergence for different levels of structural grid refinement

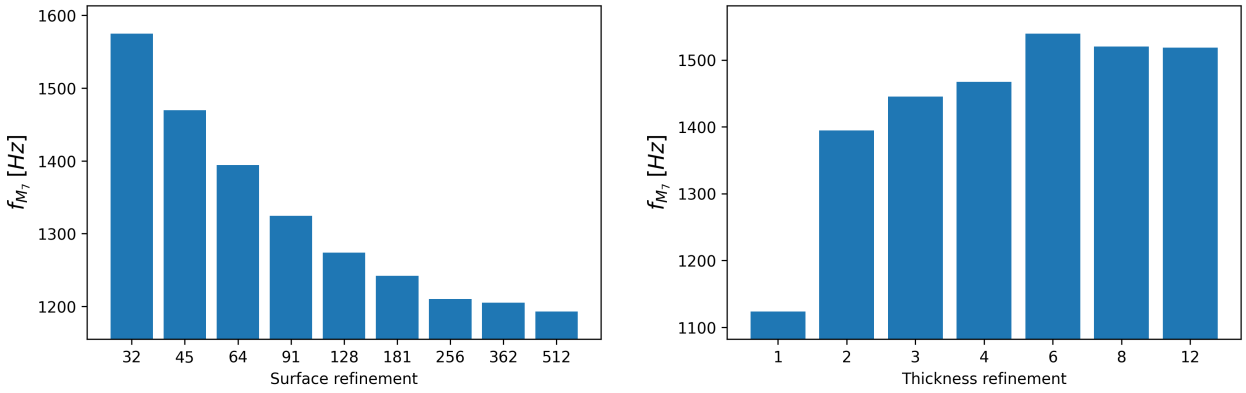

Figure 24: Mode 7 frequency convergence for different levels of structural grid refinement

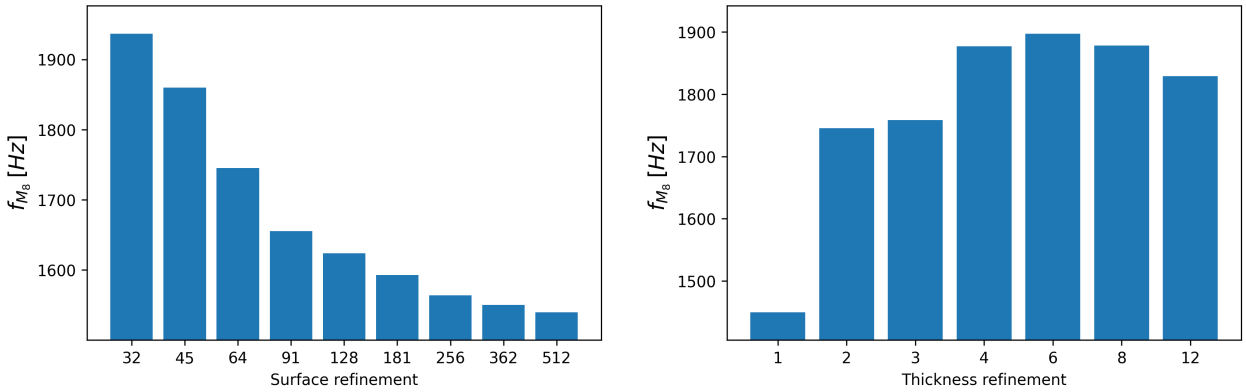

Figure 25: Mode 8 frequency convergence for different levels of structural grid refinement

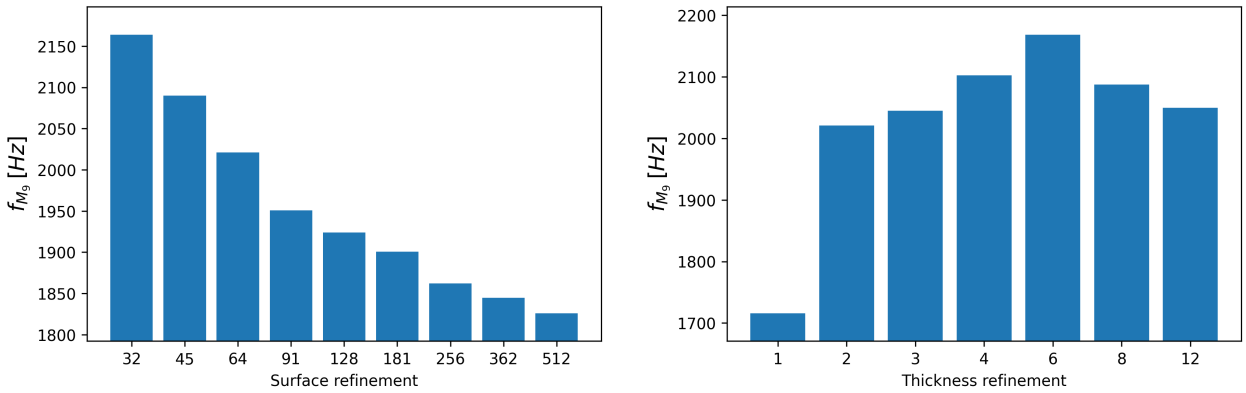

Figure 26: Mode 9 frequency convergence for different levels of structural grid refinement

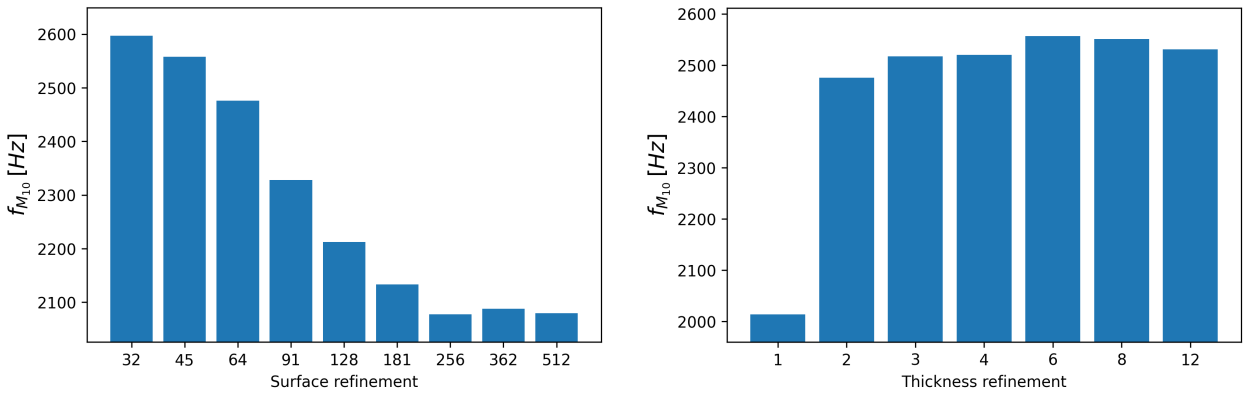

Figure 27: Mode 10 frequency convergence for different levels of structural grid refinement

D Geometric changes

This appendix shows the propeller deformation for two operational conditions and various material stiffness.

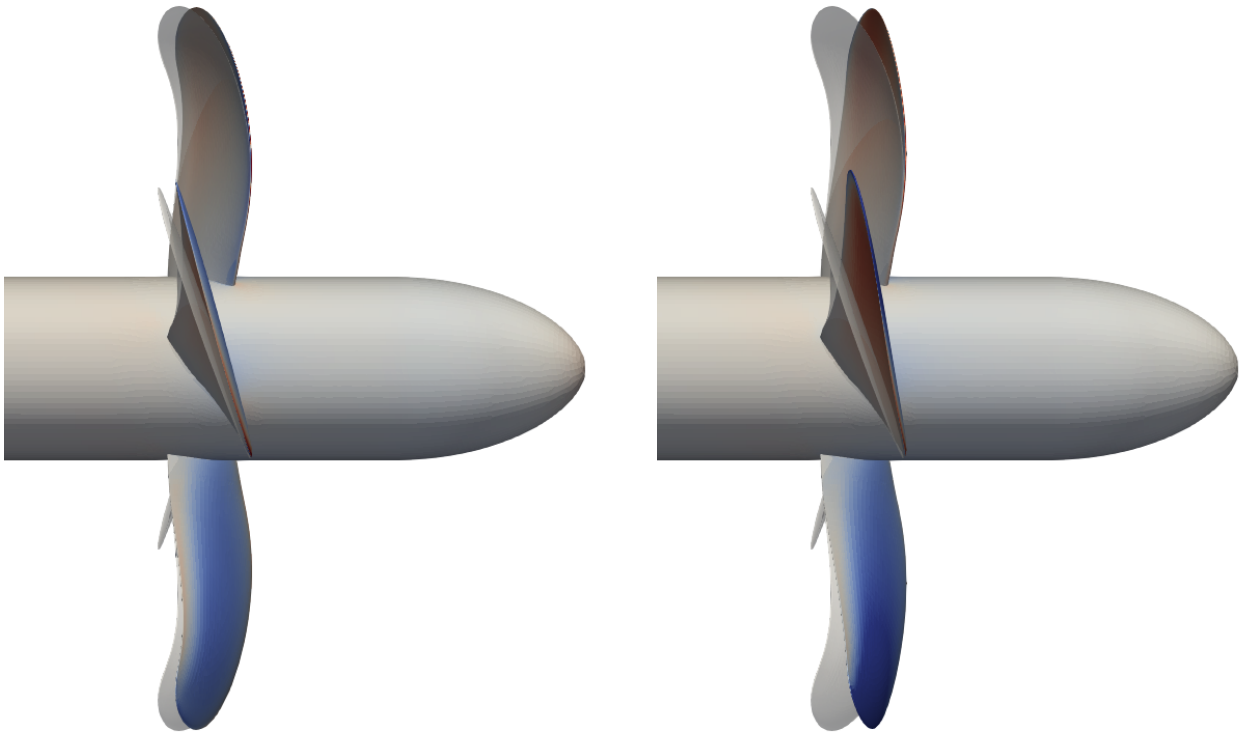

(a) $J = 0.6$ (b) $J = 0.3$

Figure 28: Propeller deformation, transparent rigid geometry and pressure distribution on the deformed blades, $E = 3[GPa]$

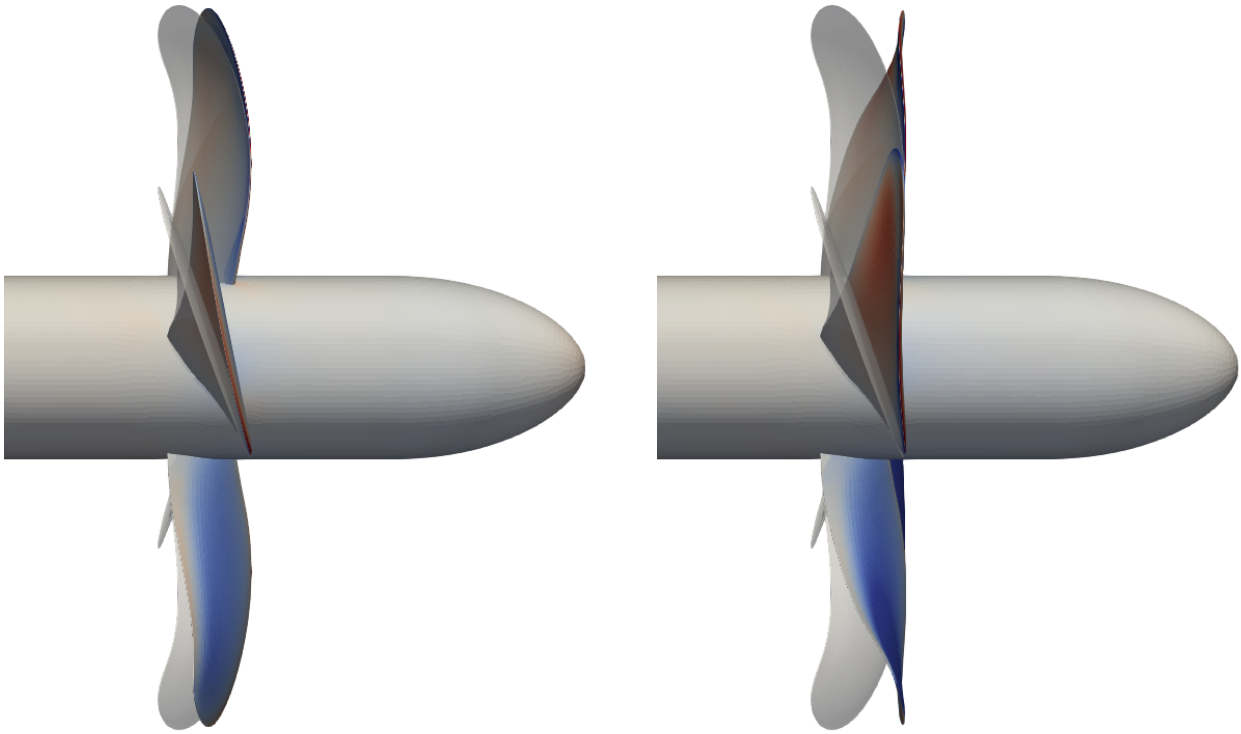

(a) $J = 0.6$ (b) $J = 0.3$

Figure 29: Propeller deformation, transparent rigid geometry and pressure distribution on the deformed blades, $E = 1[GPa]$

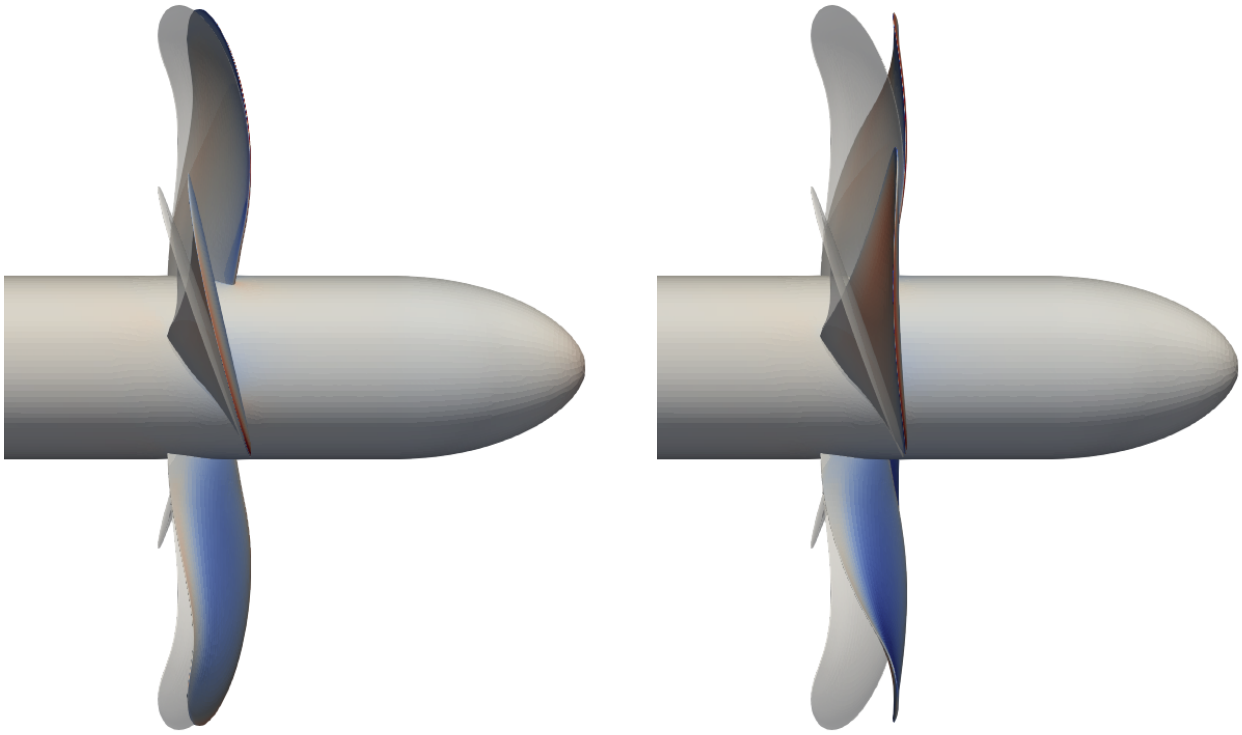

(a) $J = 0.6$ (b) $J = 0.3$

Figure 30: Propeller deformation, transparent rigid geometry and pressure distribution on the deformed blades, $E = 0.5[GPa]$

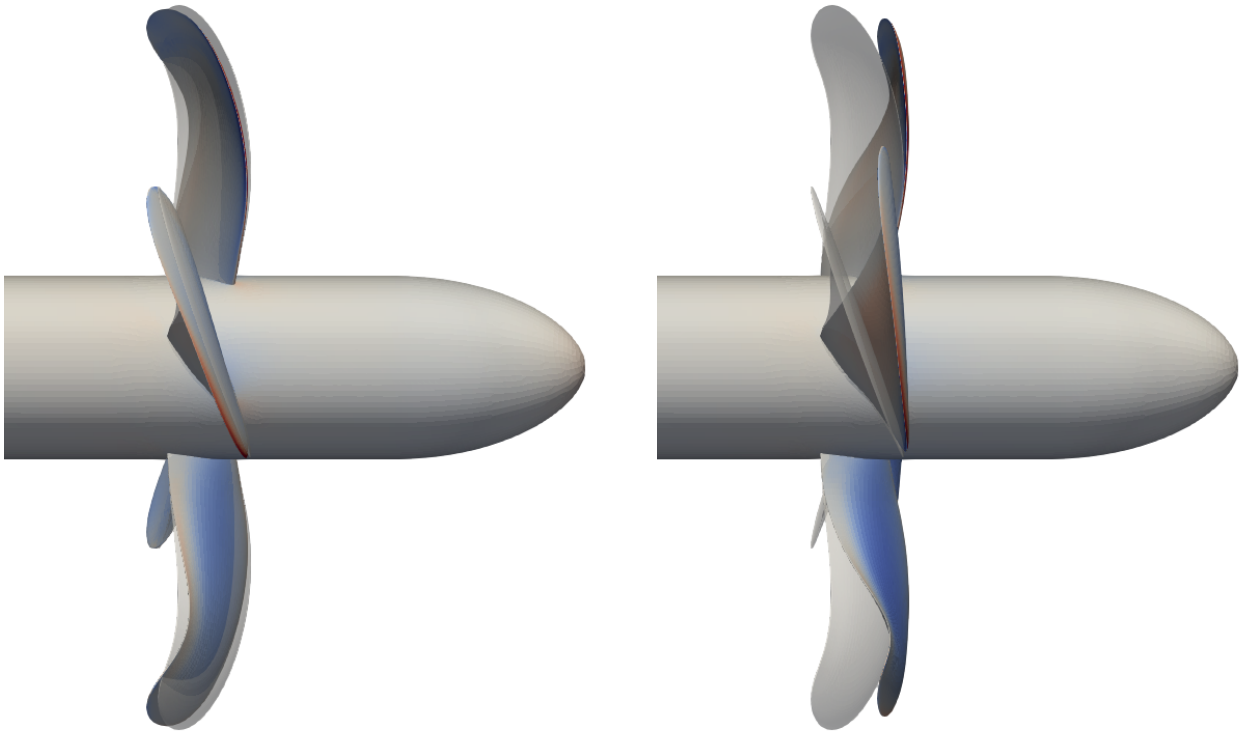

(a) $J = 0.6$ (b) $J = 0.3$

Figure 31: Propeller deformation, transparent rigid geometry and pressure distribution on the deformed blades, $E = 0.125[GPa]$

E Parametric geometry changes

This appendix shows the radial changes in propeller design parameters for flexible propellers of various stiffness and for two different operating conditions.

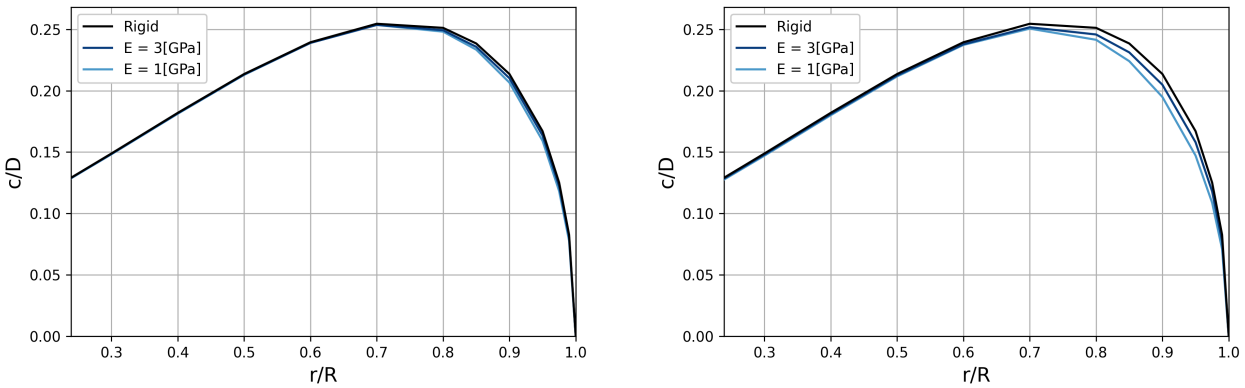

(a) $J = 0.6$ (b) $J = 0.3$

Figure 32: Propeller chord distribution for various material stiffnesses

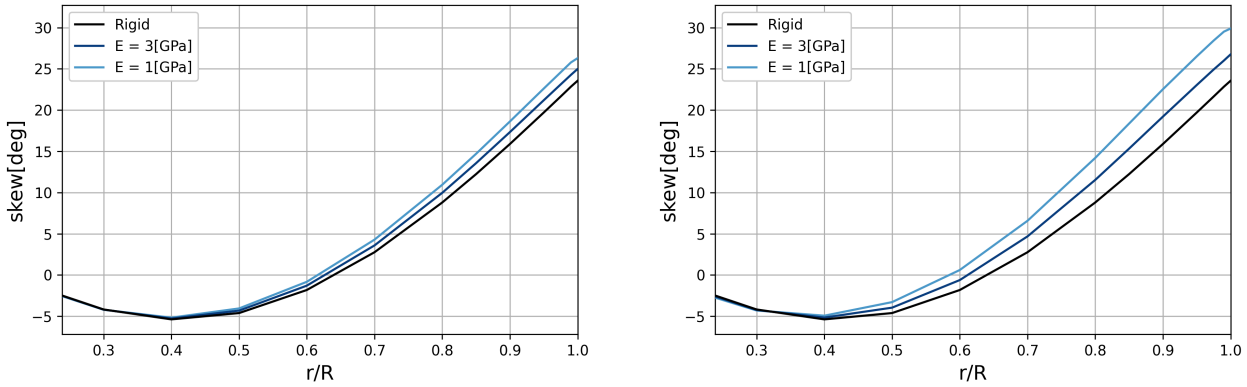

(a) $J = 0.6$ (b) $J = 0.3$

Figure 33: Propeller skew distribution for various material stiffnesses

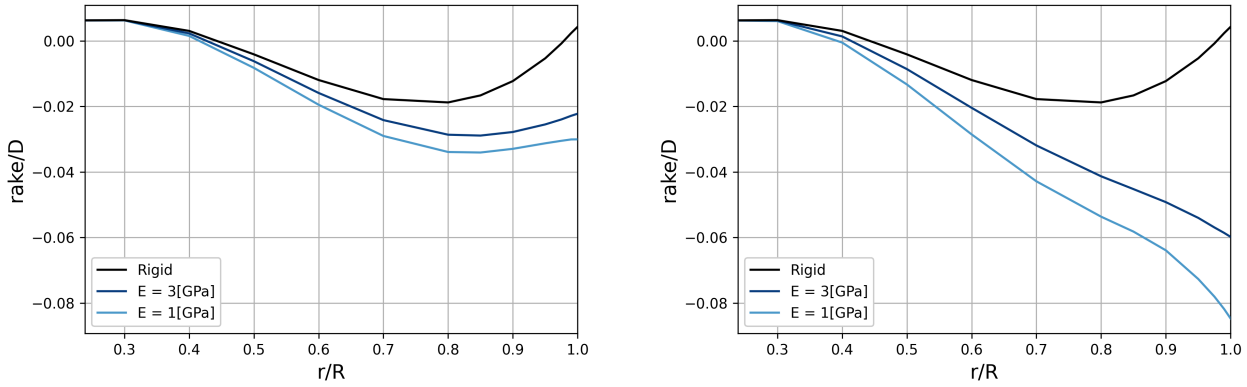

(a) $J = 0.6$ (b) $J = 0.3$

Figure 34: Propeller rake distribution for various material stiffnesses

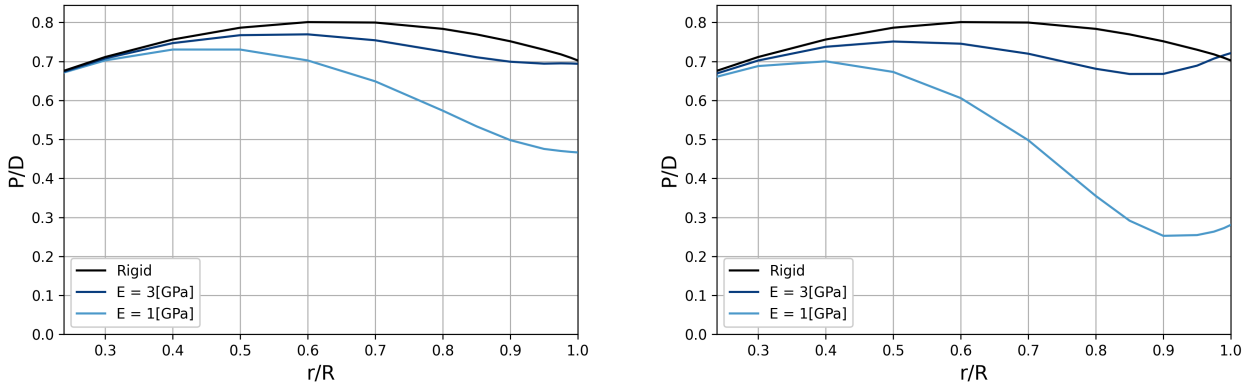

(a) $J = 0.6$ (b) $J = 0.3$

Figure 35: Propeller pitch distribution for various material stiffnesses

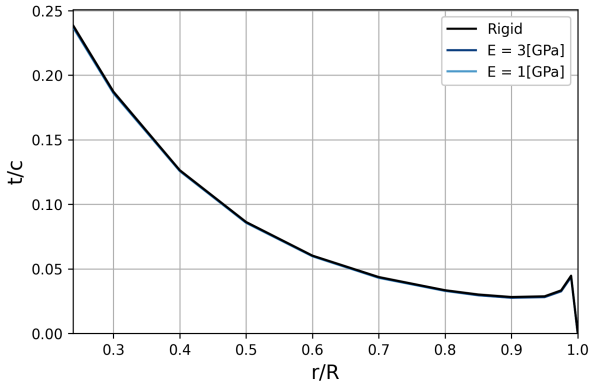

(a) $J = 0.6$

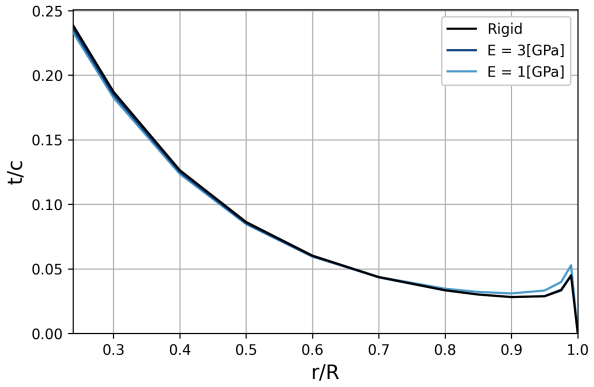

(b) $J = 0.3$

Figure 36: Propeller thickness distribution for various material stiffnesses

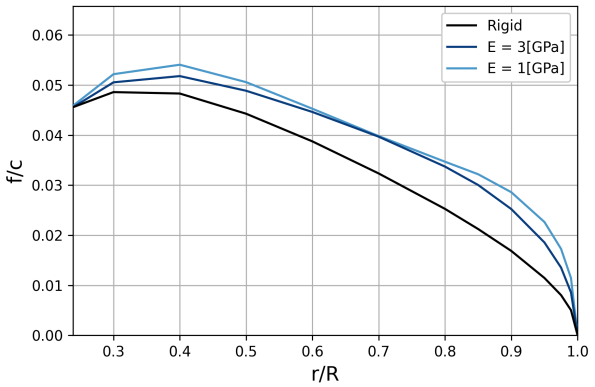

(a) $J = 0.6$

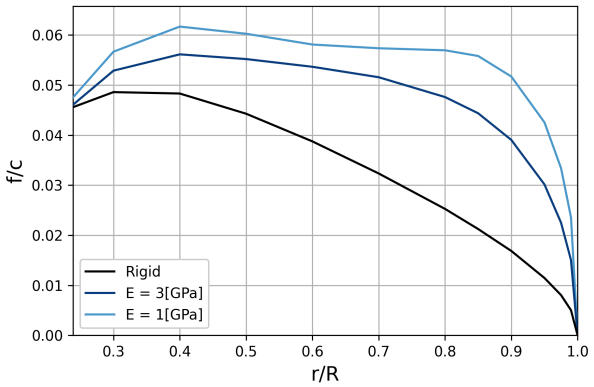

(b) $J = 0.3$

Figure 37: Propeller camber distribution for various material stiffnesses

26th Numerical Towing Tank Symposium (NuTTS)
23-25 October 2024- Duisburg, Germany

Optimization of the Open Water Performance of a Ducted Propeller

Negin Donyavizadeh[1], Arash Eslamdoost[1], Rickard Bensow[1]
[1]Department of Mechanics and Maritime Sciences, Chalmers University of Technology, Sweden

1 Introduction

Ducted propellers are crucial in enhancing the efficiency of marine propulsion systems, especially for vessels requiring high thrust at low speeds, such as tugboats and ships in harsh conditions. Ducts like 19A and 37A have gained attention due to their ability to improve thrust by effectively directing water flow, but their performance is highly dependent on key geometrical factors, such as chord length and angle of attack. Optimizing these parameters is essential, as poor design can lead to inefficiencies like flow separation and increased drag, reducing overall propulsion effectiveness. The integration of tools like CAESES for parametric modeling, STARCCM+ for simulation, and HEEDS Multidisciplinary Design Optimization that enables the exploration of how these factors influence the hydrodynamic performance of ducted propeller systems.

This study focuses on determining the optimal duct geometry, specifically examining the chord length and angle of attack, to maximize thrust and minimize torque for greater propulsion efficiency. An optimal design is crucial to avoid problems like cavitation, vibration, and increased wear, which can significantly impact vessel performance. Using STARCCM+ to solve RANS equations with the SST k-omega turbulence model, the numerical simulations are validated against experimental data. The research explores the influence of geometric parameters on thrust, torque, and efficiency, offering valuable insights into the development of more efficient and sustainable marine propulsion systems.

2 Numerical Approach

2.1 Computational Fluid Dynamics (CFD) phase

This research investigates the impact of duct geometry on marine ducted propulsion performance. To optimize the design and reduce computational cost, the study validates a CFD solution using the Moving Reference Frame (MRF) method alongside the steady-state RANS equation. The MRF technique simplifies the problem by treating rotating parts, such as propellers, as moving reference frames, assuming steady rotation. This approach eliminates the need for high-cost transient calculations, making it a more efficient solution for studying ducted propulsion. Therefore, the propeller's rotational speed, n, was kept constant at 15 revolutions per second (rps), while the advance velocity, U, was systematically varied to examine its effect on the prediction of open-water curve characteristics for a range of advance ratios, $J = U/(n\,D)$. The propeller Reynolds number is based on the chord length at $0.7R$ defined as $Re = C_{0.7R}\sqrt{U^2 + (0.7\pi Dn)^2}/\nu$, was estimated to be approximately 5.6×10^5.

The simulations maintain a Y^+ below 3, with a low wall Y^+ treatment that relies on the assumption that the boundary layer near the propeller is adequately resolved by the near-wall mesh.

A representative ducted propeller system, consisting of a KA4-55 propeller within a Wageningen 19A accelerating duct, is identified for a validation study. Numerical results are compared with experimental data reported by Stark and Shi (2021). Figure 1 shows the 3D geometry, and Table 1 provides the system specifications. The computational domain is modeled as a cylinder, following the approach reported by Donyavizadeh et al. (2024). The computational domains are shown in Figure 2. The grid for the RANS simulation consists of 12 million individual cells, divided into two regions: a rotating cylindrical region around the propeller and the inner surface of the duct, comprising 7 million cells, and a fixed region encompassing the outer surface of the duct and the rest of the domain, consisting of 5 million cells.

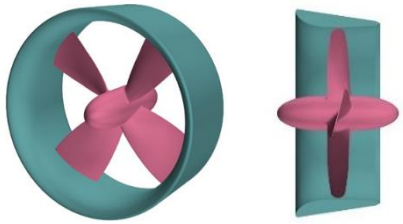

Figure 1: Geometry of propeller KA4-55 and duct of 19A (Carlton 2018).

Table 1: Geometric Specifications for propeller KA4-55 with duct 19A.

Propeller KA4-55			
Type of Section	Kaplan	Expanded Area (EAR)	0.55
Blade Number (N)	4	Pitch Ratio (P/D)	1
Diameter (D)	0.25 m	Tip Clearance (t)	2 mm
Duct 19A			
Type of Duct	19A	Duct Chord (L_D)	0.125 m
Outer Diameter (D_O)	0.306 m	Inner Diameter (D_i)	0.254 m

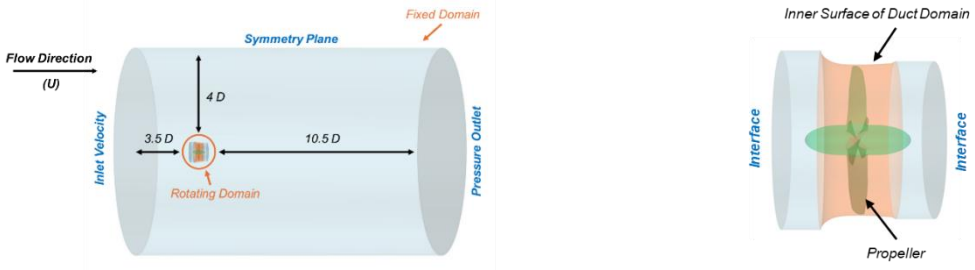

(a) **(b)**

Figure 2: Computational Domain including Fixed Domain (a) and Rotating Domain (b).

An unstructured hexahedral mesh is used for the fixed domain, while a polyhedral mesh is applied to the rotating domain. Prism layers are carefully implemented to capture and resolve the boundary layer effectively. The height of the first boundary layer adjacent to the wall was calculated under the assumption of $Y^+ = 1$, with 24 layers considered within the boundary layer flow. The grid's first layer height is set at 4.5×10^{-6} m near the blade surface and 1.5×10^{-5} m near the duct wall. Figure 3 illustrates the mesh on the blade and duct surfaces. To check the accuracy of the numerical solution, the obtained results are compared with the available experimental results. The results are expressed as hydrodynamic coefficients defined as the propeller's thrust coefficient $K_{T_{Propeller}} = T_{Propeller}/\rho.n^2.D^4$, duct's thrust coefficient $K_{T_{Duct}} = T_{Duct}/\rho.n^2.D^4$, torque coefficient $K_Q = \mathrm{Q}/\rho.n^2.D^5$, total thrust $K_T = K_{T_{Propeller}} + K_{T_{Duct}}$., open-water efficiency $\eta_o = \mathrm{J}.K_T/2\pi\,.K_Q$, where ρ is the fluid density around the propeller, n is the rotational speed of the propeller, and D is the diameter of the propeller. In Figure 4, The acquired numerical data is displayed and compared with experimental data.

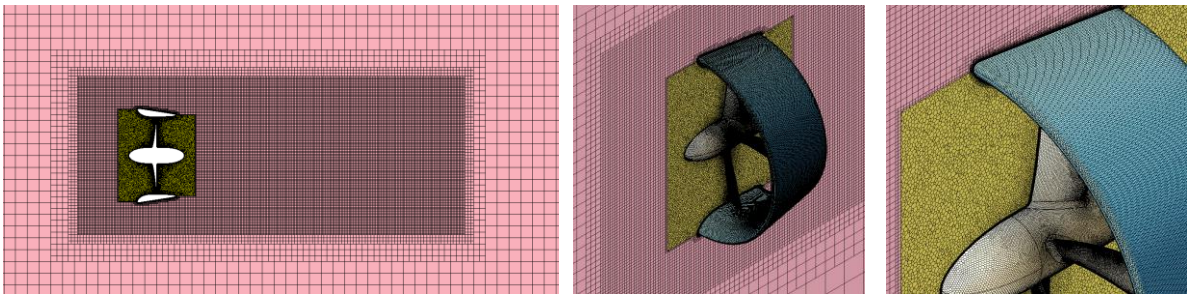

Figure 3: Grid used for the simulation of propeller KA4.5 and duct 19A.

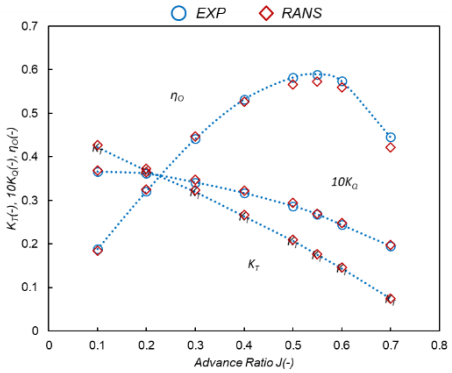

Figure 4: Comparison of the numerical results of K_T, $10K_Q$, and η_o for propeller KA4-55 and 19A duct with experimental results.

2.2 Integration Tools and Optimization Phase

One of the key goals of this study is to optimize the design of the ducted propeller. To achieve this, HEEDS MDO 2310 is employed to link the CAD generation process with CFD simulations, allowing to identification of the optimal duct geometry based on predefined parameters.

The workflow was structured in three steps:

1. *Geometric Parameter Definition and CAD Generation:* CAESES 5.2.6 is employed to define geometrical parameters. The finalized CAD file is then exported for further analysis.
2. *Mesh Generation and CFD Setup:* The CAD file is imported into STAR-CCM+. The CFD setup has been established. Hydrodynamics characteristics are considered as the output parameters of the simulation.
3. *Optimization Coupling with HEEDS:* HEEDS facilitates the coupling of CAESES and STAR-CCM+. HEEDS is responsible for managing design variables and responses based on the defined CAD and CFD parameters, leading to the identification of the optimal duct geometry.

This integration of tools allows for a streamlined and efficient optimization process of the ducted propeller. Two different duct geometries, Duct 19A, and Duct 37A, are analyzed in conjunction with a Kaplan 4-blade propeller, which is widely utilized in marine propulsion. The geometries of both ducts are illustrated in Figure 5. In this study, the angle of attack of the duct profile and the chord length are treated as key parameters for investigation.

(a) **(b)**

Figure 5: Cross Sections of two types of ducts with defined parameters: a) Duct19A, b) Duct 37A.

Objective: The objective of this study is to optimize the performance of a system by considering two main Objectives:

- Maximizing Thrust T
- Minimizing Torque Q

Design Variables: The optimization process is influenced by varying the following parameters:

- Two different profiles of the duct: *Duct 19A, and Duct 37A.*
- The angle of attack of the duct AOA: $-5° \leq AOA \leq 5°$
- The chord length of the duct C_D: $87.5\ mm \leq C_D \leq 162.5\ mm$

Number of Simulations:

The design space for the problem is extensive and complex, requiring a total of 10,201 simulations based on a resolution of 101 for each variable. This number reflects the diverse combinations of angle

of attack and various duct profiles that must be assessed to find an optimal solution. However, conducting all these simulations is computationally demanding, necessitating significant time and resources, which presents a considerable challenge due to the extensive evaluations or population in design space required.

To mitigate this issue, the Multi-Objective SHERPA (MO-SHERPA) optimization method is utilized. This method is integrated within HEEDS MDO and stands for Simultaneous Hybrid Exploration that is Robust, Progressive, and Adaptive. MO-SHERPA is designed specifically for multi-objective optimization, effectively balancing conflicting objectives such as weight and load-carrying capacity. It employs a Pareto-based search strategy, which allows the exploration of trade-offs among multiple objectives without relying on a simple weighted sum, thus ensuring independent optimization of each objective for a more comprehensive solution. Additionally, MO-SHERPA incorporates SHERPA's hybrid search strategies that adapt dynamically to the problem at hand, eliminating the necessity for user-defined tuning parameters. This results in a highly efficient process, enabling both engineers and non-experts to achieve optimal results with reduced computational time. The method is particularly adept at balancing trade-offs among crucial objectives such as thrust, efficiency, and torque through Pareto-optimal front identification (Chase et al. 2010). In Table 2, the specification of the optimization method is available. The resolution of the Pareto front is determined by the archive size (Population-the number of points on the plot, per cycle).

Table 2: Optimization Setup Specification.

Optimization Study	SHERPA Multiple-objective tradeoff
Number of Evaluations	180
Archive Size	12
Number of Variables	2 for each duct (Duct19A and 37A)

3 Results

The Pareto front trade-off diagram (Figures 6 and 7) illustrates the relationship between T and Q for various ducted propeller designs at $J = 0.55$, where the x-axis represents thrust and the y-axis represents torque. The color gradient corresponds to AOA (a) and C_D (b). The curve formed by the points shows a clear trade-off between thrust and torque: as T increases, Q also increases. In the Right-hand figure, Designs closer to the top-right exhibit higher performance in terms of both thrust and torque but likely at the cost of greater energy consumption, while designs in the lower-left region, associated with larger C_D, represent more energy-efficient configurations with lower thrust and torque.

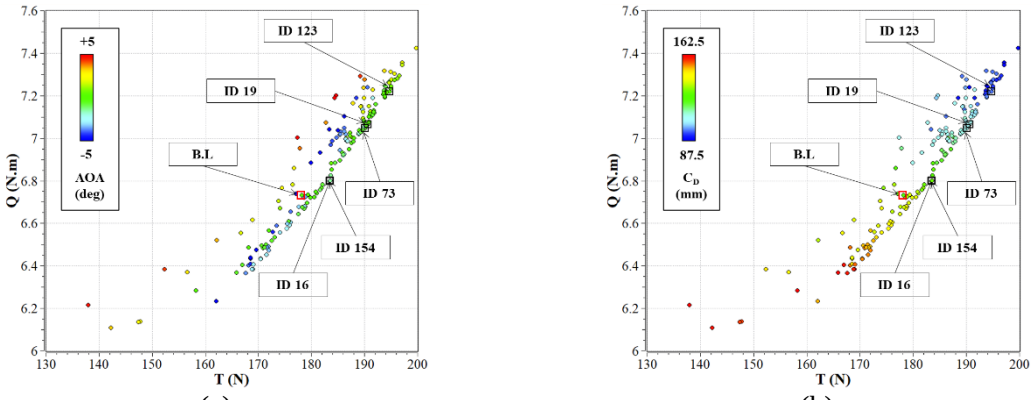

(a) (b)

Figure 6: Pareto diagrams of duct 19A at $J = 0.55$: a) Effect of AOA, b) Effect of C_D on thrust and torque.

In Figure 6, several best designs are labeled, highlighting specific performance characteristics. ID 16 and ID 154 are located near the lower thrust-torque region, indicating designs with smaller ducts and lower thrusts. Conversely, IDs like 123 and 73, positioned in the upper-right portion of the diagram,

represent high-performance propellers with smaller ducts. The B.L. point is the baseline design, as marked in Figure 6-8. This diagram helps to visualize the design space to make well-informed choices about how to balance different design goals, showing that larger ducts yield lower thrust and torque, while smaller ducts offer more efficient design points, to help.

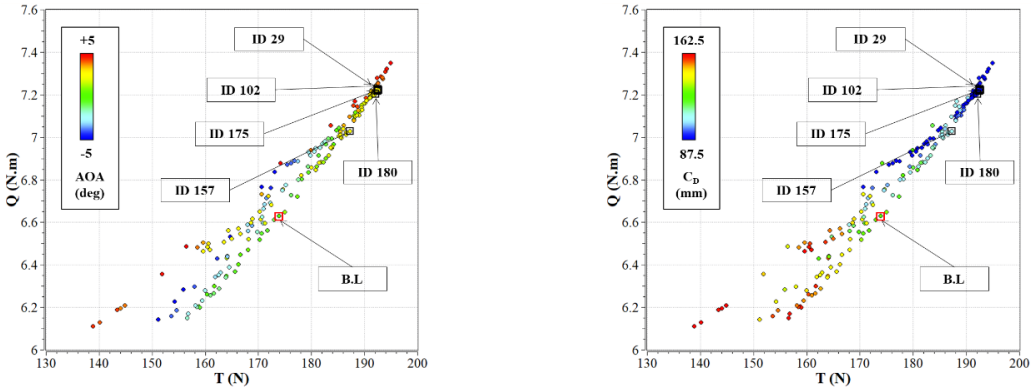

(a) **(b)**

Figure 7: Pareto diagrams of the duct 37A at $J = 0.55$: a) Effect of AOA, b) Effect of C_D on thrust and torque.

A surrogate model is obtained using the Kriging method with a second-order Gaussian function and Gaussian Process Tuning. Table 3 presents the specifications of the surrogate model.

Table 3: Surrogate Study Specification of Efficiency.

Type of Duct	Surrogate Type	Fitting Function	Polynomial Order	R2	RMSE
19A	Kriging	Gaussian	2	0.993	0.0012
37A	Kriging	Gaussian	2	0.994	0.0013

Duct19A and Duct37A, with R^2 values of 0.993 and 0.994, respectively, which are close to 1, and RMSE values of 0.0012 and 0.0013, respectively, which are near zero, demonstrate the surrogate model's high accuracy in capturing the variability in the response. In Figure 8, the surrogate 3D surface diagram for duct 19A and 37A at $J = 0.55$ is presented. The surrogate surface model demonstrates a rather smooth response, indicating a well-behaved relationship between the input parameters and the output response.

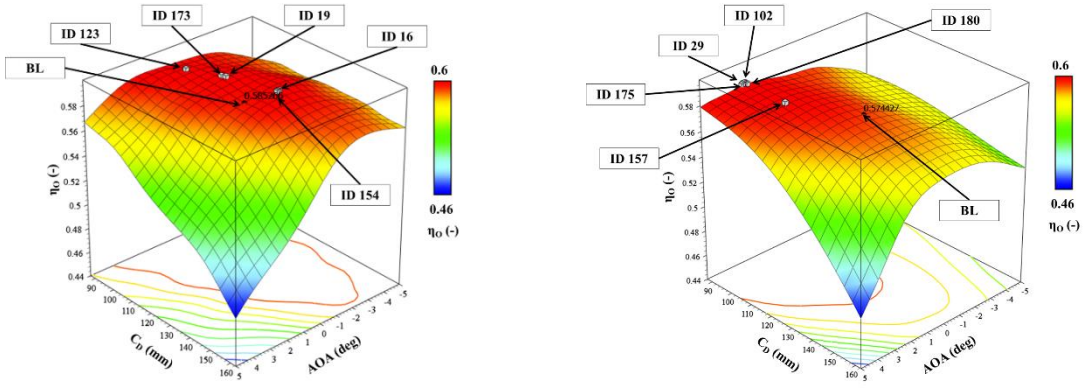

(a) **(b)**

Figure 8: 3D response surface of surrogate study at $J = 0.55$: a) Duct 19A, b) Duct 37A.

In Figure 9, The importance of AOA and C_D on response values of thrust, torque, and open water efficiency is illustrated to identify the most influential variables in a study with a Boruta method. Boruta is a method for determining how much each design variable affects responses, which allows the response influence plot to be available for any study type (Miron 2011). The analysis indicates that variations in the duct AOA significantly enhance efficiency in comparison to C_D. In contrast, changes in chord length predominantly influence torque. Overall, the results emphasize the necessity of a

balanced optimization approach to maximize thrust and minimize torque while improving open-water efficiency.

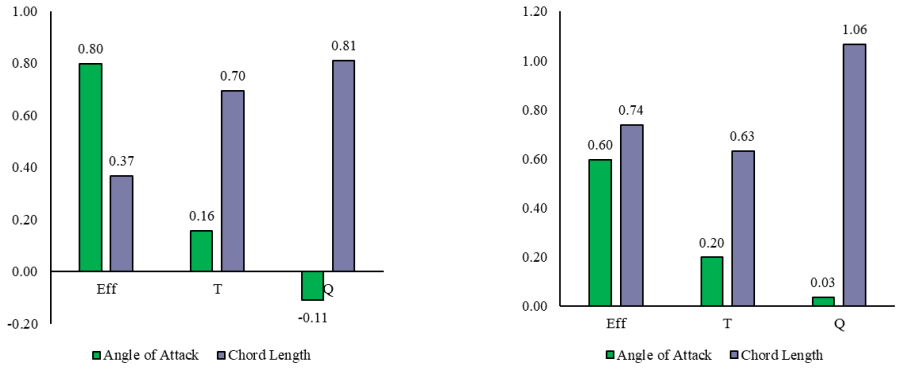

(a) **(b)**

Figure 9: Importance of AOA and C_D on Hydrodynamics characteristics at $J = 0.55$: a) 19A, b) 37A.

In Table 4, the best design points for Duct 19A and Duct 37A have been extracted, and their hydrodynamic performances have been compared.

Table 4: Optimal Design Results for Ducts 19A and 37A.

	Design ID	AOA (deg)	C_D (mm)	T (N)	Q (N.m)	η_O (%)
Duct 19A	BL	0	125	178.17	6.73	57.912
	154	-1.5	129.5	183.54	6.80	59.062
	16	-1.4	129.5	183.42	6.80	59.049
	19	-0.6	108.5	190.60	7.06	59.043
Duct 37A	BL	0	125	173.83	6.63	57.383
	180	2.5	87.5	192.64	7.22	58.374
	102	2.4	87.5	192.44	7.22	58.344
	175	2.4	88.25	192.04	7.20	58.342

4 Conclusions

The conclusion of the study highlights the successful optimization of the open-water performance of ducted propellers, focusing on geometric parameters like the chord length and angle of attack. By employing advanced numerical simulations and optimization tools like HEEDS MDO and STAR-CCM+, the study identified optimal configurations to maximize thrust and minimize torque. Specifically, for Duct 19A, the optimal design achieved an efficiency of 59.02% at an AOA of -1.5 deg and C_D of 129.5 mm. Similarly, for Duct 37A, the optimal design yielded an efficiency of 58.37% at an AOA of 2.5 deg and C_D of 87.5 mm. These findings demonstrate a clear trade-off between thrust and torque, with smaller ducts providing more efficient designs. The study's results, validated against experimental data, offer valuable insights for improving marine propulsion efficiency, laying the groundwork for further advancements in sustainable ducted propeller design.

References

J. Carlton (2018). Marine propellers and propulsion. Butterworth-Heinemann.

N. Chase, M. Rademacher, E. Goodman, R. Averill, and R. Sidhu (2010). A benchmark study of optimization search algorithms. Red Cedar Technology, MI, USA, 1–15.

N. Donyavizadeh, R. E. Bensow, and A. Eslamdoost (2024). Open water performance of two different ducted propellers in oblique flow. In *8th International Symposium on Marine Propulsors*, SMP 2024 (pp. 667–675). Norwegian University of Science and Technology, Department of Marine Technology.

B. Miron Kursa and W. R. Rudnicki (2010). Feature Selection with the Boruta Package. *Journal of Statistical Software*, 36(11).

C. Stark and W. Shi (2021). The influence of leading-edge tubercles on the sheet cavitation development of a benchmark marine propeller. In *International Conference on Offshore Mechanics and Arctic Engineering* (Vol. 85161, p. V006T06A025). American Society of Mechanical Engineers.

26th Numerical Towing Tank Symposium (NuTTS)
23-25 October 2024 - Duisburg, Germany

Ship Hydrodynamic Simulations Using an Upgraded Direct Forcing Immersed Boundary Method

Ahmet Soydan, Widar W. Wang, and Hans Bihs
Department of Civil and Environmental Engineering,
NTNU/Trondheim
Høgskolereingen 7A,7491 Trondheim, Norway, web page: http://www.reef3d.com/
ahmet.soydan@ntnu.no

Abstract

Ship performance in waves has become a main concern in reducing emissions from global sea transport. When ships operate in real sea conditions, emissions are higher than in calm water. Therefore, it is crucial to calculate ship performance in waves accurately and efficiently. This work focuses on the numerical investigation of the interaction between ships and waves. The six degrees of freedom (6DOF) motions of the vessels are simulated using a direct forcing immersed boundary method (DF-IBM) within the computational fluid dynamics (CFD) model REEF3D::CFD. The DF-IBM has been upgraded with a new density interpolation method to account for the sharp density gradient at the solid-fluid interface. This upgrade eliminates unphysical spurious phenomena and improves the stability and accuracy of ship simulations. The hydrodynamics are solved from the Navier-Stokes equations on a staggered structured grid. The water-air interface is captured using a level-set method (LSM). The LSM, combined with high-order discretization methods and initialization steps, can capture the complex free surfaces of ocean waves and their interactions with structures. In this study, the capability of the upgraded direct forcing immersed boundary method for ship hydrodynamics is investigated and the results are presented.

1 Introduction

The energy efficiency of newly designed vessels has gained great importance in recent years. The International Maritime Organization (IMO) has introduced a policy called the Energy Efficiency Design Index (EEDI), which aims to limit ships-sourced CO_2 emissions in the global sea. Thus, a vessel's EEDI must comply with a certain required value. However, the calculation procedure of EEDI is based on calm water conditions despite being the exception in the ship's lifetime. In contrast, vessels are often exposed to waves in real sea conditions, causing increased fuel consumption or reduced ship speed (Ley et al. (2014)). From this point of view, it becomes very crucial to calculate the ship performance in real sea conditions rather than calm water. With the rapid growth in computational power and advanced numerical methods, as well as rising safety concerns for vessels in extreme weather conditions, the number of studies using CFD for calculating ship motion and added resistance has increased over the past two decades. Orihara and Miyata (2003) solved the RANS equations using the finite volume method (FVM) on an overlapping grid system to evaluate the added resistance of a hull form. The free surface was calculated using the density-function method. Deng et al. (2010) also performed RANS simulations using FVM to calculate the added resistance and heave and pitch motion of KVLCC2 tanker in head wave. Simonsen et al. (2013) investigated KRISO Container Ship (KCS) in regular head sea conditions both experimentally and numerically. For the CFD study, CFDSHIP-IOWA and Star-CCM+ were used for RANS calculations, and AEGIR was used for potential flow simulations. Ley et al. (2014) examined the added resistance of two different types of ships in waves using the RANS-based solvers, Comet and OpenFOAM. Moctar et al. (2017) also conducted studies on the added resistance of DTC in waves, both experimentally and numerically. Furthermore, Sigmund and el Moctar (2017) presented the effect of head waves on propulsion characteristics. Sigmund and El Moctar (2018) also published experimental and numerical data on four different ship types in short and long waves. Tezdogan et al. (2016) carried out full-scale RANS simulations of the ship's motion in shallow water, revealing that the ship motion in shallow water differs significantly. Islam and Guedes Soares (2021) performed head wave simulations of KCS using OpenFOAM. The numerical results show that the sea margin value should be determined

considering real sea conditions. Most recently, there is an also uptake on seakeeping simulations in complex wave conditions like a bi-directional cross wave (Huang et al. (2021)) or irregular waves (Gatin et al. (2019)) besides uni-directional regular waves.

In this study, sea-keeping simulations of David Taylor Model Basin (DTMB) model 5415 at a 1/46.6 scale are performed using an upgraded direct forcing immersed boundary method (DF-IBM) within the numerical framework REEF3D::CFD (Bihs et al. (2016)). REEF3D is an open-source hydrodynamic framework developed at NTNU, focusing on wave hydrodynamics and coastal and marine applications. The objective of this research is to evaluate the capabilities of the numerical model for ship sea-keeping simulations. The numerical results are compared with experimental measurements for Fr = 0 and Fr = 28 under regular wave conditions.

2 Numerical Model

The Navier-Stokes (N-S) equations with the continuity equation are solved to ensure the conservation of mass and momentum as below:

$$\nabla \cdot \mathbf{u} = 0 \tag{1}$$

$$\frac{\partial \mathbf{u}}{\partial t} + \mathbf{u} \cdot \nabla \mathbf{u} = -\frac{1}{\rho}\nabla p + \mathbf{g} + \mathbf{f} \tag{2}$$

where $\mathbf{u}$ is the velocity vector, ρ is the density of the fluid, p is the pressure, $\mathbf{g}$ the acceleration vector due to gravity. A direct forcing immersed boundary method (Soydan et al., 2024) is implemented for the fluid-structure interaction and forcing term $\mathbf{f}$ is added to the momentum equation to take into account the rigid body velocity field in the fluid domain.

$$\mathbf{f} = \begin{cases} \frac{\partial \mathbf{P(u)}}{\partial t} + \mathbf{P(u)} \cdot \nabla \mathbf{P(u)} + \frac{1}{\rho}\nabla p - \mathbf{g} & \text{if } \Phi_s < 0 \\ \nabla \cdot \left(\nu \left[\nabla \mathbf{u} + \nabla \mathbf{u}^T\right]\right) & \text{if } \Phi_s > 0 \end{cases} \tag{3}$$

The forcing term $\mathbf{f}$ is calculated in solid and fluid domains as in Eq. 3. Here, Φ_s is the level set function that is used for tracking the fluid-solid interface, and $\mathbf{P(u)}$ is the rigid body velocity field. The forcing term $\mathbf{f}$ is smeared out through the solid and fluid interface with a smoothed Heaviside function $H(\Phi_s)$ as in Eq. 4.

$$\mathbf{f}^{(n+1)} \approx \mathbf{f}^{(*)} = H\left(\Phi_s^{(*)}\right) \cdot \left(\frac{\mathbf{P}(\mathbf{u}^{(*)}) - \mathbf{u}^*}{2\alpha_k \Delta t}\right) \tag{4}$$

The intermediate velocity field $\mathbf{u}^{(*)}$ is calculated with an explicit third-order low-storage Runge-Kutta scheme. (Spalart et al., 1991). Here, α_k is a Runge-Kutta coefficient and Δt is time-step. The intermediate rigid-body velocity field $\mathbf{P}$ $(\mathbf{u}^{(*)})$ is calculated as in Eq. 5 with the translational rigid-body velocity vector $\dot{\boldsymbol{x}}_i$, the angular rigid-body velocity vector $\boldsymbol{\omega}$ and the distance vector to the center of gravity of the rigid body $\boldsymbol{r}$.

$$\mathbf{P}\left(\mathbf{u}^{(*)}\right) = \dot{\boldsymbol{x}}_i + \boldsymbol{\omega}_i \times \boldsymbol{r} \tag{5}$$

By integrating the fluid properties (pressure p, the viscous stres tensor τ) over the solid surface Ω, the body forces and momenta are calculated as below:

$$\boldsymbol{F_i} = \int_\Omega (-\mathbf{n}p + \rho\nu\mathbf{n}\tau) d\Omega(\mathbf{x}) = \sum_{i=1}^{N} (-\mathbf{n}p + \rho\nu\mathbf{n}\tau)_i \cdot \Delta\Omega_i \tag{6}$$

$$\boldsymbol{M_i} = \int_\Omega \mathbf{r} \times (-\mathbf{n}p + \rho\nu\mathbf{n}\tau) d\Omega(\mathbf{x}) = \sum_{i=1}^{N} \mathbf{r}_i \times (-\mathbf{n}p + \rho\nu\mathbf{n}\tau)_i \cdot \Delta\Omega_i \tag{7}$$

where $\mathbf{n}$,p and τ are the surface normal vector on the solid body, the pressure and the viscous stress tensor, respectively.

The system of equations is discretized with finite differences on a rectilinear staggered grid. The convection term is solved with a fifth-order accurate weighted essentially non-oscillatory (WENO) scheme (Jiang and Shu (1996)), while the second-order accurate central finite difference scheme is used for diffusion terms. The pressure gradient in the RANS equation is solved using an incremental pressure-correction algorithm (Timmermans et al. (1996)), as explained in Martin et al. (2021). To improve computational efficiency, the fully parallelized BiCGStab algorithm from the HYPRE library (van der Vorst (1992)), coupled with a geometric multigrid pre-conditioner (Ashby and Flagout (1996)), is employed to solve the Poisson equation.

2.1 Density Interpolation Method

The DF-IBM is upgraded with a new density interpolation method to handle the sharp density gradient at the solid-fluid interface. As shown in Fig. 1.a, the material properties of the solid body can be assigned in the fluid domain. Due to the high-density gradient in the vicinity of the solid body, spurious velocities can occur in the interface leading to numerical instability. To maintain the numerical stability, the transition layer ($\epsilon = 2.1dx$) between the solid and fluid interface should be relatively large, decreasing numerical accuracy. In order to upgrade the method , the new density interpolation method is implemented as illustrated in Fig. 1.b. Here, the density and viscosity of the fluid are set the same inside and outside the solid body. Thus, the artificial density gradient in the interface is removed and numerical stability can be obtained with a thinner transitional layer ($\epsilon = 0.6dx$). In this way, the accuracy of the method is also increased. In this study, this method is subjected to a test for the ship-seakeeping simulations.

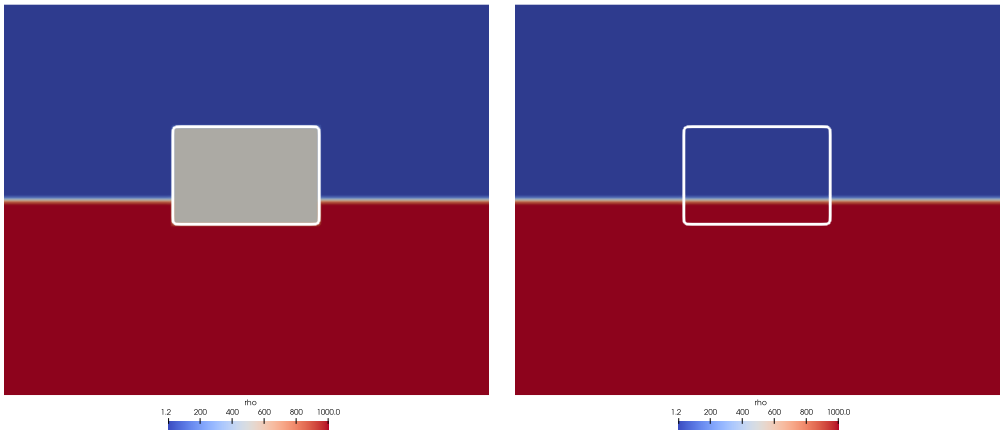

(a) Discontinuous solid density (b) Continuous fluid density

Fig. 1: Floating body density treatment

3 Numerical Results

The David Taylor Model Basin (DTMB) 5415 ship at a 1/46.6 scale is used for the ship-seakeeping simulations. This model is a well-known benchmark case used for the validation of the numerical algorithms for ship hydrodynamic simulations. The main properties of the ship are given in Table 1. The numerical

Table 1: Maain dimensions of DTMB 5415

$\lambda = 46$	Model	Full Scale
$L_{pp}(m)$	3.048	142.0
$B_{wl}(m)$	0.405	19.06
T (m)	0.123	6.15
V (m^3)	0.827	8424.4
$C_B(-)$	0.506	0.506
$S_w(m^2)$	1.371	2972.6

wave tank (NWT) is created to represent the experimental wave basin. Numerical framework REEF3D

has different types of wave generation and absorption methods, including the relaxation method, the Dirichlet-type method, and the active wave absorption method, as explained in (Miquel et al., 2018). In this study, the Dirichlet-type method is used for the wave generation and absorption and a 2nd-order Stokes wave is generated. The computational domain, grid stretching applied around the ship and the free surface are given in Fig. 2. Previously, the method was validated under a regular wave condition

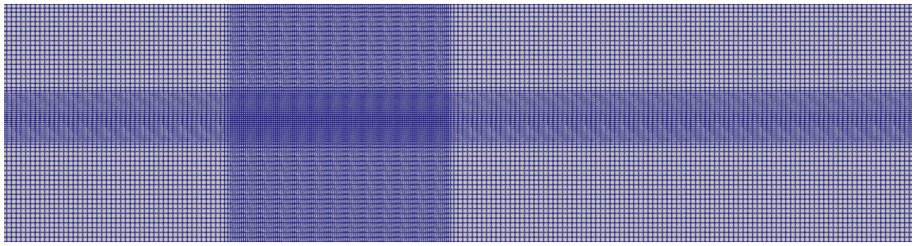

Fig. 2: Computational grid for simulations

(T=1.712 s, H=0.072 m) with Fr=0 and the results were presented in (Soydan et al., 2023). Experimental measurements were obtained from Irvine (2008). Three different grid sizes were used for the convergence study. Fig. 3 shows the numerical results with the experimental measurements. For the wave and current simulation, the mesh size $dx = 0.025$ is used. The Froude number is 0.28 and the wave height is H=0.0364 m and the wave period is T=1.089. Fig. 4 presents the numerical results of the experiment, showing a good agreement. Fig. 5 shows the vertical velocity field on the free-surface. As can be seen, the Kelvin wave is captured with the numerical method. 20 seconds simulation takes 2 hours on a M1 Max Macbook5 Pro, using 8 processors.

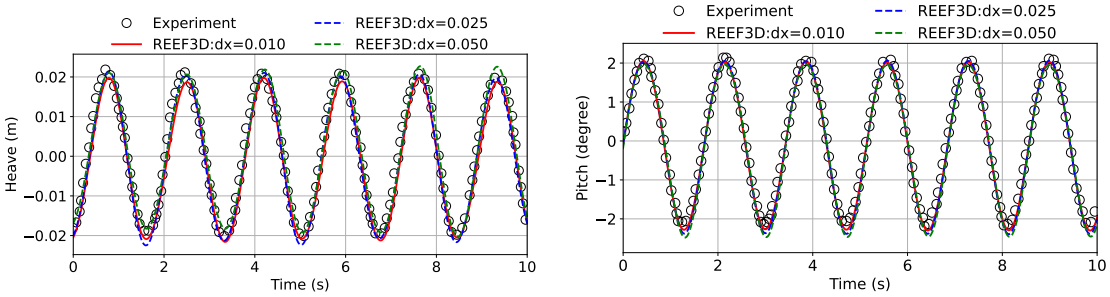

(a) Heave Motion (b) Pitch Motion

Fig. 3: Ship motion responses, Fr=0.0

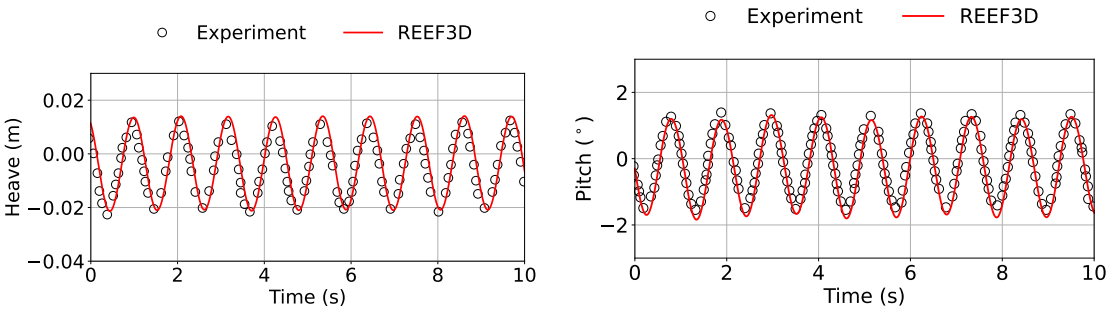

(a) Heave Motion (b) Pitch Motion

Fig. 4: Ship motion responses, Fr=0.28

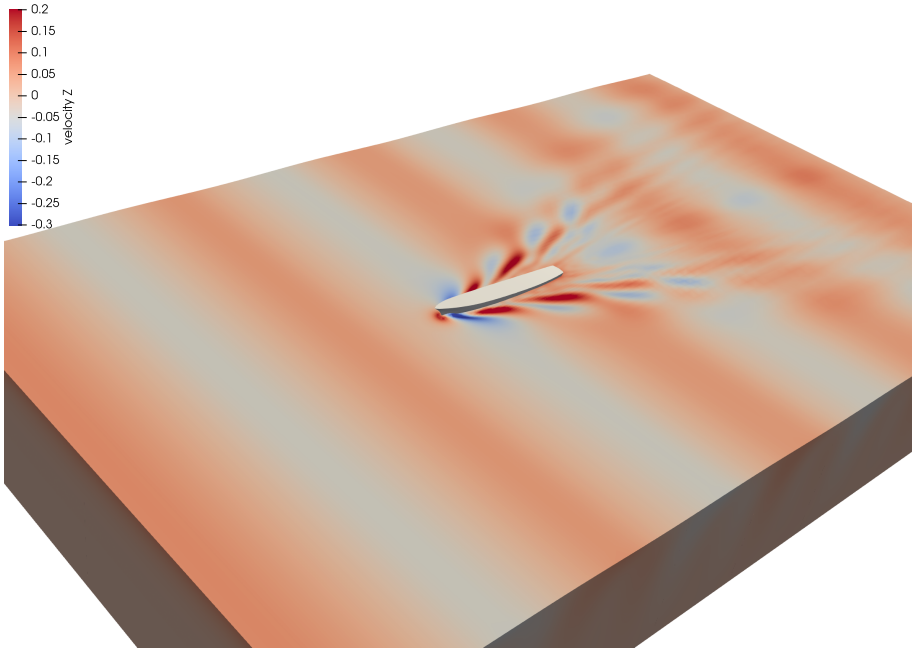

(a) t/T=5.0

Fig. 5: Ship motion with vertical velocity z

4 Conclusion

An upgraded direct-forcing immersed boundary method was tested and validated for the ship-seakeeping simulations. The method was upgraded with a new density interpolation method to improve stability and accuracy. Simulations were carried out in pure regular wave conditions and wave-current conditions at Fr=0.28. In both cases, the numerical results show a good trend with the experimental data, showcasing the applicability of the numerical method for the ship-seakeeping simulations.

Acknowledgements

The authors are grateful for the grants provided by the Research Council of Norway under the IPIRIS project (no. 308843). The simulations is performed on resources provided by Sigma2 - the National Infrastructure for High Performance Computing and Data Storage in Norway

References

Ashby, S. and Flagout, R. (1996). A parallel mulitgrid preconditioned conjugate gradient algorithm for groundwater flow simulations. *Nuclear Science and Engineering*, Volume 124(1):145–159.

Bihs, H., Kamath, A., Chella, M. A., Aggarwal, A., and Arntsen, Ø. A. (2016). A new level set numerical wave tank with improved density interpolation for complex wave hydrodynamics. *Computers & Fluids*, 140:191–208.

Deng, G., Queutey, P., and Visonneau, M. (2010). Rans prediction of the kvlcc2 tanker in head waves. *Journal of Hydrodynamics*, 22(1):459–464.

Gatin, I., Vladimir, N., Malenica, Š., and Jasak, H. (2019). Green sea loads in irregular waves with finite volume method. *Ocean Engineering*, 171:554–564.

Huang, S., Jiao, J., and Chen, C. (2021). Cfd prediction of ship seakeeping behavior in bi-directional cross wave compared with in uni-directional regular wave. *Applied Ocean Research*, 107:102426.

Irvine, M. (2008). Pitch and heave tests and uncertainty assessment for a surface combatant in regular head waves. *Journal of Ship Research*, 52(02):146–163.

Islam, H. and Guedes Soares, C. (2021). Head Wave Simulation of a KCS Model Using OpenFOAM for the Assessment of Sea-Margin. Volume 8: CFD and FSI. V008T08A036.

Jiang, G.-S. and Shu, C.-W. (1996). Efficient implementation of weighted eno schemes. *Journal of computational physics*, 126(1):202–228.

Ley, J., Sigmund, S., and el Moctar, O. (2014). Numerical prediction of the added resistance of ships in waves. In *International Conference on Offshore Mechanics and Arctic Engineering*, volume 45400, page V002T08A069. American Society of Mechanical Engineers.

Martin, T., A., T., and Bihs, H. (2021). numerical framework for modelling the dynamics of open ocean aquaculture structures in viscous fluids. *Applied Ocean Research*, 106:102410.

Miquel, A. M., Kamath, A., Alagan Chella, M., Archetti, R., and Bihs, H. (2018). Analysis of different methods for wave generation and absorption in a cfd-based numerical wave tank. *Journal of Marine Science and Engineering*, 6(2):73.

Moctar, O. e., Sigmund, S., Ley, J., and Schellin, T. E. (2017). Numerical and experimental analysis of added resistance of ships in waves. *Journal of Offshore Mechanics and Arctic Engineering*, 139(1).

Orihara, H. and Miyata, H. (2003). Evaluation of added resistance in regular incident waves by computational fluid dynamics motion simulation using an overlapping grid system. *Journal of Marine Science and Technology*, 8(2):47–60.

Sigmund, S. and el Moctar, O. (2017). Numerical and experimental investigation of propulsion in waves. *Ocean Engineering*, 144:35–49.

Sigmund, S. and El Moctar, O. (2018). Numerical and experimental investigation of added resistance of different ship types in short and long waves. *Ocean Engineering*, 147:51–67.

Simonsen, C. D., Otzen, J. F., Joncquez, S., and Stern, F. (2013). Efd and cfd for kcs heaving and pitching in regular head waves. *Journal of Marine Science and Technology*, 18(4):435–459.

Soydan, A., Wang, W., and Bihs, H. (2023). Numerical Applications of Wave-Structure Interaction Problems Using a Direct Forcing Immersed Boundary Method in REEF3D::CFD. *25th Numerical Towing Tank Symposium (NuTTS)*.

Soydan, A., Wang, W. W., and Bihs, H. (2024). An Upgraded Direct Forcing Immersed Boundary Method With Integrated Mooring Algorithm for Floating Offshore Wind Turbines. Volume 7: Ocean Renewable Energy:V007T09A043.

Spalart, P. R., Moser, R. D., and Rogers, M. M. (1991). Spectral methods for the navier-stokes equations with one infinite and two periodic directions. *Journal of Computational Physics*, 96(2):297–324.

Tezdogan, T., Incecik, A., and Turan, O. (2016). Full-scale unsteady rans simulations of vertical ship motions in shallow water. *Ocean Engineering*, 123:131–145.

Timmermans, L. J., Minev, P. D., and Van De Vosse, F. N. (1996). An approximate projection scheme for incompressible flow using spectral elements. *International journal for numerical methods in fluids*, 22(7):673–688.

van der Vorst, H. (1992). BiCGStab: A fast and smoothly converging variant of Bi-CG for the solution of nonsymmetric linear systems. *SIAM Journal of Scientific Computing*, Volume 13:631–644.

Assessment of hydrodynamic characteristics and computational resources for submarine resistance analysis: A comparative study between CFD Codes with application of BB2 Submarine

Noh Zainal Abidin[1,2,3], Frederic Grondin[2], Pol Muller[3] and Jean-François Sigrist[4]

[1]Faculty of Defence Science and Technology, National Defence University of Malaysia, Malaysia
[2]Research Institute in Civil and Mechanical Engineering (GEM), Ecole Centrale de Nantes, France
[3]Modelling and Simulation in Hydrodynamics, Sirehna, Naval Group, France
[4]Naval expert, eye-pi, France
noh.bin-zainal-abidin@ec-nantes.fr (NZ Abidin), frederic.grondin@ec-nantes.fr (F Grondin)

1.0 Abstract

Submarines are vital for maritime defense, requiring optimized hydrodynamic performance to minimize resistance. Advancements in Computational Fluid Dynamics (CFD) enable accurate predictions of submarine hydrodynamics for optimal design. This study compared the meshing capabilities of OpenFOAM and commercial software as well as the performance of High-Performance Computing (HPC) and standard PC resources upon hydrodynamic characteristics. The RANS turbulence model with $k-\omega\ SST$ was employed to analyze the resistances of the MARIN's BB2-class submarine. CFD simulations were conducted at a model scale (1:35.1) at a speed of 1.8235 m/s (U_S of 21 knots) upon various mesh densities from 1 to 97 million cells. Empirical equations were initialized for turbulence parameters. Mesh sensitivity and iteration convergence ensured validated results. The findings showed that the results were validated with errors ranging from 0.3% to 10% across different mesh densities. The lowest error (0.3%) was achieved with 97 million cells generated by the commercial meshing tool with HPC, while 13 million cells by OpenFOAM with a standard PC resulted in a 3.4% error. Accuracy improved with precise initialization of turbulence parameters, mesh strategy, numerical schemes, and computing resources. The application of a standard PC with the OpenFOAM meshing tool was able to produce an acceptable accuracy, with less than 5% error for lower mesh densities. Thus, it can be suggested that using a standard PC was beneficial for preliminary hydrodynamic simulations. However, HPC with commercial software was essential for detailed industrial analyses, such as full-scale resistance and propulsion simulations.

2.0 Introduction

In 1872, William Froude revolutionized maritime engineering by constructing the world's first physical basin for testing ship models. This innovation spurred the development of numerous tank facilities globally dedicated to examining various aspects of ship hydrodynamics, such as resistance, propulsion, maneuverability, and seakeeping. While more economical and quicker than full-scale measurements, these model tests paved the way for advancements in virtual testing through computer simulations. Numerical simulations offer distinct advantages due to their speed and ease of optimization, significantly reducing the time needed for conceptual design analysis to mere days (Gao et al., 2018). The 28th ITTC (2017) introduced comprehensive guidelines for applying CFD in ship analysis to address cost concerns further. CFD not only cuts expenses but also yields highly detailed data, enriching fluid dynamics insights. Selecting appropriate turbulence models, such as RANS, is crucial for accuracy in CFD simulations. Additionally, ensuring a properly set mesh with high cell density is vital for reliable and convergent results, although computational power limits the number of cells that can be used (Jasak et al., 2019). Recent advancements in High Performance Computing (HPC) have significantly enhanced CFD methods, allowing for higher grid densities, more parallel processors, and accelerated convergence times. Despite these benefits, the high costs associated with acquiring and maintaining HPC systems remain a significant challenge, particularly for smaller organizations and research institutions. The research explored CFD methodology by conducting numerical simulations on the SSK class attack submarine BB2 at a 1:35.1 model scale (Overpelt et al., 2015). MARIN provided the 3D CAD of the full-scale submarine, while Sirehna, Naval Group supplied lab-scale data and high mesh density for verification. The Nautilus HPC system from GeM, ECN, was used for simulations, processed with OpenFOAM 11. Mesh generation, ranging from 1 to 97 million cells, was done using SnappyHexMesh and the Cadence Fidelity meshing tool. The results of both approaches were validated with experimental and highest mesh density. A summary of the comparison between PC and HPC was also studied. Eventually, the local viscous and pressure forces along the hull were investigated to determine the spot that experienced the highest stress.

3.0 Numerical CFD setup

This study applied the finite volume method to discretize the computational domain of the Navier-Stokes (NS) equation into small control volumes. All the solution fields were stored in the centroid of the control volume. The segregated solver was utilized to solve the scalar matrix equations in an iterative sequence. The RANS turbulence

model with wall function (y^+ >30) and wall resolved (y^+ <5) was utilized in this research. The numerical parameters were configured in the open-source CFD code, OpenFOAM11. In this study, we simulated the submarine in a fully submerged isovolume and isothermal in steady state condition to simplify the equation of NS equation as follows:

$$\nabla.(\boldsymbol{u}) = 0 \quad (1)$$

$$\frac{\partial(\boldsymbol{u})}{\partial t} + \nabla.(\boldsymbol{uu}) = \frac{-\nabla p}{\rho} + \nu\nabla^2(\boldsymbol{u}) \quad (2)$$

The closure equations, typically derived from experimental data and adjusted for optimal performance across various flow conditions (Wilcox, 2008). The initialization of k and ω is significance to ensure the solution reach convergence and avoid numerical diffusion. In this study, the value of k and ω can be initialized approximately according to viscosity ratio, $\frac{\mu_t}{\mu}$ and turbulence intensity, I as follows:

$$\omega_{far} = \frac{\rho k}{\mu}\left(\frac{\mu_t}{\mu}\right)^{-1} \quad , \quad k_{far} = \frac{3}{2}(UI)^2 \quad (3)$$

Since this case was incompressible and in a steady-state condition, the transient term was set to be steady state. The RANS of $k-\omega$ SST was utilized as a turbulence model, which is capable of solving for both low and high y^+ values (Menter et al., 2003). The solution solver employed was the Semi-Implicit Method for Pressure-Linked Equations with Consistence (SIMPLEC). For the initial stage of verification and validation, the free stream velocity, U, utilized was 21 knots at real scale, as referred to by Overpelt et al. (2015), and was scaled down by Froude similitude as recommended by ITTC (2014) at $U_m = U_s/\sqrt{\lambda}$ with a ratio of (1:35.1) to ensure similarity with the model test (Lab-scale) provided by Sirehna, Naval Group. The BB2 submarine particulars were as shown in Table 1, while the initialization of physics and turbulence parameters was as shown in Table 2.

Table 1. Submarine BB2 particulars

Description	Symbol / unit	Full (1:1)	Model (1:35.1)
Length overall	L (m)	70.2	2
Beam	B (m)	9.6	0.2735
Depth (to deck)	D(m)	10.6	0.3020
Depth (to top of sail)	Dsail(m)	16.2	0.4615

Table 2. Initialization physic and turbulence

Parameter	Unit	Value
U_m	m/s	1.8235
k	m^2/s^2	0.0005
ω	$1/s$	498.77
ν_w	m^2/s	1e-06
ρ	kg/m^3	1000
μ_t/μ	-	1
I	-	1%
Re	-	3.65e06

The submarine simulation is in fully submerged domain as constructed the computational domain w.r.t to L= 2m as (8m x 14m x 8m) referred to 28th ITTC (2017) that is affordable to simulate the flow efficiently as shown Fig.1. An adequate computational domain ensures numerical stabilities, avoiding the backflow and numerical oscillations may arise that affecting the accuracy and reliability of the simulation results.

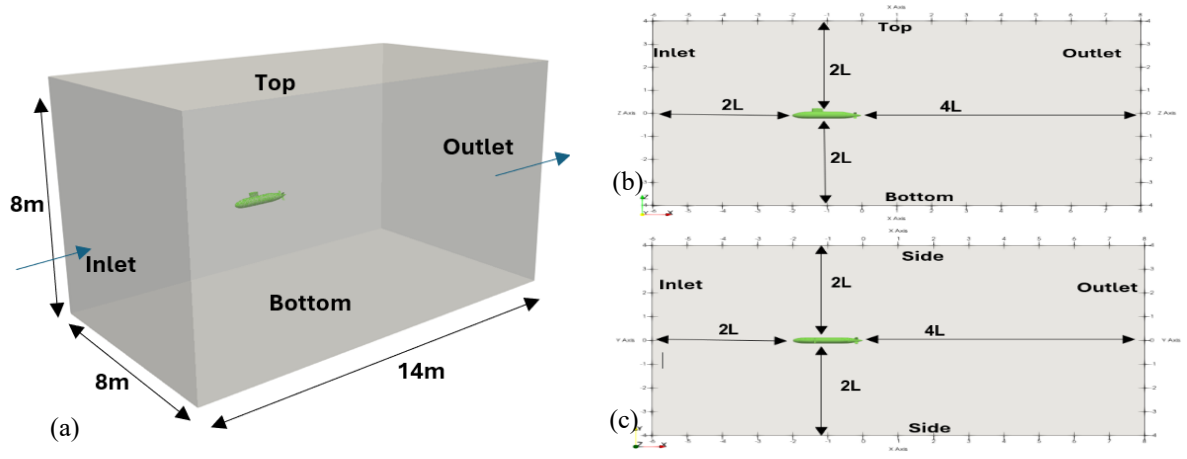

Fig.1: (a) 3D Computational Domain and Boundary Conditions, (b) Side view, (c) Top View

The near-wall treatment on the submarine hull was set based on the y^+ value. In this study, the mesh was generated in 3 cases, including (*i*) mesh from 1 to 13 million cells, which was generated by snappyHexMesh in OpenFOAM using a standard PC, (*ii*) mesh of more than 20 million cells, which was generated by snappyHexMesh in OpenFOAM using HPC, and (*iii*) mesh of more than 20 million cells, which was generated by Cadence using HPC. For (i), initially, a hexahedral background mesh was created by the blockMesh utility to set up the global base size, Δ (dx, dy, dz), at the ratio of Δ/L =0.05. The ratio could be modified to refine or reduce the mesh density globally throughout the domain by $\Delta/\sqrt{2}$ based on ITTC (2017) and (Paredes et al., 2021), from low to high mesh densities. Then, snappyHexMesh was utilized to produce the castellated mesh, surface mesh snapping, and to add boundary layer configuration. The targeted boundary layer was 6 to 8 layers, as suggested by prior studies conducted by Paredes et al. (2021) and Jasak et al. (2019). Refinement on mesh surfaces with levels (5,6) was used to achieve a smooth surface and curvature. The refinement region tool was employed for two regions near the submarine wall, in which each region reduced the size of the cells, $\Delta/2^n$ as they approached closer to the submarine's hull, as presented in Fig. 2. The size of the elements in the inner refinement region, Δ_{ir} was adjusted according to the targeted y^+ value. The stretching factor, *r,* of 1.2 for boudary layer generation was utilized. The targeted first layer thickness, y_1, boundary layer thickness, δ, and number of prism layers, m, could be approximated based on the targeted y^+ (White & Majdalani, 2022), as represented in the equation below.

$$\frac{y^+}{y_1} = \frac{0.0487.U_m}{\nu.\ln(0.06.Re)} \; ; \quad \delta = \frac{0.16L}{Re^{1/7}} \; ; \quad m = \frac{\ln\left(1-(1-r)\frac{\delta}{y_1}\right)}{\ln(r)} \tag{4}$$

In Fig. 2, (i) indicates the inner refinement region, $\Delta_{ir} = \Delta_{or}/2^n$, while (o) shows an outer region, $\Delta_{or} = \Delta_b/2^n$ and (b) background region, Δ. The same strategy is utilized for case (*iii*) generated by Cadence for high mesh density.

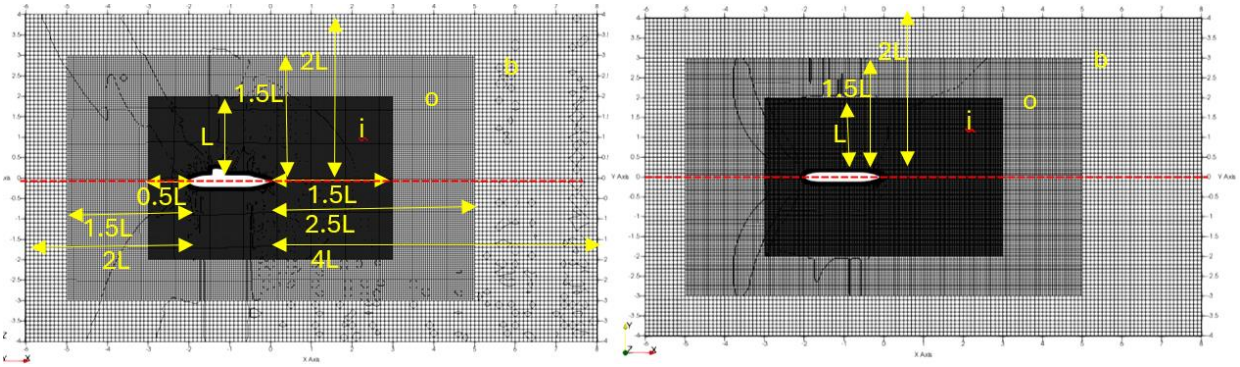

Fig. 2: Meshing Strategy, refinement zone dimension (Side and Top View). 13,705,468 cells (snappyHexMesh)

All the meshes generated for each case were processed in CFD code of OpenFOAM 11.The SIMPLEC with under relaxation factors on parameters U=0.9, k and ω are 0.7 were utilized. For the gradient, divergence and Laplacian schemes were discretized using the second-order scheme: cellLimited Gauss linear 1, bounded Gauss linearUpwindV, and Gauss linear corrected. The simulation has been monitored up to 1000 iterations for convergence. Two iterations of non-orthogonal mesh correctors have been utilized to have stable solution. The geometric-algebraic multigrid solver (GAMG) with Gauss Seidel for smoother solver has been used for quantities of the transport equation. By varying the mesh density via mesh refinement factor systematically according to the targeted y^+, mesh convergence study has been conducted. Note that, by applying the mesh refinement, the numeric setup remains the same for all the cases as illustrated in Table 3.

4.0 Results and Discussion - Submarine hydrodynamic assessment

The HPC resources were employed for computations involving high mesh density, while a standard Pc was used for simulations with lower mesh density. The specifications of the resource utilized are shown in Table 3. While the summary of sample cases conducted is presented in Table 4. The global resistance of submarine is taken for studying the hydrodynamic assessment. The global resistance, F_t contributed by integration of two components along the submarine which are pressure, F_p and viscous, F_v forces that solve in x-direction. Then the F_t can be compared it with experimental results for verification and validation process (Overpelt et al., 2015). Initially, the mesh convergence study was conducted on Case 1 to 7 (1 – 13) million using snappyHexMesh with 6 cores of CPU. Then, the mesh for Case 5, 6 and 7 taken as a base for determining the order of convergence, p, estimated extrapolated solution, relative error, e_{21} and grid convergence index (GCI) computed based on Richardson extrapolation referred to prior study (Celik et al., 2008) and ITTC guidelines (ITTC, 2017). It is shown that, the

average y^+ reduces from 478 till 7.5 when increase the mesh density as shown in Fig. 3 and Table 6. Thus, the wall function is utilized for wall treatment in viscous sub layer region. However, the Avg. y^+ less than 10 for mesh of Case 5 -7 can be acceptable as referred from Paredes et al. (2021), which used a mesh of Avg. y^+= 16.48 for his submarine computation.

Table 3. Computing resources

Resources	Type	Computing
HPC	Nautilus cluster in Glicid, 5376 AMD Genoa cores, 28TB RAM, 16 A100-80GB GPUs, 8 A40 GPUs, 100GB infiniband network	High Mesh Density (>20 millions)
Pc	Dell, 13th Gen Intel(R) Core(TM) i7-13850HX, 2100 Mhz, 20 Core(s), 32GB RAM	Lower Mesh Density (<20 millions)

Table 4. Sample Cases

Case	Mesh tool	Resources	Target y^+
1 - 7	SnappyHex Mesh	Standard PC	5
8 -9	SnappyHexMesh	HPC	1
10 - 13	Cadence	HPC	1

Fig.4 presents Case 1 – 7 simulation results using standard Pc. The trends are significant in providing information on mesh and iterative convergence concerning the quantity of interest (Qoi), F_p and F_v getting constant at specific iterations when mesh densities increase (Abidin et al., 2021). The results of the mesh sensitivity study for Mesh Cases 5 to 7 are shown in Table 6.

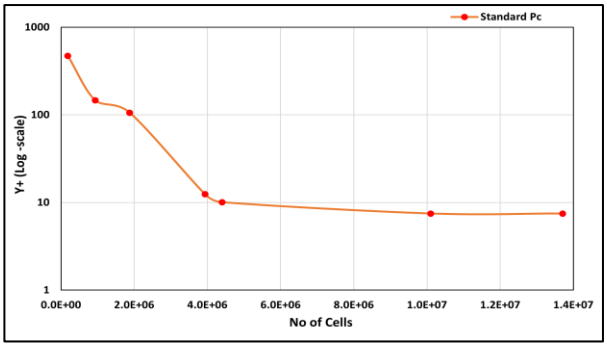

Fig.3: The average Log-Scale (y^+) for Cells (180k – 13 million)

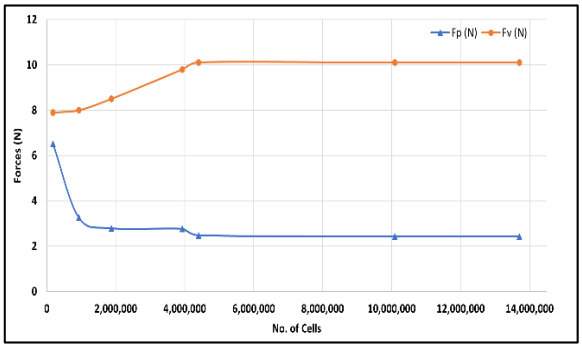

Fig.4: The prediction F_p and F_v

The results of the mesh sensitivity study and Richardson extrapolation procedure are shown in Table 5. It shown that the fine mesh of Case 7 is well converged in terms of the relative error, e_{21} and the CGI_{21}. The parameter of s=1 indicates the monotonic convergence, as presented by Eça & Hoekstra (2014). While the refinement ratio, r_{21} and r_{32} are both greater than 1.1 indicating the meshes are sufficient for good mesh sensitivity study**.** As an error of 0.44% is likely to be acceptable for most engineering studies, the solution on an infinitely fine mesh can be used with confidence. Furthermore, the order of convergence, p = 2, is the ideal order of convergence. Therefore, the extrapolated global resistance approximates as $F_0 \approx F_t$=12.48N**.** Hence, any further mesh refinement is likely to give noticeable improvements in the accuracy of global resistance and could be worthwhile if the computational cost is reasonable.

Table 5. Results of Mesh Convergence Study

r_{21}(-)	r_{32}(-)	s (-)	e_{21}(%)	${e_{21}}^{ext}$(%)	p(-)	CGI_{21}(%)	F_0 (N)
1.107	1.369	1	0.08	0.35%	2	0.44%	12.4758

Case 7 illustrated good CGI. Nevertheless, the verification and validation can be achieved by comparing them with experimental data from Sirehna, Naval Group. The summary of errors and computation times obtained for the entire study is presented in Table 6. Cases 8 and 9 generated the high mesh density using snappyHexMesh via HPC. While for cases 10 to 13, the high mesh density generated by Cadence can target the maximum Avg. y^+ less than 1. Thus, wall resolved was applied to compute the viscous sub-layer accurately. It can be observed that Cases 4 to 7 (standard Pc) and 10 to 13 (HPC) illustrated errors of less than 5%. A comparison between the accuracy, computing times and meshing tool for standard Pc and HPC is presented in Fig. 5. As discussed earlier, the mesh of Case 7 obtained good CGI and produced error of 3.4% using the OpenFOAM meshing tool. However, in Cases 8 and 9, the error increased to 9.4%, and the accuracy did not improve. This was due to poor generation and collapsing of cells vertex onto surface in the boundary layer zone, which negatively affected the interpolation of solution.While for Case 10 to 13, with high mesh density presented accuracy improve until the error reduces to 0.3%. Fig. 5 (right) illustrates the comparison between accuracy and computation on both resources utilized. It can be observed the computation time of Case 7 (13 million) had overtaken by Case 10 (26 million) due to contribution number of cores in HPC. The time spent increases with increment of mesh density. In addition, Table

6 and Fig. 5 presented the comparison on surface mesh generation between both tools. We discovered the OpenFOAM meshing tool has difficulty on generating the targeted boundary layer of y^+ in contrast to Cadence.

Table 6. Summary of Simulation on Various Mesh Densities

						yplus						
Case	Cells No.	CPU	Station	Tool	Wall/No	Min	Max	Avg	Ftcfd	Error (%)	Clock (s)	CPU (h)
1	180,348	6	Pc	OF	Wall	3.941	471.464	474	14.41	19.07	84.00	0.14
2	929,873	6	Pc	OF	Wall	1.10591	189.734	147	11.26	6.97	489.00	0.82
3	1,873,262	6	Pc	OF	Wall	0.28105	153.16	106	11.29	6.75	1143.70	1.91
4	3,932,029	6	Pc	OF	Wall	0.12336	131.199	12.5	12.59	4.00	2475.00	4.13
5	4,400,222	6	Pc	OF	Wall	0.13336	120.059	10.1	12.56	3.70	2950.00	4.92
6	10,092,709	6	Pc	OF	Wall	0.13369	113.702	7.51278	12.53	3.52	7314.00	12.19
7	13,705,468	6	Pc	OF	Wall	0.1086	113.713	7.51383	12.52	3.44	10118.00	16.86
8	38,185,848	50	HPC	OF	No	0.00199	88.3181	1.06215	10.95	9.51	6492.44	90.17
9	39,233,777	50	HPC	OF	No	0.00228	96.4607	1.22428	10.96	9.42	6509.73	90.41
10	26,724,343	50	HPC	Cadence	No	0.005	4.50451	0.85224	12.49	3.22	4300.38	59.73
11	50,071,757	50	HPC	Cadence	No	0.01051	4.50564	0.95853	11.78	2.68	8631.01	119.88
12	88,115,356	50	HPC	Cadence	No	0.00378	1.7943	0.22413	12.19	0.69	16479.10	228.88
13	97,092,477	50	HPC NG	Cadence	No	0.00244	0.77986	0.24248	12.13	0.24	18358.40	254.98

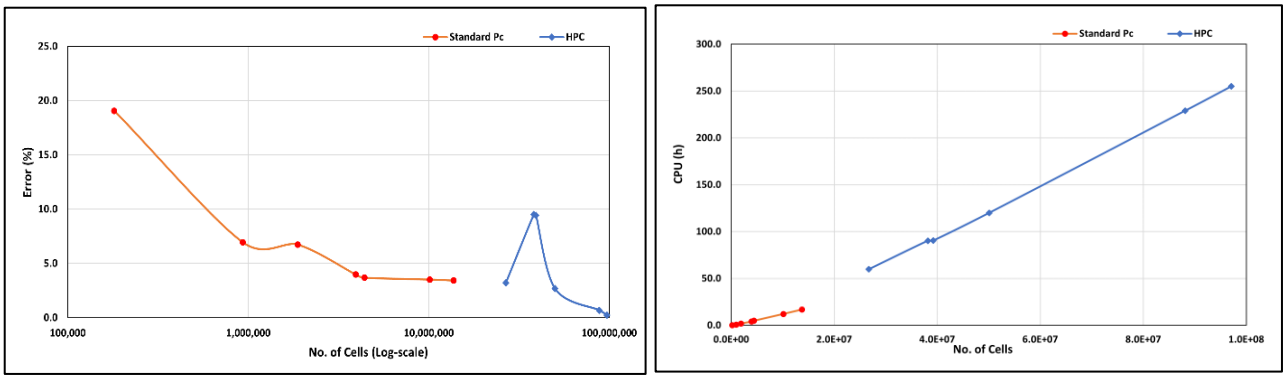

Fig.5: The accuracy and CPU time for standard PC (6 cores) and HPC (50 cores)

Detailed observation on sail planes or rudder planes showed an unsmooth surface at the edges that was expected to influence the accuracy of wall shear stress as shown in Fig. 6. Fig. 7 illustrated the hydrodynamic forces of F_v and F_p distributed along the hull for each section from bow to tail of submarine. It was observed the F_v is dominated over F_p contributing as 85% towards global resistance. The F_v is highest at the sail (x/L = 0.8 – 0.5) and tail (x/L = 0.1 – 0) regions. The turbulent field was substantially altered by the sail, sail planes, and rudder planes, which significantly modified the flow and influenced the distribution of F_v. The wake was influenced by the shear layer from the sail planes of fins' trailing edge as shown in Fig 8 (at straight ahead speed, U_m = 1.8235). The sail on the upper side of the hull generates an adverse pressure gradient, which results in the formation of a horseshoe vortex that travels downstream and interacts with the boundary layer of the hull. The sail on the upper side of the hull generated an adverse pressure gradient, which resulted in the formation of a horseshoe vortex that traveled downstream and interacted with the boundary layer of the hull. The sail's trailing edge and rudder section also generated additional vortices, as shown in similar studies by Rocca et al., (2022). Nevertheless, the flow structure was unable to clearly visualize the vortices generated accurately due to the steady solver and RANS assumption utilized in this study.

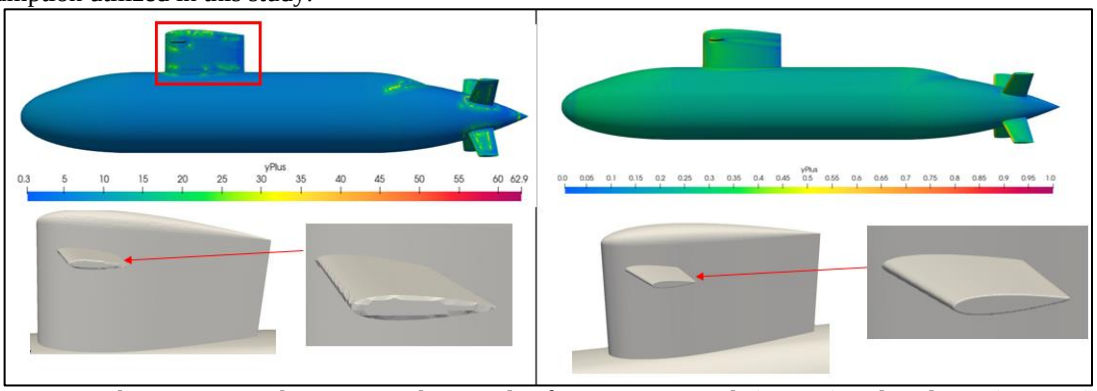

Fig.6: The comparison between meshing tools of SnappyHexMesh (Case 7) and Cadence (Case 11)

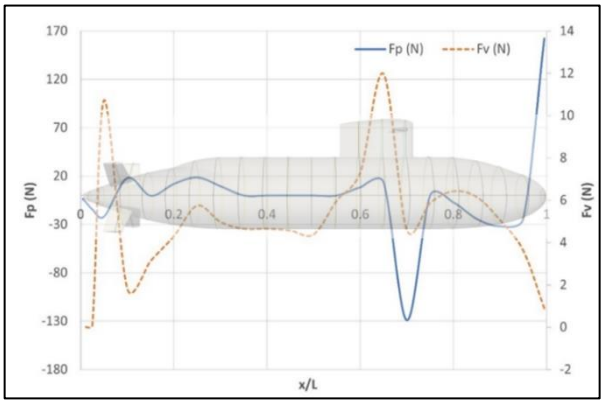

Fig.7: The Local Forces Distribution

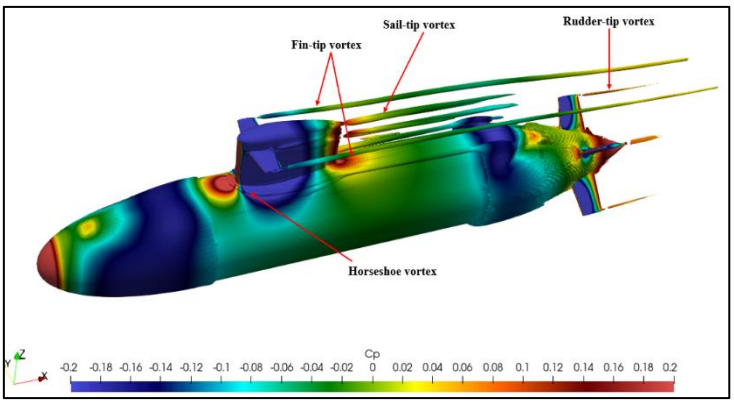

Fig.8: The Flow characteristic along the hull (Q criterion)

5.0 Conclusion

A good agreement is observed between the CFD predictions and experimental data, particularly with the high density of mesh, regarding the hydrodynamic characteristics of the submarine hull with integral of F_v and F_p at various mesh densities. It is concluded that the mesh generated by OpenFOAM with standard Pc is acceptable, with an error less than 5%. Case 7 exhibiting a 3.4% error with GCI of 0.44% demonstrates an acceptable value and approximate by Richardson extrapolation method according to ITTC standards. However, the OpenFOAM meshing tool appeared to be unable to improve the accuracy of solution even though able to generate high density mesh such Case 8 and 9 as in Fig. 5. While the utilization of HPC shows advantages like flexibility in generating high-density mesh and allows for larger computation times. Moreover, the usage of commercial meshing tools such as Cadence is shown to accurately generate boundary layers according to targeted y^+ based on Eq.4, leading to an increase in global mesh density and a reduction of error to 0.3%. Rigorous assessment on Cases 1 to 7 demonstrates that standard Pc is significance for conducting preliminary ship hydrodynamic simulations while HPC systems are indispensable for handling more intricate and detailed industrial analyses, such as full-scale resistance and propulsion simulations. However, results obtained from standard Pc should be verified against high mesh density results (Case 13) or experiment before being utilized for further analysis. However, it is imperative to ensure correct initialization and boundary condition values, as discussed in the previous section. The choice of numerical scheme for discretizing transport equations significantly influences stability, accuracy, and solution boundedness based on specific cases. The investigation on global and local contributions of hydrodynamic components shows that the sail and rudder experience highest F_v due to strong turbulent field, steep pressure gradients, and high velocity gradients. Our findings highlight the complementary roles of HPC and standard Pc, as well as the utilization of both commercial and open-source meshing tools, in optimizing the overall accuracy and cost-effectiveness of CFD simulations for ship hydrodynamics.

References

28th ITTC. (2017). Practical Guidelines for Ship CFD Applications. *ITTC – Recommended Procedures and Guidelines*, 1–20.

Abidin, N. Z., Leblond, C., Yolhamid, M. N. A. G., Zarim, M. A. U. A. A., Ibrahim, F., & Suhel, A. (2021). Investigation of numerical hydrodynamic performance of deformable hydrofoil (Applied on blade propeller). *Transactions on Maritime Science*, *10*(2), 414–438. https://doi.org/10.7225/toms.v10.n02.012

Celik, I. B., Ghia, U., Roache, P. J., Freitas, C. J., Coleman, H., & Raad, P. E. (2008). Procedure for estimation and reporting of uncertainty due to discretization in CFD applications. *Journal of Fluids Engineering, Transactions of the ASME*, *130*(7), 0780011–0780014. https://doi.org/10.1115/1.2960953

Eça, L., & Hoekstra, M. (2014). A procedure for the estimation of the numerical uncertainty of CFD calculations based on grid refinement studies. *Journal of Computational Physics*, *262*, 104–130. https://doi.org/10.1016/j.jcp.2014.01.006

Gao, T., Wang, Y., Pang, Y., Chen, Q., & Tang, Y. (2018). A time-efficient CFD approach for hydrodynamic coefficient determination and model simplification of submarine. *Ocean Engineering*, *154*(May 2017), 16–26. https://doi.org/10.1016/j.oceaneng.2018.02.003

Menter, F. R., Kuntz, M., & Langtry, R. (2003). Ten Years of Industrial Experience with the SST Turbulence Model Turbulence heat and mass transfer. *Cfd.Spbstu.Ru*, *4*(July 2014), 625–632.

Overpelt, B., Nienhuis, B., & Anderson, B. (2015). Free Running Manoeuvring Model Tests On A Modern Generic SSK Class Submarine (BB2). *Pacific International Maritime Conference*, 1–14.

Paredes, R. J., Quintuña, M. T., Arias-Hidalgo, M., & Datla, R. (2021). Numerical flow characterization around a type 209 submarine using OpenFOAM. *Fluids*, *6*(2), 1–23. https://doi.org/10.3390/fluids6020066

Rocca, A., Cianferra, M., Broglia, R., & Armenio, V. (2022). Computational hydroacoustic analysis of the BB2 submarine using the advective Ffowcs Williams and Hawkings equation with Wall-Modeled LES. *Applied Ocean Research*, *129*(May), 103360. https://doi.org/10.1016/j.apor.2022.103360

Wilcox, D. C. (2008). Formulation of the k-ω turbulence model revisited. *AIAA Journal*, *46*(11), 2823–2838.

Calibration of RANS Wall Model for Accuracy Improvement of Submarine CFD Resistance Prediction

C.E. Badoe[1], M. Stanley[1], P.W. Bull[1] and R.J. Pattenden[1]*
[1]QinetiQ, Haslar, UK
Email: cebadoe@qinetiq.com

1 Introduction

A study was conducted to understand the sensitivity of and a mitigation for CFD predictions of submarine resistance to variations in near-wall grid. This has become necessary during previous work on model scale submarine CFD resistance studies which showed that a very fine near-wall grid is required to obtain accurate estimation of the residuary resistance. Whilst this is feasible for simple geometries, it is difficult to achieve on a more complex fully appended submarine hull form due to the high aspect ratio cells that are required.

In this paper, a method to mitigate the sensitivity of submarine CFD solution to the near-wall grid spacing is proposed using roughness. A small roughness height is calibrated as a function of first cell height against a high resolution, low y^+, and solution to obtain consistent skin friction. The methodology was first developed on a flat plate and tested on the SUBOFF hull form with control surfaces. The method is compared with experimental results of SUBOFF AFF1 body of revolution, to confirm the behaviour on a simple submarine hull form, and to test the implementation of the method. Finally, it is then compared with experimental results on the SUBOFF AFF3 appended hull form, to verify the predictions of wake and to assess the effect of turbulence model parameters.

2 Developed methodology using roughness

A number of studies [1-3] have been conducted into the sensitivity of different turbulence models to near wall mesh spacing. These studies show that there is a consistent behaviour of the ω based turbulence models to exhibit a very strong sensitivity to the near wall spacing, which is not observed in other types of turbulence model. To make the solution less sensitive to the near wall grid spacing, it is necessary to modify the boundary condition of the ω equation. One way to modify the ω boundary condition is to treat the boundary as a rough wall, leading to a constant value of ω at the wall rather than an infinite value. As Hellsten showed [4], this roughness can also be a function of y+ to respond to variations in the near wall grid spacing. A variation of this approach was chosen for adoption in this task, due to the simplicity of applying a roughness value in STAR-CCM+ with no modification of the code required. For a very low wall y+ (0.01), C_f was measured on a flat plate. Wall y+ was then increased with added roughness to replicate the C_f value obtained at the very low wall y+. This was repeated for a range of Reynolds number and wall y+ values. A relationship was then found to derive a relation between required calibration roughness with Reynolds number and wall y+. An initial model was to use two separate equations to determine roughness, *r* in metre for low wall y+ (Equation 1) and high wall y+ (Equation 2) where L is the body length and the same length used for the Reynolds number, Re.

$$r = \frac{50L}{\mathrm{Re}^{0.927}} \quad \text{Equation 1}$$

$$r = \frac{26L}{\mathrm{Re}^{0.918}} \quad \text{Equation 2}$$

The model was then adjusted to account for body length since the original data was collected for a 1-metre flat plate. To account for this a new model was developed which utilised non-dimensionalised r^+ instead defined as

$$r^+ = \frac{r\rho u_\tau}{\mu} \quad \text{Equation 3}$$

where ρ is the density, u_τ is the friction velocity and μ is the viscosity. The friction velocity utilises a wall shear stress value which is calculated from:

$$\tau_w = c_f \times 0.5\rho V_0^2 \quad \text{Equation 4}$$

The wall shear stress coefficient c_f is then calculated from:

$$c_f = 0.2 \times (\log \mathrm{Re})^{-2.262} \quad \text{Equation 5}$$

The results of the study to create a model which is $r^+ = f(\mathrm{Re}, y^+)$ are presented in Figure 1 and the proposed roughness model based on Reynolds number and wall y^+ is presented in Equation 6. Where A_1 is defined in Equation 7 and B_1 is defined in Equation 8.

$$r^+ = (A_2 y^+ + A_3) \log \mathrm{Re} + B_2 (y^+)^2 + B_3 y^+ + B_4 \quad \text{Equation 6}$$

$$A_1 = A_2 y^+ + A_3 \quad \text{Equation 7}$$

$$B_1 = B_2 (y^+)^2 + B_3 y^+ + B_4 \quad \text{Equation 8}$$

This model has been utilised for the CFD results in this paper.

2 SUBOFF AFF1

SUBOFF AFF1 is a body of revolution submarine hull form. Full details of the geometry and experimental conditions can be found in [5]. Since the geometry is symmetrical about the central axis, an axisymmetric approximation can be utilised to perform simulations more efficiently. All studies into the effect of y+ and roughness on SUBOFF AFF1 were conducted using a 2D axisymmetric geometry. Several studies were conducted to understand the effect of y+ on skin friction coefficient. Initial studies were carried out using SUBOFF AFF1 modelled as a smooth surface across a range of Reynolds numbers from 10^6 to $10^{9.5}$. The rough-wall boundary condition (RWBC) was then added to observe the effect on skin friction across a range of Reynolds numbers and y+ values. A comparison was made between SUBOFF AFF1 CFD simulations and experimental data carried out by DARPA [5] where skin friction along the hull was analysed along with velocity data, and coefficient of pressure.

2.1 SUBOFF AFF1 results

Simulations were carried out with a smooth hull to understand the effect of y+ on the total resistance and skin friction coefficients. At values of y+ <3, it can be seen from Figure 2a and Figure 2b that, in general, both the total and frictional resistance decreased as target y+ increased. However, for higher target y+ >30, there was a small positive increase in resistance as y+ increased. It is clear that the near wall first cell height had an impact on the value of the skin friction coefficient. To address this, the RWBC was developed, to reduce this variance in C_F. The first implementation of the roughness model is denoted as RWBC1 in the figures. The effect that the rough wall boundary condition had on the value of C_F at a range of target y+ values can been in Figure 2b. In comparison to the smooth hull values, C_F remained more consistent across the range of y+ values. There was some variation at lower Reynolds number. However, at higher Reynolds numbers the variance in C_F was reduced. One issue with this model is that the predicted resistance at y+~0.1 does not match the smooth solution. Since it has been shown that the smooth wall solution with very low y+ is consistent with other codes, this should be taken as the reference. Therefore, when the mesh is refined, it should tend towards the smooth wall, very low y+ solution. Additional simulations were carried out at a Reynolds number of 1.2×10^7 to match experiments carried out on SUBOFF AFF1. A comparison with experimental data of the C_f profile across the hull is shown in Figure 2c, where x/L=0 represents the bow of the submarine and x/L=1 represents the stern. This shows that a target y+ value of 0.1 reproduced the

experimental data fairly well, with some deviation from x/L=0.1 to x/L=0.4 where the experimental data was lower than the CFD data. In comparison, the CFD results for a target y+ value of 1 yielded a skin friction which was lower than the experimental data across most of the hull except beyond x/L = 0.9 where it began to reproduce the experimental results and between x/L=0.15 and x/L=0.25. The results with RWBC1, with y+ of 1, gave skin friction close to the measured values and the y+~0.1 smooth hull results over the majority of the hull. However, there was an over prediction of skin friction over the fore-body, within the first 5% of the length. This is likely to be due to the use of a constant roughness height, causing a disproportionate increase in friction where the boundary layer is thin on the fore-body. To address this, and the fact that the model did not recover the smooth wall solution at low y+, a new version, hereafter denoted RWBC2, was developed.

The predicted total and frictional resistance coefficients are shown in Figure 2a and Figure 2b respectively. These show that the results with RWBC2 match the smooth wall results at y+~0.1, albeit slightly below the measured total resistance. The predicted resistance is very consistent between y+~0.1 and y+~2, which is a reasonable usable range. It is important to note that the aim of the RWBC was not to match the measured value, but simply to remove the y+ sensitivity from the solution. Although, the RWBC1 appears closer to the measured value, this is as a consequence of the over-prediction of shear stress around the bow. The difference in resistance between the y+~0.1 prediction and the measured value can be attributed to other choices in the turbulence model, such as the use of curvature correction and the realisability constant, both of which tend to lead to underestimates in the turbulence around leading edges with default settings. Differences could also be caused by the fact that neither the turbulence stimulation on the model, nor any regions of laminar flow, are represented in the CFD predictions, and other uncertainties in the experiment. Figure 2c shows that with RWBC2, the wall shear stress is very close to the smooth wall, low y+ result, even around the bow where the previous model over-predicted the shear stress. Figure 2d shows the radial variation of axial velocity at x/L = 0.978 in comparison to experimental data. Across the four conditions, the variation in axial velocity was minimal and showed a similar trend to the experimental data.

3 SUBOFF AFF3

SUBOFF AFF3 is an appended version of the SUBOFF AFF1 bare hull. It has a cruciform tail section, but with no bridge fin or forward hydroplanes. All simulations carried out on SUBOFF AFF3 were conducted as a half-hull to save simulation time. Simulations using STAR-CCM+ were carried out on the SUBOFF AFF3 geometry. A mesh study was carried out at a target y+ value of 0.1. The existing methodology was used on a smooth hull across a range of y+ values. An updated definition for the first cell height was then used on a smooth hull and a rough hull with the proposed roughness model. A mesh study was carried out with the rough wall boundary condition at a target y+ value of 1. A further set of studies were carried out using the k-ω Shear Stress Transport model, quadratic constitutive relation, with default curvature correction (SSTQCRCC) turbulence model. RANS simulations are performed using the k-ω Shear Stress Transport turbulence model with the quadratic constitutive relation and curvature correction options (SSTQCRCC) and the Realizable k-ε (RKE) turbulence model. Simulations are monitored for residuals, forces, and moments for convergence.

3.1 SUBOFF AFF3 results

All results presented here are for a Reynolds number of 1.2×10^7 corresponding to an inlet velocity of 3 m/s. The effect of the rough wall boundary condition on the skin friction coefficient for SUBOFF AFF3 is shown in Figure 3 across a range of y+ values. Adding roughness to the hull provided a more consistent value of skin friction across the y+ values. In comparison to the smooth hull where y+ increased, the skin friction coefficient decreased. Figure 3 also shows the change in C_F between the standard k-ω SST turbulence model and the SSTQCRCC model. For a given y+ value, the SSTQCRCC turbulence model produced a lower value of C_F by an offset of between 0.000135 and

0.00015. Figure 4 shows the circumferential profiles of axial velocity at two radial positions, $r/R_{max} = 0.25$, and with three different numerical methods. Firstly, the results with the modified prism layer settings, but the standard smooth wall boundary condition; secondly, the results with the rough wall boundary condition, and lastly results with the rough wall boundary condition and a non-linear variant of the SST turbulence model. These results show that using the rough wall boundary condition caused the axial velocity profiles for the different y+ values to become closer in value to each other. However, there were still small differences between y+ values. Comparing the axial velocity profile, at a radius of $r/R_{max} = 0.25$, for the SSTQCRCC turbulence model to the standard SST model, the profile between 20 degrees and 70 degrees for the standard SST model increased to a peak and then decreased. However, for the SSTQCRCC model, there was a flat region in this part of the velocity profile at this specific radius; this matches the trends observed in the experimental data.

Circumferential profiles of turbulent kinetic energy at $r/R_{max} = 0.25$ with three different numerical methods are presented in Figure 5. The CFD turbulent kinetic energy was normalised with the free-stream velocity of 3 m/s. This was to compare against the measured data, which was provided as normalised velocity fluctuations. The turbulent kinetic energy profiles were similar across the different y+ values tested. With the smooth wall definition, the experimental data was slightly above the CFD data at the peaks of the profile. Adding roughness to the hull causes the difference in turbulent kinetic energy, seen between the target y+ values, to be reduced. Using the k-ω SSTQCRCC turbulence model yielded differing results for the turbulent kinetic energy. The turbulent kinetic energy profile matched the measured data fairly well, except between 20 and 60 degrees where the CFD data increased and the experimental data remained flat.

4 Conclusions

A study has been conducted to understand the sensitivity of CFD predictions of resistance to variations in the near-wall mesh, when using STAR-CCM+. This sensitivity has become apparent during recent studies on resistance of model scale submarines, and means that a very fine near-wall mesh is required to obtain accurate predictions of the residuary resistance. While this is feasible for simple, fair, unappended hull forms, it is difficult to achieve on a more detailed, realistic hull form due to the extremely high aspect ratio cells that are required. To mitigate the sensitivity of the solution to the near-wall mesh spacing, a slightly rough-wall boundary condition was implemented, with roughness heights calibrated as a function of the first cell height. This approach enabled more consistent predictions of resistance with different mesh densities, as shown on the SUBOFF test cases. A further update has been made which better recovers the smooth wall behaviour on very fine near wall meshes, as well as improving the prediction of wall shear stress around the fore-body of the submarine. The method was tested on the SUBOFF AFF1, axisymmetric body, and the AFF3 variant, with aft control surfaces. These also showed the sensitivity of the skin friction to the near-wall mesh spacing with the smooth wall, but the rough wall boundary condition successfully reduced the sensitivity, and hence the uncertainty in the predictions. Comparisons of flow quantities showed good agreement with the measured data, particularly when using the SST model with quadratic constitutive relation.

Acknowledgements

The authors gratefully acknowledge the support provided by the SDA of the UK MoD, which enabled the research and development under the Maritime Strategic Capability Agreement. The authors are also grateful to Samvir Thandi and Mark Beal for discussions during the early stages of this work.

References

[1] NASA Langley Research Center Turbulence Modeling Resource, 2D Zero Pressure Gradient Flat Plate Verification or Validation Cases, https://turbmodels.larc.nasa.gov/flatplate_val_ypluseffect.html, 2024.
[2] Eca, L., Pereira, F.S, Vaz, G., Viscous flow simulations at high Reynolds numbers without wall functions: is y+~1 enough for the near wall cells, Computers and Fluids, Vol. 170, pp.157-175, 2018.
[3] Korkmaz, K.B., Werner, S., Bensow, R., Numerical friction lines for CFD based form factor determination, VIII International Conference on Computational Methods in Marine Engineering, MARINE 2019, 2019.
[4] Hellsten, A., Some improvements in Menter's k-ω SST turbulence model, 29th AIAA Fluid Dynamics Conference, AIAA 98-2554, 1998.
[5] Liu, H.-L. and Huang, T. T., Summary of DARPA SUBOFF Experimental Program Data, DARPA, CRDKNSWC/HD-1298-11, June 1998.

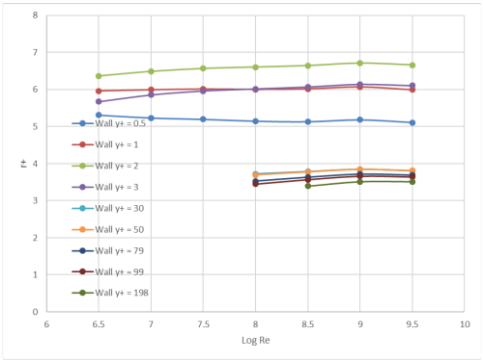

Figure 1: r+ as a function of Reynolds number and wall y+.

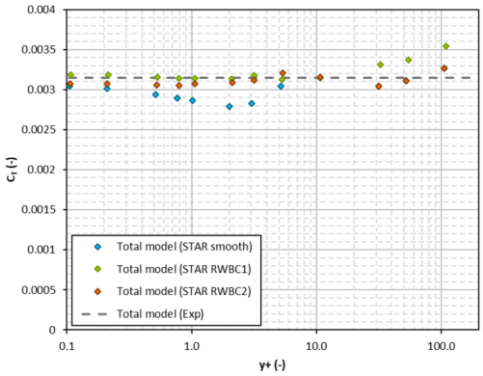

[a]

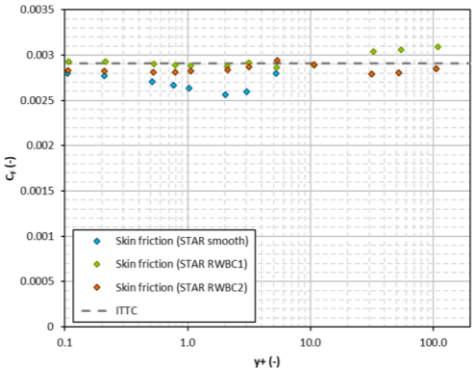

[b]

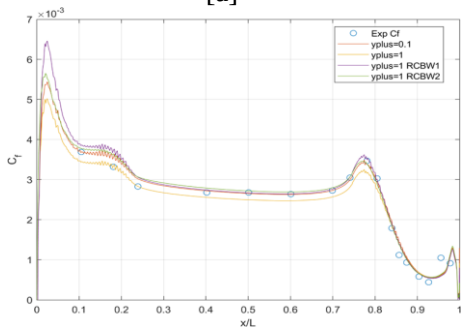

[c]

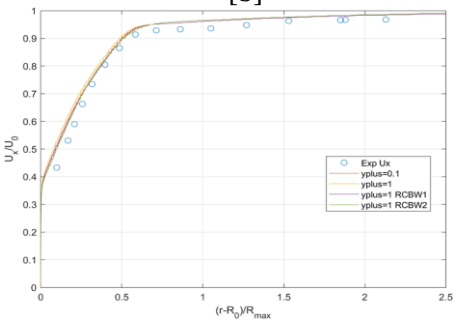

[d]

Figure 2: [a] Total resistance coefficient for SUBOFF AFF1, with and without RWBC [b] Frictional resistance coefficient for SUBOFF AFF1, with and without RWBC [c] Experimental comparison of skin friction coefficient along the hull surface [d] Experimental comparison of radial variation of axial velocity at x/L = 0.978.

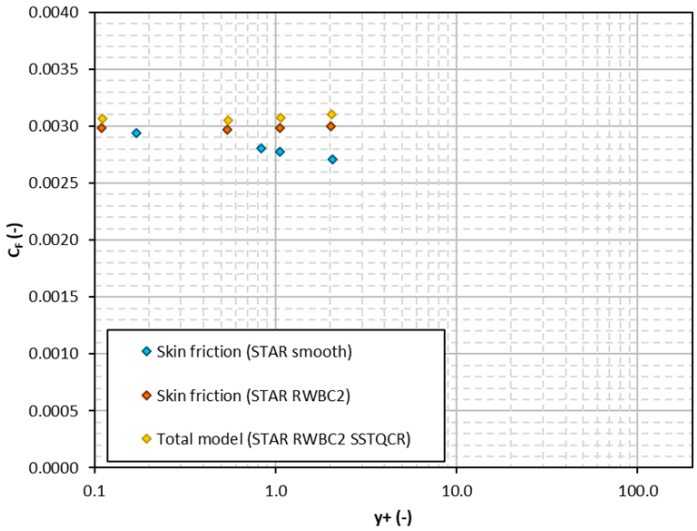

Figure 3: : Effect of rough wall boundary condition on skin friction coefficient.

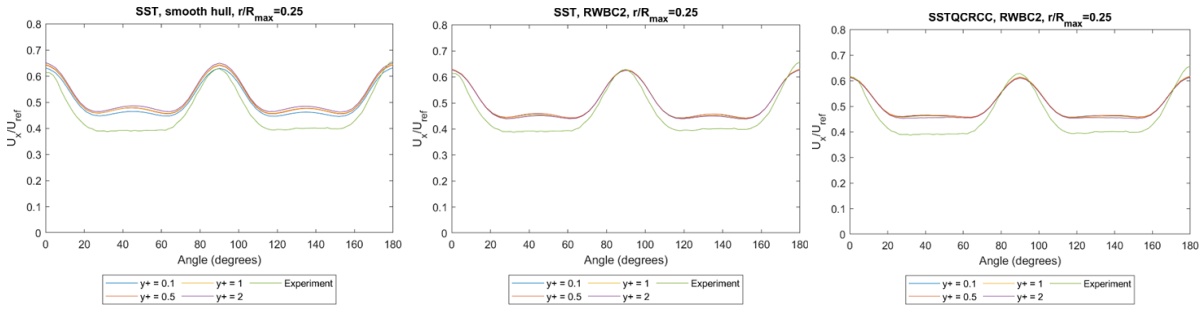

Figure 4: Axial velocity profiles at x/L=0.978.

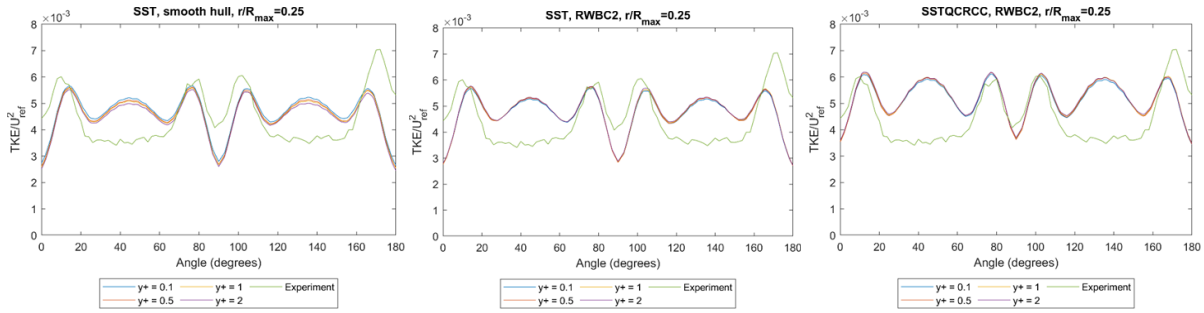

Figure 5: Turbulent kinetic energy profiles at x/L=0.978.

26th Numerical Towing Tank Symposium (NuTTS)
23-25 October 2024 - Duisburg, Germany

Quantifying the effect of turbulence intensity on turbulence-interaction noise of an airfoil using scale-resolving simulations

Gert J. Dekkers*†, Artur K. Lidtke†, Thomas P. Lloyd†, Fernanda L. dos Santos†, and Gabriel D. Weymouth*

*TU Delft, Delft/The Netherlands, † MARIN, Wageningen/The Netherlands
gertdekkers07@gmail.com

1 Introduction

Noise pollution from ships is known to negatively impact wildlife. It is the low-frequency broadband noise component that can travel over large distances and is mostly relevant for marine wildlife. In the absence of cavitation, such as for tidal turbines, naval surface vessels and submarines, the low-frequency noise component is dominated by the interaction of the body with a turbulent inflow. The inflow turbulence generates pressure fluctuations on and near the surface of the body, thereby radiating sound to the far-field. This turbulence-interaction phenomenon is not fully understood yet.

The semi-analytical model by Amiet (1975) can be used to predict far-field turbulence-interaction noise for an airfoil, which predicts the far-field sound pressure level (SPL) as a function of the square of the turbulence intensity (TI). Amiet's model, however, does not account for the geometrical properties of the airfoil. This work presents the results of a numerical study that aims to determine the effect of the turbulence intensity on the far-field turbulence-interaction noise for a NACA0008 airfoil. A comparison of the numerically predicted far-field noise to Amiet's work is performed to evaluate the accuracy of Amiet for different receiver angles. The Ffowcs Williams and Hawkings (1969) (FW-H) acoustic analogy, which separates the generation and propagation of the sound, is adopted to estimate the SPL. Validation of the inflow turbulence and generated sound are performed by comparing one of the cases to a published experimental and numerical investigation for the same airfoil.

2 Methodology

2.1 Numerical method and turbulence generation

Numerical simulations are performed using the finite volume code ReFRESCO developed by MARIN in collaboration with universities and other partners. It solves the unsteady, incompressible Navier-Stokes and mass continuity equations using a finite-volume and time-implicit framework. ReFRESCO allows the use of both structured and unstructured meshes as well as turbulence and cavitation models. Pressure-velocity coupling based on the SIMPLE scheme is used. The FW-H framework has been implemented as a run-time postprocessing tool with a solid data surface coincident with the surface of the airfoil.

A scale-resolving simulation (SRS) setup is used already validated in the work by Lidtke et al. (2022). The change between resolving and modelling of the turbulence is made by the improved delayed detached eddy simulations (IDDES) model based on Gritskevich et al. (2012). It employs the $k-\omega$ shear stress transport model, switching between LES and RANS based on the turbulent length scale. A SRS approach is preferred due to its accuracy in the bulk of the flow (LES) and low computational time near the airfoil due to the lower spatial resolution required by RANS, which is sufficient for the current work.

All simulations are run with a fixed time step of $\Delta t = 3.55 \times 10^{-5}$ s, or based on the chord and set inflow speed $\Delta t^* = \Delta t \cdot U_\infty / c = 3 \times 10^{-3}$. Simulations with a larger timestep showed unsatisfactory results regarding the turbulence resolution and the Courant number, which remains lower than 15 for the current timestep with high values only sporadically found near the airfoil in the RANS region. In the bulk of the flow (LES region), the Courant number was significantly lower averaging below 1.

Turbulence is generated using an inflow turbulence generator (ITG) that synthetically generates turbulence based on the work of Kim et al. (2013) and implemented in ReFRESCO by Klapwijk et al. (2020). At each timestep, body forces are applied at points (i) on a plane with its normal in the direction of the flow. At each point, desired Reynolds stresses are converted to velocity fluctuations (u_i'), which in turn

determine the body forces ($F_{b,i}$) based on the instantaneous velocity (u_i) according to

$$F_{b,i} = \frac{\rho \overline{u_i}(\overline{u_i} + u_i' - u_i)}{L_{ITG}} \cdot b. \tag{1}$$

Here, L_{ITG} is the thickness over which the body forces are spread in the flow direction, and b is the amplification factor used to assure faster convergence to the desired values. One can recognise the Reynolds decomposition in the numerator of Eq. (1). In this case if the instantaneous velocity fluctuation (u_i') is readily achieved at that point ($\overline{u_i} - u_i = -u_i'$) the body force term iterates towards zero within the timestep, thereby improving the solver's convergence behaviour. This is also required for divergence-free turbulence, which, if not met, can otherwise lead to spurious numerical noise that can pollute the solution.

2.2 Case description

Fig. 1 shows a side view of the numerical setup used. The coordinate system has its origin at the leading edge of the airfoil (with x in the flow, y in the vertical and z in the spanwise directions). The boundary conditions of the sides are periodic to prevent interactions between them as much as possible, making the total span $d = 0.67c$. Dampening boxes are placed upstream of the ITG and downstream of the airfoil to drive the local flow velocity to freestream conditions, thereby reducing interactions with the inlet and outlet boundaries. Inflow turbulence is not generated over the full height of the domain to prevent strong interactions with the top and bottom boundary conditions and to save computational time. The acoustic receivers for the FW-H computations are placed at 1.5 m in a circle around the airfoil at every two degrees with the array's centre at midspan and half of the chord. The angle defining the placement of the probes is θ with $\theta = 0$ degrees in the direction of the trailing edge. Table 1 presents a comprehensive overview of the inputs for the four numerical cases investigated in this paper. These cases only differ in turbulence intensity calculated based on the local mean velocity ($\overline{u}$) and the root-mean-square (RMS) of the local velocity fluctuations (u_{rms}); all other inputs remain constant. A mesh[1] resolution study has shown mesh convergence for the inflow turbulence, wall pressure on the airfoil and far-field acoustics. Similar results were also found for a study in which the spanwise domain size was varied. Those results are not included in this paper for brevity. More details, also about the setup, can be found in the work by Dekkers (2024).

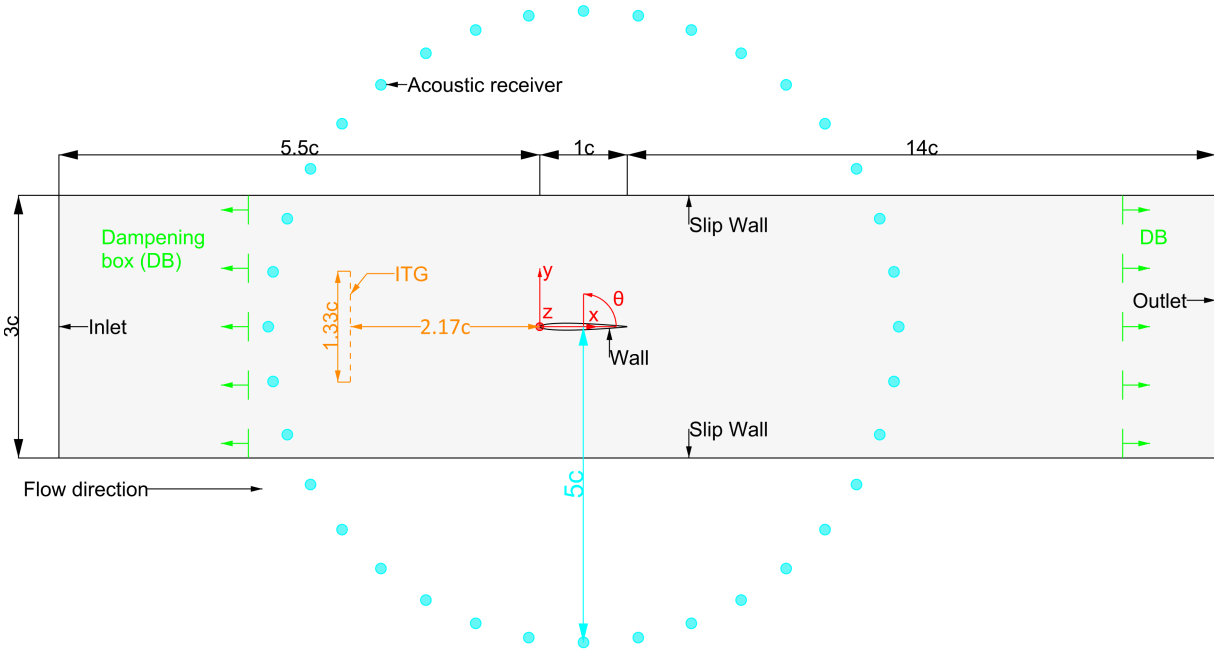

Fig. 1: Side view of the numerical setup. All distances are visualised based on the chord of the NACA0008 airfoil (c = 300 mm). The slice is taken at midspan of the airfoil.

[1]The term *mesh* refers to the computational mesh used in the numerical simulations. A *grid* refers to the grid used for turbulence generation by the ITG as explained in Section 2.1.

Table 1: Parameters of the four numerical turbulence intensity cases. Case C2 is used for validation.

Parameter	**Symbol**	**Case 1**	**Case 2**	**Case 3**	**Case 4**
Label figures	N.A.	C1: TI=13.5%	C2: TI=11.4%	C3: TI=7.6%	C4: TI=4.1%
Airfoil type	N.A.	NACA0008			
Airfoil chord [m]	c	0.3			
Airfoil span [m]	d	0.2			
Airfoil leading edge radius [mm]	r_{LE}	2.1			
Turbulence intensity [%] At $x/c = 0$ in empty domain	$TI = u_{rms}/\overline{u}$	13.5	11.4	7.6	4.1
Inflow velocity [m/s]	$U_\infty = U_{inf}$	25.26 ($Re_c \approx 5.1 \times 10^5$)			
Integral length scale [-]	Λ_f / r_{LE}	22.6	14.9	14.3	10.6

3 Validation results

Two separate sets of validation are performed. First, validation of the inflow turbulence is performed to show that the current setup can exercise realistic homogeneous isotropic turbulence downstream of the ITG. This was done in an empty domain (without the airfoil) to allow for more accurate tuning of the ITG. Numerical results are compared to experimental results by Dos Santos et al. (2022), who used grid-generated turbulence. Fig 2a shows the turbulence intensity over the domain with a peak just after the ITG. A clear decay after the ITG is visible, signifying the need for a development length for the turbulence. From $x/c = -0.5$ onwards, there is a good agreement between numerical and experimental results, showing that the ITG has been accurately tuned so that the turbulence can develop to its intended state.

Fig. 2b depicts the mean decidecade band power density[2] of the streamwise velocity. Experimental spectral levels and frequencies have been scaled based on the difference in inflow velocity, local velocity fluctuations and local integral length scale. For $f < 50$ Hz the numerical spectral level is occasionally lower relative to the experimental levels. For $50 < f < 1400$ Hz, an over-prediction of a maximum of five decibels is observed. A similar slope of the numerical spectrum relative to the experimental spectrum and the power law with slope -5/3 is found in this frequency range. Both are indicative of isotropic turbulence at this point in the flow. It was also observed that the RMS of the velocity fluctuations in all directions are similar, indicating the isotropy of the turbulent flow generated. An under-prediction of the numerical spectrum relative to the experimental spectrum is observed for $f > 1400$ Hz. This aligns with an estimate of the mesh cut-off frequency of $f_{mesh} = \frac{0.6 \cdot U_\infty}{8 \cdot \Delta x} \approx 1100$ Hz, with $0.6 \cdot U_\infty$ an estimate for the convection velocity and Δx the average cell size between the ITG and the airfoil. Generally, good agreement within +/- 5 dB is found between the numerical and experimental spectra for $60 < f < 1400$ Hz.

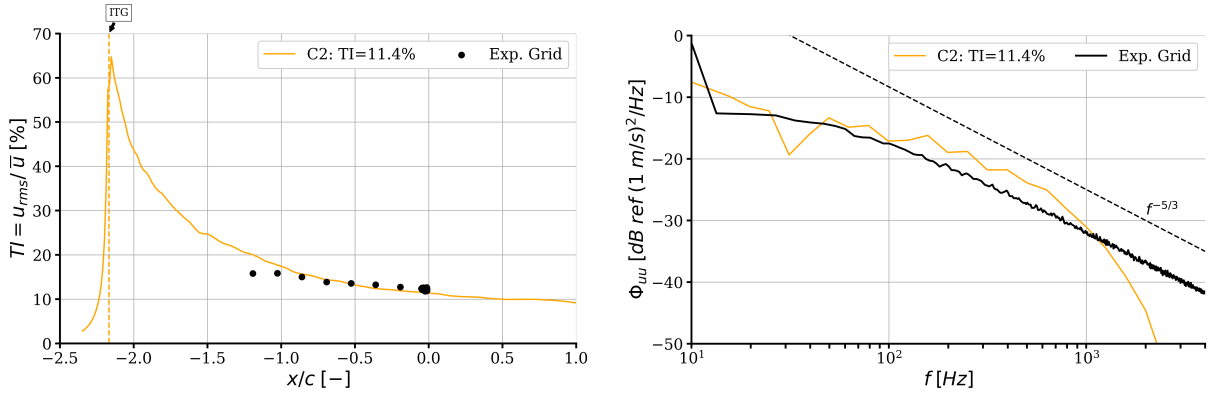

(a) Turbulence intensity at midspan in the direction of flow.

(b) Mean decidecade band power density of the streamwise velocity at the intended leading edge and midspan.

Fig. 2: Numerical and experimental results. Experimental data by Dos Santos et al. (2022) is scaled for (b) due to a difference in inflow velocity, local velocity fluctuations and local integral length scale.

[2]This is a smoothing of the power spectral density (PSD) as calculated by the Welch algorithm implemented in Python assuming a 50% overlap between each segment. Smoothing operations are performed using a bandwidth top hat filter.

The second validation set regards the airfoil acoustics. Experimental far-field noise results for grid-generated turbulence were not available, therefore comparison is made to far-field noise results for rod-generated turbulence by Dos Santos et al. (2023). Due to its similarity, a comparison is also made to a lattice-Boltzmann method (LBM) simulation by Ribeiro et al. (2023). Fig. 3 shows the noise spectra for a receiver at $\theta = 90$ degrees. Experimental data outside the bounds indicated by 2 and 4 is to be disregarded since the wind tunnel background noise dominates the signal outside these bounds. Any data around the rod-shedding frequency, indicated by 1, is also irrelevant since the associated coherent turbulent structures are absent in the numerically-generated isotropic turbulent flow. Experimental validation data is, therefore, only available for $400 < f < 2500$ Hz. Experimental acoustic data is scaled for the difference in local mean velocity and RMS of the local velocity fluctuations.

For $600 < f < 2500$ Hz the overlap between the numerical and experimental sets is very good with a maximum difference of about 5 dB. The numerical data also shows the same trend observed from the experimental data regarding the high-frequency decay of the noise. The slope of the numerical spectrum is similar to that of the experiments, indicating that the solver can accurately capture the high-frequency decay. The difference in spectral levels for $160 < f < 600$ Hz is likely explained by the coherent turbulent structures that carry energy to higher frequencies, which are not present in the simulation.

Comparison of numerical data to the LBM results shows excellent overlap for $10 < f < 1500$ Hz. This is expected since both sets are for grid-generated turbulence with similar inflow velocities. The difference for $f > 1500$ Hz shows that the current methodology can better capture the high-frequency decay behaviour when compared to experimental trends. The LBM result also shows that the solver can capture the low-frequency trend, which could not be observed from experimental data.

The key takeaway is that the current methodology can accurately capture the high-frequency trend of far-field noise for $600 < f < 2500$ Hz as observed from the experimental data. Additionally, the current setup is accurate for $10 < f < 1500$ Hz compared to the LBM simulation data. For $f > 2500$ Hz, does the numerical data decay faster compared to experimental results, where the latter might already be influenced by the wind tunnel background noise.

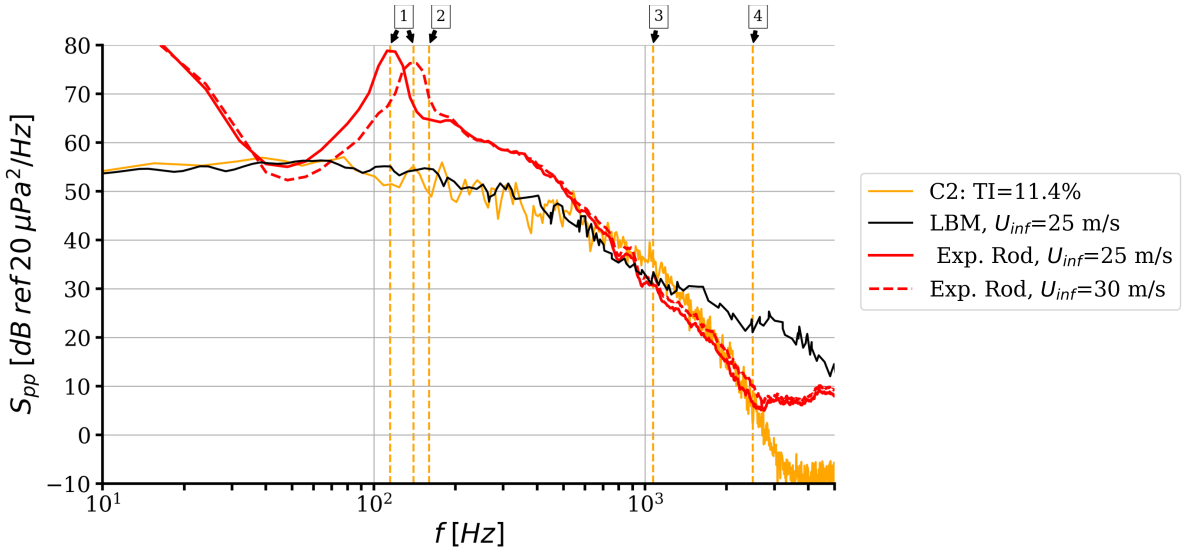

Fig. 3: PSD of the far-field noise for the numerical, LBM (Ribeiro et al. (2023)) and scaled experimental (Dos Santos et al. (2023)) cases. Data is for a receiver at $\theta = 90$ degrees. The numerical case C2 is scaled for the limited span. The dashed vertical lines signify the rod-shedding frequencies 1, lower and upper bounds of experimental acoustic data 2 4 and estimated mesh cut-off frequency 3.

4 Comparison with the Amiet model

Four cases, with parameters shown in Table 1, are evaluated. The labels in all of the presented plots refer to the turbulence intensity levels obtained from empty domain simulations. Fig. 4a shows the turbulence intensity up to the leading edge for these cases. As the TI level decreases from 13.5% to 4.1%, the TI behavior becomes more uniform along the x-direction as seen from the leading edge ($x/c = 0$).

Fig. 4b shows the far-field noise spectra for the four cases at $\theta = 90$ degrees. For $100 < f < 2000$ Hz, cases C1, C2 and C3 show similar differences and decay behaviour. Case C4 shows far-field energy levels much lower than expected while the difference in intensity is similar between the cases, see Fig. 4a. From the full work by Dekkers (2024), it became clear that there is a distinct coupling between the turbulence intensity and the integral length scale. Case C4 has the lowest length scale, likely too small for the mesh to resolve accurately thereby significantly underpredicting the energy levels.

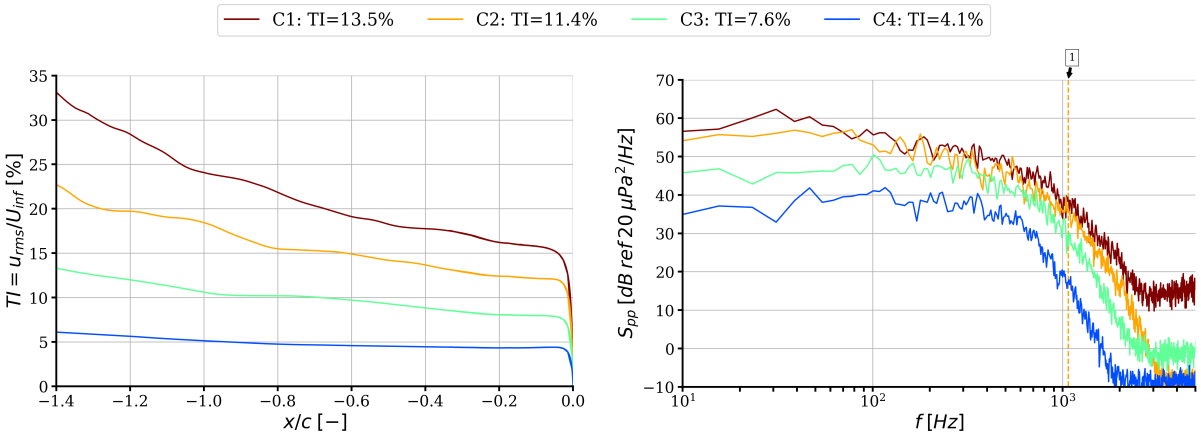

(a) Turbulence intensity at midspan as a function of the distance upstream of the leading edge.

(b) PSD of the far-field noise at $\theta = 90$ degrees. The dashed line 1 is the estimated mesh cut-off frequency.

Fig. 4: Numerical results for TI and acoustics. Numerical data in (b) is scaled for the limited span.

Integration of the mean decidecade band power density gives the broadband sound pressure level (SPL) in dB. Fig. 5 shows the SPL for the numerical cases at receiver angles $0 \leq \theta \leq 90$ degrees. The starting points for the Amiet scaling ($SPL = f(TI^2)$) are arbitrarily chosen and do not represent the actual outcomes of the Amiet model. Fits through the data are only performed for cases C1, C2 and C3 since case C4 likely contains errors induced by the mesh/solver. Fitting is performed using the curve-fit procedure from the scipy.optimize library in Python. The baseline curve to fit was chosen as

$$SPL(TI) = a + 10 \cdot log_{10}(TI^b), \tag{2}$$

where a and b are coefficients determined by the fitting procedure. For clarity, data is only presented for the quadrant $0 \leq \theta \leq 90$ degrees. Similar results are, however, found for all three other quadrants.

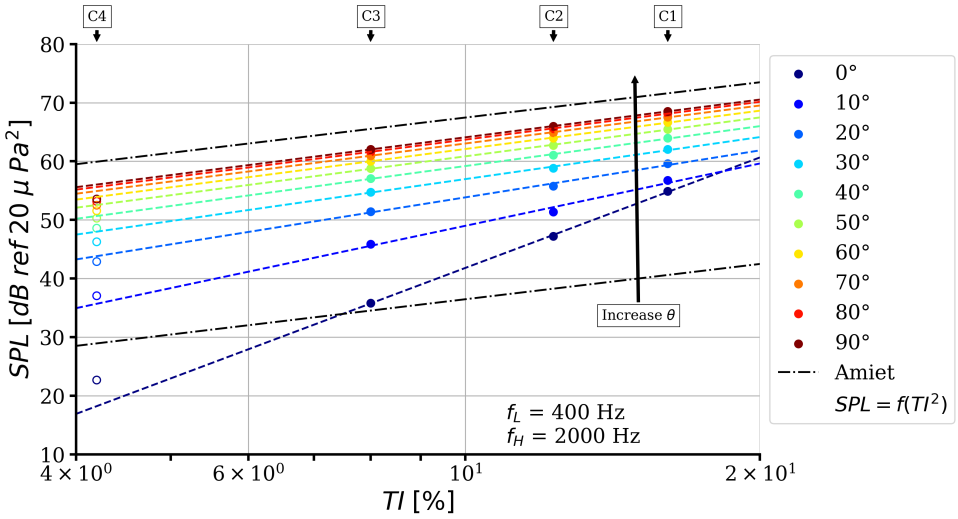

Fig. 5: Sound pressure level (SPL) against turbulence intensity (TI) at different receiver angles for the numerical cases. The Amiet curve depicts the theoretical increase of SPL for a linear increase of turbulence intensity. Dashed lines represent fits through the solid data points; hollow data points are excluded from the fits. f_L and f_H signify the lower and upper bound for the SPL integration, respectively.

For a receiver at $\theta = 90$ degrees a limited increase in SPL is observed with increased turbulence intensity. On the other hand, at $\theta = 0$ degrees a much steeper increase of the SPL is observed for the same increase in intensity. Table 2 lists the coefficients b for the fits performed following Eq.2, thereby representing the relation $SPL = f(TI^b)$. Note that the coefficient, as predicted by Amiet, independent of the receiver angle, is $b = 2$. It can be concluded that the scaling, as introduced by Amiet, is accurate for receiver angles closer to 90 degrees. The theory becomes less accurate for receivers aligned more closely with the flow direction. This connects with Amiet's assumption that the airfoil is a flat plate of negligible thickness, meaning that the interaction is not considered in the model. These interaction effects seem to dominate for receiver angles in the flow direction.

Table 2: Fitting coefficient b based on the numerical fits for different receiver angles.

Receiver angle θ [degrees]	0	10	20	30	40	50	60	70	80	90
Slope, fitting coefficient b [-]	6.26	3.53	2.66	2.38	2.26	2.20	2.17	2.15	2.14	2.14

5 Conclusion

The turbulence intensity effect on the far-field radiated noise for a NACA0008 airfoil has been addressed. Results from the FW-H acoustic analogy have been compared to the semi-analytical model by Amiet. The IDDES turbulence model, in combination with the inflow turbulence generator, has been shown to produce an accurate representation of homogeneous isotropic turbulence upstream of the airfoil. Reasonable results on far-field acoustics have been found, with agreement relative to both experimental and numerical (LBM) values available in literature to within approximately five decibels. Predicted far-field noise levels have been shown to follow the experimentally observed trends and exhibit the expected high-frequency decay behaviour. Results show that the far-field noise scaling with the turbulence intensity proposed by Amiet holds for receiver angles directly above the airfoil, but the theory fails to predict the noise levels accurately for receiver angles that are more closely aligned with the flow direction.

Future work should focus on further optimising the current inflow turbulence generator to allow decoupling of the turbulence intensity from the integral length scale. Also, effort should be put into allocating the acoustic far-field noise to the surface pressure distribution on the airfoil. One way to do so is by dividing the FW-H surface into strips. This will ensure a better understanding of the turbulence-interaction phenomenon that generates the noise from the interaction with the airfoil, thereby allowing investigations into more complex problems, such as a propeller in a ships wake. Finally, different airfoils should be evaluated to investigate the validity of Amiets predictions for small directivity angles further.

References

R.K. Amiet (1975). Acoustic radiation from an airfoil in a turbulent stream. *J. of Sound and Vibration*, **41**(4), 407–420.

J. Ffowcs Williams and D. Hawkings (1969). Sound Generation by Turbulence and Surfaces in Arbitrary Motion. *Philosophical Transactions of the Royal Society of London. Series A, Mathematical and Physical Sciences*, **264**(1151), 321–342.

A.K. Lidtke, T. Lloyd, F.H. Lafeber, and J. Bosschers (2022). Predicting cavitating propeller noise in off-design conditions using scale-resolving CFD simulations. *Ocean Engineering*, **254**, 111176.

M.S. Gritskevich, A.V. Garbaruk, J. Schutze, and F.R. Menter (2012). Development of DDES and IDDES Formulations for the $k - \omega$ Shear Stress Transport Model. *Flow, Turbulence and Combustion*, **88**(3), 431–449.

Y. Kim, I.P. Castro, and Z.T. Xie (2013). Divergence-free turbulence inflow conditions for large-eddy simulations with incompressible flow solvers. *Computers & Fluids*, **84**, 56–68.

M. Klapwijk, T. Lloyd, G. Vaz, and T. van Terwisga (2020). Evaluation of scale-resolving simulations for a turbulent channel flow. *Computers & Fluids*, **209**, 104363.

G.J. Dekkers (2024). Numerical Predictions of Airfoil Acoustics with Inflow Turbulence. *MSc Thesis TU Delft*, **MT.23/24.030.M**. Available at `https://repository.tudelft.nl/`.

F.L. Dos Santos, L. Botero-Bolivar, C. Venner, and L.D. De Santana (2022). Modeling the Turbulence Spectrum Dissipation Range for Leading-Edge Noise Prediction. *AIAA J.*, **60**(6), 3581–3592.

F.L. Dos Santos, L. Botero-Bolivar, C.H. Venner, and L.D. De Santana (2023). Inflow turbulence distortion for airfoil leading-edge noise prediction for large turbulence length scales for zero-mean loading. *The J. of the Acoustical Society of America*, **153**(3), 1811–1822.

A.F.P. Ribeiro, F.L. Dos Santos, K. Venner, and L.D. De Santana (2023). Numerical study of inflow turbulence distortion and noise for airfoils. *Physics of Fluids*, **35**(11), 115112.

26th Numerical Towing Tank Symposium (NuTTS)
23-25 October 2024 - Mülheim an der Ruhr, Germany

A VOF-PLIC Algorithm for Modelling the Impact of Breaking Waves on Structures

Fabian Knoblauch*, Widar Wang*, and Hans Bihs*
*Norwegian University of Science and Technology, Norway
fabian.knoblauch@ntnu.no

1 Introduction

The Dynamics of breaking waves are generally of significant interest for coastal engineering disciplines, since they result in considerable slamming forces on structures, when interacting with them (Kamath et al., 2016). A key point for physically accurate modelling of breaking waves is the representation of the free surface. Especially over-topping breaking waves put high demands on the capabilities of the free surface representation method, due to their complex geometries and features such as air cavities and reconnecting surfaces.
Regarding methods for free surface representation, a great variety of different approaches has been developed and implemented in solvers, as the field of Computational Fluid Dynamics has progressed and grown (Düz et al., 2016). One of the methods which have celebrated success over the last decades is the Volume-of-Fluid approach (VOF), which was first described by Hirt and Nichols (1981). A key advantage of the VOF method is the strict fulfilment of mass conservation given by its approach (Pilliod and Puckett, 2004). An inherited problem of VOF are numerical smearing and diffusion of the interface, resulting from its sensitivity regarding the discretisation of fluid advection (Düz et al., 2016). Therefore representation methods have been developed, that shall ensure a sharp interface and capture the phase distribution with sub-grid accuracy. The basic idea is, that in each cell the free surface interface is represented by a line in 2D, or a plane in 3D. The first variant of this approach was given by the Simple Line Interface Calculation method (SLIC), which was first presented by Noh and Woodward (1976). Due to problems arising from SLIC's limitation to orientate its lines along the cartesian coordinate directions, the approach was advanced towards the Partial Linear Interface Calculation method (PLIC), allowing for an arbitrary orientation of the interface (Youngs, 1982).
The VOF-PLIC algorithm consists of three major steps, which feature their own distinct methods (Düz et al., 2016). In the first step, the orientation of the plane, representing the free surface interface within its cell is determined based on the volume fraction field in the surrounding cells. Here a broad spectrum of different approaches on how to determine the plane's normal vector can be found in literature (Düz et al., 2016). The second step is to set the distance of the plane to the cell's centre point, in such a manner that the volume under the plane is the same, as given by the volume fraction field. Again multiple approaches exist, but as the most efficient and precise ones can those be regarded, that solve the given problem analytically, without any iterational solving routines. The original analytical solution was presented by Gueyffier et al. (1999). Recent improvement and simplification of the method done by Lehmann and Gekle (2022) result in an algorithm, that is fast, and straight forward to implement. The final step in the VOF-PLIC method is the advection of the fluid volume fractions by the velocity field. A general problem in the advection of the volume fractions in three-dimensional space is, that the same fluid volume might be transported into multiple cells, which would lead to a violation of mass conservation, finding a suitable scheme for the volume advection is thus a non-trivial problem (Weymouth and Yue, 2010). While schemes for transporting the volumes in three dimensions in a single step exist, they are often considered to be too intricate for implementation (Mohan and Tomar, 2024), which is why the majority of literature focuses on operator split advection schemes (Mohan and Tomar, 2024). In operator split advection schemes, the volume fraction field is advected along each spatial direction individually, resulting in three one-dimensional advection steps. The geometrical advection of the volumes themselves in one dimension is straight forward, though additional terms need to be added to the transport equation, to prevent mass loss in-between the three steps by over or underfilling a cell along one dimension (Weymouth and Yue, 2010).

Even though the principle of the VOF-PLIC method seems to be straight forward, the variety of literature concerning itself with deriving new methods for solving the problems of the normal vector determination and the volume fraction field advection shows, that building a VOF-PLIC method for representation of the free surface in a multi-phase solver is non-trivial and considerations regarding the method's used for realising steps one and three need to be selected and adapted based upon the solver's intended field of usage. The goal of this project is the implementation of a VOF-PLIC method for free surface representation in the existing FDM Navier-Stokes solver REEF3D::CFD presented in Bihs et al. (2016), with the intention of improving the solver's capabilities to resolve the complex free surface deformation and convection in violent breaking waves. Since the current free surface representation in the solver is realised with a signed-distance function level-set method (Sussman et al., 1994), a preliminary version of the VOF-PLIC algorithm can utilise the already existing signed-distance function for extended stability, as it is described by Wang et al. (2009) and Griebel and Klitz (2016).

2 Numerical Methods

2.1 The Numerical Solver

The solver in which the VOF-PLIC algorithm shall be implemented is the Finite Differences Method based Navier-Stokes solver REEF3D::CFD presented in Bihs et al. (2016). As a computational domain, the solver uses a structured staggered grid. Boundary conditions are enforced with an Immersed Boundary Method (Peskin, 1972). For the spatial discretisation of the convection terms in the Navier-Stokes Equations, 5th order Weighted Essentially Non-Oscillatory stencils (Jiang and Shu, 1996) are used. Temporal discretisation is realised with a third order Runge-Kutta scheme (Shu and Osher, 1988). The pressure term in the Navier-Stokes Equations is handled with the Projection Method introduced by Chorin (1968). The resulting Poisson equation for the pressure is solved with the Jacobi-preconditioned BiCGStab algorithm by van der Vorst (1992). Parallelisation is achieved by domain decomposition and Ghost Cells using a Massage Passing Interface (MPI). The free surface is represented with a signed-distance function level-set method (Sussman et al., 1994).

2.2 Free Surface Interface Reconstruction

The free surface interface reconstruction, is the problem of finding the parameters of the plane-equation, that defines the free surface interface in each plane.

$$n_x x + n_y y + n_z z = d \tag{1}$$

The parameters on the left hand side of equation 1 are the plane's normal vector, defining the plane's incline. In a coupled VOF-PLIC/level-set method, as it is described by Griebel and Klitz (2016), the normal vector can be obtained by the gradient of the signed-distance function.

$$\vec{n} = -\nabla\phi \tag{2}$$

Alternate methods, based exclusively on the volume fraction field are given by Youngs (1982), Scardovelli and Zaleski (2003), Cervone et al. (2011) and Weymouth and Yue (2010).

With the normal vector set, the parameter d on the right hand side of equation 1 defines the plane's distance to the cell's centre along its normal vector. This distance needs to be determined such as that the volume in the cell under the plane equals the volume given by the volume fraction. The main issue with this problem is the fact, that different parameters d result in different geometrical cases of the plane cutting the cell, with different equations for the volume, as it is illustrated in figure 2. An analytical solution for this problem is an algorithm given by Lehmann and Gekle (2022), which manages to reduce the number of possible cases down to five, utilising coordinate transformation and symmetry considerations. With the analytical algorithm presented by Lehmann and Gekle (2022), the distance d can be determined precisely without need for further iterative solving methods.

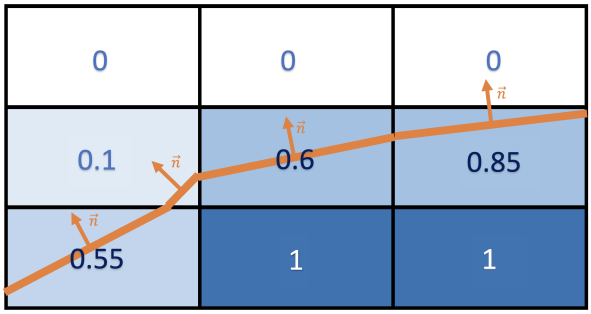

Fig. 1: Schematic illustration of the VOF-PLIC planes representing the free surface, with the free surface interface reconstruction and the normal vector being based upon the volume fraction field in the surrounding cells.

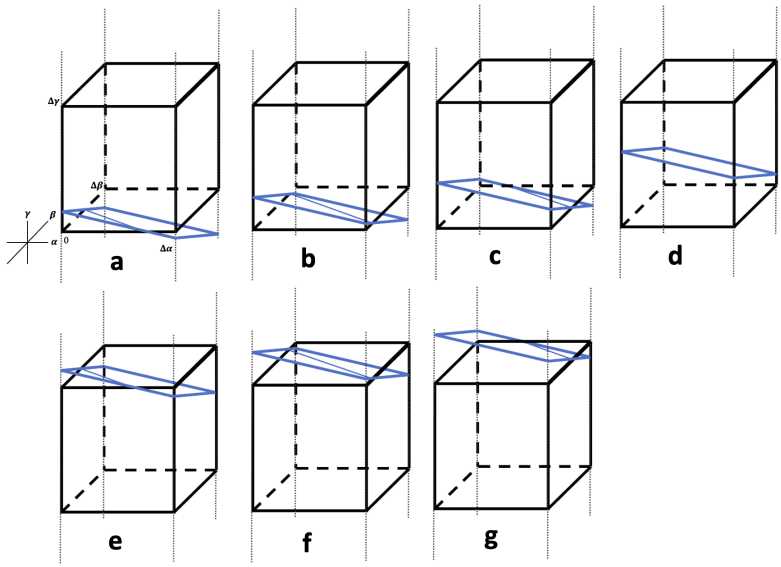

Fig. 2: Schematic illustration of different cases of a plane cutting a cell resulting in different geometrical equations for the volume inside the cell, under the plane.

2.3 Volume Fraction Advection

Following the suggestions of Düz et al. (2016) and Mohan and Tomar (2024), an operator-split advection scheme is chosen. The volume fraction field is thus advected separately along each spatial dimension, with a free surface interface reconstruction occurring before each step. For maintaining the possibility of combining the VOF-PLIC algorithm with the implemented signed-distance function, the same advection scheme is used for transporting the signed-distance function, as it is described by Griebel and Klitz (2016).

$$\xi^{*} = \frac{\xi^{n} - \frac{\partial t}{\partial x}\left(G_{i+1/2} - G_{i-1/2}\right)}{1 - \frac{\partial t}{\partial x}\left(u_{i+1/2} - u_{i-1/2}\right)} \tag{3}$$

$$\xi^{**} = \xi^{*}\left(1 + \frac{\partial t}{\partial y}\left(v_{j+1/2} - v_{j-1/2}\right)\right) - \frac{\partial t}{\partial y}\left(G^{*}_{j+1/2} - G^{*}_{j-1/2}\right) \tag{4}$$

$$\xi^{n+1} = \xi^{**} + \xi^{*}\frac{\partial t}{\partial z}\left(w_{k+1/2} - w_{k-1/2}\right) - \frac{\partial t}{\partial z}\left(G^{**}_{k+1/2} - G^{**}_{k-1/2}\right) \tag{5}$$

Hereby ξ represents both the volume fraction field and the signed-distance function ϕ and G denotes the respective flux across the cell's facet (e.g. $G_{i+1/2} = \xi_{i+1/2}u_{i+1/2}$). Since ϕ is defined in the cell's centre, an interpolation is used to determine the values on the facets (Griebel and Klitz, 2016). For the volume fraction field, the fluxes at the facets are geometrical properties given by the fluid volume under the plane,

that is transported across the facet in one time step, as it is illustrated in figure 3. Hereby, the transported

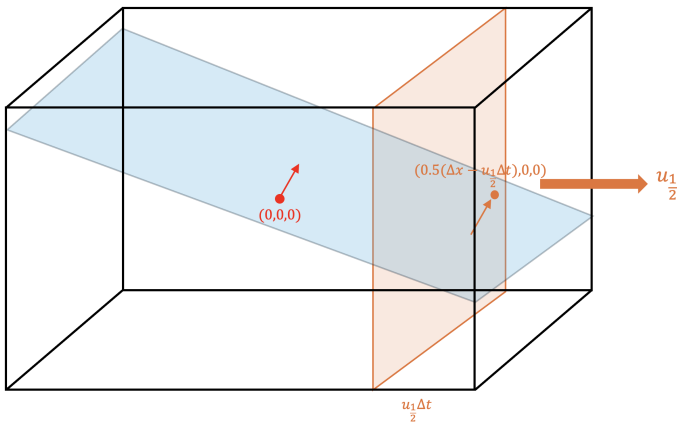

Fig. 3: Schematic illustration of the volume advected across a cell's facet given by the velocity at the facet and the plane in the cell.

volume is given by defining a region of the cell with a length of $u_{i+1/2}\Delta t$ from the facet and considering the volume under the plane inside this advection region. The volume can be determined by rewriting the plane equation 1 with the centre of the advection region as the new coordinate origin and using the volume calculation algorithm given by Lehmann and Gekle (2022) scaled to the advection region as the cell size.

While in the scope of a standalone VOF-PLIC algorithm the entire methodology would be now described, a coupled VOF-PLIC/level-set approach, as it is suggested by Griebel and Klitz (2016) implements additional steps. The transported signed-distance function can be used for additional stability, by serving as a reference for the region in which the free surface should be situated. Artificial diffusion resulting from instabilities in the volume fraction field advection can thus be corrected, by allowing volume fractions only in a band of a certain width around the approximate free surface location given by ϕ. As it is described by Griebel and Klitz (2016), a reasonable width is found by considering the region in which density and viscosity are smoothed for improved robustness.

In return the signed-distance function ϕ is redefined around the free surface by the VOF-PLIC method.

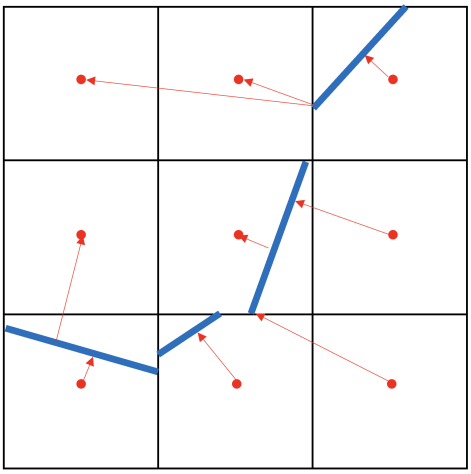

Fig. 4: Schematic illustration of the redistancing of the signed-distance function ϕ based upon the reconstructed interface of the VOF-PLIC method.

Therefore the free surface interface is reconstructed a last time after the complete advection and the closest distance from a cell's centre to a free surface interface plane is determined geometrically using

an algorithm described by Griebel and Klitz (2016). This results in increased precision of ϕ, which is beneficial for the smoothing of density and viscosity, as well as the calculation of the plane's normal vector.

3 Conclusion & Outlook

Preliminary test results of the current implementation of the VOF-PLIC algorithm in the FDM Navier-Stokes solver REEF3D::CFD show an improvement regarding capability of resolving smaller details of the free surface deformation and convection, while retaining numerical robustness. Preliminary test-case results can be seen in figure 5 for a plunging wave breaking on a slope, as well as in figure 6 for a three-dimensional dam-break featuring an obstacle.

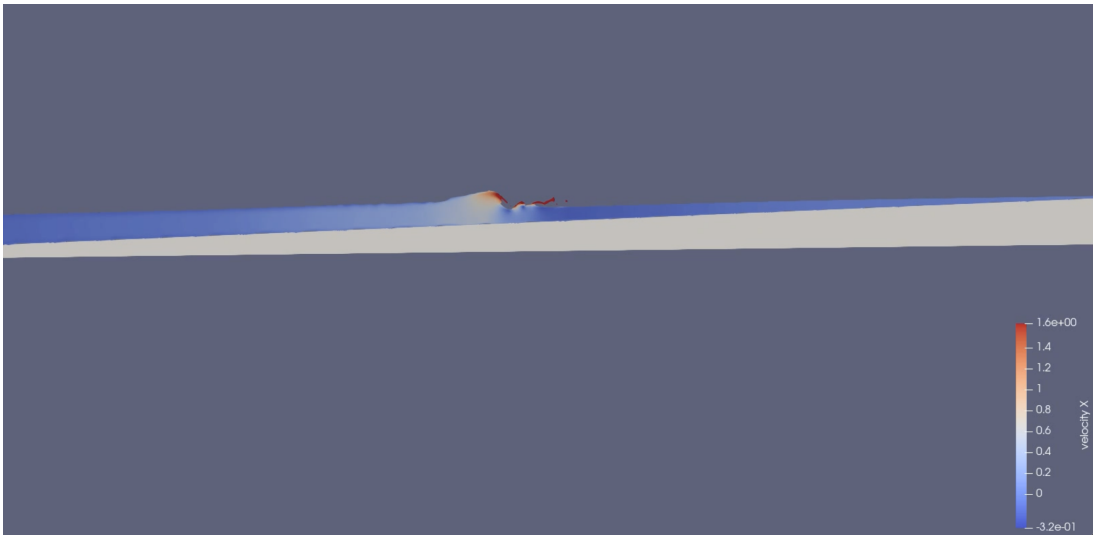

Fig. 5: Test-case of a plunging wave breaking over a slope with the colouration given by the velocity in x-direction

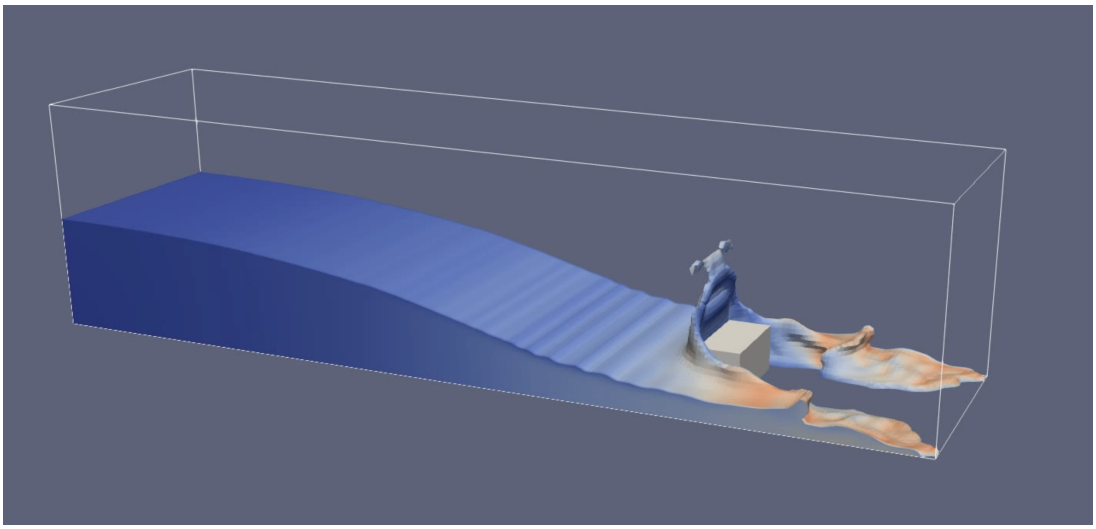

Fig. 6: Test-case of a three-dimensional dam-break with an obstacle

Further work of the project is focused on two separate goals, testing and validating the implemented VOF-PLIC algorithm regarding its precision and numerical stability, as well as the development of a standalone VOF-PLIC version without the transport of the signed-distance function. For the second aspect, emphasis lies on finding a suitable method for defining the normal vector based on the volume fraction field, as well as on finding a suitable advection scheme for the volume fraction field itself. Also

the smoothing of density and viscosity needs to be defined in a way that is independent of the signed-distance function.

Acknowledgements

The authors are grateful for the grants provided by the Research Council of Norway under the IPIRIS project (no. 308843). Some simulations were performed on resources provided by Sigma2 - the National Infrastructure for High Performance Computing and Data Storage in Norway.

References

Bihs, H., Kamath, A., Alagan Chella, M., Aggarwal, A., and Arntsen, Ø. (2016). A new level set numerical wave tank with improved density interpolation for complex wave hydrodynamics. *Computers Fluids*, 140.

Cervone, A., Manservisi, S., and Scardovelli, R. (2011). An optimal constrained approach for divergence-free velocity interpolation and multilevel vof method. *Computers Fluids*, 47(1):101–114.

Chorin, A. J. (1968). Numerical solution of the navier-stokes equations. *Mathematics of Computation*, 22(104):745–762.

Düz, B., Borsboom, M. J. A., Veldman, A. E. P., Wellens, P. R., and Huijsmans, R. H. M. (2016). Efficient and accurate plic-vof techniques for numerical simulations of free surface water waves.

Griebel, M. and Klitz, M. (2016). Clsvof as a fast and mass-conserving extension of the level-set method for the simulation of two-phase flow problems. *Numerical Heat Transfer, Part B: Fundamentals*, 71:1–36.

Gueyffier, D., Li, J., Nadim, A., Scardovelli, R., and Zaleski, S. (1999). Volume-of-fluid interface tracking with smoothed surface stress methods for three-dimensional flows. *Journal of Computational Physics*, 152(2):423–456.

Hirt, C. W. and Nichols, B. D. (1981). Volume of fluid (vof) method for the dynamics of free boundaries. *Journal of Computational Physics*, 39:201–225.

Jiang, G.-S. and Shu, C.-W. (1996). Efficient implementation of weighted ENO schemes. *Journal of Computational Physics*, 126(1):202–228.

Kamath, A., Alagan Chella, M., Bihs, H., and Arntsen, Ø. (2016). Breaking wave interaction with a vertical cylinder and the effect of breaker location. *Ocean Engineering*, 128.

Lehmann, M. and Gekle, S. (2022). Analytic solution to the piecewise linear interface construction problem and its application in curvature calculation for volume-of-fluid simulation codes. *Computation*, 10:21.

Mohan, A. and Tomar, G. (2024). Volume of fluid method: A brief review. *Journal of the Indian Institute of Science*, 104.

Noh, W. F. and Woodward, P. (1976). SLIC (Simple Line Interface Calculation). In van de Vooren, A. I. and Zandbergen, P. J., editors, *Some Methods of Resolution of Free Surface Problems*, volume 59, page 330.

Peskin, C. S. (1972). Flow patterns around heart valves: A numerical method. *Journal of Computational Physics*, 10(2):252–271.

Pilliod, J. E. and Puckett, E. G. (2004). Second-order accurate volume-of-fluid algorithms for tracking material interfaces. *Journal of Computational Physics*, 199(2):465–502.

Scardovelli, R. and Zaleski, S. (2003). Interface reconstruction with least-square fit and split eulerian-lagrangian advection. *International Journal for Numerical Methods in Fluids*, 41:251 – 274.

Shu, C.-W. and Osher, S. (1988). Efficient implementation of essentially non-oscillatory shock-capturing schemes. *Journal of Computational Physics*, 77(2):439–471.

Sussman, M., Smereka, P., and Osher, S. (1994). A level set approach for computing solutions to incompressible two-phase flow. *Journal of Computational Physics*, 114(1):146–159.

van der Vorst, H. A. (1992). Bi-CGSTAB: a fast and smoothly converging variant of bi-cg for the solution of nonsymmetric linear systems. *Society for Industrial and Applied Mathematics.SIAM Journal on Scientific and Statistical Computing*, 13(2):631–14. Copyright - Copyright] © 1992 Society for Industrial and Applied Mathematics; Zuletzt aktualisiert - 2022-10-20.

Wang, Z., Yang, J., Koo, B., and Stern, F. (2009). A coupled level set and volume-of-fluid method for sharp interface simulation of plunging breaking waves. *International Journal of Multiphase Flow*, 35:227–246.

Weymouth, G. and Yue, D. (2010). Conservative volume-of-fluid method for free-surface simulations on cartesian-grids. *J. Comput. Physics*, 229:2853–2865.

Youngs, D. (1982). *Time-Dependent Multi-material Flow with Large Fluid Distortion*, volume 24, pages 273–285.

Comparison of different approaches to couple the high-order spectral (HOS) method with computational fluid dynamics solvers

Eric Heilshorn[1], Kevin J. Maki[1], Robinson Perić[2], Jannes Berndt[2], and Moustafa Abdel-Maksoud[2]

[1]Aaron Friedman Marine Hydrodynamics Lab, University of Michigan, MI 48109, USA
ejheilsh@umich.edu

[2]Institute for Fluid Dynamics and Ship Theory, Hamburg University of Technology (TUHH), Am Schwarzenberg-Campus 4, 21073 Hamburg, Germany
robinson.peric@tuhh.de

1 Introduction

Realistic ocean waves are typically short-crested and nonlinear, and the accurate simulation of ship motions under such conditions is challenging. To model the related physics in computational fluid dynamics (CFD), the typical approach is to model irregular waves as a superposition of linear waves. Reasonable results have been reported even for wave steepnesses outside the theoretical range of validity of linear wave theory (cf. e.g. Knight et al., 2024). However, the range of applicability for linear superposition as the far-field solution is not clear, for two reasons:

First, realistic ocean waves can occur for a wide range of wave steepnesses, including highly nonlinear (possibly breaking) waves. Linear superposition cannot be expected to be valid for typical extreme sea-states, which may be critical for the survivability of ships. Furthermore, numerically, the use of linear theory to prescribe steep waves can result in non-physical wave breaking or other disturbances. Therefore, it can be expected that *after a certain limiting wave steepness, a more accurate far-field solution is required to obtain highly accurate CFD results*. But at what steepness, for which application, and under which wave conditions this limit is reached, is at present unknown.

Second, it was found that the use of *inaccurate far-field solutions can be numerically problematic*. Problems can occur when there is a mismatch between the far-field solution and the computed flow within the domain, as shown in Fig. 1: The wave elevations and phases computed within the domain do not match the far-field solution at the domain boundaries. The consequences are that a) the computed wave may differ substantially from the desired wave and that b) disturbances may be radiated into the domain in the form of undesired wave components (cf. Perić, 2019).

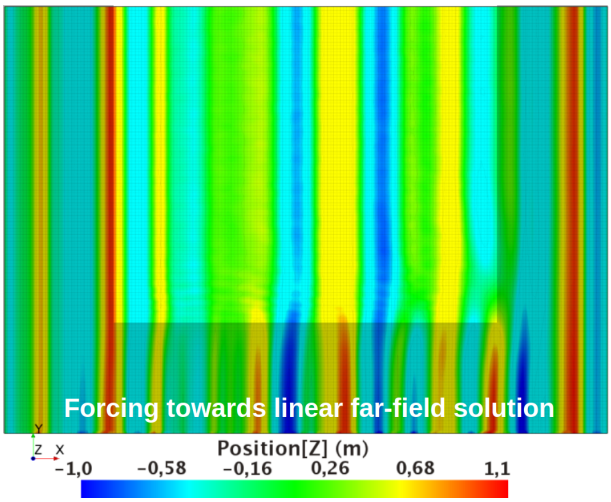

Fig. 1: CFD results for the surface elevation of long-crested irregular waves, generated by forcing the flow solution near the domain boundaries towards the far-field solution from linear wave theory; the case corresponds to pure 2D wave propagation, without wave-disturbing bodies; a strong mismatch between linear solution (bottom boundary) and computed flow (within domain) is visible

To clarify the concerns related to linear superposition as boundary conditions for CFD simulations, and to obtain a more accurate solution approach for steeper irregular waves, the High-Order Spectral (HOS) method is a promising approach. It was developed independently by Dommermuth and Yue (1987) and West et al. (1987) and provides an efficient approach to simulate phase-resolved nonlinear wave evolution over comparatively large distances (hundreds of wavelengths) and simulation durations (hours). Although in principle only applicable to non-breaking waves up to ca. 80% of maximum steepness, extensions have been presented that also model breaking wave events (e.g. Seiffert and Ducrozet, 2018).

The HOS method has been widely used to investigate nonlinear wave phenomena, such as wave-wave interactions due to modulational instability or the occurrence of extreme-wave events. Although the HOS method is nearly 40 years old and well-established in geophysical and mathematical fluid dynamics, it is comparatively rarely applied in CFD simulations.

Coupling of HOS to CFD solvers has been done in several proprietary packages, such as foamStar-SWENSE (Monroy et al., 2010), Naval Hydro Pack (Gatin et al., 2017), or naoe-FOAM-SJTU (Zhuang and Wan, 2021). Bonnefoy et al. (2010) and Ducrozet et al. (2016) published HOS codes as open-source software and developed the Grid2Grid software intended for coupling HOS to various flow solvers. However, in commercial flow solvers like ANSYS Fluent or Simcenter STAR-CCM+, the HOS method is not yet integrated, and efficiently coupling HOS and CFD appears to be not entirely possible 'out-of-the-box', especially for short-crested seas.

Therefore, the aim of the present work is to compare two techniques for coupling the HOS code HOS-OCEAN (Bonnefoy et al., 2010) to commercial flow solver Simcenter STAR-CCM+, i.e. via CFD General Notation System (CGNS) files and via CSV files.

The research questions are:

1. *How large is the increase in computational effort when importing HOS results into STAR-CCM+ via CGNS and CSV files?*

2. *Which options exist to speed up this process?*

For this, 2D-flow simulations of wave propagation are performed. First, a regular wave is generated by applying Stokes 5th-order wave theory at the inlet. Then, the simulation is repeated, storing the solution in a CGNS file. Subsequently, the first simulation is repeated, using flow fields imported as initial and boundary conditions from the stored CGNS solution. It was also repeated using flow fields from the HOS method through CSV files and size-reduced CSV files (vertically thinned-out). The computational efforts are compared and discussed. Finally, results from a 3D-flow simulation are presented, illustrating that the coupling of HOS-OCEAN to STAR-CCM+ was achieved.

2 Methods

Two-dimensional CFD simulations are performed based on a similar setup as in Perić and Abdel-Maksoud (2018), using the software Simcenter STAR-CCM+ version 18.02.008-R8. All fluids were incompressible and the volume of fluid (VOF) method was used to account for the two phases, liquid water and gaseous air, using the High Resolution Interface Capturing scheme (HRIC, cf. Muzaferija and Perić, 1999).

All discretization approximations were of second order. The linearized equation system was solved by the iterative STAR-CCM+ implicit unsteady segregated solver, using an algebraic multigrid method with a Gauss-Seidel relaxation scheme, V-cycles for pressure and volume fraction of water, and flexible cycles for velocity calculation. The under-relaxation factor was 0.9 for velocities and volume fraction and 0.4 for pressure. Per time step, 5 iterations were performed.

The domain was discretized using a rectilinear grid with local mesh refinement around the free surface (cf. Fig. 2). The free surface remained within the region of the finest mesh. The coordinate system was located with $z = 0$ at the calm-water level, z pointing upwards, x pointing in the wave propagation direction, and $x = 0$ at the inlet boundary (left boundary in Fig. 2). The computational domain was a box with dimensions $-0\lambda \leq x \leq 4.8\lambda$ and $-1\lambda \leq z \leq 0.25\lambda$, where λ denotes the wavelength; for irregular

waves, the wavelength corresponding to the peak of the wave-energy spectrum was used. The simulations were performed as quasi 2D, i.e. with symmetry boundary conditions for y-normal boundaries and only 1 cell in y-direction.

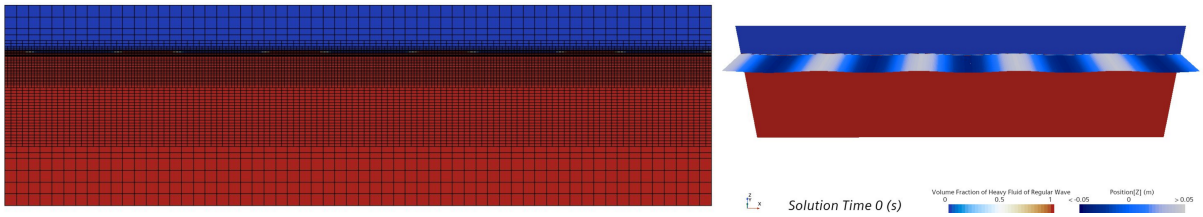

Fig. 2: Left: Reference grid for 2D simulations with air (blue) and water (red) phases; right: initialized surface elevation for regular wave case

For the regular wave simulations, the far-field solution was obtained by Fenton's (1985) Stokes 5th-order theory for wave period $T = 1.6\,\mathrm{s}$, wave height $H = 0.08\,\mathrm{m}$ and water depth 4 m. For the irregular wave simulations, the far-field solution was obtained by HOS-OCEAN for a JONSWAP spectrum with peak wave period $T = 1.6\,\mathrm{s}$, significant wave height $H_\mathrm{s} = 0.055\,\mathrm{m}$ and water depth 4 m.

As boundary conditions, velocity and volume fraction were specified at the inlet and outlet (left and right boundaries left figure from Fig. 2), pressure and volume fraction at the top, no-slip wall boundary condition at the bottom and symmetry conditions on the front and back boundaries.

To minimize undesired wave reflections, forcing zones were attached to the outlet boundary by introducing the source terms

$$q_i = \gamma b(\mathbf{x})(u_{i,\mathrm{ref}} - u_i) \quad , \tag{1}$$

$$q_\alpha = \gamma b(\mathbf{x})(\alpha_\mathrm{ref} - \alpha) \quad , \tag{2}$$

in the conservation equations for horizontal momentum and transport equation for volume fraction, respectively, with reference velocity $u_{i,\mathrm{ref}} = 0$, reference volume fraction α_ref, zone thickness $x_\mathrm{d} = 1.5\lambda$, exponential blending $b(\mathbf{x})$ and forcing strength $\gamma \approx 10\,\mathrm{rad/s}$ optimized as described in Perić and Abdel-Maksoud (2018).

The interface was discretized via ca. 25 (coarse), 50 (medium), and 100 (fine grid) cells per wavelength and 1.5 (coarse) 3 (medium) and 6 (fine grid) cells per wave height. The simulation duration was $t_\mathrm{sim} = 20\,\mathrm{s}$, or 12.5 (peak) periods. The reference simulation was completed within 0.5 hours using 8 processors.

Additionally, 3D-flow simulations were performed of the KCS ship in model scale in long-crested irregular waves using the reference solution computed by HOS-OCEAN. Overset grids were used to model the ship's motions at a Froude number of 0.

3 Results

Figure 3 shows the time required for the 2D-flow simulations to complete, where the abbreviations denote:

- 'Normal': Regular waves using Stokes 5th-order theory
- 'Write CGNS': Same as 'Normal', except that wave fields are written by STAR-CCM+ to CGNS file during simulation
- 'CGNS': Same as 'Normal', except that solution from CGNS file is used as initial and boundary conditions
- 'CSV': Same as 'Normal', except that solution from CSV file is used as initial and boundary conditions; 'Thin' and 'Thin2' denote CSV files with 0.5 and 0.25 times the number of lines; 'Coarse' and 'Fine' denote twice as coarse or fine mesh and time-step

- ‘HOS’: Time to run (‘run’), post-process (‘post’) and export to CSV files (‘CSV’) HOS simulation of long-crested irregular waves; ‘Fine’ denotes a grid with 4x as many cells

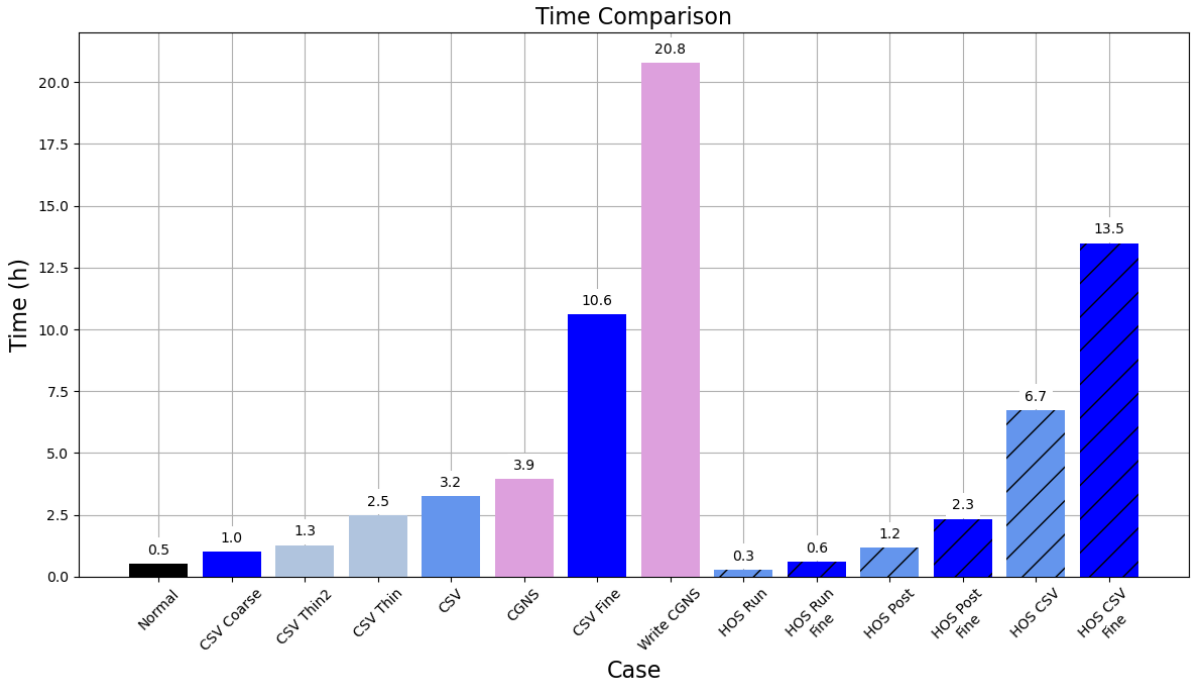

Fig. 3: Durations of 2D-flow simulations and HOS computations

Figure 4 shows that, when the grid and time-step of the CFD simulations are refined, the percentage of time occupied by importing and reading CSV files decreases. This indicates that for typical 3D-flow simulations, the additional effort (e.g. 0.8 hours for the twice thinned CSV file in Fig. 3) due to importing and reading the CSV file will be negligible compared to the total simulation duration (e.g. days or weeks for ship maneuvering in long-crested irregular waves).

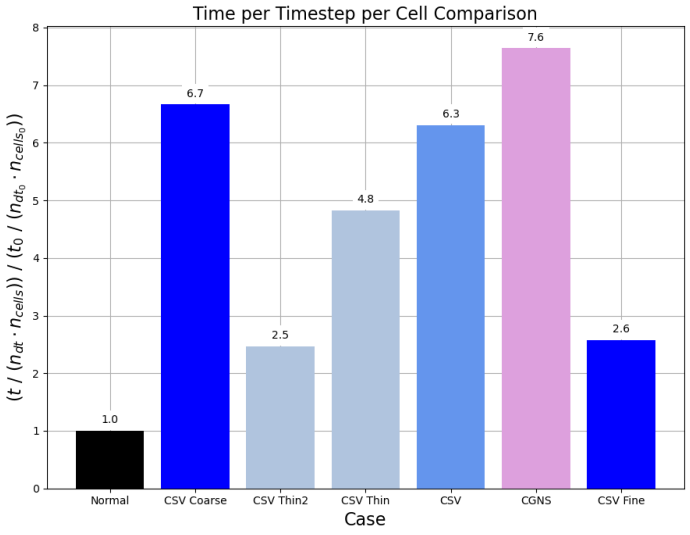

Fig. 4: Simulation durations t from Fig. 3 divided by number of time steps n_{dt} and by number of grid cells n_{cells}, normalized by the corresponding value for case ‘Normal’

Figure 5 shows the computed wave elevation from a 3D-flow simulation with the KCS ship in long-crested irregular waves and demonstrates the feasibility of using the current approach for simulating ship motions in long-crested waves. The contours on the left correspond to the mapped (cell-aligned) solution from the HOS code used as a reference for forcing and boundary conditions. On the right, the results from the CFD computation are presented resulting in smooth contours.

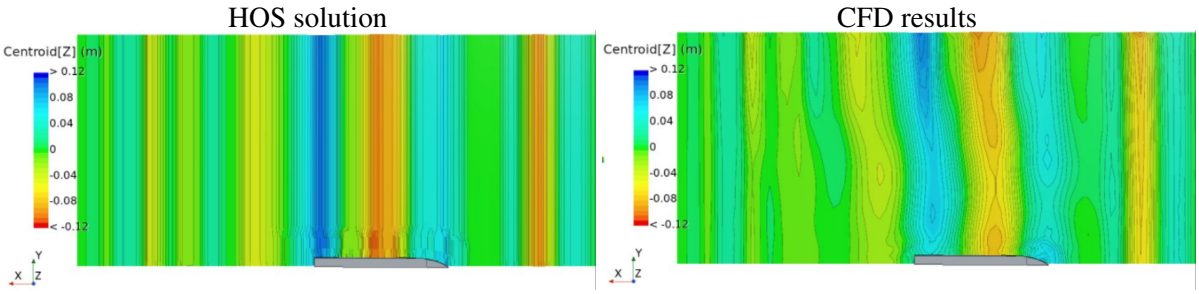

Fig. 5: Surface elevation in 3D-flow simulation with freely floating KCS ship and symmetry condition; left: reference solution from HOS simulation mapped onto the whole domain; right: actual simulation results with forcing zones at all vertical boundaries excluding the lower boundary in the image, where symmetry conditions are applied

4 Discussion

4.1 How large is the increase in computational effort when importing HOS results into STAR-CCM+ via CGNS and CSV files?

Importing and reading the flow fields from CGNS vs. CSV files increased the duration of the 2D-flow simulations substantially, by factor 7.6 (CGNS) and 6.3 (CSV). In practice, though, this is acceptable, because for 3D-flow simulations with the same long-crested irregular waves, importing and reading time will be similar, but the computational effort will be orders of magnitude larger. Hence if the simulation duration is several days, a few hours increase of simulation duration to import and read HOS data appears to be an acceptable trade-off for the increase in accuracy of the far-field solution. However, for short-crested irregular waves, the additional effort can be substantial, particularly when the solution in a large domain is required (e.g. for a ship maneuver).

Although CGNS files were marketed as particularly efficient storage for flow fields, they also contain various other data (boundary conditions, solver settings, etc.). This may be an explanation of why importing flow fields as CSV files was faster and why CSV files had a smaller size.

Writing CGNS files during the 2D STAR-CCM+ simulations increased the computational effort by factor 40, which appears impracticable for most applications. Future studies could investigate how this scales with the number of cells. Storing the data as CSV files could be a more efficient alternative.

4.2 Which options exist to speed up this process?

Importing and reading the flow fields from CSV files has the advantage that these can be easily shortened, e.g. by removing grid points further away from the water surface. By default, HOS-OCEAN writes the flow-field data onto a Cartesian grid, which increases the size of the output files unnecessarily. Therefore, the size of the CSV files can be reduced by removing data points further away from the free surface, as demonstrated in the present work. Discarding 75% of the CSV file reduced the simulation duration by more than 60%. It is expected that the simulation duration can be reduced by > 80% by this approach.

Future research will also investigate importing only the modal data, i.e. wavelengths, amplitudes, and phases of the wave components for each time step. Thus, the HOS solution can be described as a superposition of linear waves, with amplitudes and phases that change at each time step. It is expected that this approach can substantially reduce the time required to import and read the HOS results, particularly for large, short-crested wave fields.

If the aforementioned techniques for increasing the efficiency and memory usage of approaches to import short-crested wave solutions into CFD codes are demonstrated to be effective, CFD simulations

of ship maneuvers in nonlinear short-crested seas could become routine practice both with commercial and research codes in the years to come.

References

Bonnefoy, F., Ducrozet, G., Le Touzé, D. and Ferrant, P. (2010). Time domain simulation of nonlinear water waves using spectral methods, pages 129-164. World Scientific, 04 2010. URL: https://www.worldscientific.com/doi/abs/10.1142/9789812836502_0004, doi:10.1142/9789812836502_0004.

Dommermuth, D. G., and Yue, D. K. (1987). A high-order spectral method for the study of nonlinear gravity waves. Journal of Fluid Mechanics, 184, 267-288.

Ducrozet, G., Bonnefoy, F., Le Touzé, D., and Ferrant, P.. Hos-ocean: open-source solver for nonlinear waves in open ocean based on high-order spectral method. Computer Physics Communications, 203:245–254, 2016. URL: https://www.sciencedirect.com/science/article/pii/S0010465516300327, doi:https://doi.org/10.1016/j.cpc.2016.02.017.

Fenton, J. D. (1985). A fifth-order Stokes theory for steady waves. *Journal of waterway, port, coastal, and ocean engineering*, 111(2), 216-234.

Gatin, I., Vukčević, V., and Jasak, H. (2017). A framework for efficient irregular wave simulations using Higher Order Spectral method coupled with viscous two phase model. Journal of Ocean Engineering and Science, 2(4), 253-267.

Knight, B. G., Mohammadi, Y., Silva, K. M., Heilshorn, E., and Maki, K. J. (2024). ONR Tumblehome Maneuvering in Large-Amplitude Irregular Waves. Proc. 35th Symposium on Naval Hydrodynamics, July 8-12, 2024, Nantes, France.

Monroy, C., Ducrozet, G., Bonnefoy, F., Babarit, A., Gentaz, L., and Ferrant, P. (2010, June). RANS simulations of a CALM buoy in regular and irregular seas using the SWENSE method. In ISOPE International Ocean and Polar Engineering Conference (pp. ISOPE-I). ISOPE.

Perić, R., and Abdel-Maksoud, M. (2018). Analytical prediction of reflection coefficients for wave absorbing layers in flow simulations of regular free-surface waves. *Ocean Engineering*, 147, 132-147.

Perić, R. (2019). Minimizing undesired wave reflection at the domain boundaries in flow simulations with forcing zones. Dissertation at Hamburg University of Technology (TUHH), Germany. DOI: https://doi.org/10.15480/882.2394

Seiffert, B. R., and Ducrozet, G. (2018). Simulation of breaking waves using the high-order spectral method with laboratory experiments: wave-breaking energy dissipation. Ocean Dynamics, 68(1), 65-89.

West, B. J., Brueckner, K. A., Janda, R. S., Milder, D. M., and Milton, R. L. (1987). A new numerical method for surface hydrodynamics. Journal of Geophysical Research: Oceans, 92(C11), 11803-11824.

Zhuang, Y., and Wan, D. C. (2021). Parametric study of a new HOS-CFD coupling method. Journal of Hydrodynamics, 33, 43-54.

WATER WAVE SIMULATIONS USING FULLY NONLINEAR POTENTIAL FLOW: SPECTRAL/*hp* ELEMENT MODELS IMPLEMENTED IN NEKTAR++

Claes Eskilsson
Maritime Department, RISE - Research Institutes of Sweden (claes.eskilsson@ri.se)

Allan P. Engsig-Karup
Department of Applied Mathematics and Computer Science, Technical University of Denmark (apek@dtu.dk)

Using high performance computing (HPC) today it is possible to use fully nonlinear potential flow (FNPF) models for tasks that previously was restricted to asymptotic wave modelling, such as models based on Boussinesq-type or Green-Nadgy equations, due to computational effort. Indeed, as shown in [11] the dispersion properties of a FNPF model can be tuned by the vertical resolution. Thus, the FNPF model can use numerical truncation similar to the analytical truncation of the depth-integrated shallow water models. By means of scalable iterative solver strategies [9] and HPC, cost-efficient screening of extreme waves in larger areas can be performed [6] or in large regional areas [10, 14], e.g. such as fjord regions with complex topography [21].

Looking into existing wave models based on the FNPF equations there is a clear demarcation between numerical models based on classical numerical methods with low-order and high-order convergence rates. Such low-order numerical models are usually employed for wave-body interaction, while the high-order models are used for wave propagation. Lately, this demarcation is starting to be broken down by e.g. for wave-focusing events on a floating FPSO [8, 9].

The use of high-order discretizations are not new in the FNPF modelling community. The high-order spectral (HOS) model [5] is based on analytical truncation resulting in polynomial spectral methods and was introduced already back in 1987. It has been used and was recently extended to incorporate variable depth. Recently, pseudospectral models have been developed that resort to numerical approximations that can be tuned by solely adjusting the polynomial order in the basis [3] and using Fourier truncation to efficient simulate in the context of numerical wave tank and utilizing geometric p-multigrid for acceleration of the iterative solver [15]. Also, the open-source OceanWave3D model [7] that is based on a high-order finite difference scheme and a sigma-transformed computational domain have seen wide adoption due to it's numerical efficiency and the possibility to couple with Navier-Stokes based solvers.

This paper is based on the fundamental work presented in [11] and later extended to three dimensions in [12]. Those two work were proof-of-concepts implemented in Matlab. The present paper describes the development of a 3D fully nonlinear potential flow solver in the open-source spectral/*hp* element framework Nektar++ [18, 2, 22]. The implementation in Nektar++ will facilitate large-scale applications as parallelism is inherent in the framework.

Fully nonlinear potential flow (FNPF) modelling

We consider a three-dimensional time-dependent fluid domain (Ω) bounded by the boundary Γ consisting of a free surface (Γ^{FS}) and an arbitrary number of solid boundaries ($\Gamma\backslash\Gamma^{\mathrm{FS}}$). Without loss of generality, we assume that any vertical boundary represents either rigid offshore structures or walls, and the bottom boundary is a sea floor (Γ^{B}). The problem is stated in an Eulerian (fixed) frame of reference with governing equations for unsteady free surface boundaries derived from potential flow theory. A scalar velocity potential $\phi(x,z,t)$ function is introduced from which the velocity field can be computed $\mathbf{u} = \nabla\phi$, and it is required to satisfy the Laplace equation for mass continuity

$$\nabla^2\phi + \partial_{zz}\phi = 0 \quad \text{in} \quad \Omega, \tag{1}$$

in all parts of the fluid domain. The unsteady nonlinear kinematic and dynamic free surface boundary conditions can be expressed in the Zakharov form [23] as

$$\partial_t\eta = -\nabla\eta\cdot\nabla\tilde{\phi} + \tilde{w}(1+\nabla\eta\cdot\nabla\eta) \qquad \text{in} \quad \Gamma^{\mathrm{FS}}\times T, \tag{2a}$$

$$\partial_t\tilde{\phi} = -g\eta - \frac{1}{2}\left(\nabla\tilde{\phi}\cdot\nabla\tilde{\phi} - \tilde{w}^2(1+\nabla\eta\cdot\nabla\eta)\right) \quad \text{in} \quad \Gamma^{\mathrm{FS}}\times T, \tag{2b}$$

where the '$\sim$' symbol is used to denote variables evaluated at the free surface. On the bottom as well as on structures we assume zero normal flow

$$\partial_n\phi = 0 \quad \text{on} \quad \Gamma\backslash\Gamma^{\mathrm{FS}}. \tag{3}$$

In order to shift to a time-constant computational domain: $\Omega(t) \rightarrow \Omega^{\sigma}$ Following [1] we introduce a σ-transformation of the vertical coordinate

$$\sigma \equiv \frac{z+h(x)}{d(x,t)}, \quad 0 \leq \sigma \leq 1, \tag{4}$$

where $d(x,t) = \eta(x,t) + h(x)$ is the height of the water column above the bottom. This implies that the free surface elevation needs to be non-singular, and thus excludes the geometric modelling of overturning or breaking waves. The σ-transformed Laplace equation reads

$$\nabla^{\sigma} \cdot (\mathscr{K} \nabla^{c} \Phi) = 0 \quad \text{in} \quad \Omega^{\sigma}, \tag{5}$$

where $\nabla^{\sigma} = (\nabla, \partial_{\sigma})$ is introduced and the symmetric coefficient matrix is

$$\mathscr{K}(x,t) = \frac{1}{\det \mathscr{J}} \mathscr{J} \mathscr{J}^{T} = \begin{bmatrix} d & 0 & -\sigma \partial_x \eta \\ 0 & d & -\sigma \partial_y \eta \\ -\sigma \partial_x \eta & -\sigma \partial_y \eta & \frac{1+(\sigma \partial_x \eta)^2 + (\sigma \partial_y \eta)^2}{d} \end{bmatrix}. \tag{6}$$

Finally, from the scalar velocity potential $\Phi(x, \sigma, t) = \phi(x, z, t)$ the velocity field inside the fluid volume can be recovered as

$$(\mathbf{u}, w) = (\nabla + \nabla \sigma \partial_{\sigma}, \partial_z \sigma \partial_{\sigma}) \Phi. \tag{7}$$

Spectral/hp element FNPF model

We start by forming a partition of the spatial domain Ω^{σ} by a tessellation $\mathscr{T}_h$ of the horizontal xy-plane into N^k non-overlapping shape-regular elements $\mathscr{T}_k$ such that $\cup_{k=1}^{N^k} \mathscr{T}_k = \mathscr{T}_h$ with k denoting the k'th element. We then introduce the space of continuous, piece-wise polynomial functions

$$V = \{ v_h \in C^0(\Omega^{\sigma}); \forall k \in \{1, ..., N^k\}, v_{h|\mathscr{T}_k} \in \mathbb{P}^p \}, \tag{8}$$

where $\mathbb{P}^p$ is the space of polynomials of degree at most p. It is possible to exploit duality in the representation of the polynomials in the form of either modal (hierarchical and orthogonal) or nodal (Lagrange) basis functions.

The weak formulation of the free surface boundary conditions takes the following form. Find $f \in V$ where $f = \eta, \tilde{\phi}$ such that

$$\iint_{\Gamma^{\text{FS}}} \partial_t \eta \, v(x) dx = \iint_{\Gamma^{\text{FS}}} [-\nabla \eta \cdot \nabla \tilde{\phi} + \tilde{w}(1 + \nabla \eta \cdot \nabla \eta)] v(x) dx \tag{9a}$$

$$\iint_{\Gamma^{\text{FS}}} \partial_t \tilde{\phi} \, v(x) dx = \iint_{\Gamma^{\text{FS}}} \left[-g\eta - \frac{1}{2} \left(\nabla \tilde{\phi} \cdot \nabla \tilde{\phi} - \tilde{w}^2 (1 + \nabla \eta \cdot \nabla \eta) \right) \right] v(x) dx \tag{9b}$$

for all $v \in V$. We introduce the finite-dimensional approximations

$$f_h(x,t) = \sum_{i=1}^{N^{FS}} f_i(t) N_i(x), \tag{10}$$

where $\{N_i\}_{i=1}^{N_{FS}} \in V$ is the set of global finite element basis functions with cardinal property $N_i(\mathbf{x_j}) = \delta_{ij}$ at mesh nodes with δ_{ij} the Kronecker Symbol. Substitute these expressions into (9) and choose $v(x) \in \{N_i\}_i^{N_{FS}}$. The discretization in two spatial dimensions becomes

$$M' \frac{d}{dt} \eta_h = -\left(A_x^{\tilde{\phi}_x} + A_y^{\tilde{\phi}_y} \right) \eta_h + M' \tilde{w}_h + \left(A_x^{\tilde{w}_h (\eta_h)_x} + A_y^{\tilde{w}_h (\eta_h)_y} \right) \eta_h, \tag{11a}$$

$$M' \frac{d}{dt} \tilde{\phi}_h = -M' g \eta_h - \frac{1}{2} \left[\left(A_x^{(\tilde{\phi}_h)_x} + A_y^{(\tilde{\phi}_h)_y} \right) \tilde{\phi}_h + M^{\tilde{w}_h} \tilde{w}_h - \left(A_x^{\tilde{w}_h^2 (\eta_h)_x} + A_y^{\tilde{w}_h^2 (\eta_h)_y} \right) \right] \eta_h, \tag{11b}$$

where the following global matrices have been introduced

$$M'_{ij} = \iint_{\Gamma^{\text{FS}}} N_i N_j dx, \;\; M^b_{ij} = \iint_{\Gamma^{\text{FS}}} b(x) N_i N_j dx, \;\; (A^b_q)_{ij} = \iint_{\Gamma^{\text{FS}}} b(x) N_i \frac{\partial}{\partial q} N_j dx. \tag{12}$$

To obtain closure in the time-stepping problem of the free surface equations, we need to solve the σ-transformed Laplace problem to recover the vertical free surface velocity. The weak formulation of (5) is expressed as find $\Phi \in V$ such that

$$\iiint_{\Omega^c} \nabla^c \cdot (K\nabla^c \Phi) v dx = \oint_{\Gamma^c} v\mathbf{n} \cdot (K\nabla^c \Phi) dx - \iiint_{\Omega^c} (K\nabla^c \Phi) \cdot \nabla^c v dx = 0, \tag{13}$$

for all $v \in V$. The discretization leads to a sparse linear system of the form

$$L\Phi_h = \mathbf{b}, \quad L \in \mathbb{R}^{N\times N}, \quad \Phi_h, \mathbf{b} \in \mathbb{R}^N, \tag{14a}$$

where N is the total degrees of freedom in the discretisation and

$$L_{ij} = -\iiint_{\Omega^c} (\mathscr{K}\nabla^c N_j) \cdot \nabla^c N_i dx = -\sum_{k=1}^{N^k} \iiint_{\Omega^{c,k}} (\mathscr{K}\nabla^c N_j) \cdot \nabla^c N_i dx \tag{14b}$$

$$b_i = \oint_{\Gamma^c} N_i \mathbf{n} \cdot \left(\mathscr{K}\nabla^c \left(\sum_{j=1}^{N} \phi_j N_j \right) \right) dx = \sum_{s=1}^{N^s} \oint_{\Gamma^{c,s}} N_i \mathbf{n} \cdot \left(\mathscr{K}\nabla^c \left(\sum_{j=1}^{N} \phi_j N_j \right) \right) dx \tag{14c}$$

and where N^s is total number of segments of the domain boundary of the computational domain constituted from the surfaces of the elements used to tesselate the domain.

(a)

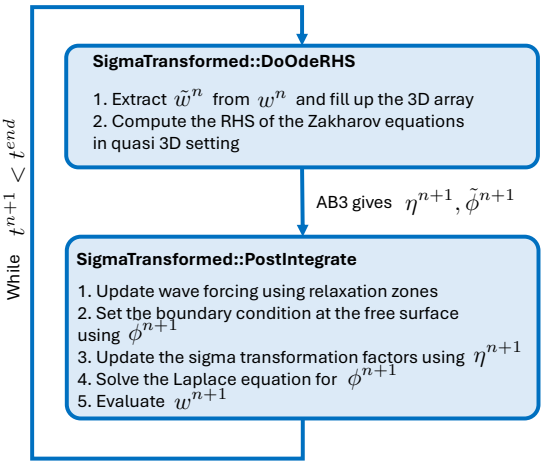

(b)

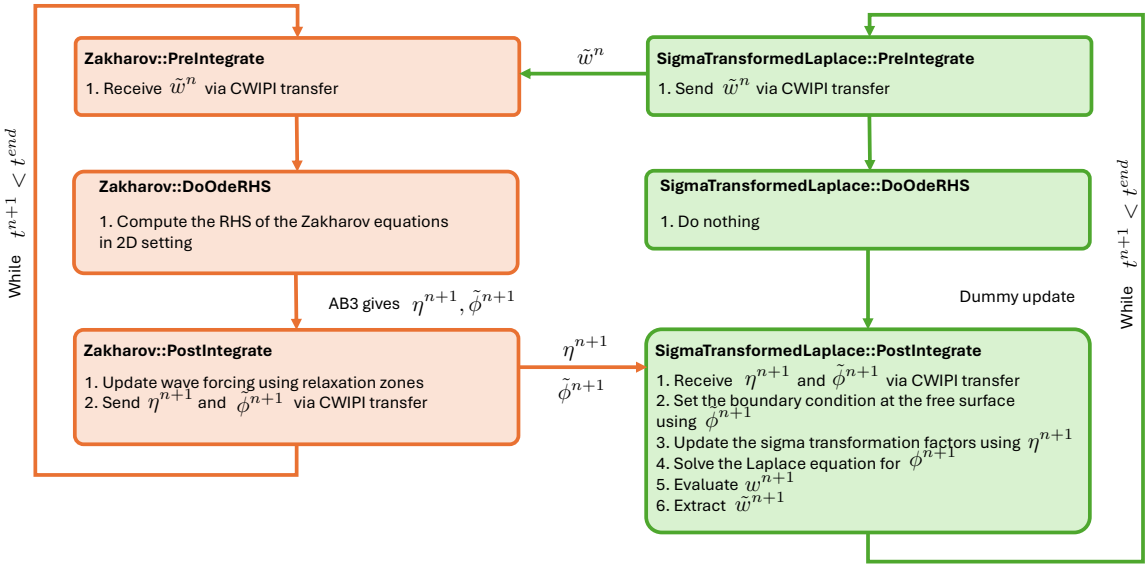

Figure 1: Flow chart of the FNPF solvers: (a) a 3D approach in which the free surface equations are solved in quasi 3D, and (b) 2D-3D co-simulation approach using a 2D free surface solver and a 3D kinematic solver.

Implementation in Nektar++

It should be noted that [16] implemented a FNPF solver in Nektar++ in 2015. In that model the 2D Zakharov solver was the 'lead' solver and the 3D domain associated with the Laplace solve was indeed created within the Zakharov solver by reading a 3D mesh. However, such an approach is no longer accepted by the communicator class in Nektar++, as it cause a MPI fork when run in parallel.

We thus apply two different approaches to implement the FNPF solver in Nektar++. The first is to initiate the model using a 3D domain. We use here the approach of solving the Zakharov equations in quasi-3D in order to be able to use the time-stepping schemes that are available in Nektar++. The second approach relies on co-simulation of two separate solvers: the 2D Zakharov solver and the 3D sigma-transformed Laplace solver. The models are coupled using the CWIPI (Coupling With Interpolation Parallel Interface) developed by Onera [19], which communicates through MPI. It should be noted the Nektar++ have an existing CWIPI implementation [17]. Here we extend the implementation from coupling 'domain-to-domain' to coupling 'domain-to-boundary', i.e. to only transfer the free surface boundary data to/from the Zakharov solver. The fundamental flow chart of the two approaches are presented in Figure 1. As can be seen both the models perform the Laplace solve as a post-integrate step – meaning that multi-step explicit methods should be used and not multi-stage. In the simulations we use the explicit third-order Adam-Bashfort (AB3) scheme. For the co-simulation the pre- and post-integration stages are also used to send-and-receive data.

The Laplace problem is solved using either a conjugate gradient iterative solver with static condensation or, for more unstable cases, the parallel direct solver XXt [20]. In ongoing work, this solver strategy can be improved by utilizing geometric p-multigrid acceleration [9] which is beneficial for wave-structure interaction applications.

Semi-circular channel

Waves propagating in a semi-circular channel give rise to a complex wave pattern caused by interacting diffracted and reflected waves. Here we model the case of channel with an inner radius of 2.5 m, an outer radius of 5 m and a constant water depth of 1 m. The linear waves with a wave length of 1.5 m are generated and absorbed in relaxation zones extending from the circular channel. These are deep water waves as $kh \approx 4$. Figure 2a shows the computational mesh. It consists of 99 structured hexahedral elements with uniform polynomial order of 4. The simulations are run for 50 s using an AB3 time step of 0.01 s. Please note that the boundary edges are straight-sided, as the model at the present does not fully support iso-parametric elements.

Figure 2b shows the resulting wave pattern obtained by the two models. It is clear that there is virtually no difference in the results and both models favorably agrees with the analytical solution in Figure 1c. Even though there is an overhead in transferring data between the solvers in the 2D-3D co-simulation it is faster than the quasi-3D approach.

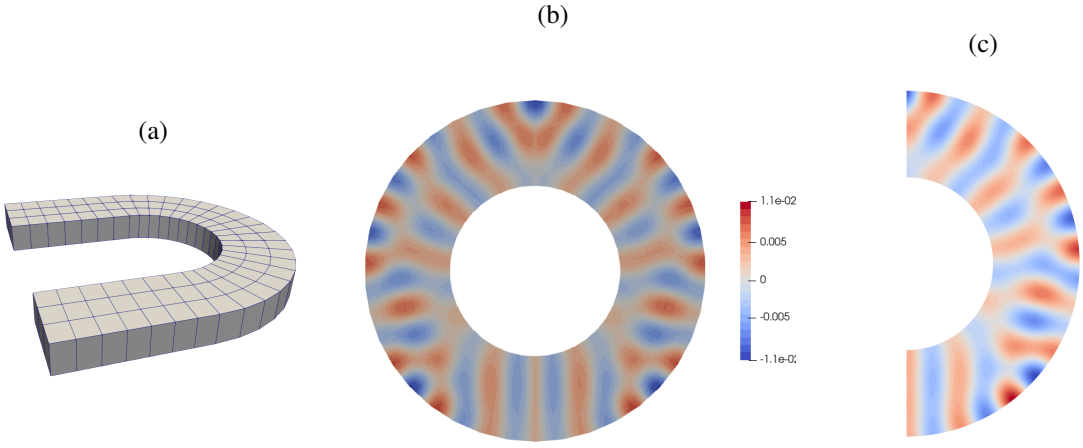

Figure 2: Semi-circular channel case. (a) hexahedral mesh, (b): free surface elevation at $t = 50$ s. Comparison between the 2D-3D coupled approach (left half) and quasi 3D approach (right half) and (c) analytical solution [4].

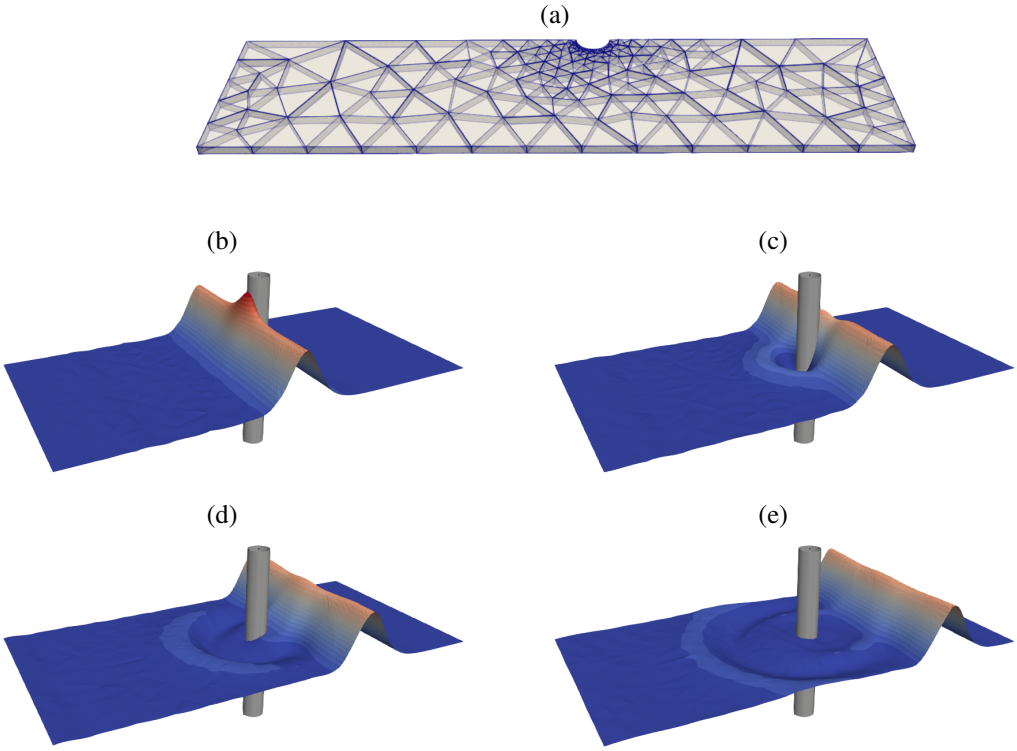

Figure 3: Solitary wave impinging on a cylinder case. (a) computational mesh, and free surface elevation at (b) $t = 4.5$ s; (c) $t = 6.5$ s; (d) $t = 8.5$ s and (e) $t = 12.5$ s.

Solitary wave scattering by a cylinder

We let a solitary wave with amplitude 0.1 m propagate in a fluid of 1 m depth and impact cylinder with 2 m radius. The computational domain is $x \in [-42, 33]$ m and $y \in [0, -19.2]$ m (symmetry condition). The solitary wave is initially located at $x = -17$ m . This case has been used in many studies, e.g. [13, 12]. The domain is partitioned into a single layer of 513 prismatic elements with horizontal polynomial order of 5 and vertical order of 3, see Figure 3a. The mesh is heavily clustered towards the cylinder. The AB3 time step is 0.025 s and the simulation time is $t \in [0, 12.5]$ s.

Figure 3 shows 4 snapshots of the wave-structure interaction. The solitary wave has a maximum wave run-up at around 4.5 s, a radiated wave is created, and the solitary wave recover its crest amplitude after the scattering. The solutions presented in Figure 3 appear similar to previously published results, e.g. [12]. We note that the solution has a tendency to become unstable when representing the cylinder with straight sided elements. Using curved elements typically alleviates this issue, see [13].

Acknowledgement

This work is supported by the Swedish Energy Agency through grant no. 51388-1 obtained by CE. This work is supported by the Danish COWIFONDEN through project no. A-165.19 obtained by APEK.

References

[1] X. Cai, H.P. Langtangen, B.F. Nielsen, and A. Tveito. A finite element method for fully nonlinear water waves. *Journal of Computational Physics*, 143(2):544–568, 1998.

[2] C.D. Cantwell, D. Moxey, A. Comerford, A. Bolis, G. Rocco, G. Mengaldo, D. De Grazia, S. Yakovlev, J.-E. Lombard, D. Ekelschot, B. Jordi, H. Xu, Y. Mohamied, C. Eskilsson, B. Nelson, P. Vos, C. Biotto, R.M. Kirby, and S.J. Sherwin. Nektar++: An open-source spectral/*hp* element framework. *Computer Physics Communications*, 192:205–219, 2015.

[3] T. B. Christiansen, H. B. Bingham, and A. P. Engsig-Karup. High-Order Finite Difference Solution of Euler Equations for Nonlinear Water Waves. volume Volume 4: Offshore Geotechnics; Ronald W. Yeung Honoring

Symposium on Offshore and Ship Hydrodynamics of *International Conference on Offshore Mechanics and Arctic Engineering*, pages 519–528, 07 2012.

[4] R. A. Dalrymple, J. T. Kirby, and P.A. Martin. Spectral methods for forward-propagating water waves in conformally-mapped channels. *Applied Ocean Research*, 16(5):249–266, 1994.

[5] D.G. DOMMERMUTH and D.K.P. YUE. A high-order spectral method for the study of nonlinear gravity waves. *Journal of Fluid Mechanics*, 184:267–288, 1987.

[6] G. Ducrozet, F. Bonnefoy, D. Le Touze, and P. Ferrant. 3-D HOS simulations of extreme waves in open seas. *Natural Hazards and Earth System Sciences*, 7:109–122, 2007.

[7] A. P. Engsig-Karup, H. B. Bingham, and O. Lindberg. An efficient flexible-order model for 3D nonlinear water waves. *Journal of Computational Physics*, 228(6):2100–2118, 2009.

[8] A. P. Engsig-Karup and C. Eskilsson. Spectral element fnpf simulation of focused wave groups impacting a fixed fpso. In *Proceedings of the Twenty-eighth (2018) International Ocean and Polar Engineering Conference*, pages 1443–1450, Sapporo, Japan, 2018. International Society of Offshore and Polar Engineers (ISOPE).

[9] A. P. Engsig-Karup and W. Laskowski. Efficient p-multigrid spectral element model for water waves and marine offshore structures. *International Journal for Numerical Methods in Fluids*, 93(3), 2021.

[10] A. P. Engsig-Karup, M. G. Madsen, and S. L. Glimberg. A massively parallel GPU-accelerated model for analysis of fully nonlinear free surface waves. 70(1), 2011.

[11] A.P. Engsig-Karup, C. Eskilsson, and D. Bigoni. A stabilised nodal spectral element method for fully nonlinear water waves. *Journal of Computational Physics*, 318:1–21, 2016.

[12] A.P. Engsig-Karup, C. Eskilsson, and D. Bigoni. Unstructured spectral element model for dispersive and nonlinear wave propagation. International Ocean and Polar Engineering Conference, pages ISOPE–I–16–455, 06 2016.

[13] C. Eskilsson and S.J. Sherwin. Spectral/hp discontinuous Galerkin methods for modelling 2D Boussinesq equations. *Journal of Computational Physics*, 212(2):566–589, 2006.

[14] S. L. Glimberg, A. P. Engsig-Karup, and L. N. Olson. A massively scalable distributed multigrid framework for nonlinear marine hydrodynamics. *The International Journal of High Performance Computing Applications*, 33(5):855–868, 2019.

[15] A. Melander and A. P. Engsig-Karup. A p-multigrid hybrid-spectral model for nonlinear water waves. *Water Waves*, 2024.

[16] A. Mieritz. Robust massively parallel free surface simulation using the spectral element method. Master's thesis, Department of Applied Mathematics and Computer Science, Technical University of Denmark, 2015.

[17] M.A. Moratilla-Vega, K. Lackhove, J. Janicka, H. Xia, and G.J. Page. Jet noise analysis using an efficient LES/high-order acoustic coupling method. *Computers & Fluids*, 199:104438, 2020.

[18] Nektar++. https://nektar.info, 2024.

[19] ONERA. https://github.com/onera/cwipi, 2024.

[20] H. M. Tufo and P. F. Fischer. Fast parallel direct solvers for coarse grid problems. *Journal of Parallel and Distributed Computing*, 61(2):151–177, 2001.

[21] W. Wang, C. Pákozdi, A. Kamath, and H. Bihs. Fully nonlinear phase-resolved wave modelling in the Norwegian fjords for floating bridges along the E39 coastal highway. *Journal of Ocean Engineering and Marine Energy*, 9:567–586, 2023.

[22] H Xu, C.D Cantwell, C. Monteserin, C. Eskilsson, A.P. Engsig-Karup, and S.J. Sherwin. Spectral/*hp* element methods: recent developments, applications, and perspectives. *Journal of Hydrodynamics*, 30(1):774–786, 2018.

[23] V.E. Zakharov. Stability of periodic waves of finite amplitude on the surface of a deep fluid. *Journal of Applied Mechanics and Technical Physics*, 9:109–194, 1968.

Effects of Density Ratio on Sloshing-Induced Impact Pressures

Andreas Peters, Bettar Ould el Moctar, Robert Potthoff

With upgrades of global energy supply, the demand of natural gas (NG) as well as the sea transport of liquefied natural gas (LNG) have been increasing notably. In the meanwhile, renewable and clean energy, such as solar energy, wind energy, Hydrogen etc. have a growing share in global energy production. Among them, hydrogen is gaining more attention because of its storability and transportability liquified in vessels, and it is foreseeable that the production and transportation of liquified Hydrogen (LH2) will increase significantly in the future. Vessels transporting liquified gas in extremely low temperature (-162°C for LNG and -253°C for LH2, respectively) are nowadays normally structural equipped with membrane tanks, which are vulnerable to high local pressure caused by liquid impact. Thus, loads on walls of LH2- or LNG-tanks caused by the partially filled fluid motions in tanks excited by ship motions need to be paid more attention to in the design process of ships to ensure the transport safety. Numerical methods can be used to investigate the impact pressure induced by sloshing in principle; however, several physical phenomena must be modeled. Experiments investigating aspects, which may affect the impact pressure and the free surface instability such as density ratio (DR), viscosity of the liquid as well as phase transition between gas and liquified gas need to be carried out.

In this work, the effects of density ratio between gas and liquid on sloshing impact pressure acting on partially filled tanks were investigated numerically and experimentally. The influence of density ratio between gas and liquid were studied in a similar range as that of liquified natural gas and liquified hydrogen (LH2). To investigate experimentally the influence of the density ratio between liquid and gaseous phases on impact pressure loads acting on tank walls, we varied the composition of the gas phase. SF6 and air were mixed to obtain different gas densities. Complying with the international sloshing benchmark test case, systematic investigation in terms of excitations by single-wave, harmonic motions and irregular motions was conducted. Numerical simulations were performed based on solving the equations of conservation of mass, momentum and energy as well as a transport equation for the volume fraction considering the compressibility of both phases. Experimental measurements were reproduced numerically by choosing the same geometrical setup, motions, and fluid properties as used in the experiments. Additionally, effects of temperature, compressibility, and density were studied numerically.

MESHFREE Simulations for Maritime Applications

Chaitanya Sanghavi*, Isabel Michel*, Fabian Castelli*, Jörg Kuhnert*

Fraunhofer ITWM, Fraunhofer-Platz 1, 67663 Kaiserslautern, Germany,
chaitanya.sanghavi@itwm.fraunhofer.de, isabel.michel@itwm.fraunhofer.de,
fabian.castelli@itwm.fraunhofer.de, joerg.kuhnert@itwm.fraunhofer.de

Despite significant progress in mathematical and numerical modeling, applying these techniques to maritime industries remains a complex challenge. Over the years, Fraunhofer has been working on a MESHFREE software to address such issues.

The Fraunhofer software MESHFREE (https://www.meshfree.eu/) is a powerful simulation tool for fluid dynamics, continuum mechanics, and multiphase scenarios that is based on a Generalized Finite Difference Method (GFDM). This enables efficient virtualization as well as optimization of processes and products even before physical prototypes are built.

This presentation will provide a brief overview of MESHFREE's capabilities, specifically in maritime applications.

MESHFREE is based on a general continuum mechanics approach[1,2], which allows it to model a wide range of nonlinear physical phenomena, such as non-Newtonian fluids and complex materials. This makes it suitable for diverse applications, including water management, avalanches, foam formation, metal cutting, advanced fluid-structure interactions, and more. In contrast to classical mesh-based approaches, MESHFREE uses an automatically managed point cloud that is efficiently adapted to the simulation domain – even if the domain changes rapidly due to moving geometries or large deformations. The unique features of MESHFREE enable numerical simulations of scenarios that are currently completely out of reach of other tools: reliably simulating a car crossing puddles and small streams[1], or abrasion in water turbines. Also, the computation can be considerably faster in scenarios that are difficult for mesh-based methods, such as free surface flows.

In maritime applications, MESHFREE excels in simulating a wide range of scenarios, including moving ships[1] and their interactions with waves, tank sloshing, ship stability, spray cleaning processes, tsunamis, flooding events, and floating bridges used in disaster control.

The talk will begin with a brief introduction to the mathematical theory behind GFDM, followed by a summary of various maritime applications that can be effectively modeled using MESHFREE.

[1] J. Kuhnert. MESHFREE Simulations in Car Design: Closing the Gaps of Classical Simulation Tools. In: H.G. Bock, KH. Küfer, P. Maass, A. Milde, V. Schulz, editors, German Success Stories in Industrial Mathematics. Mathematics in Industry, vol 35. Springer, Cham (2021).

[2] J. Kuhnert, I. Michel, R. Mack. Fluid Structure Interaction (FSI) in the MESHFREE Finite Pointset Method (FPM): Theory and Applications. In: M. Griebel, A. M. Schweitzer, editors, Meshfree Methods for Partial Differential Equations IX, Vol. 129, pages 73–92. Springer International Publishing (2019).

26th Numerical Towing Tank Symposium (NuTTS)
23-25 October 2023
Mühlheim an der Ruhr, Germany

Effects of gas pockets on nucleation and growing of nanobubbles

Mazyar Dawoodian, Bettar el Moctar
Institut für Nachhaltige und Autonome Maritime Systeme (INAM), University of Duisburg-Essen
mazyar.dawoodian@uni-due.de

This study addresses the disparity between experimentally measured and theoretically predicted tensile strengths by examining the role of nanoscale gaseous nuclei in cavitation. Despite efforts to remove dissolved gases and nanoscale contaminants from liquids, these nuclei remain as key sites for cavitation initiation. Using Molecular Dynamics (MD) simulations, we explored cavitation induced by nanoscale nuclei to evaluate their influence on the cavitation process. Our simulations provided a detailed examination of the microscopic dynamics of cavitation, building on the established effectiveness of MD for modeling both homogeneous and heterogeneous cavitation in water. The results suggested that existing models, such as the equivalent void assumption, may not fully capture the behavior of gaseous nuclei. For example, at 298 K, the equivalent void assumption model (Gao et al., 2021) predicted cavitation onset at -120 MPa for a void with a radius of 1 nm, whereas our simulations showed cavitation occurring at -48 MPa for a gaseous nucleus of the same size. By comparing these findings, we identified potential shortcomings in current models, emphasizing the need for more accurate representations of gaseous nuclei in cavitation studies. Our analysis could support the development of more reliable models for predicting and controlling cavitation in water.

Simulation approach and scale effects for sail-driven cargo ships in sideslip

Jeroen Wackers*, Gaétan Rousseau*†, and Ganbo Deng*
*LHEEA Lab – Centrale Nantes/CNRS, † GMP, IUT de Nantes
jeroen.wackers@ec-nantes.fr

1 Introduction

With the need to reduce carbon emissions in shipping, wind-assisted or fully sail-driven cargo transport is a major subject for naval architecture in the coming years. This requires research on CFD analysis for these ships. The pioneering work of Van der Kolk (2020) shows that, hydrodynamically, sailing hulls operate in sideslip conditions to counteract the lateral force of the sails, so sideslip is no longer restricted to manoeuvring, but has to be considered for the optimisation of calm-water resistance.

This paper considers if common CFD practices for calm-water resistance and local flow simulation can be used for sail-driven cargo ships. Specifically: (1) are the numerical setup protocols that were developed for straight-ahead sailing, valid for moderate sideslip? And (2), do the same scaling rules from model scale (MS) to ship size (FS) apply? These points are tested on a Series 60 $C_b = 0.6$ hull, which has earlier been studied by Queutey and Visonneau (2007).

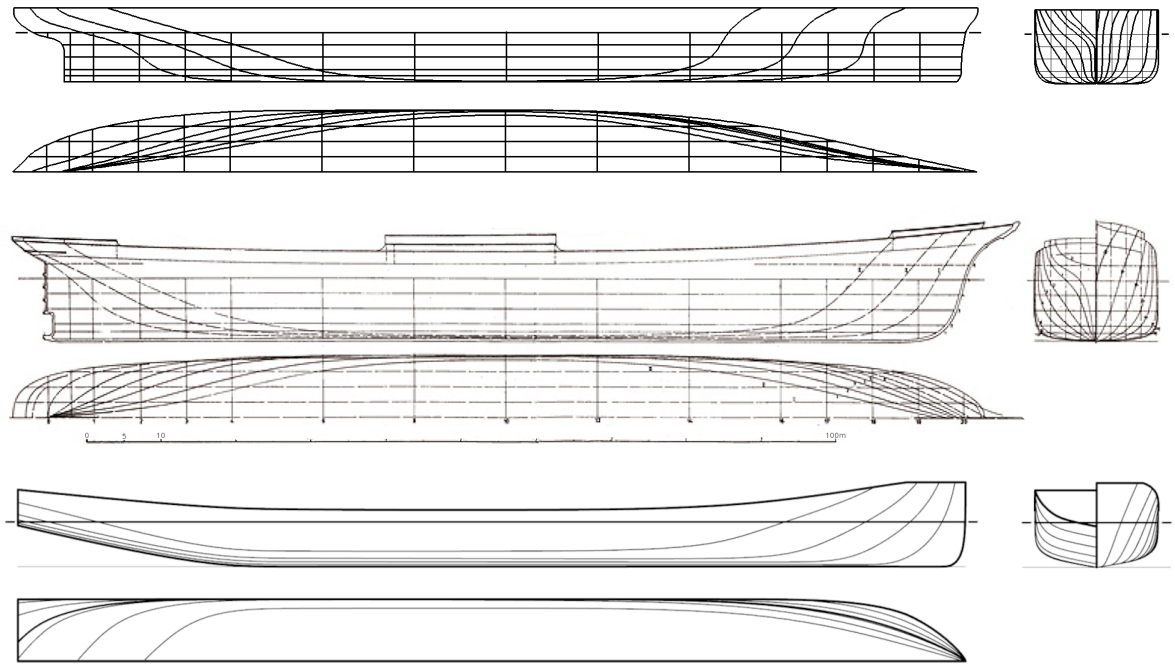

Fig. 1: Line plan of the Series 60 $C_b = 0.6$ (top), the 5-mast full-rigged bulk carrier *Preußen* (middle), and the DWA hull #34 from Van der Kolk (2020) (bottom).

2 Test case

Finding the right case The best example of modern sailing cargo hulls in the open literature is probably the DWA series (Van der Kolk (2020)). However, the tests in the current paper require high-quality local flow data, which are not available for the DWA series and, indeed, hard to find in general. The Series 60 $C_b = 0.6$ ship (Todd (1963)) is motor-driven, but it closely resembles the sailing cargo hulls of the 19th and early 20th century. Apart from the sharper bow, its lines are close to the bulk carrier *Preußen* (figure 1). In terms of size, proportions, and performance (table 1), the similarity with *Preußen* and the famous tea clipper *Cutty Sark* is confirmed, while modern ships are close enough (although these tend to have smaller drafts, flatter transom sterns, and more prudent cruising speeds than their predecessors).

Table 1: Characteristics of the Series 60 $C_b = 0.6$ hull compared with different sailing cargo vessels.

	L_{wl} [m]	L/B	L/D	C_b	$V_{\max}$ [kts]	$Fr_{\max}$
Cutty Sark (1869)	64.8	5.90	10.12	0.62	17.5	0.357
Preußen (1902)	122.0	7.44	14.77	0.67	20.0	0.297
Series 60 $C_b = 0.6$ (1951)	121.9	7.50	18.75	0.60	21.3	0.316
DWA hull #34 (2020)	138.0	7.67	21.28	0.64	15.0	0.210
Neoliner (2025)	136.0	5.67	24.73	0.60	11.0	0.155

Regarding suitable sideslip angles β for the tests, the capacity to sail upwind is determined by the ratio of sideforce to drag C_S/C_T, which in the experiments by Longo and Stern (2002) is highest at $\beta = 10^{\circ}$. However, high sideslip angles carry a significant drag penalty, so cargo ships are likely to choose routes which limit the amount of upwind sailing. A ratio $C_S/C_T = 1$, which corresponds to beam reaching, is obtained for β around 3°. Thus, $\beta = 10^{\circ}$ cannot be excluded but $\beta \leq 5^{\circ}$ in most operational conditions.

Test case definition The test is based on the experimental setup of Longo and Stern (2002). For the reasons stated above, the sideslip angles are $\beta = 0^{\circ}$ to 10°. Froude and Reynolds numbers are $Fr = 0.16$ ($Re_{MS} = 2.68 \cdot 10^6$, $Re_{FS} = 5.68 \cdot 10^8$) and $Fr = 0.316$ ($Re_{MS} = 5.30 \cdot 10^6$, $Re_{FS} = 1.12 \cdot 10^9$). The model scale is $1:40$. The hull is fixed, in the experimentally measured attitude for the model-scale force tests and in the design position for the local flow and scale effect studies.

Reynolds-averaged Navier-Stokes (RANS) equations are solved with the anisotropic EASM turbulence model (Duvigneau et al. (2003)) and a wall law with first-cell thickness $y^+ = 60$ for MS and $y^+ = 300$ for FS. The computational domain runs from $1L_{pp}$ in front of the bow to $2.5L_{pp}$ behind it, sideways to $\pm 2L_{pp}$, and vertically from $1.5L_{pp}$ below the waterline to $0.5L_{pp}$ above it. Far-field (velocity) conditions are prescribed on the lateral domain faces, with imposed pressure on the top and bottom. Sideslip angles are imposed by rotating the entire domain and forces are given in body-aligned coordinates. With the wetted area $S = 2526.4m^2$ in FS and $1.579m^2$ in MS, the force coefficients are:

$$C_T = F_x/(\tfrac{1}{2}\rho U_\infty^2 S), \qquad C_S = F_y/(\tfrac{1}{2}\rho U_\infty^2 S). \tag{1}$$

3 Flow solver and numerical setup

Solver The unsteady finite-volume Navier-Stokes solver ISIS-CFD is developed by Centrale Nantes / CNRS and distributed by Cadence Design Systems as part of FINE/Marine, which also contains the mesher Hexpress. ISIS-CFD features a mixture-fluid formulation to model the water-air interface (Queutey and Visonneau (2007)), various RANS and hybrid RANS/LES turbulence models, 6-DoF resolved or imposed body motion, and mesh deformation or overset meshing to handle moving bodies.

Adaptive grid refinement (Wackers et al. (2022)) allows the mesh to be automatically refined locally, during the computation, according to the needs of the flow. The mesh is adapted by anisotropic local division of the cells, based on a metric-tensor refinement criterion which is a real-valued tensor field computed from the flow. The mesh is refined until the mesh size times the criterion is equal to a constant threshold T_r throughout the mesh. Varying this T_r allows the mesh size to be adjusted globally.

Calm-water resistance protocol Wackers et al. (2022) define a standardised simulation setup protocol based on mesh adaptation for the resistance of bare-hull displacement ships. This protocol provides consistent, reliable simulations, since the adaptation ensures that all flow features are captured. Furthermore, results were shown to be more accurate than on non-adapted meshes, for the same numbers of cells.

The mesh adaptation in the protocol is based on combined free-surface adaptation (threshold $T_{rS} = 1.3L_{pp}/1000$) and refinement based on the second derivatives of pressure and velocity (threshold $T_{rH} \in [0.2L_{pp}, 0.025L_{pp}]$ for coarse to fine meshes). Cells smaller than $L_{pp}/1000$ are no longer refined and horizontal refinement is suppressed from $0.3L_{pp}$ behind the stern. The initial mesh is kept coarse, with cubic cells of $L_{pp}/128$ on the hull and no initial free-surface refinement. The time step is chosen such that the ship passes its own length in $100\Delta t$, and it is accelerated from rest in the first 100 time steps.

4 Grid convergence and applicability of the protocol

First, the numerical uncertainty and correspondence with measurements are evaluated in model scale. For this, each condition is simulated with a series of 5 meshes using thresholds T_{rH} from $0.2L_{pp}$ to $0.05L_{pp}$. Depending on β and Fr, the meshes have $320k$–$1.1M$ cells ($T_{rH} = 0.2L$), $490k$–$1.6M$ ($T_{rH} = 0.14L$), $880k$–$2.4M$ ($T_{rH} = 0.1L$), $1.7M$–$4.0M$ ($T_{rH} = 0.07L$), and $2.9M$–$6.4M$ ($T_{rH} = 0.05L$).

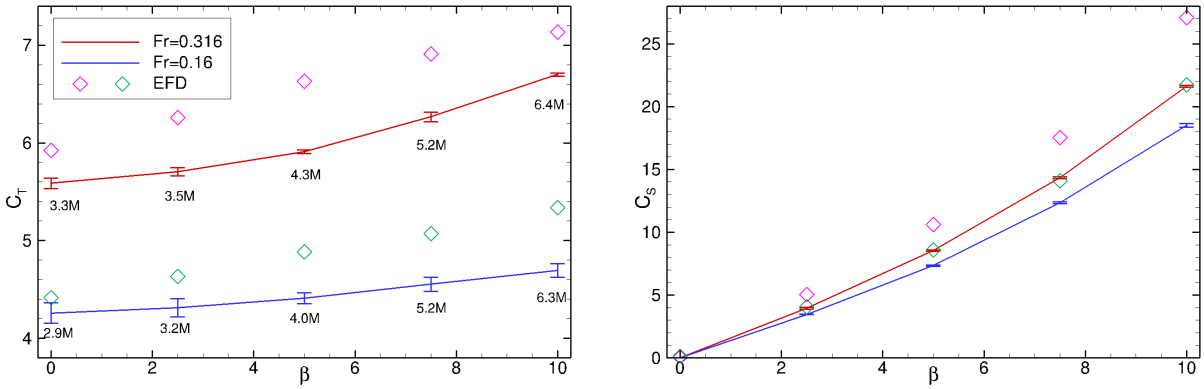

Fig. 2: Model-scale resistance (left) and sideforce (right) at $T_{rH} = 0.05L$ as a function of the sideslip angle, with numerical uncertainty, experiments, and numbers of cells.

Forces Figure 2 shows the resistance and side force as a function of β, compared with the measurements of Longo and Stern (2002) and with numerical uncertainty estimations based on the 2023 version of the Eça & Hoekstra approach (Eça et al. (2023)). The uncertainty for C_T on the finest meshes ($T_{rH} = 0.05L$) is 1–2% for $Fr = 0.316$ and 3–5% for $Fr = 0.16$, while for C_S it is always below 1%. The uncertainty shows no systematic increase with β; the variations are caused by the strong reaction of the estimation to small fluctuations in the data, since the difference between coarse- and fine-mesh solutions (not shown) is similar for all β. However, the mesh size increases with sideslip: the adaptive refinement detects that the flows become more complex and increases the number of cells to conserve numerical accuracy.

Given estimated experimental uncertainties below 1% Longo and Stern (2002), the difference between simulations and experiments is dominated by modelling error. For the resistance, the small-size model required a transition stimulator of 10×3.2 mm studs at 9.5 mm intervals to obtain the desired boundary layer behaviour. These studs, which are not simulated, probably add at least 10% to the experimental resistance. For the sideforce, the propeller axis and hub (which are absent from the CAD model) could explain part of the difference. However, the difficulties in predicting separated flows, discussed below, doubtlessly contribute to the modelling error.

Local flow Figure 3 shows the model-scale wave field for $Fr = 0.316$, comparing coarse and fine grids. At $\beta = 0^o$ the agreement between simulations, and with the experiments, is exceptional: all lines nearly overlap. At $\beta = 5^o$ the agreement between the simulations remains the same, while for $\beta = 10^o$ it is locally degraded around the bow wave. This is due to the strong breaking wave, which is sensible to the grid size: for $Fr = 0.16$ and $\beta = 10^o$ where no breaking occurs, the agreement is as good as for $\beta = 0^o$, considering the very small amplitude of the waves. The correspondence with the experiments behaves the same way, showing that the wave physics are well represented for all β.

For the wake (figure 4 shows $Fr = 0.316$), the numerical accuracy is again similar for different β. However, the flow varies strongly with the sideslip. At $\beta = 0^o$, the wake is essentially a flat-plate flow, which is perfectly simulated except for the missing propeller hub which can be seen in the experiments. For $\beta = 10^o$, at $x/L = 0.1$ the main vortex is well captured but the leeward boundary layer near the free surface has a bulge which is too low. This bulge is related with a complex separation bubble at the bow, involving vortex separation with a Froude-dependent topology, and ventilation at $Fr = 0.16$ (figure 5). Further back, the features of the open-type separation at the stern are all represented, but not perfectly captured. This illustrates the increased complexity of the flow, compared with $\beta = 0^o$.

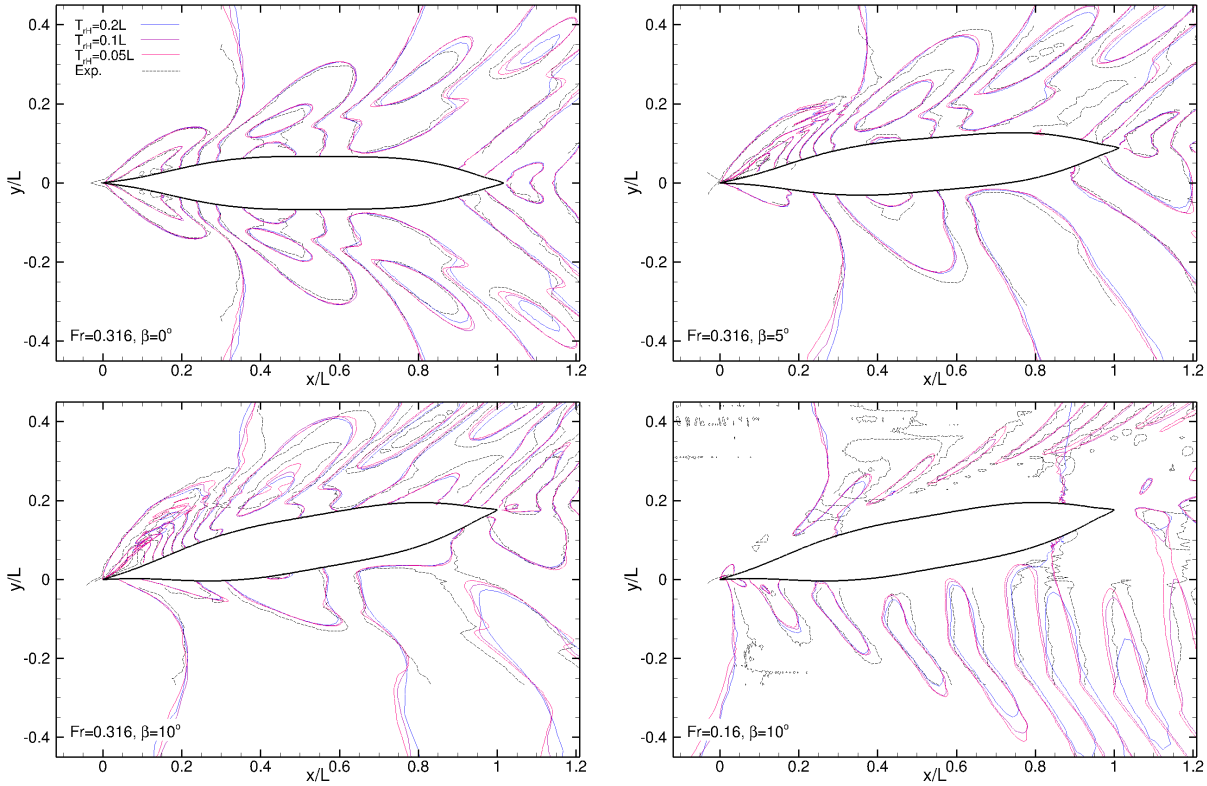

Fig. 3: Grid convergence and experiments for the wave field, as a function of β and Fr. Model scale.

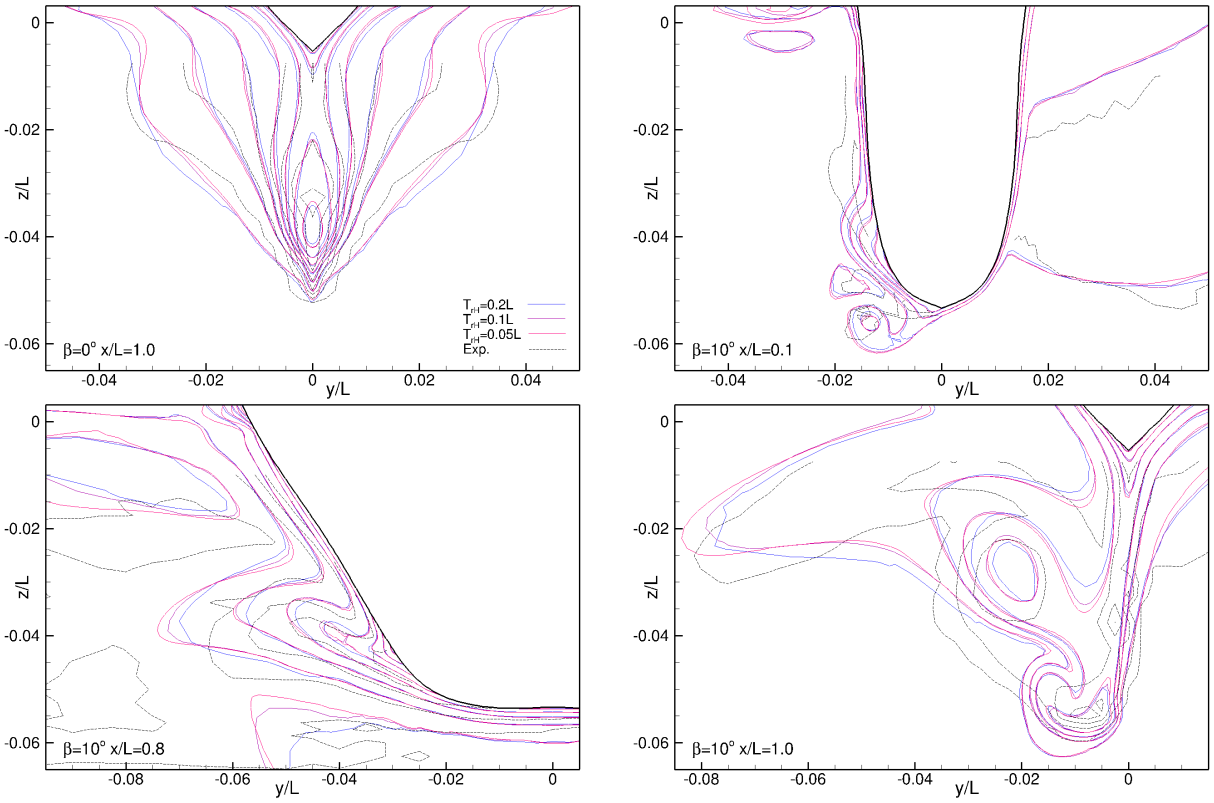

Fig. 4: Grid convergence and experiments for the axial flow in x-constant planes (body frame). Model scale, $Fr = 0.316$.

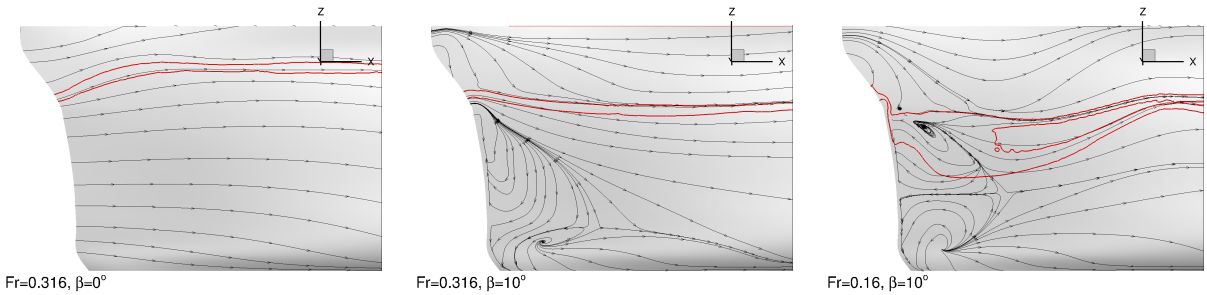

Fig. 5: Streamlines and water volume fractions 0.1 / 0.9 (red) on the leeward (port) bow. Model scale.

5 Scale effects

Figure 6 presents full-scale forces and compares them with standard extrapolations from model scale. The MS resistance is corrected following ITTC (2021) with the ITTC-1957 friction line and a form factor estimated with Prohaska's method based on $Fr = 0.16$ and 0.316. C_S is considered the same in MS and FS. The MS-based estimations are remarkably accurate, with errors close to the numerical uncertainty, and hardly degrade for increasing β. The full-scale numerical uncertainty is comparable to MS and the adapted meshes are larger than for MS, but the number of cells remains reasonable.

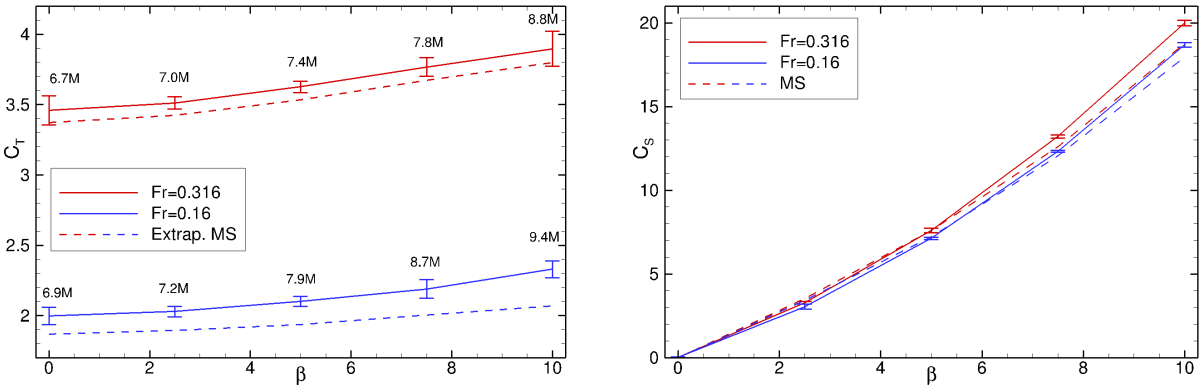

Fig. 6: FS resistance and extrapolated MS (left), FS and MS sideforce (right), $T_{rH} = 0.05L$.

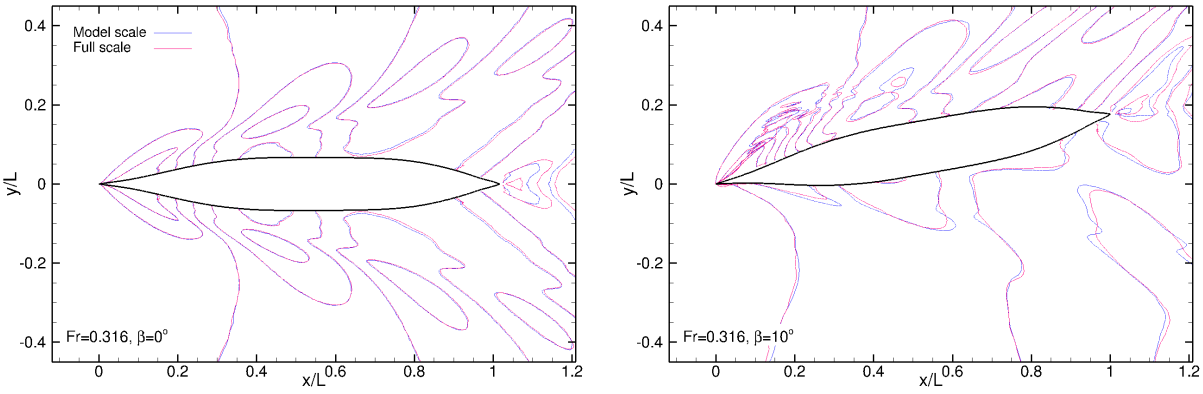

Fig. 7: Scale dependence of the wave field for $Fr = 0.316$.

Froude's hypothesis is also confirmed for the wave field (figure 7), which only shows small differences near the stern. For the wake (figure 8) the scale effect at $\beta = 0^o$ is only a reduction of the boundary-layer thickness. However, it is more complex in sideslip. The velocity defect is reduced, and confined to a smaller region, but the main vortical structures remain in place. Thus, the wake is a mixture of *Re*-independent vorticity, induced by the sideward lift created by the sideslip, and scale-dependent wake flow, which is hard to extrapolate between model and full scale.

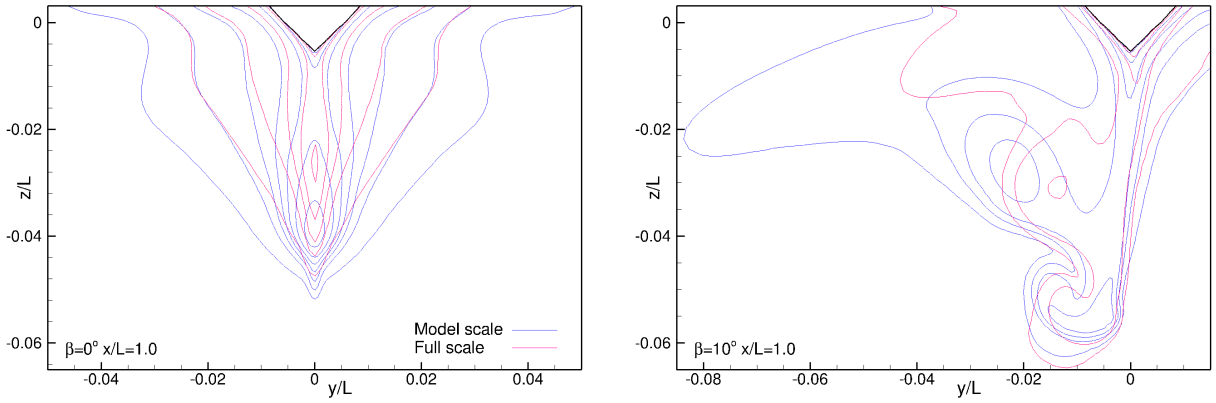

Fig. 8: Scale dependence of the wake at $x/L = 1.0$, $Fr = 0.316$.

6 Conclusions

The tests show that, thanks to the adaptive meshing, the numerical uncertainty has little dependence on β, which implies that our standard numerical protocols apply to sailing cargo ships. However, flows with sideslip exhibit complex physics, which may require more sophisticated modelling than RANS with wall laws. Extrapolation from MS to FS (and by inference, using model tests for design) appears valid for the forces and the wave fields. However, accurately representing the wake, which is crucial for the design of appendices, and propellers of wind-assisted ships, requires FS simulation.

These findings are preliminary, and have to be confirmed by more extensive studies, considering for example modern transom-stern hulls. Accurate local-flow measurements for such hulls in sideslip conditions would be very helpful.

Acknowledgements

We thank Prof. Frederick Stern for providing the Series 60 experimental data and Dr. Luis Eça and Dr. Serge Toxopeus for their help with the uncertainty estimation.

References

R. Duvigneau, M. Visonneau, and G.B. Deng (2003). On the role played by turbulence closures in hull shape optimization at model and full scale. *J. Mar. Sci. Tech.*, **8**(1), 1–25.

L. Eça, S.L. Toxopeus, and M. Kerkvliet. *Procedures for the estimation of numerical uncertainties in the simulation of steady and unsteady flows*. IST Report IST-M 8, Lisbon, Portugal. See also https://www.marin.nl/en/research/free-resources/verification-and-validation

International Towing Tank Committee (2021). *Resistance Tests*. ITTC Procedure 7.5-02-02-01.

N. van der Kolk (2020). *Sailing Efficiency and Course Keeping Ability of Wind Assisted Ships.* Ph.D. thesis, Delft University of Technology.

J. Longo and F. Stern (2002). Effects of drift angle on model ship flow. *Exp. Fluids*, **32**, 558–569.

P. Queutey and M. Visonneau (2007). An interface capturing method for free-surface hydrodynamic flows. *Comput. Fluids*, **36**(9), 1481–1510.

F.H. Todd (1963). *Series 60. Methodical experiments with models of single-screw merchant ships*. David Taylor Model Basin, report 1712.

J. Wackers, G.B. Deng, C. Raymond, E. Guilmineau, A. Leroyer, P. Queutey, and M. Visonneau (2022). Adaptive grid refinement for ship resistance computations. *Ocean Eng.*, **250**, 110969.

Evaluation of The Performance of A Model-Based Identification Method of Ship Manoeuvring Parameters Using Convex Programming

MSc. Ricardo Francisco Suarez Fernandez[1]
Prof. Dr.-Ing. Moustafa Abdel-Maksoud[2]
Prof. Dr.-Ing. Carlos Jahn[3]

*Corresponding author, ricardo.suarez.fernandez@cml.fraunhofer.de[1]
m.abdel-maksoud@tuhh.de[2], carlos.jahn@cml.fraunhofer.de[3]

ABSTRACT

Advancements in ship Model-Based System Identification (SI) over recent decades have led to the development of algorithms capable of learning complex relationships from data. This paper evaluates the predictive capabilities and robustness of a convex programming model in SI, specifically focusing on ability parameter prediction. The study evaluates the model's prediction capabilities for both deep and shallow water conditions. The model employed in this research is the MOERI Container Ship (KCS), utilizing data from a 3-DOF numerical manoeuvring model based on the Abkowitz mathematical model [1]. The results of the study demonstrate the model's effectiveness in predicting ship performance, offering valuable insights for its application in SI.

Keywords: Ship manoeuvrability, Convex programming model, System Identification (SI), Abkowitz Mathematical model, Predictive performance, Manoeuvre data.

1 INTRODUCTION

Manoeuvrability is essential in ship design, operation and safety, recognized by the IMO through resolution MSC.137(76) in 2002, which set standards for evaluating manoeuvring performance [2]. Accurate ship manoeuvrability models require understanding ship dynamics, as the ITTC [3] outlines methods like Captive Model Testing, free-running tests, empirical formulas, and computational simulations (Figure 1). System Identification (SI), particularly Model-Based SI, is the most reliable for determining hydrodynamic coefficients, using prior knowledge to focus on parameter identification rather than creating new models.

Hayes [4] introduced the model reference method for ship SI, followed by Åström and Källström [5] using probabilistic methods, including recursive prediction [6]. Wang [7] applied the Kalman Filter, and Rhee et al. [8] used the Least Squares method for the Equation Error approach. Traditional methods, however, face challenges like dependence on initial parameters and multicollinearity, leading to unreliable outcomes.

In last decade, machine learning models has been implemented in ship SI, as demonstrated by studies such as Luo and Zou [9], who applied machine learning for parameter prediction and optimized the LS-SVR algorithm to address issues like drift and multicollinearity. The data for this study was generated using a numerical ship manoeuvring simulator based on the Abkowitz model, featuring the Mariner Class Vessel and a zig-zag manoeuvre. Luo et al. [10] used free-running model tests to train an LS-SVM combined with Particle Swarm Optimization, while Luo and Li [11] minimized drift in predicted coefficients using SVM. Ban et al. [12] develop a method to handle variant Gaussian noise and outliers using epsilon support vector regression ϵ-SVR and the sequential minimal optimization algorithm. Xu et al. [13] implemented LS-SVM for real-time parameter estimation using free-running models, and Wang et al. [14]

introduced the Nu-SVM model for improved algorithm performance by controlling sparseness. Xue et al. [15] adopted a Bayesian approach for hydrodynamic parameter identification, and Alexandersson et al. [16] presents a method for identifying ship maneuvering dynamics using parameter estimation, inverse dynamics regression, and an Extended Kalman filter with a Rauch Tung Striebel smoother.

Present study uses the Model-Based SI Method, using prior knowledge of ship dynamics to develop a precise model for parameter identification. Despite progress, traditional methods remain limited in accuracy and reliability, prompting the exploration of convex optimization models to enhance these aspects in parameter estimation and manoeuvring performance prediction.

The present research evaluates the predictive capability of a linear model for estimating hydrodynamic coefficients of the KCS container ship, using convex optimization through the 'cvxpy' library. This model effectively captures linear and nonlinear relationships in data, offering reliable generalization and robustness in parameter identification.

2 PREDICTION ALGORITHM

According to ITTC [3] (Figure 1), methods for deriving manoeuvring parameters must balance reliability, accuracy, and computation time. Some methods suit online predictions, while others do not meet real-time requirements. The most notable methods are free and captive model tests, which, while highly accurate, are also costly and time-consuming.

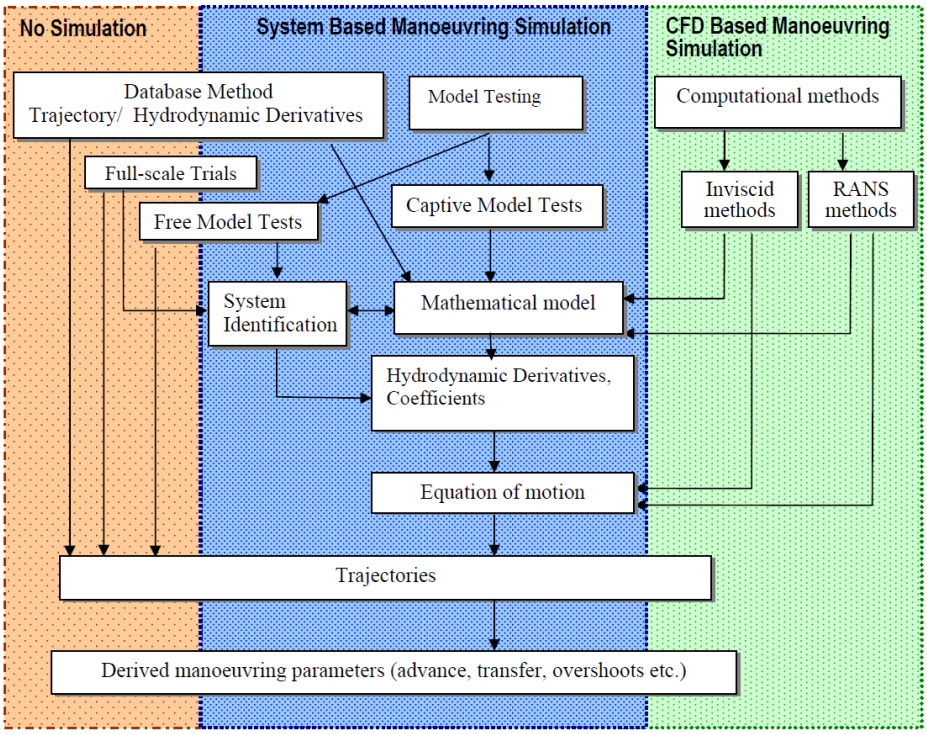

Figure 1: (ITTC) 2005. Overview prediction methods

Another approach is based on Computational Fluid Dynamics (CFD). Although CFD is less costly than model tests, it remains resource-intensive. Recent advancements combining convex optimization with CFD have maintained acceptable accuracy, suggesting potential for future online application.
Empirical methods, requiring minimal computation time, are ideal for online simulation but have reduced accuracy compared to other methods. System-based manoeuvring models, despite their limitations, remain a good option for online tools.

Convex optimization techniques have gained attention in ship SI, particularly through the SVM algorithm, which has demonstrated strong predictive performance [9, 13]. These techniques show improvements over conventional methods, establishing them as valuable tools in advancing SI [14].

This research focuses on evaluating the performance of a convex programming model for predicting ship hydrodynamic parameters.

2.1 CVXPY Model for Linear Regression

The CVXPY model solves convex optimization problems and is well-suited for predicting parameters in multiple linear regression, offering an intuitive interface for working with complex datasets. Multiple linear regression aims to find coefficients that best fit the dependent variable, minimizing the difference between observed and predicted values:

$$\min_{\beta} \frac{1}{2}\|X\beta - y\|_2^2 \tag{1}$$

Where X is the input feature matrix, β is the vector of coefficients, and y is the vector of outputs.

In this implementation, an intercept term is added to the feature matrix to improve the model's flexibility in adjusting to the data. This intercept, represented as a column of ones, allows the regression line to better fit the observed values by accounting for the baseline value of the response variable when all predictors are zero.

Data preprocessing is crucial, typically involving dataset splitting and feature scaling to ensure equal contribution from all predictors. Feature scaling helps stabilize the optimization process by ensuring that all input features have comparable ranges, which is especially important when using solvers that rely on numerical precision, as in the case of CVXPY. In this implementation, StandardScaler was used to normalize the input features before fitting the model, and the transformation was also applied to the test data to maintain consistency.

Once the data is preprocessed, the model's objective function was formulated and minimized directly using CVXPY's syntax, defining the mean squared error (MSE) between predicted and actual values. The optimization in this implementation was carried out using the OSQP solver (Operator Splitting Quadratic Program), which was automatically selected by CVXPY based on the problem's characteristics. OSQP is particularly efficient for large and sparse datasets due to its operator splitting technique, which breaks the problem into smaller subproblems to enhance computational performance. These characteristics make OSQP well-suited for handling quadratic objectives like in this regression problem, providing a good balance of efficiency, flexibility, and robustness.

The model's performance is evaluated using metrics such as mean absolute error (MAE), and R-squared (R^2), which provide insights into the quality of the model fit and its ability to generalize to unseen data. These metrics were calculated for both the training and test datasets to evaluate how well the model performs in both contexts.

Visualization and interpretation of model coefficients were conducted to assess their relative influence on the output variable. Coefficient analysis allows understanding of how changes in input features affect the target variable, providing valuable insight for decision-making in applications where the magnitude and direction of impact are significant. In this case, both the original and optimized coefficients were compared to evaluate how well the optimization replicated the known parameter values.

In conclusion, the CVXPY model provides a robust approach to multiple linear regression, offering flexibility in solver selection, data preprocessing, and model interpretation. The use of the OSQP solver in this implementation enabled efficient parameter estimation and reliable evaluation, making CVXPY a powerful tool for tackling regression problems with a strong focus on precision, robustness, and interpretability.

3 MODEL-BASED SYSTEM IDENTIFICATION METHOD

3.1 Ship Motion Mathematical Model

The selected SI approach for this research is the Model-Based Method, based on K. Wolff's work [17], which extends Abkowitz's mathematical model [1] using a Taylor Series Expansion for a polynomial representation. Knowledge of these structural models is essential to assess the regression model. Ship motion is analyzed in the horizontal plane for three degrees of freedom (surge, sway, and yaw), represented by the dynamic equations (2), (3), and (4).

The numerical model uses two reference frames based on the right-hand convention: an earth-fixed reference frame (x_0, y_0, z_0) and a body-fixed reference frame (x, y, z). In the body-fixed frame, the x-axis points forward, the y-axis to starboard, and the z-axis downward.

$$m(\dot{u} - vr - x_G r^2) = X \tag{2}$$
$$m(\dot{v} + ur + x_G \dot{r}) = Y \tag{3}$$
$$I_z \dot{r} + m x_G(\dot{v} + ur) = N \tag{4}$$

In these equations, m represents the ship's mass, I_z is the moment of inertia around the z-axis, and x_G is the longitudinal center of gravity in the body-fixed frame. The variables u, v, and r indicate surge speed, sway and yaw speed, respectively. The right-hand side of equations (2), (3), and (4) denote the hydrodynamic forces (X, Y) and moment (N). Each term is represented as a function of multiple variables using a Taylor Series expansion, as shown in Equation (5):

$$X, Y, N = f(u, v, r, \dot{u}, \dot{v}, \dot{r}, \delta) \tag{5}$$

The original hydrodynamic forces and moments were obtained from Simonsen et al. [18], using Planar Motion Mechanism (PMM) tests to determine the forces for surge, sway, and yaw. This research uses the well-known KCS container ship model. The coefficients in the following equations are consistent with those derived from these PMM tests, but they were used using K. Wolff [17] approach.

$$\begin{aligned} X = {} & X_u u\Delta u + X_{uu}\Delta u^2 + X_v uv + X_v v^2 + X_r ur + X_{rr} r^2 \\ & + X_{vr} vr + X_\delta u^2\delta + X_{\delta\delta} u^2\delta^2 + X_{u\delta} u\delta\Delta u + X_{u\delta\delta} u\delta^2\Delta u \\ & + X_{v\delta} uv\delta + X_{v\delta\delta} uv\delta^2 + X_{vv\delta} v^2\delta + X_{r\delta} ur\delta + X_{r\delta\delta} ur\delta^2 + X_{rr\delta} r^2\delta \\ & + X_{\dot{u}}\dot{u} \end{aligned} \tag{6}$$

$$\begin{aligned} Y = {} & Y_o u^2 + Y_u u\Delta + Y_v uv + Y_{vv} v^2 + Y_{v|v|} v|v| + Y_{vu} v\Delta u \\ & + Y_r ur + Y_r r^2 + Y_{r|r|} r|r| + Y_{rrr} r^3/u + Y_{vvr} v^2 r/u + Y_{vrr} vr^2/u \\ & + Y_\delta u^2\delta + Y_{\delta\delta}\delta^2 u^2 + Y_{\delta\delta\delta} u^2\delta^3 + Y_{\delta u} u\delta\Delta u + Y_{\delta\delta u} u\delta^2\Delta u \\ & + Y_{\delta\delta\delta u} u\delta^3\Delta u + Y_{v|\delta|} uv|\delta| + Y_{v\delta\delta} uv\delta^2 + Y_{r\delta} ur\delta + Y_{rr\delta} r^2\delta + Y_{r\delta\delta} ur\delta^2 \\ & + Y_{\dot{v}}\dot{v} + Y_{\dot{r}}\dot{r} \end{aligned} \tag{7}$$

$$\begin{aligned} N = {} & N_o u^2 + N_u u\Delta + N_v uv + N_{vv} v^2 + N_{v|v|} v|v| + N_{vu} v\Delta u \\ & + N_r ur + N_r r^2 + N_{r|r|} r|r| + N_{rrr} r^3/u + N_{vvr} v^2 r/u + N_{vrr} vr^2/u \\ & + N_\delta u^2\delta + N_{\delta\delta}\delta^2 u^2 + N_{\delta\delta\delta} u^2\delta^3 + N_{\delta u} u\delta\Delta u + N_{\delta\delta u} u\delta^2\Delta u \\ & + N_{\delta\delta\delta u} u\delta^3\Delta u + N_{v|\delta|} uv|\delta| + N_{v\delta\delta} uv\delta^2 + N_{r\delta} ur\delta + N_{rr\delta} r^2\delta + N_{r\delta\delta} ur\delta^2 \\ & + N_{\dot{v}}\dot{v} + N_{\dot{r}}\dot{r} \end{aligned} \tag{8}$$

For shallow water conditions, the hydrodynamic coefficients are based on Simonsen et al. [18], with corrections from the 23rd ITTC Proceedings [19]. Specifically, corrections by Sheng et al. [20] are applied

to the added mass terms for sway $Y_{\dot{v}}$ and yaw $N_{\dot{r}}$, while corrections by Clarke et al. [21, 22] relate to sway terms Y_v and Y_r, and yaw terms N_v and N_r.

3.2 Data Selection

To evaluate the performance of the convex model, it was trained using data generated from a ship numerical simulator developed in Python, simulating ship manoeuvres in the horizontal plane for three degrees of freedom (3-DOF). The numerical simulator is based on the nonlinear K. Wolff mathematical model [17], with hydrodynamic coefficients derived from the study by Simonsen et al. [18]. The training manoeuvres included zig-zag tests with a rudder angle and course angle of 30°-20°, conducted at a design speed of 24.0 knots to the starboard side. Table 1 shows the main characteristics of the ship model.

Main Particulars	**Symbol**	**Full Scale**
Length between perpendiculars	L_{pp} [m]	230
Maximum beam of waterline	B_{WL} [m]	32.2
Draft	T [m]	10.8
Displacement volume	∇ $[m^3]$	5203
Block coefficient	(C_B) [-]	0.6505
Longitudinal Centre of Gravity	LCG [m]	111.6
Moment of inertia	K_{zz}/L_{PP}	0.25

Table 1: KCS Container Ship Main Particulars

The benchmark model used to simulate the manoeuvres is the KCS container ship designed at the Maritime and Ocean Engineering Research Institute (MOERI). This model was developed to study and explain the dynamics of fluid flow and serves as a benchmark for validating Computational Fluid Dynamics (CFD) models, specifically for a contemporary container ship equipped with a bulbous bow and stern.

The performance of the model for parameter prediction was evaluated by comparing the original and predicted hydrodynamic coefficients, as well as the trajectories, speed, forces, and moments.

The data used to generate the linear regression model follows the matrix representation in Equation (1). Here, X is the matrix of input features (independent variables) corresponding to the right side of equations (2), (3), and (4), while y is the vector of observed outcomes (dependent variable). The prediction vector β corresponds to the hydrodynamic coefficients, excluding the velocity terms from equations (2), (3), and (4).

4 RESULTS

This section presents the results obtained for both deep and shallow water conditions. The selected manoeuvres for evaluating the original and predicted values were the same for both conditions: a turning circle manoeuvre with a rudder angle of 35 degrees to starboard and a zig-zag manoeuvre with a rudder angle of 30 degrees and a heading (psi) of 20 degrees. The shallow water condition considered in this study has a water depth-to-draft ratio (h/T) of 1.2.

4.1 Parameter Identification in Deep Water Conditions

The deep water simulation manoeuvres were based on the zig-zag manoeuvre for a rudder angle of 30 degrees and a course angle of 20 degrees, at a design speed of 24.0 knots. The model's performance was assessed by comparing the predicted and original ship trajectories, using the MAE as the metric to quantify differences. The results indicate varying prediction accuracy across parameters, with sway and yaw coefficients generally having higher MAE values, reflecting significant discrepancies. Surge coefficients tend to have smaller errors, although some, such as X_v and X_{v2}, exhibit relatively high errors. Yaw predictions also show variability, with parameters like N_{rIrI} and N_{vdlt2} showing considerable errors, suggesting these are among the most challenging to predict accurately.

Param. Surge	C.O.	C.P.	MAE (%)	Param. Sway	C.O.	C.P.	MAE (%)	Param. Yaw	C.O.	Predicted	MAE (%)
Xu	-2709	-2886	6.52	Y0	11	0	100.00	N0	-9	5	159.33
Xu2	1314	1129	14.08	Yu	-15	-31	109.33	Nu	31	24	21.29
Xv	-411	-49	88.00	Yv	-11670	-11442	1.96	Nv	-5087	-5181	1.84
Xv2	-3557	-5571	56.63	Yv2	169	118	30.22	Nv2	42	128	204.84
Xr	516	685	32.71	YvIvI	-29447	-28866	1.97	NvIvI	-4802	-5463	13.77
Xr2	-662	-834	26.01	Yvu	-1630	-1778	9.06	Nvu	-2441	-2380	2.49
Xvr	6007	5579	7.12	Yr	2049	1617	21.07	Nr	-2518	-2396	4.83
Xdlt	-17	0	100.00	Yr2	54	0	100.00	Nr2	-245	-251	2.26
Xdlt2	-1255	-1123	10.53	YrIrI	1445	3283	127.16	NrIrI	-48	-741	1444.05
Xdltu	-300	-395	31.57	Yr3	-1411	-3182	125.50	Nr3	-1964	-1282	34.70
Xdlt2u	2684	2659	0.94	Yv2r	-12317	-15395	24.99	Nv2r	-34725	-32868	5.35
Xvdlt	1731	2560	47.88	Yvr2	-31398	-35983	14.60	Nvr2	-1593	-32	98.02
Xv2dlt	-2180	-3498	60.48	Ydlt	3102	3098	0.12	Ndlt	-1561	-1495	4.26
Xvdlt2	-1191	-1187	0.31	Ydlt2	177	194	9.59	Ndlt2	-83	-96	15.90
Xrdlt	-564	0	100.00	Ydlt3	-2065	-2157	4.44	Ndlt3	1402	1343	4.22
Xr2dlt	-561	-545	2.88	Ydltu	-3972	-3990	0.44	Ndltu	1630	1548	5.06
Xrdlt2	2929	2863	2.25	Ydlt2u	240	264	10.13	Ndlt2u	-162	-174	7.33
				Ydlt3u	940	1175	25.01	Ndlt3u	864	834	3.48
				YIvIdlt	1424	1832	28.63	NIvIdlt	-1305	-1437	10.13
				Yvdlt2	4391	3520	19.83	Nvdlt2	-34	143	519.25
				Yrdlt	403	347	13.96	Nrdlt	-168	-159	5.53
				Yr2dlt	1964	4031	105.27	Nr2dlt	-1178	-1968	67.04
				Yrdlt2	153	917	499.65	Nrdlt2	-458	-902	96.88

Table 2: Surge, sway, and yaw prediction of hydrodynamic coefficients for deep water condition with MAE. Results are shown in non-dimensional units and must be multiplied by 10^{-6}.

Figures 2, 3, 4, and 5 provide different perspectives of the turning circle manoeuvre at 35 degrees to starboard. Figure 2 illustrates the comparison between the predicted and original trajectories, showing a general alignment with minor deviations. Figuring the manoeuvre, where slight discrepancies are noted, particularly during high rudder deflection. Figure 4 shows the comparison of heading (psi) and rudder angle, demonstrating the model's ability to capture the vessel's changes in course effectively. Figure 3 shows the surge and sway forces comparison during the manoeuvre, highlighting slight discrepancies during high rudder deflection. Finally, the Figure 5 presents the yaw force, indicating that while the general trends align well, there are challenges in accurately predicting specific rapid changes.

Table 3 provides a detailed summary of the MAE for each parameter at key registration points during the turning circle manoeuvre. These reference points (1, 2, 3, and 4) correspond to the moments when the heading reaches 90, 180, 270, and 360 degrees, respectively. The analysis reveals significant deviations in the longitudinal coordinate (x) at Register 3, while lateral dynamics (the y coordinate) present challenges mainly at Register 4.

Description	Register 1	Register 2	Register 3	Register 4
x (m) (Original)	748.09	437.73	-81.19	213.50
x (m) (Predicted)	741.33	427.36	-95.47	203.51
MAE (x (m)) (%)	0.90	2.37	17.59	4.68
y (m) (Original)	-373.14	-899.78	-601.27	-84.05
y (m) (Predicted)	-373.47	-902.99	-600.74	-78.23
MAE (y (m)) (%)	0.09	0.36	0.09	6.93
Surge velocity (m/s) (Original)	9.93	8.32	7.73	7.54
Surge velocity (m/s) (Predicted)	10.12	8.53	7.96	7.78
MAE (surge velocity (m/s)) (%)	1.90	2.64	2.97	3.13
Sway velocity (m/s) (Original)	-2.44	-2.22	-2.12	-2.09
Sway velocity (m/s) (Predicted)	-2.47	-2.25	-2.16	-2.13
MAE (sway velocity (m/s)) (%)	1.33	1.74	1.87	1.94
Yaw velocity (deg/s) (Original)	1.33	1.16	1.09	1.07
Yaw velocity (deg/s) (Predicted)	1.35	1.18	1.11	1.09
MAE (yaw velocity (deg/s)) (%)	1.47	1.67	1.82	1.92
Time (s) (Original)	78.80	151.82	232.30	315.94
Time (s) (Predicted)	77.68	149.59	228.57	310.72
MAE (time (s)) (%)	1.42	1.47	1.60	1.65

Table 3: Detailed MAE for key parameters at registration points during the Turning Circle manoeuvring at 35 degrees starboard.

Figures 6, 7, 8, and 9 illustrate different aspects of the zig-zag maneuver at 30/20 degrees to starboard. Each figure compares original and predicted values, providing a comprehensive view of the vessel's behavior during the maneuver.

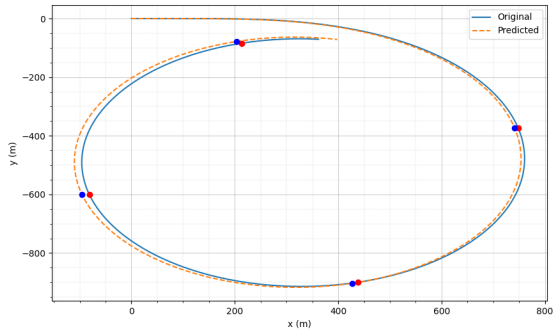

Figure 2: Turning circle trajectory comparison.

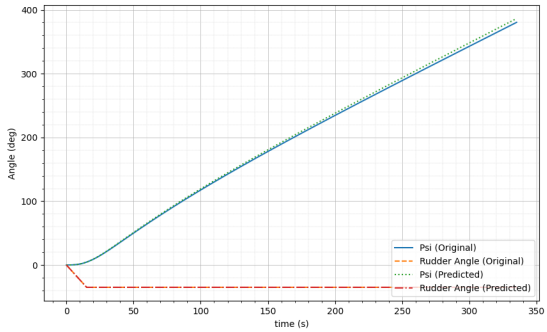

Figure 4: Heading and rudder angle comparison.

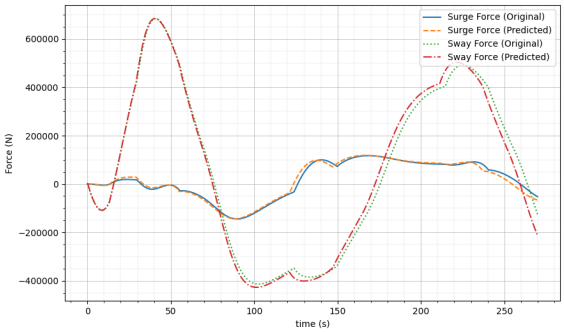

Figure 3: Surge and sway forces comparison.

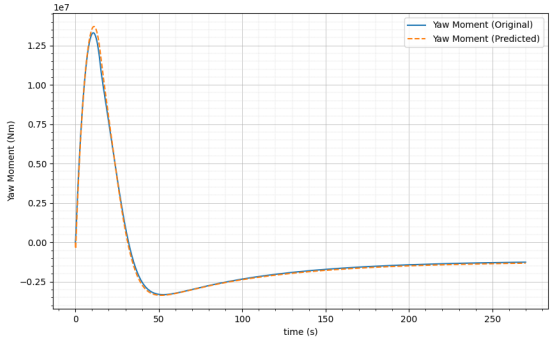

Figure 5: Yaw moment comparison.

Table 4 presents the detailed MAE values at each registration point, including original and predicted values for position, velocities, and time. Six key reference points were selected. The first point corresponds to when the vessel reaches a heading of 20 degrees with a rudder angle of 30 degrees, marking the start of changing the rudder to the opposite side. The second, fourth, and sixth points correspond to the first, second, and third overshoots, respectively. The third and fifth points mark when the vessel again reaches a heading of 20 degrees with the rudder at 30 degrees on the opposite side, initiating a new change of rudder.

Description	Reg. 1	Reg. 2	Reg. 3	Reg. 4	Reg. 5	Reg. 6
x (m) (Original)	361.13	645.50	1203.41	1391.14	1897.60	2118.47
x (m) (Predicted)	356.77	640.15	1192.89	1382.07	1890.60	2111.11
MAE (x (m)) (%)	1.21	0.83	0.87	0.65	0.37	0.35
y (m) (Original)	-18.48	-163.54	-443.10	-382.78	-208.40	-295.33
y (m) (Predicted)	-18.59	-161.98	-432.21	-369.78	-193.56	-279.53
MAE (y (m)) (%)	0.60	0.95	2.46	3.40	7.12	5.35
Surge velocity (m/s) (Original)	12.04	11.17	7.34	7.52	8.68	8.91
Surge velocity (m/s) (Predicted)	12.09	11.28	7.49	7.63	8.83	9.05
MAE (surge velocity (m/s)) (%)	0.42	0.95	2.06	1.47	1.80	1.62
Sway velocity (m/s) (Original)	-1.77	-0.94	1.97	1.06	-2.01	-1.01
Sway velocity (m/s) (Predicted)	-1.73	-0.98	1.98	1.08	-2.02	-1.06
MAE (sway velocity (m/s)) (%)	1.84	3.91	0.77	2.69	0.59	4.99
Yaw velocity (deg/s) (Original)	1.32	0.01	-1.03	0.00	1.16	0.01
Yaw velocity (deg/s) (Predicted)	1.34	0.01	-1.06	0.00	1.17	0.01
MAE (yaw velocity (deg/s)) (%)	1.06	29.41	3.12	182.11	1.30	16.00
Time (s) (Original)	29.43	57.19	123.69	150.33	214.41	241.43
Time (s) (Predicted)	29.06	56.44	121.09	147.54	211.06	237.51
MAE (time (s)) (%)	1.27	1.30	2.11	1.86	1.56	1.62

Table 4: Detailed MAE for key parameters at registration points during the Zig-Zag manoeuvring at 30/20 degrees starboard.

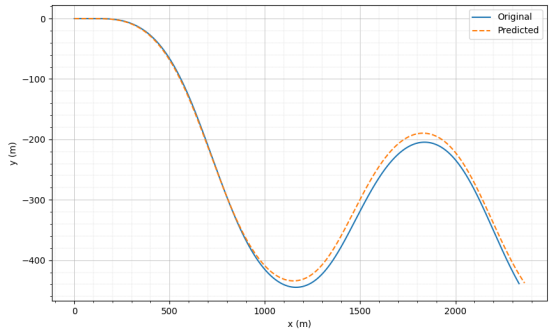

Figure 6: Zig-Zag trajectory comparison.

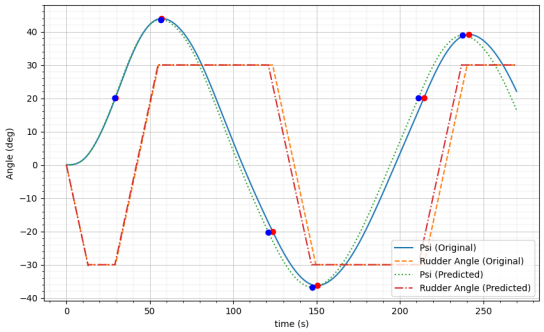

Figure 8: Heading and rudder angle comparison.

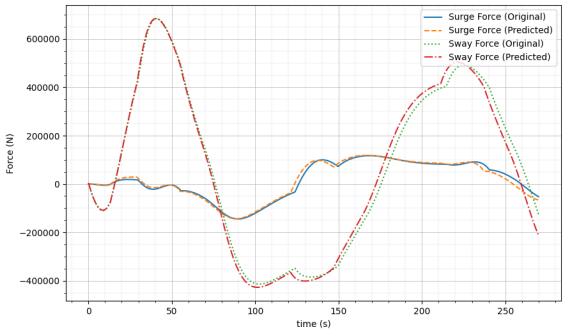

Figure 7: Surge and sway forces comparison.

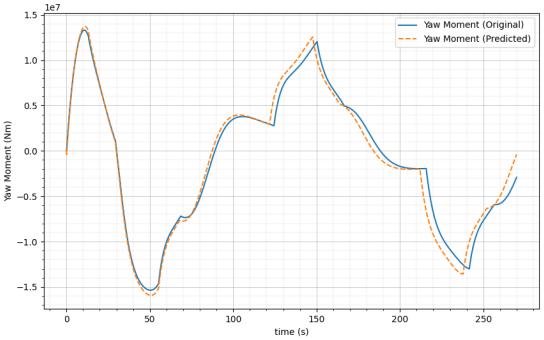

Figure 9: Yaw moment comparison.

The results indicate consistent accuracy for the longitudinal position (x), with MAE values ranging from 0.35% to 1.21%. In contrast, the lateral position (y) shows greater variability, with the MAE reaching up to 7.12% at Register 5, highlighting challenges in predicting lateral movements during repeated changes in direction. Surge velocity exhibits good accuracy, with a maximum MAE of 2.06%, while sway velocity shows higher discrepancies, particularly at Registers 2 and 6. Yaw velocity is the most challenging to predict, with an elevated MAE of 182.11% at Register 4, likely due to complex rotational responses and non-linear hydrodynamic effects.

Figures 6, 7, 8, and 9 provide visual insights into these dynamics. In Figure 6, the trajectory comparison shows good alignment between the original and predicted paths, with slight deviations during sharp directional changes. Figure 7 illustrates the surge and sway forces acting on the vessel, where surge forces are well predicted, while sway forces show discrepancies during high rudder deflection. Figure 8 shows the relationship between rudder angle and heading (psi), capturing the vessel's response, though with some deviations during abrupt heading changes. Figure 9 highlights significant discrepancies in yaw force at Registers 4 and 6, consistent with the high MAE values for yaw velocity.

In summary, the zig-zag maneuver at 30/20 degrees to starboard is effectively predicted by the model in terms of surge velocity and longitudinal positioning. However, lateral dynamics and yaw response show notable inaccuracies during abrupt direction changes, indicating the need for model improvements, particularly in representing non-linear and coupled hydrodynamic forces.

4.2 Parameter Identification in Shallow Water Condition

The shallow water simulation manoeuvre corresponds to the zig-zag manoeuvre with a rudder angle of 30 degrees and a course angle of 20 degrees. The simulation was carried out for a model ship at a design speed of 24.0 knots, with a water depth-to-draft ratio (h/T) of 1.2. The results presented in Table

5 indicate a some important variations across some parameters, particularly for sway and yaw coefficients, which display high MAE values. Parameters such as Y_{v2} and N_{vdlt2} exhibit significant deviations, with MAE values exceeding 100%. Surge coefficients, as in the deep water predictions, generally show smaller errors, though some, like X_{v2}, still have relatively high discrepancies. Overall, yaw coefficients again display substantial variability, with N_{vIvI} and N_{rdlt2} showing significant differences from the original values, highlighting ongoing challenges in achieving precise predictions.

Param. Surge	**C.O.**	**C.P.**	**MAE (%)**	**Param. Sway**	**C.O.**	**C.P.**	**MAE (%)**	**Param. Yaw**	**C.O.**	**Predicted**	**MAE (%)**
Xu	-2709	-2797	3.26	Y0	11	4	65.36	N0	-9	0	100.00
Xu2	1314	1100	16.26	Yu	-15	-112	644.59	Nu	31	54	72.58
Xv	-411	0	100.00	Yv	-38617	-41750	8.11	Nv	-12840	-8904	30.66
Xv2	-3557	-14140	297.51	Yv2	169	-3415	2120.64	Nv2	42	6314	14933.18
Xr	516	633	22.65	YvIvI	-29447	-26331	10.58	NvIvI	-4802	-13597	183.16
Xr2	-662	-1974	198.23	Yvu	-1630	-3534	116.83	Nvu	-2441	-1083	55.65
Xvr	6007	0	100.00	Yr	5172.2	4400	14.93	Nr	-5495	-4417	19.62
Xdlt	-17	-3	83.94	Yr2	54	-72	233.33	Nr2	-245	-606	147.53
Xdlt2	-1255	-1177	6.20	YrIrI	1445	397	72.53	NrIrI	-48	0	100.00
Xdltu	-300	-384	28.11	Yr3	-1411	-18481	1209.80	Nr3	-1964	-4398	123.96
Xdlt2u	2684	2504	6.70	Yv2r	-12317	-369942	2903.51	Nv2r	-34725	-52860	52.22
Xvdlt	1731	3793	119.13	Yvr2	-31398	-211959	575.07	Nvr2	-1593	0	100.00
Xv2dlt	-2180	0	100.00	Ydlt	3102	2976	4.06	Ndlt	-1561	-1380	11.61
Xvdlt2	-1191	-927	22.19	Ydlt2	177	135	23.72	Ndlt2	-83	-74	10.84
Xrdlt	-564	0	100.00	Ydlt3	-2065	-1702	17.56	Ndlt3	1402	1067	23.87
Xr2dlt	-561	-1064	89.63	Ydltu	-3972	-3619	8.88	Ndltu	1630	1221	25.10
Xrdlt2	2929	2849	2.74	Ydlt2u	240	485	102.19	Ndlt2u	-162	-232	43.48
				Ydlt3u	940	1330	41.52	Ndlt3u	864	1060	22.72
				YIvIdlt	1424	229	83.91	NIvIdlt	-1305	-1098	15.86
				Yvdlt2	4391	84	98.08	Nvdlt2	-34	0	100.00
				Yrdlt	403	184	54.34	Nrdlt	-168	-185	10.06
				Yr2dlt	1964	7899	302.18	Nr2dlt	-1178	-5296	349.55
				Yrdlt2	153	1516	891.14	Nrdlt2	-458	-2035	344.41

Table 5: Surge, sway, and yaw prediction of hydrodynamic coefficients for shallow water condition with MAE. Results are shown in non-dimensional units and must be multiplied by 10^{-6}.

Figures 10, 11, 12, and 13 illustrate different aspects of the maneuver. Each figure compares the predicted and original values, providing insights into the model's performance under shallow water conditions.

Table 6 shows the MAE for each parameter at key registration points during the maneuver, including original and predicted values for position, velocities, and time. The results indicate that the x coordinate has a maximum MAE of 4.23% at Register 3, showing some difficulty in predicting longitudinal positioning at the point of maximum deviation. The y coordinate presents a notable error of 11.55% at Register 4, suggesting challenges in predicting lateral dynamics, especially in shallow waters, where increased hydrodynamic resistance affects lateral force generation.

Description	Register 1	Register 2	Register 3	Register 4
x (m) (Original)	1160.97	378.04	-499.78	272.85
x (m) (Predicted)	1172.89	374.28	-520.91	270.48
MAE (x (m)) (%)	1.03	1.00	4.23	0.87
y (m) (Original)	-830.85	-1719.80	-943.96	-68.76
y (m) (Predicted)	-844.02	-1746.97	-954.39	-60.82
MAE (y (m)) (%)	1.59	1.58	1.10	11.55
Surge velocity (m/s) (Original)	11.73	11.60	11.56	11.55
Surge velocity (m/s) (Predicted)	11.80	11.70	11.67	11.66
MAE (surge velocity (m/s)) (%)	0.61	0.84	0.92	0.94
Sway velocity (m/s) (Original)	-0.73	-0.73	-0.73	-0.73
Sway velocity (m/s) (Predicted)	-0.72	-0.72	-0.72	-0.72
MAE (sway velocity (m/s)) (%)	1.11	1.24	1.28	1.29
Yaw velocity (deg/s) (Original)	0.80	0.80	0.80	0.80
Yaw velocity (deg/s) (Predicted)	0.79	0.79	0.79	0.79
MAE (yaw velocity (deg/s)) (%)	1.01	1.14	1.19	1.20
Time (s) (Original)	133.75	246.46	358.60	470.56
Time (s) (Predicted)	135.06	248.88	362.32	475.77
MAE (time (s)) (%)	0.97	0.98	1.04	1.11

Table 6: Detailed MAE for key parameters at registration points during the Turning Circle manoeuvring at 35 degrees starboard in shallow waters.

The surge velocity is predicted effectively, with MAE values below 1% across all registers, while sway velocity errors remain consistent at around 1.1-1.3%. Yaw velocity also shows minor discrepancies, with

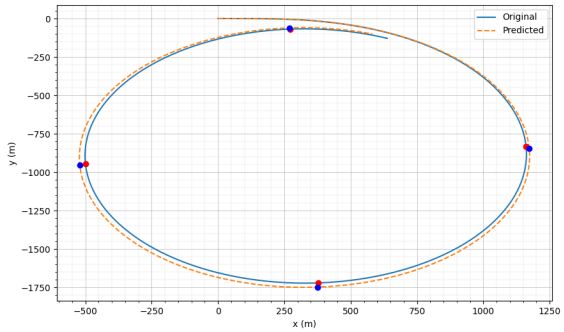

Figure 10: Turning circle trajectory comparison.

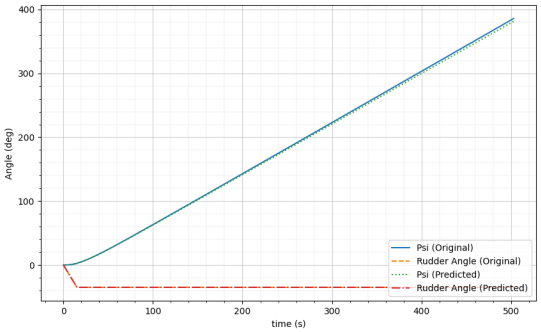

Figure 12: Heading and rudder angle comparison.

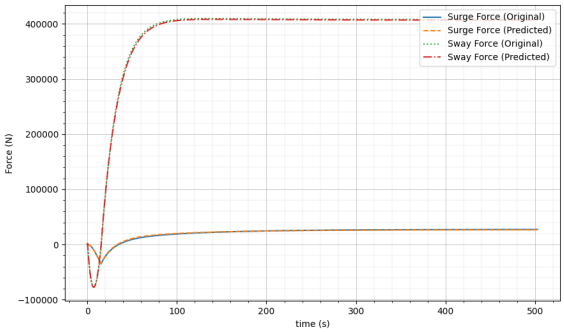

Figure 11: Surge and sway forces comparison.

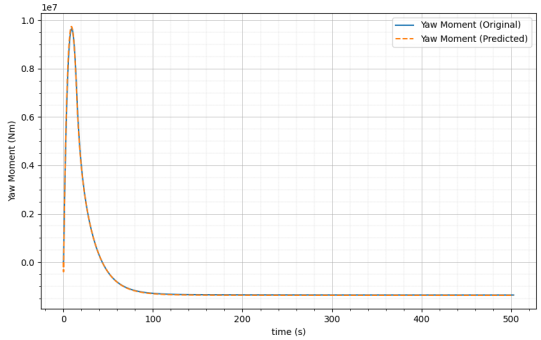

Figure 13: Yaw moment comparison.

MAE values between 1.01% and 1.20%. The timing predictions are accurate, with MAE under 2%, indicating good temporal prediction throughout the maneuver.

Figures 10, 11, 12, and 13 provide visual representations of these dynamics. Figure 10 shows that the trajectory is generally well-aligned, with some deviations at Register 3. Figure 11 illustrates the surge and sway forces, which align well except for minor discrepancies during periods of high rudder input. Figure 12 compares heading (psi) and rudder angle, demonstrating effective prediction of the vessel's response to steering inputs. Finally, Figure 13 highlights the yaw force, indicating good prediction accuracy with some deviations during rapid heading changes.

In summary, the model performs well in predicting surge velocity and yaw under shallow water conditions, while the lateral dynamics, particularly the y coordinate, present greater challenges. Improvements in modeling hydrodynamic effects, especially for shallow water, could help reduce these discrepancies.

Next Figures 14, 15, 16, and 17 represent different aspects of the zig-zag maneuver at 30/20 degrees to starboard in shallow water. Each figure compares the predicted and original values, providing insights into the model's performance.

Table 7 shows the MAE for each parameter at key registration points during the maneuver. The x coordinate shows good accuracy across all points, with MAE values ranging from 0.19% to 1.29%, indicating effective prediction of longitudinal positioning. In contrast, the y coordinate has significant variability, with a peak MAE of 19.34% at Register 5, suggesting challenges in capturing lateral positioning, especially during rapid direction changes. This discrepancy could be due to increased hydrodynamic resistance and shallow water effects.
Surge velocity is well-predicted, with a maximum MAE of 0.78%, while sway velocity shows slightly higher errors, ranging from 1.00% to 1.87%, particularly at Registers 3 and 4. Yaw velocity presents greater

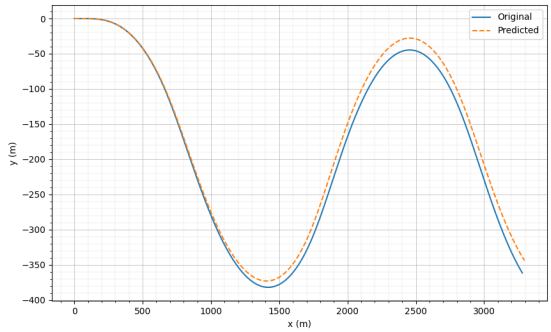

Figure 14: Zig-Zag trajectory comparison.

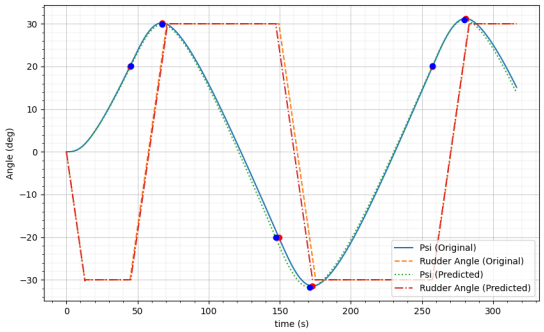

Figure 16: Heading and rudder angle comparison.

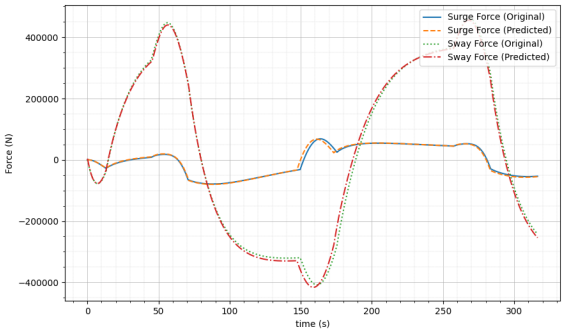

Figure 15: Surge and sway forces comparison.

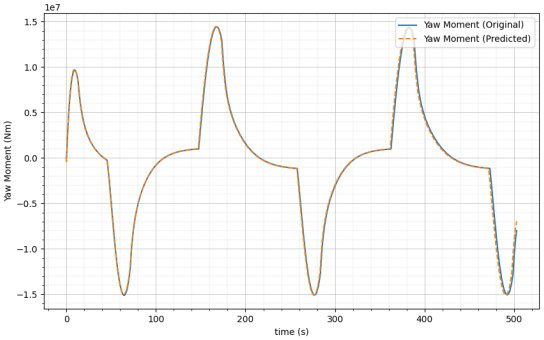

Figure 17: Yaw moment comparison.

Description	Reg 1	Reg 2	Reg 3	Reg 4	Reg 5	Reg 6
x (m) (Original)	541.63	787.75	1635.95	1846.63	2691.82	2926.07
x (m) (Predicted)	548.61	791.59	1619.92	1832.93	2701.05	2931.70
MAE (x (m)) (%)	1.29	0.49	0.98	0.74	0.34	0.19
y (m) (Original)	-54.48	-165.48	-351.54	-255.98	-79.13	-186.18
y (m) (Predicted)	-55.79	-164.59	-343.32	-245.82	-63.83	-168.48
MAE (y (m)) (%)	2.41	0.54	2.34	3.97	19.34	9.51
Surge velocity (m/s) (Original)	12.10	12.08	9.72	9.99	11.03	11.29
Surge velocity (m/s) (Predicted)	12.12	12.12	9.77	10.03	11.12	11.37
MAE (surge velocity (m/s)) (%)	0.19	0.31	0.51	0.41	0.78	0.71
Sway velocity (m/s) (Original)	-0.59	-0.20	0.67	0.23	-0.68	-0.22
Sway velocity (m/s) (Predicted)	-0.58	-0.20	0.68	0.23	-0.67	-0.22
MAE (sway velocity (m/s)) (%)	1.73	1.00	1.87	1.21	1.79	1.67
Yaw velocity (deg/s) (Original)	0.69	0.01	-0.76	-0.01	0.76	0.01
Yaw velocity (deg/s) (Predicted)	0.68	0.00	-0.78	-0.01	0.75	0.01
MAE (yaw velocity (deg/s)) (%)	1.51	97.15	2.64	22.14	1.68	30.03
Time (s) (Original)	44.71	67.06	149.40	173.06	257.45	280.55
Time (s) (Predicted)	45.27	67.25	147.17	171.01	257.26	279.80
MAE (time (s)) (%)	1.25	0.28	1.50	1.18	0.07	0.27

Table 7: Detailed MAE for key parameters at registration points during the Zig-Zag manoeuvring at 30/20 degrees starboard in shallow waters.

challenges, with a notable MAE of 97.15% at Register 2, indicating difficulty in predicting the rotational dynamics under rudder-induced forces, possibly influenced by shallow water effects. Timing errors are relatively low, with a maximum MAE of 1.50%, indicating that temporal dynamics are well captured throughout the maneuver.

Figures 14, 15, 16, and 17 provide visual insights into these dynamics. Figure 14 shows the trajectory comparison, highlighting more pronounced deviations during sharp changes in heading. Surge and sway forces (Figure 15) are mostly well-aligned, though discrepancies occur during high rudder deflection.

Figure 16 shows the heading (psi) and rudder angle, demonstrating the model's ability to follow rudder input, with some deviations during rapid changes. Figure 17 highlights the yaw force, where discrepancies are notable at Registers 2 and 6, consistent with the high yaw velocity MAE values.

In summary, the zig-zag maneuver at 30/20 degrees to starboard in shallow water shows effective prediction of surge velocity and longitudinal positioning, while lateral and yaw dynamics present greater inaccuracies. The increased resistance and seabed interactions in shallow water appear to affect the model's ability to predict lateral forces and rotational dynamics accurately. Future improvements should focus on better modeling non-linear forces and coupled dynamics to enhance prediction accuracy under shallow water conditions, particularly during sharp directional changes.

5 CONCLUSIONS

5.1 Conclusions

The analysis conducted using the CVXPY model for linear regression and parameter identification in ship manoeuvres shows promising results for predicting trajectories and hydrodynamic forces in both deep and shallow water conditions. The model's ability to adjust hydrodynamic coefficients and predict the ship's response during different manoeuvres, such as turning circles and zig-zag manoeuvres, is demonstrated by the generally low MAE rates across most evaluated parameters. To further improve the model, several avenues of research are suggested.

It is essential to develop models that more accurately represent shallow water effects, including additional resistance and altered flow around the hull and rudder. This may involve using more advanced flow models or incorporating additional data from CFD simulations specific to these conditions. Additionally, exploring more advanced machine learning techniques, such as support vector regression or Bayesian regression, could help identify patterns in manoeuvrability data and adjust hydrodynamic coefficients more precisely, particularly for predicting lateral and yaw forces, due to their robustness in capturing non-linear relationships. To further assess and improve the model's accuracy, it would be beneficial to compare the obtained results with more extensive experimental data, including full-scale trials under various environmental conditions and ship loading scenarios. Furthermore, identifying and incorporating the influence of environmental conditions, such as current and wind, into the model could provide significant improvements. The effects of wind are particularly important for identifying aerodynamic coefficients, which directly affect the ship's manoeuvrability and stability.

These future research directions focus on addressing the observed limitations, particularly in representing complex forces and shallow water effects, contributing to the enhancement of safety and efficiency in ship operations under varying environmental conditions and manoeuvres. Overall, the results indicate that the model performs well in predicting surge velocity and longitudinal position (x), with low errors that are crucial for accurate trajectory planning. However, challenges were observed in predicting lateral dynamics (sway) and yaw, particularly during manoeuvres involving sharp directional changes and large rudder angles. These challenges were more pronounced in shallow water conditions, where non-linear hydrodynamic forces and additional resistance significantly affect model accuracy.

REFERENCES

[1] M. Abkowitz. "Lectures on Ship Hydrodynamics - Steering and Manoeuvrability". In: *Hydro- and Aerodynamics Laboratrory, Report No. Hy-5, Denmark.* (1964).

[2] IMO. "Standards for Ship Manoeuvrability. International Maritime Organization (IMO)". In: *Resolution MSC, 137(76)* (2002).

[3] IMO. "The manoeuvring committee final report and recommendations to the 24th ITTC". In: *ITTC (International Towing Tank Conference)* (2005).

[4] M. N. Hayes. "Parameter Identification of Nonlinear Stochastic Systems Applied to Ocenan Vehicle Dynamics, Ph.D. thesis". In: *Massachusetts Institute of Technology, Cambridge, MA* (1971).

[5] K. Åström and C. Källström. "Identification of Ship Steering Dynamics". In: (1976).

[6] C. Källström and K. Åström. "Experiences of System Identification Applied to Ship Steering Dynamics". In: (1979).

[7] W. Y. Hwang. "Application of System Identification to Ship Maneuvering". In: *SNAME* (1980).

[8] Y. Rhee K.P. Lee S.Y. Sung. "Estimation of maneuvring coefficients from PMM test by genetic algorithm." In: *Proceedings, International Symposium and Workshop on Force Acting on a Maneuvring Vessel.* (1998).

[9] W. L. Luo and Z. J. Zou. "Parametric Identification of Ship Maneuvering Models by Using Support Vector Machines". In: *Journal of Ship Research* (2009).

[10] W. Luo. "Parameter Identification of Ship Maneuvering Model Based on Support Vector Machines and Particle Swarm Optimization". In: *J. Offshore Mech. Arct. Eng.* 2016 (2016).

[11] W. Luo and X. Li. "Measures to Diminish the Parameter Drift in the Modeling of Ship Manoeuvring Using System Identification". In: *Applied Ocean Research* (2017).

[12] B. Ban, J. Yang, P. Chen, J. Xiong and Q. Wang. "Ship Track Regression Based on Support Vector Machine". In: *IEEE Access* 5 (2017).

[13] H. Xu, V. Hassani, M. A. Hinostroza and C. Guedes Soares. "Real-Time Parameter Estimation of Nonlinear Vessel Steering Model Using Support Vector Machine". In: *Volume 11B: Honoring Symposium for Professor Carlos Guedes Soares on Marine Technology and Ocean Engineering.* Madrid, Spain: American Society of Mechanical Engineers, 2018.

[14] Z. Wang, Z. Zou and C. Guedes Soares. "Identification of Ship Manoeuvring Motion Based on Nu-Support Vector Machine". In: *Ocean Engineering* (2019).

[15] Y. Xue, Y. Liu, C. Ji and G. Xue. "Hydrodynamic Parameter Identification for Ship Manoeuvring Mathematical Models Using a Bayesian Approach". In: *Ocean Engineering* ().

[16] M. Alexandersson, W. Mao and J. W. Ringsberg. "System Identification of Vessel Manoeuvring Models". In: *Ocean Engineering* (2022).

[17] K. Wolff. "Ermittlung der Manövriereigenschaften fünf repräsentativer Schiffstypen mit Hilfe von CPMC-Modellversuchen". In: (1981).

[18] C. D. Simonsen, J. F. Otzen, C. Klimt, N. L. Larsen and F. Stern. "Maneuvering Predictions in the Early Design Phase Using CFD Generated PMM Data". In: *29th Symposium on Naval Hydrodynamics, FORCE Technology, Denmark and IIHR, University of Iowa, USA* (2012).

[19] The Manoeuvring Committee. *Proceedings of the 23rd ITTC – Volume I: The Manoeuvring Committee Final Report and Recommendations to the 23rd ITTC.* Vienna: 23rd International Towing Tank Conference, 2002.

[20] Z. Sheng. "Contribution to the discussion of the Manoeuvrability Committee report". In: *16th International Towing Tank Conference, Proceedings.* Leningrad, Soviet Union, 1981.

[21] D. Clarke, P. Gedling and G. Hine. "The application of manoeuvring criteria in hull design using linear theory". In: (1983).

[22] D. Clarke. “he shallow water effect on linear derivatives”. In: (1997).

Development of an Azimuth Propeller Duct for Shallow Water Applications

Benjamin Kossmann, Ould el Moctar, University of Duisburg-Essen, Germany

Abstract

The specially shaped sterns of inland waterway vessels allow for the accommodation of relatively large propellers, which is a consequence of the vessels' design. In particular, the diameter of the propellers that can be accommodated is up to 20 % larger, thus enabling operation without ventilation. Nevertheless, in the case of an azimuth thruster with a freely positioned propeller, ventilation may occur due to the small distance between the water surface and the propeller. Such circumstances may result in dangerous operational situations, including an inability to manoeuvre. A systematic investigation was conducted, comprising model testing and numerical URANS simulations, with the objective of analysing the open water characteristics of a typical azimuth thruster fitted with the newly invented shallow water duct. The newly invented shallow water duct was developed with the objective of preventing the air drawing of the thruster's propeller, thereby avoiding the inception of propeller free surface ventilation (aeration). A typical thruster equipped with this duct was examined at an immersion depth below the minimum immersion depth recommended by the ITTC for open water tests. In comparison to a thruster equipped with a conventional standard duct, the performance of the thruster equipped with this shallow water duct was demonstrated to be markedly enhanced. At lower propeller advance coefficients, especially during bollard pull conditions, the duct generated more continuous thrust and torque with the propeller operating at the same operating point. However, at higher propeller advance coefficients, the duct caused the thruster to act like a brake. In particular, when equipped with the shallow water duct, thrusters installed on inland waterway vessels represent a constructive solution to enhance the manoeuvrability and operational safety of ships navigating in confined waters of limited depth. It is anticipated that the installation of the shallow water duct will enhance the thruster's capacity to accelerate the vessel.

Nomenclature

A_e	Projected propeller area (m²)	P	Pitch of the propeller (-)
A_0	Propeller disc area (m²)	P/D	Pitch ratio (-)
A_e/A_0	Area ratio of the propeller (-)	Q_P	Propeller torque (Nm)
$c_{0.7R}$	Profile length of the propeller blade at 70% of the radius (m)	r	Radius (m)
		r_x	Grid refinement factor in the x-direction (-)
c	Chord length (mm)	R_e	Reynolds number (-)
c_{TH}	Thrust loading coefficient (-)	T	Ship draft (m)
D	Propeller diameter (m)	T_D	Duct thrust (N)
D_A	Outer duct diameter (m)	T_P	Propeller thrust (N)
D_I	Inner duct diameter (m)	T_T	Total thrust (N)
D_P	Propeller diameter (m)	v_a	Propeller inflow velocity (m/s)
h	Water depth (m)	Y	Grid refinement ratio (-)
Hz	Frequency (1/s)	Z	Number of blades (-)
J	Advance coefficient (-)	η_{0P}	Propeller open water efficiency (-)
K_{QP}	Propeller moment coefficient (-)	η_{0T}	Total open water efficiency (-)
K_{TD}	Duct thrust coefficient (-)	ν	Kinematic viscosity (m²/s)
K_{TP}	Propeller thrust coefficient (-)	μ_0	Kinematic viscosity (m²/s)
K_{TT}	Total thrust coefficient (-)	ρ	Density of water (kg/m³)
L_D	Duct length (m)		
n	Rotational speed (1/s)		

Introduction

In recent years, water levels on numerous European inland waterways have declined to such an extent that the navigation of vessels has been restricted or even prohibited. It is anticipated that low water levels will occur with greater frequency in the future, resulting in the creation of novel operating scenarios and the necessity for revised specifications for inland waterway vessels. For extended periods, these vessels will be operating in waters of limited depth, i.e. at h/T ratios of less than 2.0. Conventional deep-submerged propellers are confronted with a significant challenge regarding ventilation when the distance from the upper blade edge to the free surface falls below a distance of 2D. This is since no additional structure, such as a hull or a similar obstruction, exists to impede

the flow of ventilation. In inland waterway shipping, navigating in shallow waters may result in the propeller emerging from the water surface, which can cause a loss of thrust and a sudden propeller race. The conventional shaft system, situated within the specially designed stern section of inland waterway vessels, typically permits the propeller to be submerged up to 20% of its diameter. The aft ship design enables the propeller to operate without ventilation by drawing in water. Nevertheless, the occurrence of ventilation may be observed in the case of small ship drafts, which ultimately gives rise to difficulties in manoeuvring. The operation of azimuth thrusters in close proximity to the water surface may also give rise to ventilation issues. It is anticipated that the recently developed shallow water duct, as proposed by Kossmann et al. (2022), will prove beneficial for azimuth thrusters installed on inland waterway vessels navigating in areas where draft limitations restrict the immersion depth of the propeller. To circumvent this issue, the utilisation of this duct represents a practical alternative to a conventional duct, as it modifies the flow into the propeller to generate a more homogeneous thrust and torque, and, in comparison to a conventional duct, to circumvent ventilation. The initial investigation focused on the open water characteristics of a propeller equipped with a conventional duct positioned just below the water surface. For comparison, an investigation was conducted into the open water characteristics of the same propeller with the recently invented shallow water duct. When installed just below the water surface, the duct serves to prevent the inception of ventilation and the drawing of air from the propeller, which is otherwise known as aeration. Computational Fluid Dynamics (CFD) analyses were conducted in accordance with the guidelines set forth by the ITTC (2022) for open water tests. The objective of the simulation was to investigate the effects of the free surface on propeller characteristics, specifically the two-phase flow of air and water. In general, CFD methods are effective for analysing flow problems and optimising newly developed devices, such as this duct. Furthermore, URANS methods and their associated flow models offer a favourable and efficient way of simulating flow phenomena. The selection of an appropriate flow model and the related computational meshing are of paramount importance for achieving accurate results. In accordance with the ITTC guidelines, open water tests are to be conducted at propeller immersion depths of at least 1.5 to 2.0 D (ITTC, 2022) in order to circumvent free surface effects, such as incoming ventilation at low propeller rotations. Tests conducted with pod propellers adhere to the same methodology as tests performed with conventional propellers. An immersion depth of 1.0 D was considered in order to investigate the ventilation of the propeller and the ability of the newly invented duct to avoid such ventilation. The objective of our tests was to emulate a realistic operational scenario applicable to inland navigation. The novel duct design incorporates a dome positioned in front of the duct, which, when viewed from a position between nine o'clock and three o'clock, regulates the inflow to the propeller. The dome, which has been shaped to optimise the flow, is approximately 1.5 times longer than that of a conventional duct. The inlet of the shallow water duct is situated at a lower vertical position in order to guarantee that a safe distance is maintained to the free surface in areas where the intake velocity is high. This prevents the occurrence of ventilation during bollard pull operations, thereby increasing and ensuring uniformity of propeller thrust. This is especially advantageous in critical scenarios, such as when a vessel accelerates or operates at low speeds, as it minimizes the probability of impaired manoeuvrability. The newly developed duct is integrated into an azimuth drive, thereby representing a propulsion system that is universally applicable. It is not necessary to have a particular ship design to install this system. The system may be operated just below the water surface and can be retrofitted to existing inland vessels or vessels underway in shallow waters that would otherwise be unable to manoeuvre with their primary propulsion. Also, the system may be employed as a starting aid, providing the ship with an initial impulse and enabling the primary propeller to be adequately loaded while simultaneously facilitating ventilation at increased speeds.

Geometric Description

Table 1: Principal particulars of the P189 propeller.

Principal dimensions	Symbol	Value	Unit
Propeller	-	P189	-
Propeller diameter	D_P	0.100	*m*
Ratio of Pitch to Propeller Diameter	P/D	1.052	-
Area ratio of the propeller	A_e/A_0	0.710	-
Profile length of the propeller blade at 70% of the radius	$c_{0.7R}$	0.042	-
Blade thickness	-	0.004	*m*
Number of Blades	Z	4	-

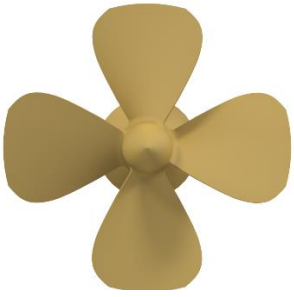

We selected the four-bladed inland waterway stock propeller P189 for our experimental and numerical simulations. This propeller is designed for use on a pod propeller drive system. Table 1 lists principal particulars of the P189 propeller. A picture of the model propeller is also shown.

Table 2: Principal particulars of the standard duct D399 and the shallow water duct FWD-1.

Principal dimensions	**Symbol**	**Value**		**Unit**
Duct		D399	FWD-1	
Profile	-	19a	19a	-
Inner duct diameter	D_I	0.101	0.101	*m*
Outer duct diameter	D_A	0.122	0.122	*m*
Duct length	L_D	0.050	0.129	*m*
Ratio duct length to inner diameter	L_D/D_i	0.500	1.280	-

The standard duct commonly used on inland waterway vessels is a stock duct. It is flattened on the outer circumference at the six o'clock position to maintain a flat vertical geometry and to provide ample distance from the riverbed. Although the flow around the duct is reduced, it is still acceptable. Table *2* lists principal particulars of the standard duct and the new shallow water duct. Both ducts have the same cross-sectional geometry as the standard duct D399. To reduce ventilation entering from the water surface, caused by the suction of the propeller at small advance ratios, a spherical cap encases the shallow water duct in the front area between the nine o'clock and three o'clock position. The spherical cap flushes with the duct, and its front end has a duct inlet profile. The entrance to the calotte is circular. The duct inlet at twelve o'clock position of the spherical cap is deeper than that of the conventional duct. As a result, under calm water conditions or even in small amplitude waves, no air is drawn in. The water primarily enters from the front and the lower sides. Figure *1* presents technical drawings showing the arrangement of a MARIN azimuth thruster (Maritime Research Institute Netherlands), the P189 propeller, and the shallow water duct.

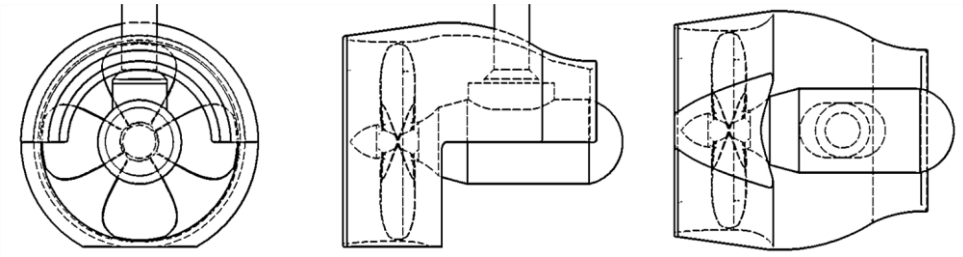

Figure 1: Arrangement of the MARIN azimuth thruster, the P189 propeller, and the shallow water duct FWD-1.

Numerical Method

The simulations were conducted using version 2302 of the Siemens StarCCM+ numerical flow solver. The unsteady Reynolds-Averaged Navier-Stokes (URANS) equations were solved using the k-ω SST turbulence model. The conservation equations were discretised using a second-order method, with spatial and temporal discretisation employed. The Volume of Fluid method was utilised for the representation of the free surface. In accordance with the sliding interface method, the computational mesh was locally refined in both the horizontal and vertical directions in the vicinity of the azimuth thruster. The computational domain was divided into two subdomains. The outer (stator) surrounding rectangular domain was designed with a trimmed cell mesh. The inner domain, representing the rotor of the propeller, was meshed with polyhedral cells. By employing suitable initial and boundary conditions and a series of discrete approximations, an algebraic system of equations was derived, which was subsequently solved numerically. The spatial solution domain was initially divided into a finite number of contiguous control volumes (CVs). The equations of interest were found to contain surface and volume integrals, as well as temporal and spatial derivatives. The derivatives were suitably approximated for each control volume at each time step. It was assumed that the Reynolds-Averaged Navier-Stokes (RANS) equations adequately described the flow, with turbulence effects accounted for via an eddy viscosity model. The equations to be solved comprised the continuity equation, the three momentum component equations, and the two equations for turbulence properties. Furthermore, the conservation laws were upheld as the control volumes underwent changes in position and shape within the rotating propeller domain (Ferziger et al., 2019).

Numerical Setup

As in the model tests, the computational domain's bottom boundary was situated 10 D below the water surface; its inlet boundary, 10 D ahead of the propeller; its outlet boundary, 20 D behind the propeller; and its left and right-side boundaries, 5 D beside the propeller. At the outlet boundary, the distribution of pressure was defined by hydrostatic pressures. At the inlet boundary, the advance speed and the free surface elevation were predetermined. Figure 2 illustrates the computational domain from two perspectives: a lateral view and a frontal view.

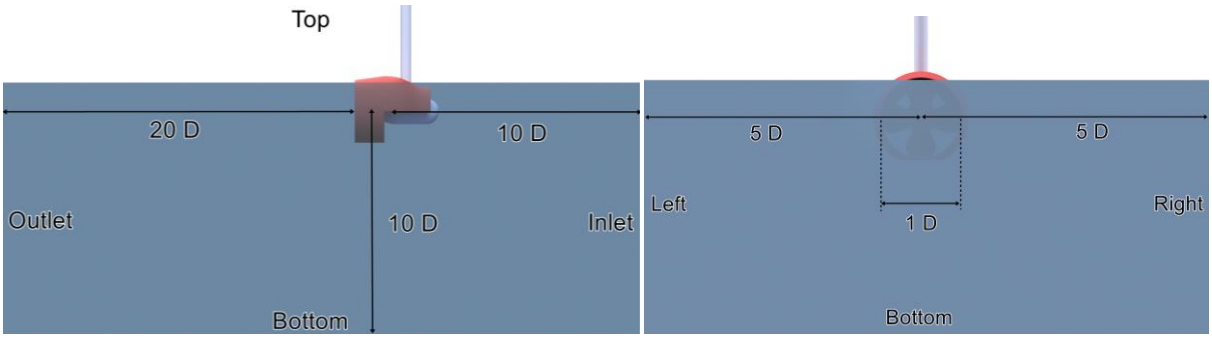

Figure 2: Side view (left) and front view (right) of the computational domain.

The flow within the numerical domain was discretised using small control volumes. The trimmed cell mesher in Simcenter STAR-CCM+ (Siemens 2302) was employed to generate hexahedral cells within a grid that spanned the entire region under consideration. Local refinement was employed for the mesh at the azimuth thruster, the duct, and the free surface. Ten prismatic cell layers were necessary to adequately resolve the boundary layer physics. A cylindrical volume was created and subtracted from the background domain to represent a rotating grid enclosing the propeller. To reduce the number of cells required, the domain was meshed using polyhedral cells in comparison to a trimmed cell mesh. This resulted in the formation of a non-conformal interface. The mesh at the propeller was locally refined via feature curves at its leading and trailing edges. Once more, the requisite number of cell layers was found to be ten, thus ensuring adequate resolution of the boundary layer physics on the surfaces of the propeller blades. By resolving the boundary layer down to the laminar sublayer with a $y+$ of less than unity, the diffusive and dissipative effects were captured.

Discretisation Study

To ensure adequate grid quality for our simulations, we carried out space and time discretization studies. We used the approach of Oberhagemann et al. (2016) to calculate discretization errors. Following his procedure, we performed our simulations on three successively finer grids, starting with a coarse grid. The absolute thickness of the boundary layer and the cell closest to the wall were kept the same for all three grids. For the propeller at an advance ratio of $J = 0.6$ and a rotational speed of $n = 25$ s-1, Table 3 lists the number of control volumes of each grid and the associated grid spacings Δ_{x1}, Δ_{x2}, Δ_{x3} and time step sizes Δ_{t1}, Δ_{t2}, Δ_{t3}. This table also lists the spatial grid refinement ratio γ, as well as the propeller thrust T_P and the propeller moment Q_P obtained on these three grids. Also listed are the comparative extrapolated (grid-independent) and the measured propeller thrust and torque and their absolute and percentage errors. The grid refinement ratio was determined as follows:

Table 3: Grid spacing, time step size, number of cells, refinement ratio, propeller thrust, and propeller moment obtained on the coarse, the medium, and the fine grids and the extrapolated (grid-independent) and measured errors for the ducted propeller at $J = 0.6$ and $n = 25$ s^{-1}.

	Δx [m]	**Δt [s]**	**Number cells [-] Mio**	**γ [-]**	**T_P [N]**	**Q_P [Nm]**
Coarse	$\Delta x_1 = 0.45$	$\Delta t_1 = 0.00028$	2.93	1.00	- 11.78	0.26
Medium	$\Delta x_2 = 0.32$	$\Delta t_2 = 0.00020$	4.51	0.66	- 11.25	0.25
Fine	$\Delta x_3 = 0.23$	$\Delta t_3 = 0.00014$	7.58	0.44	- 11.17	0.23
Extrapolated	-	-	-	0.00	- 10.60	0.21
Measured	-	-	-	-	- 11.08	0.21
Computed error absolute	-	-	-	-	0.48	0
Computed error %	-	-	-	-	- 4.53 %	0 %

$$\Upsilon_i = \frac{\Delta x_i}{\Delta x_1} = \frac{1}{r_x^{i-1}} \qquad (1)$$

where subscript i refers to the particular grid, and r_x is the grid's refinement factor in the x-direction. We performed our discretization study for turbulent flow conditions. The solution variables of interest were propeller thrust T_P and propeller torque Q_P. With increasing grid fineness, i.e., with decreasing refinement ratio γ, computed propeller thrust T_P, obtained on the three grids, as well as the extrapolated (grid-independent) and measured propeller variables converged monotonically towards the grid-independent solution at $\gamma = 0$. Absolute values of propeller thrust T_P and propeller moment Q_P decreased with increasing grid fineness. The largest error of propeller thrust occurred at T_P = -11.08 N on the extrapolated mesh. With increasing load, the measurement uncertainty of the MARIN azimuth thruster turned out to be about 1 percent in the range between 10 and 100 percent for propeller thrust and between 0.5 and 0.05 percent for propeller torque. This meant that our computed thrust and torque measurements were below measurement uncertainty. Computed values of thrust and torque showed that a coarser mesh overestimated both values. Therefore, we performed all subsequent numerical simulations on the medium-sized grid, thereby representing a compromise between accuracy and computing effort. Simulations of the medium size grid were performed with 4032 core-hours.

Numerical Results

We have carried out tests on the standard and shallow water ducts in accordance with ITTC open water testing guidelines. In general, at a depth of 1.0D, a standard propeller duct arrangement tends to be heavily ventilated at low propeller speeds. To counteract this ventilation, the ITTC guidelines recommend a traditional minimum immersion depth of 1.5D for all thrusters and preferably 2.0D for azimuth thrusters. However, additional design measures for inland waterway vessels are unrealistic in shallow water. Such measures include specially designed stern tunnels to regulate the flow to the propeller and prevent ventilation. Azimuth thrusters often make these measures difficult to implement, especially if they are not located at the stern of the vessel. We therefore considered a shallow water azimuth thruster fitted with a standard duct and the newly developed shallow water duct under the operating conditions described below.

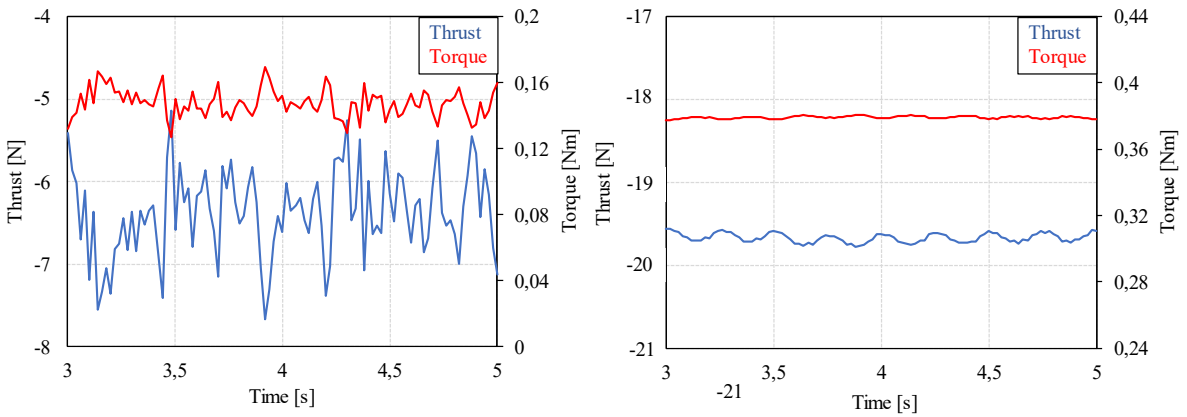

Figure 3: Exemplary computed time series of thrust (blue) and torque (red) obtained with the standard duct (left) and shallow water duct (right) for the propeller at $J = 0.1$.

Starting from standstill is a challenging operating condition because ventilation occurs rapidly at low propeller immersion depths, resulting in a decrease in thrust and torque due to the non-existent inflow velocity and low propeller advance coefficients. Figure 3 shows a computed time series of propeller thrust (blue) and propeller torque (red) obtained with the standard duct (left) and the shallow water duct (right) for the propeller with an advance coefficient of $J = 0.1$. The standard duct propeller developed significantly less thrust and torque than the shallow water duct propeller. This was due to the strong ventilation that occurred. The effect of the shallow water duct significantly reduced the fluctuations in thrust and torque. Often, accelerating an inland waterway vessel with conventional azimuth thrusters is difficult or even impossible. For this purpose, the shallow water duct was developed as it prevents ventilation at low propeller immersion depths. The dome-like protrusion in front of this duct regulates the inflow to the propeller without causing ventilation.

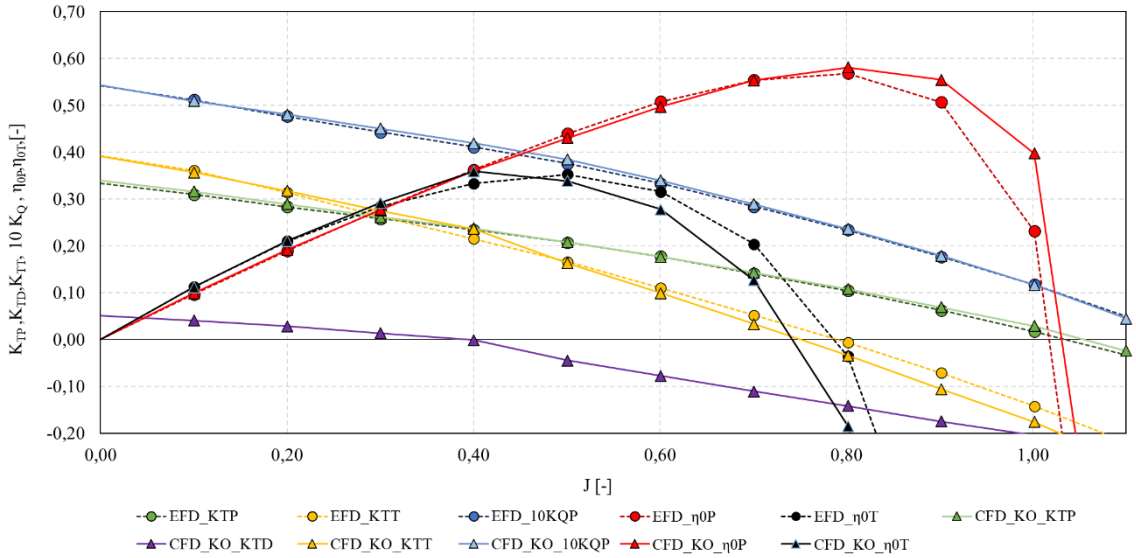

Figure 4: Comparative coefficients K_{TP}, K_{TD}, K_{TT}, $10K_{QP}$, η_{0P}, and η_{0T} versus J obtained from experimental measurements and numerical simulations for the MARIN azimuth thruster with the P189 propeller and the shallow water duct FWD-1.

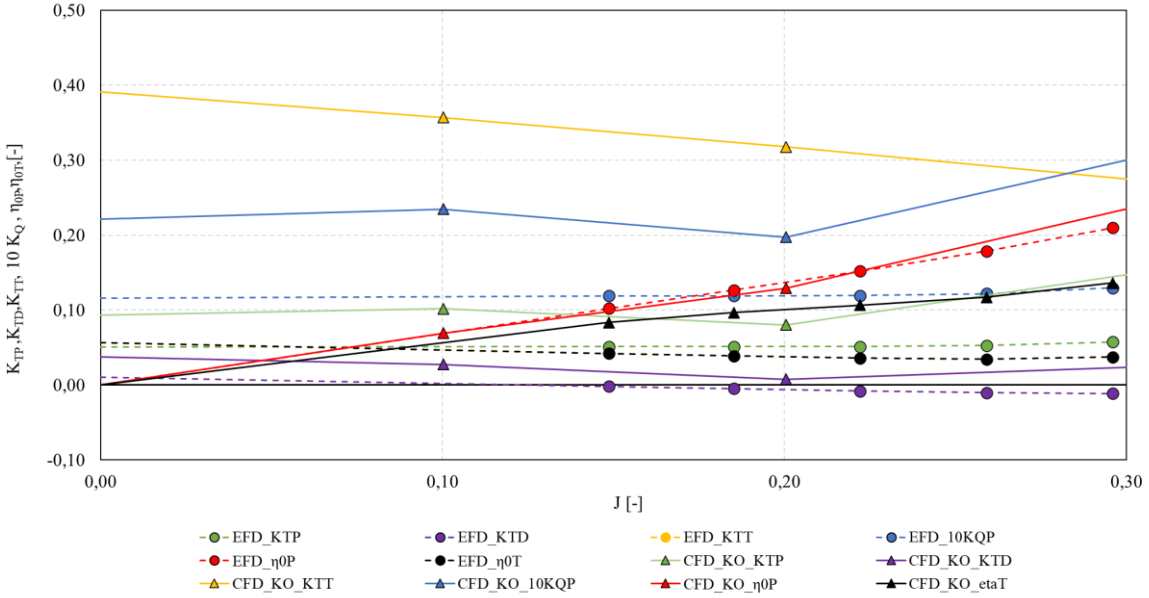

Figure 5: Comparative coefficients K_{TP}, K_{TD}, K_{TT}, $10{\cdot}K_{QP}$, η_{0P}, and η_{0T} versus J obtained from experimental measurements and numerical simulations for the MARIN azimuth thruster with the P189 propeller and the standard duct D399.

Figure 4 plots comparative values of propeller thrust coefficient K_{TP}, duct thrust coefficient K_{TD}, total thrust coefficient K_{TT}, moment coefficient $10{\cdot}K_{QP}$, propeller open water efficiency η_{OP} and total open water efficiency η_{OT} versus advance coefficient J obtained from experimental measurements and numerical simulations for the MARIN azimuth thruster with the open water P189 propeller and shallow water duct FWD-1. Figure 5 plots the results for standard duct D399. Dashed lines identify measured values, solid lines, computed values. As described above, computed values relied on the k-ω-SST model to account for turbulence. As seen in Figure 4, computed thrust coefficient K_{TP} is close to the measured value. The propeller thrust was slightly overestimated at advance coefficients $0.3 < J < 0.8$, and the propeller moment coefficient K_{QP} was slightly overestimated over the entire range of advance coefficient J. Although the propeller's open water efficiency was slightly overestimated, generally, our simulations compared favourably to the experimental model test measurements. Computed thrust coefficient K_{TT} for the thruster with the shallow water duct was slightly overestimated at advance coefficients around $J = 0.4$ and, at $J > 0.5$, they were increasingly underestimated. This underestimation of total thrust coefficient K_{TT} at higher advance coefficients caused the total open water efficiency η_{0T} to also be underestimated. The gap between the azimuth thruster's vertical axis and the shallow water duct was filled with wax to prevent air

from entering. Therefore, the duct thrust could not be determined in the model test. At $J = 0.4$ the shallow water duct no longer contributed to total thrust. Indeed, it had a retarding effect. This meant that the duct was effective only at the propeller's advance coefficients of $0 < J < 0.8$. Nevertheless, for the extremely shallow water depth scenario we examined here, this range of the propeller's advance coefficient sufficed.

As there was strong ventilation in the standard configuration, the tests were only conducted up to an advance coefficient of $J = 0.3$. The propeller did not develop sufficient thrust due to ventilation. This occurred repeatedly. The situation is similar for propeller torque. At larger advance coefficients, propeller thrust, and torque increased at a flat rate. Completely ventilation-free operation could not be achieved, even at higher advance coefficients. Measuring the duct thrust was feasible in the configuration with the standard duct. As seen in Figure 5, at an advance coefficient of $J = 0.1$, the standard duct no longer contributed to thrust. However, a strong braking effect was not detected. Due to the strong ventilation, only an extremely low total thrust was generated. This resulted in an exceptionally low overall open-water efficiency of $\eta_{0T} = 0.2$ at an advance coefficient of $J = 0.3$. As the k-ω-SST turbulence model is less accurate for two-phase flow regimes as it was developed for single-phase flows, it caused the CFD simulations to predict significantly larger deviations compared to the setup using the shallow water duct. The deviation could be explained by insufficient grid resolution for ventilation and vortices. In general, such characteristics are undesirable for azimuth thrusters at low immersions. A ship equipped with such thrusters would have difficulty accelerating and starting under such conditions. For this reason, fitting the developed shallow water duct is a viable solution for propellers operating close to the water surface. Under bollard pull conditions, a direct comparison between the standard duct and the shallow water duct showed that the use of the shallow water duct significantly increased the propeller thrust, in our case by more than 560 % compared to the use of the conventional duct. Even at higher lift coefficients of $J > 0.3$, the propeller still generated 350 % more thrust with the shallow water duct than with the standard duct. The standard duct did not contribute significantly to the thrust under these operating conditions. Under bollard pull conditions, the use of the standard duct produced a maximum thrust of 0.60 N, which was approximately 20 per cent of the propeller thrust of 3.17 N. This 20 % of propeller thrust was an excellent value under deep water conditions of 1.5D and is evidence of a well-designed propeller duct configuration. In this case, however, the total thrust of the system was insufficient due to strong ventilation.

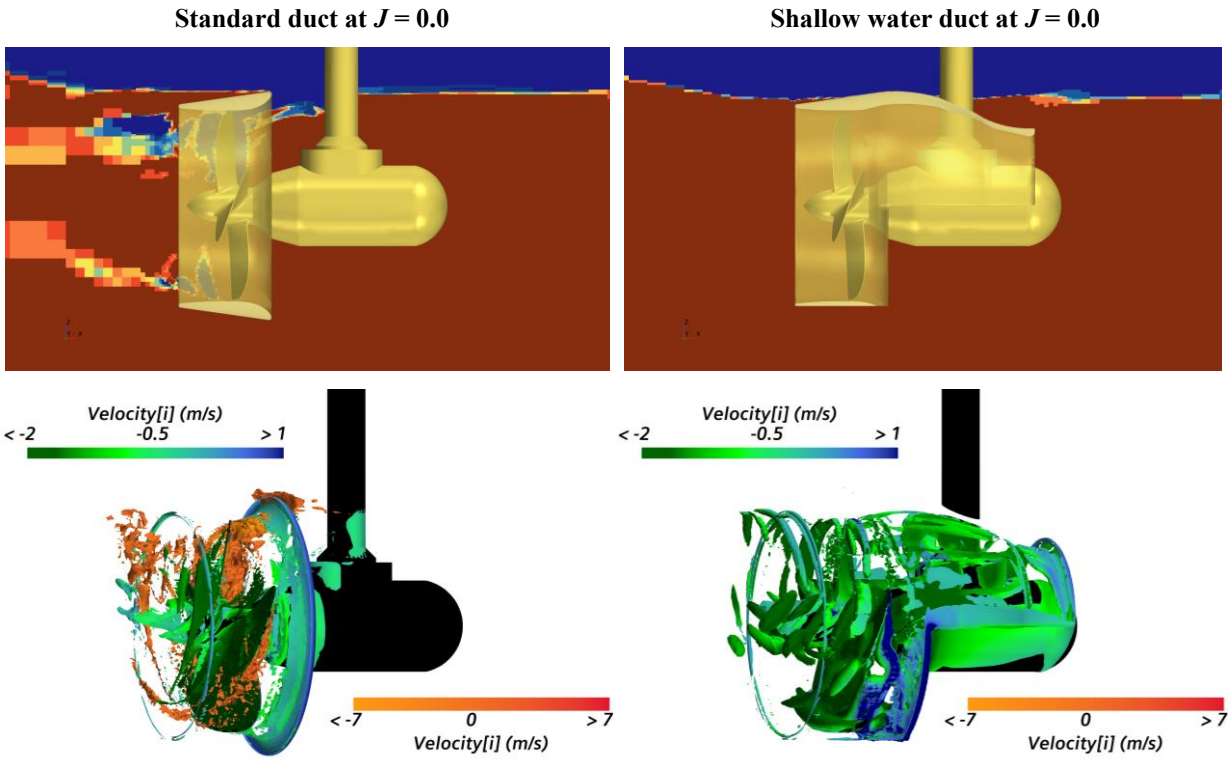

Figure 6: Comparative free surface elevation and volume fraction of water (red) and air (blue) of a shallow-immersed azimuth thruster with a standard duct (top left) and with the shallow water duct (top right) from CFD simulations and Q-Criterion of volume fraction of water (green-blue colour bar) and air (orange-red colour bar) of velocity [i] in *m/s* with standard duct configuration (bottom left) and shallow water duct (bottom right) under bollard pull condition at $J = 0.0$.

For a propeller thrust coefficient of $J = 0.0$, Figure 6 shows the free surface elevation for the shallow submerged azimuth thruster with a standard duct and with the shallow water duct. The duct in the CFD simulations was deliberately made 50% transparent to visualise the azimuth thruster and propeller. Water is shown in red, air in blue. Areas of mixture are shown in orange-yellow-green. For the standard duct thruster, the experimentally measured free surface shows a vortex generated at the twelve o'clock position of the free surface. As can be seen, this vortex passes through the propeller plane and then continues behind the propeller due to the strong formation of air bubbles. However, for the shallow water duct engine, no vortex formation is visible on the free surface and no air bubbles are formed behind the duct. The shallow water duct did not ventilate, because the distance between the duct inlet and the free surface was sufficiently large although the duct's highest inlet point, i.e., its twelve o'clock position, was located merely under 20 mm beneath the smooth free surface. This small distance was sufficient to reduce the velocity at the shallow water duct's critical twelve o'clock position, thereby directing the flow vertically downwards, which successfully prevented ventilation. As a standard duct does not have a corresponding dome extension, the flow velocity at a standard duct's inlet was not only higher, but also closer to the free surface, and this promoted ventilation. Figure 6 also shows the Q-criterion of the standard duct configuration on the left and the shallow water duct configuration on the right side. Vortices are visible at the tip and hub of the propeller. The shallow water duct shows flow separation at the duct inlet and strong interactions with the propeller pod. The geometric design of the shallow water duct can be optimised in the future. It can be seen that the vortices of the water volume fraction (green blue) are much more pronounced and have a higher velocity (dark green area behind the propeller). The vortices of the water volume fraction can therefore continue much better behind the propeller. It can be seen that, in contrast to the standard duct, there is no air volume fraction (orange red) in the shallow water duct (right). This successfully prevents air from entering the duct and the propeller plane. The standard duct, on the other hand, has a high vortex fraction of the air volume fraction. This continues along the propeller tips and reduces the thrust of the propeller. The protruding dome of the shallow water duct reduced the flow velocity at its inlet sufficiently to suppress ventilation. However, this also meant that not enough water could be sucked in at higher advance coefficients. The shape of the dome created a back pressure area on the outer surface of the duct at the nine o'clock to three o'clock position. Although irrelevant at small advance coefficients, this created a braking effect at larger advance coefficients. The particular shape of the calotte of the shallow water duct favoured a build-up of the wave at higher advance coefficients. This increased the water level locally at the duct inlet. The combination of the lower intake point, the accumulated wave and the reduced flow velocities above the duct prevented the formation of ventilation during propeller operation.

Conclusion

A newly invented shallow water duct was presented which, due to its geometric shape, was shown to prevent propeller ventilation of shallow water azimuth thrusters. This duct was used to systematically investigate the influence of ventilation on propeller and open water characteristics. Compared to a conventional duct, this so-called shallow water duct improved the performance at the relatively low propeller thrusts considered, although at higher thrusts the duct acted as a break. Direct comparisons for a typical azimuth thruster fitted with this shallow water duct resulted in significantly higher and more continuous thrust and torque. This should improve the starting conditions of a vessel in shallow water, thereby increasing not only the manoeuvrability of a particular vessel, but also its operational safety. The effects of a standard duct and this newly developed shallow-water duct were systematically investigated by carrying out open-water model tests and numerical CFD calculations, solving the URANS equations and using the k-ω-SST model to account for turbulence. These comparative results demonstrated the advantage and suitability of fitting an azimuth thruster to this shallow water duct. At low advance rates, the upper edge of the duct inlet of the shallow water duct is sufficiently distant from the free surface. Due to the low coefficient of advance combined with the geometric design of the duct, no ventilation is observed. At higher J, a damming wave forms on the outside of the duct, locally increasing the free surface around the duct inlet. This counteracts ventilation. Due to the geometric design of the duct, there is a larger frontal area than in a conventional duct. At higher lift coefficients, water accumulates on this surface, which means that the duct can no longer contribute to the thrust from J = 0.4 but has a braking effect. However, in direct comparison to a standard channel, much more and more continuous thrust can be generated.

References

1 Califano, A., & Steen, S. (2009, June). Analysis of different propeller ventilation mechanisms by means of RANS simulations. In Proceedings of The First International Symposium on Marine Propulsors.

2 Ferziger, J. H., Perić, M., & Street, R. L. (2019). Computational methods for fluid dynamics. Springer.

3 Hagesteijn, G., van der Meij, K., & Thill, C. (2015, May). Distributed Propulsion: A Novel Concept for Inland Vessels. In International Conference on Offshore Mechanics and Arctic Engineering (Vol. 56598, p. V011T12A012). American Society of Mechanical Engineers.

4 Kossmann, B. & Wierczoch, B. (2022) Düsenpropeller für Propulsionssysteme (DE 10 2022 129 372). Deutsches Patent- und Markenamt.

5 Kossmann, B., el Moctar, O., & Schellin, T. E. (2024). Effects of ventilation on open water characteristics of azimuth propellers under shallow water conditions. Ocean Engineering, 311, 118888.

6 Oberhagemann, J. (2017). On prediction of wave-induced loads and vibration of ship structures with finite volume fluid dynamic methods (Doctoral dissertation, Dissertation, Duisburg, Essen, Universität Duisburg-Essen, 2016).

7 Palm, M., Jürgens, D., & Bendl, D. (2011, June). Numerical and experimental study on ventilation for azimuth thrusters and cycloidal propellers. In Proc. 2nd Int. Symp. Marine Propulsors smp (Vol. 11).

8 Yang, D., Ren, Z., Guo, Z., & Gao, Z. (2018). Numerical analysis on the hydrodynamic performance of an artificially ventilated surface-piercing propeller. Water, 10(11), 1499.

9 Yvin, C., Muller, P., & Koushan, K. (2017). Numerical study of propeller ventilation. In Proceedings of the Fifth International Symposium on Marine Propulsors Smp (Vol. 17).

10 ITTC 08. 7.5-02-03-01.3, Propulsion, Performance Podded Propulsion Tests and Extrapolation, 2008.

11 Siemens 2302. Siemens Simcenter STAR-CCM+ 2302, User Guide.

Contact:

Benjamin.kossmann@uni-due.de

26th Numerical Towing Tank Symposium (NuTTS)
23-25 October 2024 - Mülheim an der Ruhr, Germany

Hydrodynamic Characteristics of a Gate Rudder During Straight-sailing and Sailing With a Ship Drift Angle

Wout Opdam[1], **Maarten Bijlard**[1], **Bart van Esch**[2], **Themistoklis Melissaris**[1]
[1] Hydrodynamics R&D, Wärtsilä Netherlands B.V.
[2] Eindhoven University of Technology
wout.opdam@wartsila.com

1 Introduction

In order to help reach the IMO's emission reduction goals for the maritime industry (IMO, 2023), Energy Saving Devices (ESD) can be used. An example of a relatively new ESD is the gate rudder, which was first introduced by Sasaki in Japan (Sasaki, 2013). In this new rudder configuration, two separate rudder blades are placed at the sides of the propeller instead of a single blade placed behind the propeller in the case of a conventional rudder. Ships equipped with the gate rudder show significant energy savings during operation (Sasaki et al., 2018, Celik et al., 2023). However, large discrepancies are observed between energy saving predictions from simulations and experiments, and what is observed during full scale sea-trials and actual operation.

The aim of this research is to increase the understanding of the physical principles of the gate rudder by examining the hydrodynamic characteristics when sailing straight-ahead and with a ship drift angle. One theory is that the situation in which the ship sails with a drift angle, so not perfectly straight through the water, results in favourable operating conditions for the gate rudder. Only a limited amount of research has been devoted to investigating this theory (Bulten, 2024).

2 Numerical Model

The research is carried out in the form of CFD RANS simulations of a 200 m long reference vessel with a propeller diameter of 6.5 m in STAR-CCM+. The double body approach is employed and only the stern part of the ship is simulated to reduce computational cost. No trim of the ship is taken into account, which means that the hull geometry is fixed and remains parallel to the water surface (even keel condition). The simulation uses the realizable $k - \epsilon$ two-layer turbulence model with all y+ wall treatment. The mesh uses trimmed hexahedral cells with prism layer cells near the walls. Wall functions are used to model the boundary layer, so the aim is to achieve y+ values above 30. The mesh consists of about 9.1 million cells, divided in 4.3 million cells for the rotating region and 4.8 million cells for the static region. An impression of the stern geometry and mesh is given in Fig. 1, showing the mesh and the refinements around the propeller and gate rudder:

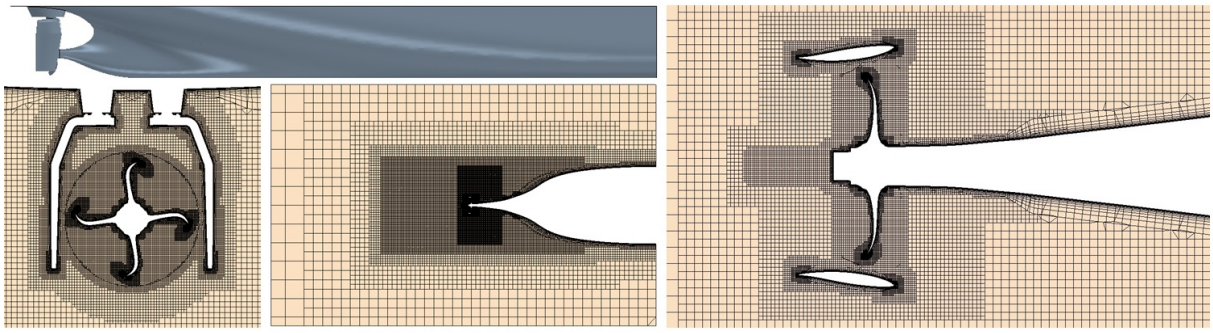

Fig. 1: Stern geometry of the reference vessel (upper left picture) and mesh refinements around the propeller and gate rudder.

The ship speed and propeller rotational speed are fixed at 19.5 knots and 105 RPM respectively, and the direction of inflow into the domain is varied in order to simulate various ship drift angles. Rudder steering angles are introduced that correspond to a steering action that corrects for the drift direction. The transient moving mesh with sliding interface approach along with the actual propeller geometry is used to include the effect of the propeller. The numerical approach has been validated in an open-water setup by making a comparison with experimental open-water measurement data of a propeller with gate rudder, and the mesh dependency has been investigated. In the current work, the rudder performance is monitored for the relatively high ship speed of 19.5 knots.

3 Results

In this section, first the characteristics during straight-sailing conditions (no ship drift) without rudder steering are briefly explored. Then results for various combinations of ship drift- and rudder steering angle are discussed.

3.1 Straight-sailing conditions

Under straight-sailing conditions, the direction of flow past the ship and the direction of travel of the ship align with each other. Note that in their neutral 'no steering action' position, the gate rudder blades on this particular reference ship have a slight toe-out rotation angle. The x-direction (longitudinal ship direction) velocity field for the reference vessel sailing straight-ahead without rudder steering and with a speed of 19.5 knots can be seen in Fig. 2:

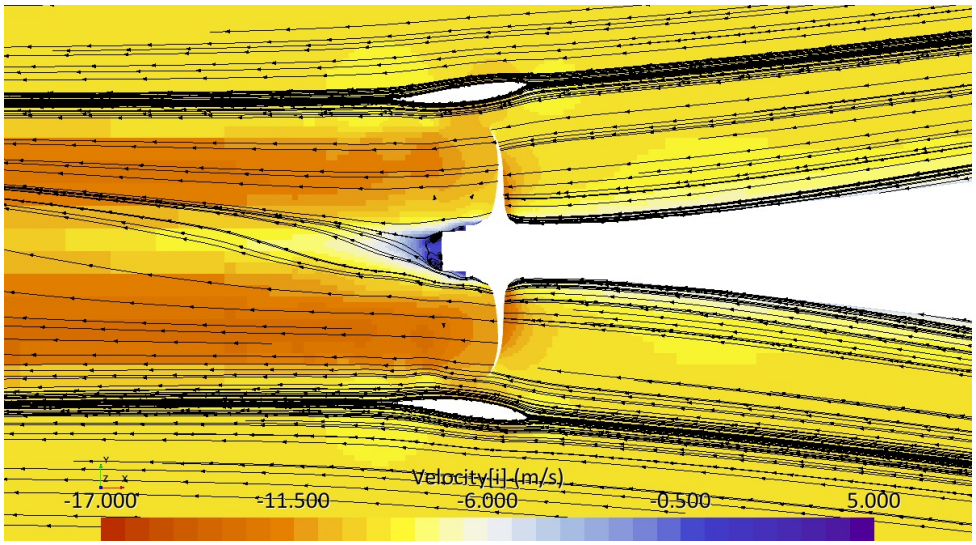

Fig. 2: Resulting x-direction velocity field with streamlines for the reference vessel sailing straight-ahead with a speed of 19.5 knots.

It can be seen in Fig. 2 that, due to the slight toe-out rotation angle of the rudder blades, they do not face the incoming flow head-on in their neutral positions but have a slight negative angle of attack of $-1.8°$ for the port blade and $-1.4°$ for the starboard blade. The angle of attack is determined by monitoring the flow conditions in a small sampling volume located right before the leading edge of the lower vertical section of the gate rudder blades. In straight-sailing conditions without rudder steering, the drag force experienced by the gate rudder blades is not that significant (0.22% of the propeller thrust). It might be interesting to dedicate an optimization study to finding a more optimal neutral toe-out rudder angle for this vessel.

3.2 Sailing with Ship Drift- and Rudder Steering Angles

The effect of a ship drift angle on the performance of the gate rudder will be investigated by introducing an angle to the flow entering the domain. The ship drift angles that are simulated are 5° and 10° both from port and starboard. The left picture in Fig. 3 shows the definition of the (positive, from starboard) ship drift angle Ψ:

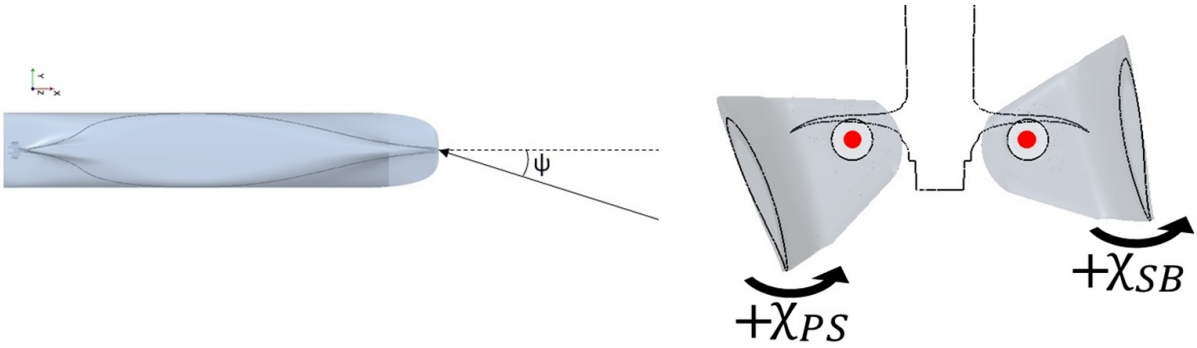

Fig. 3: Definition of the (positive) ship drift angle Ψ (left picture) and definitions of the (positive) gate rudder blade steering angle χ_{PS} for the port gate rudder blade and χ_{SB} for the starboard gate rudder blade. The red dots indicate the rotation axis of the rudder blades. As seen from above (right picture).

An example of a velocity field with a ship drift angle of 10° can be seen in the left picture in Fig. 4:

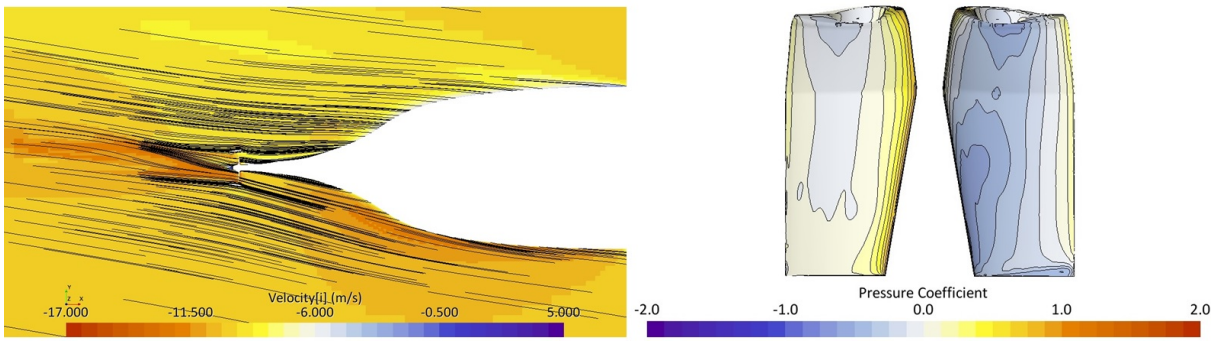

Fig. 4: Resulting x-direction velocity field with streamlines for the reference vessel sailing with a ship drift angle of 10° without rudder steering (left picture) and for the same conditions the right picture shows the pressure coefficient on the insides of the port (left) and starboard (right) gate rudder blades.

For the various ship drift angles, rudder steering angles of 5°, 10° and 15° are simulated. The positive gate rudder blade steering angle χ that brings the trailing edge towards the starboard side is indicated in the right picture in Fig. 3. The steering action of the gate rudder will change the effective angle of attack of the rudder blades with the flow and is therefore expected to impact the flow characteristics around the blades and thus the thrust or resistance they produce.

When a ship drift angle is introduced, the 'upstream' gate rudder blade (the blade on the side from where the current comes) will experience more favourable inflow conditions compared to the 'downstream' blade. This upstream blade (the starboard/right blade in case of a positive drift angle from starboard) will have a positive angle of attack with the incoming flow (e.g. 12.6° in the case of a 10° drift from starboard without rudder steering), while the downstream blade will have a negative angle of attack (−18.8° in the case of a 10° drift from starboard). Since the profile of the gate rudder blades is based on an aerofoil profile, this positive angle of attack will result in a region of higher velocity and thus lower pressure

near the leading edge on the inside of the vertical section of the blade. This can be seen in the right picture in Fig. 4 showing the pressure coefficient on the inside of the gate rudder blades for a drift angle of 10° without rudder steering.

The simulation results for a 10° ship drift angle without rudder steering are here used to show the trends that are also observed for the upstream- and downstream rudder blades in the case of other drift- and rudder steering angles. Laser Doppler Anemometry (LDA) measurements by Sasaki et al. of the velocity field for a scale model ship equipped with a gate rudder also confirmed this strong higher velocity, and thus low pressure region on the gate rudder (Sasaki et al., 2017). The lower pressure region on the upstream blade results in a lift force on the rudder profile oriented perpendicular to the flow. This lift force will have a component in the positive x-direction of the ship which is larger than the force components in the negative x-direction, which are due to for example drag on the rudder blade. This rudder blade thus has a net positive contribution to the thrust force.

The upstream rudder blade will experience a less disturbed inflow field compared to the downstream blade since, due to the drift angle, the flow reaching this blade mostly originates from parts of the domain away from the ship. This can be seen from the plot of streamlines reaching the gate rudder blades in the left picture in Fig. 5:

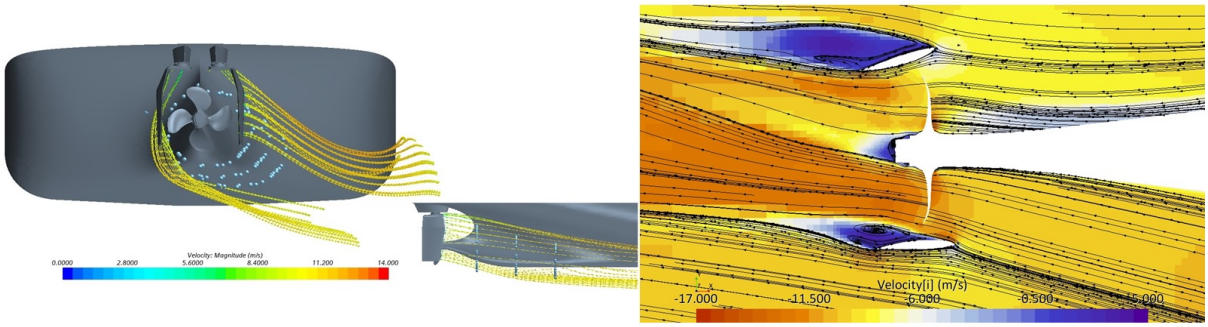

Fig. 5: Streamlines reaching the gate rudder blades, and points reaching the edges of the propeller plane, for a drift angle of 10° without rudder steering (left picture) and resulting x-direction velocity field with streamlines for the reference vessel sailing with a ship drift angle of 10° with a rudder steering angle of 10° (right picture).

This flow has a higher velocity when it reaches the upstream gate rudder blade because it is less disturbed by the boundary layer on the hull compared to the flow reaching the downstream blade. The downstream blade operates more in the wake of the hull and thus encounters a more disturbed, lower velocity flow. As mentioned, the downstream blade will experience a negative angle of attack with the incoming flow. This results in a region of high pressure on the inside of the leading edge of the vertical section (as can be seen in the right picture in Fig. 4). The result of this high pressure region is a net negative force in the x-direction of the ship on this blade (thus an extra resistance). Whether the force on a gate rudder blade results in a positive contribution to the thrust or in an additional resistance thus depends on the exact flow conditions around the rudder blades.

The force in the x-direction (forward direction) of the ship for the port- and starboard blade individually for the various combinations of ship drift- and rudder steering angles can be seen in the left plot in Fig. 6:

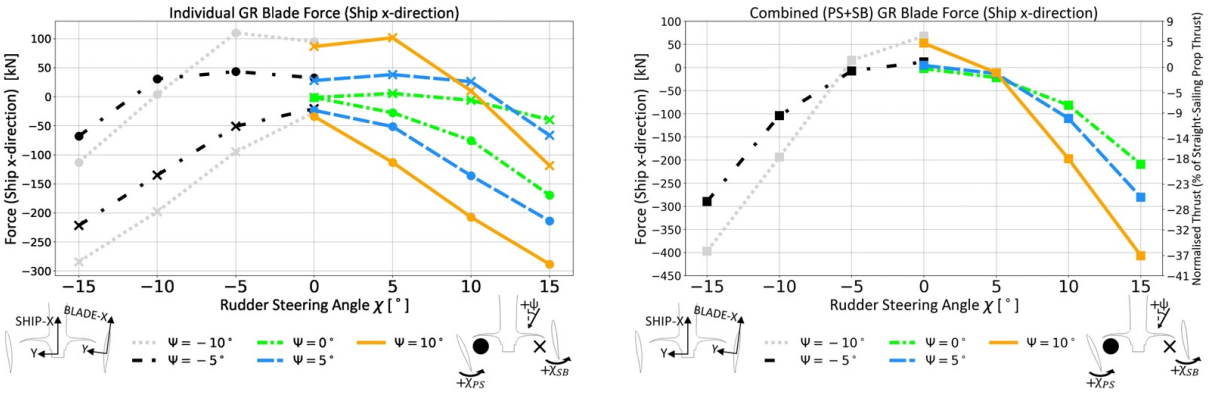

Fig. 6: Thrust in the x-direction of the ship for the port- and starboard rudder blades individually (left plot) and total combined rudder thrust (right plot) for various combinations of ship drift- and rudder steering angles.

The downstream blade always experiences a negative force in the ship x-direction. The upstream blade has a positive contribution for lower steering angles, and in most cases this is compensated by the negative force on the downstream blade (with some exceptions having a slight positive total rudder thrust). For higher steering angles, the force on the upstream blade can also become negative. Furthermore, it can be seen at lower (or zero) steering angles that for increasing drift angle, the positive thrust contribution of the upstream blade increases more rapidly than the extra resistance contribution of the downstream blade, resulting in an increase of the combined rudder force in the x-direction of the ship with increasing drift angle. At combinations of high drift angles and high rudder steering angles, flow separation on the rudder blades is observed, as can be seen for example in the right picture in Fig. 5 for the case of a 10° drift angle from starboard with a 10° rudder steering angle, indicated by the dark blue areas. This flow separation leads to a significant increase in rudder resistance.

The total combined (port + starboard) rudder force in the x-direction of the ship can be seen in the right plot in Fig. 6. In general it is observed that, with some exceptions, the overall combined rudder thrust for the various combinations of ship drift- and rudder steering angles is negative. For most of the cases the rudders thus do not result in a positive thrust force in the forward direction of the ship when a rudder steering angle is present. For the cases with a ship drift angle without rudder steering, and the case of a −10° ship drift angle and a −5° rudder steering angle, the gate rudder does result in a thrust force in the x-direction of the ship. However, the question can be raised if these cases provide a realistic image because, when sailing at these ship drift angles, almost certainly a (higher) rudder steering angle is required to keep the ship on course. These cases will therefore in reality probably only be encountered for relatively short periods of time. Note however that for the more realistic case of straight-sailing without rudder steering, the rudder resistance is relatively low, while for a conventional rudder a significantly higher resistance is expected. It can also be seen that for higher drift angles, the rudder force starts dropping earlier at lower rudder steering angles than for lower drift angles. This is because for these higher drift angles, stall/flow separation occurs sooner (at lower steering angles).

The second y-axis in the right picture in Fig. 6 shows the force contribution of the rudder blades as a percentage of the propeller thrust at the straight-sailing condition without rudder steering. It can be seen that, in the cases where the contributions of the two rudders result in a positive rudder thrust, this total thrust of the rudders compared to the propeller thrust is relatively small. The highest percentage of rudder thrust compared to propeller thrust is about 8% for the case of a 10° drift angle from starboard without rudder steering. For the cases where the combined contributions of both rudder blades result in a net rudder resistance, this negative rudder force can become relatively large compared to the propeller thrust.

Only looking purely at the forces of the gate rudder blades in the x-direction of the ship does not give

the complete picture since most of the thrust of the ship is coming from the main propulsor, which in this case is the propeller. Initial investigations into the interactions between the propeller and gate rudder seem to indicate that the gate rudder has an effect on the pre-swirl of the flow going into the propeller plane, and thereby influences the propeller performance.

4 Conclusion and Recommendations

Significant differences in flow conditions between the port and starboard rudder blades are observed for the various combinations of ship drift- and rudder steering angles at this relatively high ship speed. It is found that when sailing with a drift angle, one of the gate rudder blades can result in a positive rudder thrust force due to the angle of attack with the incoming flow. In most cases, this thrust is compensated by the resistance of the other rudder blade.

The reported energy savings achieved by the gate rudder during real-life operation are significant. However, these energy savings are not reflected in the here presented simulation results of sailing with a drift angle, so the discrepancy between numerical predictions and observed operational performance remains. In order to say if the benefit of the gate rudder is based on the effect of sailing with a drift angle, a comparison with a conventional rudder needs to be made, including the influence on the propeller (due to the suspected influence of the gate rudder on the pre-swirl of the flow into the propeller plane). This could then be repeated at a lower ship speed to see if a possible duct-like working of the gate rudder then becomes more apparent. Note that comparing two vessels with different rudder types is not straightforward since in reality these ships will be optimised for that specific rudder type, so they will have different configurations in terms of the propeller- and aft design of the ship. This will have an influence on the results and makes it difficult to isolate the influence of the rudder type. It could also be that the benefit of the gate rudder is not captured adequately in these rather limited static CFD simulations, and that more dynamic simulations (including ship motion and moving rudders) are required in order to capture a possible influence of the gate rudder on the yaw and roll motions of the ship. Future work may also include investigating different neutral toe-out rudder angles or investigating steering actions in which different steering angles are used for each blade.

References

Bulten, N. (2024). Upgraded MMG-Methodology to Capture Gate-Rudder Performance Aspects. *8th International Symposium on Marine Propulsors*.

Celik, C., Özsayan, S., Köksal, Ç., Danışman, D., Korkut, E., Gören, Ö., and Atlar, M. (2023). On the evaluation of the model test extrapolation by sea trial measurements. *7th International Conference on Advanced Model Measurement Technology for the Maritime Industry*.

IMO (2023). 2023 IMO Strategy on Reduction of GHG Emissions from Ships. Available at https://www.imo.org/en/OurWork/Environment/Pages/2023-IMO-Strategy-on-Reduction-of-GHG-Emissions-from-Ships.aspx#

Sasaki, N. (2013). ZEUS and NOAH Projects of NMRI. *3rd International Symposium on Marine Propellers*.

Sasaki, N., Kuribayashi, S., Asaumi, N., Fukazawa, M., Nonaka, T., Turkmen, S., and Atlar, M. (2017). Measurements and calculations of gate rudder performance. *5th International Conference on Advanced Model Measurement Technology for the Maritime Industry*.

Sasaki, N., Kuribayashi, S., Atlar, M., and Co, K. S. (2018). Gate rudder. *3rd International Naval Architecture and Maritime Symposium*.

26th Numerical Towing Tank Symposium (NuTTS)
23-25 October 2024 - Mülheim a. d. Ruhr, Germany

Extreme-event analysis of a floating structure with mooring dynamics in an irregular sea state

Qi Zhang, Ould el Moctar and Changqing Jiang*
Institute for Sustainable and Autonomous Maritime Systems
University of Duisburg-Essen, Duisburg/Germany
*changqing.jiang@uni-due.de

1 Introduction

Ocean wave energy is a promising renewable source with significant potential to contribute to the global energy mix. As the world shifts toward sustainable solutions, the development of wave energy converters (WECs) has accelerated, categorized into attenuating, point-absorbing, and terminating devices (Drew et al., 2009). Accurate prediction of motions and loads on WECs, particularly in relation to mooring systems, is crucial for structural integrity and safety (Jiang et al., 2020). Mooring systems play a critical role in maintaining device stability under wave-induced forces, but their design is challenging due to nonlinear hydrodynamic effects and fatigue forces in harsh sea conditions. Reliable assessment of these systems requires interdisciplinary expertise in hydrodynamics and mooring dynamics, typically approached through both physical testing and numerical methods (Davidson and Ringwood, 2017). Various numerical methods have been developed to model wave-structure interactions, such as mid-fidelity potential solvers and high-fidelity computational fluid dynamics (CFD) tools. Potential flow solvers, despite their inability to directly model viscous effects, are commonly employed in marine hydrodynamics because of their reliability and computational efficiency. In contrast, CFD methods can simulate the intricate interactions between nonlinear waves and floating structures, offering detailed insights into the complex flow behaviors around floating bodies.

Traditional numerical approaches can be computationally intensive, prompting the use of surrogate models for faster predictions without sacrificing accuracy. These models are especially important for real-time monitoring of mooring line tensions to prevent damage. In our previous work, we developed a data-driven model to predict the nonlinear dynamics of a floating body moored with catenary lines (Jiang et al., 2024). This study builds on that work by evaluating the model's performance in predicting the motions and loads of a floating power system (FPS) under various irregular wave conditions (Zhang et al., 2024). We assess the model's generalizability to different sea states and its ability to predict nonlinear hydrodynamics, with a focus on higher-order harmonic components of extreme events. This is crucial for ensuring the safety and reliability of offshore structures.

2 Test case description

To evaluate the performance of a FPS for the Galway Bay wave energy test site, physical wave basin tests were conducted at University College Cork, Ireland, using the National Ocean Energy Test Facility (Bosma et al., 2014). The FPS, designed to support data acquisition and supply power at the test site, also acts as a local grid connection point, enabling the integration of multiple WECs. Figure 1 gives a diagram of the experimental setup. The FPS model was built at a 1:25 scale with a draft of 30 mm, height of 90 mm, and diameter of 200 mm, constructed from thermoplastic polycarbonate and weighing 766.4 g (excluding mooring lines). A three-point catenary mooring system, with three symmetrical mooring lines, was used, each with a linear density of 45.5 g/m and a length of 3 m. Tests were conducted in a wave basin measuring 25 m by 17.2 m, with a water depth of 1 m. A flap-type ocean wave generator features 40 individually controlled paddles, capable of generating a diverse array of waves, such as regular and irregular single direction waves, as well as directional-spread waves. Long-duration irregular wave tests were conducted during the experimental campaign and they are analyzed in detail in this study. Here, only waves propagating in the x-direction (parallel to line 2) are presented, where all conditions are long-crested waves. Measurements of free-surface elevations as well as motions and loads on the FPS were recorded at the frequency of 32 Hz (Bosma et al., 2015).

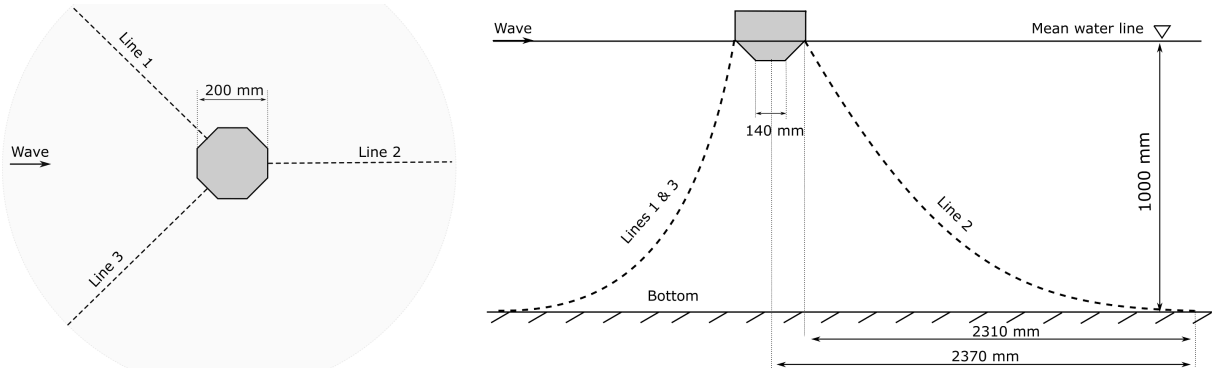

Fig. 1: Diagram of the experimental setup, adapted from Zhang *et al.*, Phys. Fluids 36, 082119 (2024). Copyright 2024 Authors, licensed under a Creative Commons Attribution (CC BY) license.

3 Results and Discussion

The effectiveness of the data-driven approach for predicting the motions and forces of the FPS in irregular waves is evaluated by examining the accuracy of the surrogate model. This includes verifying its ability to predict the temporal responses of the moored FPS and the associated extreme events. For example, Fig. 2 presents the training and validation results of the model for an irregular sea state. The model was trained using time-series data from 0 to 250 s and validated on the remaining 30% of the dataset, covering 250 to 350 s. While some discrepancies exist between the actual and predicted local crests and troughs, the model generally demonstrates strong accuracy in predicting the tensile forces on the mooring lines for previously unseen wave conditions.

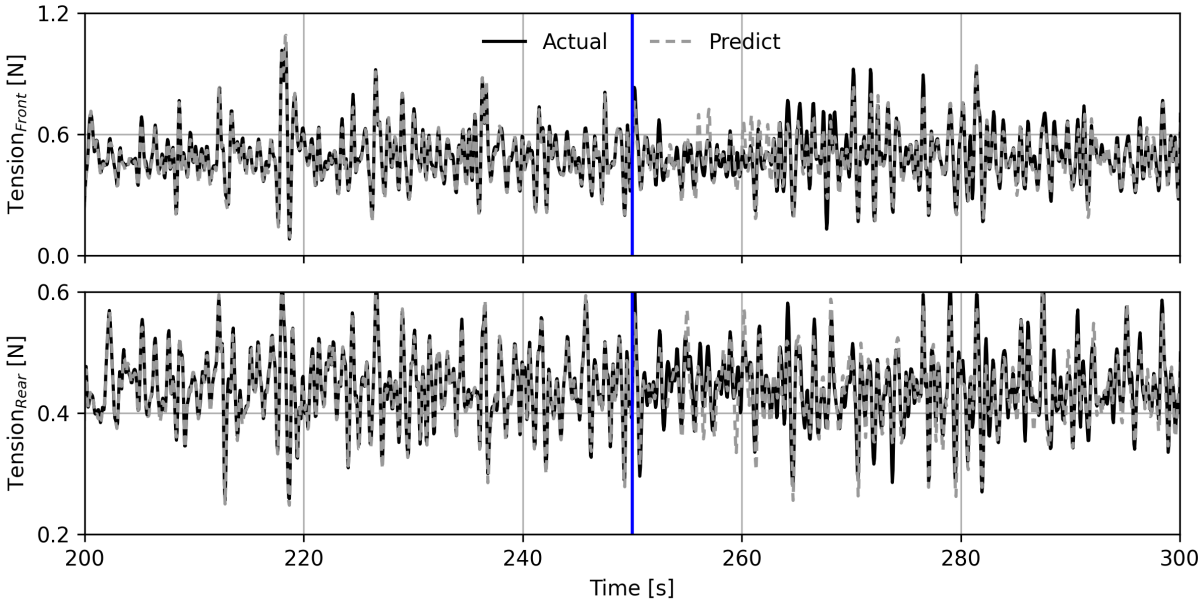

Fig. 2: Performance of the data-driven model in simulating the hydrodynamics of a floating power system with mooring dynamics in an irregular sea state. The model was trained on time-series data from 0 to 250 s and tested on data from 250 to 350 s.

While the overall accuracy of the surrogate model is essential for predicting the temporal responses and mooring tensions of a floating body in waves, its ability to capture nonlinear dynamics, particularly during extreme events, is even more critical. Extreme motions and loads can pose significant risks to floating structures in high sea states. To assess this, detailed comparisons between actual and predicted results, based on exceedance probability, are shown in Fig. 3. The model, trained on 70% of the dataset

for an irregular sea state, shows strong overall agreement between predicted and actual values. However, when focusing on extreme events, the tensile forces on the mooring lines are slightly overpredicted during these extreme conditions by the surrogate model. Overall, the model successfully captures the physical relationships between wave elevations, body motions, and mooring loads in an irregular sea state.

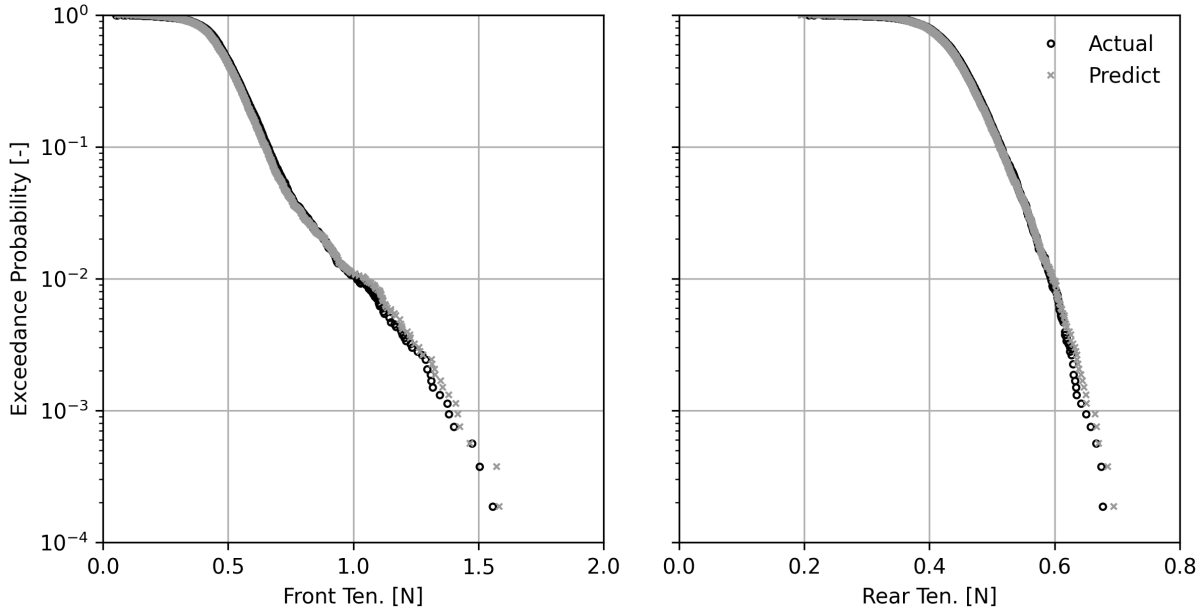

Fig. 3: Comparison of exceedance probabilities for the actual and the predicted tensile forces of the mooring lines in an irregular sea state.

4 Conclusion

The LSTM-based data-driven model demonstrates significant computational efficiency and effectively models FPS dynamics in irregular sea states. However, its performance needs to be further assessed across various sea states, particularly when the conditions differ from those in the training dataset. While the model can predict low to moderate responses in different sea states, it struggles with large amplitude motions due to the strongly nonlinear interactions between waves, structure, and mooring dynamics. These extreme events are rare, providing limited data for training, which results in poor performance in such cases. A more detailed analysis of the model's ability to predict extreme events for moored floating structures can be achieved through harmonic analysis, which will be addressed in future research. This study highlights the potential of machine learning for marine applications, including real-time monitoring and the development of digital twins for offshore structures, with opportunities for future improvements in capturing extreme nonlinearities.

Acknowledgements

This research was funded by the German Research Foundation (DFG) under grant number 448471847. We acknowledge Bret Bosma from the O.H. Hinsdale Wave Research Laboratory at Oregon State University for providing the experimental data.

References

Bosma, B., Sheng, W., and Thiebaut, F. (2014). Performance study of the galway bay wave energy test site floating power system. International Conference on Ocean Energy.

Bosma, B., Thiebaut, F., and Sheng, W. (2015). Comparison of a catenary and compliant taut mooring system for marine energy systems. In *Proceedings of the 11th European Wave and Tidal Energy Conference (EWTEC2015), 6-11 September 2015, Nantes, Frances*, pages 08B5–4.

Davidson, J. and Ringwood, J. V. (2017). Mathematical modelling of mooring systems for wave energy converters-a review. *Energies*, 10(5):666.

Drew, B., Plummer, A. R., and Sahinkaya, M. N. (2009). A review of wave energy converter technology.

Jiang, C., el Moctar, O., Paredes, G. M., and Schellin, T. E. (2020). Validation of a dynamic mooring model coupled with a rans solver. *Marine Structures*, 72:102783.

Jiang, C., Zhang, Q., el Moctar, O., Xu, P., Iseki, T., and Zhang, G. (2024). Data-driven modelling of wave–structure interaction for a moored floating structure. *Ocean Engineering*, 300:117522.

Zhang, Q., Jiang, C., el Moctar, O., and Bosma, B. (2024). Data-driven modeling and extreme-event analysis of a floating power system with mooring dynamics in random waves. *Physics of Fluids*, 36(8).

Modelling turbine-turbine interactions using techniques learned from Naval Engineering

João Muralha, Tiago Gomes, António Maximiano, Guilherme Beleza Vaz
blueOASIS, Ericeira/Portugal
jmuralha@blueoasis.pt

1 Introduction

In naval and maritime engineering, Computational Fluid Dynamics (CFD) has been used for a long time to study numerous different types of problems. The present paper focuses on the CFD approaches used to model relative motion between different bodies and their application in studying turbine-turbine interaction.

In the open literature, the three most common approaches used to model a rotating body are Actuator Disk (AD), Moving Reference Frame (MRF), and Sliding Interfaces (SI) or overset grids (OG). The AD model is the simplest and least computationally expensive. In this approach, the rotating body is replaced by a body-force distribution, while in the remaining two approaches, the body geometry is modelled, making them more computationally expensive. Improvements to the simple AD model can be achieved by coupling the CFD solver with a potential flow code to obtain a better body force approximation. In the MRF and SI approaches, the computational domain is divided into two parts: one around the static body and another around the rotating body. For the MRF model, steady flow is considered in both domains, with the equations in the rotating domain being solved in a moving reference frame formulation. The SI and OG models are the most physically complete and computationally expensive approach. Calculations are intrinsically unsteady, and the interaction between the bodies is modelled using a moving grid approach for the case of the SI method or overset grids in the OG approach. A large part of the research on wind turbine-turbine interaction or the study of wind turbine wakes employs more advanced body-force distribution methods, such as the generalised actuator disk, actuator line or actuator surface models, or the coupling of CFD solvers with Blade Element Momentum or Lifting Line codes. Although a clear improvement on the standard AD model, these approaches require the knowledge of the turbine geometry and detailed information on the airfoil, input data that is often not public available for industrial turbines.

The present study goal is to use ReFRESCO Reynolds Average Navier Stokes (RANS)/URANS flow solver to compare the wake generated by modelling a wind turbine using the AD, MRF, and SI approaches. The turbine selected for this study is the model-scale DTU 10MW tested during the UNAFLOW project. The experimental data publicly available from this wind tunnel campaign will be used in this paper to validate the different models. Besides comparison with experimental data, the results will also be compared with QBlade's Lifting Line Free Vortex Wake (LLFVW) model generally used in wind turbine farm layout optimization software.

2 Mathematical Models

The mathematical model used in the present work is the RANS equations, and the Reynolds stress tensor is modelled using the k-ω SST 2003 turbulence closure model. In this study, three approaches are used to model the effect of the turbine in the incoming flow. The simplest model used in this study is the Actuator Disk (AD) model. In this approach, the turbine blades are replaced by an equivalent body-force distribution, making this a straightforward model for the turbine. Although it cannot be used to capture the flow characteristics near the AD, it is useful to study the downstream region due to its reduced computational cost (Maciel et al., 2013; Koop et al., 2017). This approach does not need previous knowledge of the propeller geometry but requires knowledge of the thrust and torque of the turbine. The remaining two approaches require a detailed geometry characterization of the turbine, which makes them more computationally expensive and difficult to implement in industrial projects, where this information is proprietary to the turbine manufacturer. In the Moving Reference Frame (MRF) model, the RANS equations are solved in the moving reference frame but written in absolute reference frame quantities. In this approach, the flow is considered steady, so all the time-history effects of the turbine flow are neglected. It is cheaper than the more computationally intensive Sliding Interface (SI) but provides a good first

approximation for the interaction phenomena (Maciel et al., 2013). In the SI model, no approximations are made, resulting in unsteady calculations in the entire domain and a high computational cost. This approach provides estimates of the turbine torque and thrust and predicts correct flow characteristics downstream of the turbine (Maciel et al., 2013; Koop et al., 2017).

3 ReFRESCO Flow Solver

ReFRESCO discretizes the transport equations using a finite volume method with cell-centred collocated variables. The use of meshes with arbitrary cell shapes, as well as hanging nodes, is possible by the use of a face-based implementation. Mass conservation is ensured using a SIMPLE-type algorithm through a pressure correction equation. At each non-linear iteration, a linear system of equations is obtained using Picard's method. The linearised Navier-Stokes equations are solved in a segregated way, i.e., the equations for velocity, pressure correction, and if required energy, turbulence model and air volume fraction are solved in turn, and when solving for one of the variables, the others are considered known. Time integration is performed through the first or second-order Backward Differentiation Formulas BDF1 and BDF2. Mesh handling techniques such as moving, sliding, deforming and overset meshes are available, as well as automatic mesh refinement and coarsening.

4 Test Case

The model-scale version of the DTU 10MW wind turbine used during the UNAFLOW campaign is used in the present study. Fig. 1 illustrates the turbine CAD model (left image) and the computational domain (right image), in these illustrations is possible to see that open flow conditions were used throughout this study and that only the turbine blades and hub are modelled. These choices were made to reduce the computational costs of the simulations. These simplifications don't allow for a direct comparison with the experimental results obtained by Fontanella et al. (2021). Nevertheless, the experimental results will be used as a guideline, mainly for the values of thrust and torque obtained for the MRF and SI approaches. Table 1 presents the turbine characteristics and operating conditions.

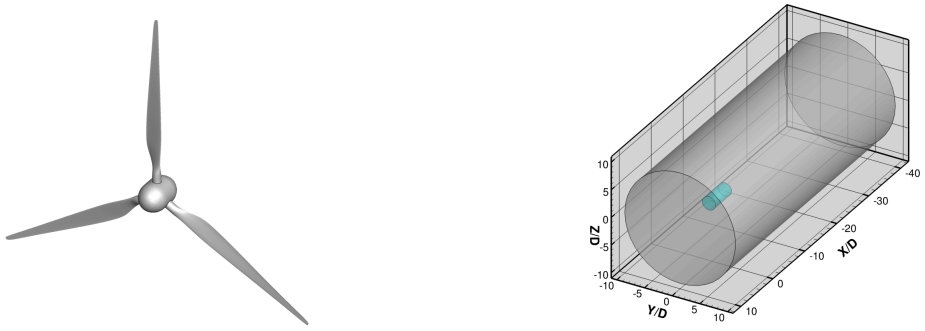

(a) (b)

Fig. 1: Wind turbine geometry (a) and domain dimensions showing the inner domain in light blue and the outer domain in light grey (b).

Table 1: Wind Turbine Characteristics and Operating Conditions.

Diameter,	D [m]	2.38
Density,	ρ [kg/m^3]	1.177
Viscosity,	μ [Pa/s]	1.84×10^{-5}
Inflow Velocity,	U_∞ [m/s]	4
Rotational Speed [RPM]	-	240

Based on previous studies (Make and Vaz, 2015; Ye et al., 2022), the cylindrical computational

domain has a length of 50D and a radius of 20D. Furthermore, the turbine was placed in the centre line of the cylinder and at a distance of 10D from the inlet. An interior subdomain was added to use the SI approach and was kept for all simulations to keep the same grid topology. This subdomain is, again, cylindrical with a length of 5D and a radius of 1.2D.

5 Numerical Settings

The Total Variation Diminishing (TVD) Van Leer's harmonic and first-order upwind schemes were used in the momentum and turbulent quantities equations, respectively, to discretize the convective term, and Gauss's theorem was used in all equations to calculate the gradients. The coupling between the outer and inner domains is done using Halo Cells, and the interpolation of quantities between the two domains's boundary cells is done using a third order accurate Least Square scheme. For the SI approach the second order BDF2 time discretization scheme was used.

For the AD and MRF approaches, the simulations were stopped after 20000 thousand iterations, a sufficient number of iterations to establish the turbine wake. For the unsteady SI approach, ten turbine revolutions were performed for the coarsest grid and 14 for the remaining grids. In a previous study conducted with the same turbine but modelling the wind tunnel, this number of rotations was sufficient to remove the effect of the initial condition (uniform flow) (Sileo et al., 2023). In the present study, this was not the case, and extra turbine rotations were performed for the finer grids. The time steps used range from 2.78×10^{-3}s to 1.82×10^{-3}, which correspond to turbine rotation ranging from 4° to 2.6° at each timestep. In the AD approach, the torque and thrust of the turbine were considered to be the experimentally obtained values. For all the simulations, the L_2 norm of the normalised residuals decreased to 4×10^{-3} or lower. Fig. 2 exemplifies the residual evolution for each approach.

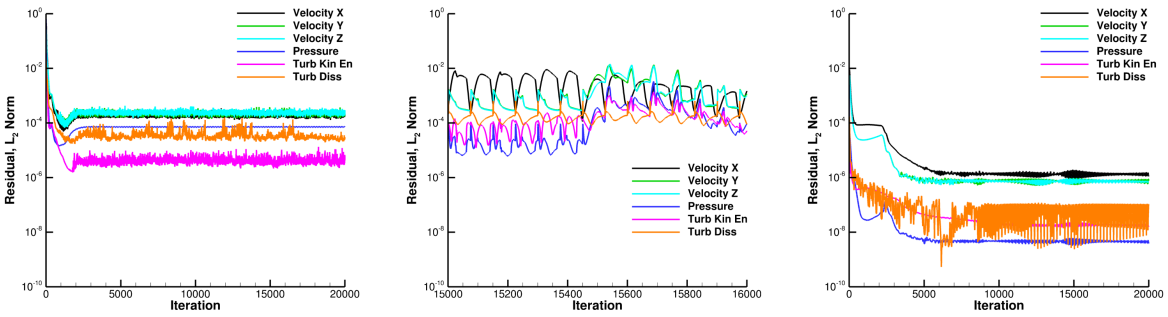

(a) MRF (b) SI (c) AD

Fig. 2: Residuals at each iteration for the MRF (left plot), SI (middle plot) and AD (right plot).

Two sets of four grids were generated using Hexpress, the simulations for the MRF and SI approaches use the same grids, but when using the AD approach different grids had to be generated without the turbine blades, but keeping the same grid topology in the wake region. The total number of cells N_{total}, the number of cell in the turbine surface N_{surf} and the grid refinement ration $r_i = h_i/h_1 = \sqrt[3]{N_1/N_i}$ are presented in Table 2. The grids topology are illustrated in Fig. 3.

Table 2: Grid Characteristics.

Grid	MRF and SI			Grid	AD	
	N_{total}	N_{surf}	r_i		N_{total}	r_i
4	17.83M	0.82M	1.53	1	4.72M	1.71
3	34.32M	0.91M	1.23	2	9.62M	1.35
2	49.04M	1.58M	1.09	3	15.58M	1.15
1	63.79M	1.89M	1.00	4	23.49M	1.00

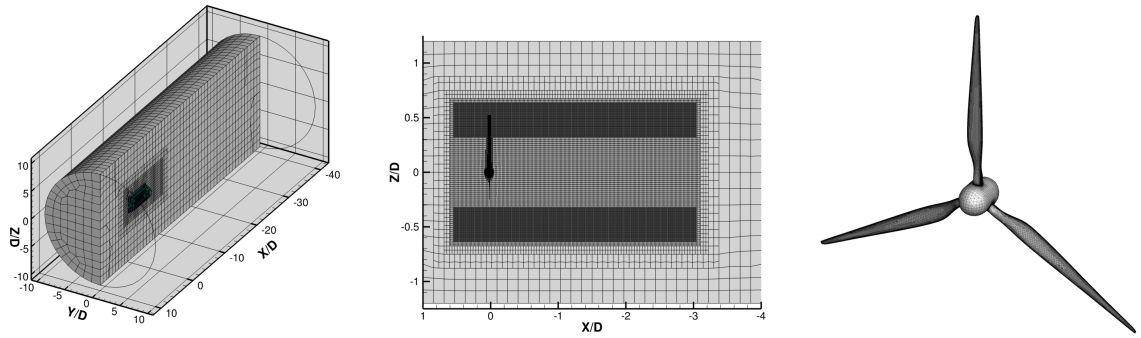

(a) Mesh overview (b) Inner Domain (c) Turbine Surface

Fig. 3: Mesh for the MRF and SI approaches: overview (left figure), inner domain mesh (middle figure) and surface mesh of the wind turbine (rigth figure).

6 Results

In the present paper, the result section focuses on the analysis of the wake for the different approaches, analysing the wake qualitatively, using illustrations of the velocity field, and quantitatively, using velocity distributions along the wake (AW) and across the wake (CW). All numerical uncertainties will be calculated using the procedure presented by Eça and Hoekstra (2014), and unless otherwise stated the shown quantities are averaged using the tool made available by Lemaire and Klapwijk (2021).

Before analysing the wake, the grid convergence studies of the torque and thrust produced by the turbine are shown in Fig. 4. Although there are significant differences between the numerical and experimental set-ups, the differences between the experimental and numerical values of thrust and torque are inferior to 6% and 13%. The purple line represents results obtained using the lower fidelity code QBlade, which are in agreement with the results obtained using the RANS models.

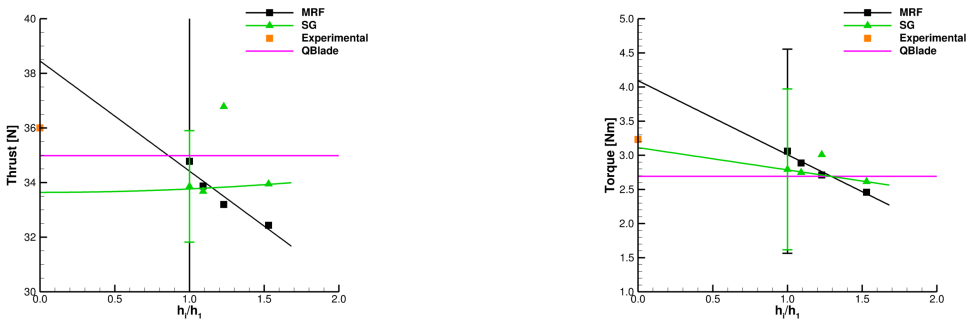

(a) Thrust (b) Torque

Fig. 4: Grid convergence of the thrust (left plot) and torque (right plot) for the MRF and SI approaches.

Figs. 5 and 6 allow a qualitative comparison between the three models by presenting the normalized velocity component along the x-axis field at the x/D=-2.36 and the z/D=0 planes. Two aspects are important to take notice of. The first is that the AD approach underpredicts the velocity magnitude, and the second is that the SG approach presents a low-velocity region downstream of the turbine. This low-velocity region is believed to be due to the initial condition of the simulation as this region is convected with the flow. Figs. 5(d) and 6(d) also show the results obtained using QBlade, which agree well with the higher fidelity models in the outer domain regions.

Fig. 7 presents a more quantitative analysis of the flow field in the wake by plotting the velocity distributions along (AW) and across (CW) the wake at specific measurement locations, x/D=-2.30 for the across wake and y/D=0.38 for the along wake distance. It is again clear that the AD approach under-

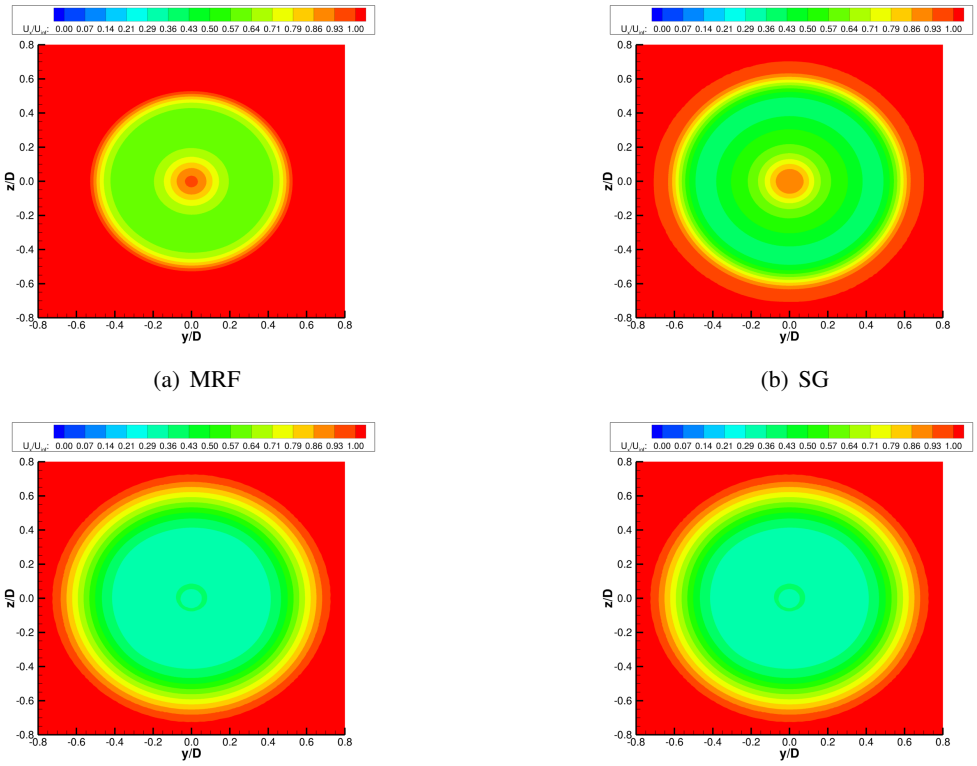

(a) MRF (b) SG

(c) AD (d) QBlade

Fig. 5: Normalized velocity field at the downstream plane x/D=-2.30 for the difference tested approaches.

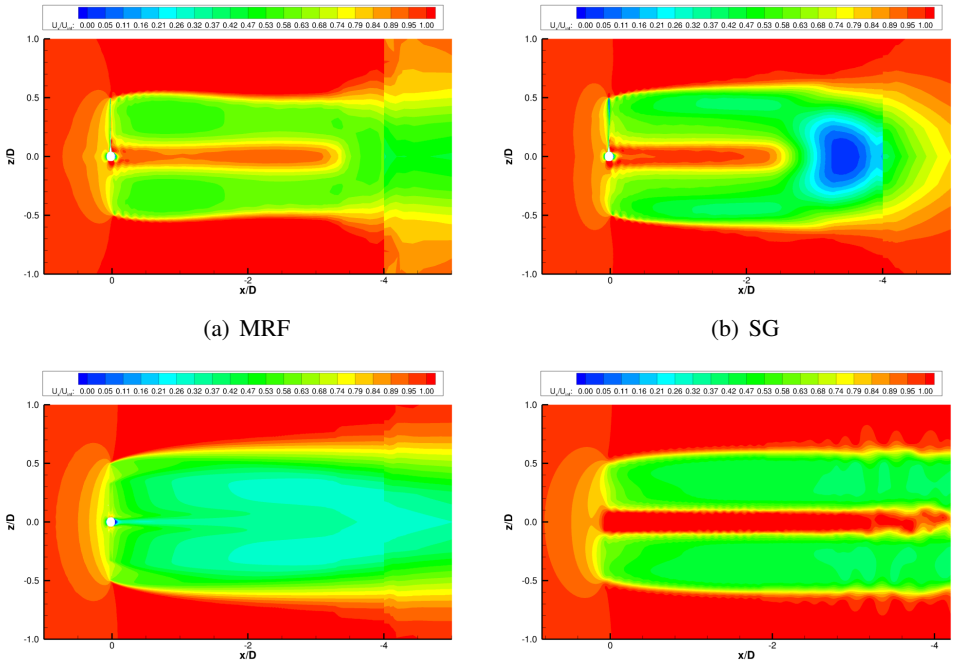

(a) MRF (b) SG

(c) AD (d) QBlade

Fig. 6: Normalized velocity field at the middle plane y/D=0 for the difference tested approaches.

predicts the wake recovering. The results obtained with the MRF and SI approaches are similar, with the main differences appearing across the wake near the hub location. These differences can be explained

by the inability of the MRF to capture the flow field's unsteady behaviour. Again, it is possible to see that QBlade's LLFVW model is capable of predicting the wake velocity field, with the exception of the locations near the hub, as in the present work, the hub was not modelled. Compared to the experimental measurements, the same conclusions as in previous studies, mainly the work of Sileo et al. (2023), can be observed: The numerical models fail to capture the wake behaviour near the centre location and overpredict the axial velocity level. Regarding the numerical uncertainties presented in the bottom row of Fig. 7, it can be seen that the AD model presents, in general, higher uncertainty estimations and the SI approach the lowest values. The estimated numerical uncertainties for the MRF and SI approaches have similar behaviour for the CW measurements. They present maximum values near the centre and the blade tip locations. Along the wake, the opposite happens, the numerical uncertainty of the the MRF tends to increase with the distance to the turbine.

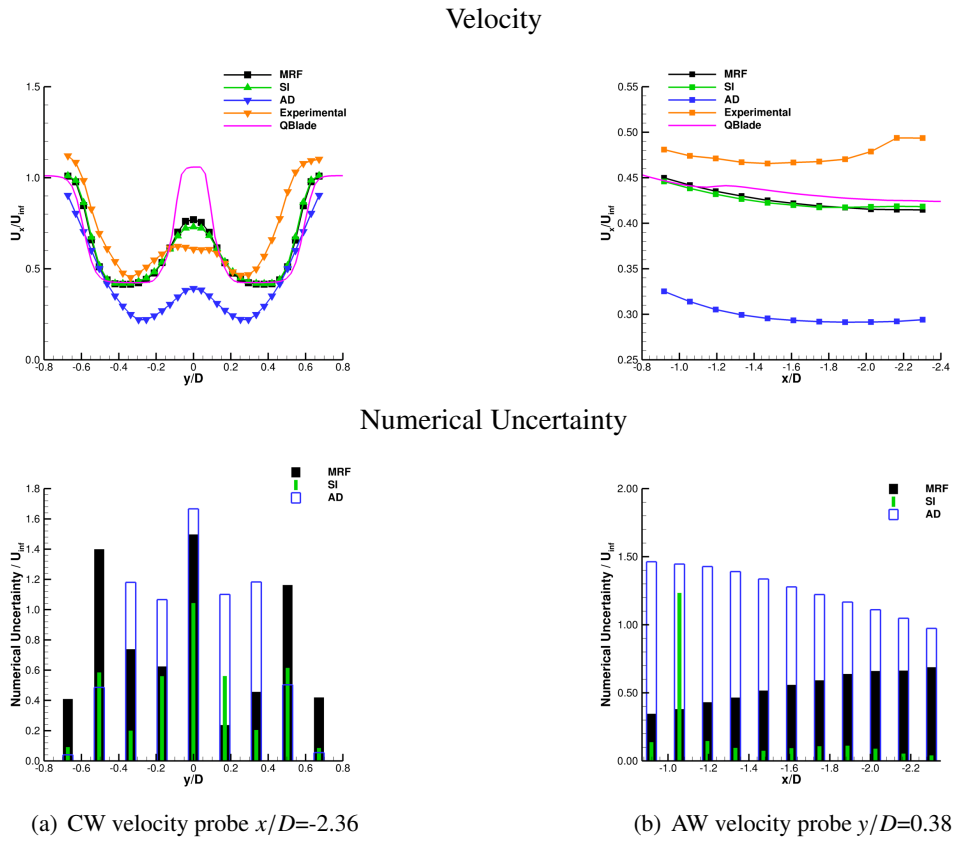

(a) CW velocity probe x/D=-2.36 (b) AW velocity probe y/D=0.38

Fig. 7: Velocity measurements (top row) and estimated numerical uncertainty (bottom row).

7 Conclusion

In the present paper, three approaches to model turbine-turbine interactions were studied. Based on the presented results, it can be concluded that using an actuator disk approach results in an underprediction of the velocity in the wake region. This simplified approach can possibly be improved by using more complex axial and tangential force distributions than the simple volumetric distribution of the thrust and torque used in this study. In future work, it would be interesting to compare these results with the empirical approaches used in software to optimize wind farm layouts. Lastly, it is important to mention the excellent agreement between QBlade's results and the MRF and SI approaches, at a fraction of the computational cost.

Acknowledgements

The authors would like to acknowledge the computational resources made available by FCT through the grant number 2022.15647.CPCA.A2.

References

Eça, L. and Hoekstra, M. (2014). A procedure for the estimation of the numerical uncertainty of cfd calculations based on grid refinement studies. *Journal of Computational Physics*, 262:104–130.

Fontanella, A., Bayati, I., Mikkelsen, R., Belloli, M., and Zasso, A. (2021). Unaflow: a holistic wind tunnel experiment about the aerodynamic response of floating wind turbines under imposed surge motion. *Wind Energy Science*, 6(5):1169–1190.

Koop, A., Cozijn, H., Schrijvers, P., and Vaz, G. (2017). Determining thruster-hull interaction for a drill-ship using CFD. In *Volume 2: Prof. Carl Martin Larsen and Dr. Owen Oakley Honoring Symposia on CFD and VIV*, page V002T08A022. American Society of Mechanical Engineers.

Lemaire, S. and Klapwijk, M. (2021). pytst.

Maciel, P., Koop, A., and Vaz, G. (2013). Modelling thruster-hull interaction with CFD. In *Volume 7: CFD and VIV*, page V007T08A024. American Society of Mechanical Engineers.

Make, M. and Vaz, G. (2015). Analyzing scaling effects on offshore wind turbines using CFD. 83:1326–1340.

Sileo, L., Gomes, T., Krasilnikov, V., and Maximiano, A. (2023). Towards the CFD validation and analysis of aerodynamic loads acting on the rotor of a floating wind turbine subject to forced motions. In *Numerical Towing Tank Symposium (NuTTS2023)*.

Ye, M., Chen, H.-C., and Koop, A. (2022). Comparison of different wind turbine modeling strategies in CFD simulations.

Hydroelasticity Effects During Helicopter Ditching

Eduardo T. Katsuno, Simon Tödter, Jörn Linde, Andreas Peters, and Bettar el Moctar
University of Duisburg-Essen, Duisburg/Germany, eduardo.katsuno@uni-due.de

1 Introduction

Ditching is the process of a planned and controlled emergency landing of an aircraft in the water. National Transportation Safety Board (1998) classifies this as "a planned event in which a flight crew knowingly makes a controlled emergency landing in water. (Excludes floatplane landings in normal water landing areas.)". In other words, aircrafts designed to land on the water, such as floatplanes and flying boats, are not defined as ditching accidents. As ditching is in an emergency situation, it is not unusual to encounter injuries and fatalities.

Generally, all helicopters must be designed to be compliant with the Certification Specification (CS) of different authorities (e.g. European Union Aviation Safety Agency (EASA), Federal Aviation Administration (FAA), Civil Aviation Authority(CAA)). As a guide for a showing of compliance, the authorities have published the Means of Compliance (AMC) for Small Rotorcraft (European Union Aviation Safety Agency, 2023) as a recommendation for helicopters in offshore operations. These rules define requirements for helicopters to withstand impact loads during ditching and to remain dynamically stable (floating stability) in irregular sea states.

As far as it is observed, there are limited studies on ditching considering fluid-structure interaction (FSI). The published studies on ditching deal almost exclusively with airplanes or simple geometries. Climent et al. (2017) and Viana et al. (2017) experimentally investigated the hydrodynamic loads during ditching on flexible structures of an airplane. The authors proposed a simple approach to correct the loads when simulating using the Finite Element Method (FEM) by using synthetic pressure-time curves to generate the loads. Iafrati et al. (2019) discussed the importance of FSI, as well as the difficulty of reproducibility of measured loads in ditching tests.

Previous numerical investigations on helicopter ditching have been carried out in earlier studies, focusing on ditching dynamics (Katsuno et al., 2022, 2024) and flotation stability analysis (Katsuno et al., 2023, 2025). The objective of this paper is to study the hydroelasticity effects of slamming during helicopter ditching, with an emphasis on the physics of both the fluid and structural components of the system, as well as their coupling. Observations are made regarding the maximum displacements that occur during the slamming process.

2 Description of the condition

The studied geometry is based on a realistic representation of a helicopter, with realistic dimensions and mass distribution. This geometry is composed of the helicopter fuselage, skid, and emergency flotation system (EFS), composed of four floaters already activated and the gas cylinder. The mass configuration of $m = 3175$ kg is such that it represents one of the heaviest conditions on the envelope of flight.

Figure 1 shows the main dimensions of the helicopter. Note that the center of gravity (CG) is not aligned with the symmetry plane of the fuselage, being slightly to the right, because of the weight of the cylinder used to fill the floaters.

3 Numerical Methods

3.1 CFD: Computational Fluid Mechanics

To simulate the helicopter ditching into the water using CFD, the overset mesh technique was used to account for the helicopter's motions. The associated numerical domain consisted of two regions: one region represented the ocean and another region surrounded the helicopter's geometry. An essential advantage of this method was that the region surrounding the helicopter can be moved relative to the domain mesh with appropriate interpolations being carried out at each time step. This allowed simulating the six degrees-of-freedom motions of the helicopter without the need to remesh the numerical domain.

Figure 2 shows the domain mesh, represented by a cube of 100 m-side length. Also shown is a cross-section of the mesh with its refined region close to the water surface, where the helicopter impacts

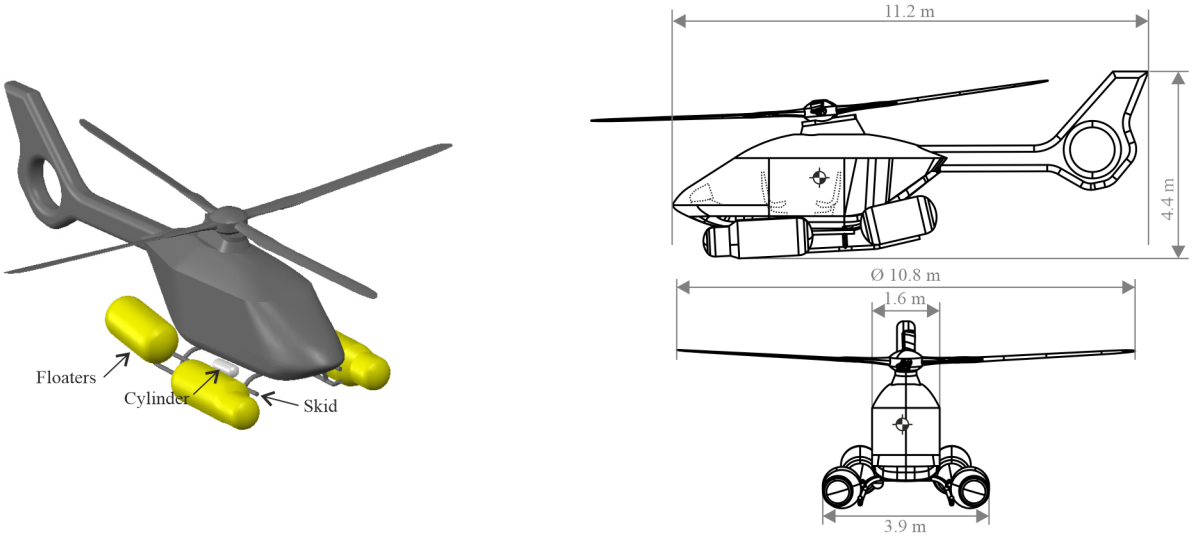

Fig. 1: Perspective view of the test-case helicopter, indicating the floaters, cylinder, and skid (left); and main dimensions of the studied helicopter

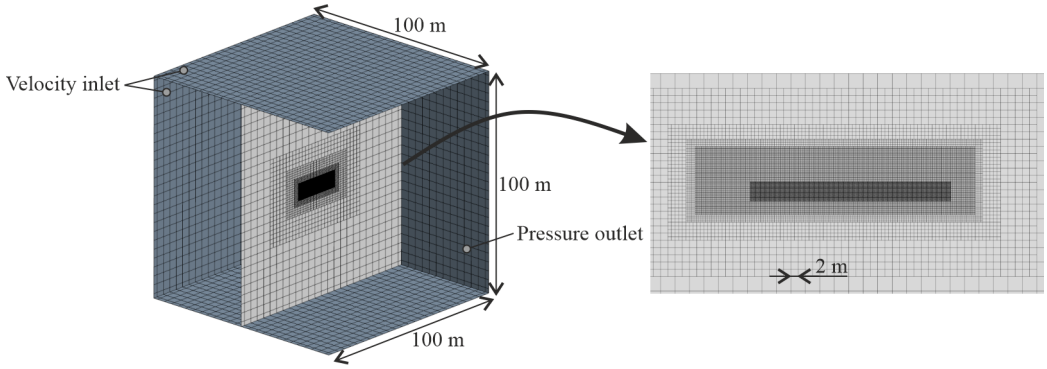

Fig. 2: CFD mesh overview of the domain region (left) and a cross-sectional view of the mesh (right)

occur.

Figure 3 shows the helicopter mesh region and, on the right-hand side, both the domain and the helicopter mesh after the interpolation. Hexahedral mesh topology was employed in both regions. Also, the elements were refined in the waterline region to more accurately represent the water-air interface; and to cover the possible trajectories of the helicopter trajectory. As recommended by Siemens (2018), the same element size was maintained to perform the overset interpolation. Numerical regions beyond the helicopter's motion accounted for overlaps of the helicopter's mesh. Beyond the edge of the helicopter's mesh, its motions were interpolated between these two meshes.

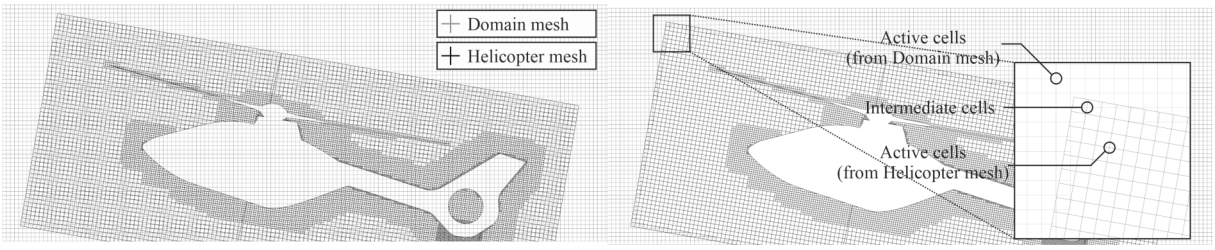

Fig. 3: CFD mesh overview of the helicopter region and an example of the overset mesh after the interpolation process

Air and water are modeled as inviscid. As exemplified by several researchers, an inviscid fluid model is suitable to estimate maximum impact pressures. For example, to reduce computational costs, Almallah et al. (2021) relied on an inviscid approach to simulate the slamming of a full-scale high-speed catama-

ran in irregular head seas. They demonstrated that it is reasonable to approximate the CFD results by verifying and validating them against model experiments. An implicit unsteady model was adopted, and each equation was solved in a segregated manner. The Volume of Fluid (VOF) model represented the phase mixture.

The simulated case employed a calm water model. The numerical treatment for velocity inlet boundary conditions is that velocity is specified, while the pressure gradient is zero. This boundary condition is applied to the top, bottom, left, right, and front surfaces of the domain region. For pressure outlet boundary conditions, velocity gradients are zero, while the pressure is defined. This boundary condition is applied in the back surface of the domain region. The wave model defines the volume of fractions on the boundary conditions, as well as velocities and pressures. Numerical wave damping was at the inlet and outlet boundary conditions to minimize the effect of wave reflection and to improve numerical convergence. Wave damping was accounted for by adding a source term to the momentum equation, which influenced the calm water surface based on the method of Choi and Yoon (2009). A two-way coupled interaction between the body and the fluid flow was simulated. The body motions were numerically computed by considering hydrodynamic, inertial, and gravitational effects.

3.2 CSM: Computational Structural Mechanics

The Computational Structural Mechanics (CSM) part of this study focuses on the deformation of the skid and the floaters (which are attached to the skid). The elements used in the mesh are tetrahedral, forming a volumetric mesh. The fuselage is assumed to be rigid for this study, therefore not being meshed.

A top and frontal view of the mesh used for Finite Element Method (FEM) calculations is provided in Fig. 4. Volumetric elements are also employed to represent the hollow of the tube on the skid part. The skid is a tubular structure with a thickness of 3 mm and a radius of 45 mm. The aim is to have at least two elements in the thickness direction. The elements on the skid and the junction with the floater part are illustrated in Fig. 5.

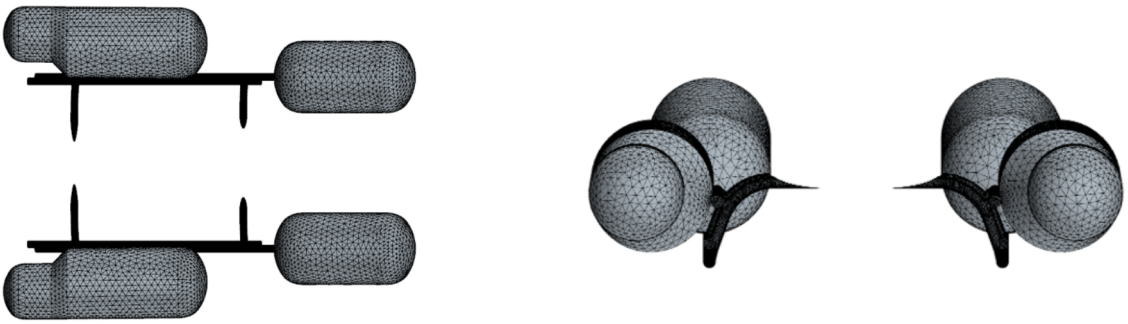

Fig. 4: CSM mesh overview of the skid and the floaters: top view (left); and front view (right)

Different material properties are assigned to the floater and skid. However, the accuracy of the properties is primarily given to the skid, which is the main focus of this study: it is assumed to be made of aeronautical aluminum 7075.

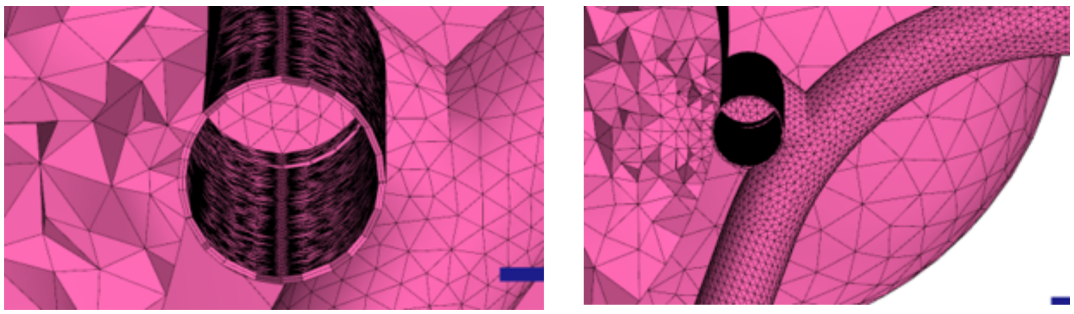

Fig. 5: Cross-section view of the CSM mesh details on the skid tube

3.3 FSI: Fluid-Structure Interaction

The simulations are coupled using a two-way implicit coupling algorithm. The loads generated by the pressure distribution in the fluid flow are applied as input forces for the structural analysis. The resulting deformation of the solid, in turn, iteratively modifies the geometry of the fluid flow.

Three main physical phenomena are considered: fluid flow, structural mechanics, and body motion. At each time step, the solution to the body motion equation determines the movement of the helicopter, displacing the domain region surrounding it. The new mesh position is interpolated using the overset mesh approach. The pressure field from the fluid flow solver is then mapped to compute the forces acting on each node in the solid stress solver. Based on the deformation results from the solid stress solver, the helicopter mesh is morphed, altering the geometry of the fluid flow. Through the two-way coupling approach, this process runs iteratively until the convergence criteria are met.

The coupling is performed using the STAR-CCM+ software. In this software, fluid flow is solved using the cell-centered finite volume method, while structural mechanics are handled using the finite element method.

4 Results

According to the CS AMC 27.563: structural ditching provisions (European Union Aviation Safety Agency, 2023), the specified vertical velocity is 1.5 m/s and a horizontal velocity of 30 kt. These are also the velocities adopted by the simulation of the helicopter before touching the water.

As a proof of concept, this initial study focuses on fictional materials, which are considerably softer than aeronautical aluminum 7075: the Young's modulus is set to 1.2×10^8 Pa. This approach is taken to induce and observe significant deformation, check the morphing of the CFD mesh, and test the limits of the model.

Figure 6 allows for the observation of the interpolation between meshes using the overset approach on the first time frame, $t = 0.01$ s. At this time, on the extreme left, it shows the domain mesh in light gray, and an intermediate zone. Figure 7 presents the front view of the helicopter. Notable is the deformation of the skid, opening and spreading to the outside. As a consequence, the back floaters are displaced to a position below.

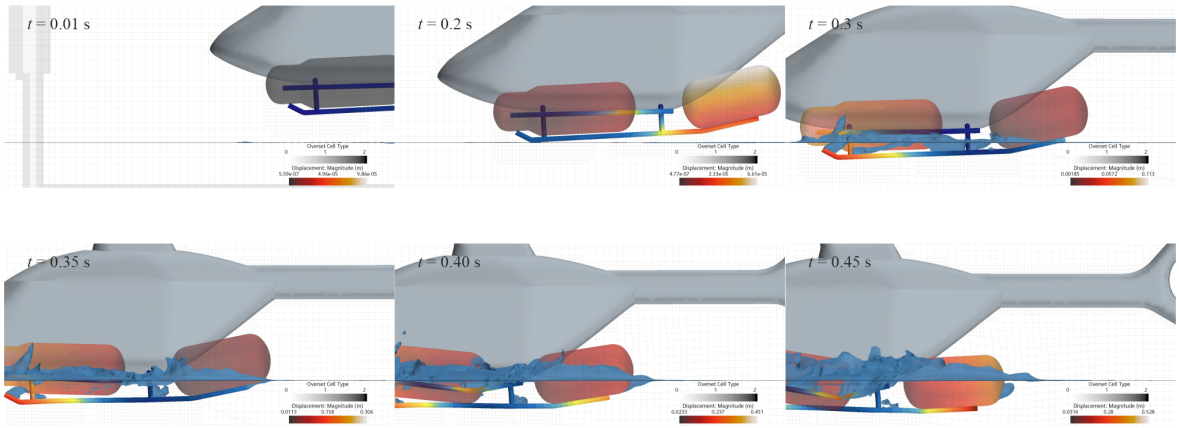

Fig. 6: Lateral view of helicopter ditching, considering the hydroelasticity of the skid and floaters

On the lateral view, it is noticeable that the stepping part of the skid (the top horizontal tube) suffers severe deformation. To further observe the deformation, Fig. 8 displays the CFD mesh being deformed, as a coupled result of the output from the CSM part. The original skid is also shown in black for reference. It is observable that the elements between the two horizontal bars mesh are squeezed due to the morphing process. Some empty zones appear in the middle of each frame because of the translation of the frontal floater. This figure shows a slicing on the CFD mesh. As the mesh gets morphed, the frontal floater enters inside the slicing plane, resulting in this empty zone (it is important to note that there are only elements inside the floaters for the CSM mesh, not the CFD).

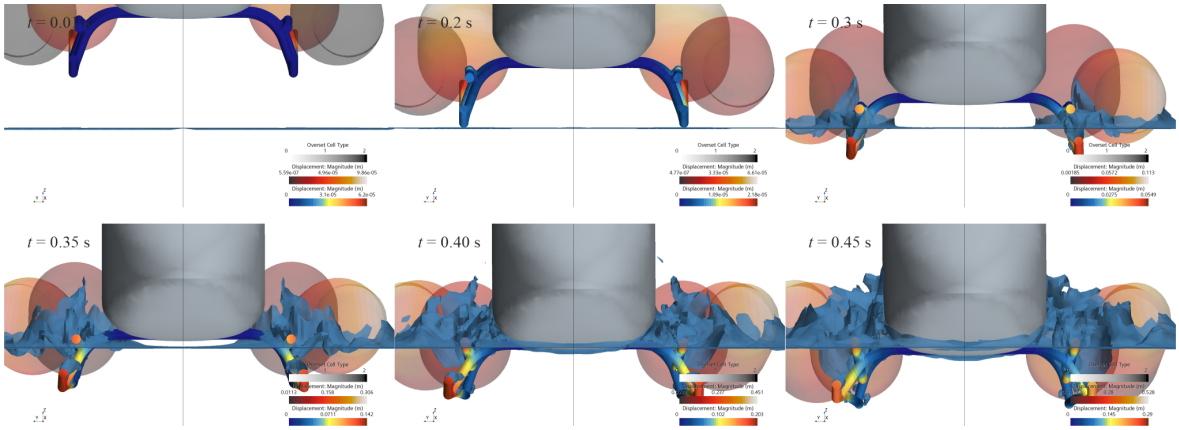

Fig. 7: Frontal view of helicopter ditching, considering the hydroelasticity of the skid and floaters

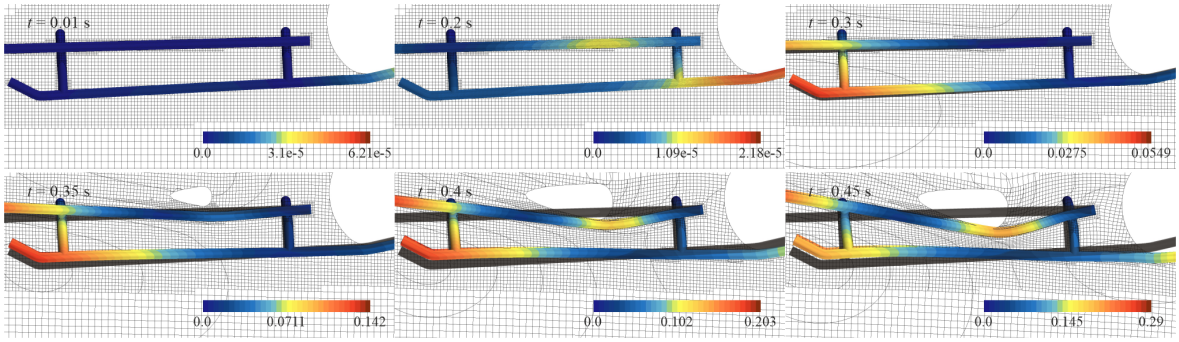

Fig. 8: View of the skid during the helicopter ditching, colorized based on the displacement (units in meters) and the undeformed skid (in black) as reference

5 Conclusions

This study examines the hydroelasticity effects of helicopter ditching, with a focus on fluid-structure interaction (FSI) during the slamming process. A realistic representation of the helicopter's dimensions and shape, along with an emergency flotation system, is employed. A two-way implicit coupling algorithm is used to simulate the interaction between computational fluid dynamics (CFD) and computational structural mechanics (CSM), with particular emphasis on FSI. The results demonstrate that the proposed methodology effectively simulates the hydroelasticity effects during helicopter ditching, providing insights into maximum displacements and pressure distribution during slamming. Although the study uses fictional material properties, the current findings serve as a proof-of-concept to test the limits of the proposed numerical method. Future work will incorporate the actual properties of Aluminum 7075 and include a comparison of slamming behavior in a rigid body, as well as validation of the numerical model with experimental results. Additionally, future work will investigate the effects of plastic deformation.

Acknowledgments

The authors thank Airbus Helicopters for providing the initial geometry and some characteristics of the helicopter used in this work.

This project is supported by the Bavarian Aviation Research Programme (BayLu25) and the Bavarian Ministry of Economic Affairs, Regional Development and Energy (StMWi), under grant ROB-2-3410.20-04-10-36 / BLU-2109-0036.

The authors gratefully acknowledge the computing time granted by the Center for Computational Sciences and Simulation (CCSS) of the Univeristy of Duisburg-Essen and provided on the supercomputer magnitUDE (DFG grants INST 20876/209-1 FUGG, INST 20876/243-1 FUGG) at the Zentrum für Informations- und Mediendienste (ZIM).

References

Almallah, I., Ali-Lavroff, J., Holloway, D. S., and Davis, M. R. (2021). Slam load estimation for high-speed catamarans in irregular head seas by full-scale computational fluid dynamics. *Ocean Engineering*, 234:109160.

Choi, J. and Yoon, S. B. (2009). Numerical simulations using momentum source wave-maker applied to RANS equation model. *Coastal Engineering*, 56(10):1043–1060.

Climent, H., Pastor, G., and Viana, J. T. (2017). Experimental Ditching Loads on Aeronautical Flexible Structures. In *International Forum on Aeroelasticity and Structural Dynamics - IFASD*, Como, Italy.

European Union Aviation Safety Agency (2023). Certification Specifications and Acceptable Means of Compliance for Small Rotorcraft, CS-27, Amendment 10. Technical report, European Union Aviation Safety Agency.

Iafrati, A., Grizzi, S., and Olivieri, F. (2019). Experimental investigation of fluid-structure interaction phenomena during aircraft ditching. In *AIAA Scitech 2019 Forum*, Reston, Virginia. American Institute of Aeronautics and Astronautics.

Katsuno, E. T., Peters, A., and El Moctar, O. (2023). Seakeeping Behavior of a Helicopter Landing in Waves. In *Volume 7: CFD & FSI*. American Society of Mechanical Engineers.

Katsuno, E. T., Peters, A., and el Moctar, O. (2025). Numerical Seakeeping Analysis for a Floating Helicopter After Ditching in Water. *Journal of Offshore Mechanics and Arctic Engineering*, 147(1):1–45.

Katsuno, E. T., Peters, A., Lantermann, U., Beham, A., Harms, S., and Ould El Moctar, B. (2022). Numerical simulations of helicopter ditching. In *24th Numerical Towing Tank Symposium*.

Katsuno, E. T., Tödter, S., Neugebauer, J., Peters, A., and El Moctar, O. (2024). Investigating Helicopter Ditching and Flotation Stability using CFD: Analysis of Mass Configurations, Door Openings, and Floater Conditions. In *50th European Rotorcraft Forum 2024*, Marseille.

National Transportation Safety Board (1998). Aviation Coding Manual. Technical report, National Transportation Safety Board.

Siemens (2018). STAR-CCM+ Documentation - version 13.06.

Viana, J. T., Pastor, G., and Climent, H. (2017). Flexible Structures Response to Ditching Loads. In *Aerospace Structural Impact Dynamics International Conference*.